Diols under Investigation: Benchmarking their Monomers, Dimers and Chirality Recognition

Dissertation

for the award of the degree
"Doctor rerum naturalium"
of the Georg-August-Universität Göttingen

within the doctoral program chemistry
of the Georg-August University School of Science (GAUSS)
as part of the BENCh Research Training Group (RTG 2455)

submitted by
Beppo Hartwig
from Bamberg

Göttingen, 2022

Thesis Advisory Committee:

Prof. Dr. Martin A. Suhm, Institut für Physikalische Chemie

Prof. Dr. Ricardo A. Mata, Institut für Physikalische Chemie

Prof. Dr. Melanie Schnell, Deutsches Elektronen Synchrotron Hamburg

Members of the Examination Board

Reviewer:

Prof. Dr. Martin A. Suhm, Institut für Physikalische Chemie

Second Reviewer:

Prof. Dr. Ricardo A. Mata, Institut für Physikalische Chemie

Further Members of the Examination Board:

Jun.-Prof. Dr. Daniel Obenchain, Institut für Physikalische Chemie

PD Dr. Oliver Bünermann, Institut für Physikalische Chemie

Jun.-Prof. Dr. Anna Krawczuk, Institut für Anorganische Chemie

Dr. Tim Schäfer, Institut für Physikalische Chemie

Date of the Oral Examination: 17.11.2022

Acknowledgements

First of all, I would like to thank my supervisor Martin A. Suhm who has been a continuos source of inspiration, encouragement and guidance ever since I first joined his group for my bachelor thesis in 2016. Secondly, I would like to thank my co-supervisor Ricardo A. Mata who helped to spark my interest in computational chemistry. Special thanks also goes to Melanie Schnell in whose group I spend a great month learning a lot about microwave spectroscopy. The supervision of Daniel Obenchain made my research stay even more enjoyable. Furthermore, I would like to thank the other members of the examination board Oliver Bünermann, Anna Krawczuk, Daniel Obenchain and Tim Schäfer.

For making my research possible, I would like to thank the German Research Foundation (Deutsche Forschungsgemeinschaft, DFG; projects 389479699/GRK2455 and 405832858 for computational resources) for its financial support. Furthermore, I would like to thank all members of the Research Training Group (RTG) "2455 Benchmark Experiments for Numerical Quantum Chemistry" (BENCh) for the nice atmosphere and group events. Here, special thanks goes to my fellow RTG member Xaiza Aniban (Mata group) with whom it was a pleasure to work on a joint publication.

Additionally, I would like to thank the institutes workshops for always helping out with any issues that came up. Here, I would like to especially thank Reinhard Hildebrandt and Mike Zippert of the mechanical workshop. The former helped to design a custom heat-exchanger and the latter helped with the acquisition of new pressure regulators. Furthermore, I would also like to thank Rainer Oswald for helping out when problems arose with the Chemie-Cluster and making quantum-chemistry programs available as modules. Thanks also go to Stefan Grimme who allowed for the use of the xTB and CREST programs on the Chemie-Cluster which have been developed by his group.

Special thanks also goes to Laura N. Schiebel, for whom I had the pleasure to supervise her bachelor thesis. She also continued researching open questions of her bachelor project as a research assistant (Junior Bencher), funded by the DFG as part of the RTG. I would also like to thank her for proof-reading large parts of this work.

Furthermore, I would like to thank the entire Suhm group for the great atmosphere, be it during conferences, table football games, group trips or game nights. I am also grateful

to Robert Medel for proof-reading the monomer chapter and providing computational data for tri-*tert*-butyl-methanol. Further thanks go to Maxim Gawrilow, Arman Nejad, Sophie Schweer and Taija Fischer for help and advise regarding experimental and non-experimental work. Additionally, I would like to thank the entire Schnell Group for the warm welcome during my research stay in Hamburg.

Last but not least, I would like to thank my family and friends for their support.

Contents

1 Introduction

Chirality, the property of molecules behaving like mirror images, has been an active research topic since the 19th century for chemists and physicists alike[1]. Despite this long history of research, chirality and its function in nature are still puzzling in many aspects. For instance, the so called parity violation, a predicted small energy difference between enantiomers, could not yet be experimentally confirmed[2–8]. If this phenomenon were to be proved, it could explain life's strong preference for homo-chirality. This preference can be seen by, for example, the almost exclusive presence of (S) amino acids in naturally occurring proteins. Moreover, the human nose can distinguish between different enantiomers of some molecules, such as limonene. Here, the (R) enantiomer smells like oranges, while its mirror image smells like lemons[9]. The different olfactory response must be linked to distinct molecular interactions with the receptors. This phenomenon is referred to as chirality recognition and is ubiquitous in modern synthesis, chromatography, biochemistry, pharmacology and toxicology[10–14]. A grim example of the sometimes vastly different effects that enantiomers can have on the human body is provided by thalidomide. (R)-thalidomide acts as a sedative, while the (S) enantiomer has teratogenic effects[15,16]. In the 1950s, racemic thalidomide was sold as *Contergan* and was explicitly marketed to be effective against morning sickness and safe to use during pregnancy. The (S) enantiomer, contained in the racemic mixture caused (also produced in the body from the R form[17]), subsequently caused a massive spike in malformations in children. This goes to show that, it is crucial to understand the interactions of chiral molecules. The enantiomers of limonene and thalidomide are shown in Fig. 1.1.

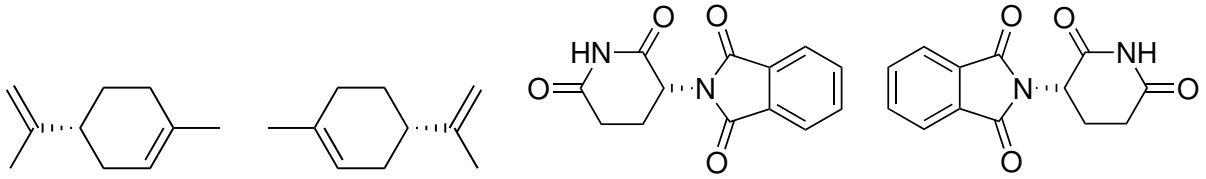

(a) (R)-limonene **(b)** (S)-limonene **(c)** (R)-thalidomide **(d)** (S)-thalidomide

Fig. 1.1: Enantiomers of limonene and thalidomide.

To investigate chirality recognition, this work examines the self-aggregation of vicinal diols. Diols or vicinal diol subunits play an important role in nature. For instance, they are present in many hormones, such as estradiol, estriol, dopamine and adrenalin. Strictly speaking, none of these examples is a pure vicinal diol, whereas almost any sugar has a vicinal diol subunit. Therefore, vicinal diols can be used as test systems for sugars, with ethane-1,2-diol (ethylene glycol) being an important fragment of most sugars. The simple ethane-1,2-diol (0-0) system is of particularly prototypical nature because its dimers have been found to display energetic chirality recognition[18]. 0-0 constitutes a transiently chiral system, where the *gauche* + and − O-CC-O angles correspond to mirror images. This is illustrated in Fig. 1.2a. Hetero-chiral refers to dimers of molecules with opposite signs of the dihedral angles and homo-chiral refers to ones with the same sign. The experimental spectra recorded in Ref. [18] showed limited evidence of homo-chiral dimers. However, since a supersonic expansion was used, it would be expected that conformers with the same and opposite sign collide at an equal rate. Hence, homo- and hetero-dimers should form in equal proportions. To investigate the apparent lack of homo-chiral dimers, the permanently chiral *trans*-cyclohexane-1,2-diol (t6-6, see Fig. 1.2b) will be used for this work. By measuring the enantiopure compound, the formation of homo-dimers can be enforced. This spectral analogy may allow to solve the homo-dimer mystery. If homo-dimers are formed at an equal rate, it can be concluded that 0-0 behaves like a permanently chiral system under supersonic jet-conditions, due to the low temperatures that can be reached.

Moreover, chemical substitution will be used to understand the occurrence of energetic chirality recognition. The effect of different methyl substitutions (2,3-dimethyl-butane-2,3-diol (pinacol), butane-2,3-diol, propane-1,2-diol and 2-methyl-propane-1,2-diol) and ring size (*trans*-cyclopentane-1,2-diol, *trans*-cyclohexane-1,2-diol and *trans*-cycloheptane-

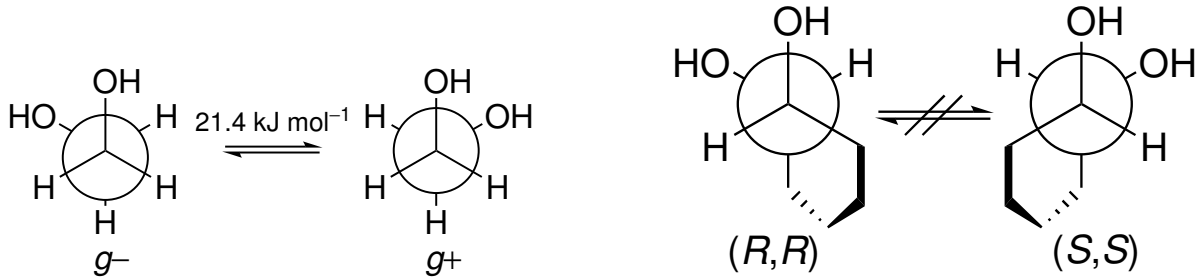

(a) ethane-1,2-diol **(b)** *trans*-cyclohexane-1,2-diol

Fig. 1.2: Newman projections to illustrate the transient and permanent chirality of ethane-1,2-diol (0-0) and *trans*-cyclohexane-1,2-diol (t6-6), respectively. The barrier was calculated at the B3LYP-D3(BJ,abc)/ma-def2-TZVP level of theory.

1,2-diol) is investigated. Additionally, the influence of a π-system is studied *via* 3-butene-1,2-diol. All these systems are benchmarked using density functional theory and Raman spectroscopy in the OH-stretching region.

Furthermore, the influence of dispersion on chirality recognition is investigated in cooperation with the group of R. Mata. Dispersion has been found to be crucial in many enantioselective reactions[19–25] as well as in host-guest interactions in chiral chromatography[26–29]. Therefore, dispersion may also be crucial for the energetic chirality recognition, as it was found for ethane-1,2-diol. Additionally, *trans*-cyclohexane-1,2-diol and pinacol are investigated in the same way. By employing a local orbital framework to Møller-Plesset perturbation theory of second order (MP2), one of several possible rigorous definition of dispersion is used and compared to Grimme's D3 dispersion correction of a few common density functionals. In this way, the suitability of the D3 term to gauge dispersion can be determined. The general importance of dispersion for chemistry is outlined in Ref. [30].

However, before dimers are investigated, different theoretical methods are first tested with regards to a large variety of monomeric systems characterised by Raman spectroscopy. Here, an empirical fitting strategy is used, that was previously applied to mono-ols in a recent study[31]. The commonly used BP86, PBE, PBE0 and B3LYP functionals (dispersion corrected) are used and their predictive capabilities for OH-stretching vibrations tested. The different systems include varying methylation patterns, cyclic arrangements and π as well as halogen (F, Cl and Br) contacts (see Fig. 2.5 (page 25)). Furthermore, Cl and Br containing systems are also investigated *via* microwave spectroscopy. A broader set of variables allows to judge the different methods more accurately, since coincidental agreements are less likely. For the quadrupolar nuclei Cl and Br, it is also attempted to link the asymmetry parameter of the nuclear quadrupole coupling constants (η) with the band position of the OH stretching mode that interacts with the halogen atom. In this way, the potential of η as a probe for the hydrogen bond strength is investigated.

Moreover, OH stretching frequencies and rotational constants are properties largely determined by the valence electrons. Nuclear quadrupole coupling constants, on the other hand, depend on the core electrons as well. Chemists often focus purely on valence electrons and little attention is paid to core properties[a]. However, a good method should describe both cases well. Hence, methods can be benchmarked with regards to a good description of valence and core electrons simultaneously with the process described above.

[a] A SciFinder search for "core electrons" and "valence electrons" in the top 15 chemistry journals (determined by SCImago Journal Rank 2021), yields 65 and 482 results, respectively. Since the concern with valence electrons is often not explicitly stated, these results are likely biased to favour "core electrons".

The experimental methods used in this work are especially suited for a comparison with theory. With supersonic expansions, conditions very close to the theoretical ideal can be reached, *i.e.* a temperature of 0 K and the isolated gas-phase. Hence, the complex simulation of solvation and thermal motion effects can be avoided. Such accurate reference data is needed to complement the trend towards benchmarking theory with theory[32] and is a fundamental part of the BENCh research training group agenda. Some of the experimental as well as theoretical data shown in this work have been made available in Ref. [33].

2 Experimental and theoretical techniques

2.1 Experimental techniques

2.1.1 Supersonic jet expansion

The description given here is largely based on Ref. [34]. The experimental techniques in this work revolve around so called supersonic jet expansions. The name stems from the fact that the expansion is cooled to such a degree that the speed of the molecular beam exceeds the local speed of sound. A simplified illustration of a jet expansion is shown in Fig. 2.1. Inside the reservoir (black box) the system is in thermal equilibrium, *i.e.* the translational (T_{Trans}), rotational (T_{Rot}), vibrational (T_{Vib}) and conformational

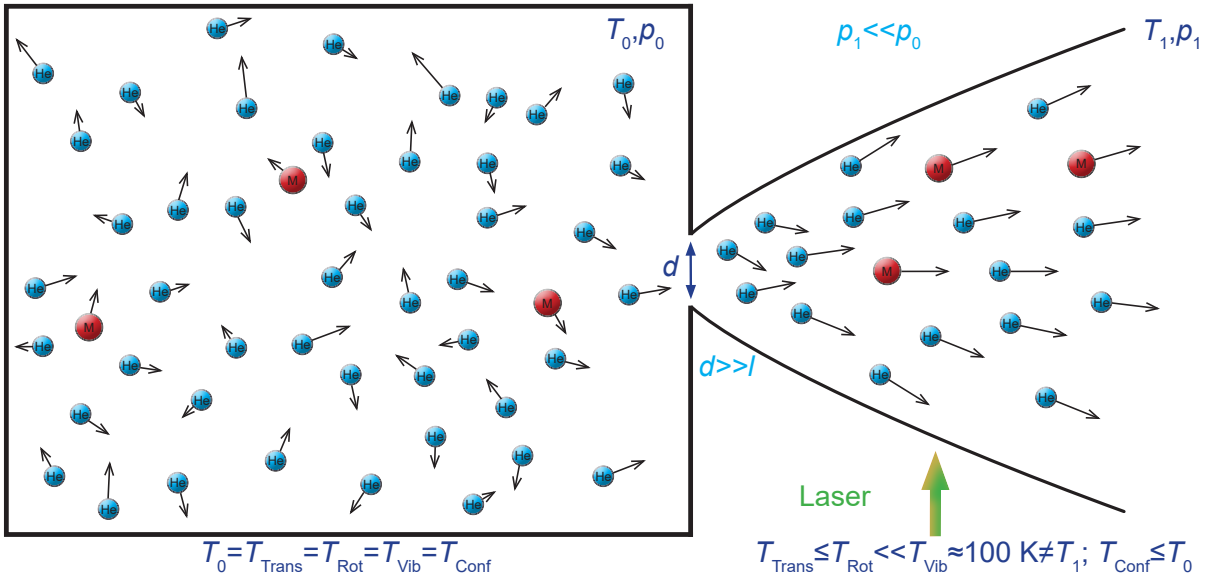

Fig. 2.1: Illustration of a supersonic jet expansion. The index 0 denotes conditions in the reservoir while 1 indicates the situation outside of the reservoir, but not within the expansion. The image is not to scale.

temperatures (T_{Conf}) are equal to the reservoir temperature (T_0). p_0 indicates the pressure within the reservoir, which is filled with an excess of a rare gas. In the example shown helium is used which acts as a carrier gas. The analyte to be studied is shown as M. The arrows indicate the random thermal motion and the Maxwell-Boltzmann distributed velocities within the reservoir. If the outside pressure p_1 is chosen to be much lower than p_0 ($p_1 \ll p_0$) and the diameter of the nozzle d (opening of the reservoir) exceeds the mean free path l ($d \gg l$) of the molecules, a supersonic expansion can form.

While transiting the nozzle, many collisions can take place and the random thermal motion is converted to a directed flow, as indicated by the arrows in Fig. 2.1. This conversion leads to a cooling of the expansion, while simultaneously the molecular beam is accelerated. The temperature dependent speed of sound will eventually decrease so much that the average flow velocity surpasses it and the expansion becomes supersonic and the velocity distribution narrows strongly. The cold molecular beam can then be probed by a laser (Raman spectroscopy), IR-beam, or microwave radiation. At some point, the molecular density will drop so much that collisions can no longer take place. This part of the expansion is referred to as the "zone of silence" where molecules are isolated and ultracold. Hence, supersonic expansions lend themselves to a comparison with theoretical methods, which usually assume the isolated gas phase and a temperature of 0 K. Colder conditions also lead to a narrowing of vibrational bands and rotational lines, making the interpretation of spectra easier. At some stage collisions with the background gas occur and the flow is recompressed in a so called shock-wave. The shock-wave is associated with a density and temperature increase and may expand again.

It is important to note, that a thermodynamic equilibrium can no longer be maintained in the jet. The vibrational degrees of freedom cannot be cooled as efficiently as the rotational and translational ones, so that T_{Vib} quickly starts diverging from the others. Rotation starts to diverge next from T_{Trans}, but can remain very close. This leads to the order shown in Fig. 2.1 of $T_{\mathrm{Trans}} \lesssim T_{\mathrm{Rot}} \ll T_{\mathrm{Vib}}$. Judging T_{Conf}, on the other hand, is more difficult. For monomers with high conversion barriers ($> 20\,\mathrm{kJ\,mol^{-1}}$) between conformers, T_{Conf} can equal T_0, but otherwise will be lower. From experience and the study of Ruoff *et al.*[35], barriers below $5\,\mathrm{kJ\,mol^{-1}}$ can easily be overcome under jet conditions, leading to smaller T_{Conf}. Surmountable barriers will be indicated by angled arrows in the energy-matrices (*e.g.* Fig. 3.6 (page 39)) of section 3.1 (page 29). Clusters, with a few exceptions (*e.g.* formic acid[36]), are formed during the expansion itself and therefore will generally have T_{Conf} below T_0 for their intermolecular degrees of freedom.

The collision rate and therefore the cooling can be increased by using a higher pressure in the reservoir. More generally, this quantity is called backing or stagnation pressure

(p_S) and a reservoir as such is not strictly necessary. Similarly, probing later stages of the expansion, *i.e.* increasing the distance from the nozzle (d_N), leads to a stronger cooling. However, once the "zone of silence" is reached, this effect subsides. Furthermore, going along the series He, Ne, Ar, Kr and Xe, the cooling effect increases[35,37]. This is generally attributed to the velocity slip effect, which is due to a mismatch of the velocities of light carrier gases and heavier analyte molecules[37]. Moreover, the propensity to cluster onto the analyte also increases.

2.1.2 *curry*-jet

The *curry*-jet (*C*lassical *U*n*r*estricted *R*aman Spectroscop*y* in a Jet) gets its name from the discoverer of the Raman effect Sir C. V. Raman, who was Indian and from the generated distribution of differently-sized particles in a carrier fluid. Five years prior to Raman's discovery the effect was hypothesised by the Austrian physicist A. Smekal in 1923[38]. The *curry*-jet employs linear Raman spectroscopy, *i.e.* the signal intensity depends linearly on the intensity of the laser and the concentration of scattering molecules, and in that sense is classical. It is unrestricted in the sense that no chromophores or permanent dipole moments are necessary, as would be the case for UV-IR techniques or microwave spectroscopy. If a sufficiently high vapour pressure can be reached, any molecular system can be measured and Raman active bands are always present. Ever since its inception in 2006[39], the *curry*-jet underwent many changes constantly improving the signal-to-noise ratio of the setup[40,41]. Further improvements were made to measure non-volatile substances by introducing a heatable saturator and improving the signal quality[42–46]. M. Gawrilow introduced mass flow controllers to the setup simplifying the creation of mixtures[46]. Additional information about the *curry*-jet can be found in the cited sources.

A schematic representation of the *curry*-jet is shown in Fig. 2.2. As the vapour pressure is the only limiting factor, two coolable saturators (S1, glass) for very volatile and a heatable saturator (S2, stainless steel) for non-volatile substances can be used. In this way temperatures (T_S) as low as 240 K and as high as 395 K can be reached. By adjusting the temperature, the concentration can be varied and therefore the clustering propensity. Using the corresponding bypass (BP) the flow can be directed towards both, a single one or none of the saturators. When the heatable saturator is used the tubing temperature (T_T) is kept 10 K – 20 K above the saturator to avoid condensation. Higher T_T can also be used to avoid larger clusters or to populate meta-stable conformers. Hence, a heating series can provide valuable information about different oligomers. The tubing can be

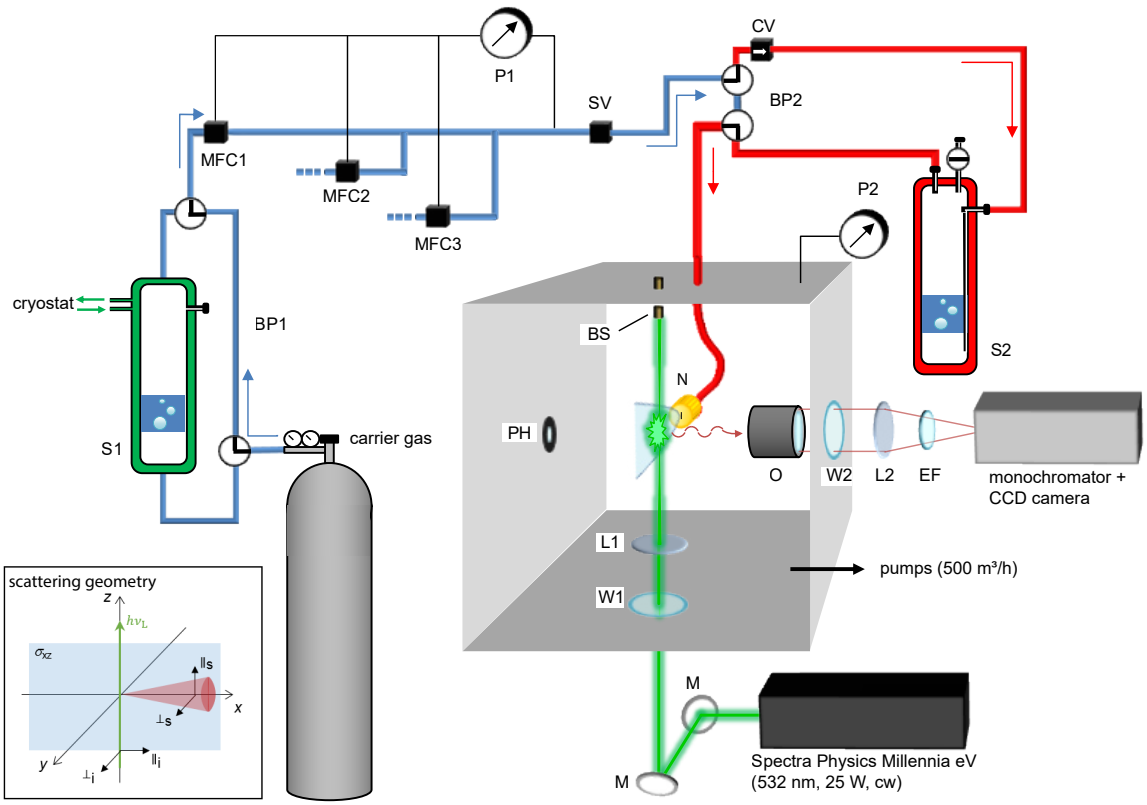

Fig. 2.2: Scheme of the *curry*-jet. Parts highlighted in red are heatable and the arrows indicate the flow direction. Abbreviations used are: S = saturator, BP = bypass, MFC = mass flow controller, SV = solenoid valve, CV = check valve, PH = pinhole, W = window, L = lens, N = nozzle, BS = beam stop, O = objective lens, EF = edge filter and P = pressure gauge. The scattering geometry is shown in the bottom left. The graphic was adapted to English and slightly modified from the versions of M. Gawrilow[47] and T. Forsting[45,48].

heated up to 465 K, although some parts are limited to 425 K. The nozzle body itself can even be heated up to 555 K. Furthermore, a check valve (CV) only allows gas flow in the indicated direction (see Fig. 2.2), to avoid possible condensation in the non-heated parts of the setup.

A pressure gauge (P1) coupled to mass flow controllers (MFC) allows for the control of the stagnation pressure (p_S), while under continuous operation. Multiple MFCs can be used to create gas mixtures. In this way He and Ar ad-mixtures can be created on the fly or the relative content of two substances can be changed. Due to the high gas throughput of the *curry*-jet, measurements with Ne are not conducted, given the high cost of Ne in comparison to He and Ar. Furthermore, the MFCs are limited to a maximum p_S of 1.4 bar. The expansion itself can be controlled *via* a solenoid valve (SV). Each MFC is controlled by an additional solenoid valve, which are not shown in Fig. 2.2. Pressure gauge P2 is used to monitor the background pressure (p_{BG}) in the vacuum chamber, with

p_{BG} ranging from 0.3 mbar to 2.2 mbar under normal operation.

Moreover, the distance of the slit nozzle (4.0×0.15 mm^2) to the laser (d_N) can be varied. Typically, nozzle distances range from 0.5 mm to 3 mm. At these distances the "zone of silence" is generally not reached. For $d_N = 1$ mm, T_{Rot} of 30 K – 60 K and T_{Vib} of ca. 100 K were achieved in a He expansion with water and 2,2,2-trifluoroethanol[43]. For N_2 (1%) in He, ca. 6 K and 20 K translational and rotational temperatures were achieved, respectively[40]. A frequency doubled Nd:YVO_4 laser (Spectra Physics Millennia eV), operating at 25 W and continuous wave mode, is used. However, during warm weather the operation had to be limited to 20 W, since the air-water chiller used could not provide sufficient cooling. In cooperation with R. Hildebrandt, of the mechanics workshop, a water-water chiller alternative was developed, in which the hot exhaust liquid was pre-cooled before entering the regular chiller. The developed chiller used the on-site cooling circuit. In this way the laser could be operated at full power and its temperature stabilised, even at high ambient temperatures. Later on a commercial water-water chiller was adopted.

The scattered photons are detected orthogonal to the nozzle, which is also indicated in the drawing of the scattering geometry (see Fig. 2.2 bottom left). Here i indicates the incident radiation and s the scattered case. $\perp$ shows an orthogonal and $\parallel$ a parallel polarisation relative to the scattering plane σ_{xz}. The photons are collected by an objective lens (O, Nikon Nikkor) and then focused on the entry slit of the monochromator (McPherson Inc. Model 2051, f/8.7, grating 1200 lines/mm). An edge filter (EF) in front of the slit removes the much more intense Rayleigh scattering. This leads to a distortion of the baseline and intensity at small wavenumbers (< 40 cm^{-1}). The monochromator itself has a spectral window of about ± 10 nm around the central wavelength (λ_{CWL}), which translates to about 450 cm^{-1} in the OH stretching region. The aperture of the monochromator (d_M) is set to 75 µm. Increasing d_M leads to a signal increase at the cost of resolution. The Raman scattering itself is then detected by a CCD (charged coupled device) camera (Princeton Instruments, PyLoN®:400, 1300 × 400 Pixels). To suppress electronic noise, the camera is cooled with liquid nitrogen and kept at a temperature of 153 K (-120 °C). The combination of these parameter results in a resolution of about 1 cm^{-1}. Furthermore, the exposure time (t_{exp}) can be increased, leading to an almost linear increase in intensity. However, due to the build up of spikes, very intense signals mostly due to cosmic rays, more exposures are necessary to reliably "despike" (remove cosmic rays) the spectra. Moreover, electronic noise increases with the exposure time leading to somewhat limited returns with regards to the signal-to-noise ratio. However, read-out noise can be reduced by using longer t_{exp}. Additionally, one may overexpose the CCD chip at long t_{exp}.

To obtain the spectral information, the pixel-dimension has to be converted into wavenumbers. The monochromator gives a rough estimate for the spectral range, but is not sufficiently accurate. To calibrate the spectra a Ne and/or Kr lamp is placed in front of the pinhole (PH) depicted in Fig. 2.2. The Ne and Kr lines are then compared with known values of the NIST (National Institute of Standards and Technology) database[49]. The laser wavelength (λ_L) can be measured with a recently acquired wavemeter and the spectral dimension can then be determined. The line assignment of the calibration spectra is done automatically using a Python script called madras. By comparing different exposures, the script also removes spikes automatically. The script was initially developed by T. Forsting[45], with further improvements made by M. Gawrilow[46], A. Nejad and N. O. B. Lüttschwager.

Details regarding the measurement conditions of all discussed Raman spectra can be found in chapter H (page 311).

2.1.3 Microwave setups in Hamburg

In the Schnell group the *COMPACT* (*Com*pact-*P*assage *A*cquired *C*oherence *T*echnique)[50,51] and *18 – 26*[51] setups were used. The former covers frequency ranges of 2 GHz – 8 GHz, 8 GHz – 13 GHz, 13 GHz – 15.5 GHz and 15.5 GHz – 18 GHz, while the latter covers the 18 GHz – 26 GHz range, as its name suggests. Both setups employ the so called chirped-pulse Fourier transform microwave (CP-FTMW) spectroscopy, as developed by the Pate group[52,53] in 2006 and utilise supersonic jet expansions. The chirped-pulse technique allows for fast and intense pulses of microwave radiation. This can be used to sample broad frequency ranges at once in comparison to traditional cavity setups, which cover about 500 kHz. Hence, this technique is also referred to as broadband rotational spectroscopy. Moreover, given the high pulse rates possible with chirped-pulse instruments and advancements in signal processing, very high sampling rates can be achieved. For instance, in case of 3-chloro-propane-1,2-diol 5 400 000 free induction decays (FID) have been collected in the 2 GHz – 8 GHz range. A drawback of the CP-FTMW technique is an inferior resolution in comparison to cavity setups. Resolutions of 25 kHz (2 GHz – 8 GHz) and 100 kHz can be achieved with the *COMPACT* and *18 – 26* setups, respectively. In the 8 GHz – 18 GHz range the resolution of the *COMPACT* instrument roughly doubles. Cavity setups can achieve a resolution of a few kHz. However, CP-FTMW still provides a very high resolution suitable for most purposes (25 kHz $\approx 8.3 \times 10^{-7}\,\mathrm{cm}^{-1}$). Moreover, cavity instruments can be used to detect very weak signals. Therefore, cavity measurements can be a helpful tool to refine fits obtained from CP-FTMW spectra.

In the following, a brief description of some key details of the setups will be given. More technical information can be found in Refs. [50, 51]. In the 2 GHz – 8 GHz region a pulse rate for the expansion of 8 Hz is used. During each pulse, the expansion is irradiated eight times, orthogonally to the direction of travel of the flow, with 4 µs long microwave chirps. The microwave pulse is amplified by a 300 W amplifier before entering the vacuum chamber. A horn antenna is used to broadcast the chirped pulse, with another antenna opposite to the broadcasting one collecting the FID. The FID is collected over a duration of 40 µs. This way, a combined repetition rate of 64 Hz can be achieved. The 8 GHz – 18 GHz region is sampled stepwise as was mentioned above. Here, a less powerful amplifier (50 W) is used and the chirped pulse duration is halved. Moreover, due to data handling limitations, the FID is collected for only 20 µs, resulting in the lower resolution as previously mentioned. As a result of this limitation gas pulses are also reduced to 4 per second yielding an overall repetition rate of 32 Hz.

A key difference between the *18 – 26* and the *COMPACT* setup is the fact that a segmented chirp pulsed approach is used. Instead of using a single broad pulse, ten pulses covering 800 MHz each are used with durations of 1.5 µs. The combinations of these pulses are referred to as pulse trains and are amplified using a 6 W amplifier. Horn antennas are used in the same manner as is the case for the *COMPACT* setup. Per gas pulse, three pulse trains are used at a gas pulse rate of 10 Hz. Hence, a combined rate of 30 Hz can be achieved. The FIDs are collected over a duration of 10 µs, resulting in a resolution of 100 kHz.

In comparison to the *curry*-jet, the major differences that have been covered so far are the pulsed operation and the resolution. Moreover, the horn antennas are placed significantly more downstream than the laser is for the *curry*-jet. For the *curry*-jet, nozzle distances of 3 mm are not exceeded under normal operation, while the horn antennas probe the expansion in the order of cm away from the nozzle. Additionally, the antennas also probe a larger area of the expansion simultaneously, also in the order of cm. The laser used for the Raman experiments, on the other hand, is highly focussed with a beam diameter of about 16 µm. Moreover, for the microwave experiments neon has been used as a carrier gas throughout at a p_S up to 2.4 bar. For the Raman setup, helium is used with occasional ad-mixtures of argon, with at most 1.4 bar. These factors indicate that the microwave expansions are colder than those in the *curry*-jet. In fact rotational temperatures of 1 K or 2 K can be achieved. Additionally, the nozzle head itself contains the sample and acts as a saturator. To reach sufficiently high vapour pressures the nozzle head can be heated.

Furthermore, a slit nozzle is used in case of the *curry*-jet, while an annular/circular one is used for the microwave setups. In slit nozzles, the molecular density decreases slower

than for annular nozzles. This is due to the fact that the former have only one transverse dimension (two dimensional in total) and the latter have two (three dimensional in total). Hence, the collisions rates remain high even at larger distances for slit nozzles. This would generally favour the formation of clusters and the cooling of vibrational ("stubborn") degrees of freedom[34]. However, rotation can be cooled very efficiently in either case and temperatures very close to the translational temperature can be achieved. Moreover, in principle, Doppler broadening can be reduced by using a slit nozzle, although given the low resolution of the *curry*-jet, the effect would not be significant. It may be of use to employ slit nozzles for the microwave setups.

To analyse the microwave spectra, the PGOPHER (version 10.1) fitting program by C. M. Western[54,55] is used. The systems studied in this work all constitute asymmetric rotors, as indicated by Ray's asymmetry parameter κ_{R}[56]. κ_{R} can be calculated in the following way:

$$\kappa_{\mathrm{R}} = \frac{2B - A - C}{A - C} \tag{2.1}$$

with A, B and C being rotational constants. Values of -1, 0 and $+1$ describe the symmetric prolate ($A > B = C$), most asymmetric ($A = B + C$ with $B = 2C$) and symmetric oblate ($A = B > C$) limiting cases, respectively. The systems studied here range between $-1 < \kappa_{\mathrm{R}} < 0$ and therefore are asymmetric. In fact, most conformers tend towards the prolate limit ($\kappa_{\mathrm{R}} \approx -0.9$). Based on this observation the Ir representation is used. The choice of a representation is necessary due to the fact that the mapping of the principal inertial system (a, b, c) to the cartesian axis system (x, y, z) is no longer clearly defined. The choice of Ir ($z \mapsto a$, $x \mapsto b$, $y \mapsto c$) is advantageous since it most closely resembles the prolate description (a corresponds to the quantisation axis of K) and improves the quality of the fit. Additionally, the symmetric top reduction of the Hamiltonian is used, because it provides better convergence behaviour for near symmetric (prolate) systems[57]. The symmetric top reduction is also referred to as Watson S reduction. Values obtained with the S reduction can be easily converted to the asymmetric top reduction (Watson A reduction)[58].

Given the large number of different quantities that can be fitted, a brief overview of the constants important to this work is given in Tab. 2.1. Details regarding the measurement conditions of all discussed microwave spectra can be found in chapter H (page 311).

Tab. 2.1: Summary of relevant constants in the Watson *S* and *A* reduction for the microwave spectra.

S reduction	*A* reduction	explanation
A, B, C		rotational constants
D_J, D_{JK}, D_K	$\Delta_J, \Delta_{JK}, \Delta_K$	diagonal quartic centrifugal distortion constants
d_1, d_2	δ_J, δ_K	off-diagonal quartic centrifugal distortion constants
χ_{aa}, χ_{bb-cc}		diagonal nuclear quadrupole coupling constants
$\chi_{ab}, \chi_{ac}, \chi_{bc}$		off-diagonal nuclear quadrupole coupling constants
χ_J, χ_K		quartic nuclear quadrupole coupling distortion constants
C_{aa}, C_{bb}, C_{cc}		nuclear spin - rotation interaction constant

2.2 Used chemicals

Tab. 2.2: Overview of the used chemicals with common names in parentheses. CAS-numbers, suppliers and purity are also given. 70% purity indicates technical grade.

compound	CAS-number	supplier	purity
(*R*,*R*)-butane-2,3-diol	24347-58-8	ChemPur	98%
(*S*,*S*)-butane-2,3-diol	19132-06-0	Sigma-Aldrich	97%
2-methylbutane-2,3-diol	5396-58-7	abcr	95 – 98%
3-butene-1,2-diol	497-06-3	Sigma-Aldrich	99%+
cis-cyclohexane-1,2-diol	1792-81-0	Sigma-Aldrich	99%
(*R*,*R*)-1-phenyl-*cis*-cyclohexane-1,2-diol	125132-75-4	Santa Cruz	> 98%
(*R*,*R*)-*trans*-cyclobutane-1,2-diol	35358-34-0	Sigma-Aldrich	97%
trans-cycloheptane-1,2-diol	65678-03-7	Sigma-Aldrich	⩽ 100%
(*R*,*R*)-*trans*-cycloheptane-1,2-diol	108268-28-6	Sigma-Aldrich	⩽ 100%
trans-cyclohexane-1,2-diol	1460-57-7	Alfa Aesar	> 97.5%
(*S*,*S*)-*trans*-cyclohexane-1,2-diol	55794-08-8	Sigma-Aldrich	99%
trans-cyclopentane-1,2-diol	5057-99-8	Sigma-Aldrich	97%
(*R*,*R*)-*trans*-cyclopentane-1,2-diol	930-46-1	Key Organics	95%+
ethane-1,2-diol (ethylene glycol)	107-21-1	abcr	99%
1-phenyl-ethane-1,2-diol	93-56-1	ChemPur	97%
1-bromopropan-2-ol	19686-73-8	Sigma-Aldrich	70%
2-bromopropan-1-ol	598-18-5	BLD	97%
1-chloropropan-2-ol	127-00-4	TCI	70%

(*R*)-1-chloropropan-2-ol	19141-39-0	BLD	98%
(*R*)-2-chloropropan-1-ol	37493-14-4	BLD	95%+
propane-1,2-diol (propylene glycol)	57-55-6	Merck	99%+
(*S*)-propane-1,2-diol	4254-15-3	ChemPur	95%
3-bromo-propane-1,2-diol	4704-77-2	Sigma-Aldrich	97%
3-chloro-propane-1,2-diol	96-24-2	Sigma-Aldrich	98%
(*S*)-3-chloro-propane-1,2-diol	60827-45-4	abcr	97%
3,3,3-trifluoro-propane-1,2-diol	431-39-0	abcr	97%
2-methylpropane-1,2-diol	558-43-0	ChemPur	98%
2,3-dimethyl-butane-2,3-diol (pinacol)	76-09-5	ChemPur	98%
1-(1-hydroxy-1-methylethyl)-cyclopentanol	5607-45-4	abcr	95%
[1,1'-bicylopentyl]-1,1'-diol	5181-75-9	Sigma-Aldrich	97%
2,2,4,4-tetramethyl-3-*t*-butyl-pentane-3-ol (tri-*tert*-butylmethanol/carbinol)	41902-42-5	BLD	98%+

2.3 Quantum chemical methods

If not otherwise stated calculations utilise the Born-Oppenheimer approximation (nuclear and electronic wavefunctions are treated separately)[59], frozen core approximation (only valence electrons are included in the correlation treatment; not applicable to DFT) and without the inclusion of relativistic effects.

2.3.1 Structure search

Given the conformational flexibility of the systems studied in this work, automated search algorithms have been used for the monomers and dimers. To this end, the CREST (Conformer-Rotamer Ensemble Sampling Tool, version 2.10.2) program, developed by S. Grimme and co-workers[60,61], was used. CREST itself uses the GFN2-xTB (Geometries Frequencies Non-covalent interactions extended Tight Binding, version 6.3.3) functional[62,63]. The structural searches ran with CREST are based on meta-dynamics (MTD) simulations, which allow for an efficient sampling of the conformational space. The iMTD-GC (iterative Meta-Dynamics - Genetic Crossing) and NCI routines were employed. The NCI procedure introduces a wall potential around the molecular system to prevent the dissociation of clusters, allowing for a meaningful sampling of oligomers. Furthermore, the energy introduced into the system is reduced as to not break weak

intramolecular hydrogen bonds, for instance. Both iMTD-GC and NCI were used for each system and in case of the dimers a variety of starting structures were employed. Given that a single simulation run can easily exceed 300 structures, in some cases pre-optimisations have been conducted. For these, the cheap but still reasonably accurate, B97-3c[64] functional was utilised and followed by calculations as outlined in section 2.3.2. All of the resulting structures were checked by hand for missing conformers.

With permission of S. Grimme the CREST and xTB packages were made available on the in-house compute cluster (Chemie Cluster). To streamline these calculations a submit script has been written.

2.3.2 Density functional theory methods

Density functional calculations have been performed with the ORCA 4.2.1[65–67] and 5.0.3[65,68] as well as Gaussian 16 (Rev. A.03)[69] program packages. Most calculations have been conducted with the former and its use can be assumed if not otherwise stated. Example inputs for all calculations can be found in chapter G (page 305).

Out of the "zoo" of different density functionals a few common ones have been chosen. This includes the BP86[70–72] and PBE[73] methods, which both utilise the generalized gradient approximation (GGA). This constitutes the lowest level of density functional theory (DFT) used in this work. GGAs can be improved by mixing in a constant amount of exact exchange from Hartree-Fock (HF) theory, which is a wavefunction theory (WFT) based method. Such a combination is referred to as a hybrid functional and the very popular B3LYP[74–76] and PBE0[77,78] functionals have been chosen here. Hybrid functionals can be further refined by mixing in HF exchange dependent upon the electron-electron distance, instead of using a constant ratio. These methods are referred to as range-separated hybrid functionals[79], of which CAM-B3LYP[80] has been employed in this work. HF by definition does not include any correlation energy and in principle the DFT description could be improved by additionally including parts of the correlation energy of wavefunction methods. A comparatively cheap way of obtaining the correlation energy is the use of second-order Møller-Plesset perturbation theory (MP2)[81]. Functionals including parts of the MP2 correlation energy are called double-hybrid functionals and were first proposed by S. Grimme[82,83]. His initially proposed B2PLYP functional was used in this work. In principle this approach can also be combined with range-separation (*e.g.* ωB2PLYP[84]), but no such method was used here.

A big shortcoming of DFT is the inability to describe dispersion properly, with the characteristic R^{-6} decay of the interaction missing. The term dispersion was inspired by F. London's work, who gave the first theoretically treatment of the interaction of two induced dipoles[85,86]. In his honour, dispersion is also referred to as London forces or London dispersion. A computationally cheap way of correcting for this fact was established by S. Grimme with the so called D3 dispersion correction. Here, R^{-6} and higher order energy terms are added to the electronic energy of the functional. These terms are parametrised empirically and differ for each functional. To prevent divergence at short distances the interaction is damped towards a constant value (not 0), using the so called Becke-Johnson damping function (BJ).[87,88] This dispersion correction works in a pairwise manner but can be extended to three body interactions using the Axilrod-Teller-Muto expression (abc)[89,90]. Calculations with the ORCA program package utilise both BJ and abc (-D3(BJ,abc)), while no three body terms (-D3(BJ)) are included in case of Gaussian. These distinctions will be dropped for brevity if calculations have been conducted by the author. Despite this shortcoming, DFT already includes some dispersion at short distances and cannot be considered "dispersion free" without a correction.

It should be kept in mind, that DFT relies on empirical fitting strategies and at best can be as good as its reference data. Hence, many functionals are only good at describing a few properties of a system included in the reference data and completely fail for others outside it. Furthermore, the reference data often only includes higher level computations and no experimental data. Moreover, it may be the case that a GGA functional performs better than a double hybrid functional for a specific property. The success of DFT is based to a large extent on error cancellation. A comprehensive look at the "zoo" of functionals and their performance can be found in Refs. [91–93]. Mixing and matching functionals and basis sets will also eventually lead to a desired outcome. A brief description with regards to the choice of basis set will be given in the following paragraphs.

A large variety of different basis set families can be used in conjunction with the different functionals, but also with wavefunction based methods. Some initial testing was done for the Ahlrichs (Karlsruhe)[94–96], Dunning[97,98] and Jensen[99] basis set families in their augmented (includes diffuse basis functions) and unaugmented variants, with double up to quadruple zeta quality. Ahlrichs basis sets are for general purposes and suitable for both DFT and WFT. Dunning basis sets have been designed to be correlation consistent, *i.e.* to recover the correlation energy in a consistent manner when its size is increased and are primarily aimed at WFT methods. The Jensen family sets out to recover the polarisation of the electron density upon the formation of a bond in a similar manner, but with DFT in mind and are called polarization consistent. It should be noted, that both Dunning and Jensen basis sets also systematically recover the HF energy in a systematic

manner.[100] The testing was conducted by comparing the relative energies of the different basis sets with B3LYP-D3(BJ,abc) as the baseline method and the Dunning aug-cc-pVQZ (aVQZ) basis set as the reference. The aVQZ basis set was chosen due to it being the largest. Therefore, providing the best description in principle. 8 different ethane-1,2-diol dimers are included in the dataset. To judge the time domain, the length of the analytical frequency calculation is taken as a reference.

The results of the testing are shown in Fig. 2.3. It can be seen, that Dunning and Ahlrichs basis sets show a similar convergence behaviour, while the Jensen basis sets significantly differ. Furthermore, the importance of augmented functions becomes clear. For instance, the aVDZ (292 basis functions) basis set performs better than the much larger VQZ basis set (800 basis functions). Of the unaugmented basis sets def2-QZVP performs the best. def2-TZVP, on the other hand, shows much larger deviations. This can be attributed to the Basis Set Superposition Error (BSSE), an artificial stabilisation

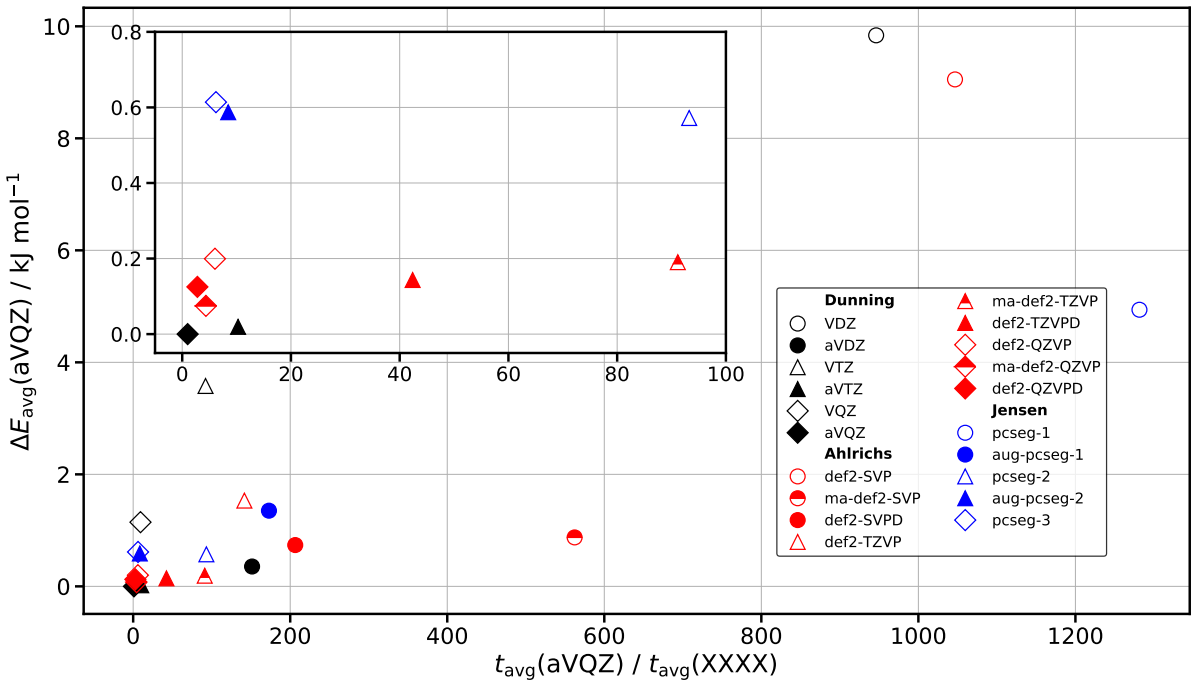

Fig. 2.3: Correlation between the average deviation of the relative zero point corrected energies for a given functional with aVQZ as a reference (ΔE_{avg}) and the ratio of the average time of a aVQZ calculation (t_{avg}(aVQZ)) and any other basis set (t_{avg}(XXXX)). Empty symbols indicate no augmentation, half full symbols slight augmentation and full symbols heavy augmentation. Basis sets in black, red and blue correspond to Dunning, Ahlrichs and Jensen families, respectively. The aug-pcseg-3 calculations did not converge. SV in def2-SVP stands for split valence and refers to a double zeta basis set. The zeta level for Jensen basis sets correspond to the number at the end +1. The calculations have been performed with ORCA. This figure is taken from Ref. [101].

due to the incompleteness of the basis set. The conformers included in the test set have a global minimum with four intermolecular hydrogen bonds (het4), while all other structures have three or two hydrogen bonds. The BSSE is strongest for the one with four hydrogen bonds, leading to an artificial lower energy of the conformer relative to the others. This can be further demonstrated by changing the reference point to another structure and excluding het4. Even unaugmented double zeta basis sets perform significantly better, with average deviations of about $2\,\mathrm{kJ\,mol^{-1}}$. For intramolecular hydrogen bonds, this phenomenon has been previously investigated by Reiling *et al.*[102] for ethane-1,2-diol and by Jensen[103] for ethane-1,2-diol and propane-1,3-diol at the MP2 level of theory. A very good compromise between accuracy and computational cost is provided by the minimally augmented ma-def2-TZVP basis set, being almost at aVQZ level in terms of accuracy but about 90 times as fast. Hence, ma-def2-TZVP will be used preferably in this work and is abbreviated as maTZ.

Calculations using the ORCA 4.2.1 program package utilised the Grid5 integration grid and the TightOpt setting for the geometry optimisations. The optimisation was followed by an analytical frequency calculation[104] within the double harmonic approximation. For the analytical frequency calculations no density fitting was applied for B3LYP and PBE0, while for PBE and BP86 the RI-J approximation was used with the corresponding auxiliary basis set[105]. For the frequency calculations the Mass2016 was always included, to ensure the use of the mass of the most stable isotope instead of an averaged one. Since ORCA can only compute Raman activities using numerical frequency calculations, these have been conducted for energetically relevant structures with B3LYP. Due to numerical frequency calculations being significantly more time demanding than analytical ones, density fitting (RI-JCOSX)[106] was applied in these cases.

However, the Raman activities obtained in this manner cannot be directly compared to the experiment. Using a script written by M. Gawrilow the activities are converted to differential (per unit angle) cross sections (σ' in $\mathrm{m^2\ sr^{-1}}$), which take setup specific factors into account. These include the orthogonal laser polarisation relative to the scattering plane (see $\perp_\mathrm{i}$ in Fig. 2.2 (page 8)), method of detection (photon counting), angle of detection, an approximate vibrational temperature (100 K) and the frequency and polarisation dependence of the grating of the monochromator. The latter is done with a recently empirically determined polynomial function, which corrects for the fact that parallelly polarised light (see $\|_\mathrm{S}$ in Fig. 2.2 (page 8)) is less efficiently transmitted by the grating[46,107]. σ' obtained in this manner is then combined with the corresponding vibrational mode from the analytical frequency calculations to simulate the spectra. The recorded intensities have not been adjusted with regards to the differing spectral dimensions of individual pixels, as was done in Refs. [46, 107]. However, given that bands have been compared in

a narrow frequency range the effect is small. A comprehensive theoretical treatment of the Raman effect can be found in Ref. [108].

Furthermore, the NEB-CI (Nudged Elastic Band - Climbing Image) method[109] has been employed to find starting structures for transition state searches. For the transition state calculations, the exact Hessian-matrix is computed at every third step.

ORCA 5.0.3 has been used for tri-*tert*-butylmethanol, were convergence issues arose for ORCA 4.2.1. Utilising the newly introduced TRAH (Trust Radius Augmented Hessian) method[110] these could be avoided. Furthermore, the integration grid definitions have been overhauled and the newly devised DefGrid3 (largest default grid) was used. Additionally, the RI-JCOSX method was significantly improved, so that it was also employed for the analytical frequency calculation. Furthermore, the VeryTightOpt keyword was used. As part of her bachelor thesis L. Schiebel[111] conducted a lot of testing with calculations relevant to the Suhm group. Two bugs were discovered, which have been quickly fixed by the developers and are no longer present in ORCA 5.0.3. Moreover, the new SHARK integral package[112] leads to significant speed-ups, while yielding the same results as the previously used integral package. Hence, ORCA 5.0.3 can generally be recommended to be used within the Suhm group.

The ORCA submit script, written by A. Poblotzki and H. Gottschalk, has been overhauled and adapted to be used with the Chemie Cluster, as well as the GWDG cluster. Furthermore, with the help of R. Oswald centralised ORCA distributions were made available to the Suhm Group, so that users no longer need ORCA within their own home directory.

The Gaussian calculations were conducted to utilise its vibrational perturbation theory of second order (VPT2)[113] implementation[114,115]. The SuperFine (largest grid) integration grid was used coupled with the VeryTight optimisation criteria. Anharmonic VPT2 calculations are significantly more costly than harmonic frequency calculations and are therefore limited to small systems. For instance, at the B2PYLP-D3(BJ)/aVTZ level of computation a VPT2 calculation takes about a week (36 cores; 2× Intel Xeon Gold 6240 (18) @ 3.9 GHz) for 3-bromo-propane-1,2-diol (13 atoms, 6 non-hydrogen). A harmonic calculation, on the other hand, is finished within hours. The VPT2 calculations are preceded by analytical harmonic frequency calculations. It was noted in Ref. [36] that for DFT the VPT2 calculations varied strongly with different optimisation criteria, but also when slightly different input structures (still leading to the same minimum) were used for the optimisation directly followed by the frequency calculation. It was found that these variations can be greatly reduced by separating the optimisation from the frequency calculation[116]. For the VPT2 calculations the aug-cc-pVTZ has been used throughout,

Tab. 2.3: Overview of the used functionals, including the typer of dispersion correction, basis set, frequency calculation, functional type and program. RI refers to the use of resolution of identity, *i.e.* density fitting. GGA corresponds to a functional within the generalised gradient approximation.

method	dispersion	RI	basis set	frequencies	functional type	program
BP86	D3(BJ,abc)	RI-J	maTZ	harmonic	GGA	ORCA
PBE	D3(BJ,abc)	RI-J	maTZ	harmonic	GGA	ORCA
PBE0	D3(BJ,abc)	no RI	maTZ	harmonic	hybrid	ORCA
B3LYP	D3(BJ,abc)	no RI	maTZ	harmonic	hybrid	ORCA
PBE0	D3(BJ)	no RI	aVTZ	VPT2	hybrid	Gaussian
B3LYP	D3(BJ)	no RI	aVTZ	VPT2	hybrid	Gaussian
B2PLYP	D3(BJ)	no RI	aVTZ	VPT2	double hybrid	Gaussian

which is shortened to aTZ. Besides the frequencies, the quartic distortion constants (see Tab. 2.1 (page 13)) can also be obtained *via* VPT2.

An overview of the different functionals and their parameters is shown in Tab. 2.3.

2.3.3 Wavefunction theory methods

Wavefunction theory (WFT) methods have been used in conjunction with the ORCA 4.2.1[65–67], Gaussian 16 (Rev. A.03)[69], MOLPRO 2020.2[117–119] and 2021.2[117,118,120] program packages.

For Gaussian 16, VPT2 calculations have been performed at the MP2 level of computation. The gradients[121,122] and the harmonic frequencies have been calculated analytically[123]. The same parameters as for the DFT calculations have been used, excluding the inapplicable D3(BJ) and grid options.

SCS-LMP2 and LCCSD(T0)-F12a calculations have been made with MOLPRO 2021.2. SCS-LMP2 refers to the MP2 variant utilising spin-component scaling (SCS)[124] and localised orbitals (L)[125–127]. The SCS approach, where parallel and anti-parallel spin components are scaled separately in an empirically manner, helps to improve MP2 energies. In comparison to standard canonical orbitals, that extend over the entirety of the molecular system, local orbitals are spatially restricted. In this way the computational scaling with the number of basis functions can be reduced from M_{basis}^5 to near linear behaviour. Furthermore, intermolecular BSSE can be greatly reduced in the local framework, by excluding BSSE prone double excitations (see Fig. 2.4), but also by the spatial

limitations[100,128–130]. The localisation is done according to the procedure outlined by Pipek and Mezey[131], but other schemes such as the method of Foster and Boys[132] could be applied. To speed up the calculations, density fitting was used in conjunction with the corresponding auxiliary basis sets[133,134]. The geometries are optimised using analytical gradients[135–137], while the frequency calculations were done numerically[138]. The aVTZ basis set was used for all non hydrogen atoms, while VTZ was used for hydrogen. The optimisation parameters can be taken from the example inputs for all MOLPRO calculations (see section G.3 (page 307)).

LCCSD(T0)-F12a[139,140] is the local variant of coupled cluster (CC), which includes single S, double D and pertubative triple excitations (T0). The 0 of (T0) indicates an approximation, wherein the triples do not have to be computed iteratively. In comparison to the full iterative perturbative triples the time savings are substantial, while the loss of accuracy is minimal[141]. Canonical CCSD(T) scales with M_{basis}^7 and as was the case for MP2 this scaling can be greatly reduced by the localisation. F12a is a variant of so called explicitly correlated methods. Here, an explicit dependence upon the interelectronic distance ($\exp(-r_{12})$) is introduced into the wavefunctions, which greatly accelerates the basis set convergence. With specially adapted basis sets, results near the basis set limit can already be achieved at the double-zeta level. For the calculations in this work, the VDZ-F12[142] basis set has been employed, which behaves favourably with the F12a variant in comparison to F12b. Both the geometry optimisation and the frequency calculations were done numerically. Furthermore, density fitting was applied using the corresponding auxiliary basis sets[133,143,144]. Moreover, CCSD(T) is often referred to as the "gold standard" of quantum chemistry able to reach chemical accuracy (for energies $1\,\text{kcal}\,\text{mol}^{-1} \equiv 4.184\,\text{kJ}\,\text{mol}^{-1}$), frequently leading to theory benchmarking theory with CCSD(T) as reference[32]. However, the ultimate goal of theory should be the replication of the experiment, highlighting the importance of providing reliable experimental reference data for such comparisons.

The local framework also allows to gain more chemical insight into a system. This is discussed in detail in Refs. [145, 146]. The double excitations present in MP2 and CCSD(T) can be divided in different types of interactions. This is illustrated in Fig. 2.4. The molecular system has to be partitioned into fragments A and B. In principle these could be any parts of the system. However, in this work fragment A and B correspond to the different monomers of a dimer (see section 4.3 (page 180)). If an electron is excited in fragment A and stays within the orbital space of A, while simultaneously an electron is excited in fragment B and stays within the orbital space of B the interaction is classified as dispersion. In a similar fashion dispersion exchange, intramolecular correlation and ionic interactions can be defined. The analysis of dispersion in section 4.3 (page 180)

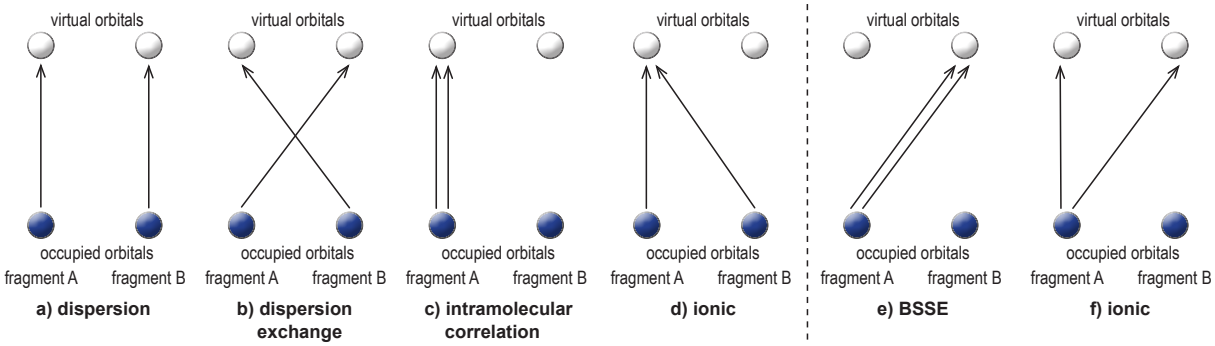

Fig. 2.4: Excitation scheme for the local energy decomposition (LED) of double excitations of WFT calculations. An arrow indicates the excitation of a single electron from the occupied orbitals to the virtual ones. Fragment A and B can correspond to any predefined part of a molecular system. In section 4.3 (page 180) A and B apply to the two monomers of a dimer. Interaction **e)** and **f)** are largely responsible for the BSSE and are excluded in the local calculations. This figure was created in analogy to Fig. 2 of Ref. [129].

focuses on "pure" dispersion, *i.e.* dispersion-exchange is not included. The contributions **e)** and **f)** in Fig. 2.4 are largely responsible for the BSSE and by excluding them this error can be greatly reduced. It is important to note, that this may only apply to the use of Projected Atomic Orbitals (PAOs) to describe the virtual orbital space. Schemes using Pair Natural Orbitals (PNOs) instead of PAOs explicitly include contributions of **e)**- and **f)**-type.[146] Furthermore, local energy decomposition (LED), in principle, can be extended to an arbitrary amount of fragments.

Moreover, for the systems involving chlorine and bromine atoms, canonical CCSD(T0)-F12a[147,148] calculations have been conducted with MOLPRO 2020.2. Local coupled cluster calculations lead to irregularities during the geometry optimisation. Hence, canonical CC was used instead. The apparent increase of computational effort, in comparison to the local variant, can at least be partially off-set by the fact that analytical gradients[149,150] are available. Frequencies are again calculated numerically and the VDZ-F12 basis set was used. Furthermore, to speed up the calculations density fitting was used, as was the case for LCCSD(T0)-F12a. For Br the VDZ-PP-F12[151] basis set was used. PP indicates the use of a pseudopotential (Stuttgart-Köln type ECP10MDF)[152] to describe the core electrons. The corresponding auxiliary basis sets provided in Ref. [151] were used together with the def2-QZVPP/JKFIT[153] basis set.

For MOLPRO a submit script was written for the Chemie and GWDG cluster.

Lastly, CCSD(T) calculations have been conducted with ORCA 4.2.1 to calculate the electric field gradient (EFG) at Cl and Br nuclei. The EFG is necessary to compute nuclear quadrupole coupling constants, which is elaborated on in more detail in section 2.3.4.

Since the EFG depends on the core electrons the specialised aug-cc-pwCVTZ[98,154,155] basis set is used, which is adjusted to describe core - valence and core - core correlation. This choice is further informed by the study of Aerts and Brown[156], who investigated small aluminium containing molecules at the coupled cluster level with the aug-cc-pVXTZ and aug-cc-pwCVXZ (X = D, T, Q, 5) basis sets. Furthermore, the frozen core approximation is not applied, which is also referred to as an all electron calculation. To judge the influence of relativistic effects, especially on the heavier Br nuclei, relativistic and non-relativistic calculations have been performed. Relativistic effects are introduced via the Douglas-Kroll-Hess of second order (DKH2) transformation[157–159]. The relativistic EFG calculations included the finite nucleus model (nuclei are no longer assumed to be point charges)[160] and picture change effects specifically for DKH2[161]. Picture change effects result from changes to the operator for a given property and changes to the wavefunction due to the DKH2 transformation. Furthermore, no density fitting was applied. For consistency, the aug-cc-pwCVTZ basis set is also used for the relativistic calculations. However, specialised basis sets designed for the use of DKH2, *e.g.* aug-cc-pCVTZ-DK[154,155,162,163] or ma-DKH-def2-TZVP (adapted for DKH use by the ORCA team), may provide better results.

2.3.4 Calculation of nuclear quadrupole coupling constants

The nuclear quadrupole coupling constants χ_{ij} (NQCC) can generally be calculated in the following way:

$$\chi_{ij} = eQq_{ij} = eQ\frac{\partial^2 V_{ij}}{\partial x_i \partial x_j} \tag{2.2}$$

with e being the elementary charge, Q the nuclear quadrupole moment and q_{ij} the electric field gradient (EFG) at the nucleus. i and j correspond to the axes in the inertial principal axis system (a, b, c). Nuclei that have a nuclear spin (I) greater than ½ have a non-zero nuclear quadrupole moment. Hence, nuclear spins greater than ½ are necessary to observe any NQCC. The nuclei studied here (^{35}Cl, ^{37}Cl, ^{79}Br and ^{81}Br) all exhibit $I = 3/2$. For the calculations, the following values for Q are used: -0.0817 barn, -0.0644 barn, 0.313 barn and 0.262 barn ($1\,\text{barn} \equiv 100\,\text{fm}^2$) for ^{35}Cl, ^{37}Cl, ^{79}Br and ^{81}Br, respectively[164]. These correspond to the recommended values of the International Nuclear Data Committee. Given the larger Q of Br in comparison to Cl, χ_{ij} is also expected to be larger for the former. q_{ij} corresponds to the second partial derivative of the electrostatic potential (V) leading to nine different components in total, which have to be computed. Generally, q_{ij} will increase when moving from Cl to Br, however, the effect is smaller than the change in Q for the systems studied here. The Gaussian program package directly computes χ_{ij}

in MHz, while in case of ORCA the EFG tensor has to be converted from atomic units to MHz ($\chi_{ij}/_{\mathrm{MHz}} = 235.541 \times Q/_{\mathrm{barn}} \times q_{ij}/_{\mathrm{a.u.}}$). Moreover, the molecule has to be moved to its inertial principle axis system first for ORCA calculations.

q_{ij} and by proxy χ_{ij} yield a traceless and symmetric tensor. Since the tensor is traceless, *i.e.* $\chi_{aa} + \chi_{bb} + \chi_{cc} = 0$, there are only two independent diagonal elements χ_{aa} and $\chi_{bb} - \chi_{cc}$ (χ_{bb-cc}). Moreover, due to the fact that the tensor is symmetric, *i.e* $\chi_{ab} = \chi_{ba}$, $\chi_{ac} = \chi_{ca}$ and $\chi_{bc} = \chi_{cb}$, five elements in total can be determined experimentally. Furthermore, algebraic rules dictate that as long as the sign of the product of the off-diagonal elements remains unchanged, their description is equivalent. For instance, $\chi_{ab}\chi_{ac}(-\chi_{bc})$ is equivalent to $(-\chi_{ab})(-\chi_{ac})(-\chi_{bc})$. As will be seen in section 3.2 determining accurate off-diagonal elements experimentally, especially for Cl, is often not possible. Additionally, changes in χ_{ij} can quickly lead to large differences in the rotational hyperfine-structure, highlighting the necessity of reliable theoretical predictions.

2.4 Nomenclature

2.4.1 1,2-Diol monomers

Given the large amount of molecules studied in this work, systematic abbreviations for the different systems are introduced which have previously been laid out in Ref. [165]. The different systems are classified according to the substitution geminal to each OH group. The unsubstituted parent is provided by ethane-1,2-diol which will be written as 0-0. A substitution with a methyl group is indicated by an M, a phenyl group by a Ph, a vinyl group by a V, a trifluoromethyl group by an F and mono-halogenated methyl groups by Cl_1 for chlorine and Br_1 for bromine. The shorthand notation puts the less substituted side first. For example propane-1,2-diol would be called 0-M, 3,3,3-trifluoro-propane-1,2-diol 0-F and 2-methyl-butane-2,3-diol M-MM. In case of *rac*-butane-2,3-diol an *r* is added to distinguish it from the *meso* compound *i.e.* rM-M.

For cyclic systems that do not close the ring at the same carbon atom (vicinal) the ring size is expressed as *X*-*X* with *X* being the number of carbon atoms of the ring. However, *trans* and *cis* arrangements of the OH-groups are possible which is indicated by a t and c, respectively. For instance, *trans*-cyclohexane-1,2-diol is designated as t6-6 and *cis*-cyclohexane-1,2-diol as c6-6. Cyclic systems closing at the same carbon atom (geminal) a cyclopentyl group is indicated by CP *e.g.* 1-(1-hydroxy-1-methylethyl)-cyclopentanol is abbreviated as CP-MM. For systems bridged in such a way no other ring sizes have been

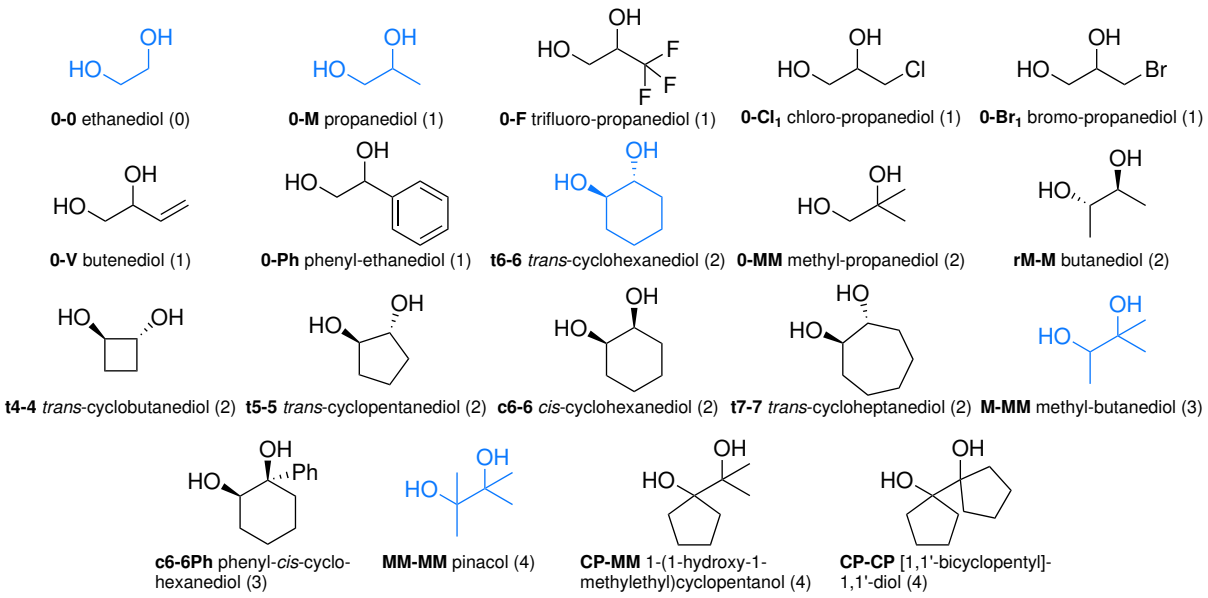

Fig. 2.5: Overview of the abbreviations used for all diol systems discussed in this work. The proper IUPAC names of all compounds used can be found in Tab. 2.2 (page 13). The degree of substitution (n_D) is shown in parentheses. The compounds used for the training set in section 3.1 are highlighted in blue and the test set in black. This figure is adapted from Ref. [165].

studied in this work. All of the different diols with their corresponding abbreviations are shown in Fig. 2.5. It also shows the degree of substitution (n_D) *i.e.* the number of exchanged H atoms of the ethane-1,2-diol backbone. Therefore, ethane-1,2-diol has a degree of substitution of 0 while pinacol, for example, has one of 4.

To distinguish between the many different conformers a few extra signifiers are added to the shorthand notation which have been previously discussed in Refs. [18, 165]. These are illustrated in Fig. 2.6 with *rac*-butane-2,3-diol (rM-M) and 1-(1-hydroxy-1-methylethyl)-cyclopentanol (CP-MM) as examples. The most common conformers can be distinguished from each other by adding a prime (primed) to rM-M where the intramolecular hydrogen

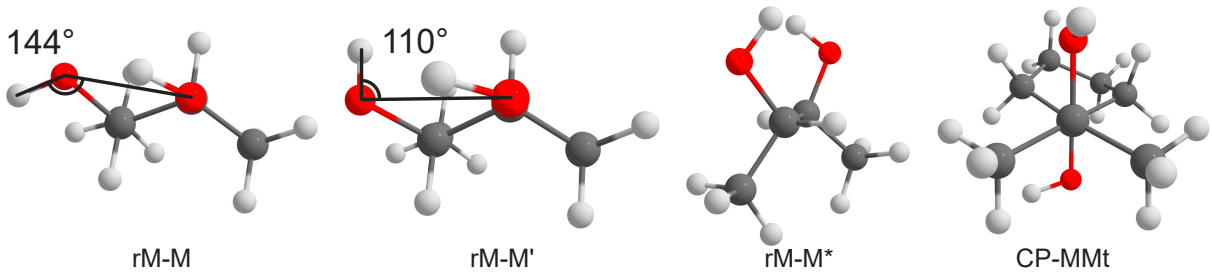

Fig. 2.6: Illustration of the nomenclature used for monomers in this work. This figure is adapted from Ref. [165].

bond is quite orthogonal, *i.e.* the donor oxygen - acceptor oxygen - acceptor hydrogen angle ($\angle O_D O_A H_A$) is fairly close to the 90° case. If no prime is added (unprimed), the intramolecular hydrogen bond is more linear, *i.e.* it follows the direction that the donor OH group and acceptor oxygen indicates. The threshold to differentiate the two cases is put at 120°, with angles below being considered primed (*e.g.* rM-M') and angles above unprimed (*e.g.* rM-M). In some instances the OH groups have a more cross like shape not actually forming a hydrogen bond, which is designated with a * (see rM-M*). Some conformers do not have an intramolecular hydrogen bond at all in which case a t is added (see CP-MMt). The t designator for *trans*-cyclobutane-1,2-diol (t4-4) implies no hydrogen bond due to an antiperi-planar OCCO dihedral angle as shown in Fig. 2.6. For *trans*-cyclopentane-1,2-diol (t5-5) this corresponds to a di-axial arrangement of the OH groups. In cases where a label would reoccur an a, b, c or d are added *e.g.* rM-Ma or rM-Ma'. As a reference point for the reoccurrence the B3LYP/maTZ calculations are used.

2.4.2 Oligomers

In this work dimers are studied in detail with a focus on chirality recognition, but the following nomenclature can be used for higher oligomers as well. Oligomers up to tetramers are elaborated on showing some interesting statistical weights that arise for their formation. Therefore, the corresponding nomenclature has to capture the (relative) chirality observed in these systems. To this end, the aggregation up to tetramers is shown in

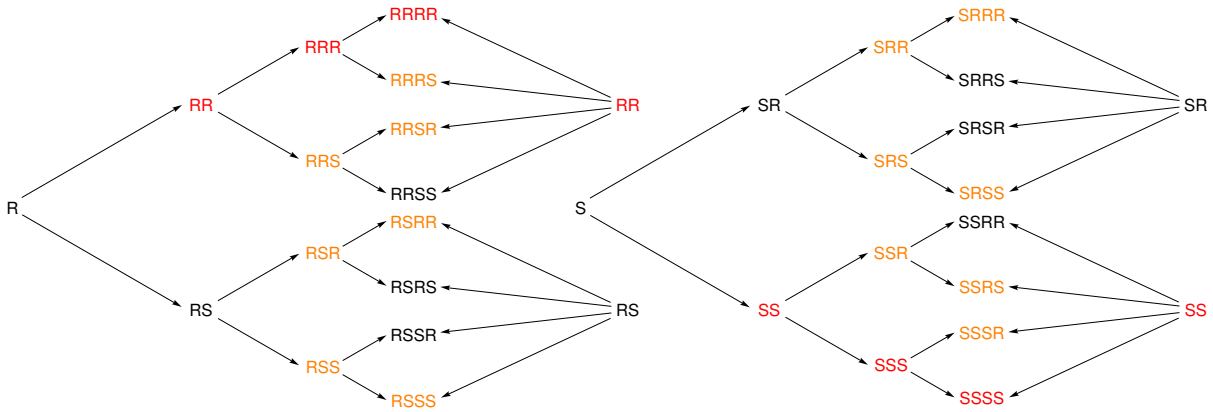

Fig. 2.7: Illustration of the sequential aggregation up to tetramers. R and S signal the chirality while arrows pointing up indicate the addition of an R enantiomer and arrows pointing down the addition of a S enantiomer. Furthermore, the formation of tetramers from dimers is shown by arrows going from right to left. The arrows add RR, RS, SR and SS dimers from top to bottom. Racemic hetero-chiral species are highlighted in black, homo-chiral ones in red and scalemic hetero-chiral ones in orange.

Fig. 2.7. It indicates that the formation of racemic hetero-chiral (black), homo-chiral (red) and scalemic hetero-chiral (orange) oligomers is possible which are abbreviated as het, hom and hot, respectively. Hetero-chiral scalemic oligomers are synonymous with enantioenriched aggregates. Assuming permanently chiral systems, statistical weights for these subclasses can also be derived since in a supersonic expansion no collisional preference would be expected, albeit in principle possible.Hence, for dimers, het and hom populations are roughly even while for trimers the scalemic hetero-chiral ones have a statistical advantage (3:1). In case of tetramers weights for het : hom : hot of 3 : 1 : 4 can be found.

Unlike the monomers, the naming convention does not include a reference to the studied system like 0-0 and so on. Instead het, hom or hot followed by the number of intermolecular hydrogen bonds is added, *e.g.* hom3. Signifiers inspired by the monomers are then used which have previously been discussed in Refs. [101, 166]. The primed/unprimed distinction is now applied to intermolecular hydrogen bonds instead. However, to simplify the nomenclature only the OOH angles to dangling OH groups are used. Any OH group is considered dangling if itself is not involved in an intermolecular hydrogen bond, excluding hydrogen bond acceptors. For clarity donor-groups involved in intramolecular hydrogen bonds are also considered dangling. As a threshold an $\angle O_D O_A H_A$ of 120° is still used. hom3 and hom3' are shown as examples in Fig. 2.8. Moreover in case of bifurcated hydrogen bonds, *i.e.* two donors have the same acceptor, a subscript b is added. The example of hom3$_b$' also illustrates that two OOH angles are now used to the same dangling OH group. Since one donor is below the threshold only one ' is added. As het4 illustrates it may be the case that no dangling OH groups exist where no additional descriptors are used. In analogy to the monomers a, b, c and so on are added should a label repeat for example hom3a'. The same principles apply to trimers and tetramers, for which the hot specifier is introduced.

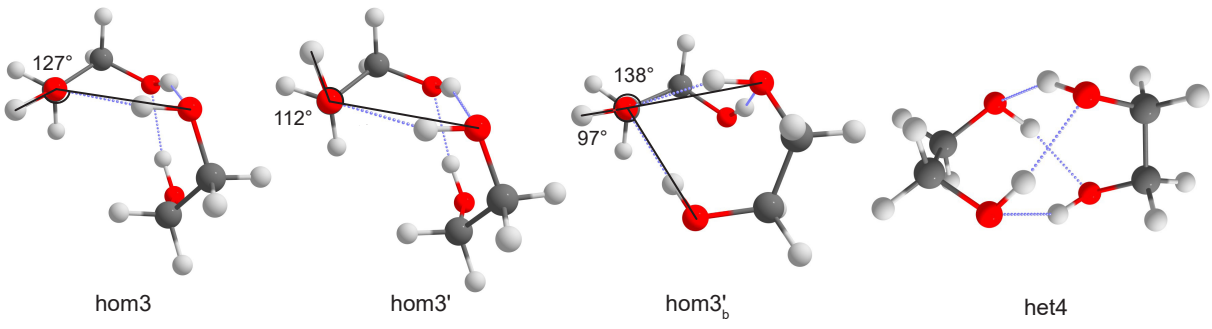

Fig. 2.8: Illustration of the nomenclature used for oligomers in this work. This figure is adapted from Ref. [101].

3 Benchmarking monomers

3.1 Vibrational data

All discussed assignments can be found in section C.1, comparing the experimental data to BP86/maTZ, PBE/maTZ, PBE0/maTZ and B3LYP/maTZ predictions. All relevant conformers are pictured in section A.1. The derived fitting constants can be found in chapter E.

3.1.1 Background

A recent publication by R. Medel and M. A. Suhm[31] showed that in case of alcohols (mono-ols) for OH-stretching modes a reliable model can be built by correlating theoretically calculated harmonic wavenumbers to experimental fundamentals, to predict yet unknown ones of the latter. The general idea of their analysis and conclusions will be briefly summarised here.

Medel and Suhm used a model of the form

$$\tilde{\nu}_l = \omega_l + \kappa \tag{3.1}$$

where ω_l is the computed harmonic wavenumber of the lth OH-stretching mode of the training set, κ an empirical anharmonic and electronic structure correction which is assumed to be constant and $\tilde{\nu}_l$ the resulting anharmonically corrected wavenumber. κ was derived from a training set taken from literature and tested with newly measured alcohols. The advantage of an additive model over a scaling model ($\omega_l + \kappa$ *vs.* $\lambda \cdot \omega_l$) is its physical interpretability, *i.e.* it can be seen as the sum of the diagonal ($x_{i,i}$) and off-diagonal anharmonicity ($x_{i,j}$) for fundamental OH-stretch transitions, as a comparison with Eq. 3.2[167] shows. This assumes that the anharmonicity is not strongly dependent on the

specific monool and κ also absorbs any systematic harmonic theory error. Additionally, it was found that the scaling model tends to perform slightly worse.

$$\tilde{\nu}_i = \omega_i + 2x_{i,i} + \frac{1}{2}\sum_{j\neq i}^{n} x_{i,j} \tag{3.2}$$

Given that the off-diagonal components are generally small and often largely compensate each other in case of OH stretching vibrations of alcohols[168,169], one may also reduce Eq. 3.2 to the simple diatomic case shown in Eq. 3.3[170]

$$\tilde{\nu}_i = \omega_i - 2\omega_\mathrm{e}x_\mathrm{e} \tag{3.3}$$

Medel and Suhms study included the commonly used B3LYP-D3(BJ) and PBE0-D3(BJ) density functionals, as well as the SCS-LMP2, LCCSD(T*)-F12a and CCSD(T)-F12a (1D OH stretching local modes)[169] wave function based methods. For B3LYP-D3(BJ) a strong dependence of κ was found upon the degree of substitution (n_D), decreasing (more negative) as n_D increases, with secondary and tertiary alcohols being only marginally separated. A similar but attenuated behaviour can be found for PBE0-D3(BJ) but with better predictive capabilities. Curiously, a new fitting strategy has to be used for SCS-LMP2. Again a dependence upon n_D is found, however, additionally separate fits for *gauche* and *trans* conformers are necessary. This dependence persists for LCCSD(T*)-F12a to a lesser degree and almost vanishes for CCSD(T)-F12a. The very uniform behaviour of CCSD(T)-F12a can at least be partially attributed to the fact that applying a harmonic model[a] to their 1D calculations includes some anharmonic contributions by construction. Specifically, this is due to the non-linear nature of the transformation from a harmonic frequency calculation involving all modes to the reduced 1D or any reduced dimensionality case[171].

Overall, PBE0-D3(BJ) is recommended since it yields reliable results at low computational cost. However, it was noted that when the derived model was tested against systems including π, N, O, F and Cl as acceptors it fails. The following sections deal with the development of an analogous model derived from and to be used for diols involving weak intramolecular hydrogen bonds/contacts, using B3LYP-D3(BJ,abc), PBE0-D3(BJ,abc), PBE-D3(BJ,abc) and BP86(BJ,abc). In their testing, Medel and Suhm already found indications that B3LYP works well for the description of ethane-1,2-diol and *trans*-cyclohexane-1,2-diol[31]. Besides the explicit inclusion of hydrogen bonding in

[a] Calculated from Vogt *et al.*[169] anharmonic 1D calculations by using their reported fundamentals ($\tilde{\nu}_\mathsf{F}$) and first overtones ($\tilde{\nu}_\mathsf{O}$), *i.e.* $\omega = 3\tilde{\nu}_\mathsf{F} - \tilde{\nu}_\mathsf{O}$. It was found that including higher order overtones has a negligible effect.[31]

the model, the substitution patterns also become more complex even leading to the same n_D but to a different local pattern in one instance (see Fig. 2.5). The results of this analysis have largely been published in Ref. [165] and will not be explicitly cited. Parts of the computed geometries at the B3LYP/maTZ level of computation have been published in Ref. [172]. The experimental Raman spectra in the 3560 cm^{-1} – 3700 cm^{-1} range have been published in Refs. [173] and [174].

3.1.2 Initial assignments

The symmetrical diols ethane-1,2-diol (0-0)[18,166], cyclohexanediol-1,2-diol (t6-6)[166] and pinacol (MM-MM)[165] lend themselves to initial fits since their assignment is unambiguous given the fact that only two conformers are energetically relevant, as the energy diagrams at the B3LYP/maTZ level of theory in Fig. 3.1 show. In this scheme, the diagonal elements give the zero point corrected energies relative to the global minimum (bottom left) and the off-diagonal elements correspond to barriers. The barriers are always given from the perspective of the less stable conformer. A row in the energy matrix corresponds to pathways away from the conformer while columns indicate pathways towards the conformer. The calculated barriers are quite small and very similar for the three systems. Hence, it is expected that the primed conformers should relax to the more stable unprimed case under jet conditions. This is illustrated by the angled arrows in Fig. 3.1. From experience and the results of Ruoff *et al.*[35], a relaxation threshold can be roughly put at 5 kJ mol^{-1}. The corresponding minima are shown in Figs. A.6 (page 224), A.17 (page 232) and A.22 (page 234) respectively.

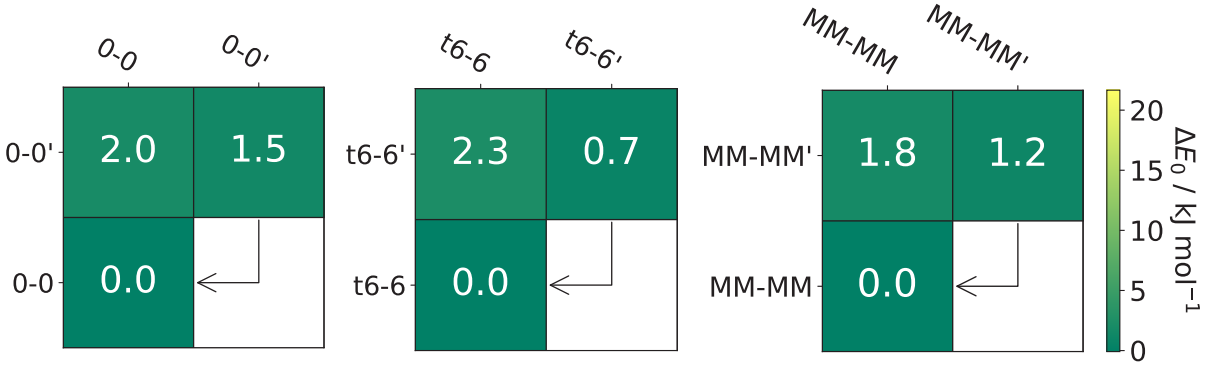

Fig. 3.1: Zero-point corrected energies as well as the corresponding barriers for ethane-1,2-diol (0-0), cyclohexane-1,2-diol (t6-6) and pincaol (MM-MM) at the B3LYP/maTZ level of computation. Barriers are given relative to the less stable conformer. The angled arrows indicate barriers that are feasible (< 5 kJ mol^{-1}) to be overcome in a jet expansion. This figure is adopted from Ref. [165].

In case of 0-0, a plethora of energetic data is available[165,166,175–183] and a comparison can be found in Tab. B.1 (page 241). The data is largely consistent with respect to the energetic order and ranges from 0.3 – 2.8 kJ mol^{-1} in favour of 0-0 over 0-0'. Paoloni *et al.* also provide computations for the conversion barrier, which are in line with those shown in Fig. 3.1. It also becomes apparent that the GGAs (BP86 and PBE) predict the primed - unprimed conformers energy splitting to be smaller in comparison to the hybrid functionals, which will emerge as a general trend for all studied systems. Similar trends can be found when comparing the computational data[165,166,184–186] for t6-6 as can be seen in Tab. B.11 (page 251), with the difference that the energetic order for the GGAs is reversed for this diol. The energetic trends for the GGAs closely resemble those of t6-6 in case of MM-MM (*cf.* Tab. B.17). Besides BP86, all methods[165,187–189] agree in terms of the energetic order of the MM-MM and MM-MM' conformers, although PBE predicts MM-MM to be more stable only after zero point correction. Olschweski *et al.*[188] also provide a conversion barrier which again is in line with the one shown in Fig. 3.1. For all three systems, where electronic energies as well as zero point corrected ones are available for a given method, it can be found that the unprimed conformer becomes less unfavourable when considering zero point energy.

In Fig. 3.2, the experimental Raman spectra are shown in comparison to the B3LYP/maTZ simulations. The simulations are Boltzmann weighted using the nozzle temperature (T_N) as the conformational temperature and the relative energies from Fig. 3.1. If barriers are sufficiently high (> 10 kJ mol^{-1}), the predicted energies and intensities are accurate as well as the partition functions of the isomers similar enough, one would expect a match with the experimental relative intensities. However, error compensation between the energies and intensities may still lead to a match despite the fact that they are inaccurate. As previously mentioned, relaxation towards the more stable unprimed conformers is expected for the three diols. A comparison of the simulated intensities and the experimental ones allows for an estimation of a shrinking factor for bands of the primed conformers that do not overlap (*cf.* arrows in Fig. 3.2 (page 33)), in line with a small barrier. Furthermore, the addition of different Ar concentrations to the He expansion in case of t6-6 clearly illustrates the relaxation. Therefore, it can be concluded that the energetic predictions for t6-6 of the GGAs are qualitatively wrong. Overall, the scaled predictions match the experiment quite well, with the needed scaling factor decreasing slightly with an increase of n_D which may be due to DFT deficiencies or anharmonicity.

In case of t6-6, the jet data can also be compared to anharmonic calculations by Barone and co-workers[186]. They used a Local-Mode (LM) approach as well as VPT2 (Vibrational Perturbation Theory of Second Order) to simulate IR and VCD spectra in solution where the PCM (Polarizable Continuum Model)[190] was used for all modes except XH stretching

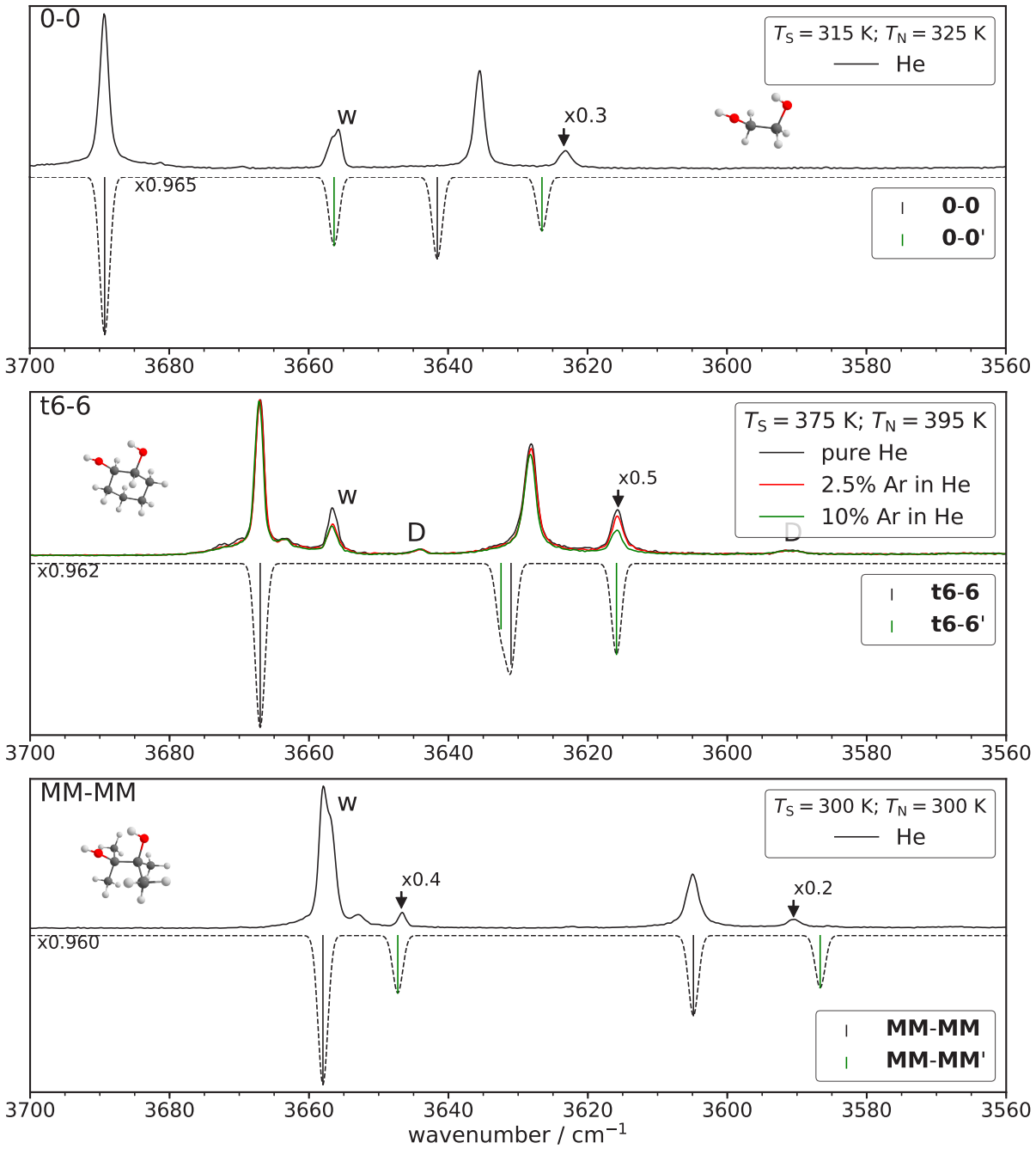

Fig. 3.2: This figure was adapted from Ref. [165]. Experimental data (plotted upwards) and simulated data (plotted downwards) of ethanediol (0-0)[166], *trans*-cyclohexanediol (t6-6)[166] and pinacol (MM-MM)[165]. In case of t6-6, different mixtures of He and Ar were used to investigate the relaxation behaviour. The saturator temperature (T_S) as well as the nozzle temperature (T_N) are given. The simulated spectra are based on B3LYP/maTZ and are Boltzmann weighted based on T_N according to the relative energies given in Fig. 3.1. Scaling factors are based on the free OH stretching vibration of the unprimed species. The shrinking factors (arrows) are based on a comparison of the experimental and predicted intensities for the primed conformers that do not overlap. w indicates a water band or overlap with one and D bands due to dimers.

modes. A comparison of their data with the results of the Raman spectrum can be found in Tab. 3.1. It can be seen that the LM approach works considerably better and shows a somewhat uniform downshift relative to the experiment, whereas VPT2 significantly underestimates the band positions in a less systematic manner.

These three diols illustrate the importance of jet data for benchmarking since computations commonly assume 0 K and the isolated gas phase. Fig. 3.3 shows a comparison of available data from solution[185,187,188,191–204], gas phase[183,187,205] and matrix IR-spectroscopy[187,199,206–209] in comparison to jet data[18,165,166]. Specifically, the intramolecular hydrogen bond shift (difference of the free OH mode relative to the bound) as well as the year of publication are shown. The corresponding shifts can be found in Tabs. C.4 (page 261) for 0-0, C.16 (page 269) for t6-6 and C.22 (page 272) for MM-MM.

In case of data in solution, differentiation between primed and unprimed conformers is not possible and even matrix data may not be able to unambiguously assign both conformers. For instance, Günthard and co-workers were not able to assign 0-0/0-0', with the energetic order still remaining unclear at that point in time based on their Ar and Xe matrix FTIR data[206,207]. Later studies by Tasumi and co-workers also using Ar matrix FTIR spectroscopy[208,209] were able to resolve this issue, with microwave data further corroborating that the unprimed conformer is more stable[178,210–213]. However, their 1991 study[209] with more accurate FTIR measurements fits the jet data worse, with the unprimed shift being too small and the primed one fitting very well. This indicates that matrix effects are not uniform and one should be very cautious when comparing to

Tab. 3.1: Comparison of the experimental wavenumbers[166] and the anharmonic calculations of Barone and co-workers[186] for *trans*-cyclohexane-1,2-diol (t6-6). $\tilde{\nu}_{\mathrm{LM}}$ are based on a Local-Mode approach and $\tilde{\nu}_{\mathrm{VPT2}}$ on Vibrational Perturbation Theory of Second Order. The Local-Mode approach was conducted at the B3LYP/TZVP level of theory while a composite scheme was used for VPT2 where the harmonic force fields are computed at the B2PLYP-D3(BJ)/jun-cc-pVTZ level and the anharmonic force fields are computed at the B3LYP-D3(BJ)/jul-cc-pVTZ level of theory. The differences (theory − experiment) of the anharmonic calculations ($\Delta\tilde{\nu}_{\mathrm{LM}}/\Delta\tilde{\nu}_{\mathrm{VPT2}}$) are also given. The indices used for the band are assigned in ascending order with regards to the frequency. All values are given in cm^{-1}. This table was adapted from Ref. [165].

	Jet-Raman[166]	$\tilde{\nu}_{\mathrm{LM}}$[186]	$\Delta\tilde{\nu}_{\mathrm{LM}}$	$\tilde{\nu}_{\mathrm{VPT2}}$[186]	$\Delta\tilde{\nu}_{\mathrm{VPT2}}$
t6-6$_1$	3628	3620.2	−7.8	3602.3	−25.7
t6-6$_2$	3667	3660.5	−6.5	3651.7	−15.3
t6-6$_1'$	3616	3603.4	−12.6	3580.5	−35.5
t6-6$_2'$	3628	3622.5	−5.5	3602.1	−25.9

predictions for the isolated gas phase. It can also be seen that B3LYP predicts these shifts quite well with PBE0 still performing reasonably well while PBE and by proxy BP86 overestimate the shifts significantly. The gas phase value is somewhat close to the jet value for the most stable conformer but cannot distinguish between 0-0 and 0-0'. Data in solution, on the other hand, differs significantly from the most stable species.

For t6-6, the shifts predicted in solution and in the matrix fit to the jet data fairly well as does the B3LYP prediction for the most stable conformer. One may assume that solution and matrix data can be used for benchmarking. However, the previous example shows that this is not the case. It can also be seen that B3LYP yet again fits best to the

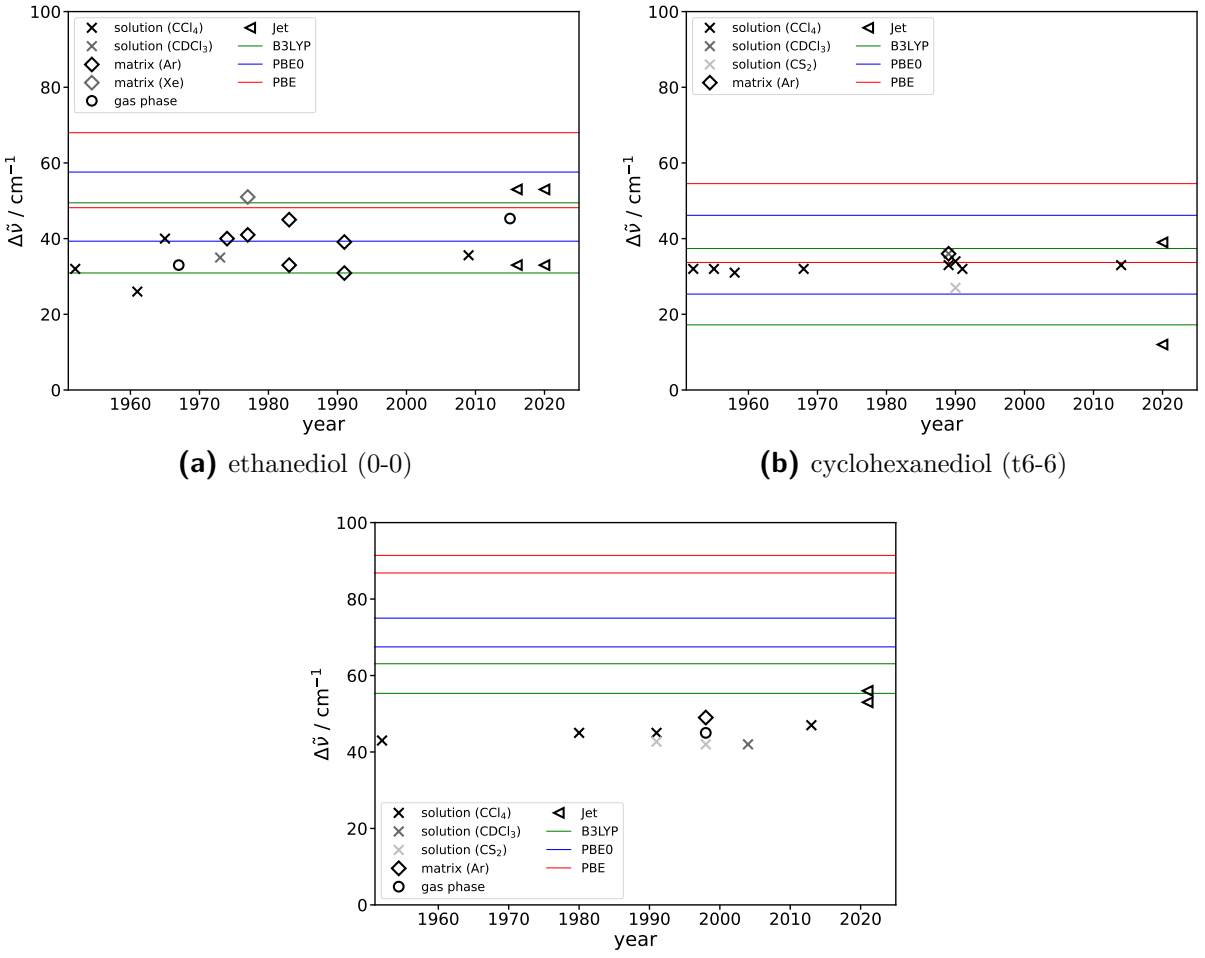

(a) ethanediol (0-0)

(b) cyclohexanediol (t6-6)

(c) pinacol (MM-MM)

Fig. 3.3: Comparison of the intramolecular hydrogen bond shifts ($\Delta\tilde{\nu}$) from literature (with year of publication) to the theoretical predictions at the B3LYP/maTZ, PBE0/maTZ and PBE/maTZ level. Since BP86/maTZ behaves very similar to PBE/maTZ it is not shown. In case of 0-0 and t6-6 the lower lines represent the primed shifts and the upper the unprimed shift while the opposite is the case for MM-MM.

experimental jet data. Furthermore, the matrix spectra could not properly resolve the two conformers, hence a peak average was used in this case.

MM-MM is another example showing that data in solution underestimates the hydrogen bond shifts in comparison to theory as well as jet measurements. Unique to pinacol even the conformer with the lower shift (here the more stable MM-MM conformer) is not covered by solution, matrix and gas phase data. Additionally, only the most stable conformer could be observed in the matrix[187] but does not differ significantly from the jet value. Overall, no clear trend emerges which could be used to empirically account for environmental effects substantiating the need for jet data.

Looking at the absolute wavenumbers provided in Tabs. C.4 (page 261), C.16 (page 269) and C.22 (page 272), it can be seen that a general downshift can be found for the solution, matrix and jet data while n_D increases. This behaviour is well known for mono-ols when going from primary to secondary to tertiary alcohols[31,214,215], although substitution patterns in diols can become much more complex as will be discussed later.

3.1.3 Model building and interpretation

In analogy to Eq. 3.3 the following formalism is used

$$\tilde{\nu}_i = h\omega_i - a2 \tag{3.4}$$

where h is an additional scaling parameter and $a2$ the anharmonic correction. Ideally, $h = 1$, as was the case throughout Ref. [31], and $a2$ equals about $175(15)\,\mathrm{cm}^{-1}$ in case of free and weakly hydrogen bonded OH groups[216]. In practice, h and $a2$ are highly correlated, hence the 12 assigned bands are fit freely. h is then frozen for subsequent individual n_D-dependent fits. For the n_D-dependent fits, h is rounded off at two decimal places since the particular value is not very significant given the parameter correlation. The exemplary covariance matrices in Tab. E.2 (page 295) illustrate this behaviour.

Fig. 3.4a shows a comparison of fits assuming that $h = 1$ at the B3LYP and PBE0 levels of theory. It is apparent that when $h = 1$, B3LYP fits quite well to the data. A continuous increase of $a2$ with n_D is also noticeable. This has previously been found for mono-ols as well[31]. However, in case of PBE0 the fits perform significantly worse as can be seen through the higher standard deviations (σ), especially for MM-MM.

This demonstrates the need for an adjustable h when intramolecular hydrogen bonds are introduced. Adjusting h reflects the systematic overestimation of hydrogen bond shifts

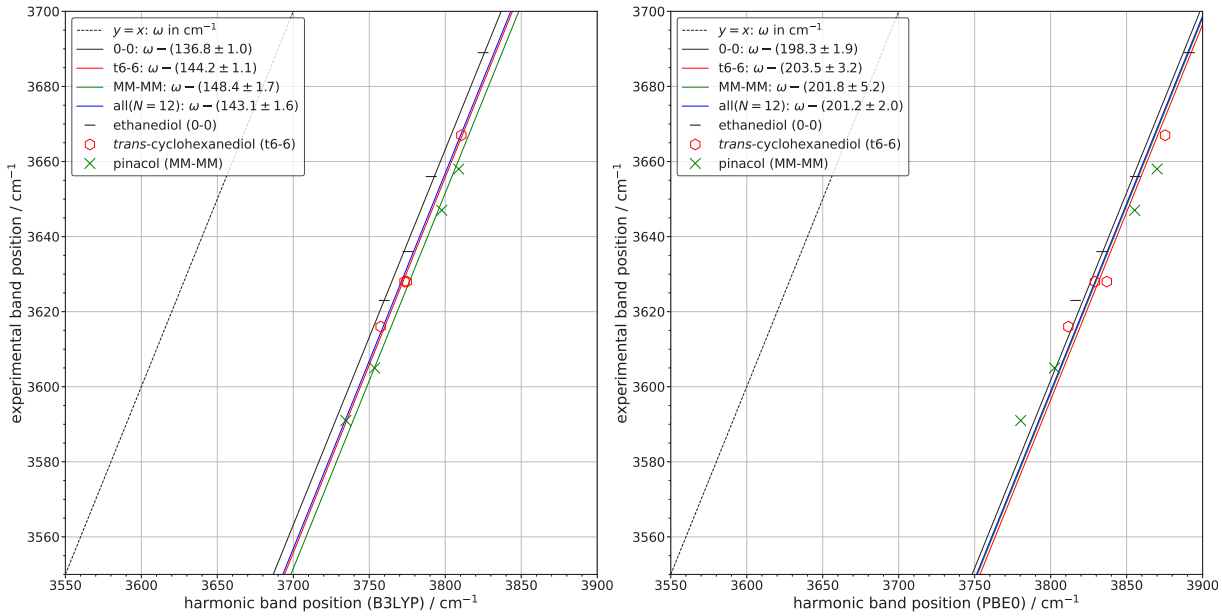

(a) $h = 1$ fit

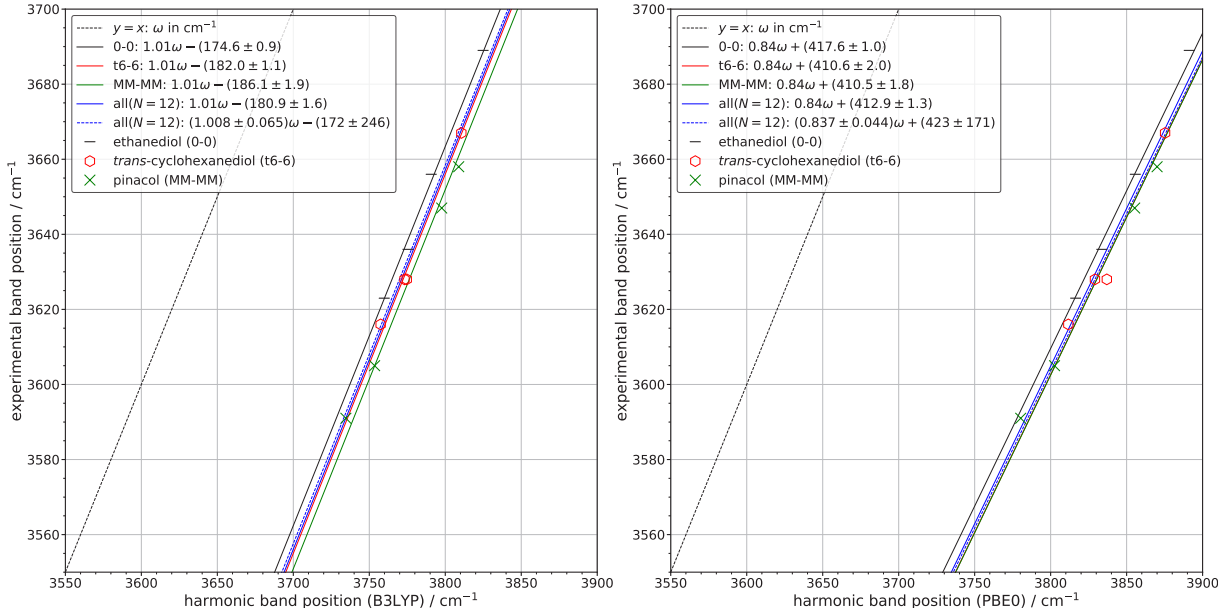

(b) free parameter fit

Fig. 3.4: The fits with $h = 1$ and the free parameter fits for ethanediol (0-0), cyclohexanediol (t6-6) and pinacol (MM-MM) are shown at the B3LYP/maTZ and PBE0/maTZ level of theory. The standard deviations (σ) as well as the number of included data points (N) are shown. The figures are adapted from Ref. [165]

(see Fig. 3.3). Additionally, as was the case for the mono-ols, PBE0 shows a smaller or no significant dependence on n_D[31] than B3LYP does (keeping in mind the small sample size considered up to this point).

In Fig. 3.4b, the results with the method initially described in this section are shown

for B3LYP and PBE0. In comparison to the fixed $h = 1$ scenario, only a very slight adjustment is necessary for B3LYP with the fit quality being very similar between each approach. However, $|a2|$ now closely resembles the doubled diagonal anharmonic constant of mono-ols[216]. The fact that some upscaling is necessary can be interpreted as B3LYP predicting slightly too soft OH bonds. The previously found increase of $a2$ with n_D is still present. For PBE0 on the other hand, a significant diversion from $h = 1$ is observed with $h \approx 0.84$, indicating that the hydrogen bond shifts are being overestimated. Playing into this is likely the common phenomenon that PBE0 predicts OH bonds that are too stiff. Additionally, PBE0 tends to overestimate wavenumber lowering in electron-rich regions such as hydrogen bonded environments. Furthermore, $a2$ now exhibits physically unreasonable values ($a2 < 0$) due to the adjusted h, but the fits perform significantly better than the $h = 1$ ones as indicated by the smaller value of σ. In analogy to the mono-ols, it can again be found that PBE0 behaves rather independently from n_D[31].

Fig. 3.5 shows the results for BP86 and PBE. Here, the behaviour previously found with PBE0 is even more exacerbated with h being about ⅔ and $a2$ exceeding $-1000\,\mathrm{cm}^{-1}$ (more negative). This indicates that the GGAs are far too sensitive with regards to hydrogen bond interactions, assuming a roughly constant anharmonicity. They may still yield reasonable predictions. However, any success of these methods is purely due to empirical fitting and no longer based on physically reasonable assumptions. Hence, the

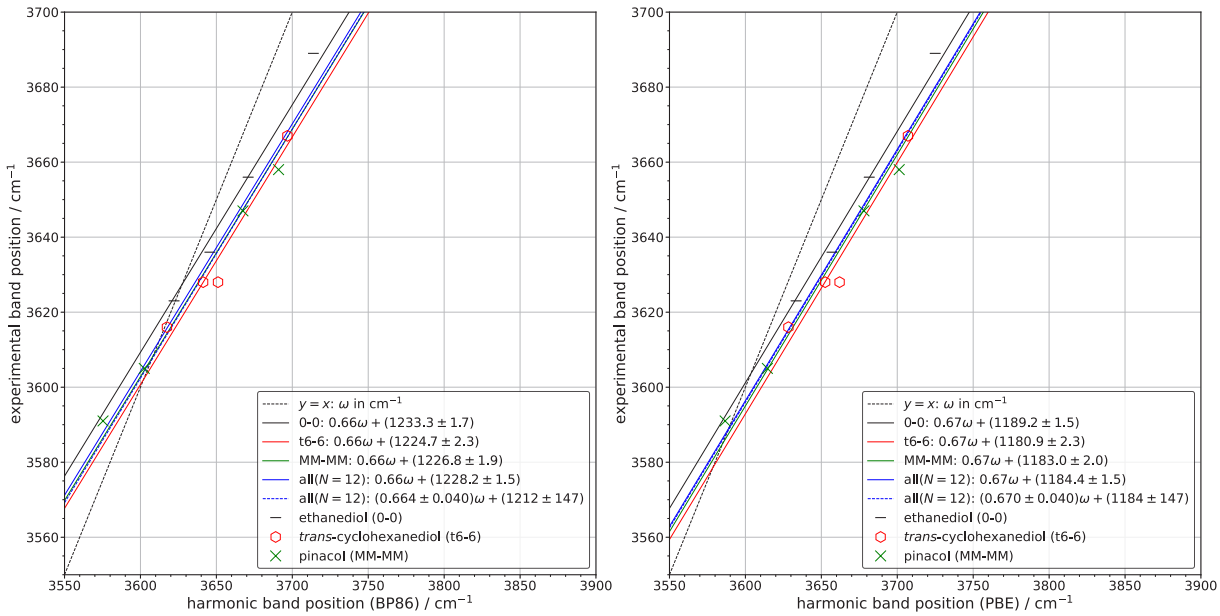

Fig. 3.5: Free parameter fits for ethanediol (0-0), cyclohexanediol (t6-6) and pinacol (MM-MM) are shown at the BP86/maTZ and PBE/maTZ levels of theory. The standard deviations (σ) as well as the number of included data points (N) are shown. This figure is taken from Ref. [165]

focus of the investigation will be on the two hybrid functionals.

3.1.4 Methyl substitution and model testing

As previously mentioned, diols provide an increased complexity in terms of substitution in comparison to mono-ols. Specifically propane-1,2-diol (0-M, $n_D = 1$) and 2-methyl-butane-2,3-diol (M-MM, $n_D = 3$) complete the series, providing a fit for $n_D = 0$ – 4. Additionally, for $n_D = 2$, two differing local substitutions are possible, *i.e.* a secondary-secondary substitution with *rac*-butane-2,3-diol (rM-M) as a test case and tertiary-primary with 2-methyl-propane-1,2-diol (0-MM) as a test case. In this section, these aspects will be discussed starting with the completion of the n_D series.

Fig. 3.6 shows the energetic landscape of 0-M (left) which is considerably more complicated than the ones discussed in section 3.1.2 given that 8 conformers can be found within 5 kJ mol^{-1}. It can be seen that the two most stable conformers are predicted to be approximately isoenergetic. Hence, despite the low barrier between them, both are expected to be present in the expansion. An analogous behaviour is expected for the conversion of 0-M' to 0-M. However, no additional conformers are expected to convert to 0-M' as is predicted for 0-Ma'. Therefore, the 0-M/0-M' and 0-Ma/0-Ma' pairs form a family of conformers that can interconvert to a certain extent. Similarly, the 0-Mb/0-Mb' and 0-Mc/0-Mc' conformers form another family that are expected to relax in the same

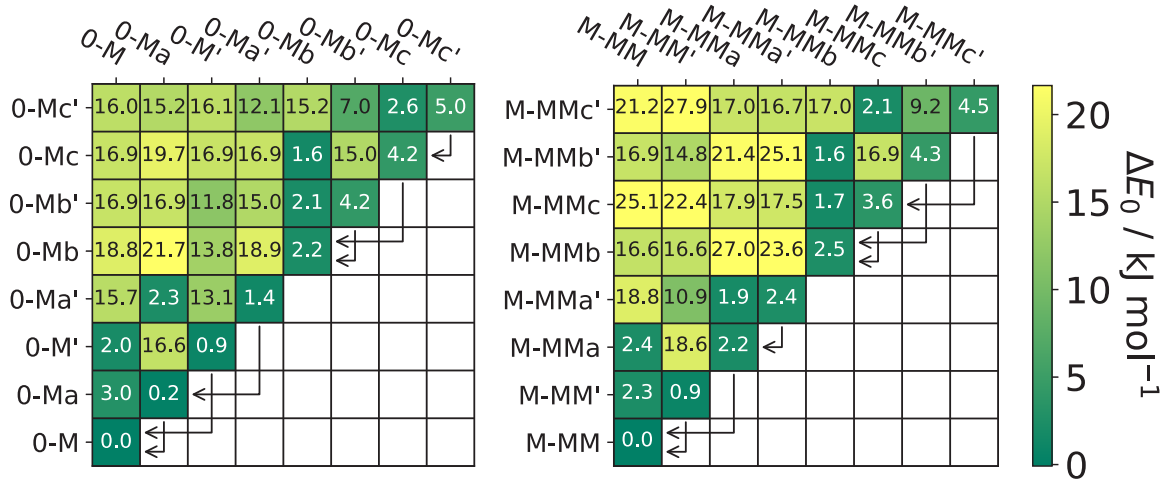

Fig. 3.6: Zero-point corrected energies as well as the corresponding barriers for propane-1,2-diol (0-M) and 2-methyl-butane-2,3-diol (M-MM) at the B3LYP/maTZ level of computation. Barriers are given relative to the less stable conformer. The angled arrows indicate barriers that are feasible (< 5 kJ mol^{-1}) to be overcome in a jet expansion. This figure is adapted from Ref. [165].

pattern as the previously mentioned one. Generally, relaxation is to be expected for all primed/unprimed pairs found within this section. The corresponding structures can be found in Fig. A.7 (page 225).

Since 0-M is of special interest to astrochemistry[217–220], given that its "smaller brother" 0-0 has been detected in space[221,222], a considerable amount of computational data exists for this compound. A comparison of such data[165,184,217,220,223–225] can be found in Tab. B.2 (page 243). The computations largely agree with each other except BP86, PBE and HF. As was the case previously, the two GGAs predict primed species to be more stable and even predict 0-M' to be the most stable conformer. HF on the other hand appears to predict primed species significantly higher in energy than the hybrid functionals and MP2 do. Furthermore, the described relaxation behaviour is in line with the results of Lovas *et al.*[217].

Earlier FTIR measurements allowed for the assignments of 0-M, 0-Ma, 0-M', 0-Ma' and 0-Mb. It was found that the band intensity of 0-M and the sum of 0-Ma and 0-Mb are very similar, whereas 0-M' and 0-Ma' were less intense. Given the significant spectral overlap as well as some degree of rotational broadening still present in the jet[225], 0-M will be revisited by Raman jet spectroscopy. To disentangle the conformers, spectra with admixture of Ar were recorded, which are shown in Fig. 3.7, where a scaling factor is applied to computed results to match the free OH mode of the most stable conformer. The two most prominent bands can be assigned to 0-M since they do not change with an increasing Ar content in the expansion. Analogous behaviour is expected for 0-Mb as the most stable member of its conformational family. Therefore, the non-changing band around 3670 cm^{-1} can be assigned to 0-Mb. Furthermore, for 0-M', 0-Ma', 0-Mb' and 0-Mc', a quick reduction in intensity is expected since no conversion pathway leads to them, while the opposite is true for 0-Ma and 0-Mc and an attenuated decrease is expected. However, 0-Mc only profits from the rather small population of 0-Mc' and in practice should decrease quickly as well. Hence, the slowly decreasing band around 3670 cm^{-1} can be assigned to 0-Ma and the quickly decreasing band next to the most intense band to 0-Mc. Additionally, the quickly decreasing band around 3655 cm^{-1} is likely caused by 0-M' and the small band towards lower wavenumbers by 0-Mb'. The bound OH mode of 0-Mb likely overlaps with 0-Ma and 0-Ma' leading to a slow decrease in intensity upon adding Ar to the expansion. The band around 3610 cm^{-1} decreases quickly and therefore matches the expected behaviour of 0-M' and 0-Ma'. These observations are in line with the findings of Lovas *et al.*[217] and Arenas *et al.*[220], although the latter did not detect 0-Mb'. It can therefore be concluded that the energetic predictions of the GGAs are qualitatively wrong as was the case for t6-6.

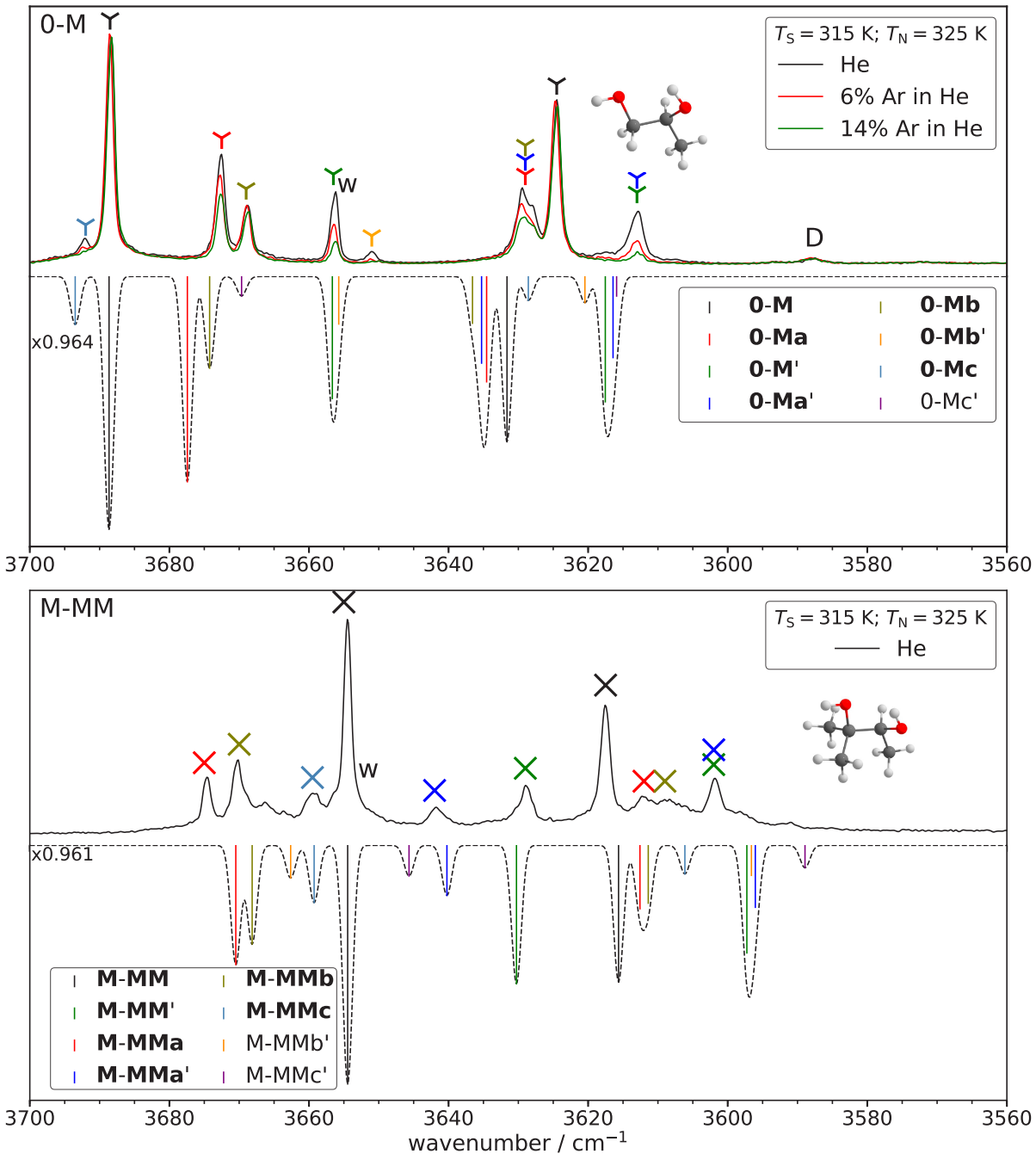

Fig. 3.7: This figure was adapted from Ref. [165]. Experimental data (plotted upwards) and simulated data (plotted downwards) of propane-1,2-diol (0-M) and 2-methyl-butane-2,3-diol (M-MM). In case of 0-M, different mixtures of He and Ar were used to investigate the relaxation behaviour. The saturator temperature (T_S) as well as the nozzle temperature (T_N) are given. The simulated spectra are based on B3LYP/maTZ and are Boltzmann weighted based on T_N according to the relative energies given in Fig. 3.6. Scaling factors are based on the free OH stretching vibration of the unprimed species. w indicates a water band or overlap with one and D bands due to dimers.

The substitution pattern of 2-methyl-butane-2,3-diol (M-MM) has the same symmetry as 0-M. Therefore, they are expected to behave quite similar in terms of their conformational complexity as can be seen in Fig. 3.6. Some slight reshuffling in the energetic order can be observed but most notably a strong preference for conformers where the donor OH group points towards the higher substituted side can be found, in line with the preference in mixed mono-ol dimers[226]. In case of 0-M, the 0 side is preferred as acceptor (0-M *vs.* 0-Ma) with around $0.2\,\mathrm{kJ\,mol^{-1}}$, whereas the MM side is preferred in M-MM (M-MM *vs.* M-MMa) with $2.2\,\mathrm{kJ\,mol^{-1}}$. However, the calculated barriers remain very similar and an analogous relaxation behaviour to 0-M is expected. A comparison of all computational data can be found in Tab. B.15 (page 254) where again the typical overestimation of the stability of primed conformers by GGAs can be observed. The corresponding structures can be found in Fig. A.20 (page 233).

Fig. 3.7 shows the spectrum of M-MM where a scaling factor is applied to the predictions in the same way as for 0-M. When looking at the scaling factors for the different n_D, a somewhat linear decrease for B3LYP can be found, *i.e.* 0-0: 0.965, 0-M: 0.964, t6-6: 0.962, M-MM: 0.961 and MM-MM: 0.960. However, it still remains unclear whether this is due to anharmonicity or intrinsic behaviour of B3LYP. The most stable conformer can yet again be easily identified due to its prominence in the spectrum. The free OH modes of M-MMa and M-MMb can be identified at similar positions as their 0-M counterparts. The lower abundance of M-MMa is in line with the expected relaxation behaviour as well. This is also the case for M-MM' and M-MMa', where the bound OH modes overlap again and can be found at a similar position as for 0-M. However, the free modes are shifted significantly in comparison to 0-M, where both do not overlap. The assignment of the rather broad bands around $3610\,\mathrm{cm^{-1}}$ is less clear. Given that B3LYP appears to underestimate the separation of M-MMa and M-MMb where the two can be distinguished, it is proposed that the two broad maxima are caused by these two conformers, likely further broadened by M-MMc. The free OH mode of can M-MMc can be found at slightly higher wavenumbers relative to the most prominent band similarly to 0-M.

The fact that the free OH modes of M-MM, M-MM' and M-MMc are strongly shifted in comparison to their 0-M counterparts, while the bound OH mode changes only slightly, due to the substitution occurring on the free OH mode side. The opposite can be found for M-MMa and M-MMb. Surprisingly, despite the fact that M-MMa' is substituted at the bound OH mode side, the free OH mode is shifted significantly. To illustrate this point, the differences between 0-M and M-MM conformers are shown in Tab. 3.2. The subscript 1 stands for a bound OH modes while 2 stands for a free OH mode. A positive sign indicates an upshift relative to M-MM and a negative sign a downshift. All functionals agree with the experimental results qualitatively. It also becomes immediately apparent

Tab. 3.2: Comparison of experimental and predicted shifts between 0-M conformers and the corresponding M-MM conformers. Positive signs indicate that the 0-M conformer is at higher wavenumbers while negative signs indicate that it is at lower ones. All values are given in cm^{-1}.

	Jet-Raman	BP86/maTZ	PBE/maTZ	PBE0/maTZ	B3LYP/maTZ
0-M_1	8	12.02	10.98	7.93	4.69
0-M_2	33	29.89	30.75	27.72	23.45
0-Ma_1	17	21.04	20.78	15.36	10.91
0-Ma_2	−2	−5.15	−5.19	−4.24	−4.87
0-M_1'	11	19.31	18.17	13.43	9.21
0-M_2'	27	20.21	19.79	19.64	15.43
0-Ma_1'	11	17.45	17.61	13.74	9.32
0-Ma_2'	−13	−13.26	−12.99	−14.21	−17.12
0-Mb_1	20	26.23	26.12	18.95	14.25
0-Mb_2	−1	−4.14	−4.00	−4.34	−5.74
0-Mb_1'	-	22.23	22.29	17.54	12.92
0-Mb_2'	-	−11.78	−11.90	−14.74	−19.19
0-Mc_1	-	22.82	21.95	15.78	11.41
0-Mc_2	33	29.58	30.37	27.30	23.48
0-Mc_1'	-	28.83	27.91	21.81	16.20
0-Mc_2'	-	16.73	16.52	15.90	12.90

that 0-Ma'/M-MMa' cannot be explained by the substitution side alone. Curiously, the system shifts are best predicted by PBE0 (MAD: 3.01 cm^{-1}) followed by PBE (MAD: 4.09 cm^{-1}), BP86 (MAD: 4.45 cm^{-1}) and B3LYP (MAD: 5.54 cm^{-1}). B3LYP consistently underestimates these shifts, while BP86 and PBE tend to overestimate for bound OH modes and underestimate for free OH modes. No clear pattern emerges for PBE0.

As previously mentioned, 2-methyl-propane-1,2-diol (0-MM) and *rac*-butane-2,3-diol (rM-M) are investigated to judge whether or not the fits depend upon a local difference in the substitution pattern. The latter also provides a first test for the derived secondary-secondary correlation. As can be seen from Fig. 3.8 (left) due to the symmetric substitution pattern the energetic landscape of rM-M is less complicated. The primed/unprimed pairs can easily convert to the more stable conformer as was the case for 0-M and M-MM, while rM-M/rM-M' and rM-Ma/rM-Ma' constitute non-interconverting families. rM-M* is expected to relax with effectively no barrier to rM-M. A comparison of available computational data[184,186,227–230] is shown in B.14 (page 253). The hybrid functional and MP2 results generally agree with each other concerning the energetic order with the excep-

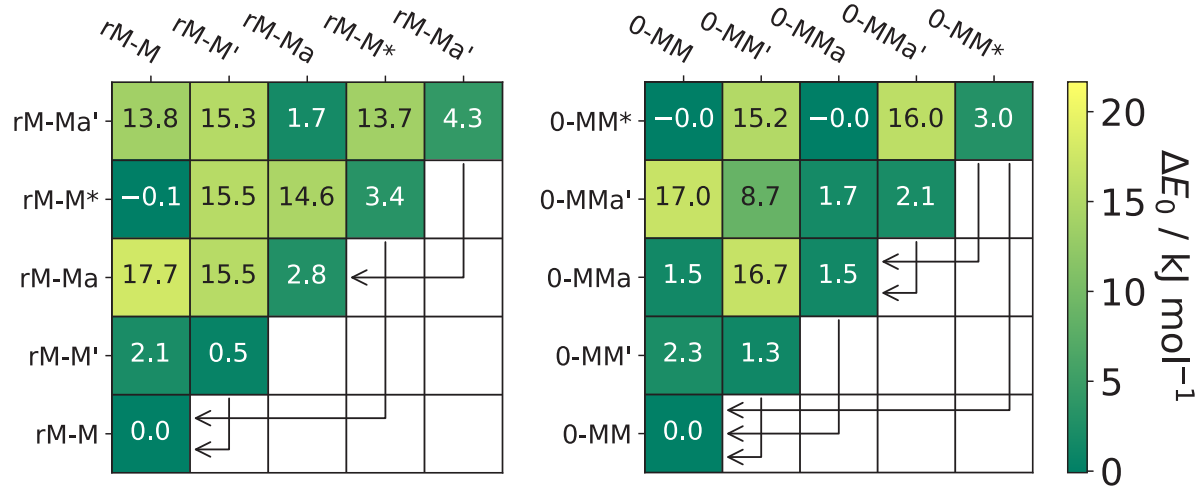

Fig. 3.8: Zero-point corrected energies as well as the corresponding barriers for 2-methyl-propane-1,2-diol (0-MM) and *rac*-butane-2,3-diol (rM-M) at the B3LYP/maTZ level of computation. Barriers are given relative to the less stable conformer. The angled arrows indicate barriers that are feasible (< 5 kJ mol^{-1}) to be overcome in a jet expansion. This figure is adapted from Fig. [165].

tion of the B3LYP/6-31G* results by Wang *et al.*[227]. As was found before, the GGAs overestimate the stability of primed conformers while HF underestimates their stability in comparison to the other results. Besides B3LYP, the rM-M* conformer is also to be a transition state. Furthermore, Paoloni *et al.* provide barriers which indicate the same relaxation behaviour as the one shown in Fig. 3.8.

The experimental results in comparison to the B3LYP predictions based on the derived $n_D = 2$ correlation are shown in Fig. 3.9. The simulations for rM-M and rM-Ma' fit quite well. For rM-Ma' the bound OH mode fits in intensity to the expected relaxation behaviour which indicates that rM-M* likely fully relaxes also overlapping with the bound mode of rM-Ma', assuming it is indeed a stable conformer. The free OH modes for rM-M' and rM-Ma are also well predicted, while the bound mode is underestimated for the former and overestimated for the latter. Based on these experimental results it can be concluded that the energetic ranking of the GGAs is qualitatively wrong as are the results by Wang *et al.*[227]. An FTIR matrix study in Ar and Xe by Jesus *et al.*[229] was able to assign rM-M and rM-Ma. A comparison of their data as well as anharmonic calculations by Barone and co-workers[186] can be found in Tab. 3.3. The matrix shifts can be up to 40 cm^{-1} and differ considerably between the different vibrations, again highlighting the importance of jet data. Additionally, more conformers survive in the expansion. The previously well performing Local-Mode approach for t6-6 (*cf.* Tab. 3.1) performs poorly with deviations of up to 86.9 cm^{-1} in magnitude. Frequencies are consistently predicted too low, however, the extent as to which varies greatly. Free OH modes appear to be less

Tab. 3.3: Comparison of experimental wavenumbers as well as FT-IR matrix[229] results and the anharmonic calculations of Barone and co-workers[186] for *rac*-butane-2,3-diol. $\tilde{\nu}_{\mathrm{LM}}$ are based on a Local-Mode approach and $\tilde{\nu}_{\mathrm{VPT2}}$ on Vibrational Perturbation Theory of Second Order. A more detailed explanation can be found in Tab. 3.1. The differences of the anharmonic calculations ($\Delta\tilde{\nu}_i$) relative to the jet data are also given. All values are given in cm^{-1}.

	Jet-Raman	FT-IR/Ar	FT-IR/Xe	$\tilde{\nu}_{\mathrm{LM}}$	$\Delta\tilde{\nu}_{\mathrm{LM}}$	$\tilde{\nu}_{\mathrm{VPT2}}$	$\Delta\tilde{\nu}_{\mathrm{VPT2}}$
rM-M_1	3622	3607	3597	3555.4	−66.6	3600.3	−21.7
rM-M_2	3673	3657	3640	3664.8	−8.2	3652.4	−20.6
rM-$M_1^{'}$	3607	-	-	3520.1	−86.9	3571.5	−35.5
rM-$M_2^{'}$	3630	-	-	3578.9	−51.1	3603.7	−26.3
rM-Ma_1	3610	3602	3587	3548.7	−61.3	3585.0	−25.0
rM-Ma_2	3673	3654	3633	3641.8	−31.2	3655.2	−17.5
rM-M_1^{*}	-	-	-	-	-	-	-
rM-M_2^{*}	-	-	-	-	-	-	-
rM-$Ma_1^{'}$	3598	-	-	3515.9	−82.1	3583.2	−14.8
rM-$Ma_2^{'}$	3661	-	-	3647.1	−13.9	3649.9	−11.1

affected which was also the case for t6-6. VPT2 also consistently underestimates the OH stretching frequencies but in a more uniform manner and over all performs better than the LM calculations. The range of these deviations also match those observed for t6-6.

2-Methyl-propane-1,2-diol (0-MM) behaves quite similar in terms of its energetic landscape, as Fig. 3.8 shows. The typical relaxation behaviour for unprimed/primed conformers can be found. However, unlike rM-M, 0-MM and 0-MMa no longer constitute non-converting families with 0-MMa being able to efficiently relax towards 0-MM. This is due to the fact that in case of rM-M the families are defined by a difference in their OCCO dihedral angle, while in case of 0-MM the difference arises from the free OH group pointing towards either the 0 or MM side. Hence, less movement of heavy atoms is required and the barrier is lower. 0-MM* is also expected to easily relax towards 0-MM and 0-MMa. A comparison with other computational data can be found in B.8 (page 249). 0-MM* is again in a special position since it is only stable at the B3LYP level of theory, while for PBE0, PBE and BP86 it reverts back to the 0-MM conformer. Given the low barriers at the B3LYP level it will not be considered for the assignments. The GGAs again overestimate the stability of primed conformers relative to the hybrid functionals. However, all functionals predict the same global minimum after zero point correction. As was found for M-MM, a preference for the MM side as an acceptor exists with about $1.5\,\mathrm{kJ\,mol^{-1}}$, being slightly lower than for M-MM ($2.2\,\mathrm{kJ\,mol^{-1}}$). However, this already constitutes a

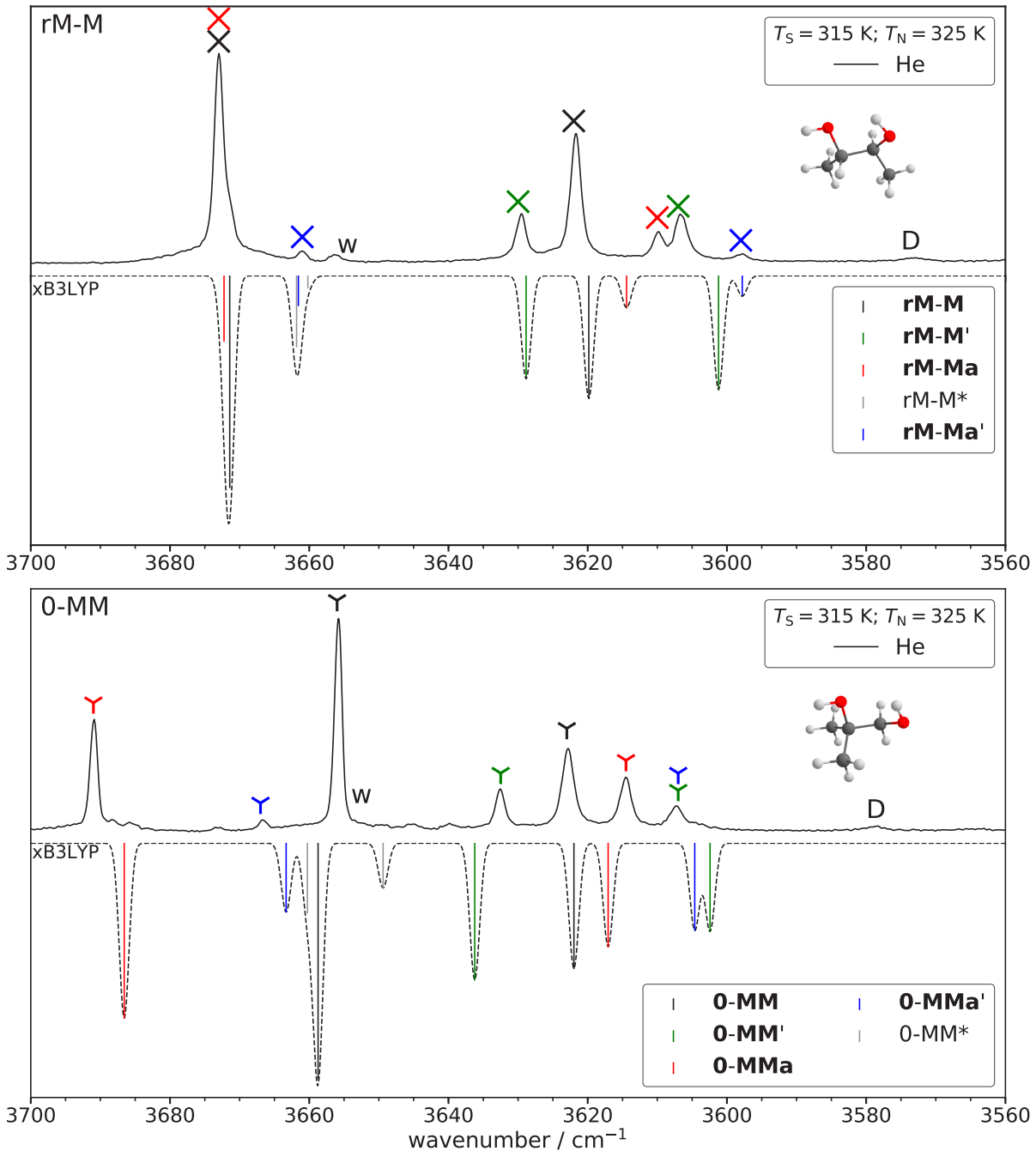

Fig. 3.9: This figure was adapted from Ref. [165]. Experimental data (plotted upwards) and simulated data (plotted downwards) of 2-methyl-propane-1,2-diol (0-MM) and *rac*-butane-2,3-diol (rM-M). In case of t6-6 different mixtures of He and Ar were used to investigate the relaxation behaviour. The saturator temperature (T_S) as well as the nozzle temperature (T_N) are given. The simulated spectra are based on B3LYP/maTZ (indicated by xB3LYP) and are Boltzmann weighted based on T_N according to the relative energies given in Fig. 3.8. The derived correlation ($n_D = 2$) for B3LYP was used for the predictions. w indicates a water band or overlap with one and D bands due to dimers.

significant change from 0-M where the 0 side was preferred by only $0.2\,\mathrm{kJ\,mol^{-1}}$. PBE0 closely corroborates these results.

Fig. 3.9 also shows the B3LYP predictions based on the $n_\mathrm{D} = 2$ correlation. Despite the different substitution pattern the predictions fit remarkably well. The general spectral signatures are very similar to rM-M, with the only major differences occurring for the free OH bands of rM-M and rM-Ma. The splitting between the free and bound OH modes of 0-MM' are again overestimated, whereas the splitting of rM-Ma is underestimated. The change in relaxation behaviour is also reflected in the experimental intensity of the band of 0-MMa. Unlike rM-Ma, the experimental intensities of 0-MMa are smaller than the simulated ones. The broader nature of the band at $3605\,\mathrm{cm^{-1}}$ can be attributed to an overlap of 0-MM' and 0-MMa'.

Some very similar spectral signatures cannot only be found between 0-MM and rM-M but also with M-MM in either case (*cf.* Figs. 3.9 and 3.7). By combining both modes of 0-MM and 0-MM'/rM-M', the bound modes of 0-MMa/rM-Ma and 0-MMa'/rM-Ma' as well as the free mode of rM-Ma, the spectrum of M-MM can be reproduced remarkably well excluding conformers that are not present for rM-M and 0-MM. A noticeable exception is the bound OH mode of M-MMa' which does not have a close equivalent and already showed an unusual behaviour for the system shift between 0-M and M-MM (*cf.* Tab. 3.2). Furthermore, the splitting between the two OH oscillators is also overestimated for M-MM' and underestimated for M-MMa. Moreover, the spectral similarities between 0-MM and rM-M are somewhat surprising since the structural motifs are not closely related (see Figs. A.13 (page 230) and A.14 (page 230)) unlike 0-M and M-MM. Major differences only occur for the free OH-mode of unprimed conformers. One could view this as a degeneracy in case of rM-M and rM-Ma that is lifted due to the different substitution pattern in case of 0-MM and 0-MMa. However, these changes would also apply to the primed species where no significant changes for either conformer can be observed. Hence, it might be the case that the substitution effects cancel with the different alignment of the intramolecular hydrogen bond.

3.1.5 Closing the training phase

Since the dataset now includes additional points for the all fit which may lead to changes of h, the analysis of section 3.1.3 is redone. The results for the GGAs are shown in Fig. 3.10 (top panels). For the GGAs, a small change of h to 0.66 can be found, still deviating from 1 significantly. In either case, the M-MM and MM-MM fits cluster closely together with the others still being substantially separated from each other.

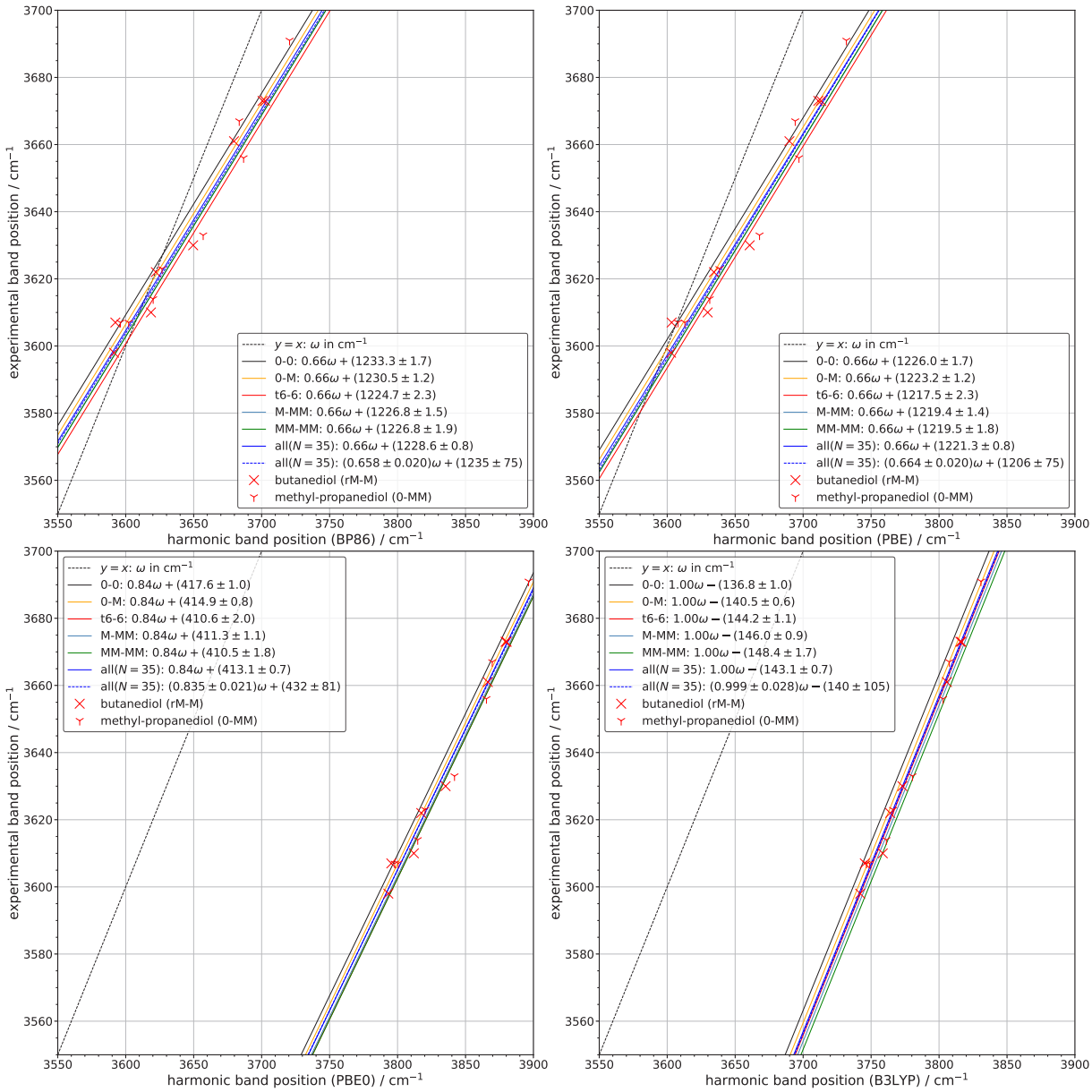

Fig. 3.10: Reevaluated free parameter fits for the systems discussed in sections 3.1.2 and 3.1.4 are shown at the BP86/maTZ, PBE/maTZ, PBE0/maTZ and B3LYP/maTZ level of theory. Only data points for the test sets are shown. The standard deviations (σ) as well as the number of included data points (N) are shown. This figure is adapted from Ref. [165].

With regards to the dependence upon differences in the local substitution pattern, the data points are found at higher experimental wavenumber than the t6-6 fits indicate. Fits for rM-M (BP86: $-1228.8(1.8)\,\mathrm{cm}^{-1}$; PBE: $-1221.5(1.8)\,\mathrm{cm}^{-1}$) and 0-MM (BP86: $-1228.8(2.2)\,\mathrm{cm}^{-1}$; PBE: $-1221.5(2.1)\,\mathrm{cm}^{-1}$) separately are very close to each other but differ considerably from the t6-6 fit. Hence, it appears that the GGAs overall do not follow any clear n_D dependence. The fits in general also perform worse than for the hybrid functionals but the all fit may still be adequate if the experimental band shifts are

significantly large.

Some slight changes can also be observed in h for the hybrid functionals shown in Fig. 3.10 (bottom right). In case of B3LYP, h now approaches 1 even more closely. The 0-M and M-MM data complements the n_D trend that was found for this functional, *i.e.* 0-M fits in between 0-0 and t6-6 while M-MM fits between t6-6 and MM-MM. Therefore, the decrease of $a2$ with an increase of n_D can be further substantiated. The data points for 0-MM and rM-M now closely cluster around the t6-6 fit. This can also be illustrated by individual fits yielding $143.4\,\mathrm{cm}^{-1}$ and $144.2\,\mathrm{cm}^{-1}$ for 0-MM and rM-M, respectively. Therefore, in case of B3LYP it can be concluded that n_D is a sufficient distinction while the local substitution pattern does not need to be included. This systematic behaviour of n_D can also be used to derive a more general correlation of the form $\tilde{\nu}_i = \omega_i - (137 + 3n_\mathrm{D})\ \mathrm{cm}^{-1}\ (\mathrm{all}(n_\mathrm{D}))$, which closely resembles the actual fits. Similar behaviour can be observed for alcohols (mono-ols)[31], where the separation between primary and tertiary alcohols amounts to $2 \times 3\,\mathrm{cm}^{-1}$. However, secondary alcohols more closely resemble tertiary ones. Although, there appears to be an underlying physicality for this behaviour, it is more likely that this is in fact an underlying deficiency of the functional itself[31]. Additionally, the implied anharmonicity ($a2$) of the OH group by the B3LYP model is expected to be larger, which is at least partially caused by the softer OH bonds computed with the maTZ basis set.

For PBE0, h does not change upon an increase of the training set (see Fig. 3.10, bottom left). It can be seen that 0-0 and t6-6 are relatively far apart from each other while t6-6, M-MM and MM-MM are in very close proximity to each other. Hence, the lower dependence of PBE0 upon n_D prevails in comparison to B3LYP, which is also indicated by the smaller error of the all fit. However, it is still possible to formulate a more general expression, *i.e.* $\tilde{\nu}_i = 0.84\omega_i + (411 + 3n_0)\ \mathrm{cm}^{-1}\ (\mathrm{all}(n_0))$, where n_0 it the amount of unsubstituted CH_2-groups in the diol unit *e.g.* 2 for 0-0, 1 for 0-M and 0 for t6-6.

Since the analysis is based upon frozen variants of the all fits their stability should be discussed. To this end leave one out fits are performed for the all fits from section 3.1.3 and this section, leading to 12 and 35 different fits, respectively. The results are shown in Fig. 3.11. It can be seen that the results for the initial fitting process show a very significant variance. In case of B3LYP, values below 1 can be found and some significantly higher making a clear assessment of the behaviour of said functional difficult. Previous statements made with regards to PBE0 also become somewhat doubtful. The improved fits, *i.e.* the extension of the training set, of this section cut the variance substantially, allowing for robust statements concerning the functionals. It is also a way of summarising the general behaviours of the functionals, with B3LYP remaining the most physically

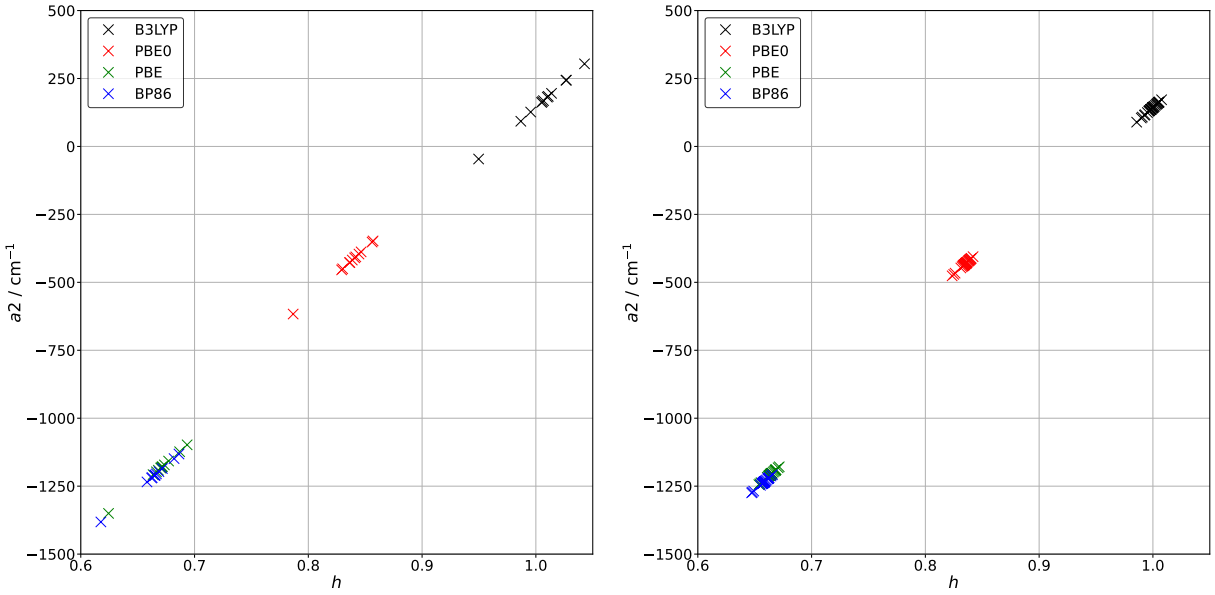

(a) section 3.1.3 **(b)** section 3.1.5

Fig. 3.11: The results of leave one out fits are shown for the all fits from section 3.1.3 and 3.1.5 for BP86, PBE, PBE0 and B3LYP.

reasonable functional followed by PBE0 and with a significant distance the GGAs. It can also be seen that BP86 and PBE behave very similar.

3.1.6 Influence of π and fluorine hydrogen contacts

As previously mentioned, the introduction of π or fluorine contacts did not lead to satisfactory results for the mono-ols. However, since the second OH group introduced with diols did not prove to be detrimental to the fitting strategy so far, the aforementioned contacts may also lead to moderately large deviations. To this end, but-3-ene-1,2-diol (0-V), 1-phenyl-ethane-1,2-diol (0-Ph) and 3,3,3-trifluoro-propane-1,2-diol will be analysed.

The energetic landscape of 0-V is shown in Fig. 3.12a and is highly complex with 9 conformers within $5\,\mathrm{kJ\,mol^{-1}}$, with all conformers being shown in A.9 (page 226). The previous commonality that primed and unprimed pairs can convert into the more stable variant no longer holds. Only a single conformer (0-Vd) is expected to strongly relax to the most stable structure (0-V). However, 0-Va' and 0-Vc' may partially convert to the 0-V conformer. For the second most stable species (0-Va), two conformers (0-Vc, 0-Va') are expected to easily relax towards it with partial contributions from 0-Vc'. Besides these conformers, only 0-Vb' is expected to easily convert to 0-Vc. Additionally, some partial

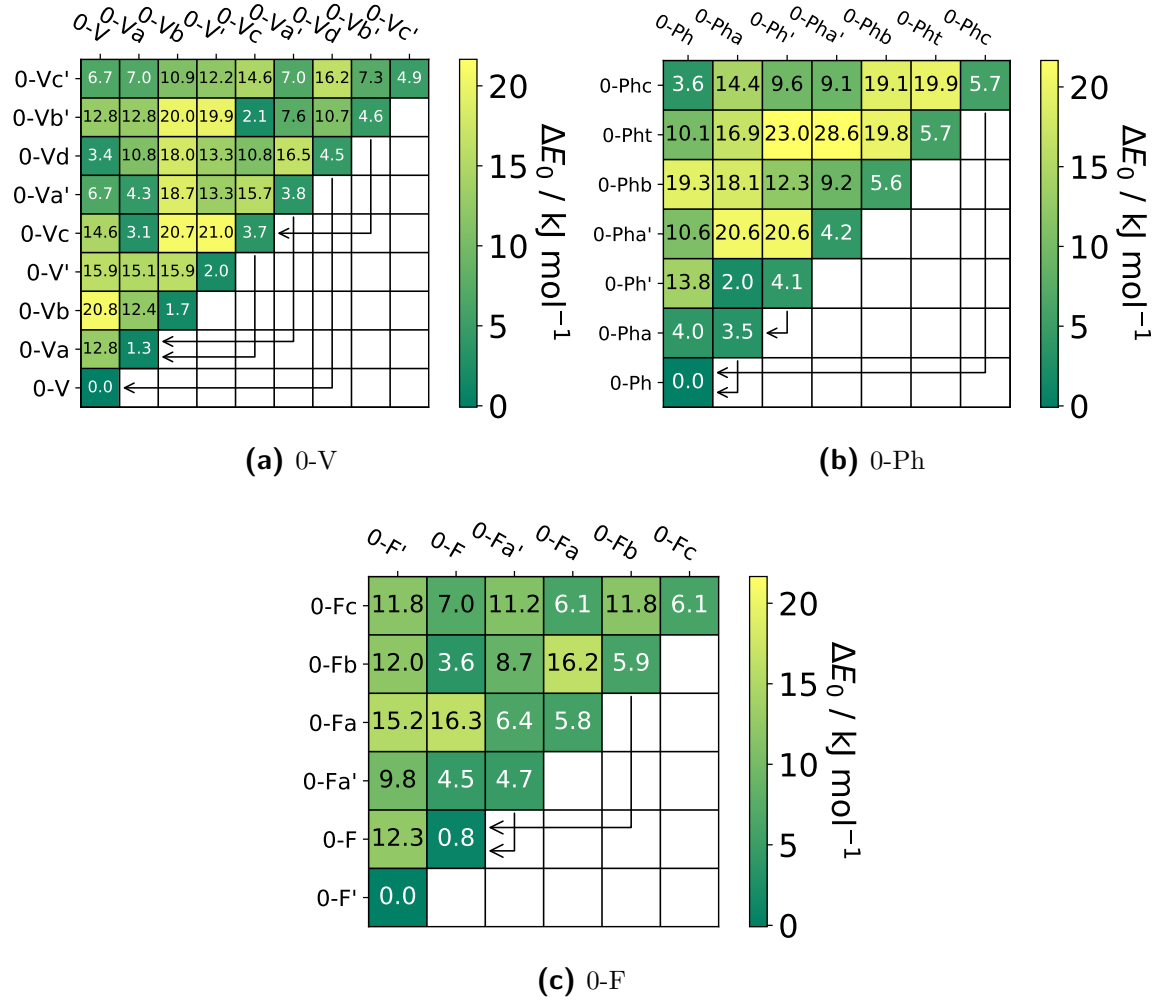

(a) 0-V **(b)** 0-Ph

(c) 0-F

Fig. 3.12: Zero-point corrected energies as well as the corresponding barriers for but-3-ene-1,2-diol (0-V), 1-phenyl-ethane-1,2-diol (0-Ph) and 3,3,3-trifluoro-propane-1,2-diol (0-F) at the B3LYP/maTZ level of computation. Barriers are given relative to the less stable conformer. The angled arrows indicate barriers that are feasible (< 5 kJ mol^{-1}) to be overcome in a jet expansion. This figure is adapted from Ref. [165].

relaxation of 0-Vc' and 0-Vb' to 0-Va' may take place, which is also the case for 0-Vc' to 0-Vb'. Hence, no significant deviations from the simulated intensities should occur for 0-V, 0-Va, 0-Vb and 0-Vc'. A comparison with other computational data can be found in Tab. B.4 (page 245). The usual stabilisation of primed conformers can be found for the GGAs relative to the hybrid functionals with the exception of 0-Vc'. Furthermore, the energetic order between the hybrid functionals now also differs considerably. Most notably 0-V and 0-V' are predicted almost isoenegetic by PBE0. 0-Vc' is also about 2 kJ mol^{-1} higher in energy for PBE0.

The experimental spectrum of 0-V is shown in Fig. 3.13. The two most prominent bands

can be assigned to the most stable conformer. The second most stable conformer can also be easily assigned with its free OH mode being slightly lower than 0-V while the bound mode is slightly higher. The non overlapping band also fits quite well to the predicted intensity, indicating that 0-Va does not relax as expected. The intensity of the band overlapping with 0-Vb on the other hand differs somewhat from the predicted intensity which can be attributed to the broader appearance of the band, with a significant shoulder towards lower wavenumbers. This appears to be also the case for the bound OH mode of 0-V which overlaps with 0-Vb and 0-Vc, where some lowering of the intensity is expected due to 0-Vc relaxing. That 0-Vc significantly relaxes can be further collaborated by the band around 3685 cm^{-1} that has a much lower experimental intensity. Furthermore, 0-Vd also overlaps with this band but is also expected to easily convert to more stable conformers. The band at 3610 cm^{-1} also has some contributions of 0-Vd with some possible overlap with 0-Va'. Lastly, 0-V' can be attributed to the remaining bands. The larger discrepancies to the experimental positions of 0-V' can be explained by the fact that the π-system is directly involved in the hydrogen bonding. Interestingly, the "free" OH mode that is making contact with the π-system is predicted more accurately than the bound OH (OH$\cdots$O) mode. Furthermore, considerably more mode coupling of the OH groups can be found for 0-V' likely contributing to the worse predictions. After the discussion of the results for 0-Ph this will be elaborated in more detail.

The energetics for 0-Ph can be found in Fig. 3.12b being less complicated than for 0-V, with all structures being shown in Fig. A.10 (page 227). Noticeably, a t conformer (anti-periplanar OCCO dihedral angle) is possibly relevant and the relative energies increase much quicker. Only limited efficient relaxation pathways exist, namely 0-Phc and 0-Pha are expected to convert to 0-Ph and 0-Ph' is expected to relax to 0-Pha. Given the steep energy increase following the most stable conformer significant relaxation is expected towards it, slightly counteracted by 0-Ph' replenishing some of the population of 0-Pha. A comparison with the computational results of Lomas[184] and others is shown in B.5 (page 246). A slight stabilisation of primed conformers can again be found for the GGAs although 0-Pha' is also predicted significantly more stable by PBE0/maTZ in comparison to B3LYP/maTZ. Otherwise, the hybrid functionals agree reasonably well with each other including the PBE0/6-311+G(d,p) of Lomas[184]. However, some energy differences are larger for the latter, possibly caused by missing dispersion correction or BSSE especially for the 0-Pht conformer.

The experimental results are shown in Fig. 3.13. To judge the relaxation behaviour different ad-mixtures of Ar are used. The two most intense bands can immediately be assigned to the most stable conformer. The two quickly decreasing bands at 3685 cm^{-1} and 3618 cm^{-1} can be assigned to 0-Pha, in line with its small predicted barrier. Similarly, the

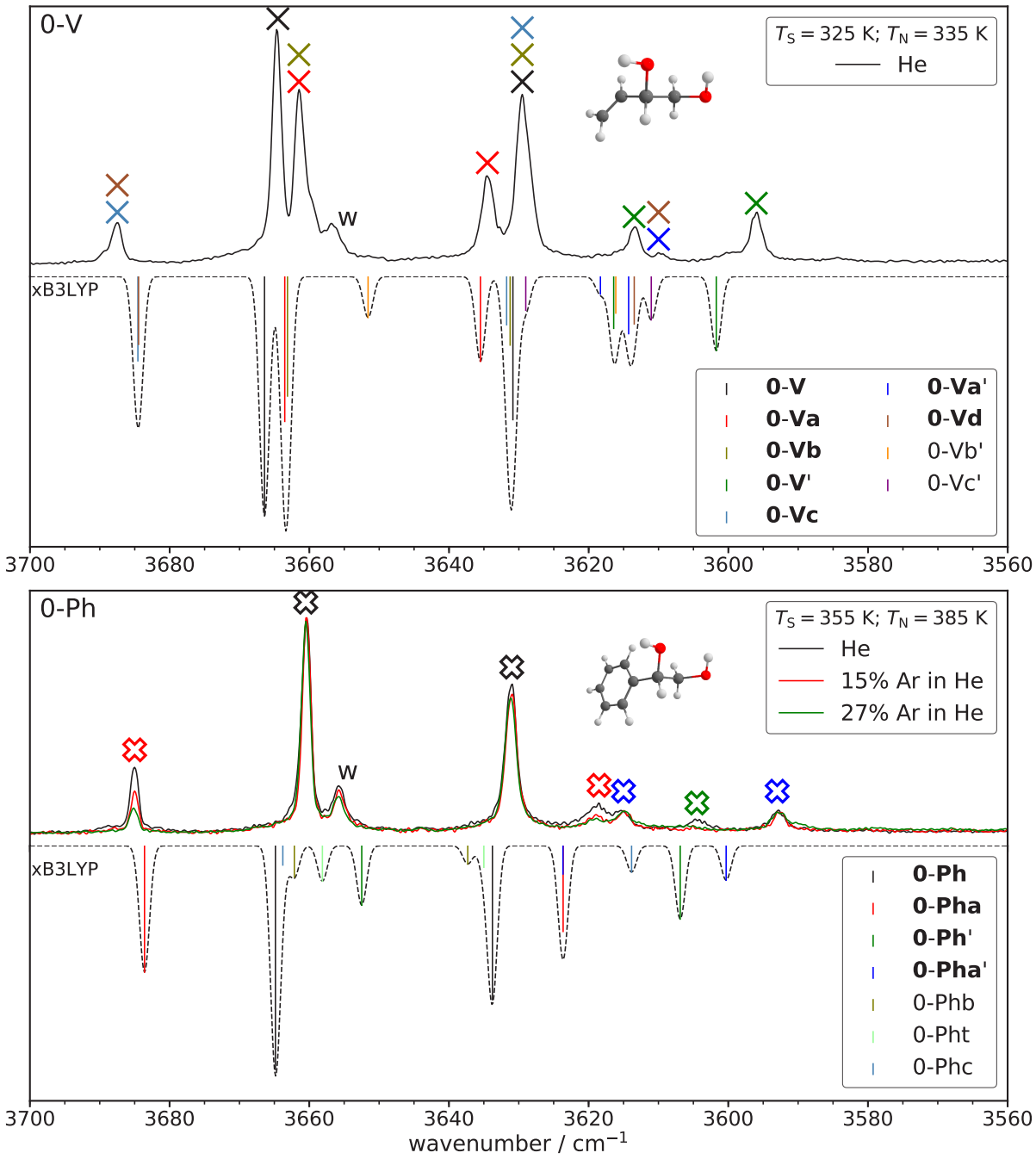

Fig. 3.13: This figure was adapted from Ref. [165]. Experimental data (plotted upwards) and simulated data (plotted downwards) of butenediol (0-V) and phenyl-ethanediol (0-Ph). In case of 0-Ph different mixtures of He and Ar were used to investigate the relaxation behaviour. The saturator temperature (T_S) as well as the nozzle temperature (T_N) are given. The simulated spectra are based on B3LYP/maTZ and are Boltzmann weighted based on T_N according to the relative energies given in Fig. 3.12. The derived correlation ($n_D = 1$) for B3LYP was used for the predictions. w indicates a water band or overlap with one and D bands due to dimers.

bound OH mode of 0-Ph' can be assigned to the band around 3605 cm^{-1} which disappears upon the addition of Ar to the expansion. The free OH mode is likely too low in intensity or possibly overlapping with a water band. The two remaining bands do not change with the Ar content and can be assigned to 0-Pha' which is expected to remain unchanged under these conditions. Other conformers may be present but cannot be distinguished due to spectral overlap.

0-Pha' also directly involves the π-system as was the case for 0-V' before. However, unlike 0-V', a fairly constant overestimation by the B3LYP correlation of about 8 cm^{-1} can be found for both the bound and free OH mode. This shift can be used as a phenyl correction for the correlation model for related systems[231]. It was noticed that for the conformers directly involving the π the OH oscillators couple significantly more than the training systems. For the training system, the OH streching modes are highly localised and might not be applicable to more strongly coupling system/conformers. To analyse this in more detail the displacement vectors are normalised and the ratio of the sum of squares of the OH displacement to the sum of squares of the entire vector is analysed and will be referred to as OH stretch locality (L_{OH}). The correlation between the OH stretch locality and the deviation of the model from the experiment is shown in Fig. 3.14a. It can be seen that in general unprimed conformers have more localised OH stretching vibrations than primed ones. Curiously, the most delocalised mode does not involve the π-system directly and belongs to the 0-Va' (see Fig. A.9 (page 226)) conformer. The two sets that are also delocalised more strongly belong to 0-V' and 0-Pha', respectively, with the model overestimating their band position in either case. In general, it can be observed that the predictive power is less adequate when L_{OH} is lower, however, the degree to which this is the case is not tied to it. The switch from a vinyl to a phenyl group appears to be more important. Additionally, the difference between the donor and acceptor locality (ΔL_{OH}) is shown in Fig. 3.14b which also includes unassigned modes to gauge a more general trend. The differences are very small in the order of 10^{-4} and no systematic changes can be observed for primed conformers. For unprimed conformers a slight preference for a higher L_{OH} in the acceptor modes can be found (more so for 0-V). In case of 0-V' and 0-Pha' the larger deviation of the free OH mode may be explained by a higher L_{OH} for the donor mode. However, no stringent systematic behaviour can be found.

Another possibility to judge the influence of mode coupling is to switch from hydrogen to deuterium or tritium for each OH group separately. In this way the modes can be decoupled due to their strong spectral separation. The decoupled hydrogen modes can then be plugged into the model again. Such an analysis can be performed in the future and may improve the predictions for hydrogen bonds involving π-systems. In case of deuterium, experimental measurements could also be conducted.

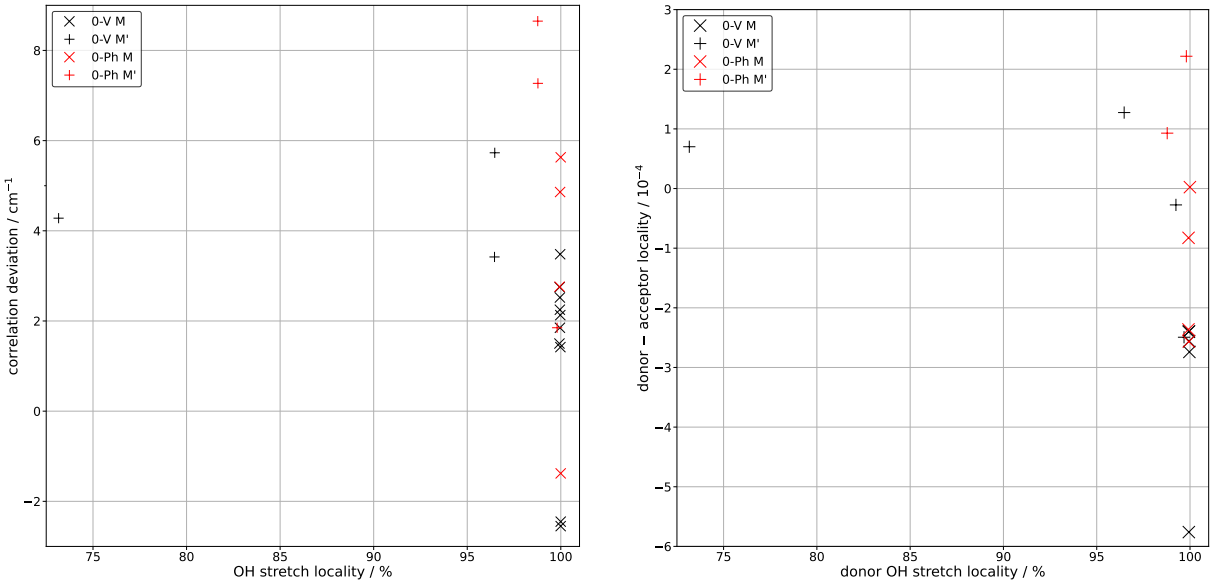

(a) correlation deviation **(b)** donor acceptor dependence

Fig. 3.14: The correlation of the OH stretch locality (L_{OH}) to the deviation of the model predictions to the experiment is shown (left), as well as the difference between the donor and acceptor locality (ΔL_{OH}) relative to the donor OH stretch locality for butenediol (0-V) and phenylethanediol (0-Ph). Furthermore, the two systems are divided into unprimed and primed conformers.

Lastly, the possible influence of fluorine contacts will be tested via 3,3,3-trifluoro-propane-1,2-diol (0-F). Its energetic landscape is shown in Fig. 3.12c and behaves very differently from 0-M (*cf.* Fig. 3.6). It is also the first system with a primed conformer (0-F') as its global minimum, which also shows a OH$\cdots$F contact (see Fig. A.8 (page 226)). Other more stable conformers involve a favourable alignment of the OH and CF dipoles. In terms efficient relaxation pathways only two exist from 0-Fb and 0-Fa' to 0-F. Besides that, some limited conversion from 0-Fc to 0-F or 0-Fa and from 0-Fa to 0-Fa' may take place. A comparison with other computational data can be found in Tab. B.3 (page 244). The overestimation of the stability of primed conformers for the GGAs can again be seen since unprimed conformers are higher in energy than for the hybrid functionals. In general, the calculations qualitatively agree with each other.

The experimental spectrum is shown in Fig. 3.15. The most stable conformer can be easily identified, although it does not exhibit the most intense signals. The bound OH mode is unusually broad, perhaps caused by some cooperative effects due to the fluorine contact. With a band position of 3575 cm^{-1} it also exhibits the strongest downshift observed so far. 0-F can also be easily assigned with the simulated intensities fitting well. The remaining band around 3690 cm^{-1} could be assigned to either 0-Fb or 0-Fc. However, since 0-Fb

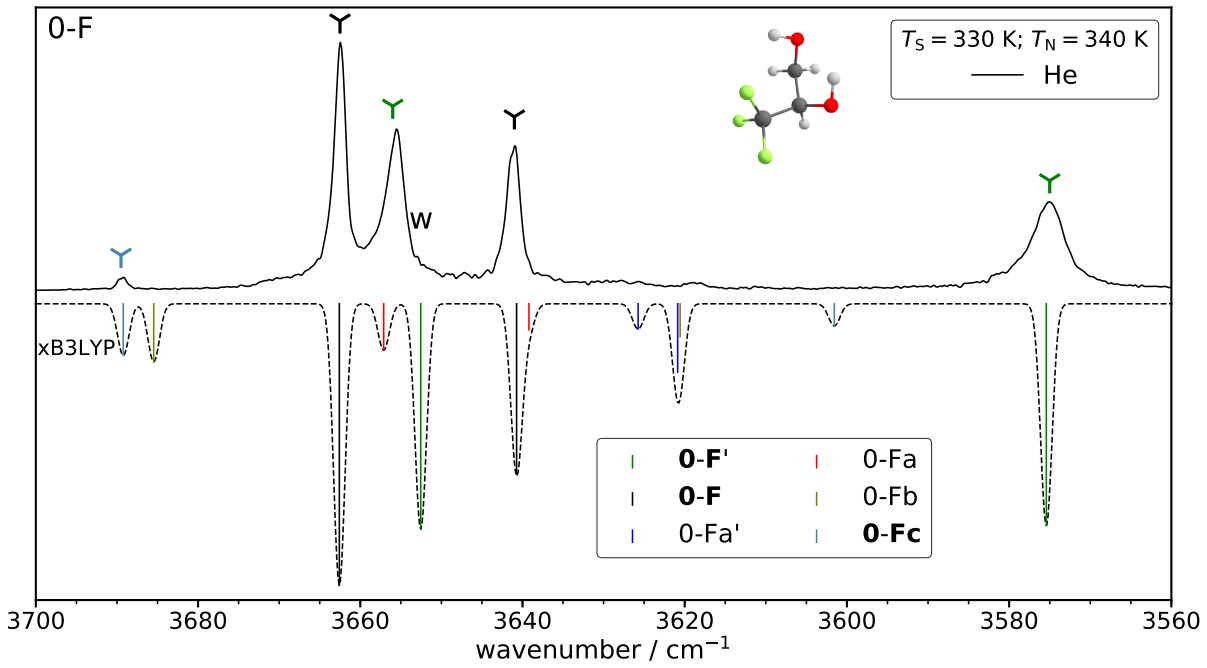

Fig. 3.15: This figure was adapted from Ref. [165]. Experimental data (plotted upwards) and simulated data (plotted downwards) of 3,3,3-trifluoro-propane-1,2-diol (0-F). The saturator temperature (T_S) as well as the nozzle temperature (T_N) are given. The simulated spectra are based on B3LYP/maTZ and are Boltzmann weighted based on T_N according to the relative energies given in Fig. 3.12. The derived correlation ($n_D = 1$) for B3LYP was used for the predictions. w indicates a water band or overlap with one and D bands due to dimers.

is expected to strongly relax it will be assigned to 0-Fc although a possible overlap of the two cannot be ruled out. The bound OH mode of 0-Fc is likely too weak to be observed. Around 3620 cm^{-1}, there are some indications that 0-Fa' might be present but an assignment would be highly speculative and therefore will not be made. Overall, the $n_D = 1$ fit performs much better than was the case for 0-V and 0-Ph, indicating that the type of hydrogen bond contact is important. A possible explanation can be found in the L_{OH} which is much higher for 0-F' (donor: 0.9983; acceptor: 0.9982) than was the case for 0-V' (donor: 0.9647; acceptor: 0.9646) and 0-Pha' (donor: 0.9878; acceptor: 0.9877).

A comparison of the data assigned in this section to the model fits is shown in Fig. 3.16. For the GGAs (top row), the data points are mostly far removed from $n_D = 1$ (0-M) correlation and no particular fit would describe the results for 0-V and 0-Ph especially well. However, in case of 0-F the $n_D = 1$ model would describe the data reasonably well even for the 0-F' conformer. Additionally, the results of 0-Pha' differ significantly from the rest and lie outside the range spanned by the different fits indicating a general problem in describing OH-π interactions of BP86 and PBE. This is also the case for the bound

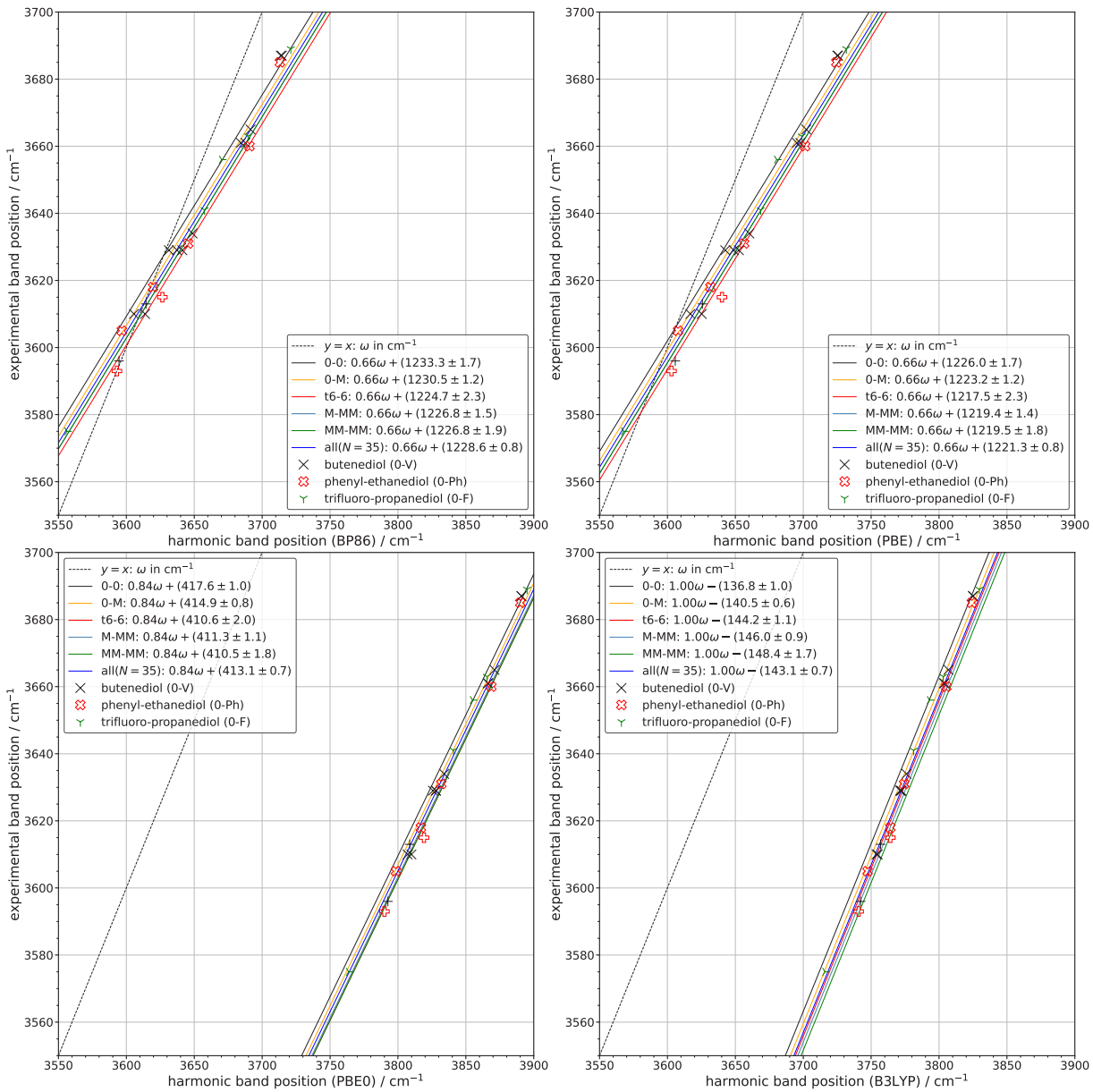

Fig. 3.16: Comparison of the data points of 0-V, 0-Ph and 0-F relative to the fits at the BP86/maTZ, PBE/maTZ, PBE0/maTZ and B3LYP/maTZ level of theory. Data points that involve the π-system or F-atom in the hydrogen bonding are tilted. The standard deviations (σ) as well as the number of included data points (N) are shown. This figure is adapted from Ref. [165].

OH mode of 0-V' but not the free OH mode.

Fig. 3.16 also shows the results for the hybrid functionals (bottom row). Compared to the GGAs, all data points cluster more closely around the fits. For PBE0, no clear favourite can be declared for the three systems as a whole. However, taking 0-F as its own system the $n_{\mathrm{D}} = 1$ correlation fits very well. For 0-Pha' and the bound OH mode of 0-V' some larger deviations can again be found. In case of B3LYP, the signals may

be adequately represented by an $n_D = 1$ or $n_D = 2$ fit. A fit for all three systems yields $a2 = 142.6(6)\,cm^{-1}$ being more akin to a $n_D = 2$ fit. However, when conformers with π or fluorine contacts are excluded, an $a2 = 141.8(5)\,cm^{-1}$ can be found being much closer to a $n_D = 1$ system. Furthermore, for 0-F alone no adjustments are needed to reach a good agreement with the $n_D = 1$ fit. Hence, it can be said that both hybrid functional models exhibit deficiencies in describing π-systems while tri-fluorinated systems appear to be well described. The strong substitution dependence of B3LYP is also further established.

As previously mentioned, the systematic overestimation of the band position when the phenyl ring is involved in the hydrogen bonding may be exploited in related systems. To this end, 1-phenyl-*cis*-cyclohexane-1,2-diol (c6-6Ph) will be studied which also provides a testcase for the $n_D = 3$ correlation. In section 3.1.7 differences between equatorial-equatorial and equatorial-axial hydrogen bond will be discussed in more detail. Fortunately, these effects are benign in context of the performance of the fit. Interestingly, only one energetically significant conformer is found for c6-6Ph with the second most stable conformer (c6-6Ph) following around $7.20\,kJ\,mol^{-1}$ at the B3LYP/maTZ level of theory. A comparison of different computational data can be found in B.16 (page 255). The GGAs again overestimate the stability of primed conformers which leads to a higher separation of the most stable primed conformer and the second most stable unprimed conformer. The three most stable structures are depicted in Fig. A.21 (page 233). The global minimum corresponds to c6-6Ph' which is closely related to 0-Pha' with the backbone being changed from ethane to cyclohexane. The structural similarity can also be seen from comparing the OCCO dihedral angle of 56° and 57° for c6-6Ph' and 0-Pha', respectively. However, the phenyl ring overlaps more strongly with the C-O group, *i.e.* the $OCCC_{Ph}$ dihedral angle is closer to 0° for c6-6Ph'.

The experimental spectrum of c6-6Ph is shown in Fig. 3.17. As can be seen, no evidence for a second conformer is found. Furthermore, a systematic overestimation by the model can again be found for both OH oscillators. However, by applying the aforementioned correction of $-8\,cm^{-1}$ a remarkably good agreement with the experiment can be achieved. The bound OH is with $3574\,cm^{-1}$ downshifted quite similarly to 0-F'. The typical downshift with a higher degree of substitution can also be observed when comparing 0-Pha' to c6-6Ph' with the bound OH mode shifting more strongly. The success of the model can also be seen as a first sign that axial-equatorial hydrogen bonds can also be described well. The next section will cover c6-6 which will tackle such hydrogen bond arrangements in more detail.

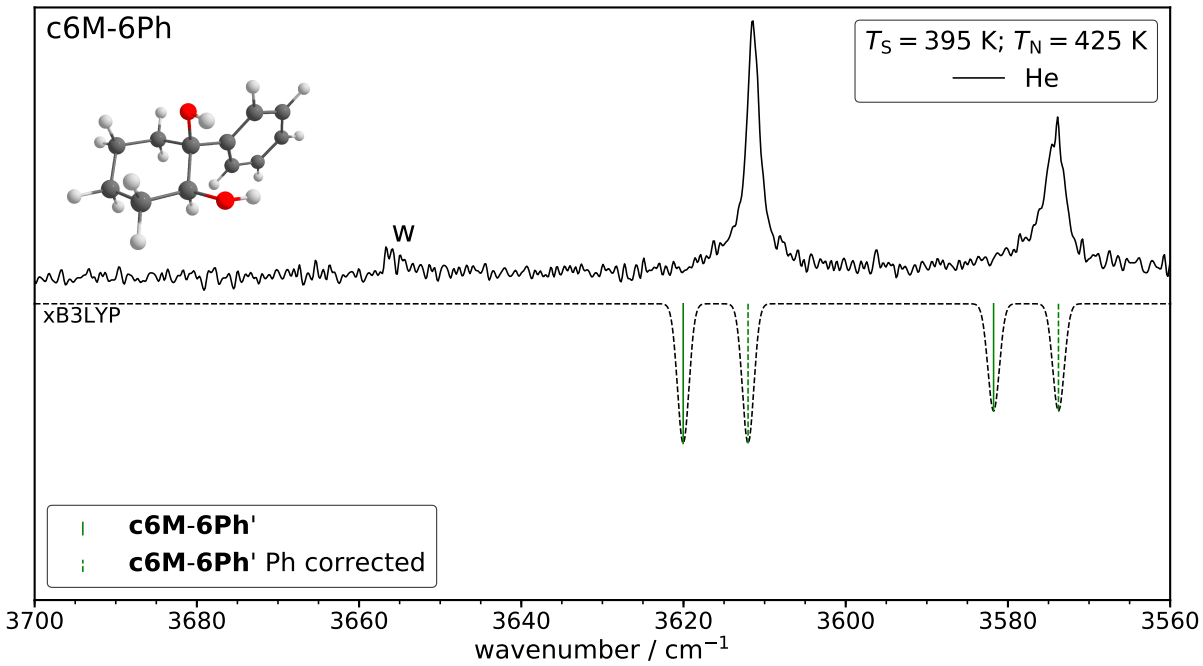

Fig. 3.17: Experimental data (plotted upwards) and simulated data (plotted downwards) of 1-phenyl-*cis*-cyclohexane-1,2-diol (c6-6Ph). The saturator temperature (T_S) as well as the nozzle temperature (T_N) are given. The derived correlation ($n_D = 3$) for B3LYP was used for the predictions. w indicates a water band.

3.1.7 Cyclic systems

Different ring sizes associated with the backbone may also provide a challenge for theory. Ring sizes are varied from *trans*-cyclobutane-1,2-diol (t4-4) up to *trans*-cycloheptane-1,2-diol (t7-7), *via* *trans*-cyclopentane-1,2-diol (t5-5) and *trans*-cyclohexane-1,2-diol (t6-6). The latter was already part of the training set and will only be invoked as a reference point. Especially, *trans*-cyclobutane-1,2-diol might be challenging due to its uniquely high ring strain compared to the other ring sizes[232]. Additionally, *cis*-cyclohexane-1,2-diol (c6-6) is investigated to look at the influence of equatorial ↔ axial hydrogen bonds, decoupled from interactions with a π-system as was the case for c6-6Ph.

Firstly, a look at the predicted OH···O distances is advisable to set the expectations for the experimental spectra. For the most stable unprimed conformer, the following distances are found: 3.34 Å for t4-4, 2.67 Å for t5-5, 2.31 Å for t6-6, 2.25 Å for c6-6 and 2.23 Å for t7-7 at the B3LYP/maTZ level of theory. Hence, it is to be expected that t4-4 and t5-5 will be at higher wavenumbers than t6-6, c6-6 and t7-7. Especially, t4-4 should be found at higher wavenumbers. t6-6, c6-6 and t7-7 would be expected to cover a fairly similar wavenumber range. A comparison with the computed hydrogen bond length of 0-0 2.38 Å (experimental estimate: 2.36 Å[211]) with t6-6 would also indicate that they should

be observed in a very similar range. However, a spectral difference of around $10\,\mathrm{cm}^{-1}$ (stronger downshift for t6-6) is found for the bound OH modes showing the importance of n_D for downshifts.

The energetic landscape of t4-4 is shown in Fig. 3.18a. Here, a larger variety of conformers are energetically relevant which do not exhibit a hydrogen bond/contact (indicated by a t) due to the large OH$\cdots$O distances. Furthermore, it is no longer possible to distinguish between di-equatorial and di-axial conformations. The calculated barriers are quite small throughout with the exception of the conversion of t4-4* to t4-4' and to a lesser extent t4-4ta to t4-4t. It should be noted, that some barriers are fairly wide reducing the conversion somewhat. For the transition of t4-4t to t4-4* and from t4-4* to t4-4, the same transition state was found based on the converged climbing image. However, for the path from t4-4t to t4-4* a negative electronic energy barrier is found and therefore this conversion is discarded. A comparison with other computational data can be found in B.9 (page 250). BP86 and PBE predict the primed conformation to be the most stable in opposition to the experimental results. Furthermore, t4-4ta is predicted higher in energy by B3LYP/maTZ while for the other functionals the energy difference is close to that of t4-4*.

The experimental spectrum is shown in Fig. 3.19. When comparing the experimental results to the simulations based on the $n_\mathrm{D} = 2$ correlation, large discrepancies can be found which can be explained by the high ring strain. Fortunately, a fairly constant underestimation is observed and the simulation can be realigned to match the two most

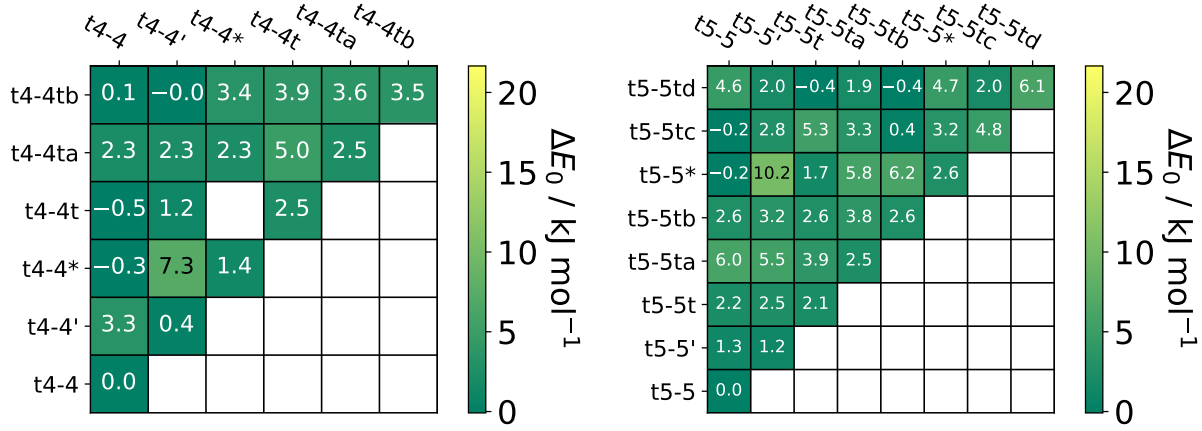

(a) t4-4 **(b)** t5-5

Fig. 3.18: Zero-point corrected energies as well as the corresponding barriers for *trans*-cyclobutane-1,2-diol (t4-4) and *trans*-cyclopentane-1,2-diol (t5-5) at the B3LYP/maTZ level of computation. Barriers are given relative to the less stable conformer. Given the large amount of relaxation pathways no arrows will be drawn. This figure is adapted from Ref. [165].

intense bands, which can be assigned to the most stable conformer. Based on this offset the bands at 3669 cm^{-1} and 3674 cm^{-1} can be assigned to t4-4* and t4-4t, respectively. The OH modes overlap in either case. The predicted intensities for these conformers are also significantly higher than the experimental ones in line with the small barriers. Assigning t4-4' on the other hand is less clear. The band overlapping with water can be assigned to the free OH mode of t4-4', however, no good candidate remains to explain the band at 3642 cm^{-1}. It appears likely that the shift between the free and bound OH mode of t4-4' is underestimated by the harmonic calculations given the intensity of the unassigned band. Given its stability and analogue development with respect to the other signals over multiple exposures, attributing it to an impurity would be very improbable. To resolve the uncertainty regarding the assignment of t4-4' anharmonic VPT2 (Vibrational Perturbation Theory of Second Order)[114] calculations at the B3LYP/def2-TZVP level were conducted with the Gaussian 16 (Revision A.03)[69] program package. A simulation based on these results is shown in D.1 (page 291) and indeed indicates that the splitting between the OH modes of t4-4' is strongly underestimated by harmonic calculations. Curiously, the GGAs predict a splitting of about 10 cm^{-1} harmonically, matching the experiment while PBE0 predicts half of that slightly higher than B3LYP (see Tab. C.13 (page 267)). t4-4ta and t4-4tb are likely responsible for some of the broadening in between the bands.

The energies and barriers for t5-5 are shown in Fig. 3.18b. t5-5 exhibits significantly less ring strain than t4-4, while at the same time being more floppy than t6-6. This increased floppiness is evident, given the energetic relevance of di-axial conformations which are indicated by a t. Furthermore, di-axial conformers are expected to relax to di-equatorial ones under jet conditions. Similar to t4-4, barriers are mostly very low with the only high barrier occurring for the conversion of t5-5* to t5-5'. A comparison of computational data can be found in Tab. B.10 (page 250). The GGAs predict t5-5' higher in energy than t5-5 in line with the experimental intensities. However, given the very close energetic proximity they can be considered quantitatively wrong. Concerning the energetic order the functionals mostly agree showing only minor differences.

Fig. 3.19 also shows the experimental results for t5-5. The general shifts appear to be captured quite well by the model. However, the signals are bunched closely together making assignments very challenging, although t5-5 can be assigned due to its prominence in the experimental spectrum and appearing somewhat isolated. The significantly separated band at 3630 cm^{-1} can be assigned to bound OH mode of t5-5'. Comparing the predicted and experimental intensities clearly indicates strong relaxation of t5-5' to t5-5 which theory corroborates. Due to the close proximity of the different signals and the limited accuracy of the harmonic approximation, further assignments are difficult. The

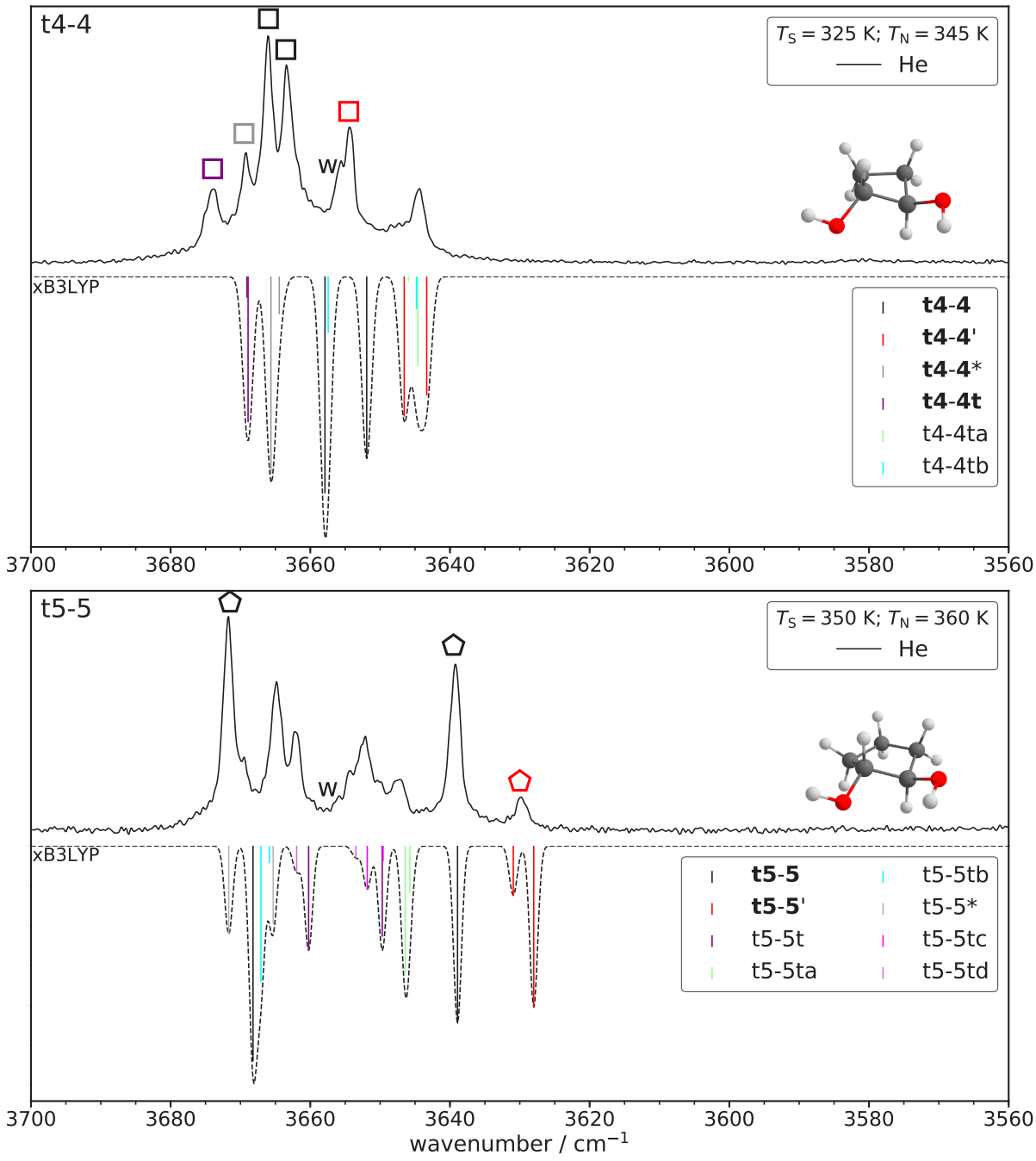

Fig. 3.19: Experimental data (plotted upwards) and simulated data (plotted downwards) of *trans*-cyclobutane-1,2-diol (t4-4) and *trans*-cyclopentane-1,2-diol (t5-5). The saturator temperature (T_S) as well as the nozzle temperature (T_N) are given. The simulated spectra are based on B3LYP/maTZ and are Boltzmann weighted based on T_N according to the relative energies given in Fig. 3.18 The derived correlation ($n_D = 2$) for B3LYP was used for the predictions. w indicates a water band. This figure is adapted from Ref. [165].

band at 3647 cm^{-1} could be assigned to t5-5ta which would be expected to relax strongly which a comparison between the experimental and theoretical intensities also indicates.

Furthermore, the three signals above can be explained by t5-5t and t5-5tc but the intensities only make sense if high barriers are assumed or that the conformers are predicted to high in energy. The latter would also increase the barrier. Specifically, the bands at 3654 cm^{-1} and 3650 cm^{-1} would be assigned to t5-5tc and 3650 cm^{-1} and the more intense centre band to t5-5t. Given the similar intensity of the already assigned band of t5-5t the signal at 3662 cm^{-1} can also be attributed to that conformer. Going once more against the computed barriers and/or relative energies, the signal at 3665 cm^{-1} can be made sense of as an overlap of t5-5tb and t5-5*. The remaining signal at 3669 cm^{-1} can be assigned to t5-5*. These assigned signals are highlighted in Fig. C.1 (page 268)

Adding to the complexity is the fact that hot bands might be involved at a nozzle temperature of 360 K, but likely only for the most stable conformer. Especially, the signal at 3669 cm^{-1} could possibly be explained by a hot band. VPT2 calculations reveal a few possible modes with suitable coupling constants which are listed in Tab. D.1 (page 292). To be suitable the coupling constant for the bound OH mode has to be smaller in magnitude since no additional signal is resolved around it. However, since all of the modes are above 1000 cm^{-1} leading to vibrational temperatures (θ_{vib}) above 1500 K the involvement of these hot bands is unlikely. Considering all this, only the safe assignments of t5-5 and t5-5' are shown in Fig. 3.19. For a clear assignment higher level electronic structure methods and/or vibrational treatment are necessary. In this regard the energetic landscape including the barriers should be revisited. Furthermore, microwave spectra of t5-5 have been recorded in the 2 GHz – 8 GHz range, which should allow for non ambiguous assignments.

To separately study the influence of axial ↔ equatorial hydrogen bonds on the quality of the predictions of the model, *cis*-cyclohexane-1,2-diol (c6-6) is investigated. As can be seen from Fig. 3.20a, the conformational landscape of c6-6 is far less complicated than the other systems studied in this section. Strong relaxation of c6-6' and c6-6a is expected towards the global minimum. Furthermore, significant conversion of c6-6a' to c6-6a is expected. All other calculated barriers are quite high with some additional relaxation from c6-6a' to c6-6' may taking place. Conformers with an axial donor and equatorial acceptor (c6-6 and c6-6') are found to be more stable. The structures can be found in A.18 (page 232). A comparison with other computational data including those of Lomas[184] can be found in Tab. B.12 (page 252). The GGAs again stabilise the primed conformers to an extent with BP86 even switching the energetic order of c6-6a and c6-6a'. The hybrid functionals agree well with each other.

The experimental spectrum of c6-6 is shown in Fig. 3.21. To further gauge the relaxation behaviour, measurements at a nozzle distance (d_N) of 1.25 mm and 2.0 mm were

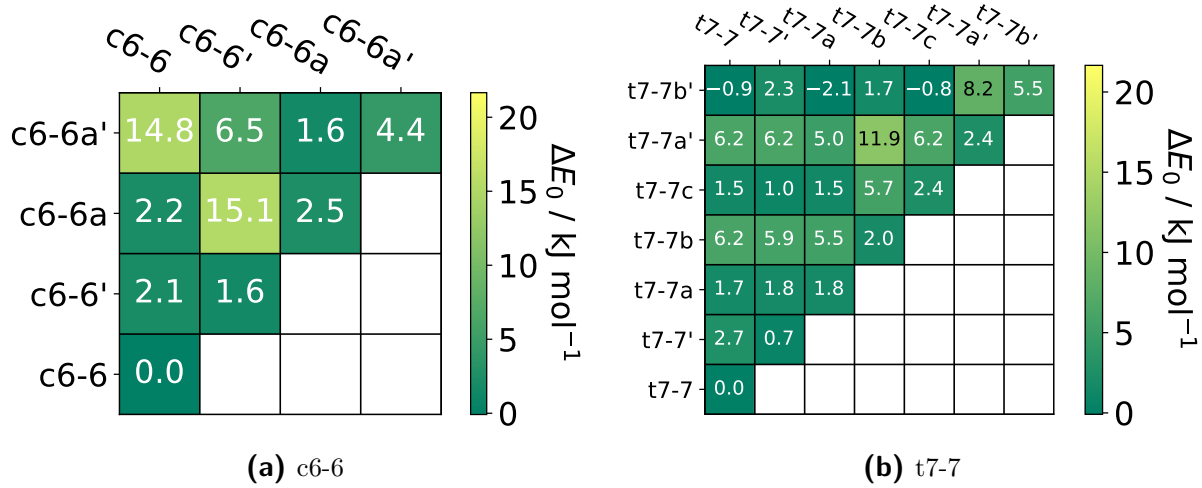

(a) c6-6 **(b)** t7-7

Fig. 3.20: Zero-point corrected energies as well as the corresponding barriers for *cis*-cyclohexane-1,2-diol (c6-6) and *trans*-cycloheptane-1,2-diol (t7-7) at the B3LYP/maTZ level of computation. Barriers are given relative to the less stable conformer. Given the large amount of relaxation pathways no arrows will be drawn. This figure is adapted from Ref. [165].

conducted. The two most intense bands can be assigned to the most stable conformer and expectedly do not change with a varying d_N. However, the signals at 3674 cm^{-1} and 3613 cm^{-1} most likely belong to c6-6a which is expected to relax, but no change in the intensity is observed. This discrepancy can be explained by the fact that for the conversion from c6-6a to c6-6 a change from an equatorial donor to an axial one is necessary resulting in a widened barrier. For the unprimed/primed pairs, this is not the case. More efficient cooling might be observed when Ar admixtures or higher backing pressures are used. Closer to the nozzle the small bands at 3648 cm^{-1} and 3604 cm^{-1} can be assigned to c6-6' which vanish at higher distances, in line with very efficient relaxation and a low barrier. Similarly, strong relaxation can be expected for c6-6a' to c6-6a explaining why it is not observed in the experimental spectrum. Overall, the $n_D = 2$ model yields very good predictions, showing that axial ↔ equatorial hydrogen bonds do not pose a problem lending further credence to the success in the predictions of c6-6Ph (*cf.* Fig. A.21).

The largest ring system studied is *trans*-cycloheptane-1,2-diol (t7-7) whose energetic landscape is shown in Fig. A.19. Given the increased flexibility, significantly more conformers are relevant in comparison to t6-6 (*cf.* Fig. 3.1), reminiscent of t5-5. However, unlike t5-5, no di-axial conformers can be found below 6 kJ mol^{-1} above the global minimum. In general, strong relaxation is anticipated for all conformers except t7-7b and t7-7a'. For these two conformers, limited to no conversion is expected. Furthermore, significantly high barriers can be found for the pathways from t7-7b' to t7-7a' and t7-7c to t7-7b. A comparison with other computational data can be found in B.13 (page 252). As is typical

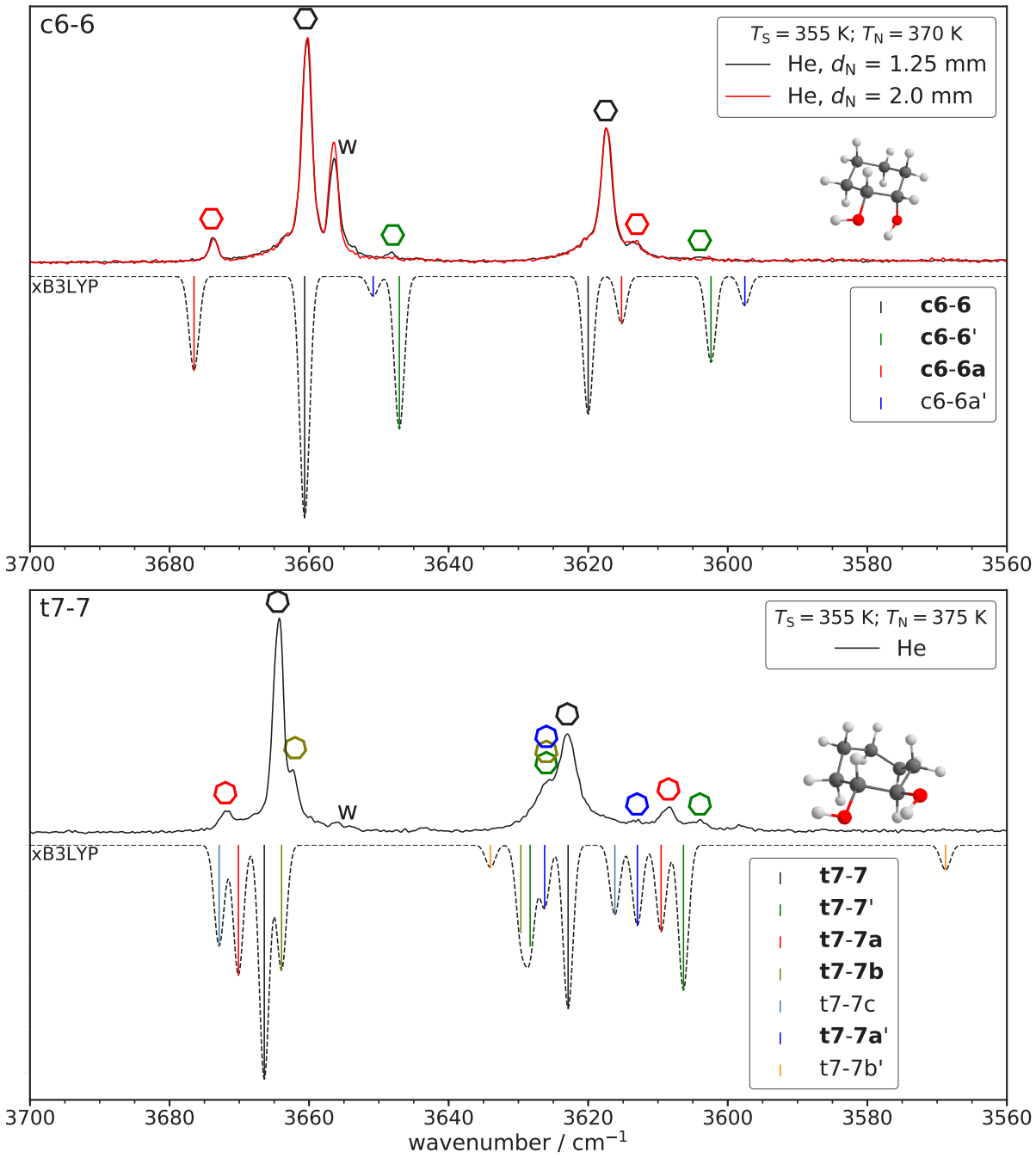

Fig. 3.21: Experimental data (plotted upwards) and simulated data (plotted downwards) of *cis*-cyclohexane-1,2-diol (c6-6) and *trans*-cycloheptane-1,2-diol (t7-7). The saturator temperature (T_S) as well as the nozzle temperature (T_N) are given. To gain insight into the relaxation behaviour of c6-6 measurements at different nozzle distances (d_N) were conducted. The simulated spectra are based on B3LYP/maTZ and are Boltzmann weighted based on T_N according to the relative energies given in Fig. 3.20 The derived correlation ($n_D = 2$) for B3LYP was used for the predictions. w indicates a water band. This figure is adapted from Ref. [165].

for the GGAs, the stability of primed conformers is overestimated with t7-7' constituting the global minimum and t7-7a' being the third most stable conformer. B3LYP and PBE0 agree reasonably well with each other. All energetically relevant structures are depicted in Fig. A.19 (page 232).

The experimental spectrum of is shown in 3.21. The two most intense bands can be easily identified as belonging to t7-7, going against the energetic predictions of the GGAs. Both of these bands exhibit a shoulder which is significantly broadened in case of the bound OH mode. These shoulders can be assigned to t7-7b which is expected to not relax very strongly in line with the experiment. The broadening can be attributed to an overlap with t7-7' and t7-7a'. The bands at $3672\,\mathrm{cm}^{-1}$ and $3608\,\mathrm{cm}^{-1}$ can be assigned to t7-7a exhibiting strong relaxation as expected. The free OH mode of t7-7c may also be a candidate explanation for the signal at $3672\,\mathrm{cm}^{-1}$ but is expected to relax more strongly, since more pathways lead away from it while at the same time less pathways lead to it. Furthermore, there is no substantial evidence for the bound OH mode of t7-7c. Therefore, it will not be considered further. The lower frequency mode could also be potentially explained by t7-7', however, the shoulder at $3626\,\mathrm{cm}^{-1}$ would be expected to be larger. This could potentially be obfuscated by the broadening but the intensity of the proposed bound OH mode of t7-7a matches the already assigned free OH mode. The two remaining small bands at $3613\,\mathrm{cm}^{-1}$ and $3604\,\mathrm{cm}^{-1}$ can be assigned to t7-7a' and t7-7' respectively. Given the very small intensity of the signal belonging to t7-7a' this assignment is tentative. It also contradicts the predicted intensity especially since relaxation behaviour more akin to t7-7b would be expected. For t7-7', strong relaxation is expected although the extent as to which it relaxes is surprising given the close energetic proximity to t7-7. This may be an indication that B3LYP struggles in predicting the correct energetic spacing and/or barriers for more floppy ring systems as was seen before with t5-5.

The initially described expectations based on the computed hydrogen bond lengths were confirmed (*cf.* Figs. 3.2 (t6-6), 3.19 (t4-4, t5-5) and 3.21 (c6-6, t7-7)). As expected, t4-4 showed very small splittings and a small spread of the bands which increases for t5-5, with an even further increase for t6-6 which behaves very similar to c6-6 and t7-7 as the hydrogen bond distances suggested.

A comparison of the assignments is shown relative to the model in Fig. 3.22 for the different tested functionals. The GGAs are shown in the top row. It is obvious that t4-4 behaves quite different than the other cyclic systems. This is further underlined by a separate fit for t4-4 which shows a significant increase in magnitude of $a2$. The data point that behaves more like the other systems belongs to t4-4', where issues have been

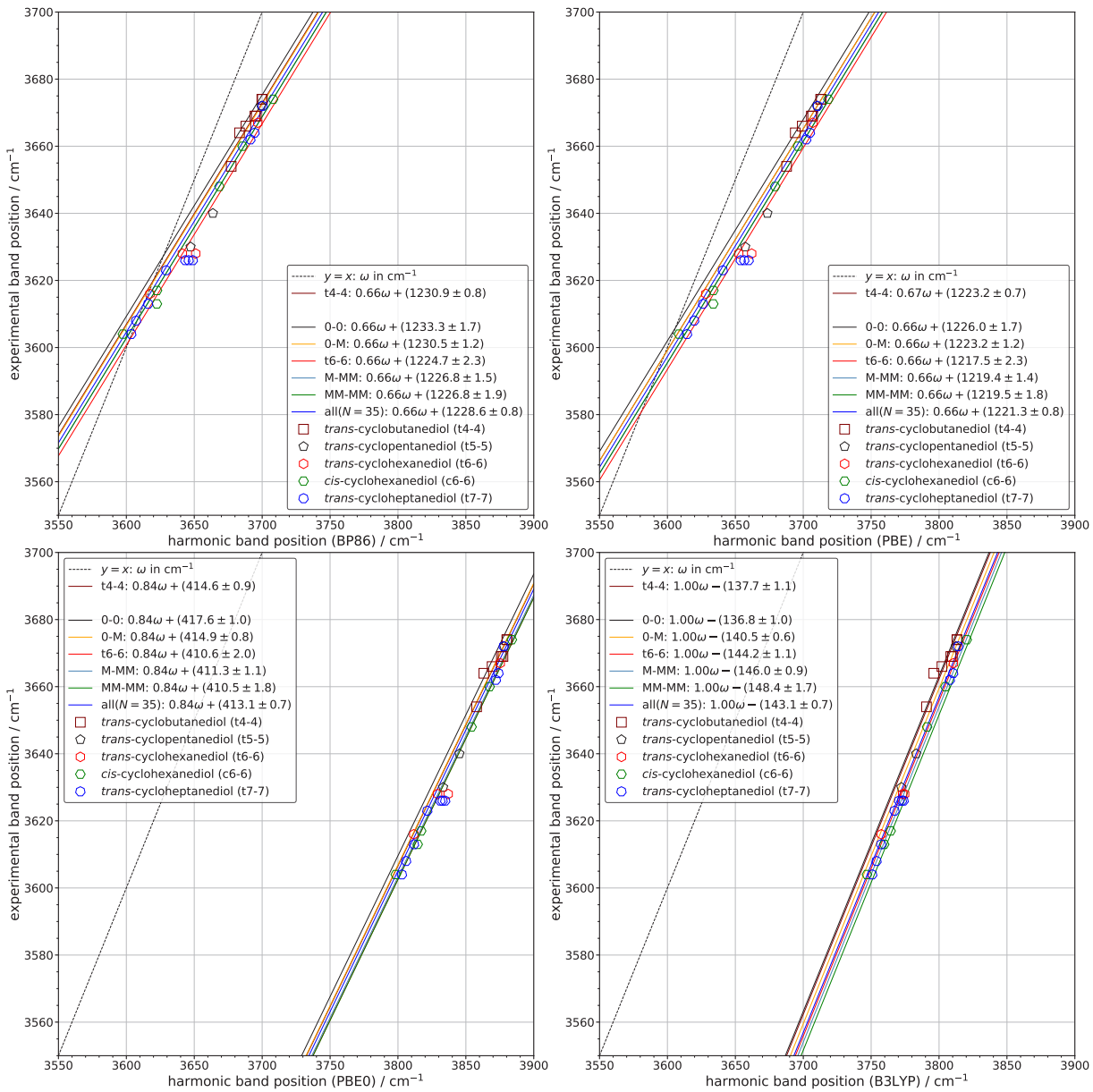

Fig. 3.22: Comparison of the data points of t4-4, t5-5, t6-6, c6-6 and t7-7 relative to the fits at the BP86/maTZ, PBE/maTZ, PBE0/maTZ and B3LYP/maTZ level of theory. The standard deviations (σ) as well as the number of included data points (N) are shown. This figure is adapted from Ref. [165].

found in the prediction of the shift between the free and bound OH mode. However, the GGAs predicted this shift well which is also the case for the other conformers. It may instead be related simply to the fact that it is a primed conformer. Again, no model fit complements the data particularly well confirming the notion that BP86 and PBE do not show a strong substitution dependence.

The bottom row in Fig. 3.22 shows the behaviour of the hybrid functionals. The trend

for t4-4 with regards to $a2$ prevails, although it appears to be more attenuated for PBE0 substantiating the lack of substitution dependence even more. Expectedly, no fit emerges that can be favoured for the description of the data. In case of B3LYP, the data points (except t4-4) cluster nicely around the $n_D = 2$ fit corroborating its strong dependence upon n_D. In general, t4-4 could be better described by $n_D = 0$ or $n_D = 1$ fits. One could also speculate that $a2$ could increase even further in magnitude for *cis* or *trans*-cyclopropane-1,2-diol.

3.1.8 Fully substituted systems

The term fully substituted systems refers to those with $n_D = 4$ for which pinacol (MM-MM) was the training dataset. To check the robustness of the $n_D = 4$ correlation, the same α carbon atom is bridged by a cyclopentane ring (CP). This added ring strain on the backbone is expected to challenge theory increasingly when first only one carbon atom is bridged, while the other is di-methylated using 1-(1-hydroxy-1-methylethyl)-cyclopentanol (CP-MM) and then both carbon atoms are bridged using [1,1'-bicylopentyl]-1,1'-diol (CP-CP).

The energetic landscape of CP-MM is shown in Fig. 3.23a. It is among the rare cases where anti-periplanar arrangements (t conformers) are energetically relevant. These conformers constitute a family that can convert to some degree within, but not to non-t conformers which form a separate family. Despite the low barriers for the t family, the fact that the energy differences are quite small. Therefore, the thermodynamic driving force is also small and some population may remain outside the most stable conformer CP-MMt. The non-t family conformers can generally relax easily towards the global minimum with the notable exception of CP-MMb'. Here, only one (CP-MMb' to CP-MMb) out of five pathways is expected to be energetically feasible under jet conditions. Other computational data is shown in Tab. B.18 (page 256). Yet again, the GGAs predict primed conformers to be more stable. They predict CP-MM' and CP-MMa' to be the two most stable conformers, whereas the hybrid functionals and the experiment shows the opposite, although CP-MM is only more stable than CP-MM' after zero point correction for the hybrid functionals. Furthermore, there are some significant differences in the energetic order of the t family, where the GGAs predict CP-MMt and CP-MMat higher in energy.

To illustrate the ring strain, the $CC_\alpha C$ angle on either side of CP-MM (see Fig. A.23a (page 235)) can be compared. At the B3LYP/maTZ level an angle of 110° is found for the MM side and 104° for the CP side, clearly showing an increased strain. To decouple

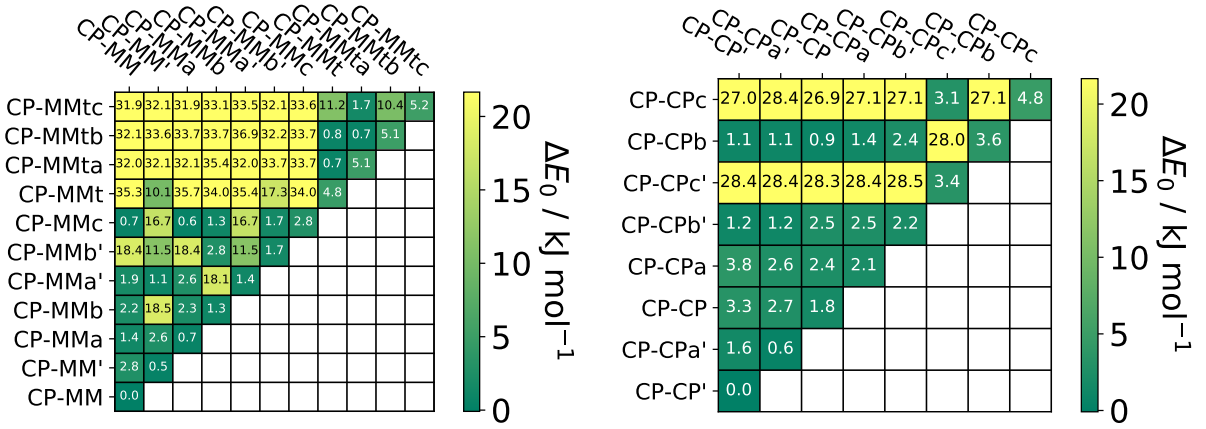

(a) CP-MM **(b)** CP-CP

Fig. 3.23: Zero-point corrected energies as well as the corresponding barriers for 1-(1-hydroxy-1-methylethyl)-cyclopentanol (CP-MM) and [1,1'-bicylopentyl]-1,1'-diol (CP-CP) at the B3LYP/maTZ level of computation. Barriers are given relative to the less stable conformer. Given the large amount of relaxation pathways no arrows will be drawn. This figure is adapted from Ref. [165].

the CP and MM interaction, one can also take a look at MM-MM (see Fig. A.22a (page 234)) and 0-MMa (see Fig. A.13c (page 230)), specifically the hydrogen bond donor side. For MM-MM an angle of 110° is found while in the most unconstrained case of 0-MMa an angle of 111° is calculated. Hence, the strain introduced by MM or CP to a neighbouring MM subgroup is only minor, highlighting the strain introduced by CP itself.

The experimental spectrum of CP-MM is shown in Fig. 3.24. The most intense band can be assigned to CP-MM with some contribution of CP-MMa and to a lesser extent CP-MMb', which explains the rather broad nature of the signal. The extended base can be attributed to an overlap with conformers of the t family, however, no clear assignments of them can be made. Further contributing is some residual water in the jet. The second most intense band can be assigned to an overlap of CP-MM' and CP-MMa', although the experimental intensities are not quite in line with the expected relaxation behaviour. Given the close energetic proximity of the conformers, the relaxation propensities might be overstated. Applying a uniform shift based on the assigned bands to the others around 3650 cm^{-1}, suggests that the signal at 3662 cm^{-1} belongs to CP-MMb. CP-MMc may also be a possibility but much stronger relaxation would be expected and the band is therefore assigned to CP-MMb. The very broad band around 3600 cm^{-1} appears to tail off towards higher wavenumbers. Given this clear asymmetry, the tail is assigned to an overlap of CP-MMa and CP-MMb and the band maximum to CP-MM. The other broad feature towards lower wavenumbers can be attributed to an overlap of CP-MM', CP-MMa'

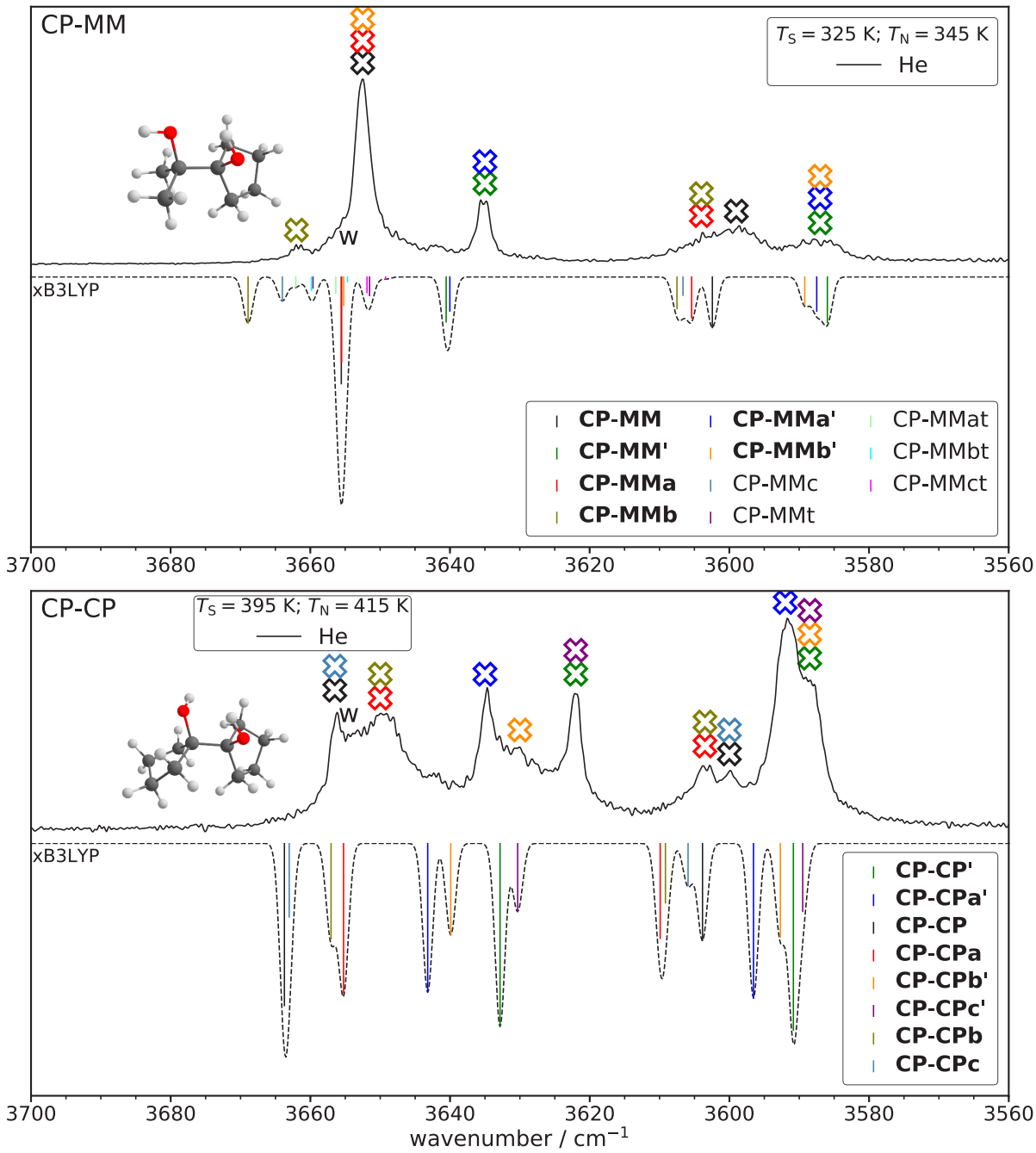

Fig. 3.24: Experimental data (plotted upwards) and simulated data (plotted downwards) of 1-(1-hydroxy-1-methylethyl)-cyclopentanol (CP-MM) and [1,1'-bicylopentyl]-1,1'-diol (CP-CP). The saturator temperature (T_S) as well as the nozzle temperature (T_N) are given. The simulated spectra are based on B3LYP/maTZ and are Boltzmann weighted based on T_N according to the relative energies given in Fig. 3.23 The derived correlation ($n_D = 4$) for B3LYP was used for the predictions. w indicates a water band. This figure is adapted from Ref. [165].

and CP-MMb'. Since the free OH modes appear to be described slightly worse, one may expect that the bridging CP ring is present at the hydrogen bond acceptor side, leading

to a similar behaviour as was the case with the methyl series (see section 3.1.4 (page 39)). Curiously, this is not the case and instead appears to be a general effect for the free OH modes of the CP-MM systems regardless of which side the acceptor group is pointing.

The energetic landscape of [1,1'-bicylopentyl]-1,1'-diol (CP-CP) is shown in Fig. A.24. Together with 0-F (see Fig. 3.12c (page 51)) and c6-6Ph' (see Fig. 3.17 (page 59)) it is the only system with a primed species as its global minimum with even the second most stable conformer being primed. Furthermore, anti-periplanar arrangements are not energetically relevant, unlike CP-MM. However, two intra-converting but not inter-converting families of conformers can again be found: CP-CPc/CP-CPc', opposed to all other conformers. For the intra-conversions of the families, low barriers can be found throughout. Other computational data is shown in Tab. B.19 (page 257). CP-CP' and CP-CPa' are predicted to be the most stable conformers by all functionals.

Fig. 3.24 shows the experimental spectrum of CP-CP and expectedly adding the second CP bridge leads to larger deviations of the $n_D = 4$ fit, but assignments can be made under the assumption that the pattern holds. Similar to CP-MM, the fit appears to describe the bound OH modes better than the free ones, further corroborating that this behaviour is caused by the bridging. The bound OH modes also are at very similar positions for CP-MM and CP-CP, however, the intensities differ quite a lot. The most intense band at $3592\,cm^{-1}$ can be assigned to CP-CPa' with the shoulder around $3589\,cm^{-1}$ being caused by an overlap of CP-CP', CP-CPb' and CP-CPc'. Given the experimental intensities, it can be concluded that CP-CPa' is the globals minimum instead of CP-CP'. In that light, the simulated intensity of the free OH mode of CP-CP' also appears more reasonable. It should be noted, that the described overlap may also be more on the side of CP-CPa', especially given the broad nature of the band. The bands at $3603\,cm^{-1}$ and $3600\,cm^{-1}$ can be explained by an overlap of CP-CPa with CP-CPb and CP-CP with CP-CPc, respectively. The observed intensities are also in line with the expected relaxation propensity. The free OH modes of CP-CP' and CP-CPc' can be assigned to the band at $3622\,cm^{-1}$. This assignment can be used as an anchor-point for the others. Subsequently, the signal at $3635\,cm^{-1}$ can be attributed to CP-CPa'. It is noticeable that the baseline between the free OH bands of CP-CP' and CP-CPa' is significantly heightened, which is not the case in the free OH region for other diols. This could be rationalised by non-resolved hot bands especially since the OH torsional modes are at lower frequencies for the free OH vibration than the bound one. A tentative assignment of the signal at $3630\,cm^{-1}$ is made to CP-CPb' based on the shift towards CP-CPa'. The remaining two signal at $3656\,cm^{-1}$ and $3650\,cm^{-1}$ can be assigned to and overlap of CP-CP with CP-CPc and CP-CPa with CP-CPb, respectively. Here, some of the broadening can also be attributed to residual water in the jet.

A comparison of the CP-MM and CP-CP data relative to the derived correlations is shown in Fig. 3.25 for the tested functionals. Both GGAs behave quite similarly and show large deviations from all fits. However, for CP-MM the discrepancies are not as large as for CP-CP. To further illustrate the unusual behaviour separate fits were made for CP-CP and show a strong increase of $a2$ (becoming less negative). Analogous behaviour can be found for the two hybrid functionals and a very clear trend with regards to $a2$ emerges, which is opposite to that of t4-4. Hence, it appears that introducing ring strain at the

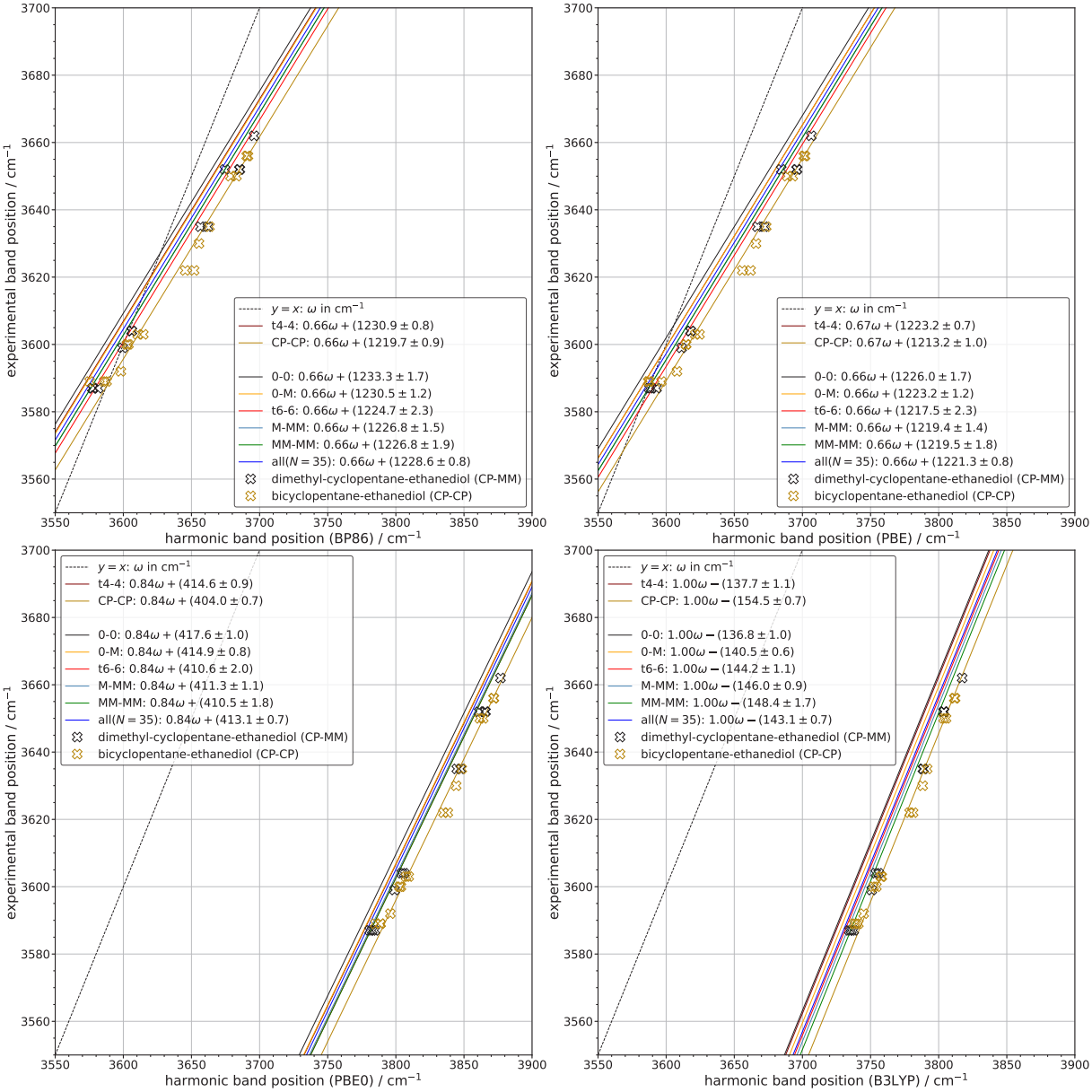

Fig. 3.25: Comparison of the data points of CP-MM and CP-CP relative to the fits at the BP86/maTZ, PBE/maTZ, PBE0/maTZ and B3LYP/maTZ level of theory. A separate fit for CP-CP is also shown. The standard deviations (σ) as well as the number of included data points (N) are shown. This figure is adapted from Ref. [165].

same carbon atom leads to an increase of $a2$ while doing so at the vicinal carbon atoms leads to a decrease of $a2$. To further prove the point [1,1'-biclobutyl]-1,1'-diol could be investigated for which an even stronger increase of $a2$ would be expected.

3.1.9 Detailed analysis

Absolute band predictions

Given the large amount of data collected, a concise comparison is difficult. To this end, box-plots will be used to visualise the deviations of absolute band predictions from the experiment including 109 such data points. The dotted blue lines in Fig. 3.26 represent the arithmetic average, while the solid blue lines represent the median. The box itself equates to the 25th up to 75th percentile of the data, with the whiskers representing at most 1.5 times the interquartile range. At 1.5 times this amounts to about 2.7σ from whisker to whisker. Everything outside of that range is considered an outlier and is marked with a cross ($\times$). Included here are such systems that do not show obvious signs of not being represented well by the fits, *i.e.* t4-4 and CP-CP. Systems that start to deviate such as CP-MM, 0-Ph and c6-6Ph are still included. The data itself is sorted according to their degree of substitution and the appropriate fit is applied. An overview of the different correlation fits can be found in chapter E. In each category the training set is also included. For $n_\mathrm{D} = 0$ no test set is available and for $n_\mathrm{D} = 3$ only two additional data points are present.

The top row in Fig. 3.26 shows the box-plots for the GGAs. The both provide very similar results at about the same computational cost. For the largest system (CP-CP), calculations finished in about 15 minutes with 18 cores for both functionals. The substitution dependent fits do not provide a significant increase in accuracy. However, based on the median a slight overestimation can be found for $n_\mathrm{D} = 1, 4$ and an underestimation for $n_\mathrm{D} = 2$. For PBE, a tendency for overestimation can also be found for $n_\mathrm{D} = 3$. In general, the all fits for BP86 and PBE may still be adequate if bands are well separated.

In the bottom row of Fig. 3.26 the results for the hybrid functional are shown. It can immediately be seen, that the deviations are smaller in comparison to the GGAs. The strong substitution dependence of B3LYP compared to all other functionals can also be seen. Subdivided fits provide a considerable improvements towards the all fit. This effect is only present to a limited extent for the other functionals. Furthermore, the all(n_D) fit improves the quality of the predictions in comparison to the all fit while all(n_0) shifts the median closer to $0\,\mathrm{cm}^{-1}$ but shows no other improvement. A detailed explanation of the

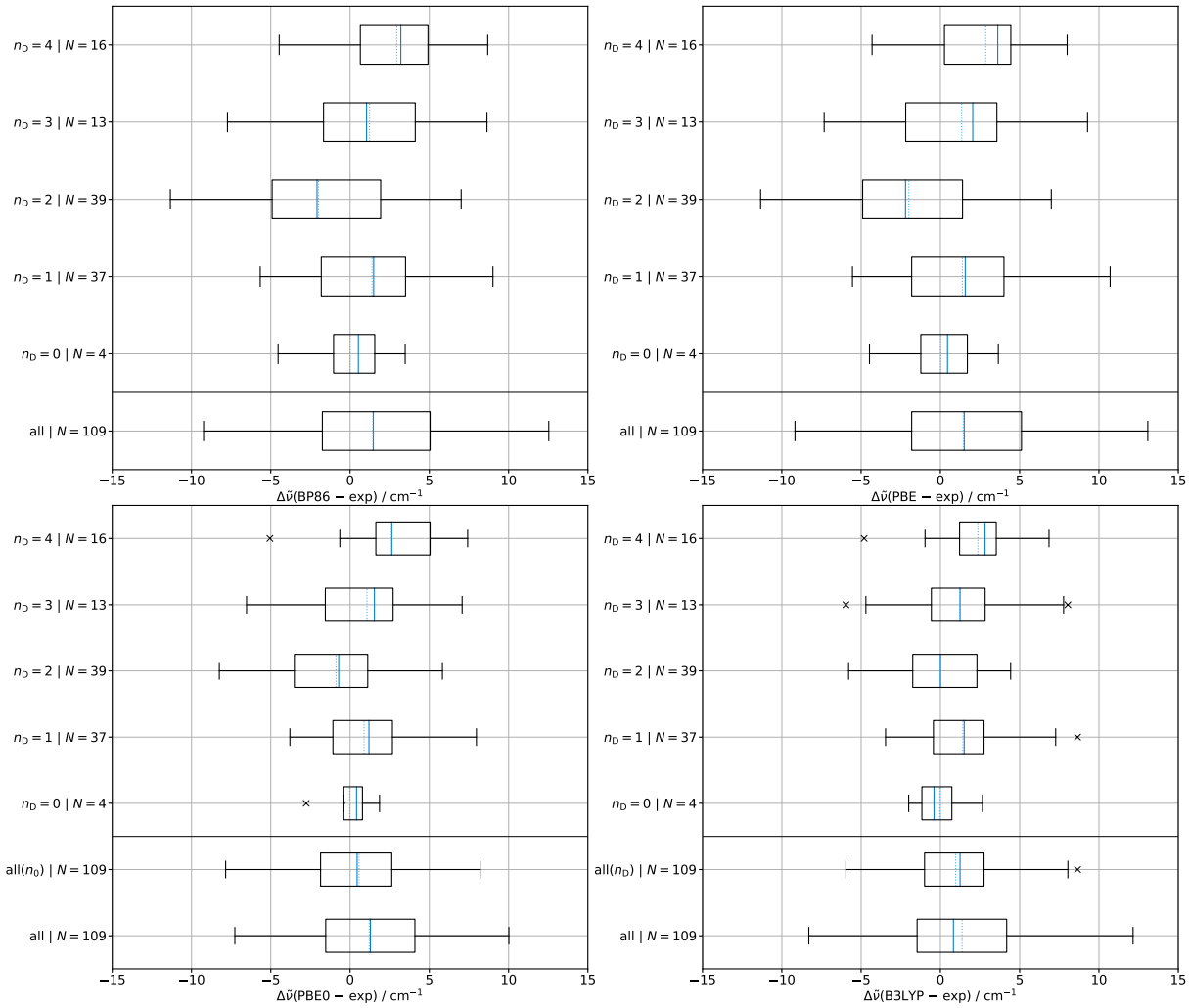

Fig. 3.26: Box-plots showing the deviation of the predicted wavenumbers at the BP86/maTZ, PBE/maTZ, PBE0/maTZ and B3LYP/maTZ level of theory with respect to the experiment, depending on the degree of substitution (n_D). N indicates the number of data points included. This figure is adapted from Ref. [165].

all(n_D) and all(n_0) fit can be found in section 3.1.5. The median of the fits mostly centres around $0\,\mathrm{cm}^{-1}$ showing no clear signs of under- or overestimation, except $n_D = 4$ which tends to overestimate.

Intramolecular hydrogen bond shift

Since empiric corrections as described in the previous sections or anharmonic calculations are often not readily available, harmonic hydrogen bond shifts are commonly investigated. Underlying this approach is the assumption that anharmonic effects will at least partially cancel when looking at spectral differences. To be most charitable to this method, the

acceptor/donor shifts for each individual conformer are considered. Here, the assumption is made that anharmonic effects are the most comparable for those instances. Hence, the anharmonicity should cancel the most fortuitous. Especially, since the hydrogen bonds are quite weak. The results are again divided according to their n_{D}. Since t4-4 and CP-CP were found to behave quite differently than their n_{D} suggests they are treated separately. However, they are still included in the all category. Box-plots are again used to visualise the deviations from the experiment.

The results of such an analysis are shown Fig. 3.27 for the GGAs (top row). Yet again, BP86 and PBE behave very similarly showing very large spreads of the data in many

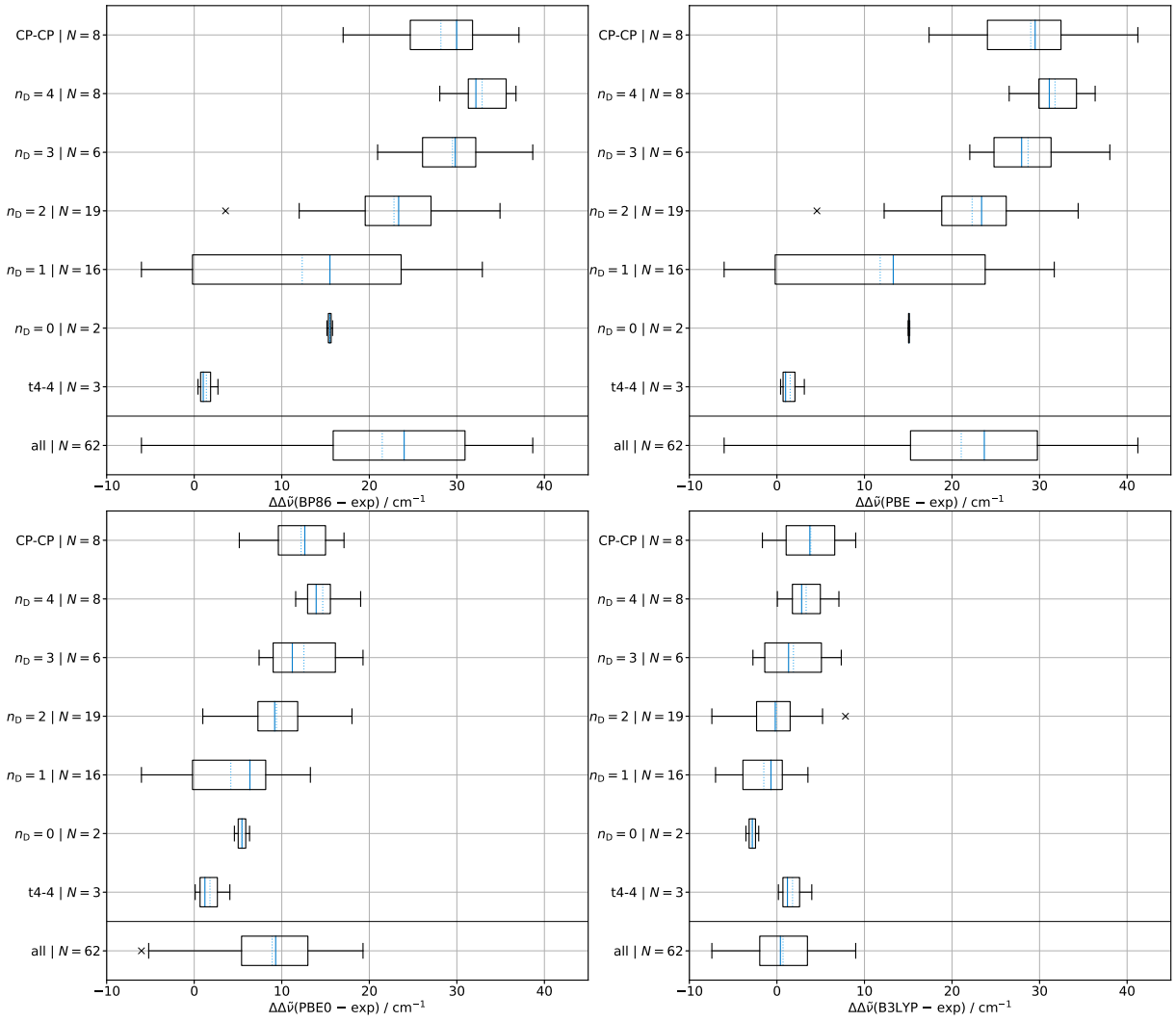

Fig. 3.27: Box-plots showing the deviation of the predicted intramolecular hydrogen bond shifts at the BP86/maTZ, PBE/maTZ, PBE0/maTZ and B3LYP/maTZ level of theory with respect to the experiment, depending on the degree of substitution (n_{D}) and t4-4 and CP-CP separately. N indicates the number of data points included. This figure is adapted from Ref. [165].

instances. It can also be seen that with an increase of n_D the overestimation of the shift increases as well. Curiously, the shifts for t4-4 are described quite accurately indicating that the GGAs are adequate for systems with very weak or no hydrogen bonds. This likely also includes the shift of t4-4' which they describe exactly considering the experimental uncertainty of $\pm 2\,cm^{-1}$ for such a shift (BP86 and PBE: $-0.5\,cm^{-1}$). The hybdrid functionals underestimated the shift (see section 3.1.7). It may also be the case that due to error cancellation introduced by the strong ring strain good results are achieved. Furthermore, CP-CP shows much larger shifts than the $n_D = 4$ category indicating that the GGAs struggle in the description of a doubly bridged system. To provide more context to the deviations they can be compared to the experimental median ($43\,cm^{-1}$) and extreme values (0 – $81\,cm^{-1}$) clearly showing that the GGAs are not very useful as a predictive tool.

The bottom row in Fig. 3.27 shows the results for the hybrid functionals. It is immediately apparent that the deviations and the spread of the data are much smaller than for the GGAs. This is especially true for B3LYP, which shows an overall very balanced behaviour with the all median being around $0\,cm^{-1}$ and the whiskers being slightly above $-10\,cm^{-1}$ and slightly below $10\,cm^{-1}$. PBE0 on the other hand, generally tends to overestimate the shifts. As was the case for the GGAs, an increase of the deviations can be found with an increase of n_D. However, the starting point for B3LYP is in the negative region opposed to PBE0. t4-4 again occupies a special position with a remarkably similar behaviour to the GGAs. It should be kept in mind that the t4-4' conformer is not included which would introduce deviations of $-4.4\,cm^{-1}$ and $-6.8\,cm^{-1}$ for PBE0 and B3LYP, respectively. Nevertheless, the other shifts are still very well described. In case of B3LYP, t4-4 also fits well into the behaviour of the $n_D = 2$ category. CP-CP fits quite well in the $n_D = 4$ category for both functionals. Furthermore, given the smaller spread of the data the median could be used to correct the shifts to improve general accuracy.

Conformational families

Instead of dividing the data points along n_D it is also possible to separate them according to conformational families. Specifically, the conformers can be differentiated between unprimed (M) and primed (M') conformers which can be further divided into hydrogen bond donors and acceptors. Such a comparison is depicted in Fig. 3.28. For simplicities sake, BP86 is not shown since it behaves very similar to PBE and no further insights can be gained. It can be seen that M and M' cover similar wavenumber ranges, although shifted from each other. However, in some instances signals can be found that behave atypical with regards to their family. For example, the two strongly downshifted bands at about

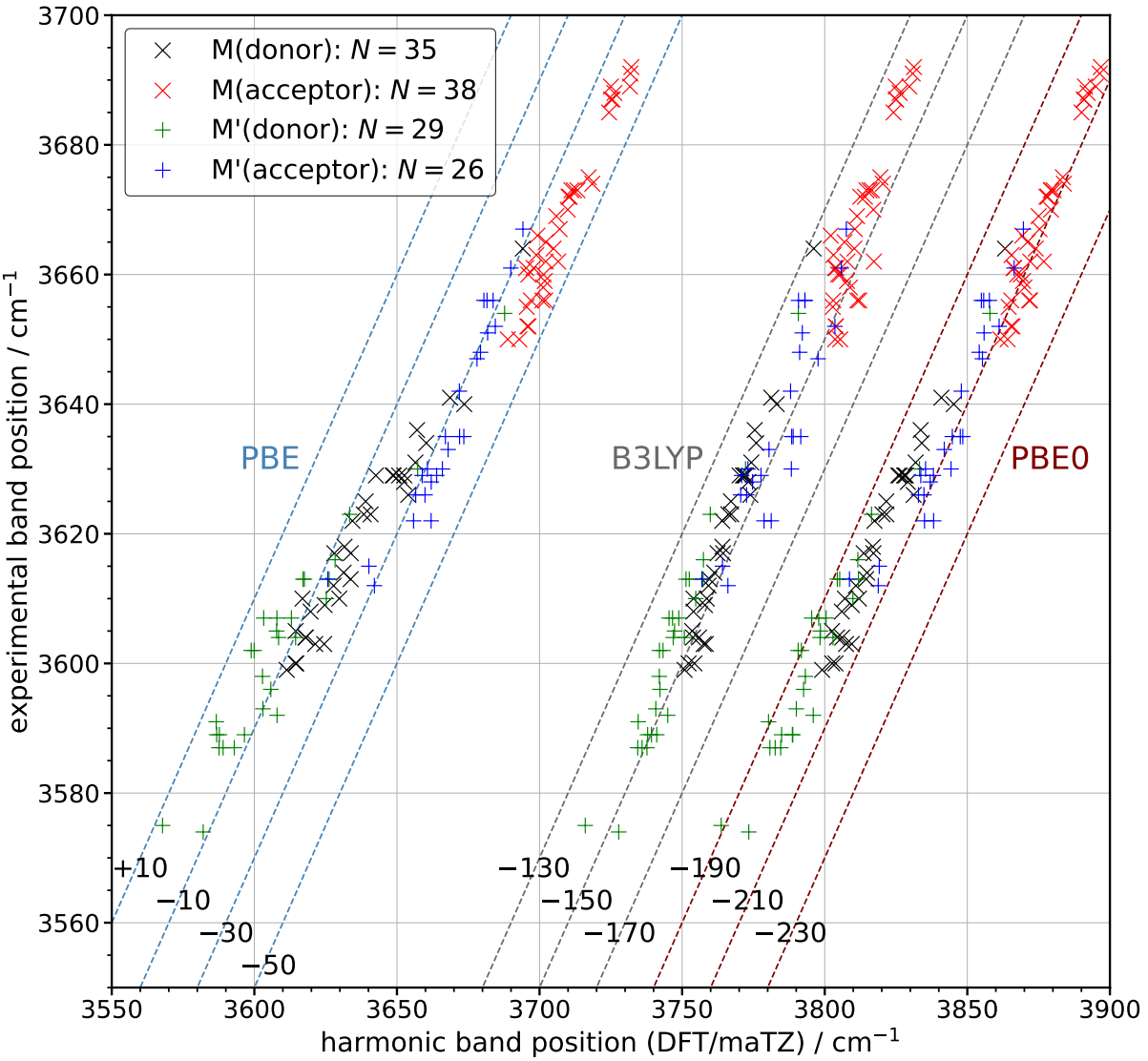

Fig. 3.28: Overview of primed hydrogen bond donors (black) and acceptors (red) as well as the corresponding unprimed donors (green) and acceptors (blue) and the correlation between their experimental and theoretical band positions. N indicates the number of data-points included. The dotted lines represent functions of the form $\omega/\mathrm{cm}^{-1} + \#$ with $\#$ being the corresponding number on the line. Data in between the blue lines corresponds to PBE, between the grey lines to B3LYP and between the brown lines to PBE0. This figure is adapted from Ref. [165].

$3575\,\mathrm{cm}^{-1}$ (experimental) of the M' donors belong to hydrogen bonds directly involving a fluorine atom (0-F') and the π-system of c6-6Ph'. In the following, the given wavenumber values are always the experimental ones. On the other hand, the unusually high signal at $3654\,\mathrm{cm}^{-1}$ belongs to t4-4' clearly highlighting the special nature of these systems, although 0-F' is quite well behaved in terms of predicting its experimental position with the derived correlation fits. Some of the substitution effects can also be seen, *i.e.* the

signal around 3690 cm^{-1} all belong to systems with $n_D = 0, 1$ except 0-MM. 0-MM is also a somewhat special case for the primed acceptors since it shows an unusually high band around 3667 cm^{-1}. Curiously, there appears to be a sizeable gap between these bands and the following ones below 3675 cm^{-1}. Furthermore, another gap can be found between the unprimed signals in between 3640 cm^{-1} and 3650 cm^{-1}. However, it remains to be seen whether or not this is a general diol property or specific to this dataset. In case of PBE and BP86 (not shown), the primed acceptor signals around 3615 cm^{-1} also appear to be somewhat offset with regards to the other bands of the family. This behaviour can be explained by the fact that in all three cases π-systems (0-V', 0-Pha' and c6-6Ph') are involved. These signals are also unusually low in comparison to the others.

This plot also allows some further comparison to mono-ols, where *gauche* isomers can be found at lower wavenumbers than *trans* isomers for primary alcohols.[31] In the case of diols, primed conformers correspond to *gauche* acceptors and donors, while unprimed conformers correspond to *trans* acceptors and *gauche* donors, which show equivalent behaviour. Secondary mono-ols behave in a similar manner, however, the references point of the nomenclature switches (*gauche* corresponds to *trans* and *vice versa* relative to primary alcohols) so that that the primed and unprimed correspondence also switches[31]. For diols, this trend also continues for tertiary systems, *i.e.* those with an n_D of 4. It is also quite clear from the behaviour of the hydrogen bond donors and acceptors that primed conformers are better acceptors than unprimed ones.

Fig. 3.28 is also illustrative of the different h values obtained for the tested functionals. In case of B3LYP, the data points cluster very closely along the dotted line which used $h = 1$, while for PBE0 a slight tilt can be observed which intensifies further for PBE and BP86. This highlights that for individual subclasses different h values would be advantageous. The fitting results for a distinction between hydrogen bond donors and acceptors is shown in Fig. C.2 (page 275). In case of the GGAs, the h values are quite different and should yield advantageous results in comparison to an all fit. For the hybrid functionals, the fits become progressively less different going from PBE0 to B3LYP. Neglecting the bands involving π-systems around 3615 cm^{-1} would further increase the description of the hydrogen bond acceptors for all functionals except B3LYP. This is illustrated in Fig. C.3 (page 276) which shows that especially for the GGAs an improvement of the predictive capabilities can be achieved relative to the all fit. Another possibility would be to simply divide between the primed and unprimed conformers which is shown in Fig. C.4 (page 277). There is little difference between the separate fits but also towards the all fit. Hence, such a division is not suitable to increase the predictive power in comparison to the all fit. A similar progression with regards to the behaviour of the functionals can be found

as was the case for the donor acceptor strategy but significantly attenuated. In this case the π-systems also do not appear to behave irregular.

Lastly, fits for all four classes for the tested functionals are shown in Fig. 3.29. For the GGAs, it can be seen that such a division would improve the predictive capabilities in comparison to the all fit. As was the case for just the acceptors the bands involving a π-system behave somewhat differently than the rest of the M' acceptors. Curiously, the unique behaviour of t4-4, CP-CP and to a limited degree CP-MM can be described reasonably well if the aforementioned π acceptors are excluded. The fits also suggest that the primed and unprimed hydrogen bond donors can be treated together given their

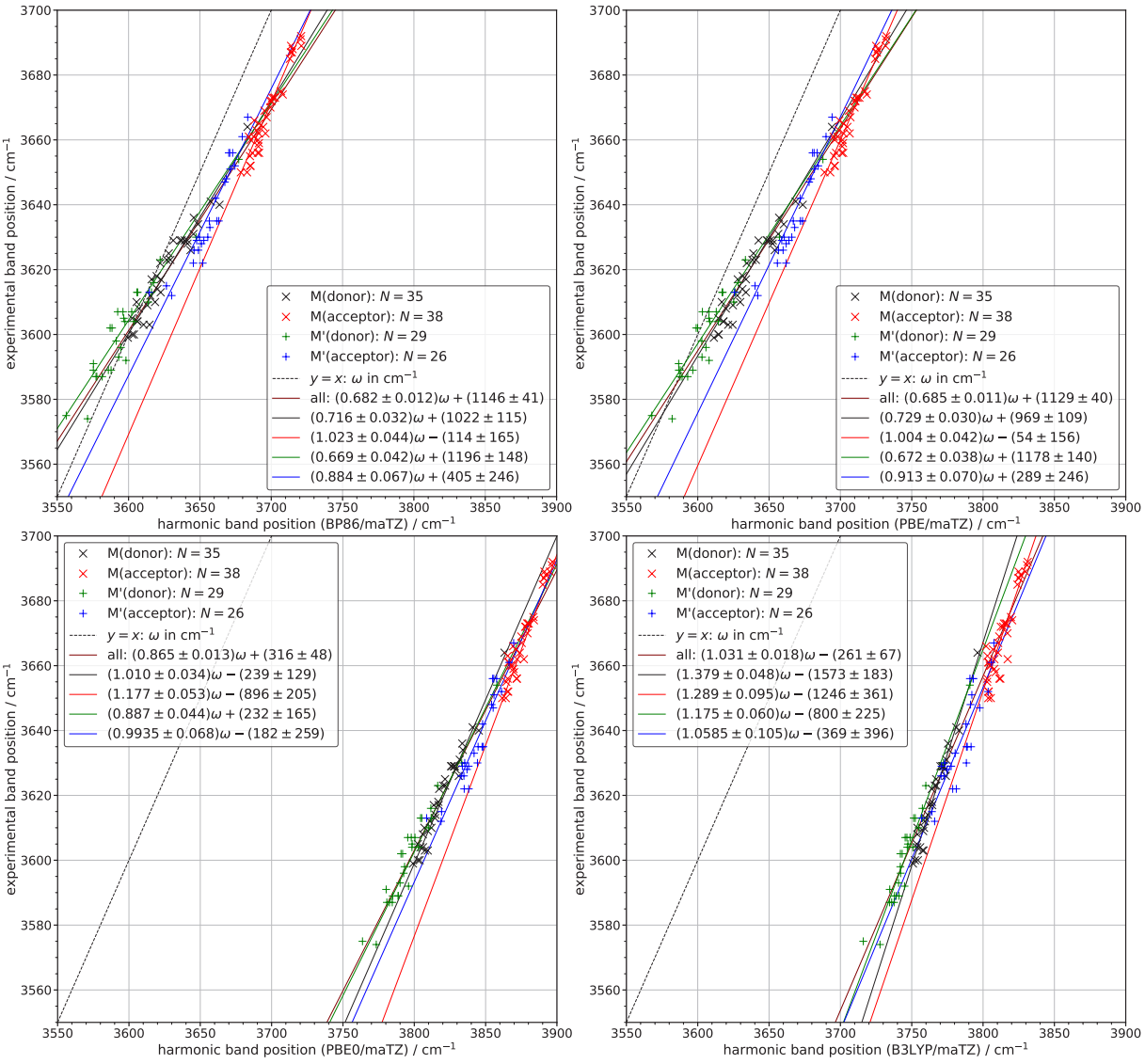

Fig. 3.29: Fits for BP86/maTZ, PBE/maTZ, PBE0/maTZ and B3LYP/maTZ for hydrogen bond donors and acceptors separately. The standard deviations (σ) as well as the number of included data points(N)are shown as well. This figure was adapted from [165].

similarity. This treatment also leads to generally more physically reasonable h values. For the hybrid functionals, it can again be found that the fits differ less than for the GGAs with B3LYP having the tightest pattern. However, the general spread of the data is also smaller for the hybrid functionals. In either case, the donors could also be treated together. For PBE0 it is also advisable to not include the previously mentioned π bands while for B3LYP changes are smaller. Fits where these bands are excluded can be seen in Fig. C.5 (page 278) for all functionals. For the GGAs, a significant improvement can be seen for the primed acceptor bands with a significantly higher h. Yet again, both of BP86 and PBE behave very similarly. For PBE0, changes are significant but less drastic than for the GGAs while for B3LYP no substantial changes can be observed. It may generally be the case that this effect is at least attenuated for hybrid functionals.

Comparing the findings for the conformational families with the dependence upon the degree of substitution some more general conclusions can be drawn. While B3LYP is highly specific towards the degree of substitution, it does not significantly differentiate between hydrogen bond donors and acceptors of the primed and unprimed families. This may be the reason why B3LYP performed so well for the description of intramolecular hydrogen bond shifts (see Fig. 3.27). The performance of the other functionals for the hydrogen bond shifts also aligns nicely with their family dependence. However, it remains unclear whether any of these behaviours are based on an actual physical property or an artefact of the tested functionals. Higher level electronic structure methods and/or anharmonic treatment as well as the measurement of overtones, combination and hot bands may resolve this issue.

Comparison with wave-function-theory

As was mentioned in section 3.1.1 (page 29), Ref. [31] investigated the behaviour of wave-function based harmonic calculations, *i.e.* SCS-LMP2, LCCSD(T*)-F12a and CCSD(T)-F12a (1D local modes) of Vogt *et al.*[169]. For SCS-LMP2, fits had to distinguish between n_{D} as well as *gauche* and *trans* conformers to perform reasonably well. This distinction becomes less necessary for LCCSD(T*)-F12a and almost vanishes for the CCSD(T)-F12a (1D local modes) case. For the latter, this can be at least partially attributed to the fact that a harmonic 1D model (derived from the anharmonic 1D model) includes some anharmonic contributions by construction due to the reduction of dimensionality in comparison to a harmonic frequency calculation involving all modes[171]. LCCSD(T0)-F12a/VDZ-F12 and SCS-LMP2/aVTZ* (aVTZ*; aVTZ=all, H=VTZ) geomtry optimisations followed by harmonic frequency calculations were conducted for some select diols. Tested systems are 0-0, 0-MM, rM-M, t6-6, M-MM and MM-MM.

The same analysis as it was done for the functionals (*cf.* Fig. 3.10 (page 48)) with regards to n_D is shown in Fig. 3.30. For both methods, h values significantly above one can be found leading to highly unphysical $a2$. In case of LCCSD(T0)-F12a, h is somewhat smaller. The fact that $h > 1$ indicates that the wave-function methods underestimate the separation between primed and unprimed conformers as well as the hydrogen bond shifts. B3LYP on the other hand, predicts these shifts remarkably well for weak hydrogen bonds, leading to $h = 1.00$. In this sense it could be considered right for the right reasons. However, the substitution dependence is an artefact of the method and is missing almost entirely for LCSSD(T0). Contrarily, PBE0 begins to struggle as soon as weak hydrogen bonds are involved. For both MP2 and coupled cluster, $a2$ of the fits differ very little in comparison to the functionals. The maximum spread between the fits amounts to $6.5\,\mathrm{cm}^{-1}$ for MP2 and only $3.8\,\mathrm{cm}^{-1}$ for the coupled cluster calculations while for B3LYP $11.6\,\mathrm{cm}^{-1}$, for PBE0 $7.1\,\mathrm{cm}^{-1}$, for PBE $8.5\,\mathrm{cm}^{-1}$ and for BP86 $8.6\,\mathrm{cm}^{-1}$ are found. It should be kept in mind that the actual spread of the data for the GGAs is not represented by the fits, *i.e.* the spread of $a2$ is smaller than that of data points. Furthermore, $a2$ generally decreases slightly with an increase of n_D while the density functionals indicate the opposite, although not entirely consistent in some cases (see Fig. 3.10 (page 48)).

The wave function theory data can also be sorted according to the conformational families and then further divided between hydrogen bond donors and acceptors (*cf.* Fig. 3.29). This is shown in Fig. 3.31. In terms of the general spread between the fits MP2 is

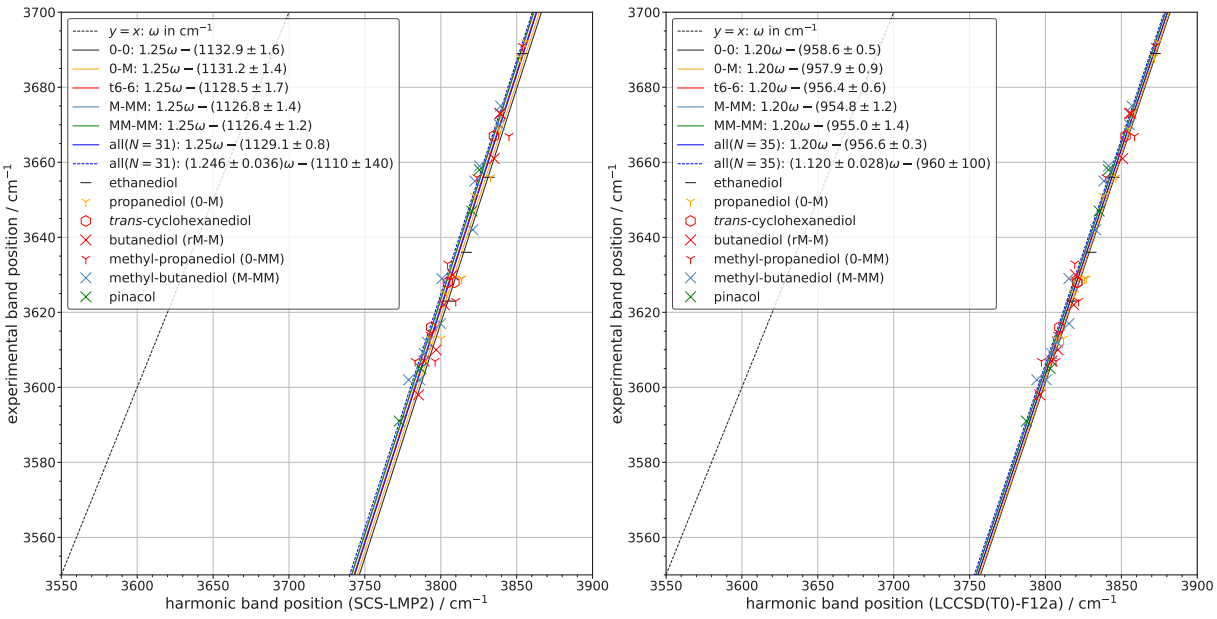

Fig. 3.30: Fits according to n_D for SCS-LMP2/aVTZ* (aVTZ*; aVTZ=all, H=VTZ) and LCCSD(T0)-F12a/VDZ-F12. All data points are shown. The standard deviations (σ) as well as the number of included data points (N) are shown as well.

somewhat akin to PBE0 and LCCSD(T0) akin to B3LYP. In case of PBE0 and MP2, the h values of the fits are also fairly similar. The major difference to DFT is that the unprimed and primed acceptors fits lie above their corresponding donors graphically in the region of interest. This reversal is reminiscent of the previously stated behaviour with regards to n_{D}. Furthermore, more physically reasonable values for h can be achieved for the unprimed conformers for LCCSD(T0). Additionally, the donors can be treated together for LCCSD(T0), which also appeared to be the case for the GGAs. This can be attributed to the fact that donor OH groups are always in a *gauche* orientation. For MP2 such a division provides some benefit to the predictive capabilities, while for coupled cluster little improvements can be made with regards to the all fit. Based on the WFT results one could speculate that a division along conformational families has a physical grounding, more so than along n_{D}. Without knowledge of the anharmonicity constants this remains speculative.

Fig. C.7 (page 280) shows the behaviour of the hydrogen bond donor and acceptor bands. The deviation of the fits relative to each other are reminiscent to the GGAs for MP2 while coupled cluster more closely resembles PBE0 (see Fig. C.2 (page 275)). However, yet again the graphical order of the fits is flipped in the region of interest with the acceptors being above the donors in the WFT case. For MP2, the two different fits provide little improvement while for coupled cluster no significant changes can be observed relative to the all fit. However, for the latter more physically reasonable h values can be obtained.

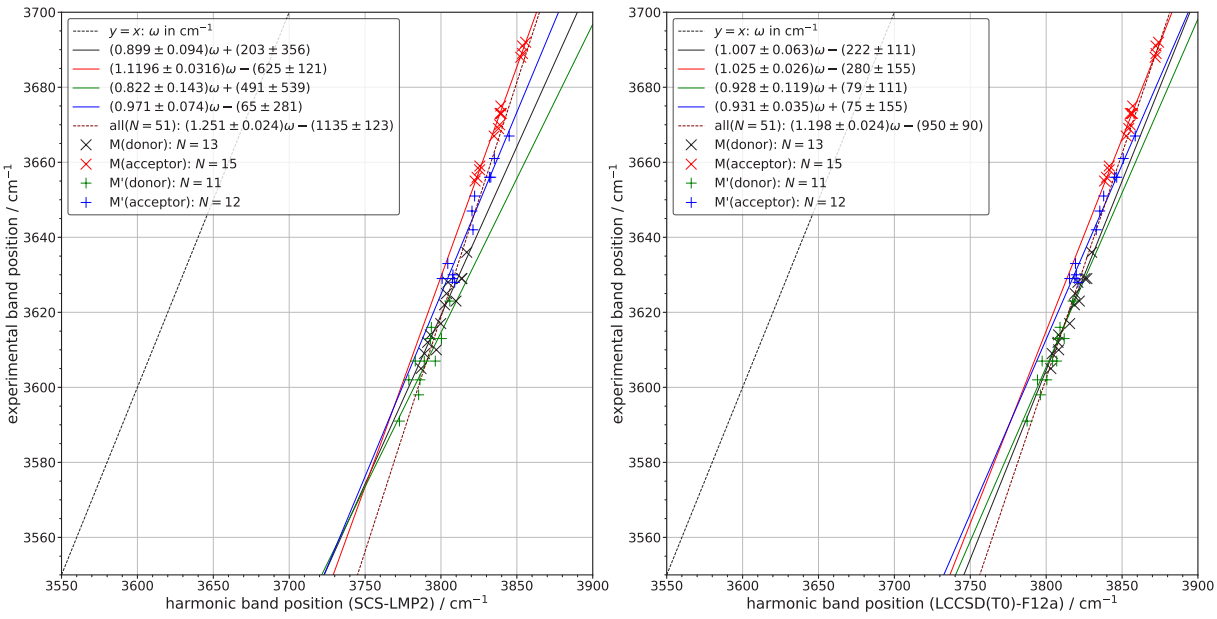

Fig. 3.31: Fit according to n_{D} for SCS-LMP2/aVTZ* (aVTZ*; aVTZ=all, H=VTZ) and LCCSD(T0)-F12a/VDZ-F12. All data points are shown. The standard deviations (σ) as well as the number of included data points (N) are shown as well.

The results for a distinction between primed and unprimed conformers are shown in C.8 (page 280). Here, the WFT results closely resemble the ones of the hybrid functionals (see Fig. C.4 (page 277)). In the region of interest very little deviations can be found between the fits with MP2 showing slightly larger ones.

For the mono-ols (see Ref. [31]), it was found that for WFT methods fits along the lines of n_D and between *gauche* (primed donor and acceptor and unprimed donor bands) and *trans* (unprimed acceptor bands) conformers can improve the predictive capabilities. Fig. C.9 (page 281) shows such a comparison for the diols. The improvement relative to the all fit is only minor similar to the donor and acceptor distinction (see Fig. C.7 (page 280)). However, for the latter the spread of the data can be reduced significantly with LCCSD(T0). It remains to be seen if a harmonic frequencies derived from a 1D local mode approach as used by Vogt *et al.*[169] could tighten the spread even further. As previously mentioned, this phenomenon is likely caused by the fact that harmonic 1D LM models include some anharmonicity by construction, but the switch from local to canonical coupled cluster calculations and possibly a different treatment of the pertubative triples provides additional unknown factors. Furthermore, the largest system studied so far with their method is *tert*-butyl hydroperoxide with six non-hydrogen atoms[233,234] indicating that systems such as MM-MM may not be computationally feasible.

may-cc-pVTZ vs. ma-def2-TZVP and the importance of *h* for B3LYP

R. Medel and M. A. Suhm used the may-cc-pVTZ basis set for their mono-ol study[31], while here the ma-def2-TZVP basis set is used. Both basis sets constitute minimally augmented variants of the Dunning and Ahlrichs family of basis sets, respectively. To gauge the differences between the approaches B3LYP-D3(BJ)/may-cc-pVTZ (B3LYP/mVTZ) calculations have been conducted with *Gaussian 16* for all underlying systems of the n_D fits. These fits are shown in Fig. C.6 (page 279). It can be seen that the change in basis set yields a higher h and $a2$ values. However, the unique n_D-dependence of B3LYP persists. An all(n_D) fit can also be proposed in the form $\tilde{\nu}_i/\mathrm{cm}^{-1} = 1.01\omega_i - (198 + 2n_\mathrm{D})$ or $\tilde{\nu}_i/\mathrm{cm}^{-1} = \omega_i - (137 + 3n_\mathrm{D})$ for B3LYP/maTZ. More details with regards to the all(n_D) fits are provided in section 3.1.5 (page 47). Hence, using the mVTZ basis set slightly attenuates the n_D dependence. Other basis sets may lower this dependence even further. Applying an LM model based on DFT calculations, as it was done by Barone and co-workers to for rM-M and t6-6[186], may also have this effect.

A summary of the different h and $a2$ values is given in Tab. 3.4. Comparing the results for the $a2$ values for a given h of the different basis sets shows an off-set of about $20\,\mathrm{cm}^{-1}$

Tab. 3.4: Formally equivalent B3LYP/maTZ fits for different n_D classes, where slightly upscaling ω yields more physical anharmonicity effects for this particular functional and basis set. $a2$ is given in cm^{-1}. Also shown for $h = 1.01$ and 1.00 are the results obtained for B3LYP/mVTZ in the lower row.

	$n_D = 0$	$n_D = 1$	$n_D = 2$	$n_D = 3$	$n_D = 4$
0.98	61.0(1.1)	64.7(6)	68.7(1.1)	70.4(8)	72.9(1.4)
0.99	98.9(1.1)	102.6(6)	106.4(1.1)	108.2(9)	110.7(1.5)
1.00	136.8(1.0)	140.5(6)	144.2(1.1)	146.0(9)	148.4(1.7)
1.00	159.2(1.1)	161.8(6)	164.9(1.2)	166.0(9)	168.2(1.5)
1.01	174.6(9)	178.4(6)	182.0(1.1)	183.8(1.0)	186.1(1.9)
1.01	197.3(1.0)	199.9(6)	202.9(1.2)	203.9(1.0)	206.2(1.7)
1.02	212.5(9)	216.3(6)	219.8(1.2)	221.6(1.0)	223.9(2.0)

that decreases with an increasing n_D. It also shows fits with slightly varied h values for B3LYP/maTZ that run counter to $h = 1.00$ as suggested by the initial all fit during the training phase (see section 3.1.5 (page 47)). As can be seen by the associated standard deviations, the quality of the fits changes very little. However, by using $h = 1.01$ a more physical $a2$ values can be achieved being closer to what would be expected for the diagonal anharmonicity of an OH oscillator ($a2 \approx x_{OH,OH} \approx 175(15)\,cm^{-1}$)[216]. In a similar vein, mVTZ with $h = 1.00$ also yields results that are closer to expected $x_{OH,OH}$ values for $a2$. Furthermore, the $h = 1.00$ fits for mVTZ are remarkably similar to those found for mono-ols with primary alcohols corresponding to $n_D = 0$, secondary to $n_D = 3$ and tertiary to $n_D = 4$. Hence, in the future the possibility of combining mono-ols and diols can be explored.

Transferability to oligomers

The intramolecular hydrogen bonds studied here are fairly weak and correlations derived for such system cannot be applied to stronger hydrogen bonds which are found in diol oligomers. This increase in strength is indicated by further downshifts, shorter hydrogen bond distances and the presence of a bond critical point, which is used by some to decide whether or not a hydrogen bond is present[235]. The most stable dimer for 0-0 and t6-6 is a hetero-chiral dimer with 4 intermolecular hydrogen bonds (called het4) exhibiting S_4 symmetry and having the same structural motif (see Figs. 4.3a (page 131) and 4.6a (page 136)). For 0-0, band positions of $3444\,cm^{-1}$ (A symmetry), $3475\,cm^{-1}$ (E symmetry) and $3513\,cm^{-1}$ (B symmetry) are found experimentally[18,166]. However, the B3LYP

$n_D = 0$ correlation yields 3419 cm^{-1}, 3452 cm^{-1} and 3493 cm^{-1}, respectively. The model considerably underestimates the signals with lower frequency modes being even less well described, which leads to an overestimation of the excitonic coupling of about 7%. This effect is even more pronounced for the GGAs *e.g.* for BP86 a deviation of more than 40% is found. Furthermore, it is to be expected that even larger deviations will be found for liquid-phase 0-0 hydrogen bonds[236].

For t6-6, 3416 cm^{-1} (A symmetry), 3448 cm^{-1} (E symmetry) and 3493 cm^{-1} (B symmetry) is found experimentally[166]. The $n_D = 2$ models perform slightly better but still show large deviations of up to 22 cm^{-1} for B3LYP and 30 cm^{-1} for BP86 from experiment. It is also noticeable that the experimental results for t6-6 are more strongly downshifted with this effect being more exacerbated at lower wavenumbers. This substitution dependence could be exploited in the future for more all encompassing harmonic DFT models.

Another approach would be to form the "diol" in a dimer, *i.e.* by the formation of a weak hydrogen bond between two mono-ols. A promising candidate for such an approach is the dimer of tri-*tert*-butyl-methanol for which claims have been made that it does not form intermolecular hydrogen bonds in its aggregates, since no evidence has been found in the liquid[237,238] and solid phase[237,239] for such interactions. Given the bulkiness of the molecule, if intermolecular hydrogen bonds are formed they are expected to be fairly weak and can possibly be described by the derived correlation model for intramolecular hydrogen bonds of diols. Calculations by R. Medel suggest that hydrogen-bonded dimers should indeed be formed in the gas phase[240].

R. Medel kindly provided his computational data and B3LYP/maTZ calculations were conducted based on these structures. The computations predict a single dominant monomer which is depicted in Fig. A.1 (page 223). This was confirmed experimentally, with the band maximum being heavily influenced by the nozzle temperature and backing pressure. As C.10 (page 281) shows under warm expansion conditions the maximum shifts by about 5 cm^{-1}, indicating a large influence of hot bands. This can be attributed to the fact that a large amount of low lying methyl torsions are present. Moreover, these modes also often involve a torsion of the OH group as well which helps to rationalise the blue-shift of the hot bands. For instance, in case of the OH-stretching frequency of ethanol, a hot band involving the OH torsion was found to be blue-shifted by 7 cm^{-1}[241]. The experimental spectrum (see Fig. 3.32) also shows an additional band at 3680 cm^{-1} which behaves like a monomer. As the monomer is not the focus of this work it will not be further analysed and its cause remains unclear. Furthermore, the tri-*tert*-butyl-methanol monomer is transiently chiral with regards to the $HOC_\alpha C_\beta$ dihedral angle of the *tert*-butyl groups.

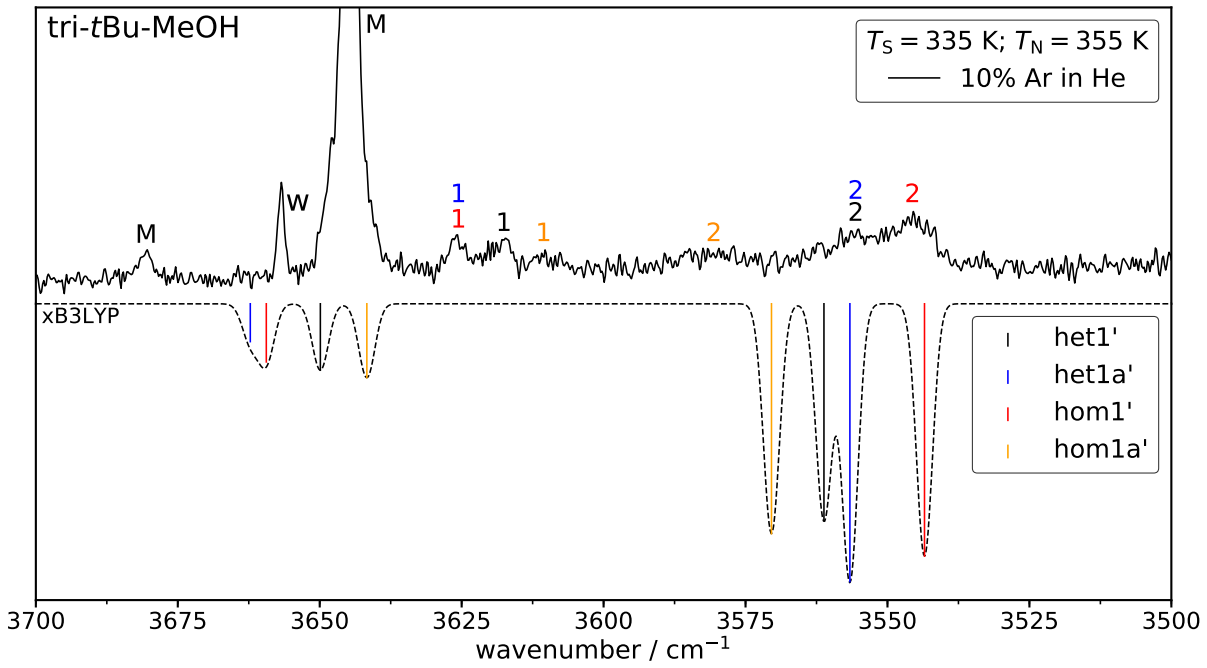

Fig. 3.32: Experimental data (plotted upwards) and simulated data (plotted downwards) of tri-*tert*-butyl-methanol. The saturator temperature (T_S) as well as the nozzle temperature (T_N) are given. The derived correlation ($n_D = 4$) for B3LYP was used for the predictions (see Fig. 3.10 (page 48) bottom left) and no additional shift introduced. w indicates a water band and M monomer bands.

However, a NMR study in solution suggests that the barrier (38.5 kJ mol^{-1}) for the libration of the *tert*-butyl group[242] is too high to be overcome under jet conditions. Therefore, it can be considered a permanently chiral system under jet conditions. A more detailed justification for this assumption can be found in section 4.1.1 (page 129).

Out of the sixteen dimer geometries provided only four structures ended up being energetically relevant at the B3LYP/maTZ level of theory, all of which exhibit intermolecular hydrogen bonds. Using ORCA 4.2.1 the calculations did not converge and ORCA 5.0.3 was used instead, where major improvements have been made to improve the convergence behaviour in difficult cases (TRAH algorithm). During the bachelor thesis of Laura Schiebel it was found that both versions yield very similar frequencies[111], so that the previously derived model can still be applied. Of the four dimers, two are homo-chiral and two are hetero-chiral so that statistical weights of 1 : 1 : 1 : 1 for het1' : het1a' : hom1' : hom1a' have been applied to the simulation shown in Fig. 3.32. The naming convention of the dimers is used which was explained in detail in section 2.4.2 (page 26). Here, hom1' is the most stable dimer closely followed by het1', hom1a' and het1a', with a hydrogen bond length of about 2.0 Å for all of them. This is generally shorter than for the diols with the typical diol having about 0.2 Å – 0.4 Å longer hydrogen bonds. However,

in case of t7-7b' lengths of a similar size have been computed, although the conformer could not be detected experimentally (see Fig. 3.21 (page 65)). All structures are shown in Fig. A.25 (page 237).

The shorter hydrogen bond lengths are also reflected in the stronger experimental downshift relative to the diols. Bands as low as $3574\,\mathrm{cm}^{-1}$ have been observed for the diols in comparison to $3545\,\mathrm{cm}^{-1}$ in this case. It should be kept in mind, that for the diols these strong downshifts are due to secondary interactions with phenyl groups or fluorine atoms. The simulation fits reasonably well for the bound OH modes but completely fails for the free ones. It may be the case that the hydrogen bonds are already too strong to be treated by the model. Instead the typical overestimation of the free OH mode is found, when frequencies are shifted (additive or multiplicative) to coincide with a bound OH mode of a dimer using B3LYP/maTZ (see section 4 (page 129)). Another cause for the deviations could be the influence of not only α but also β substituents which ties into the general strong substitution dependence of B3LYP. It remains to be seen if other methods can describe the OH modes more accurately. Furthermore, the intensities are generally hard to judge given their broad nature and spectral overlap. The experimental intensities suggest that hom1a' at least partially relaxes towards hom1' or that the populations inherently differ due to differences in energy. It may also be the case that band 2 of het1a' overlaps with hom1' instead of het1'. Neglecting the small and broad signals which have been assigned to hom1a', het1' and hom1' alone are satisfactory to explain the main features of the dimer region. However, it is evident that contrary to the solid[237,239] and liquid-phase[237,238], tri-*tert*-butyl-methanol forms hydrogen bonded dimers in the cold gas phase. The experimental Raman-spectra of the dimers discussed in this section have been made available in Ref. [243].

3.1.10 Mono halogenated systems

The systems studied in this section contain either one bromine or chlorine atom whose naturally abundant isotopes have a nuclear spin (I) of 3/2. Since $I > 1/2$ for Cl and Br, they exhibit a nuclear quadrupole moment. This quadrupole moment interacts with the electric field gradient at the nucleus and couples to the rotation of the molecule, allowing to gain information about the electronic environment at the core, *i.e.* the asymmetry parameter (η). If Cl or Br are involved as a hydrogen bond acceptor, this interaction, as characterised by the vibrational frequency of the OH oscillator, may correlate with η which will be discussed in detail in section 3.3 (page 121). Due to diols already being fairly complicated systems, the mono-ols chloropropanol and bromopropanol are characterised

first as simpler entry points for such a comparison. The two mono-ols can in the future also be analysed in the context of Ref. [31]. Since these systems either have been previously studied[244] or have been characterised for the first time in this work by microwave spectroscopy, centrifugal distortion constants are also available (see section 3.2). This enables a comparison of distortion constants and anharmonic frequencies which both can be computed with VPT2. Such a combined analysis can be performed at a later point.

Chloropropanol

Both 1-chloropropan-2-ol and 2-chloropropan-1-ol are conformationally very simple with only two energetically relevant conformers within a given enantiomer. In either case, these conformers have been previously observed by microwave spectroscopy by Goldstein *et al.*[244]. Since the previously used nomenclature for diols is not applicable here, the one of Goldstein *et al.* is used instead. They use three letter descriptors of the form *X*-*YZ*. *X* generally refers to the C-O axis and describes the group on the vicinal chiral C atom which aligns anti-periplanar to the hydrogen of the OH-group. For the methyl group an *m* is used, for a chloromethyl group a *c* and for a hydrogen atom an *h*. For 1-chloropropan-2-ol, *Y* is related to the position of the Cl and O atoms relative to each other and *Z* describes the relative positions of the terminal methyl-group and the Cl atom. *g* refers to a *gauche* angle ($\approx \pm 60^\circ$) and *a* to an anti-periplanar dihedral angle ($\approx 180^\circ$). For 2-chloropropan-1-ol, *Y* indicates the angle between the O and Cl atoms and *Z* the angle between the O atom and the terminal methyl-group. Additionally, *g* and *g'* are introduced to distinguish *gauche* angles of 60° and -60°, respectively.

In case of 2-chloropropan-1-ol, the most stable conformer is g-ga followed by g'-gg which are depicted in Fig. A.2 (page 223). The next structure follows around $7.2\,\mathrm{kJ\,mol^{-1}}$ at the B3LYP/maTZ level and will therefore not be further discussed. The relative energies for different computational methods including literature values[244] are shown in Tab. 3.5. It can be seen that the methods generally agree quite well with each other. In comparison to the highest level of computation available, *i.e.* CCSD(T0)-F12a, the relative energies computed by PBE and PBE0 are slightly higher while the MP2/6-311++G(d,p) calculations of Goldstein *et al.* are lower. Since MP2/aVTZ is very close to the coupled cluster values, the deviations can be attributed to an inadequate basis set. Zero-point correction also does not significantly influence the relative energies but systematically increases the energy difference slightly. Furthermore, using the anharmonic zero point correction makes little difference in comparison to the harmonic one. Additionally, the switch from maTZ to aVTZ also provides little changes. It should be kept in mind that differences between the basis sets could also be caused by the fact that different program packages

Tab. 3.5: Comparison of energetical computational data with literature values from Goldstein *et al.*[244] and Gonçalves *et al.*[245] for 1-chloropropan-2-ol and 2-chloropropan-1-ol. The relative electronic energy (ΔE_{el}) and harmonically zero point corrected energy (ΔE_0^{h}) as well as the anharmonically corrected energies (ΔE_0^{an}) if available are shown. In case of the literature data it is not entirely clear if zero point correction was applied. The energies are given relative to the most stable g-ga conformer in case of 2-chloropropan-1-ol and m-ga in case of 1-chloropropan-2-ol. All values are given in kJ mol^{-1}.

	2-chloropropan-1-ol			1-chloropropan-2-ol		
	ΔE_{el}	ΔE_0^{h}	ΔE_0^{an}	ΔE_{el}	ΔE_0^{h}	ΔE_0^{an}
BP86/maTZ	1.62	1.92	-	1.93	1.94	-
PBE/maTZ	1.91	2.20	-	2.71	2.70	-
PBE0/maTZ	1.75	2.07	-	2.61	2.63	-
B3LYP/maTZ	1.62	1.89	-	2.59	2.60	-
PBE0/aVTZ	1.90	2.18	2.27	2.76	2.78	2.64
B3LYP/aVTZ	1.72	1.95	1.75	2.66	2.67	2.46
CAM-B3LYP/aVTZ	1.83	2.06	2.09	3.32	3.33	3.26
B2PLYP/aVTZ	1.66	1.88	2.23	3.67	3.70	3.56
MP2/aVTZ	1.47	1.69	1.68	3.14	3.20	3.20
CCSD(T0)-F12a/VDZ-F12	1.36	1.59	-	3.22	3.26	-
B3LYP/aug-cc-pVDZ[245]	-	-	-	4.14	-	-
MP2/6-311++G(d,p)[244]	0.78	-	-	3.93	-	-
MP2/6-311++G(d,p)[245]	-	-	-	3.93	-	-

were used. However, these deviations are in line with results of a more comprehensive basis set test using the ORCA program package (see Fig. 2.3 (page 17)). For the diols, some substantial differences were found between GGAs and hybrid functionals which is not the case here.

The computational data for 1-chloropropan-2-ol is also provided in Tab. 3.5. The two energetically relevant conformers are depicted in Fig. A.3 (page 223). The next highest conformer in energy is in a similar range as was the case for 2-chloropropan-1-ol. It can be seen that all methods agree in terms of the energetic order but some larger deviations from the gold standard can be found. This is especially noticeable for BP86/maTZ and the B3LYP/aug-cc-pVDZ calculation by Gonçalves *et al.*[245]. For the latter, this could be caused by the neglect of dispersion correction or the small basis set or perhaps both. Again, the switch from maTZ to aVTZ and the inclusion of zero point correction (harmonic and anharmonic) makes no significant difference. For both chloropropanol isomers, the MP2/aVTZ values are remarkably close to the coupled cluster ones.

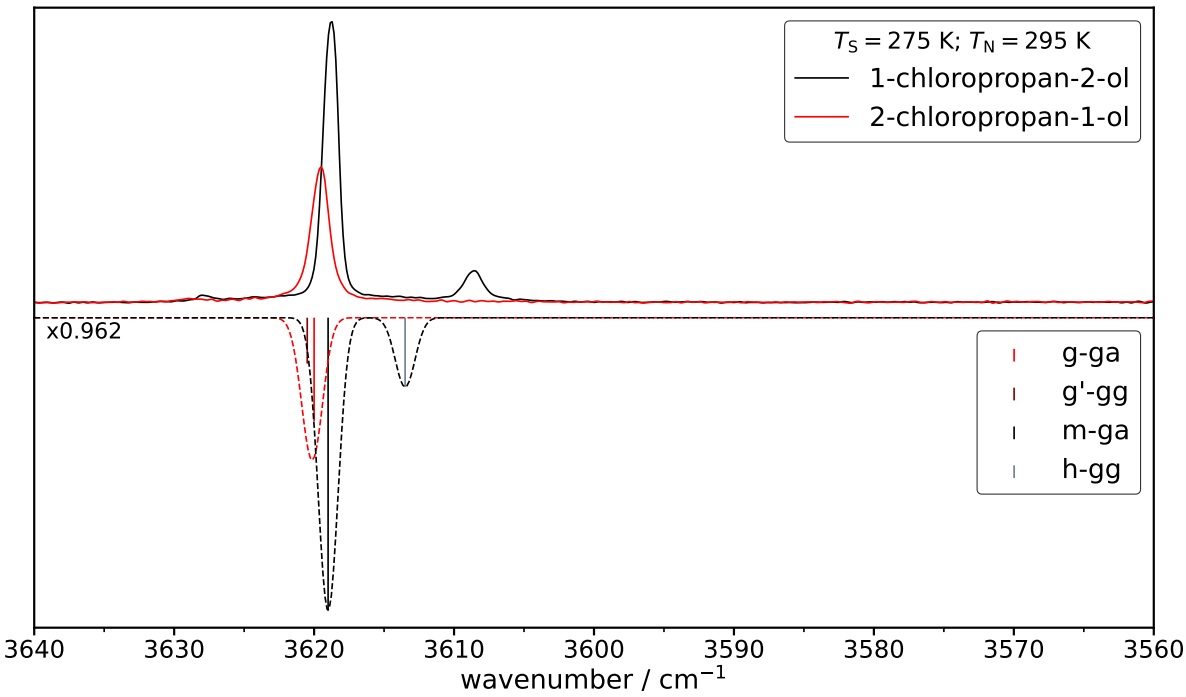

Fig. 3.33: Experimental data (plotted upwards) and simulated data (plotted downwards) of 2-chloropropan-1-ol (g-ga and g'-gg) and 1-chloropropan-2-ol (m-ga and h-gg). The saturator temperature (T_S) as well as the nozzle temperature (T_N) are given. The simulated spectra are based on B3LYP/maTZ and are Boltzmann weighted based on T_N according to the relative energies given in Tab. 3.5. A wavenumber scaling factor of 0.962 is used for both systems. The predicted intensities for 2-chloropropan-1-ol have been halved to reproduce the experimental results.

The experimental and simulated spectra are shown in Fig. 3.33 for 2-chloropropan-1-ol (red spectrum) and 1-chloropropan-2-ol (black spectrum). In both instances a scaling factor of 0.962 is appropriate to scale to the most stable conformer. The intensities of the experimental spectra are unscaled and were recorded under the same experimental conditions indicating that the vapour pressure of 2-chloropropan-1-ol is significantly lower. To simulate this fact the predicted intensities of 2-chloropropan-1-ol are halved. The experiment can be well reproduced with the exception of the splitting between m-ga and h-gg (1-chloropropan-2-ol), where B3LYP/maTZ underestimates the splitting. Since g-ga and g'-gg spectrally overlap no inference with regard to the energetic predictions can be made for 2-chloropropan-1-ol. However, for 1-chloropropan-2-ol such a distinction is possible indicating that might B3LYP/maTZ overestimates the stability of h-gg. It might also be the case that partial relaxation of h-gg to m-ga is taking place. The energy differences predicted by WFT, CAM-B3LYP and B2PLYP are more in line with the experimental intensities (see Tab. 3.5).

Tab. 3.6 shows a comparison of the experimental and predicted shifts between the band

Tab. 3.6: Comparison of the experimental and predicted shifts between the band positions of the two most stable conformers of 2-chloropropan-1-ol and 1-chloropropan-2-ol. Shifts based on harmonic and anharmonic calculations are given if available. The absolute wavenumbers by Goldstein *et al.*[244] were originally scaled by 0.95 and did not provide any decimal places. All values are given in cm^{-1}.

	$\Delta\tilde{\nu}_{21}$ = g-ga − g'-gg		$\Delta\tilde{\nu}_{12}$ = m-ga − h-gg	
	harmonic	anharmonic	harmonic	anharmonic
Jet-Raman	-	0	-	10
BP86/maTZ	−5.8	-	1.0	-
PBE/maTZ	−6.0	-	0.8	-
PBE0/maTZ	−3.9	-	4.4	-
B3LYP/maTZ	−0.5	-	5.7	-
PBE0/aVTZ	−3.3	−4.6	5.3	7.8
B3LYP/aVTZ	−3.0	−4.3	6.2	8.9
CAM-B3LYP/aVTZ	−2.5	−2.7	8.0	9.9
B2PLYP/aVTZ	−1.8	−2.9	5.6	7.5
MP2/aVTZ	−0.5	−0.6	2.7	3.4
CCSD(T0)-F12a/VDZ-F12	0.3	-	7.4	-
MP2/6-311++G(d,p)[244]	−2.1	-	0.0	-

positions of the two relevant conformers. It can be seen that for the GGAs an opposite trend towards the hybrid functionals is present, *i.e.* the shift increases in magnitude for 2-chloropropan-1-ol ($\Delta\tilde{\nu}_{21}$) while it decreases for 1-chloropropan-2-ol ($\Delta\tilde{\nu}_{12}$). Furthermore, in case of $\Delta\tilde{\nu}_{21}$ the switch of basis sets for B3LYP appears more substantial. The anharmonic calculations increase the shift in magnitude throughout which is closer to experiment for $\Delta\tilde{\nu}_{12}$, while its further away for $\Delta\tilde{\nu}_{21}$. For MP2, $\Delta\tilde{\nu}_{21}$ is predicted well while $\Delta\tilde{\nu}_{12}$ is predicted far too low, which is compensated for in the double-hybrid functional B2PLYP. The MP2 results by Goldstein *et al.*[244] also run counter to the experiment. Coupled cluster on the other hand performs well throughout. The absolute band positions can be found in Tab. C.1 (page 259) for the harmonic and Tab. D.2 (page 292) for the anharmonic case.

The VPT2 calculations also allow for a direct comparison of the anharmonic frequencies with the experiment. This is illustrated in Tab. 3.7 where the differences between theory and experiment are shown. As can be seen, MP2 and B2PLYP perform reasonably well, while larger and less consistent deviations are found for PBE0, B3YLP and CAM-B3LYP. The rather good performance of MP2 and B2PLYP was previously noted by Meyer *et al.* for formic acid, although the larger aVQZ basis set was used[246]. Espe-

Tab. 3.7: Deviations of the absolute band positions at different levels of electronic structure theory calculated with VPT2 relative to the experiment for 2-chloropropan-1-ol (g-ga and g'-gg) and 1-chloropropan-2-ol (m-ga and h-gg). A positive sign indicates overestimation while a negative one indicates underestimation. The absolute Jet-Raman band positions are given as reference points. All calculations utilise the aVTZ basis set. The arithmetic mean and standard deviation for each method are also shown.

	g-ga	g'-gg	m-ga	h-gg	mean
Jet-Raman	3620	3620	3609	3619	-
PBE0	15.89	20.49	24.68	22.52	20.9(3.8)
B3LYP	−32.19	−27.87	−24.74	−25.88	−27.7(3.3)
CAM-B3LYP	22.89	25.58	28.56	28.49	26.4(2.7)
B2PLYP	−13.77	−10.86	−10.15	−12.68	−11.9(1.7)
MP2	−8.97	−8.38	−9.40	−15.96	−10.7(3.6)

cially, the very consistent deviations, as indicated by the standard deviation, for B2PLYP would lend themselves to a possible back correction ($+12\,\mathrm{cm}^{-1}$) of related systems like bromopropanol. For B3LYP ($+28\,\mathrm{cm}^{-1}$) and CAM-B3LYP ($-26\,\mathrm{cm}^{-1}$), this may also be possible but with larger uncertainties. Furthermore, the effect that B3LYP underestimates and that PBE0 overestimates can be attributed to the previously established fact that B3LYP predict OH bonds too soft while PBE0 predicts them to be too hard. The use of the CAM method also significantly changes the B3LYP results indicating that OH bonds are now too hard, although the deviations are more consistent. In terms of the deviation from experiment the harmonic unscaled predictions of the GGAs are closer to experiment than some anharmonic calculations albeit highly irregular (see Tab. C.1 (page 259)). It is also possible to combine higher level harmonic coupled cluster calculation with the computed anharmonicity constants at lower levels which proved very helpful to predict/reproduce the bands of the methanol monomer and dimer[168] but also for small organic acids[247,248] and various other small organic molecules[249]. Such an approach can be carried out in the future for this and the following systems.

Bromopropanol

The heavier analogues 1-bromopropan-2-ol and 2-bromopropan-1-ol behave very similar to the chlorine ones where only two conformers are energetically relevant. As can be seen from Figs. A.4 (page 224) and A.5 (page 224), the structures are also very closely related. The energetics for 2-bromopropan-1-ol are shown in Tab. 3.8. In comparison to the chlorine analogue a slight stabilisation of the less stable conformer can be observed with

Tab. 3.8: Comparison of energetical computational data with literature values from Gonçalves *et al.*[245] for 1-bromopropan-2-ol and 2-bromopropan-1-ol. The relative electronic energy (ΔE_{el}) and harmonically zero point corrected energy (ΔE_0^{h}) as well as the anharmonically corrected energies (ΔE_0^{an}), if available, are shown. In case of the literature data it is not entirely clear if zero point correction was applied. The energies are given relative to the most stable g-ga conformer in case of 2-bromopropan-1-ol and m-ga in case of 1-bromopropan-2-ol. The VDZ-F12* basis set is defined as all = VDZ-F12 and Br = VDZ-PP-F12. All values are given in kJ mol^{-1}.

	2-bromopropan-1-ol			1-bromopropan-2-ol		
	ΔE_{el}	ΔE_0^{h}	ΔE_0^{an}	ΔE_{el}	ΔE_0^{h}	ΔE_0^{an}
BP86/maTZ	1.46	1.79	-	1.27	1.25	-
PBE/maTZ	1.76	2.07	-	2.29	2.22	-
PBE0/maTZ	1.61	1.94	-	2.20	2.18	-
B3LYP/maTZ	1.45	1.73	-	2.19	2.17	-
PBE0/aVTZ	1.76	2.06	2.10	2.33	2.29	2.16
B3LYP/aVTZ	1.84	2.48	2.44	2.23	2.20	1.94
CAM-B3LYP/aVTZ	1.65	1.90	1.92	3.02	3.00	2.95
B2PLYP/aVTZ	1.64	1.92	1.98	2.73	2.70	2.65
MP2/aVTZ	1.22	1.50	1.50	2.43	2.39	2.20
CCSD(T0)-F12a/VDZ-F12*	0.43	0.78	-	2.44	2.36	-
B3LYP/aug-cc-pVDZ[245]	-	-	-	4.10	-	-
MP2/6-311++G(d,p)[245]	-	-	-	4.02	-	-

the exception of B3LYP/aVTZ. All functionals predict very similar energy differences. However, as was the case for 2-chloro-propan-1-ol, the WFT methods predict smaller energy differences for 2-bromopropan-1-ol. Especially, coupled cluster predicts very close energetic proximity of the conformers. Harmonic zero point correction introduces little changes. Furthermore, switching from harmonic to anharmonic zero point correction makes no difference. Changes induced by the switch of the basis set are again quite small with some slightly larger changes for B3LYP. The next higher in energy conformers follow around 7 kJ mol^{-1} at the B3LYP/maTZ level of theory.

The relative energies of 1-bromopropan-2-ol are also shown in Tab. 3.8. The hybrid functionals and GGAs generally agree with each other with the exception of BP86, CAM-B3LYP and the B3LYP/aVDZ results of Gonçalves *et al.*[245] which was already the case for 1-chloropropan-2-ol (see Tab. 3.5). Furthermore, the energy gap is predicted to be smaller in comparison to 1-chloropropan-2-ol, except MP2/6-311++G(d,p)[245]. B2PLYP also predicts slightly higher energies than B3LYP/aVTZ and MP2/aVTZ yet again. MP2/aVTZ by itself predicts relative energies that are very close to the coupled clus-

ter results, however, with the 6-311++G(d,p) basis set the relative energy is too high. Zero point correction does not significantly change the relative energies regardless if the correction is done harmonically or anharmonically. More unstable conformers follow in a similar region as was the case for 2-bromopropan-1-ol.

Fig. 3.34 shows the experimental spectra and simulations of 2-bromopropan-1-ol and 1-bromopropan-2-ol. In case of 1-bromopropan-2-ol, only technical purity (75%) was easily commercially available with the biggest contaminant being 2-bromopropan-1-ol. This can be seen in the experimental spectrum (black spectrum) where the signal at 3608 cm^{-1} tails of towards lower wavenumbers which coincides with the spectrum of 2-bromopropan-1-ol (red spectrum). Due to this overlap an accurate judgement of the relative energies is not possible. It is also evident that the vapour pressure of 2-bromopropan-1-ol is likely significantly lower than its counterpart which was already the case for the chlorine derivative (see Fig. 3.33) as the experimental spectra are again unscaled and measured under the same experimental conditions. B3LYP/maTZ also again underestimates the

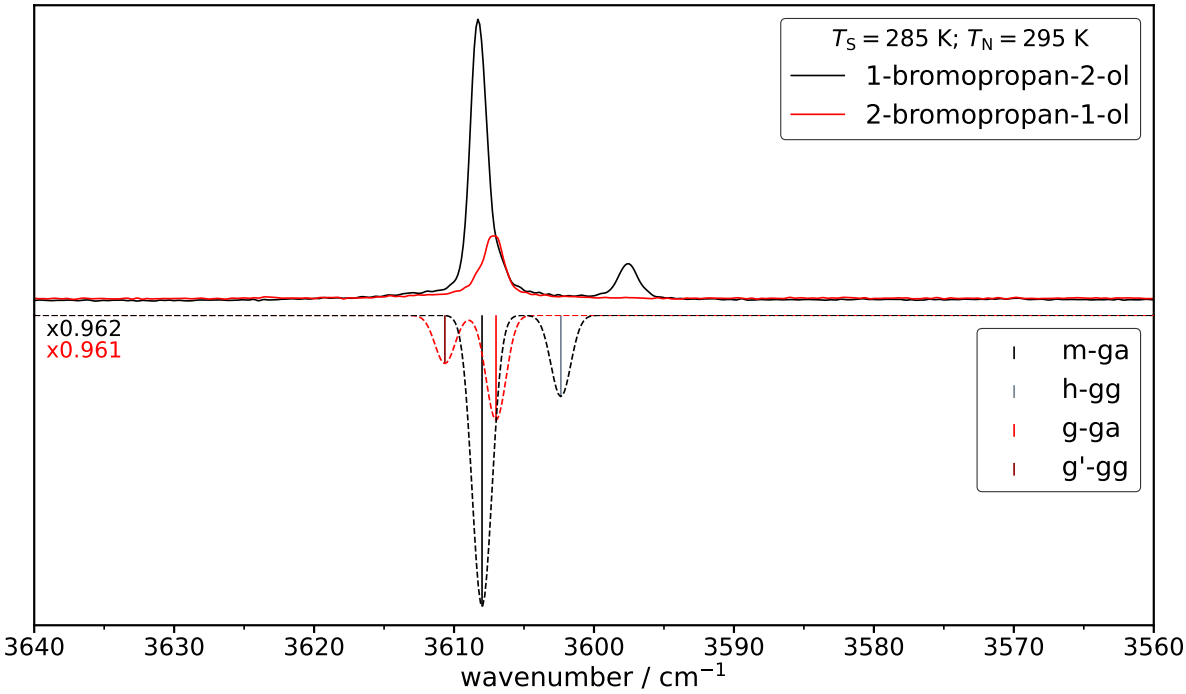

Fig. 3.34: Experimental data (plotted upwards) and simulated data (plotted downwards) of 2-bromopropan-1-ol (g-ga and g'-gg) and 1-bromopropan-2-ol (m-ga and h-gg). The saturator temperature (T_S) as well as the nozzle temperature (T_N) are given. The simulated spectra are based on B3LYP/maTZ and are Boltzmann weighted based on T_N according to the relative energies given in Tab. 3.8. The corresponding scaling factors are shown as well. The predicted intensities for 2-chloropropan-1-ol have been halved to reproduce the experimental results.

splitting between m-ga and h-gg. However, the spectral separation between g-ga and g'-gg is now overestimated. The OH stretching vibrations still overlap. However, unlike 2-chloropropan-1-ol, a shoulder around 3608 cm^{-1} can be seen with the main contributions of g-ga being at 3607 cm^{-1}. Given this overlap, the relative energies can also not be accurately assessed. For the simulated intensities the same scaling factor of 1/2 was used taken from 2-chloropropan-1-ol.

In Tab. 3.9 the band splitting between the two most stable conformers are shown for both bromine isomers. For the GGAs, similar behaviour as for the chlorine derivatives (see Tab. 3.6) can be found, *i.e.* larger shifts are expected for $\Delta\tilde{\nu}_{21}$ while they decrease for $\Delta\tilde{\nu}_{12}$ in comparison to most other methods and experiment. In case of $\Delta\tilde{\nu}_{21}$, all predicted shifts are too large in magnitude besides the coupled cluster and MP2 results. Furthermore, B3LYP/aVTZ predicts a significantly more negative value than its maTZ counterpart. For 2-chloropropan-1-ol, the absolute deviations were smaller but the relative deviations were larger. Using anharmonic shifts provides no benefit in case of $\Delta\tilde{\nu}_{21}$. In case of $\Delta\tilde{\nu}_{12}$, most methods significantly underestimate the shift again similar to the chlorine case. MP2 yet again predicts shifts far too low akin to the GGAs. Harmonically CAM-B3LYP and coupled cluster perform well while switching to anharmonic ones improves the predictions throughout for 1-bromopropan-2-ol. These results again highlight the close similarity between the chlorine and bromine systems. The absolute band positions can be found in

Tab. 3.9: Comparison of the experimental and predicted shifts between the band positions of the two most stable conformers of 2-bromopropan-1-ol and 1-bromopropan-2-ol. Shifts based on harmonic and anharmonic calculations are given if available. The VDZ-F12* basis set is defined as all = VDZ-F12 and Br = VDZ-PP-F12. All values are given in cm^{-1}.

	$\Delta\tilde{\nu}_{21}$ = g-ga − g'-gg		$\Delta\tilde{\nu}_{12}$ = m-ga − h-gg	
	harmonic	anharmonic	harmonic	anharmonic
Jet-Raman	-	−1	-	10
BP86/maTZ	−6.8	-	1.4	-
PBE/maTZ	−7.0	-	1.2	-
PBE0/maTZ	−4.6	-	4.5	-
B3LYP/maTZ	−3.8	-	5.9	-
PBE0/aVTZ	−4.3	−4.0	5.3	8.4
B3LYP/aVTZ	−8.4	−8.7	6.2	9.6
CAM-B3LYP/aVTZ	−3.1	−4.3	8.3	10.0
B2PLYP/aVTZ	−4.2	−4.9	5.4	7.7
MP2/aVTZ	−0.3	−0.7	2.2	3.1
CCSD(T0)-F12a/VDZ-F12*	−0.3	-	6.8	-

Tab. C.2 (page 260) for the harmonic and Tab. D.3 (page 293) for the anharmonic case.

The deviations of the absolute band positions predicted with VPT2 calculations relative to the experiment are shown in Tab. 3.10. As was the case for the chlorine derivatives (see Tab. 3.7), PBE0 and CAM-B3LYP overestimate while the other methods underestimate the band positions. While for B3LYP, CAM-B3LYP and B2PYLP the deviations between the Cl and Br derivatives are quite similar, large difference can be found for PBE0 and MP2 as indicated by the different means. This indicates that B3LYP and CAM-B3LYP could be back-corrected as previously suggested. B2PLYP again shows little variance and applying a correction of $12\,\mathrm{cm}^{-1}$ leads to a maximum absolute deviation of about $3\,\mathrm{cm}^{-1}$. Expectedly, slightly larger absolute deviations of up to $5\,\mathrm{cm}^{-1}$ can be found for B3LYP and CAM-B3LYP. For PBE0 and MP2, switching from chlorine to bromine leads to slight changes and it remains to be seen if this effect prevails for the diols. Furthermore, it can be seen if the back correction can be applied more generally or if it fails when moving to diols. It may also be the case that the OH oscillator involved in a hydrogen bond towards a halogen can be corrected while it fails for the OH$\cdots$O case.

Tab. 3.10: Deviations of the absolute band positions at different levels of theory calculated with VPT2 relative to the experiment for 2-bromopropan-1-ol (g-ga and g'-gg) and 1-bromopropan-2-ol (m-ga and h-gg). A positive sign indicates overestimation while a negative one indicates underestimation. The absolute Jet-Raman band positions are given as reference points. All calculations utilise the aVTZ basis set. The arithmetic mean and standard deviation for each method are also shown.

	g-ga	g'-gg	m-ga	h-gg	mean
Jet-Raman	3607	3608	3598	3608	-
PBE0	10.99	13.99	17.22	18.82	15.3(3.5)
B3LYP	−33.52	−25.85	−26.88	−26.45	−28.2(3.6)
CAM-B3LYP	25.72	28.97	31.09	31.12	29.2(2.5)
B2PLYP	−14.89	−11.03	−14.33	−12.04	−13.1(1.8)
MP2	−16.31	−16.66	−24.13	−17.19	−18.6(3.7)

3-Chloro-propane-1,2-diol

An energetic overview of the conformational landscape of 3-chloro-propane-1,2-diol (0-Cl_1) is shown in Fig. 3.35. The way in which the relative energies increase is reminiscent of 0-F, where the two most stable conformers are fairly close while all other conformers follow at significantly higher energies (see Fig. 3.12c (page 51)). It is also one of the systems where

a conformer with an anti-periplanar OCCO dihedral angle may be energetically relevant. Contrary to other diols discussed before a weak intramolecular hydrogen bond to a chlorine atom is present. Furthermore, the barriers are quite high with the only exception being 0-Cl_1b' which can easily relax to 0-Cl_1b. Here, the relaxation path is along a simple OH torsion, similar to unprimed/primed pairs for the methyl series (see section 3.1.4 (page 39)). The different structures are shown in Fig. A.11 (page 228) and demonstrate why most barriers are quite high.

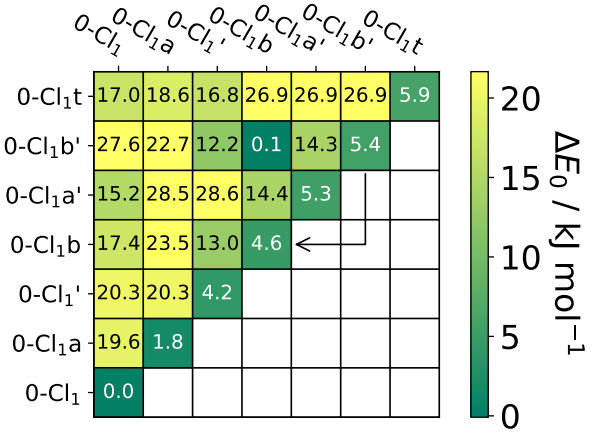

Fig. 3.35: Zero point corrected energies as well as the corresponding barriers for 0-Cl_1 at the B3LYP/maTZ level.

A large variety of other computational methods have also been employed and are summarised in Tab. B.6 (page 247). The harmonic zero point corrected relative energies are shown in Fig. 3.36. As can be seen some conformers undergo very drastic energy changes at different levels of theory. Most affected is the 0-Cl_1a' conformer which is predicted as high as 7.02 kJ mol^{-1} with MP2/aVTZ and as low as 2.65 kJ mol^{-1} for BP86/maTZ. For the GGAs, this stabilisation can be attributed to a general effect of GGA functionals observed for primed conformers. In this vein, 0-Cl_1' is also significantly over-stabilised by the GGAs. The very strong differences for 0-Cl_1a' are likely due to the fact that it has the most direct hydrogen bond towards the chlorine atom. This becomes clear when comparing the H$\cdots$Cl distances between isomers which is computed to be 2.44 Å for 0-Cl_1a' while the others range between 2.55 Å and 2.68 Å at the B3LYP/maTZ level of theory. For the simpler 2-chloro-ethanol, an experimental H$\cdots$Cl distance of 2.609(1) Å[250] has been found which fits nicely in-between the less interacting cases. PBE0 and B3LYP yield very similar results to each other.

The hybrid and double hybrid functionals as well as MP2 results closely resemble the coupled cluster data, although the energetic order switches but stays within 1 kJ mol^{-1} of the CCSD(T) relative energies, with the exception of 0-Cl_1a' where B3LYP and PBE0 show larger differences. The CAM-B3LYP, B2PLYP and MP2 results are very close to the coupled cluster results, although MP2 switches the energetic order of 0-Cl_1b' and 0-Cl_1t. As was the case for the mono-ols, a change in basis set for B3LYP and PBE0 does not significantly impact the results. Similarly, switching to anharmonically zero point corrected energies has little effect as can be seen from Tab. B.6 (page 247). Furthermore, the zero point correction (harmonic and anharmonic) consistently lowers the relative

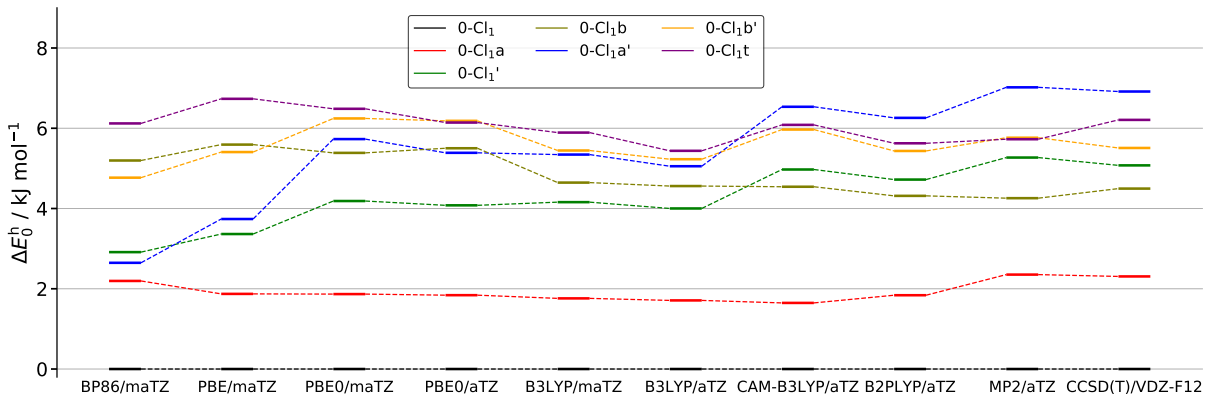

Fig. 3.36: Overview of the harmonically zero point corrected relative energies at different levels of theory for 3-chloro-propane-1,2-diol (0-Cl_1). The aVTZ basis set is shortened to aTZ.

energies with the exception of 0-Cl_1a' and 0-Br_1b' for the GGAs.

For 0-Cl_1 the previously derived B3LYP/maTZ correlation can be used for $n_D = 1$. However, the predictions are not satisfactory and open for ambiguity as can be seen from Fig. C.11 (page 282). This behaviour is more indicative of what was observed for mono-ols where halogen atoms provided a significant challenge for the models[31]. Since the correlation worked well for 0-F it might be the case that tri-chlorination would lead to a better agreement. It may also be an inherent property of fluorine leading to the agreement. Measurements of 3-fluoropropane-1,2-diol could potentially resolve this issue.

Instead of B3LYP/maTZ, the assignments are aided by VPT2 B2PLYP/aVTZ calculations since for the mono-ols very consistent deviations were found. Specifically, an upshift of 12 cm^{-1} was necessary to reach very good agreement with the experiment. Such an approach is shown in Fig. 3.37. The predictions fit remarkably well to the experiment with the largest deviation being $-2.8\,cm^{-1}$ for 0-Cl_1a'. The very broad band around 3630 cm^{-1} can be attributed to an overlap of the free OH vibration 0-Cl_1 (main peak) and 0-Cl_1a (shoulder) for which the donor and acceptor overlap. The signal at 3617 cm^{-1} can then be readily assigned to 0-Cl_1. The pair of bands at 3587 cm^{-1} and 3621 cm^{-1} can be assigned to 0-Cl_1'. The two bands close to 3700 cm^{-1} belong to 0-Cl_1b and 0-Cl_1t, respectively, where the free OH group is in no contact with the chlorine atom (see Fig. A.11 (page 228)). The somewhat unusual band profile of the signal at 3689 cm^{-1} is likely caused by similar higher energy variants of 0-Cl_1t which will not be discussed for simplicity. The counterparts of the free modes can be found at 3604 cm^{-1} and 3599 cm^{-1} for 0-Cl_1b and 0-Cl_1t, respectively. The former overlaps with 0-Cl_1a', while the latter may overlap with 0-Cl_1b' but given its low barrier it will not be assigned. Furthermore, no spectral evidence is found for the free OH mode of 0-Cl_1b'. Lastly, the small band at 3573 cm^{-1} can be

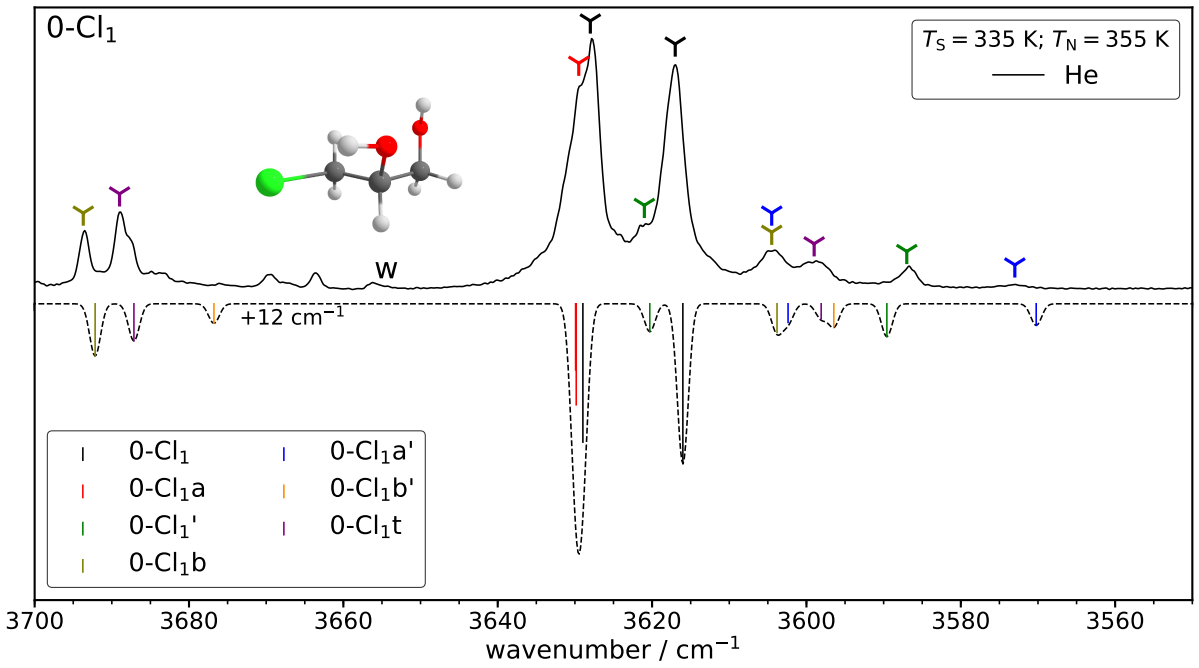

Fig. 3.37: Experimental data (plotted upwards) and simulated data (plotted downwards) of 3-chloropropane-1,2-diol (0-Cl_1). The saturator temperature (T_S) as well as the nozzle temperature (T_N) are given. The simulated intensities are based on B3LYP/maTZ and are Boltzmann weighted based on T_N according to the relative energies given in Fig. 3.35. The frequencies are taken from VPT2 B2PLYP/aVTZ calculations corrected by $+12\,cm^{-1}$ as derived in section 3.1.10 (page 88). w indicates a water band.

attributed to the bound OH mode of 0-Cl_1a'. The bands around $3665\,cm^{-1}$ could possibly be caused by 0-Cl_1b' but given its predicted relaxation propensity will not be assigned. Other possible explanations include higher energy conformers, hot bands or impurities.

Tab. 3.11 summarises the experimental and predicted harmonic intramolecular hydrogen bond shifts. It can be seen that the methods perform quite diverse. The GGAs tend to overestimate the shift especially in the case of 0-Cl_1. It appears as though this trend is attenuated for primed conformers with the shift of 0-Cl_1' being underestimated. Furthermore, the BP86 and PBE are the only methods that predict the free OH mode lower than the bound one harmonically as indicated by the negative sign. Although B3LYP previously performed very well in predicting the shifts harmonically (see Fig. 3.27 (page 75)), it performs rather poorly but still better than the GGAs. This is still the case for 0-C_1b where the Cl atom is not directly involved in the hydrogen bond arrangement. It appears that the previous fortuitous error cancellation is no longer present possibly due to different anharmonicity. A change in basis set also does not influence that behaviour. PBE0 on the other hand, now performs significantly better. There still is a tendency for overestimation but the agreement with experiment is much better than with B3LYP.

Tab. 3.11: Comparison of the experimental and computed intramolecular hydrogen bond shifts of 3-chloro-propane-1,2-diol. The shifts Δ are calculated as the difference between the free OH mode and the bound one. Harmonic (Δ^{h}) as well as anharmonic shifts (Δ^{an}) are given if available.

		0-Cl_1	0-Cl_1a	0-Cl_1'	0-Cl_1b	0-Cl_1a'	0-Cl_1b'	0-Cl_1t
Jet-Raman	Δ^{an}	−11	0	−34	90	31	-	90
BP86/	Δ^{h}	−29.0	−0.3	−27.3	116.0	31.7	97.9	108.2
maTZ	Δ^{an}	-	-	-	-	-	-	-
PBE/	Δ^{h}	−29.8	−1.5	−27.7	115.3	34.2	98.7	108.2
maTZ	Δ^{an}	-	-	-	-	-	-	-
PBE0/	Δ^{h}	−18.2	5.0	−27.1	94.1	33.5	81.0	91.6
maTZ	Δ^{an}	-	-	-	-	-	-	-
B3LYP/	Δ^{h}	−10.4	7.9	−22.5	82.1	27.7	70.8	76.8
maTZ	Δ^{an}	-	-	-	-	-	-	-
PBE0/	Δ^{h}	−21.2	0.6	−30.1	92.5	32.3	83.1	94.4
aVTZ	Δ^{an}	−20.5	6.8	−34.1	99.2	23.0	85.9	105.5
B3LYP/	Δ^{h}	−13.5	4.2	−25.0	81.3	27.6	73.1	79.4
aVTZ	Δ^{an}	−12.7	−4.6	−26.1	88.8	16.1	76.4	89.7
CAM-B3LYP/	Δ^{h}	−6.7	9.9	−22.5	84.1	37.5	77.7	77.8
aVTZ	Δ^{an}	−5.8	8.7	−25.9	90.8	31.9	85.7	85.8
B2PLYP/	Δ^{h}	−14.9	0.9	−28.5	81.0	36.5	74.5	78.4
aVTZ	Δ^{an}	−13.0	−0.1	−30.7	88.4	32.2	80.3	89.1
MP2/	Δ^{h}	−21.8	7.6	−34.4	83.1	48.6	76.5	82.5
aVTZ	Δ^{an}	−23.0	10.2	−38.5	90.0	46.9	85.2	93.0
CCSD(T)/	Δ^{h}	−11.1	2.3	−29.5	82.2	43.1	70.1	79.2
VDZ-F12	Δ^{an}	-	-	-	-	-	-	-

For instance, the mean absolute error (MAE) is $3.81\,cm^{-1}$ for PBE0/aVTZ while for B3LYP/aVTZ it is $6.43\,cm^{-1}$. Furthermore, PBE0/aVTZ performs best harmonically in comparison to all tested methods. Moving to B3LYP double hybrid variant (B2PLYP) slightly reduces the error to $6.08\,cm^{-1}$ while the range separated variant (CAM-B3LYP) increases it to $8.41\,cm^{-1}$. MP2 exhibits similar errors as CAM-B3LYP but otherwise behaves quite different, *i.e.* it overestimates the shift significantly for some instances while the opposite is the case for CAM-B3LYP. The coupled cluster results have an MAE of $6.27\,cm^{-1}$ very similar to B3LYP/aVTZ. However, the deviations are more systematic. In cases where the Cl atom is not involved in the hydrogen bonding, a consistent underestimation of about $10\,cm^{-1}$ can be found while the overestimation of again about $10\,cm^{-1}$

in case 0-Cl_1a' may occur due to a very strong interaction with the Cl atom. Despite the short distance, the bound (OH$\cdots$O) mode is lower in wavenumber than the "free" one interacting with the Cl atom. The absolute harmonic wavenumbers can be found in Tab. C.9 (page 264).

Tab. 3.11 also shows the anharmonically predicted intramolecular hydrogen bond shifts in comparison to the experiment. While PBE0 performed very well harmonically its performance suffers when moving towards anharmonic shifts increasing the MAE to 8.12 cm^{-1}. For all other methods the switch leads to some slight improvement with the exception of B2PYLP (MAE: 1.51 cm^{-1}) and CAM-B3LYP (MAE: 4.66 cm^{-1}). B2PLYP performs the best and shows at most deviations of $-3.28\,cm^{-1}$ making it the general method of choice. For the 0-Cl_1a conformer in case of B3LYP and B2PLYP changes the spectral order of the free and bound OH mode. For CAM-B3LYP and B2PYLP, no clear trends can be made out while for B3LYP a tendency towards underestimation and for MP2 as well as PBE0 a trend towards overestimation can be found. For the latter, the 0-Cl_1a' conformer shows underestimation which may be caused by the strong interaction between the OH group and the Cl atom. The absolute anharmonic wavenumbers can be found in Tab. D.4.

In Tab. 3.12 the deviations of the absolute band position predicted by VPT2 calculations relative to the experiment are shown. It can yet again be seen that PBE0 and CAM-B3LYP consistently overestimate while the other methods underestimate. The PBE0 results vary greatly, however, a tendency towards stronger overestimation can be found for the free OH modes. Since this trend is also present in 0-Cl_1b it is not tied to a direct interaction with the Cl atom with the exception of 0-Cl_1a' where this trend is reversed and the OH$\cdots$Cl distance is particularly short. In case of B3LYP, the deviations cluster around $-26\,cm^{-1}$ as was previously the case for the mono-ols (see Tabs. 3.7 (page 92) and 3.10 (page 96)) with the exception of the strongly interacting 0-Cl_1a' free OH mode. Using $+28\,cm^{-1}$ as a correction leads to deviations of at most 5.48 cm^{-1} excluding the 0-Cl_1a' free OH mode. For CAM-B3LYP, a correction of 26 cm^{-1} was proposed which is still fairly close to the calculated mean. Based on that the maximum deviation from experiment is $-5\,cm^{-1}$. Furthermore, no clear trends emerge and no exceptions for 0-Cl_1a' have to be made. B2PLYP is yet again the most consistent method with mean very close to the ones observed for the mono-ols and a very small standard deviation. However, the assignments themselves are based on B2PYLP and the results are therefore possibly biased towards its good performance. MP2 shows a considerable spread as indicated by a standard deviation of 5.37 cm^{-1} where only PBE0 performs worse. However, the mean is very close to what was observed for the chloro-propanols. Furthermore, the free OH modes tend to be less strongly underestimated. 0-Cl_1b poses an exception where the

Tab. 3.12: Deviations of the absolute band positions at different levels of theory calculated with VPT2 relative to the experiment for 3-chloro-propane-1,2-diol (0-Cl_1). A positive sign indicates overestimation, while a negative one indicates underestimation. The absolute Jet-Raman band positions are given as reference points. All calculations utilise the aVTZ basis set. The arithmetic mean and standard deviation for each method are also shown.

	Jet-Raman	PBE0	B3LYP	CAM-B3LYP	B2PLYP	MP2
0-Cl_1	3617	15.1	−28.2	26.8	−13.0	−19.8
	3628	24.7	−26.5	21.6	−11.0	−7.8
0-Cl_1a	3629	23.3	−22.5	21.1	−11.1	−16.1
	3629	30.1	−27.1	29.8	−11.2	−5.9
0-Cl_1'	3587	21.0	−22.4	29.4	−9.4	−11.6
	3621	21.0	−30.3	21.3	−12.7	−7.1
0-Cl_1b	3604	26.0	−23.6	22.4	−12.2	−11.9
	3694	35.1	−24.7	23.2	−13.8	−11.9
0-Cl_1a'	3573	14.5	−24.6	21.7	−14.8	−23.4
	3604	6.5	−39.5	22.6	−13.6	−7.5
0-Cl_1t	3599	19.3	−26.6	27.0	−12.9	−11.7
	3689	34.8	−26.9	22.8	−13.9	−8.7
mean		22.6	−26.9	24.1	−12.5	−12.0
standard deviation		8.4	4.6	3.2	1.5	5.4

deviations for the free and bound OH mode are equal which is likely due to the fact that no contact towards the Cl atom is made.

The VPT2 calculations by Barone and co-workers for butane-2,3-diol (rM-M) and *trans*-cyclohexane-1,2-diol (t6-6)[186] used B2PLYP-D3(BJ)/jun-cc-pVTZ for the harmonic and B3LYP-D3(BJ)/jul-cc-pVTZ for the anharmonic force field and are much less consistent then the pure B3LYP and B2PLYP shown in Tab. 3.12. Their results for t6-6 and rM-M are shown in Tabs. 3.1 (page 34) and 3.3 (page 45), respectively. However, a consistent overestimation can be found which would be expected from B2PYLP or B3LYP alone. Furthermore, the minimal deviations for their data are in the same range as pure B2PYLP while the maximum deviations are covered by pure B3LYP. Hence, their combination appears to be not ideal and pure B2PLYP is preferable but not computationally feasible for t6-6. Pure CAM-B3LYP would still be applicable to t6-6 as well as rM-M and exhibits more consistent differences to the experiment which could be corrected for empirically.

3-Bromo-Propane-1,2-diol

3-Bromo-Propane-1,2-diol (0-Br_1) is conformationally as well as energetically closely related to its chlorine analogue. All structures are depicted in Fig. A.12 (page 229). Given these similarities, no barriers are computed and it is assumed that they are similar to 0-Cl_1 (see Fig. 3.35 (page 97)). Barriers involving the movement of the bromine atom are expected to be even higher *e.g.* from 0-Br_1' to 0-Br_1. The only efficient pathway remains from 0-Br_1b' to 0-Br_1b.

An overview of the different harmonically zero point corrected energies for the tested methods can be found in Fig. 3.38. In comparison to the chlorine derivative (*cf.* 3.36 (page 98)), very similar energies and conformational trends can be found. Specifically, the 0-Br_1a' conformer gets destabilised and the energetic order of 0-Br_1' and 0-Br_1b switches when moving to the right. For the GGAs, a trend towards over-stabilisation of primed conformers can yet again be found. 0-Br_1a' undergoes the strongest changes ($1.90\,\mathrm{kJ\,mol^{-1}}$ – $6.75\,\mathrm{kJ\,mol^{-1}}$) which can be linked to the strong OH$\cdots$Br contact. At the B3LYP/maTZ level a distance of 2.54 Å is found while for the other conformers it ranges from 2.65 Å to 2.77 Å. The larger distances in comparison to to chlorine can be explained by the fact that the C-Br bond is about 0.17 Å longer, which is quite similar to the carbon-halogen distance change found between ethyl-chloride (C-Cl: 1.789(1) Å)[251] and ethyl-bromide (C-Br: 1.950(1) Å)[252] experimentally. Additionally, the C-Cl distance for 2-chloro-ethanol has been experimentally determined to be 1.789(4) Å[250], indicating that a comparison to the diols can be made since the effect of the OH group appears to be fairly small. Furthermore, switching the basis set introduces no significant energetic changes.

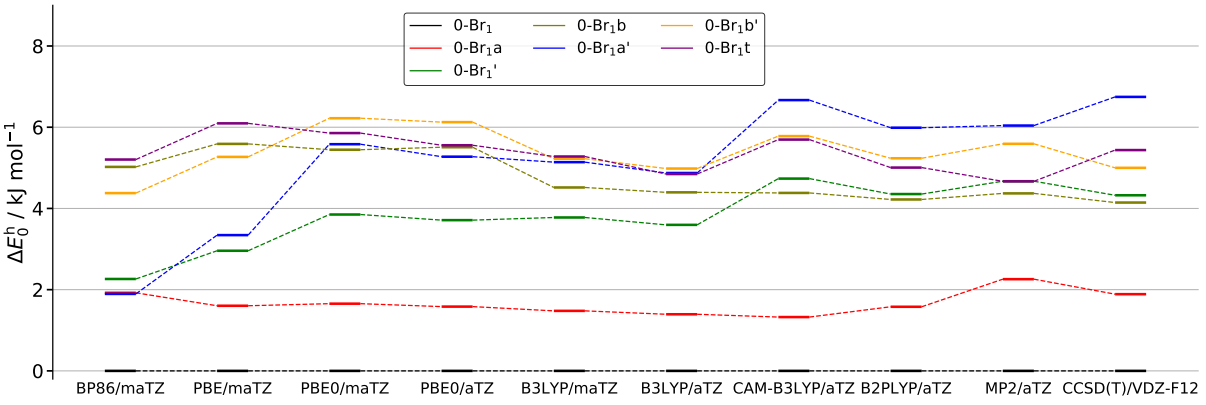

Fig. 3.38: Overview of the harmonically zero point corrected relative energies at different levels of theory for 3-bromo-propane-1,2-diol (0-Br_1). The aVTZ basis set is shortened to aTZ.

Moreover, no tested method is able to reproduce the energetic ranking of the coupled cluster results. CAM-B3LYP and B2PYLP are quite close but switch the order of 0-Br_1b' and 0-Br_1t predicting them to be almost isoenergetic. MP2 also closely resembles the coupled cluster results but as was the case for the chlorine derivative it shows larger discrepancies with regards to 0-Br_1b' and 0-Br_1t. B3LYP and PBE0 also stay within 1.5 kJ mol^{-1} of the gold standard with B3LYP performing slightly better. Overall, B2PLYP closest resembles the coupled cluster data, closely followed by CAM-B3LYP. Furthermore, switching from harmonic to anharmonic zero point correction does not significantly impact the results as can be seen from Tab. B.7 (page 248). Furthermore, the harmonic zero point correction consistently lowers the relative energies of all structures besides 0-Br_1a'. In the anharmonic case an increase can be also be found for 0-Br_1b at the B3LYP/aVTZ level of computation.

Fig. 3.39 shows the experimental and simulated spectra of 0-Br_1. The simulations are done analogously to 0-Cl_1. The derived B3LYP/maTZ $n_D = 1$ correlation again yield poor results as can be seen in Fig. C.12 (page 282). However, it is also evident that the corrected VPT2 B2PYLP results do not fit as well as for the chlorine case but still allows

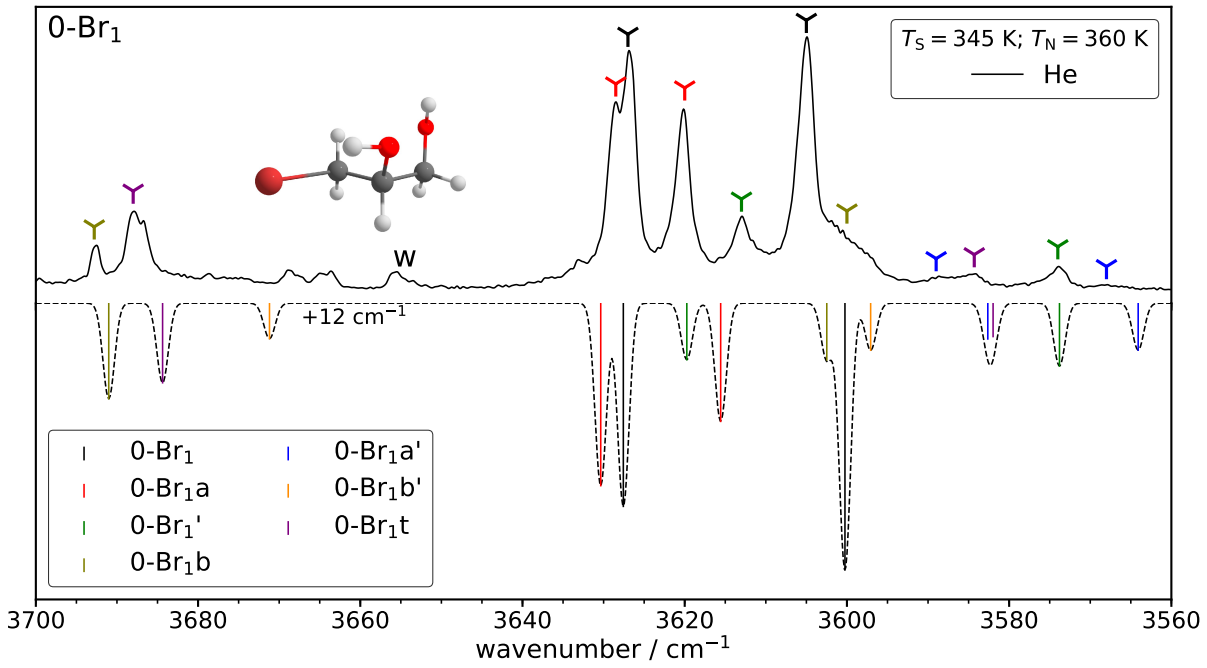

Fig. 3.39: Experimental data (plotted upwards) and simulated data (plotted downwards) of 3-bromopropane-1,2-diol (0-Br_1). The saturator temperature (T_S) as well as the nozzle temperature (T_N) are given. The simulated intensities are based on B3LYP/maTZ and are Boltzmann weighted based on T_N according to the relative energies given in Fig. 3.35. The frequencies are taken from VPT2 B2PLYP/aVTZ calculations corrected by +12 cm^{-1} as derived in section 3.1.10 (page 88). w indicates a water band.

assignments. The two most intense bands with almost equal intensity can be assigned to the most stable conformer 0-Br_1. The two bands slightly lower in intensity can be attributed to 0-Br_1a. The intensities are again about equal which is not reflected in the predicted band strengths. For both conformers the signals at higher wavenumbers are predicted quite well while the lower one are underestimated. This could be explained by the fact, that the OH modes at lower wavenumbers include interactions of the OH group with the bromine atom. For 0-Cl_1a, the bound (OH$\cdots$O) and free OH mode coincided while the free OH mode is downshifted in the bromine case. A similar pattern for an overestimated shift between bound and free OH mode can also be found for 0-Br_1'. However, in this instance the lower lying free OH mode is predicted more accurately. Therefore, a general trend cannot be established. The 0-Br_1b conformer that does not involve the Br atom in the hydrogen bond arrangement is described very well although the intensities are overestimated for the free OH mode. Furthermore, the bound OH mode appears as a very broad shoulder of the band at 3605 cm^{-1} but can be identified as such by spectral analogy to 0-Cl_1b. A rough assignment of 3600 cm^{-1} is made with an experimental uncertainty above the instrumental (± 1 cm^{-1}). The 0-Br_1t conformer is also well described in terms of the spectral positions despite a direct interaction with the Br atom. However, the intensity of the OH$\cdots$Br mode is underestimated. To better distinguish the bands in that region a zoom in is shown in Fig. D.2 (page 294). It also shows two yet unassigned small bands which are tentatively assigned to 0-Br_1a'.

Lastly, it should be noted that impurities appear in the experimental spectrum at lower and to a lesser extent at higher wavenumbers outside of the spectral range shown. However, other spectra of the compound not showing these impurities show no differences in the region of interest but with a worse signal-to-noise ratio. Further investigations showed that these impurities were not tied to the compound, although the exact origin could not be determined.

Tab. 3.13 shows an overview of the experimental and predicted intramolecular hydrogen bond shifts. The GGAs consistently overestimate the shifts in magnitude with the exception of 0-Br_1a', as was the case for the chlorine derivative (see Tab. 3.11 (page 100)). B3LYP yet again shows larger deviations as well while PBE0 is more generally applicable. For the 0-Br_1a conformer, reverse behaviour of 0-Cl_1a can be found where B3LYP predicted a significant separation of the bands opposite to experiment, while for the Br case the bands are predicted closely together but are further apart experimentally. Furthermore, B3LYP and CAM-B3LYP tend to underestimate the shifts in magnitude while PBE0, B2PLYP, MP2 and CCSD(T) tend to overestimate the shifts. In terms of the harmonic predictive capabilities PBE0/maTZ (MAE: 3.63 cm^{-1}) performs best followed by B3LYP/aVTZ (MAE: 5.56 cm^{-1}), PBE0/aVTZ (MAE: 5.60 cm^{-1}) and CCSD(T) (MAE:

Tab. 3.13: Comparison of the experimental and computed intramolecular hydrogen bond shifts of 3-bromo-propane-1,2-diol (0-Br_1). The shifts Δ are calculated as the difference between the free OH mode and the bound one. Harmonic (Δ^{h}) as well as anharmonic shifts (Δ^{an}) are given if available.

		0-Br_1	0-Br_1a	0-Br_1'	0-Br_1b	0-Br_1a'	0-Br_1b'	0-Br_1t
Jet-Raman		−22	−8	−39	93	20	-	104
BP86/ maTZ	Δ^{h}	−48.9	−17.8	−46.7	117.4	18.2	91.1	127.9
	Δ^{an}	-	-	-	-	-	-	-
PBE/ maTZ	Δ^{h}	−50.6	−19.9	−47.9	117.0	18.6	94.3	128.7
	Δ^{an}	-	-	-	-	-	-	-
PBE0/ maTZ	Δ^{h}	−33.5	−8.0	−42.8	95.0	21.3	77.3	107.2
	Δ^{an}	-	-	-	-	-	-	-
B3LYP/ maTZ	Δ^{h}	−22.6	−2.0	−35.2	83.0	17.4	67.7	89.3
	Δ^{an}	-	-	-	-	-	-	-
PBE0/ aVTZ	Δ^{h}	−36.6	−13.7	−45.7	93.3	20.0	81.0	110.2
	Δ^{an}	−36.9	−24.8	−58.6	99.8	9.9	81.9	123.5
B3LYP/ aVTZ	Δ^{h}	−25.5	−5.8	−37.1	82.2	16.8	71.1	92.1
	Δ^{an}	−24.9	−17.4	−46.7	87.2	7.4	75.8	103.7
CAM-B3LYP/ aVTZ	Δ^{h}	−15.1	−3.1	−31.5	84.5	30.6	76.6	87.1
	Δ^{an}	−16.2	−1.1	−36.2	89.8	25.1	82.5	96.4
B2PLYP/ aVTZ	Δ^{h}	−27.8	−10.0	−41.3	81.8	25.0	71.9	91.6
	Δ^{an}	−27.3	−14.8	−46.0	88.5	18.5	74.1	102.4
MP2/ aVTZ	Δ^{h}	−40.5	−24.6	−52.3	83.0	32.6	68.7	100.5
	Δ^{an}	−44.1	−28.9	−59.9	91.1	28.0	75.4	113.9
CCSD(T) VDZ-F12	Δ^{h}	−25.3	−8.2	−44.8	87.9	32.1	75.8	95.4
	Δ^{an}	-	-	-	-	-	-	-

$5.85\,cm^{-1}$). The other methods perform worse. Comparing the experimental shifts for the Cl and Br case shows a general increase of the magnitude of the shift with the exception of 0-Br_1a'. However, this behaviour is consistent with a stronger interaction of the OH group with the Br atom relative to Cl leading to a closing of the gap between the OH$\cdots$O bound mode and "free" OH$\cdots$Br. The absolute harmonic and anharmonic band positions can be found in Tabs. C.10 (page 265) and D.5 (page 294) respectively.

Switching to the anharmonic case lessens the predictive capabilities with the exception of B2PLYP ($4.43\,cm^{-1}$) and CAM-B3LYP ($5.24\,cm^{-1}$). Since the anharmonic B2PYLP calculations are the basis for the assignment this is to be expected for the former. However,

in comparison to the Cl derivative all tested methods perform worse, indicating that the accuracy of the electronic structure methods is suffering. Furthermore, the magnitude of the shifts is consistently increased in comparison to the anharmonic case with the exception of 0-Br_1a', which is likely linked to the short OH$\cdots$Br distance.

Tab. 3.14 shows the difference between the experimental and anharmonic VPT2 band positions. PBE0 and MP2 again show very inconsistent deviations from the experiment as the standard deviations suggest. This is especially true for PBE0 which shows the largest difference between the minimum and maximum deviation. Furthermore, PBE0 previously overestimated the positions throughout whereas here in case of 0-Br_1a' shows slight underestimation in one case (OH$\cdots$Br mode). MP2, on the other hand, consistently underestimates. Additionally, smaller deviations can be found for OH$\cdots$Br mode, in comparison to OH$\cdots$O ones in case of MP2. In case of 0-Br_1b no direct contact is made to the Br atom showing balanced deviations. B3LYP, CAM-B3LYP and B2PYLP behave much more consistent as was already the case for the other mono-halogenated systems. The observed means and standard deviations are akin to the chlorine case with the exception of the standard deviation of B2PLYP which more than doubles. Curiously, despite

Tab. 3.14: Deviations of the absolute band positions at different levels of theory calculated with VPT2 relative to the experiment for 3-bromo-propane-1,2-diol (0-Br_1). A positive sign indicates overestimation, while a negative one indicates underestimation. The absolute Jet-Raman band positions are given as reference points. All calculations utilise the aVTZ basis set. The arithmetic mean and standard deviation for each method are also shown.

	Jet-Raman	PBE0	B3LYP	CAM-B3LYP	B2PLYP	MP2
0-Br_1	3605	8.8	−29.9	27.8	−16.8	−31.9
	3627	23.8	−27.0	22.0	−11.4	−9.8
0-Br_1a	3620	13.0	−31.5	29.5	−16.4	−27.7
	3628	29.8	−22.1	22.7	−9.6	−6.9
0-Br_1'	3574	11.8	−26.5	32.0	−12.2	−22.4
	3613	31.4	−18.8	29.2	−5.3	−1.5
0-Br_1b	3600	28.2	−19.6	26.5	−9.5	−10.1
	3693	35.0	−25.4	23.3	−14.0	−11.9
0-Br_1a'	3568	10.1	−27.3	21.7	−15.9	−27.2
	3588	−0.1	−39.9	26.8	−17.4	−19.2
0-Br_1t	3584	15.0	−26.6	30.2	−14.0	−19.9
	3688	34.4	−26.9	22.7	−15.6	−10.0
mean		20.1	−26.8	26.2	−13.2	−16.5
standard deviation		11.7	5.6	3.6	3.7	9.5

the fact that the assignments are based on B2PYLP, CAM-B3LYP exhibits a slightly smaller standard deviation. In case of CAM-B3LYP, free OH modes are less strongly overestimated with the exception 0-Br_1a'. Additionally, the largest deviations for B3LYP and B2PLYP are found for 0-Br_1a'. Using the previously suggested back corrections CAM-B3LYP performs the best, closely followed by B2PYLP and more distant B3LYP. After the correction the largest deviations are $6.04\,cm^{-1}$, $-5.37\,cm^{-1}$ and $-11.09\,cm^{-1}$ for CAM-B3LYP, B2PLYP and B3LYP, respectively.

3.2 Microwave data

3.2.1 Bromopropanol

The energetic landscape of 1-bromo-propan-2-ol and 2-bromo-propan-1-ol was elaborated on in detail in section 3.1.10 with two energetically relevant conformers in either case. Clear evidence for both of them was found in case of 1-bromo-propan-2-ol but in case of 2-bromo-propan-1-ol due to expected spectral overlap no definitive statement can be made, although the calculated relative energies suggest both should be present. Microwave spectra do not suffer from such an overlap and allow an unambiguous assignment. Goldstein *et al.* were able to assign all four conformers for the chlorine analogues[244]. Details with regards to the calculation of the nuclear quadrupole coupling tensor (χ_{ij}; $i,j = \{a,b,c\},\{a,b,c\}$) can be found in section 2.3.4 (page 23), some of which will be restated here. The larger magnitude of the nuclear quadrupole moment Q (^{35}Cl: -0.0817 barn, ^{37}Cl: -0.0644 barn; ^{79}Br: 0.313 barn, ^{81}Br: 0.262 barn[164]) of bromine in comparison to chlorine allows for a more accurate determination of χ_{ij}. In comparison to Q the effect of the electric field gradient is minor but generally also leads to an increase of χ_{ij} for Br relative to Cl. In particular, the off-diagonal elements can often not be all determined or only with high uncertainties which is also a problem that occurred in the study of Goldstein *et al.*[244]. This issue is further exacerbated by the fact that the ^{37}Cl is about 1/3 as naturally abundant as ^{35}Cl while the bromine isotopes are equally abundant. Additionally, the sign of the off-diagonal elements cannot be directly determined by experiment and signs have to be inferred from theory. Furthermore, as long as the sign of the product of the three off-diagonal elements is kept, the description is equivalent, *e.g.* $\chi_{ab}\chi_{ac}\chi_{bc}$ is equivalent to $(-\chi_{ab})(-\chi_{ac})\chi_{bc}$. All assignments reported in this section were done in the 2 – 8 GHz frequency range.

As can be seen from Tab. F.1 (page 299), the entire χ_{ij} tensor could be determined for ^{79}Br and ^{81}Br for the most stable conformers of 2-bromo-propan-1-ol, which was not possible for

the chlorine derivatives[244]. Furthermore, smaller uncertainties can be found for the off-diagonal elements. It can also be found that the ratio of χ_{ij} for the two isotopes reflects the ratio of the corresponding Q, so that $\chi_{ij}(^{81}\mathrm{Br}) \approx {}^{Q(^{81}\mathrm{Br})}/_{Q(^{79}\mathrm{Br})} \times \chi_{ij}(^{79}\mathrm{Br}) = 0.84\chi_{ij}(^{79}\mathrm{Br})$. Moreover, the quartic centrifugal distortion constants (D_J, D_{JK}, D_K) as well as the off diagonal quartic centrifugal distortion constants (d_1, d_2) were successfully fitted. The distortion constants differ very little between the two Br isotopes. Additionally, the spin-rotation constants (C_{ii}) were determined. C_{ii} itself describes the coupling between the nuclear magnetic moment and the magnetic field produced by the rotation of the molecule. Their inclusion reduced the uncertainties of the χ_{ij} values as well as their sensitivity, *i.e.* indifference with regards to multiple fitting runs resulting in minor changes well below the experimental error. For Cl, these types of interactions are less relevant and could not be determined for Cl containing systems studied here. C_{ii} is largely determined by the nuclear magnetic dipole moments (μ_Z) and a comparison of μ_Z shows the change in magnitude: $0.8219\mu_\mathrm{N}$, $0.6841\mu_\mathrm{N}$, $2.1064\mu_\mathrm{N}$ and $2.2706\mu_\mathrm{N}$[164] for ^{35}Cl, ^{37}Cl, ^{79}Br and ^{81}Br, respectively. μ_N is the nuclear magneton ($\mu_\mathrm{N} = 5.050\,783\,699 \times 10^{-27}\,\mathrm{J\,T^{-1}}$). Instead of fitting C_{ii} the distortion constants for the NQCC χ_J and χ_K could be used instead. However, PGOPHER does not support the fitting of χ_J and χ_K and a program like SPFIT/SPCAT would have to be used. This possibility can be explored in the future.

Tab. F.1 (page 299) also shows the experimental results for 1-bromo-propan-2-ol. It was also possible to determine the entire χ_{ij} tensor although in case of h-gg the relative error of χ_{bc} is quite high given the small magnitude of the coupling. For most isotopes the quartic centrifugal distortion constants were determined with the exception of D_K for h-gg(^{79}Br). Furthermore, d_2 could not be fitted. The distortion constants again do not differ a lot when switching the Br isotope. In case of the nuclear spin-rotation coupling C_{aa} could not be determined for m-ga(^{81}Br). Including C in fits for h-gg lowered the errors for χ_{ij} but led to unreasonable ratios of the off-diagonal elements, *i.e.* they significantly deviated from the ratio of the respective Q. Therefore, C was not fitted for h-gg.

Given the large number of methods tested, box-plots are used to represent the difference between theory and experiment. A more detailed explanation regarding the box plots can be found in section 3.1.9. Moreover, it should be kept in mind that properties are calculated at the equilibrium geometry, while the experiment deals with the vibrational ground state. Therefore, perfect agreement with the experiment cannot be expected and likely would not be for the right reasons, although some properties may be more indifferent than others with regards to this fact.

Box-plots illustrating the deviations from experiment for A, B and C for the various tested methods are shown in Fig. 3.40. All assigned bromo-propanol con-

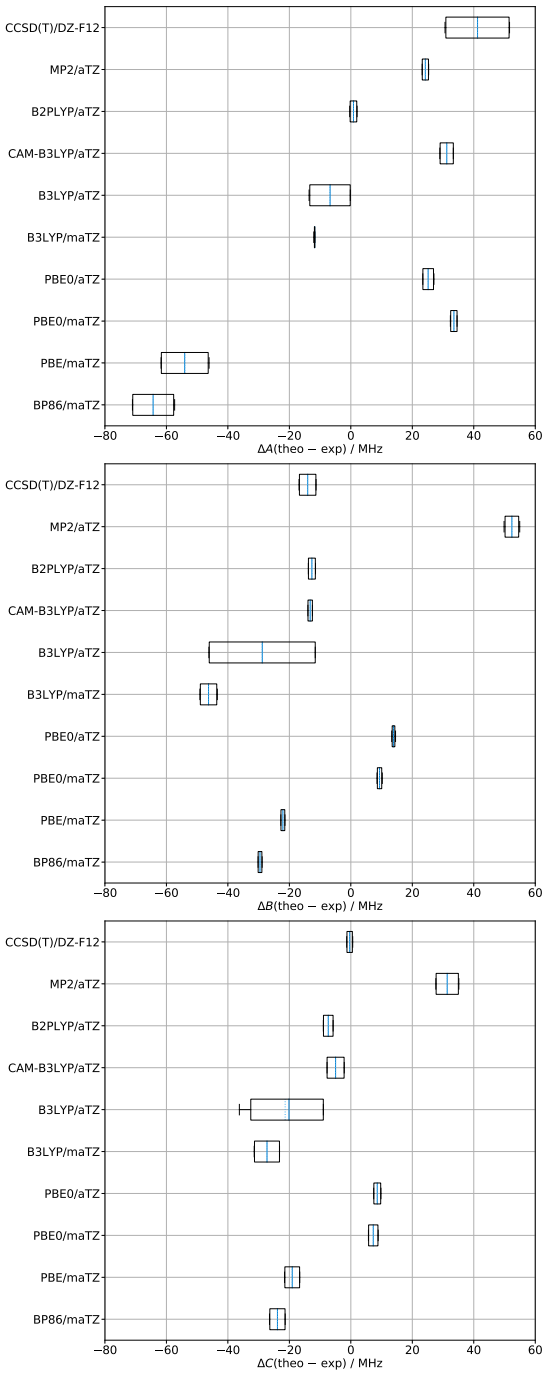

Fig. 3.40: Box-plots illustrating the deviations from experiment for A, B and C of the eight conformers of bromo-propanol.

formers (eight in total) are included in this analysis. GGAs are sticking out by significantly underestimating A. Most other methods tend to overestimate. Furthermore, the spread is generally fairly small with exception of the GGAs, B3LYP/aTZ and CCSD(T)-F12. Therefore, empirical back correction may be possible for related systems. Moreover, B2PLYP/aTZ almost perfectly predicted the experimental value. In case of B, B3LYP/aTZ shows a very large spread in comparison to all other tested methods. Back correction again might be possible. The majority of methods now underestimate. PBE0/maTZ get closest to the experiment. For C, again most methods underestimate relative to the experiment and B3LYP/aTZ again shows a very large spread. Curiously, now coupled cluster yields perfect predictions. Overall it can be found that PBE0 and MP2 consistently overestimate while the GGAs, B3LYP and CAM-B3LYP underestimate rotational constants. Furthermore, consistent deviations between B and C can be observed while for A larger discrepancy are found. This is especially true for the GGAs, PBE0 and B3LYP/aTZ, although the spread of the data is very large for the latter. The best overall predictions are provided by B2PLYP while a combination of BP2LYP for A, PBE0/maTZ for B and CCSD(T) for C would yield the best composite results.

The deviations from experiment for the different χ_{ij} values are shown in Fig. 3.41. When comparing these deviations with those shown in Fig. 3.40 it should be kept in mind that the relative deviations are considerably higher for χ_{ij}. The coupled cluster calculations were done on the CCSD(T0)-F12a/VDZ-F12 geometries employing the aug-cc-pwCVTZ basis which is designed to accurately describe core electrons. Moreover, relativistic calcu-

lations were done employing the Douglas-Kroll-Hess of Second Order (DKH2) formalism which is abbreviated as CCSD(T)-D. In case of χ_{aa}, the spread of the data is fairly small for the tested methods allowing for the possibility of empirical correction for related systems. For χ_{aa}, the largest deviations can be found and all methods besides coupled cluster DKH2 underestimate. B3LYP/maTZ and CCSD(T) reproduces the experiment quite well with a small spread.

χ_{bb-cc} is quite well described by all methods where CCSD(T) performs the worst. The inclusion of DKH2 significantly narrows the distribution of the data. Even the GGAs manage to predict χ_{bb-cc} quite well. Generally, a slight underestimation can be observed. The inclusion of DKH2 leads to slight overestimation. Some of the success of the different methods may be attributed to error compensation when taking the difference.

The sign of the off-diagonal elements does not change the overall description as long as the product yields the same sign. Given this fact the designation of under- and overestimation is arbitrary. Therefore, absolute values will be compared and are shown in Fig. 3.41. The deviations of the off-diagonal χ_{ab} coupling constant behaves more similarly to χ_{aa} with the exception of coupled cluster if underestimation is assumed. Closest to the experiment are the CCSD(T)-DKH2 calculations. χ_{ac} shows very similar behaviour to χ_{ab} with the latter showing slightly larger deviations. CCSD(T)-DKH2 again shows a very small spread fitting perfectly to the experiment. χ_{bc} is predicted quite accurately by all methods with only CCSD(T) showing somewhat larger spreads. CCSD(T)-DKH2 yields results remarkably close to experiment again. All methods show small spreads allowing again for the possibility of empirical correction for all coupling constants neglecting the sign. W. C. Bailey[253] derived such empirical models for Cl and Br with BLYP and specialised basis sets as the computational backbone, which can also be applied to the systems studied here in the future.

Overall, CCSD(T)-DKH2 yields excellent results for the off-diagonal elements but shows slightly larger ones for the diagonal ones. B3LYP/maTZ on the other hand behaves the other way round. Therefore, a combination of CCSD(T)-DKH2 and B3LYP/maTZ is the most promising approach. Additionally, it can be explored if B3LYP/maTZ geometries yield similar results as the CCSD(T0)-F12a/VDZ-F12 ones when CCSD(T)-DKH2 single point EFG calculations are done which could be applied to larger systems as well. The good performance of CCSD(T)-DKH2 also indicates that relativistic effects may be necessary to accurately describe the coupling constants. B2PLYP previously performed very well for the description of A, B and C but suffers from similar problems as MP2 does for χ_{ij} possibly due to its double hybrid character. This highlights the fact that methods may perform well for one property but cannot accurately describe another. Additionally,

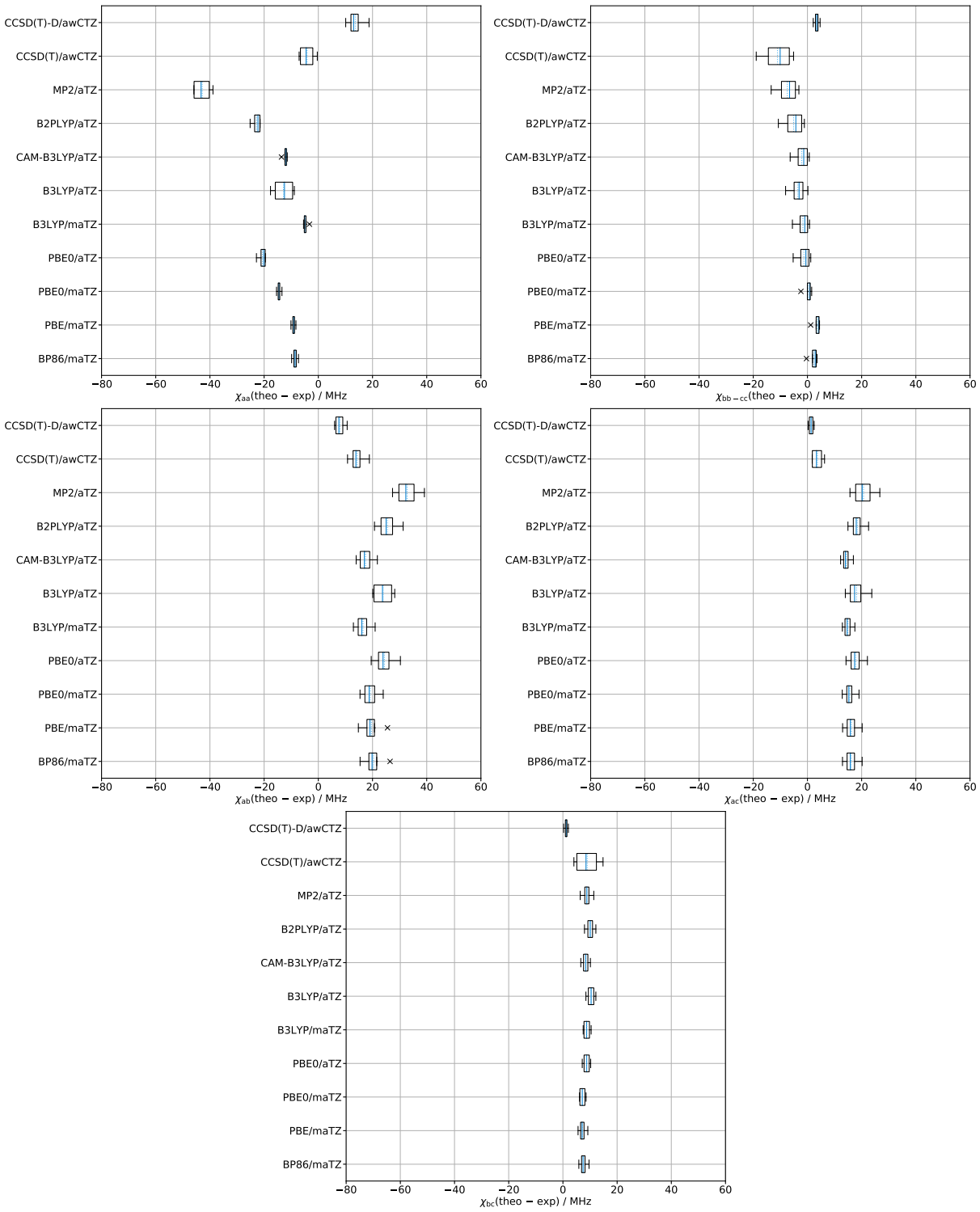

Fig. 3.41: Box-plots illustrating the deviations from experiment for χ_{aa}, χ_{bb-cc}, χ_{ab}, χ_{ac} and χ_{bc} of the eight conformers of bromo-propanol.

properties related to the core electrons are often not of interest for chemists and more experimental data to test their description by computational methods is needed. It should

also be kept in mind that neither maTZ nor aTZ were designed to predict core properties and more specialised basis sets may yield better results. DKH2 can also be easily applied to other methods presented here and may improve the results.

Furthermore, VPT2 calculations provide predictions for the vibrational ground state for both the rotational constants as well as the NQCCs. The inclusion leads to smaller A, B and C in comparison to the equilibrium geometry. However, the absolute changes are significantly larger for A, while only minor changes occur for B and C. This indicates that methods that largely overestimate A and slightly overestimate B and C do so for a physical reason. Methods yielding perfect matches do so without any physical grounding and profit from error compensation (vibrational averaging *vs.* electronic structure). From an experimentalists point of view this may be sufficient since the spectra can be accurately predicted. A theoretician might wonder about the "bad" performance of the "gold standard" method CCSD(T) for A. However, this is expected and stems from physical grounding due to neglected vibrational averaging. Similar effects can be seen for PBE0 and CAM-B3LYP in this and the other sections. In the future the zero point averaged VPT2 results can be directly compared to the experimental ones. For the averaged NQCCs on the other hand, changes remain within 1 MHz and do not lead to any significant differences. Hence, zero point effects on the NQCCs can be justifiably neglected. It should be kept in mind that this analysis hinges on the fact that VPT2 reliably predicts zero point effects.

3.2.2 3-Chloro-propane-1,2-diol

The energetic landscape of 3-chloro-Propane-1,2-diol (0-Cl_1) was previously shown in Fig. 3.36 (page 98) and barriers at the B3LYP/maTZ level in Fig. 3.35 (page 97), having 7 energetic relevant conformers and only one pathway that is expected to be overcome in a jet expansion. The experimentally determined rotational constants are summarised in Tab. F.2 (page 300). For most conformers D_J, D_K, D_{JK} and d_1 were also determined. For some conformers with the less abundant ^{37}Cl isotope d_1 could not be assigned. Moreover, d_2 was fitted for 0-Cl_1b and 0-Cl_1t. All conformers that were previously observed in the jet-Raman spectra (see section 3.1.10) can also be found in the microwave spectra, *i.e.* all conformers besides 0-Cl_1b' were assigned. However, unassigned lines are still present being possibly caused by higher energy conformers, dimers or impurities which can be examined in the future. All assignments were made in the 2 – 15.5 GHz and 18 – 26 GHz frequency ranges.

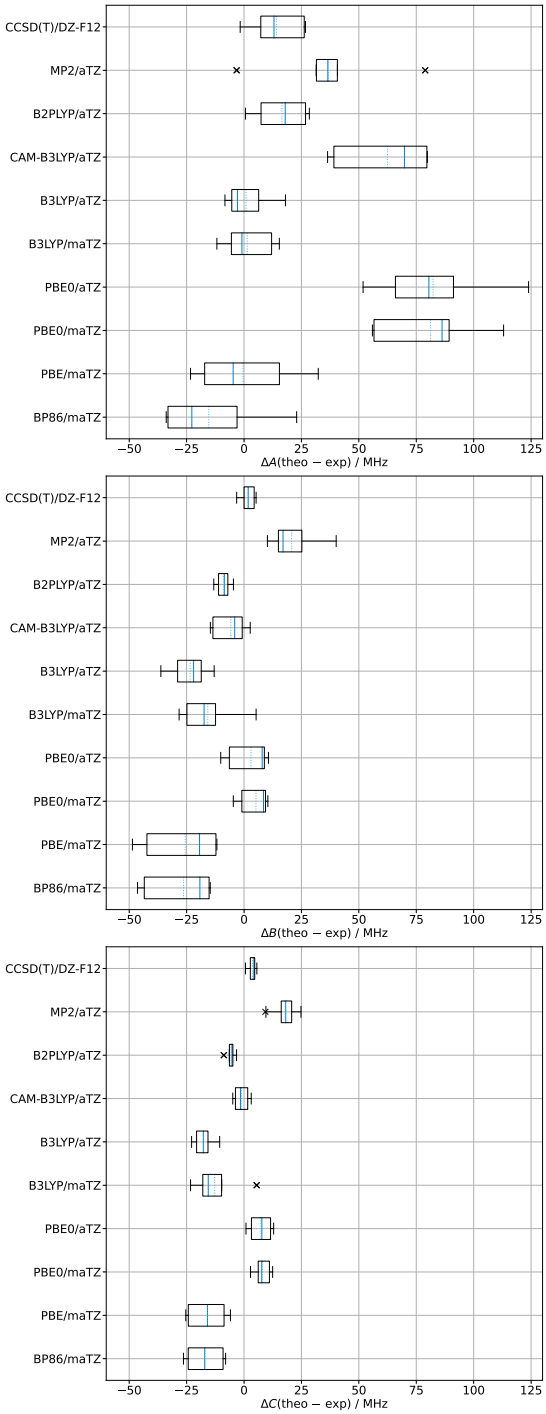

Fig. 3.42: Box-plots illustrating the deviations from experiment for A, B and C of the twelve conformers of 3-chloro-propane-1,2-diol.

From the experimental χ_{ij} shown in Tab. F.2 (page 300) typical problems in its determination for chlorine can be found, *i.e.* off-diagonal elements cannot be or only inaccurately determined. This even applies to the most stable conformer where χ_{bc} could not be determined. Furthermore, χ_{ac} also exhibits a fairly large uncertainty at the same level of magnitude as the value itself. The newly built cavity microwave spectrometer in the group of Jun. Prof. Dr. Obenchain could be used in the future to lower the uncertainties and determine χ_{bc} at all. 0-Cl_1a' is also a candidate for such an examination given some of the large errors and the inability to determine χ_{ac} for the less abundant chlorine isotope at all. Furthermore, χ_{ab} and χ_{bc} could not be determined for ^{37}Cl in case of 0-Cl_1t. Some refinement of the ^{35}Cl case for 0-Cl_1t would also be beneficial. Lines that depend heavily on these bands can identified from the simulations and searched for for with the more sensitive cavity instrument. Additionally, given the higher resolution of the cavity setup possible overlap with other bands or the collapse of the hyperfine structure with increasing J.

Fig. 3.42 shows box-plots for A, B and C for all tested methods. For the two GGAs, underestimation for all three constants can be observed as was previously the case for bromo-propanol (see Fig. 3.40). However, the description of A is more balanced for PBE. Furthermore, A showed larger deviations than B in case of bromo-propanol, while for 0-Cl_1 the opposite is the case. The other methods also behave quite similarly as was the case for bromo-propanol with the exception of coupled cluster which showed larger overestimation for bromo-propanol. Moreover, the spreads are much larger as well as the magnitude of the deviations of PBE0. For MP2, four (two for each

conformer) outliers for A also stick out which are caused by 0-Cl_1a (79 MHz) and 0-Cl_1t (-3 MHz). For the latter, this could be explained by the fact that the OCCO dihedral angle is vastly different than for the other *gauche* conformers, whereas for the former this is unclear. Of all tested methods B3LYP provides the best predictions for A. Coupled cluster and B2PLYP also perform reasonably well. For B, the overall spreads are smaller especially for coupled cluster and B2PLYP. Most methods yet again underestimate B, while MP2 and PBE0 still overestimate although PBE0 only slightly. In this instance CCSD(T) gets remarkably close to the experiment closely followed by PBE0. B2PLYP and CAM-B3LYP also yield decent results. In case of C, a very similar behaviour to bromo-propnaol can be observed with slightly lower deviations for MP2. Therefore, a back-correction for C based on the previous results would increase the accuracy considerably. CAM-B3LYP and coupled cluster are very close to the experiment with very small spreads. B2PLYP and PBE0 closely follow. The overall best description is given by coupled cluster and B2PLYP with the latter yielding a very good description for the bromo-propanols as well. CAM-B3LYP and PBE0 yield good predictions for B and C only. PBE0 already gave good predictions for B previously. The best composite description would be given by B3LYP for A, CCSD(T) for B and CAM-B3LYP/CCSD(T) for C.

Fig. 3.43 shows an overview of the deviations of χ_{ij} from experiment. The predictions of the diagonal elements are fairly accurate for the different methods but in case of χ_{bb-cc} the spread for some methods is fairly substantial especially for the GGAs. The discrepancies are smaller than for the bromo-propanols but it should be kept in mind that the values themselves are also much smaller. χ_{aa} can be as small in magnitude as 0.9102 MHz and 5.965 MHz for χ_{bb-cc} (see Tab. F.2 (page 300)). With this in mind the relative errors are quite significant. However, it is also worth noting that no tested method predicted the wrong sign despite the small values. The coupled cluster calculations match the experiment extremely well with a very small spread, followed by CAM-B3LYP and B3LYP/aTZ for χ_{aa}, closely followed by B2PLYP. For χ_{bb-cc}, coupled cluster also yields good results as well CAM-B3LYP and B3LYP/maTZ. It is also clear that relativistic effects are not important for Cl since calculations with and without DKH2 yield very similar results. This is generally assumed to be the case but can be nicely corroborated by the calculations in this instance. For both χ_{aa} and χ_{bb-cc}, coupled cluster clearly performs the best but CAM-B3LYP and B3LYP/aTZ could be used as less computational expensive alternatives.

The off-diagonal elements also exhibit smaller deviations in comparison to the bromo-propanols. They should also be put into perspective in terms of the absolute experimen-

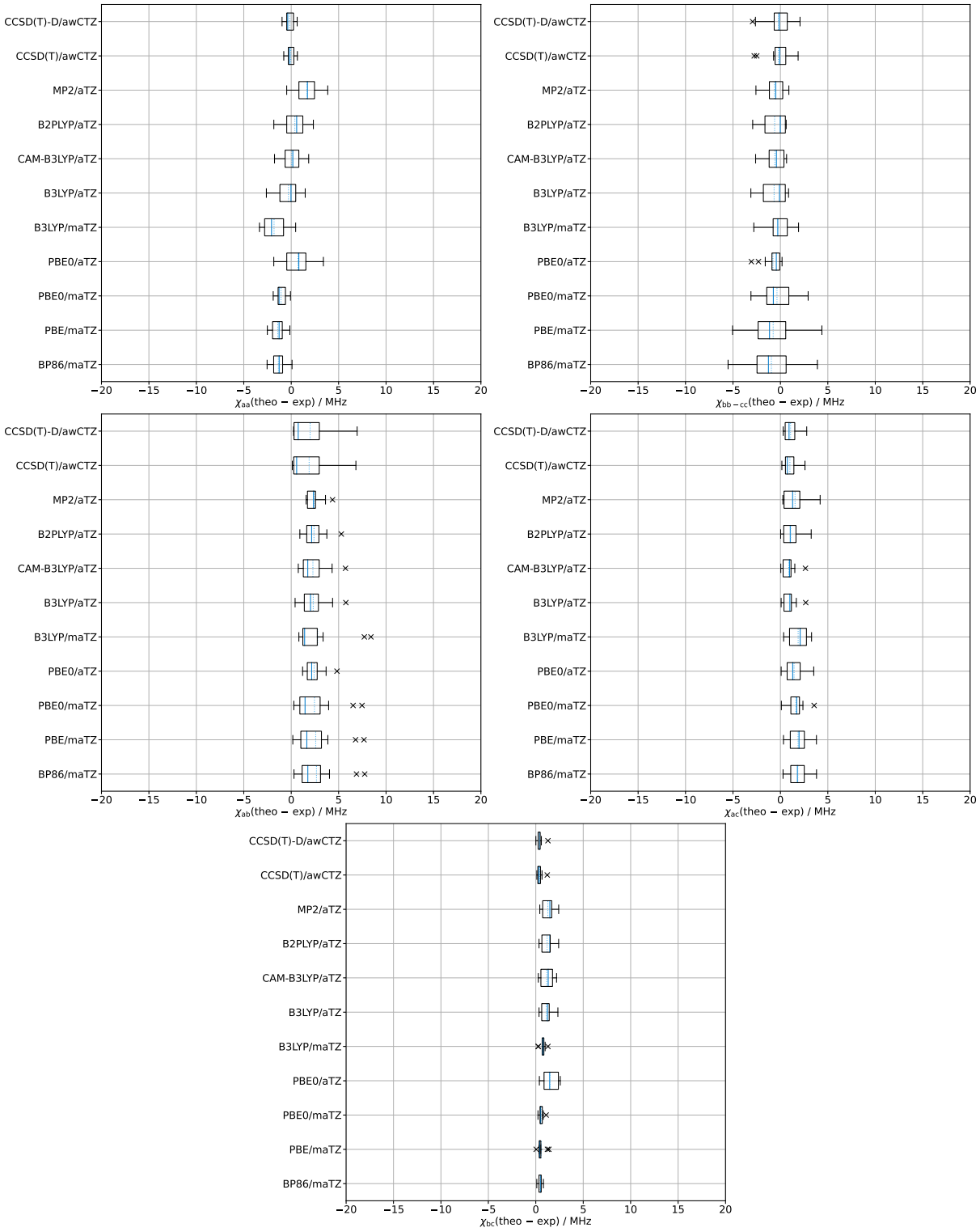

Fig. 3.43: Box-plots illustrating the deviations from experiment for χ_{aa}, χ_{bb-cc}, χ_{ab}, χ_{ac} and χ_{bc} of the twelve conformers of 3-chloro-propane-1,2-diol.

tal values. The smallest values are 14.5 MHz, 3.5 MHz and 11.19 MHz for χ_{ab}, χ_{ac} and χ_{bc}, respectively. In case of χ_{ac}, the differences between theory and experiment are in

a very similar range as the smallest value and hence the predictive capabilities are not yet satisfactory. Furthermore, all methods predict the same sign for the product of the off-diagonal elements. χ_{ab} has the largest deviations and some significant outliers are noticeable. These are caused by 0-Cl_1a' and were determined with large errors. Therefore, it appears likely that the problem is not theory but the the experiment as all other predictions match much better. Excluding that data points the spread of the data significantly decreases. Coupled cluster yields the best predictions with the other methods behaving quite similar. χ_{ac} is akin to χ_{ab} as was the case for the bromo-propanols. Coupled cluster also yet again is the most reliable. CAM-B3LYP and B3LYP/aTZ also show small difference to the experiment at a much lower computational cost. Quite similar to the bromo-propanols χ_{bc} also shows the smallest discrepancies. Coupled cluster performs very well but, curiously, BP86 is closest to the experiment and shows a very small spread. Methods like CAM-B3LYP, B2PLYP and B3LYP/aTZ now perform sligthly worse and show larger spreads. Overall, coupled cluster performs the best in all cases but decent accuracy can also be achieved with the cheaper B2PLYP, B3LYP and CAM-B3LYP methods. Since CCSD(T) is also capable of predicting A, B and C very accurately it is the clear favourite. B2PLYP provides a cheaper alternative that describes all constants reasonably well but is still considerably more expensive then hybrid-functionals. A cheaper alternative would be to use CAM-B3LYP for all constants except A which could be tackled by B3LYP. If vibrational averaging is taken into account, CAM-B3LYP also performs well for A.

3.2.3 3-Bromo-propane-1,2-diol

An overview of the energetic landscape of 3-bromo-propane-1,2-diol (0-Br_1) can be found in Fig. 3.38 (page 103) which is very similar to that of 0-Cl_1. Given this fact it is assumed that the barriers of 0-Cl_1 (see Fig. 3.35) are a good approximation for those of 0-Br_1. Therefore, 0-Br_1b' is expected not to be observed while the all other conformers should be present. However, the assignment proved to be very difficult with only the 0-Br_1, 0-Br_1a, 0-Br_1' and 0-Br_1b conformers being assigned so far. Especially, the line density makes pattern finding hard. Furthermore, the theoretical description is also more challenging in comparison to the chlorine derivative, hence, providing worse initial guesses for the fitting procedure. The respective experimental rotational constants can be found in Tab. F.3 (page 302). For all conformers D_J and D_{JK} could be determined. Additionally, for 0-Br_1 and 0-Br_1b D_K as well as d_1 and for 0-Br_1a even d_2 were fitted. Moreover, C_{ij} was assigned for all conformers except 0-Br_1'. In some cases C_{aa} could also not be determined. For C_{ij} little correlation with other fitting parameters is observed possibly

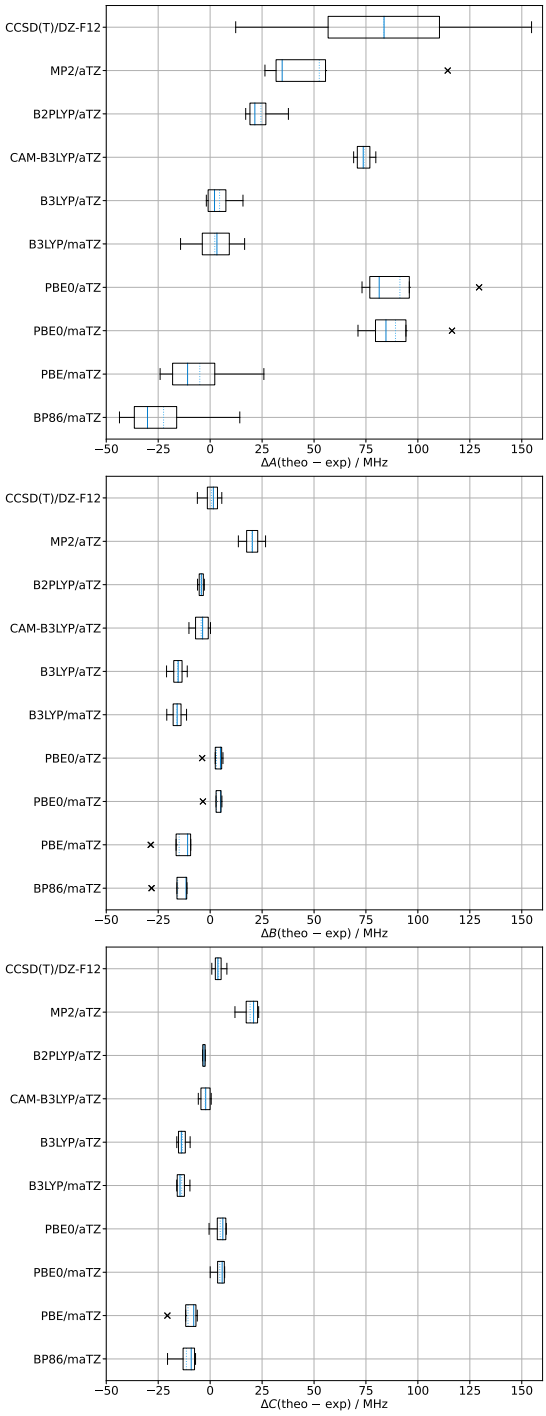

Fig. 3.44: Box-plots illustrating the deviations from experiment for A, B and C of the eight conformers of 3-bromo-propane-1,2-diol.

due to the strong overdetermination of the fit. Hence, a comparison of fits with and without C_{ij} is warranted.

The unassigned 0-Br_1a' and 0-Br_1t conformers are expected to be present, however, they are the highest in energy at the CCSD(T)-F12a level of theory. Hence, it may be the case that the populations are too small to be assigned coupled with the fact that the vapour pressure of 0-Br_1 is lower than that of 0-Cl_1. Unfortunately, increasing the temperature further to increase the likelihood of observing the less stable conformers is not a possibility since the compound started decomposing during attempts to do so. The microwave spectra have been recorded in the 2 – 8 GHz and 18 – 26 GHz frequency ranges. Recording broadband spectra in the 8 – 18 GHz range may help to find 0-Br_1a' and 0-Br_1t. Furthermore, the use of automated assignment algorithms could aid this endeavour. In the jet-Raman spectra clear evidence for 0-Br_1t was found while the assignment of 0-Br_1a' was more tentative. Therefore, finding 0-Br_1t in the existing spectra should be possible, while finding 0-Br_1a' is expected to be significantly more difficult. Lastly, in comparison to the chlorine derivative the entire χ_{ij} tensor could be determined with small uncertainties even for the less abundant 0-Br_1' conformer.

Fig. 3.44 shows the box-plots for A, B and C for the different methods. The GGAs again behave very similar for A as was the case for 0-Cl_1 (see Fig. 3.42) with a tendency toward slight underestimation, although BP86's median is closer to zero than that of PBE. The hybrid functionals also show very similar behaviour, with slightly larger spreads for PBE0 and B3LYP in case of 0-Cl_1. However, this can be attributed to the fact that two ad-

ditional conformers have been assigned for 0-Cl_1. In case of CAM-B3LYP, this change is especially substantial due to the fact that 0-Br_1a' and 0-Br_1t have not been assigned which cause the large spread for 0-Cl_1. The B2PLYP results tend to overestimate slightly more in comparison to 0-Cl_1. The MP2 results appear to be more consistent due to the fact that 0-Br_1t has been not assigned that caused the outlier close to 0 MHz. The strong overestimation for 0-Br_1a is also still present and even more pronounced. The coupled cluster results on the other hand behave very differently. A is now generally significantly overestimated with the exception of 0-Br_1' with deviations of about 12 MHz. As to why this change occurs is unclear as of yet. Furthermore, B3LYP yet again provides the best predictions for A. Curiously, for B the coupled cluster results are very similar between 0-Cl_1 and 0-Br_1 again being very close to 0 MHz with a small spread. All other methods also behave very similar with tighter spreads due to reasons previously explained. For B, CCSD(T) is the clear favourite to guide the fitting process with the computationally cheaper B2PLYP, CAM-B3LYP and PBE0 also yielding good results. For C, analogous behaviour to 0-Cl_1 is yet again found. CAM-B3LYP and B2PLYP describe the experiment the best closely followed by PBE0 and coupled cluster. Overall, B2PLYP and B3LYP are closest to the experiment for A, B and C. Considering the possibility of a back-correction based on previous results, CAM-B3LYP also performs well as it's lacklustre performance for A is no longer an issue. The best composite results are given by B3LYP for A and CCSD(T) for B and C as was the case for 0-Cl_1.

Box-plots comparing the predicted χ_{ij} to experiment are shown in Fig. 3.45. For χ_{aa} significant differences can be found between 0-Cl_1 and 0-Br_1. Besides CCSD(T)-DKH2 all methods tend to underestimate χ_{aa} and show larger spreads. MP2 shows especially large deviations. Considering that the experimental values range from 91.829 MHz to 424.054 MHz quite a few methods are not sufficiently accurate with the maximum deviations amounting to 1/3 of the smallest experimental value. CCSD(T)-DKH2 yield the best description followed by CCSD(T) and PBE0/maTZ. B3LYP/maTZ also provides a decent description. Furthermore, a substantial difference can be found between the DKH2 and non DKH2 results. B2PLYP, that previously performed quite well, now yields poor results which might be caused by the double hybrid approach since MP2 performs especially bad which was not the case before. For χ_{bb-cc} most methods again centre around 0 MHz but with a larger spread. Curiously, PBE/maTZ performs the best showing the smallest spread of all methods. For 0-Cl_1, the GGAs performed the worst. Given that the minimum experimental value is 27.788 MHz all methods show large relative errors. However, for Br χ_{bb-cc} is generally larger than for 0-Cl_1 leading to more substantial spreads. In all cases the largest deviations can be found for the 0-Br_1' conformer with the description of the unprimed conformers being considerably more accurate.

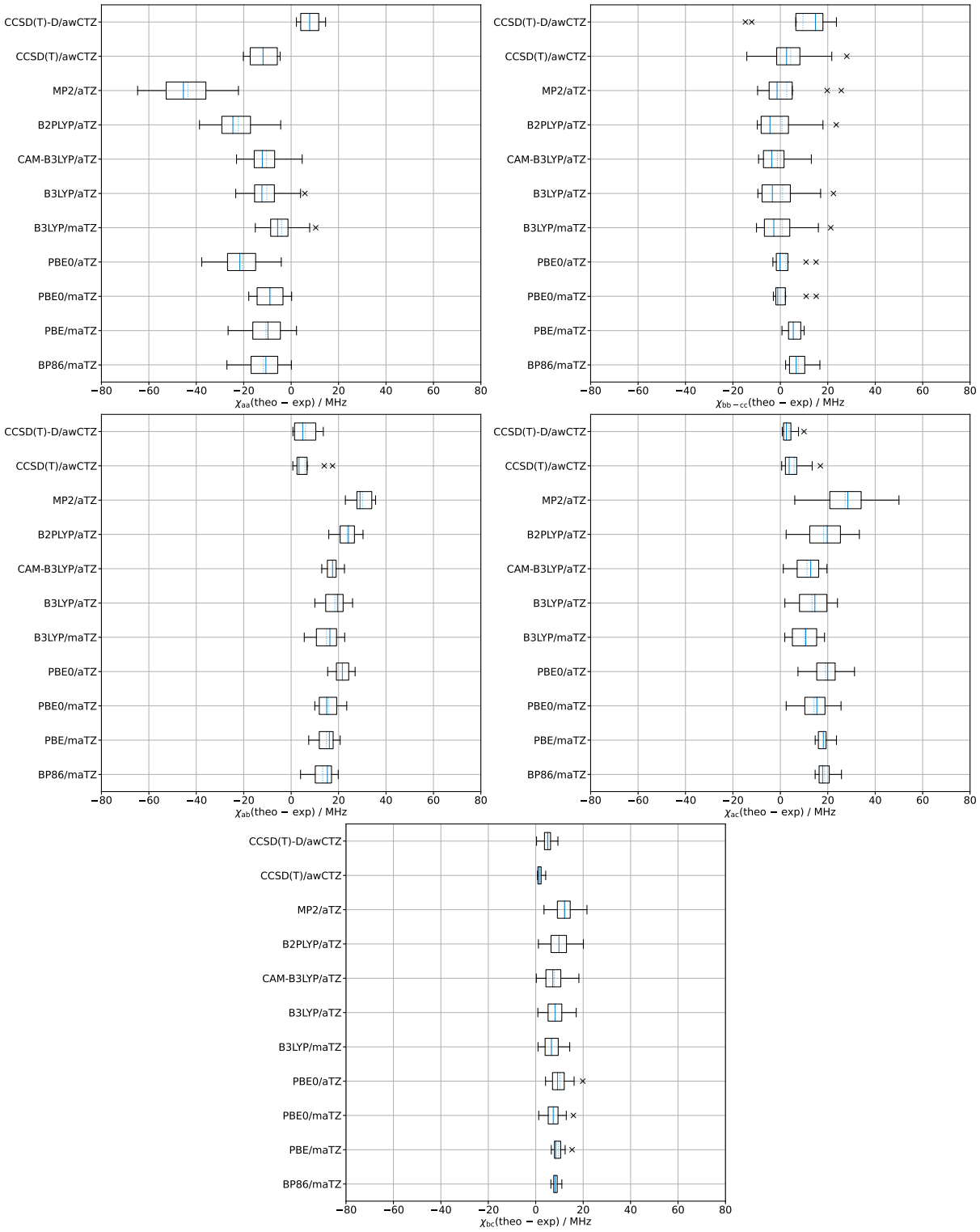

Fig. 3.45: Box-plots illustrating the deviations from experiment for χ_{aa}, χ_{bb-cc}, χ_{ab}, χ_{ac} and χ_{bc} of the eight conformers of 3-bromo-propane-1,2-diol.

For the off-diagonal elements, experimental values as small as 166.47 MHz, 25.4 MHz and 9.92 MHz in magnitude have been determined for χ_{ab}, χ_{ac} and χ_{bc} respectively. In all cases

the coupled cluster methods yield the most reliable predictions with the DKH2 variant performing slightly better for χ_{ac} while the no DKH2 variant performs better for χ_{bc}. All other methods show considerably larger deviations and spreads. Especially, for χ_{ac} large discrepancies can be found with most methods having a median deviation around 20 MHz. Since the smallest experimental χ_{ac} value is in the same range the theoretical accuracy is not sufficient. The quite large deviations are again caused by the primed conformer. For χ_{bc} only CCSD(T) yields sufficiently accurate results given the smallest experimental value. For all three elements, MP2 performs the worst and with it B2PLYP with slightly better results.

Overall, as was previously the case, the coupled cluster methods perform the best with B3LYP providing a slightly worse but computationally cheaper alternative. The best composite approach consists of CCSD(T)-DKH2 for χ_{aa}, χ_{ab} and χ_{ac}, the no DKH2 variant for χ_{bc} and PBE0 for χ_{bb-cc}. However, the description for most instances can be improved substantially when applying a back correction based on the median of the bromo-propanols (see Fig. 3.41 (page 112)). Hence, the corrected variants of BP86 and PBE would provide very cheap but accurate descriptions as they behave very consistent and show small spreads especially for the off-diagonal elements.

3.3 Combined analysis: Asymmetry parameter as a probe for hydrogen bond strength

The χ_{ij} determined in section 3.2 are in the inertial reference frame as defined by a, b and c. However, further molecular insights can be gained by transferring χ_{aa} and so on to the principal axis system (PAS) of the nucleus (quadrupole moment). The χ_{ij} tensor in the inertial reference frame has the following form:

$$\begin{pmatrix} \chi_{aa} & \chi_{ba} & \chi_{ca} \\ \chi_{ab} & \chi_{bb} & \chi_{cb} \\ \chi_{ac} & \chi_{bc} & \chi_{cc} \end{pmatrix} \tag{3.5}$$

Since the matrix is symmetric it follows that $\chi_{ab} = \chi_{ba}$, $\chi_{ac} = \chi_{ca}$ and $\chi_{bc} = \chi_{cb}$. Moreover, the matrix is traceless, *i.e.* $\chi_{aa} + \chi_{bb} + \chi_{zz} = 0\,\text{MHz}$ (Laplace equation holds). By computing the eigenvalues of Eq. 3.5 χ_{xx}, χ_{yy} and χ_{zz} can be obtained which are now in the PAS of the nucleus and also traceless. However, the mapping of the coordinates from the a, b and c axis system to the x, y and z axis system is not clearly defined and in

principle six permutations are possible. Hence, six different values can also be obtained for the asymmetry parameter (η) which is defined in the following way:

$$\eta = \frac{\chi_{xx} - \chi_{yy}}{\chi_{zz}} \tag{3.6}$$

To avoid this ambiguity, χ_{zz} is chosen to be the element with the largest magnitude which would approximately point in the direction of the C-Cl or C-Br bond axis for the systems studied here. χ_{xx} and χ_{yy} are then chosen so that η is positive. The six possible solutions for η reduce to three in absolute terms with the given convention resulting in the smallest possible $|\eta|$. This definition is equivalent to $|\chi_{xx}| \leqslant |\chi_{yy}| \leqslant |\chi_{zz}|$ since they will sum up to zero and therefore result in the smallest possible and positive η. Hence, η can range from 0 to 1 ($0 \leqslant \eta \leqslant 1$), with 0 and 1 being the ideal cylindrical symmetric and ideal cylindrical asymmetric case, respectively. From these χ information about the bonding can be gathered such as the ionic- and π-character of the C-Cl or C-Br bond which is described in more detail in Ref. [57]. However, the focus of this work is η and its relation to hydrogen bonding.

χ_{xx}, χ_{yy} and χ_{zz} are measures of the electric field gradient which will be the largest more or less along the C-Cl or C-Br bond. Hence, χ_{zz} will be aligned with the bond axis. Therefore, higher η generally indicate a stronger interaction with the rest of the molecule. In very symmetric cases such as methyl-chloride[254–257] and *tert*-butyl-chloride[258–261] or their bromine counterparts[261–268] $\eta = 0$, *i.e.* ideal cylindrical symmetry is present. For more complex cases such as ethyl-chloride and ethyl bromide values of 0.004[b] and 0.0062[252] are found respectively, showing minor deviations from the cylindrical symmetry. For the *trans*-1-chloro-propane conformer, $\eta = 0.0094(19)$[270] is observed increasing even further in comparison to its smaller counterpart. The asymmetry increases even further once hydrogen bonding gets involved. For the simple 2-chloro-ethanol $\eta = 0.02$[250] is found and for the chloro-propanols investigated by Goldstein *et al.*[244] values as high as 0.090 have been reported. Many more examples can be found in the database of W. C. Bailey[253]. Although, experimental η are often associated with large uncertainties with the same order of magnitude as the value itself, it is clear that the formation of a lose intramolecular hydrogen bond leads to an increase of η. Hence, η can be used as a qualitative measure to deduce the presence of a hydrogen bond when comparing the bonded to the non-bonded or non-alcohol case.

It should also be kept in mind that this behaviour is specific to the type of hydrogen bond arrangement found with vicinal OH$\cdots$halogen intramolecular hydrogen bonds. For

[b] Calculated based on the experimental diagonal elements by Hayashi *et al.*[251] and computed off-diagonal elements by W.C. Bailey[269].

instance, if one where to substitute the hydrogen atom involved in the intermolecular hydrogen bond of the water dimer with deuterium ($I = 1$) an increase of the cylindrical symmetry would be expected relative to the monomer. Hence, in principle information about the hydrogen bond arrangement can be inferred and indications for strained configurations found. Unfortunately, due to the very small quadrupole moment ($Q = 0.002\,86\,\text{barn}$) of deuterium coupled with a small electric field gradient, the entire NQCC tensor cannot be resolved in most cases. However, halogen atoms could provide similar direct bonding information as deuterium in case of halogen bonds.

Nonetheless, it might be possible to use η in a more quantitative fashion as a direct probe of the hydrogen bond strength. It is well established that the downshift of the OH-stretching vibration is an indicator of the strength of a hydrogen bond. In fact, this is a criterion listed to determine the presence of a hydrogen bond at all according to IUPAC[271]. Therefore, correlating η with the stretching frequency of the OH$\cdots$Cl or OH$\cdots$Br bonds allows to investigate whether or not η could be used as a probe for hydrogen bond strength. If this is the case it would be expected that as the vibrational downshift increases η increases as well. It also remains to be seen if a functional relationship can be found which could possibly aid the search for unassigned conformers if either η or the vibrational frequency is known. Moreover, such an analysis can also be done by comparing theory only which provides a unique challenge. Harmonic frequencies can also be used and may still reproduce the general behaviour well.

Tab. 3.15 shows an overview of the experimentally determined η for chloro-propanol, bromo-propanol, 3-chloro-propane-1,2-diol and 3-bromo-propane-1,2-diol. It illustrates the difficulty of determining accurate η for chlorine since the uncertainties are quite large in many cases and inconsistencies are sometimes observed between the ^{35}Cl and ^{37}Cl isotopes. However, in cases where η can be accurately determined for chlorine, similar values to their bromine counterparts are found. A comparison with Br also allows to rule out inconsistencies within the Cl-containing systems. The sometimes large discrepancies between ^{35}Cl and ^{37}Cl can be attributed to insufficient experimental data rather than an actual change introduced by the other isotope. It can also be seen that the η derived by Goldstein *et al.* who did not provide error bars are not a good basis to draw conclusions given their uncertainties. However, by analogy to the bromine cases expected behaviour can still be inferred.

In case of 1-X-propan-2-ol (m-ga and h-gg), a direct comparison to 3-X-propane-1,2-diol (X = Cl, Br) is possible since the same structural motif can be found. Specifically, m-ga is related to 0-X_1 and 0-X_1a, while h-gg is related to 0-X_1' as well as 0-X_1t. The structural similarities are illustrated in Fig. 3.46 for the Cl case, but can be directly

Tab. 3.15: Overview of the experimentally determined asymmetry parameters (η) for the different chlorine and bromine isotopes of 2-*X*-propan-1-ol (g-ga and g'-gg), 1-*X*-propan-2-ol (m-ga and h-gg), and 3-*X*-propane-1,2-diol with *X* being Cl or Br. 0-X_1 is used as a placeholder for 0-Cl_1 and 0-Br_1. The chlorine values of g-ga, g'-gg, m-ga and h-gg are taken from Goldstein *et al.*[244] with uncertainties having been additionally calculated. For 0-Cl_1, the CCSD(T)/awCVTZ values have been used for χ_{bc} and the largest experimental error of the other elements has been used in this case.

	^{35}Cl	^{37}Cl	^{79}Br	^{81}Br
g-ga	0.08(15)	-	0.039 25(42)	0.039 21(33)
g'-gg	0.056(88)	-	0.044 15(24)	0.044 30(37)
m-ga	0.0467(92)	0.040(19)	0.048 279(69)	0.048 302(94)
h-gg	0.090(60)	-	0.060 67(98)	0.0605(18)
0-X_1	0.0494(74)	0.054(18)	0.053 262(23)	0.053 289(32)
0-X_1'	0.0661(24)	0.111(18)	0.063 713(93)	0.063 52(12)
0-X_1a	0.0468(41)	0.0458(47)	0.047 546(35)	0.047 568(51)
0-X_1a'	0.138(72)	-	-	-
0-X_1b	0.0214(26)	0.066(20)	0.023 44(14)	0.023 38(20)
0-X_1b'	-	-	-	-
0-X_1t	0.046(23)	-	-	-

extended to Br. Comparing the η also bears out this similarity as the deviations are fairly small. The fact that in case of 0-X_1a larger differences are observed can be explained by the fact that the additional OH group is far outside the plane that is spanned by *X*-C-C-C, whereas for 0-X_1 this is not the case. Due to the rather large error bars for 0-X_1t no definitive statements can be made. For 0-X_1b, a comparison to *gauche*-1-*X*-propane would be of interest since no direct interactions of the OH groups take place with the halogen atom. However, experimentally determined η in this case are accompanied with large uncertainties for *gauche*-1-chloro-propane[270] or the complete tensor was not determined for *gauche*-1-bromo-propane[272]. Fortunately, for the iodine derivative η has been determined to be 0.0236(25)[273] which is indeed very close to the 0-X_1b results. For *trans*-1-iodo-propane ($\eta = 0.0075(5)$[273]) η is within the error bars of the previously stated chlorine case ($\eta = 0.0094(19)$[270]). This further demonstrates the practicality of η to judge the presence of a hydrogen bond.

Furthermore, based on the values given in Tab. 3.15 expectations for the behaviour of the OH stretching vibrations can be formulated. Since η does not differ a lot between g-ga and g'-gg it would be expected that the OH stretching vibrations should be fairly close together while for m-ga and h-gg a stronger downshift for h-gg would be expected. For the diols, an increasing downshift would be expected going from 0-X_1a to 0-X_1 and 0-X_1'.

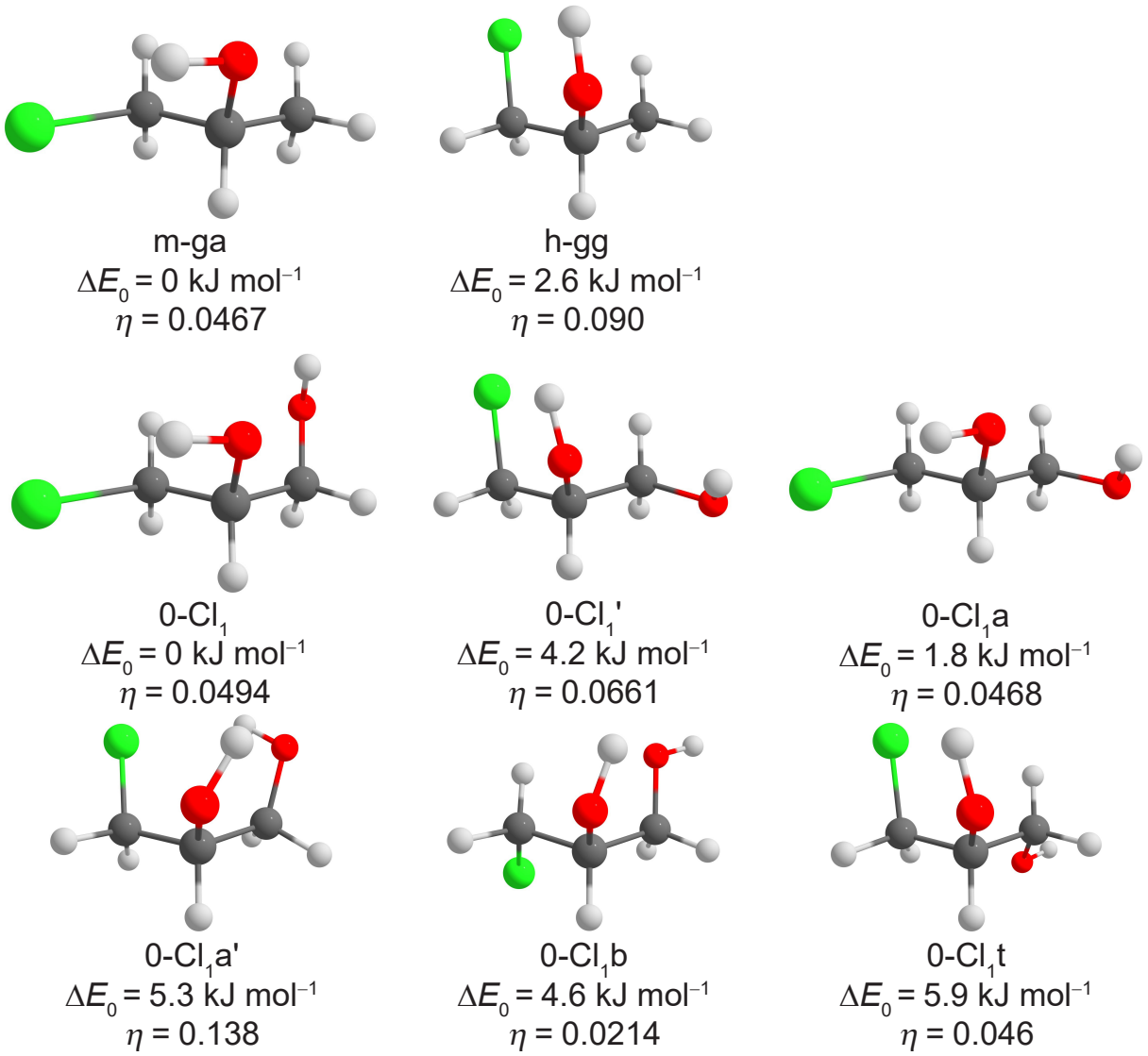

Fig. 3.46: Overview of the conformers of 1-chloro-propan-2-ol (m-ga and h-gg) and 3-chloro-propane-1,2-diol. The Br-containing counterparts are structurally very similar. The zero point corrected relative energies (ΔE_0) at the B3LYP/maTZ level of computation as well as the experimental asymmetry parameters (η) are given. The structural similarities between m-ga and 0-Cl$_1$ as well as 0-Cl$_1$a immediately become apparent. Furthermore, h-gg structurally similar to 0-Cl$_1$' and 0-Cl$_1$t.

Given the large error bar for 0-X$_1$a' and 0-X$_1$t no conclusions can be drawn for them. Furthermore, since for 0-X$_1$t no OH$\cdots$O hydrogen bond is present it may also would not fit into the series as well as the others may.

Fig. 3.47 (top) shows the correlation of the experimental OH stretching frequencies as well as the experimentally determined η for 1-X-propan-2-ol (m-ga and h-gg) and 2-X-propan-1-ol (g-ga and g'-gg). The chlorine results for g-ga and g'-gg show large uncertainties with the values by themselves indicating that the corresponding wavenumbers should be quite

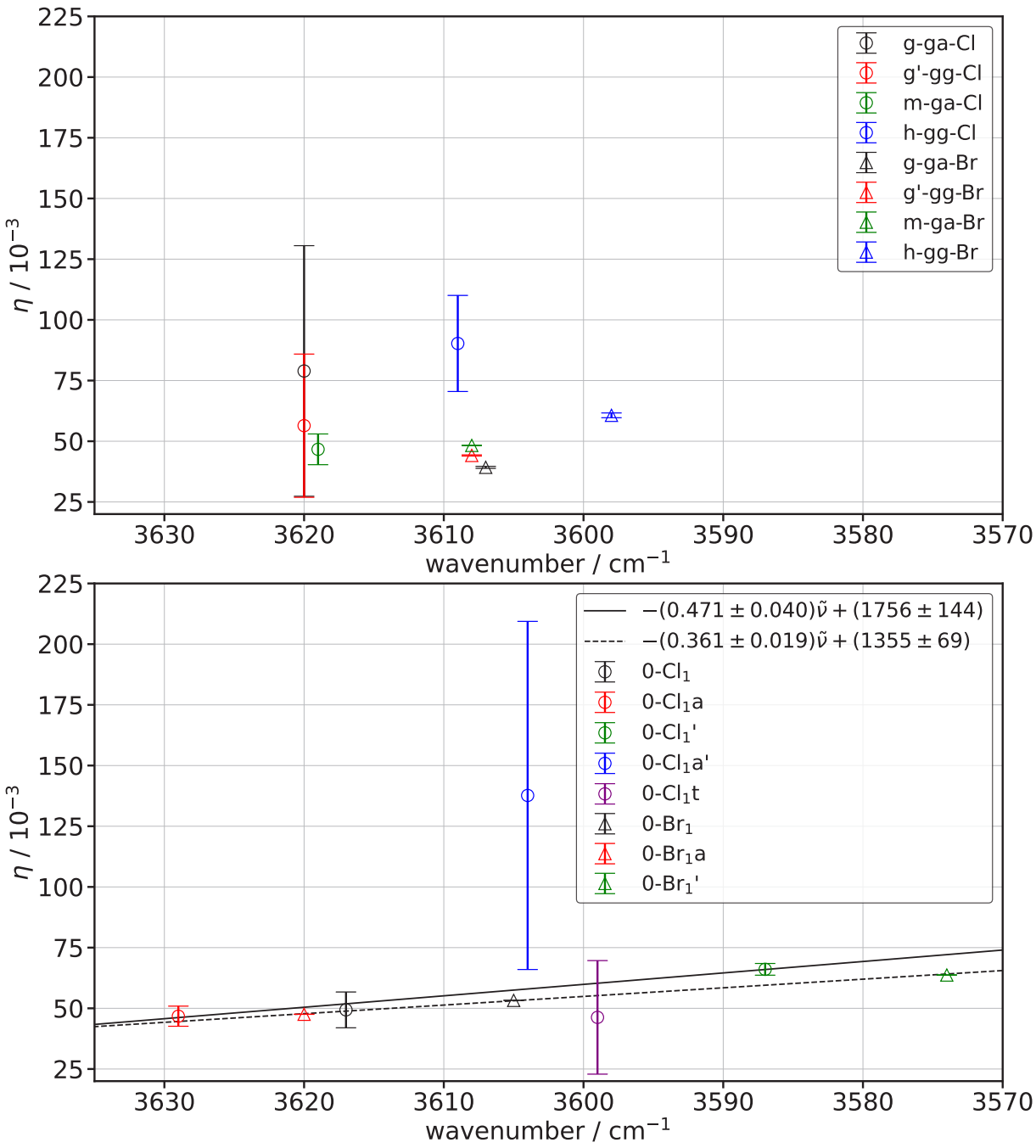

Fig. 3.47: Correlation of the experimental OH stretching vibrations of 1-*X*-propan-2-ol (m-ga and h-gg), 2-*X*-propan-1-ol (g-ga and g'-gg) and 3-*X*-propane-1,2-diol (lower panel) with the asymmetry parameter (η), where X = Cl, Br. The error-bars for the chlorine conformers of the mono-ols have been scaled by $1/3$.

different. In fact this inconsistency in the results of Goldstein *et al.*[244] was first noticed since predicted frequencies did not match the expected η behaviour. With the help of Jun. Prof. Dr. Obenchain it was found that two off-diagonal elements of g'-gg were not properly determined based on the experimental assignments Goldstein *et al.* provided

which likely lead to these discrepancies. In this context, properly determined means that if an off-diagonal element is changed by for example 10 MHz and kept frozen the quality of the overall fit does not change. Hence, such a comparison of η and the OH stretching vibration, even predicted ones, may be used as a sanity check of experimental results. The 1-chlorine-propan-2-ol values are in line with the expectations. However, they are likely overstated as a comparison with the bromine derivative shows. For 2-bromo-propan-1-ol, as expected, the OH stretching frequencies are very close to each other while the 1-bromo-propan-2-ol conformers are significantly separated. However, g-ga-Br is shifted slightly lower despite having a smaller η than g'-gg-Br. This change in wavenumber is still within the error of the experiment. Even larger deviations can be found when comparing g-ga-Br to m-ga-Br indicating that this analysis is best suited for a comparison of very analogous systems with no "absolute" scale being present.

Furthermore, Fig. 3.47 (bottom) also shows such a comparison for 3-X-propane-1,2-diol (X = Cl, Br). For chlorine it immediately becomes apparent that refinement for 0-Cl_1a' and 0-Cl_1t is necessary to draw conclusions for the entire system. However, if one focuses on 0-Cl_1, 0-Cl_1a and 0-Cl_1' which have smaller uncertainties a consistent increase of η with decreasing wavenumbers can be found. This is further illustrated by the linear regression (solid line) in Fig 3.47. It should be noted that this is only for illustrative purposes and there is no physical reasoning involved. Furthermore, the error bars of 0-Cl_1 also require some refinement. Assuming that the actual η for 0-Cl_1a' will be towards the lower end of the error bar it can be concluded that the halogen atom in primed cases is the better hydrogen bond acceptor. Fortunately, parallels to the bromine case can be drawn where η can be determined very accurately. For Br, a very good correlation can be found as can be seen by the dotted line. For these three conformers the expected behaviour is observed, however, this very limited dataset is not sufficient to make more general statements. It also highlights the importance of finding the 0-Br_1a' and 0-Br_1t conformers to complement or contradict the correlation.

Another possibility to compare the data is using η as computed by high level computations. For this purpose a comparison of the computed η with the experimental ones of 3-bromo-propane-1,2-diol is made given their small error bars. Such a comparison can be found in Fig. F.1 (page 303). CCSD(T) performs the best by far getting remarkably close to the experiment and therefore is chosen as the method of choice to correlate the experimental wavenumbers with. It should be noted though that CCSD(T) is not the best in predicting χ_{zz} but overall has the most balanced description of χ_{xx}, χ_{yy} and χ_{zz} as can be seen from Fig. F.2 (page 304). Given the similarity between the Br and Cl case it is assumed that CCSD(T) is also the most suitable method for 3-chloro-propane-1,2-diol.

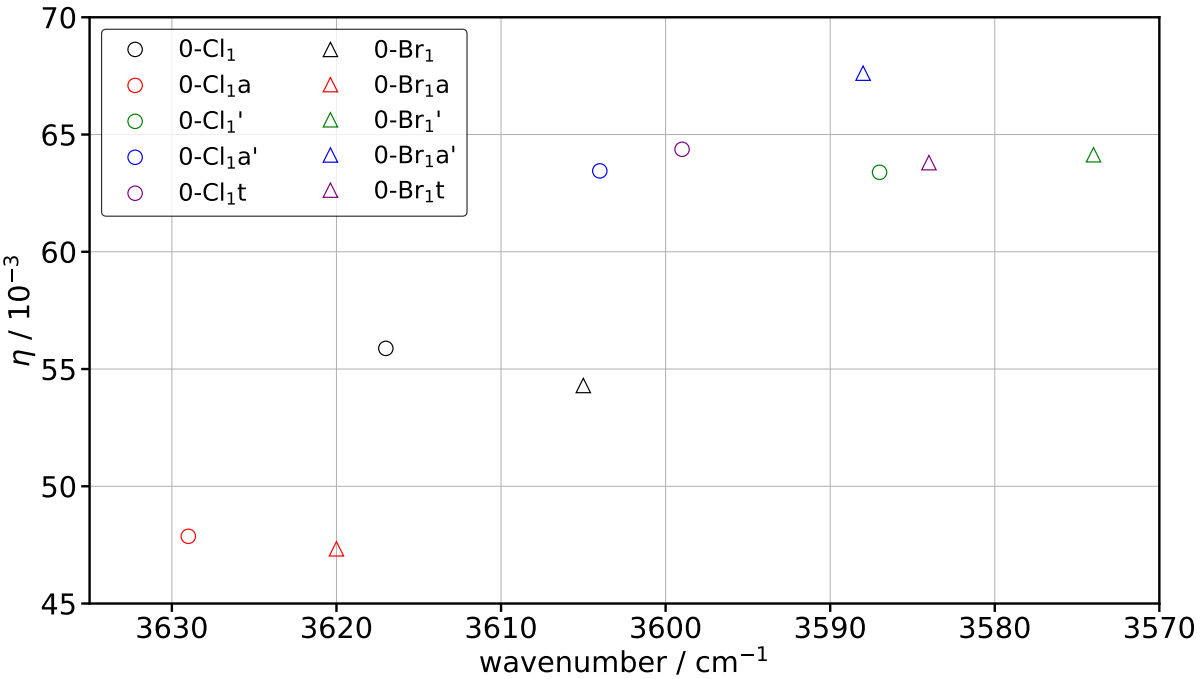

Fig. 3.48: Comparison of η computed at the CCSD(T)/awCTZ level of theory with experimental OH stretching vibrations for 3-chloro-propane-1,2-diol and 3-bromo-propane-1,2-diol.

Fig. 3.48 shows the computed η and experimental OH stretching frequencies for both diols. As was seen previously a fairly linear trend can be found if only 0-X, 0-Xa and 0-X' are taken into account (see Fig. 3.47 (page 126)). However, including 0-Xa' and 0-Xt defies this trend. Instead it appears as if once Ma' is reached η settles around 0.064. 0-Br$_1$a' differs somewhat from that behaviour but it is also the most challenging system to describe as most other methods yield unreasonably large η. Given the otherwise similar behaviour between the computed η of the two systems 0-Br$_1$a' can be considered somewhat of an outlier. Therefore, it may be the case that for these types of intramolecular OH$\cdots$halogen bonds η reaches some kind of saturation or maximal asymmetry. It can also be seen that the chlorine and bromine results are fairly consistently shifted towards each other. Hence, if a suitable method to describe the OH stretching frequency is found predictions could be made keeping this shift in mind. This could potentially be useful to make predictions for 3-iodo-propane-1,2-diol which could be used to complete the halogen series and further corroborate the idea of a potential maximum asymmetry for such systems. Moreover, η could also be correlated with results of theoretical methods that directly predict the hydrogen bond strength or the geometry of the interaction of the OH group with the halogen atom.

4 Chirality recognition within dimers

The distinction between symmetric and non-symmetric diols is made in terms of the substitution pattern on each side of the ethane-1,2-diol subunit. Therefore, the molecules with cyclic backbones also constitute symmetric diols. An overview of the systems studied in this section as well as their classification is shown in Fig. 4.1. All experimental dimer optimised Raman-spectra have been made available in Ref. [243].

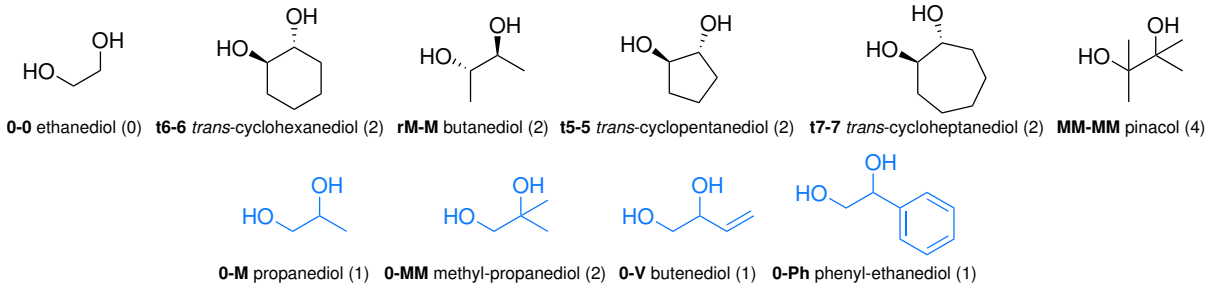

Fig. 4.1: Overview of the studied systems including the abbreviations used. Systems in black are considered symmetric and systems in light blue as non-symmetric. The degree of substitution (n_D) is shown in parentheses.

4.1 Symmetric diols

4.1.1 Ethane-1,2-diol

Ethane-1,2-diol constitutes the simplest organic vicinal diol and will be used as the baseline for the effects of substitution. Its strong energetic preference for hetero-chiral dimers was first described by Kollipost *et al.*[18] where a S_4 symmetric hetero dimer with 4 intermolecular hydrogen bonds (het4) being global minimum structure. However, IR and Raman jet-spectroscopy does not allow for a direct comparison of the energetic gap between the most stable homo-chiral and hetero-chiral dimer for permanently chiral systems. This is due to the fact that dimers are formed largely statistically in the expansion lead-

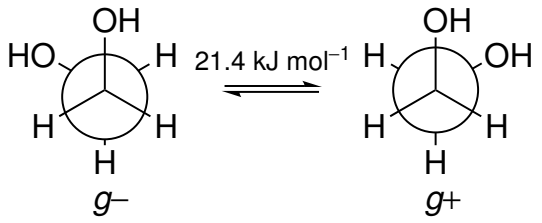

Fig. 4.2: Illustration of the transient chirality of ethane-1,2-diol.

ing to equal homo and hetero populations. In case of chirality induction (permanently chiral + transiently chiral) or chirality synchronisation (transiently chiral + transiently chiral), the energetics can be judged more directly. Since 0-0 is formally a transiently chiral system chiral synchronisation may occur. Nevertheless, due to the high barrier for conversion from *gauche* + to *gauche* − or *vice versa* of 21 kJ mol^{-1} (B3LYP/maTZ, see Fig. 4.2), the system can be treated as effectively permanently chiral under jet conditions. Keeping this in mind, it would be expected to observe both hetero and homo-chiral dimers in the jet-expansion. However, the study by Kollipost *et al.*[18] did not find strong evidence for the presence of homo-dimers which prompted the reinvestigation conducted in Ref. [166]. This elucidated the data by a comparison to the permanently chiral *trans*-cyclohexane-1,2-diol. The results and discussion presented here have largely been published in Ref. [166]. *trans*-cyclohexane-1,2-diol will be characterised in the next section and will be used to validate the assignments made here.

A selection of energetically relevant conformers at different levels of theory is shown in Tab. 4.1. A more comprehensive look at the energetic landscape and previous studies can be found in Refs. [18, 101, 166, 225]. The focus here is only on possibly relevant conformers

Tab. 4.1: Overview of computational results for the relative energies of the dimers of ethane-1,2-diol. Electronic (E_{el}) and zero point corrected (E_0) values are given. All values are given in kJ mol^{-1}.

		het4	het3	het3'	hom3'	hom3	hom3a	hom3$_b$'	hom2"
BP86/	E_{el}	0	-	11.88	12.49	13.45	15.51	16.86	14.35
maTZ[101]	E_0	0	-	8.59	8.83	9.74	11.49	12.50	11.76
PBE/	E_{el}	0	9.75	10.66	11.35	12.37	14.05	15.13	13.09
maTZ[101]	E_0	0	6.61	7.52	7.86	8.82	10.18	10.92	10.61
PBE0/	E_{el}	0	7.87	9.36	10.09	10.74	12.05	12.44	12.10
maTZ[101]	E_0	0	4.88	6.21	6.68	7.34	8.14	8.33	9.44
B3LYP/	E_{el}	0	9.45	10.80	12.19	12.78	14.20	15.27	14.56
TZ[166]	E_0	0	6.10	7.51	8.26	8.75	9.72	10.46	11.34
B3LYP/	E_{el}	0	7.84	9.20	10.15	10.74	11.98	12.06	13.67
maTZ[101]	E_0	0	4.72	5.94	6.73	7.23	8.02	8.02	10.65
B3LYP/	E_{el}	0	8.20	9.35	10.40	11.23	12.34	12.69	13.88
QZ[166]	E_0	0	5.01	6.49	7.01	7.66	8.39	8.55	10.71

for the spectra. All structures are shown in Fig. 4.3. As can be seen, all functionals predict het4 to be the most stable conformer. The next most stable hetero dimers (het3 and het3') follow after around 5 kJ mol^{-1} at the lowest, making het4 the only energetically relevant hetero dimer. Moreover, the barrier for het3 and het3' into het4 is very small. As can be seen from the molecular structures, het3 acts as an intermediate for the conversion of het3' to het4. The functionals also agree with regards to the minimum of the homochiral population namely hom3'. However, it is noticeable that the GGAs and B3LYP/TZ predict a larger het-hom gap. In case of B3LYP/TZ, this can be attributed to unaccounted BSSE which overly stabilises het4. This can also be seen by setting the reference point to hom3' which leads to very similar results to the larger basis sets, excluding het4. The less compact hydrogen bonded systems and systems with three hydrogen bonds are expected to have more similar BSSEs, therefore error cancellation can take place. Diffuse functions in case of maTZ or a higher ζ in case of QZ help to remedy this problem. This trend generally continues for B3LYP/TZ while B3LYP/maTZ, B3LYP/QZ and PBE0/maTZ

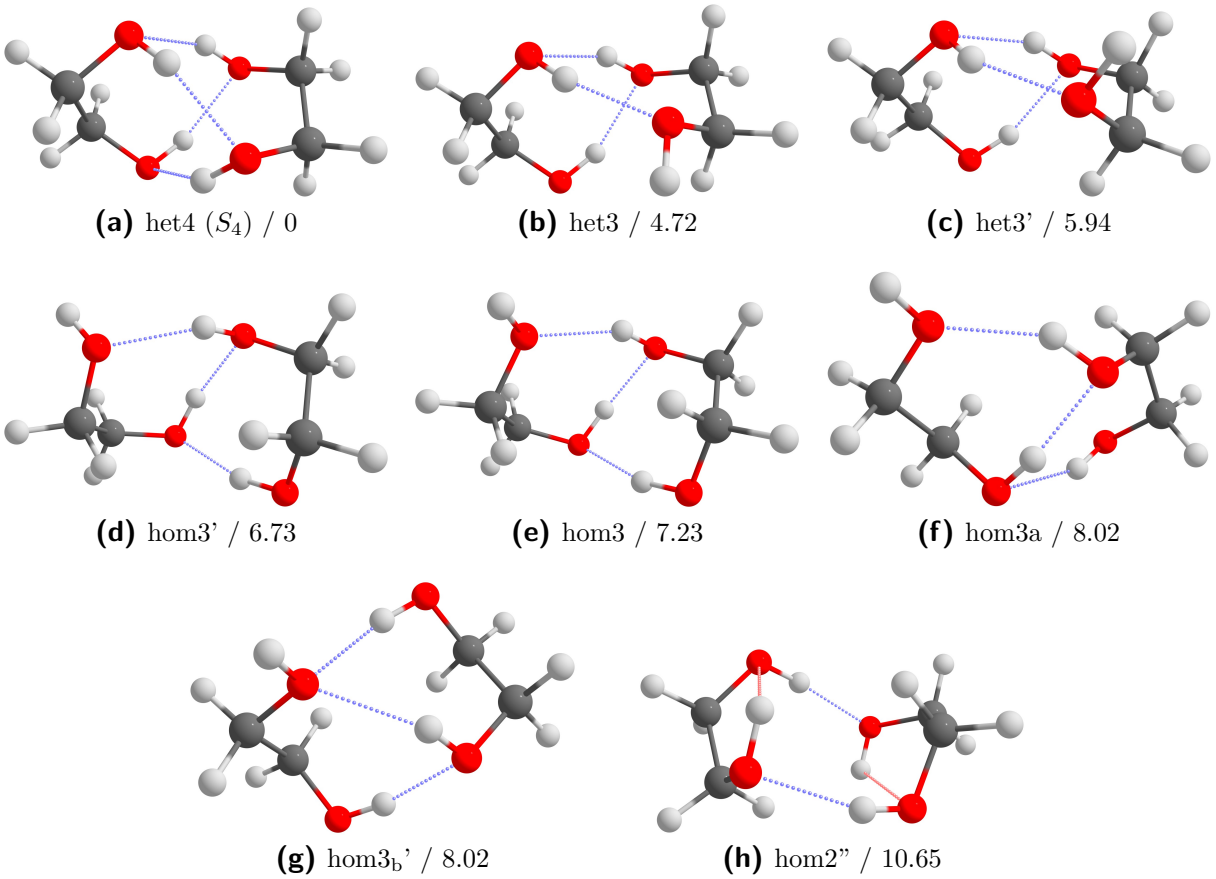

Fig. 4.3: Dimers of ethane-1,2-diol. Intermolecular hydrogen bonds are highlighted in blue and intramolecular ones in red. Relative zero-point corrected energies at the B3LYP/maTZ level are given in kJ mol^{-1}.

yield very similar results. The GGAs also overestimate however given that the maTZ basis set is used this is an inherent property of the functionals and not related to BSSE. Additionally, zero point correction significantly influences the relative energies.

Judging from the hybrid functionals with sufficiently large basis sets hom3', hom3, hom3a and hom3$_b$' are likely energetically relevant during the expansion. The major difference between hom3 and hom3a is that in hom3, the C-C backbones are oriented more perpendicular to one another than in hom3a (see Figs. 4.3e *vs.* 4.3f). hom2" is more than 2.5 kJ mol^{-1} above the the homo-chiral minimum for the hybrid functionals and will therefore not be considered. The barrier between hom3 and hom3' is quite small and could be easily overcome under jet conditions. Furthermore, their spectral signatures are very similar. All things considered, the set of relevant homo-chiral conformers can be simplified to hom3', hom3a and hom3$_b$'. Given the close energetic proximity of the three conformers it is assumed that they are roughly equally populated so that statistical weights of 3 : 1 : 1 : 1 for het4 : hom3' : hom3a : hom3$_b$' are expected. Based on the GGAs only hom3' and hom3 would be considered. Lastly, it should be mentioned that a homo-chiral C_2 symmetric het4 counterpart exists. However, it is of significantly higher energy at around 10 kJ mol^{-1} above the global minimum at the B3LYP/maTZ level of computation.

Fig. 4.4 shows the experimental and predicted Raman and IR spectra of 0-0 with the weighting mentioned above applied. het4 can be easily identified in both the IR and Raman spectra nicely showing the effects of its S_4 symmetry. Band 4 corresponds to A character which is only Raman active while Band 1 corresponds to B character which in principle allows both IR and Raman activity. However, the Raman intensities are very small. The doubly degenerate E band is both Raman and IR active and can be identified in both spectra. This interplay highlights the complementary use of Raman and IR spectroscopy.

As one would expect from the statistical weights, the homo-dimers are significantly less prominent than het4. The simulations indicate that all bands that can be observed in the Raman spectra should also be present in the IR spectra with the exception of the free OH stretching vibrations which are strongly enhanced in the Raman spectra. Band 2 of hom3', the most stable homo-chiral dimer, can be observed easily in the Raman spectrum while some overlap with het4 is found in the IR case. Band 3 is too weak to be observed and would likely be obfuscated by band 1 of het4 in the IR spectrum. Band 4 can be clearly identified in the Raman spectra and likely overlaps with band 4 of hom3a. The rather broad nature of the band may be caused by this overlap. In the IR case its presence is more tentative. Band 2 of hom3a, which overlaps with band 3 of hom3$_b$', can be identified in both cases . Band 3 of hom3a is too low in intensity to be detected.

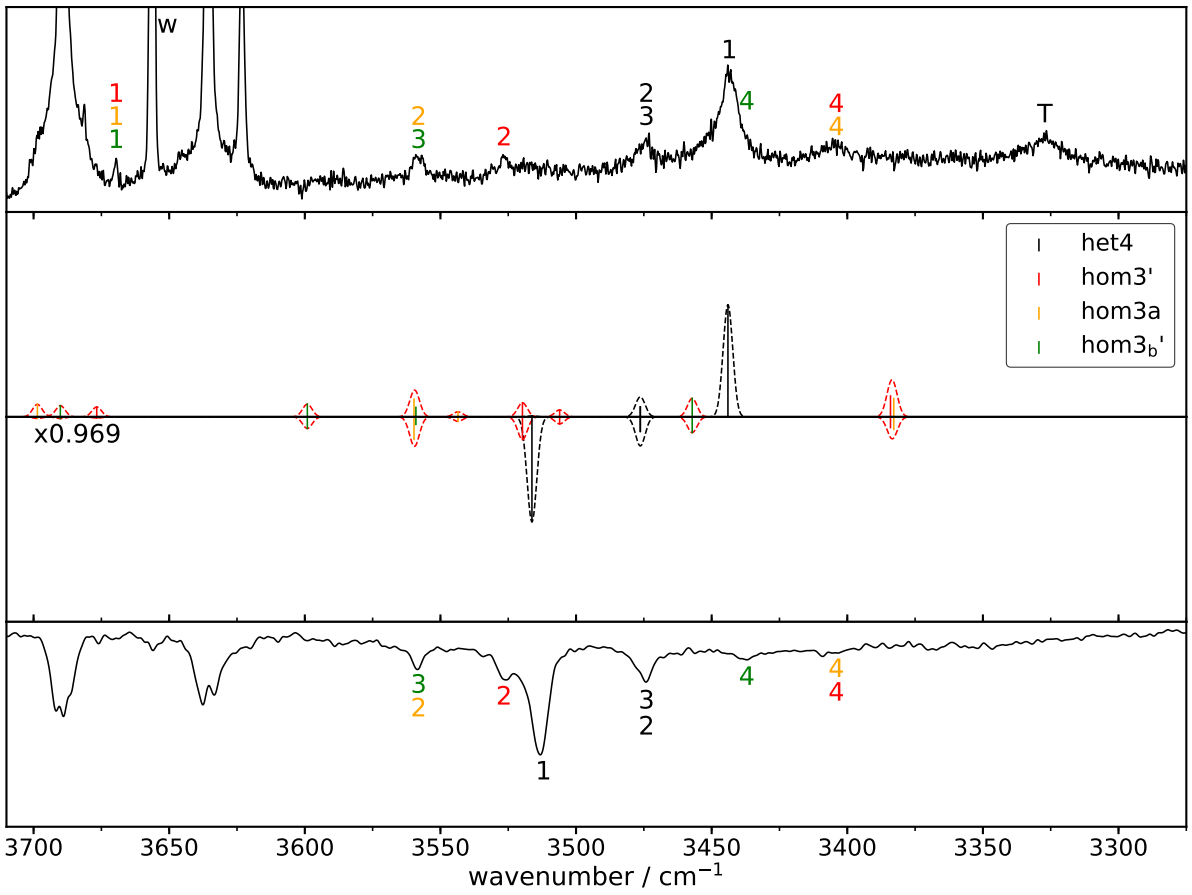

Fig. 4.4: Overview of the experimental and predicted Raman (plotted upwards) and IR spectra (plotted downwards) of ethane-1,2-diol. The predictions are based on B3LYP/maTZ calculations and scaled by 0.969 to match band 4 of het4. The experimental spectra are taken from Ref. [166] with the IR data having been recorded by M. Lange. w Indicates a water band and T a trimer band.

Furthermore, band 4 of hom3$_b$' can be identified in the IR while in the Raman case it is likely hidden underneath the very intense band 1 of het4. Lastly, the small band in the monomer region can be assigned to the free OH mode of the three homo-chiral dimers. The fact that the band can be observed at all indicates that some degree of overlap must be present here when comparing the experimental to the predicted intensities. However, it cannot be ruled out that one dimer band may be hidden underneath a monomer or water signal.

Furthermore, microwave spectra in the 2 GHz – 8 GHz and 18 GHz – 26 GHz region were recorded, which can be used to further corroborate the assignment and statistical weights. Luca Evangelisti (University of Bologna) and his group have also recorded spectra in the 2 GHz – 8 GHz and have agreed to join the data and provided some preliminary assignments and calculations. hom3' could already be assigned in the spectra. It should be

kept in mind that het4 has no permanent dipole moment due to its symmetry. Therefore, microwave data is expected to only provide evidence of homo-dimers.

4.1.2 *trans*-Cyclohexane-1,2-diol

As could already be seen for the monomers, *trans*-cyclohexane-1,2-diol (t6-6) behaves very similarly to 0-0 (see section 3.1.2). Hence, it may also be the case that the dimers show analogous behaviour. As was previously mentioned t6-6 is a permanently chiral system, hence the formation of homo-dimers can be enforced by using the enantiopure compound. Here *trans*-(*S*,*S*)-cyclohexane-1,2-diol was used in the experiments. For the racemate equal populations of homo and hetero dimers can be safely assumed. This can be used to validate the corresponding assumption for 0-0 *via* spectral analogy. The permanent chirality is illustrated in Fig. 4.5. As can be seen, only a conversion from di-equatorial to di-axial is possible. However, di-axial conformers are much higher in energy and therefore will not be considered for the formation of dimers.

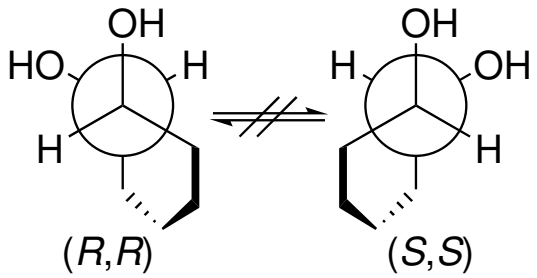

Fig. 4.5: Illustration of the permanent chirality of *trans*-cyclohexane-1,2-diol.

Possibly energetically relevant conformers are summarised in Tab. 4.2. As was the case with 0-0, a more thorough exploration of the conformational space can be found in Refs. [166] and [101]. A comparison with 0-0 (see Tab. 4.1 (page 130)) shows that both systems have a lot in common with one distinct difference *i.e.* the energetic order of hom3a and hom2" is reversed. All functionals lower hom2" and increase hom3a in energy. This similarity can also be seen when comparing the structures shown in Figs. 4.6 and 4.3 (page 131). Despite the much larger cyclohexyl backbone, structural changes are quite small, which further legitimates a comparison between the two systems. The hybrid functionals indicate that hom3', hom3$_b$' and hom2" should constitute the homo-chiral population in a jet-expansion. The GGAs on the other hand suggest that hom2" and hom3' should suffice. As was the case for 0-0, hom3 is expected to convert to hom3' under jet conditions and exhibits very similar spectral signatures and therefore will not be included in the interpretation. Moreover, the energy difference between hom3' and hom3 is even larger, increasing the thermodynamical driving force for the relaxation. The three remaining homo-chiral dimers are yet again very close in energy and hence equal populations are assumed. het4 is also the global minimum and unrivalled in terms of energy with regards to all other dimers. Easy relaxation of het3' to het4 is possible and

Tab. 4.2: Overview of computational results for the relative energies of the dimers of *trans*-cyclohexane-1,2-diol. Electronic (E_{el}) and zero point corrected (E_0) values are given. All values are given in kJ mol^{-1}.

		het4	het3	het3'	hom3'	hom3	hom3a	hom3$_b$'	hom2"
BP86/ maTZ[101]	E_{el}	0	13.03	12.71	13.05	15.18	18.27	15.59	11.57
	E_0	0	9.35	9.32	9.09	11.04	13.76	11.25	8.78
PBE/ maTZ[101]	E_{el}	0	11.47	11.18	11.95	14.04	16.53	14.11	10.32
	E_0	0	8.07	7.95	8.12	10.02	12.17	9.88	7.65
PBE0/ maTZ[101]	E_{el}	0	9.33	9.51	10.34	12.21	13.99	11.26	11.26
	E_0	0	5.98	6.18	6.48	8.18	9.53	7.08	6.29
B3LYP/ TZ[166]	E_{el}	0	-	11.42	12.16	13.74	15.05	13.22	11.34
	E_0	0	-	7.64	8.21	9.52	10.93	9.04	8.00
B3LYP/ maTZ[101]	E_{el}	0	9.42	9.37	10.47	12.23	13.73	10.94	10.45
	E_0	0	5.16	5.92	6.58	8.13	9.16	6.80	7.47
B3LYP/ QZ[166]	E_{el}	0	-	9.89	10.74	12.47	13.77	11.39	10.96
	E_0	0	-	6.37	7.05	8.27	9.63	7.58	7.44

therefore statistical weights of 3 : 1 : 1 : 1 for het4 : hom3' : hom3$_b$: hom2" can be introduced in analogy to 0-0. Therefore, it is also expected that when switching from the racemic mixture to the enantiopure compound, the homo-chiral signals should roughly double in intensity.

It can also be seen from Tab. 4.2 that BSSE artificially stabilises het4 again when using the TZ basis set. maTZ and QZ combat the BSSE and yield fairly similar results. However, maTZ is significantly smaller than QZ and given that the t6-6 dimer consists of 40 atoms in total provides huge time savings at the same level of accuracy. Furthermore, given this trend, caution is advised when using TZ for the comparison of systems with different amounts of hydrogen bonds and/or compactness. The impact of zero point correction is also quite substantial with changes around 4 kJ mol^{-1} being very common. Additionally, a study by Jesus and Redinha[185] reported computed dimer structures. However, their dimers are significantly more open and favour one or two intermolecular hydrogen bonds which are found to be not energetically competitive to the structures reported here. A more detailed discussion of their results can be found in Ref. [166].

Fig. 4.7 shows a comparison of the experimental and predicted IR and Raman spectra. The spectra shown in red correspond to enantiopure and the ones in black to racemic t6-6 for the simulations as well as for the experiment. Since het4 is still S_4 symmetric, the same intensity pattern as for 0-0 can be found. Furthermore, all het4 signals overlap to

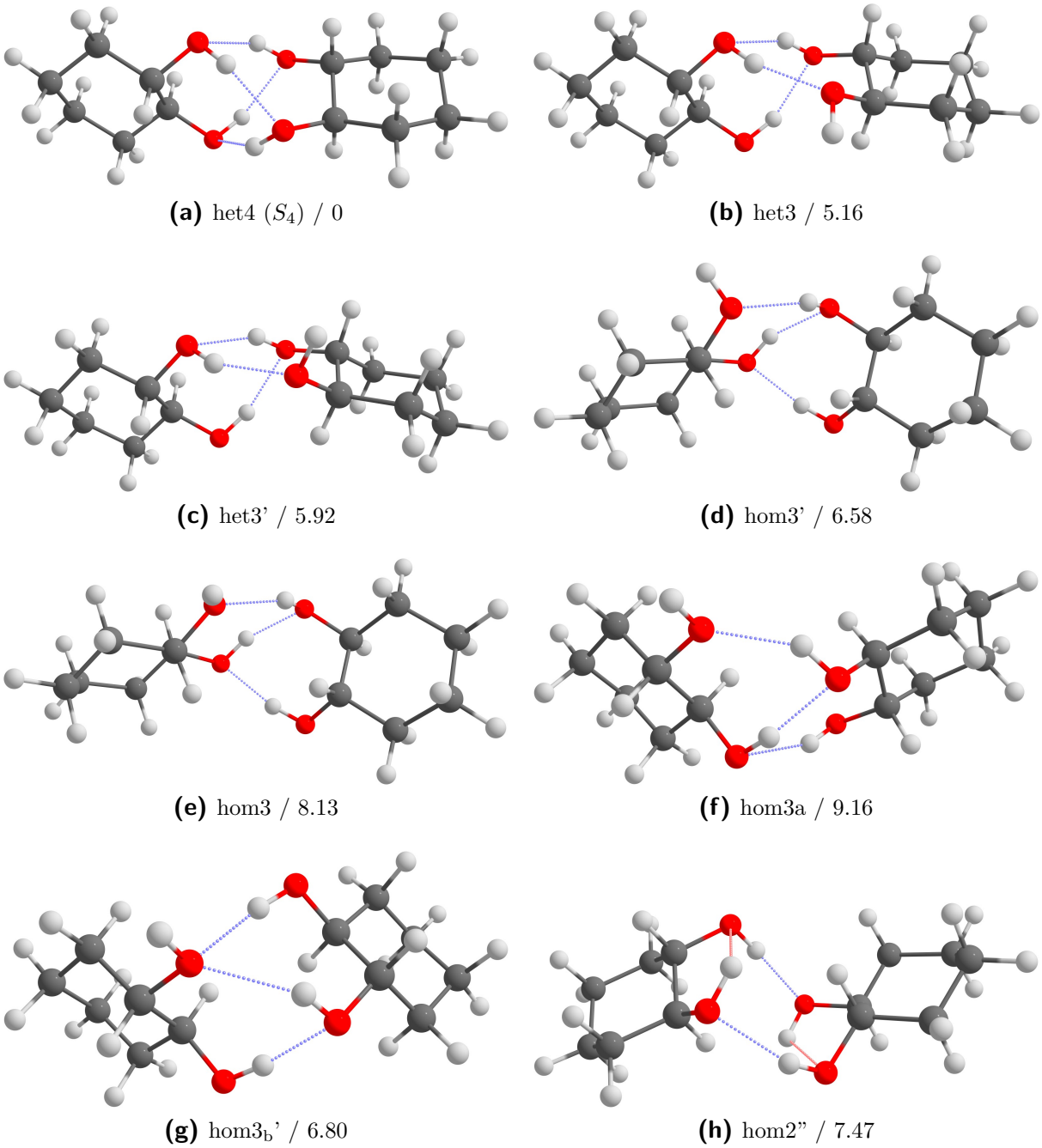

(a) het4 (S_4) / 0 **(b)** het3 / 5.16

(c) het3' / 5.92 **(d)** hom3' / 6.58

(e) hom3 / 8.13 **(f)** hom3a / 9.16

(g) hom3$_b$' / 6.80 **(h)** hom2" / 7.47

Fig. 4.6: Dimers of *trans*-cyclohexane-1,2-diol. Intermolecular hydrogen bonds are highlighted in blue and intramolecular ones in red. Relative zero-point corrected energies at the B3LYP/maTZ level are given in kJ mol^{-1}.

some degree with homo-dimers as a comparison of the racemic and enantiopure spectra shows. Hence, the assignment of het4 is quite straightforward. Band 4 of het4 overlaps with band 4 of hom2" and hom3' in the Raman spectra. No overlap is present in the IR spectra although, given the higher level of noise, hom2" and hom3' cannot be identified

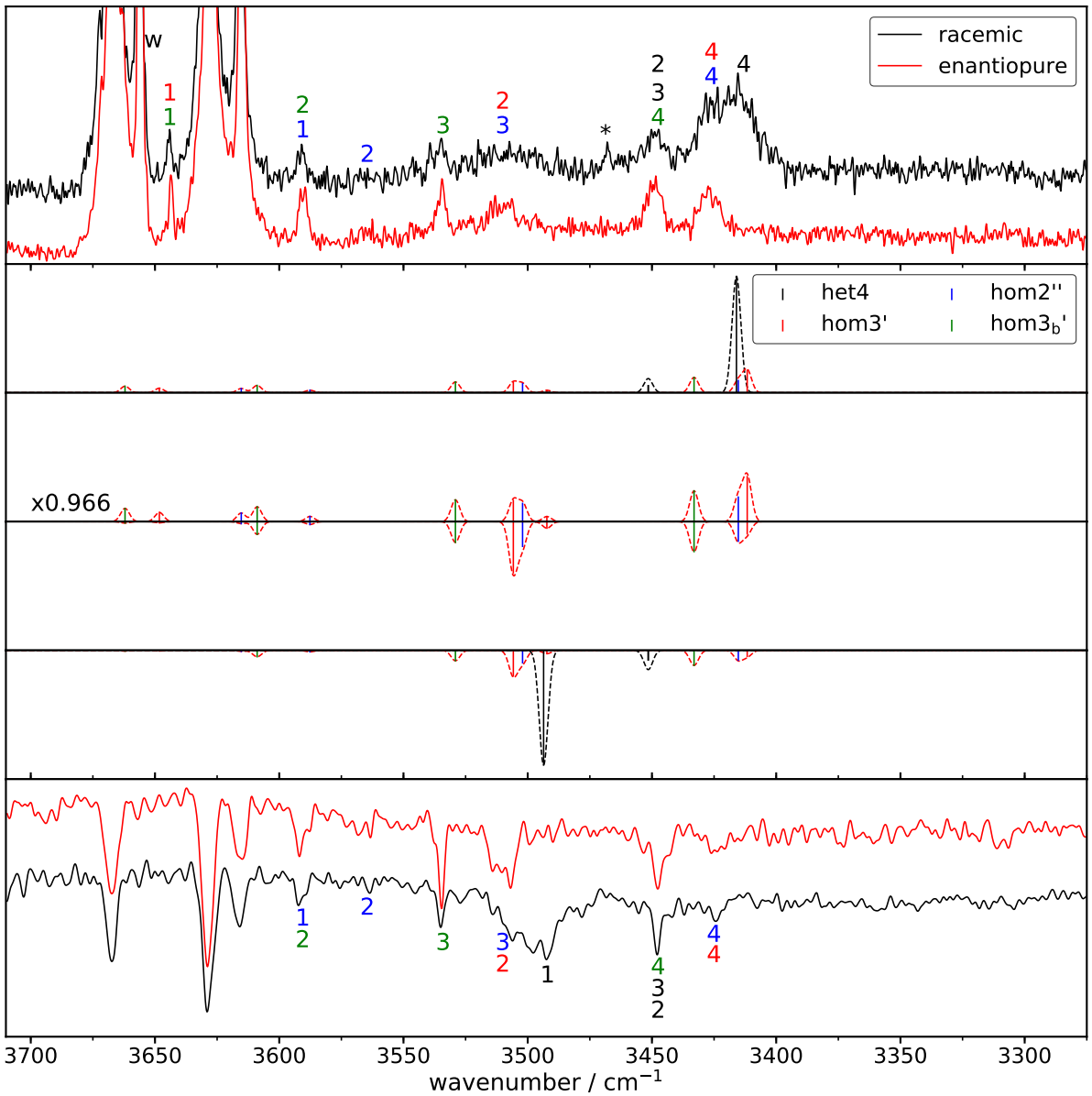

Fig. 4.7: Overview of the experimental and predicted Raman (plotted upwards) and IR spectra (plotted downwards) of *trans*-cyclohexane-1,2-diol. The racemic and enantiopure experimental spectra are scaled to match the free OH mode of the most stable monomer. The two middle spectra show the enantiopure simulations. The predictions are based on B3LYP/maTZ calculations and scaled by 0.966 to match band 4 of het4. The experimental spectra are taken from Ref. [166] with the IR data having been recorded by M. Lange. w Indicates a water band and * a residual peak due to a spike.

as clearly. The very high intensity of band 4 of the hetero-dimer can also be inferred by comparison to the enantiopure case. The E band overlaps with hom3$_b$' since a signal persist when switching to (*S*,*S*)-t6-6 both in the IR and Raman case. Band 1 of het4 is only visible in the IR and again overlaps with hom2" and hom3' with their presence being clearly shown by the enantiopure spectrum. In the racemic Raman case, the hom2" and

hom3' signal appears quite broad but adopts a similar band shape in the (*S*,*S*)-t6-6 case as the IR spectrum.

Band 3 of hom3$_b$' exists as a non overlapping band in all cases and is especially sensitive to the chirality switch. Signal 2 of hom2" is quite low in its predicted intensity and can only be observed in the enantiopure spectra albeit still with a small population. In case of the Raman spectra, a signal can be consistently observed in each of the scans that were averaged for the spectrum, validating its presence. The IR case is less clear given the noise level but can be inferred by the Raman spectrum. Band 2 and 1 of hom3$_b$' and hom2" respectively can be found slightly outside the monomer range. They also appear to be quite sensitive to the chirality switch. Based on the simulations it could be argued that hom2" is not contributing in the IR. Since hom2" exhibits either intermolecular or intramolecular hydrogen bonds no signals can be found within the monomer range. For hom3' and hom3$_b$' on the other hand, an overlap of their free OH mode can be found in the Raman spectra. As was the case for 0-0, no free OH modes can be observed in the IR spectra.

Comparing the experimental intensities of the racemic and enantiopure case reveals that the expected increase of the homo dimer by a factor of 2 is not present. However, a clear increase can be observed for the non-hetero overlapping bands. Judging overlapping bands is in principle possible by taking the difference between the spectra. Unfortunately, the resulting spectrum is too noisy for interpretation. Furthermore, the vapour pressure of (*S*,*S*)-t6-6 is likely lower since the racemic spectra had to be scaled down to match the monomer signal although literature data[274] suggest that the racemate is less volatile. Moreover, slightly different expansion conditions may also play a role. Additionally, differences in the contact areas during the sample pickup can also explain the deviations found.

Given the very similar behaviour of 0-0 and t6-6, the previously made assumption that 0-0 behaves as a permanently chiral system in a supersonic jet expansion and the formation of dimers is mostly statistical can be confirmed. Moreover, the issue of insufficient homo-dimers of 0-0 found in the jet by Kollipost *et al.*[18] could be resolved. While the hetero-population consist of a single conformer the homo population is shared among at least three dimers, hence appearing smaller in the spectrum.

For t6-6, a microwave spectrum in the 2 GHz – 8 GHz region has also been recorded and similarly to 0-0, the statistical weights of the homo-chiral dimers can be confirmed. The racemic mixture was used but het4 is again not microwave active. Hence, the racemic mixture can be considered enantiopure. This may be seen as a disadvantage but the enantiopure compound is significantly more expensive and the same results can be achieved

with the racemic mixture in the rotational spectroscopy case. In fact, hom3' and hom3$_b$ could be assigned. hom2" could not be assigned, likely due to its small permanent dipole moment. Based on the predicted dipole moments it was estimated that hom3' is slightly more populated than hom3$_b$'. It should be kept in mind that lower conformational temperatures were likely achieved in comparison to the Raman/FTIR measurements, since neon was used as a carrier gas and other differences between the setups as outlined in section 2.1.3 (page 10).

4.1.3 Pinacol

As was the case for 0-0, pinacol (MM-MM) is a transiently chiral system with a significantly bulkier backbone. The conversion from the *gauche* + to *gauche* − conformation or *vice versa* is associated with a significantly higher barrier than for 0-0, as illustrated in Fig. 4.8. The increase of the barrier is due to an eclipsed arrangement of the methyl groups in the transition state. Hence, it is also expected that MM-MM behaves like a permanently chiral system in a supersonic jet expansion. Due to the tetra-methylation, the conformational landscape of MM-MM differs significantly from that of 0-0, most notably for the homo-dimers. As can be seen in Tab. 4.3, MM-MM generally favours more open homo-chiral hydrogen bond arrangements. For the hetero-chiral dimers het4 is still energetically unrivalled but other conformers are closer in energy than for 0-0 and t6-6 (see Tabs. 4.1 (page 130) and 4.2 (page 135)).

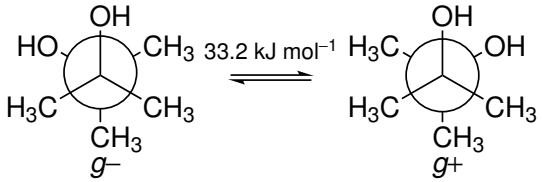

Fig. 4.8: Illustration of the transient chirality of pinacol.

It can also be seen that the homo-chiral conformational landscape is vastly more complicated than before. Within 3 kJ mol^{-1}, a total of eleven conformers were found at the B3LYP/maTZ level. hom4, the homo-chiral analogue of het4 constitutes the most stable homo conformer. Unlike het4, it is C_2 symmetric having two short hydrogen bonds (1.87 Å) and two long hydrogen bonds (2.29 Å). It should be noted though that C_2 is a subgroup of S_4. Furthermore, given its symmetry, hom4 itself is chiral while het4 is not which plays a role in the prediction of their populations. het4 on the other hand has 4 equivalent hydrogen bonds with a length in between (1.95 Å) those of hom4. The given bond lengths were all calculated at the B3LYP/maTZ level of theory. The long hydrogen bonds of hom4 are more akin to lengths found in intramolecular hydrogen bonds of monomers. For instance, the most stable monomer of pinacol has a predicted hydrogen bond length of 2.15 Å. Hence, despite the 4 intermolecular hydrogen bonds, two signals

Tab. 4.3: Overview of computational results for the relative energies of the dimers of pinacol. Electronic (E_{el}) and zero point corrected (E_0) values are given. The reported B3LYP/maTZ energies have only been partially published in Ref. [101]. A - does not indicate that a conformer is unstable at a given level of theory. All values are given in kJ mol^{-1}.

	BP86/maTZ[101]		PBE/maTZ[101]		PBE0/maTZ[101]		B3LYP/maTZ[101]	
	E_{el}	E_0	E_{el}	E_0	E_{el}	E_0	E_{el}	E_0
het4	0	0	0	0	0	0	0	0
het3$_b$'	14.27	9.26	11.95	7.32	10.05	5.50	8.67	4.14
het3'	11.82	7.15	10.56	6.25	9.47	5.14	9.64	4.80
hom4	12.61	9.31	11.97	8.21	10.77	7.01	10.63	6.96
hom2'	-	-	-	-	-	-	12.26	6.87
hom3'	15.38	10.29	13.88	8.82	12.76	7.76	12.12	7.11
hom2	-	-	-	-	-	-	13.93	7.63
hom3a	19.51	13.49	17.49	10.71	15.60	8.85	14.81	8.09
hom3a'	15.86	10.43	14.83	9.53	14.44	9.10	13.58	8.14
hom3	17.44	11.75	15.95	10.52	14.48	9.15	13.74	8.29
hom1'	-	-	-	-	-	-	14.76	8.46
hom1a'	-	-	-	-	-	-	14.81	8.76
hom3$_b$'	19.99	13.92	18.13	12.34	16.09	10.32	15.04	9.17
hom1	-	-	-	-	-	-	16.10	9.52

are expected in the monomer range. The structures with two intermolecular hydrogen bonds do not resemble the previous hom2" structures as can be seen from Fig. 4.9. Arrangements of the hom2" type are not possible due to the steric influence of the methyl groups, although the hetero-chiral analogue is stable but much higher in energy. The fact that these insertion complexes are still energetically competitive is likely due to dispersion interactions of the backbone. In a similar fashion, the structures with just a single intermolecular hydrogen bond are also stabilised by London forces.

The structures with three intermolecular hydrogen bonds still closely resemble those of 0-0 as a comparison of Figs. 4.3 (page 131) and 4.9 shows. As was the case before relaxation of hom3 to hom3' is expected under jet conditions, although the spectral signatures are no longer as similar as before. In the same vein, hom3a' can relax to hom3a. However, it should be noted, that they are predicted to be almost isoenergetic. Therefore, no strong thermodynamic driving force is present and given the uncertainty of the calculation the energetic order could easily be reversed. Given the complexity of the homo-chiral dimers it is quite difficult to determine statistical weights. To gain a general idea of the spectrum it is assumed that all homo-chiral dimers have the same population and that het4 is three times as populated as the homo-chiral population, in analogy to 0-0. Moreover, zero

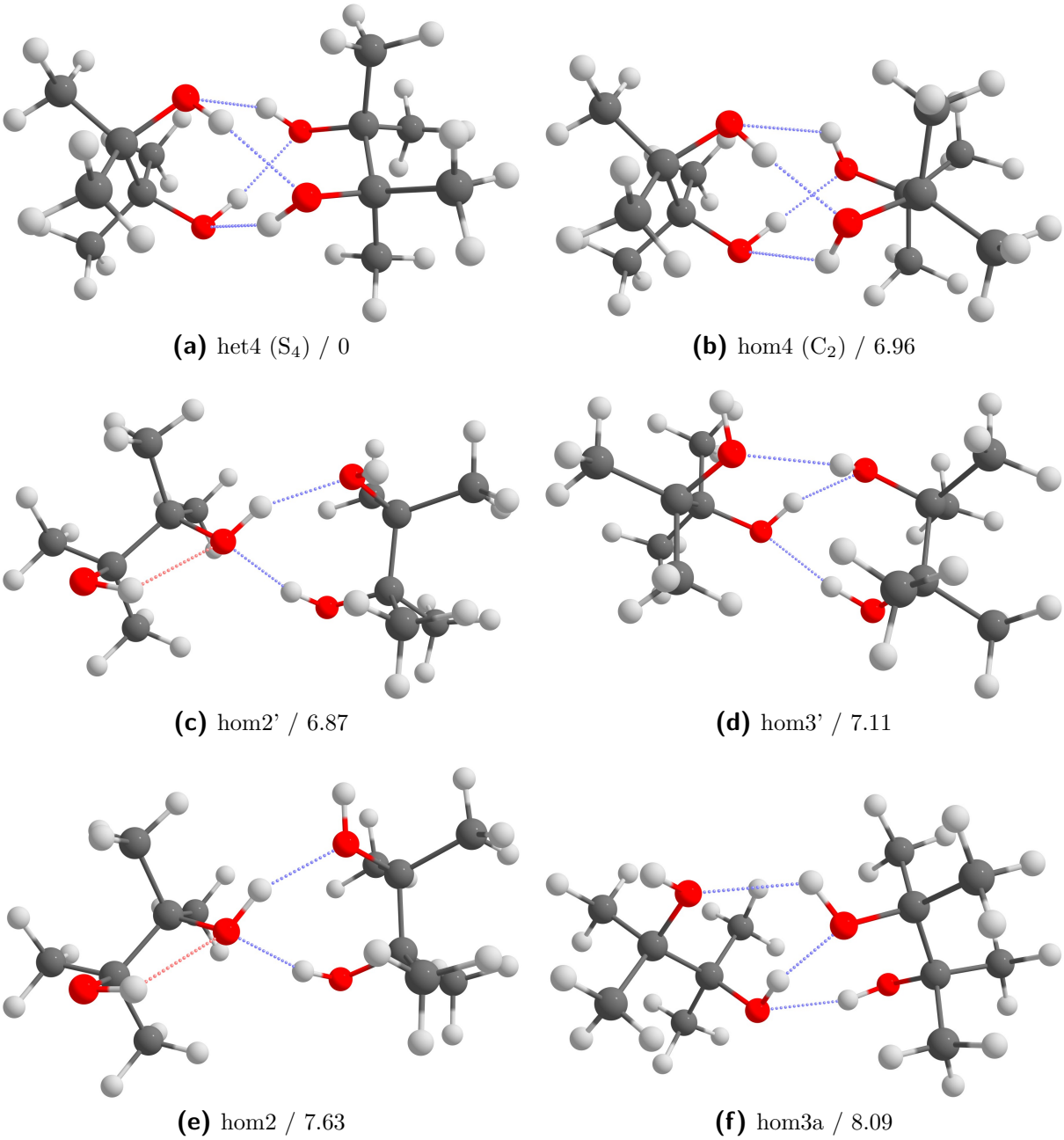

(a) het4 (S_4) / 0 **(b)** hom4 (C_2) / 6.96

(c) hom2' / 6.87 **(d)** hom3' / 7.11

(e) hom2 / 7.63 **(f)** hom3a / 8.09

Fig. 4.9: Dimers of pinacol. Intermolecular hydrogen bonds are highlighted in blue and intramolecular ones in red. Relative zero-point corrected energies at the B3LYP/maTZ level are given in kJ mol^{-1}.

point correction becomes even more important reaching differences of up to 6.71 kJ mol^{-1} at the B3LYP/maTZ level. In comparison to B3LYP/maTZ, PBE0 predicts slightly larger energy differences while with PBE and BP86 they are significantly larger. Especially BP86 shows larger discrepancies. Curiously, for the hom3'/hom3 and hom3a'/hom3a pairs, the GGAs suggest that the primed conformers are more stable, which was already observed for the monomers.

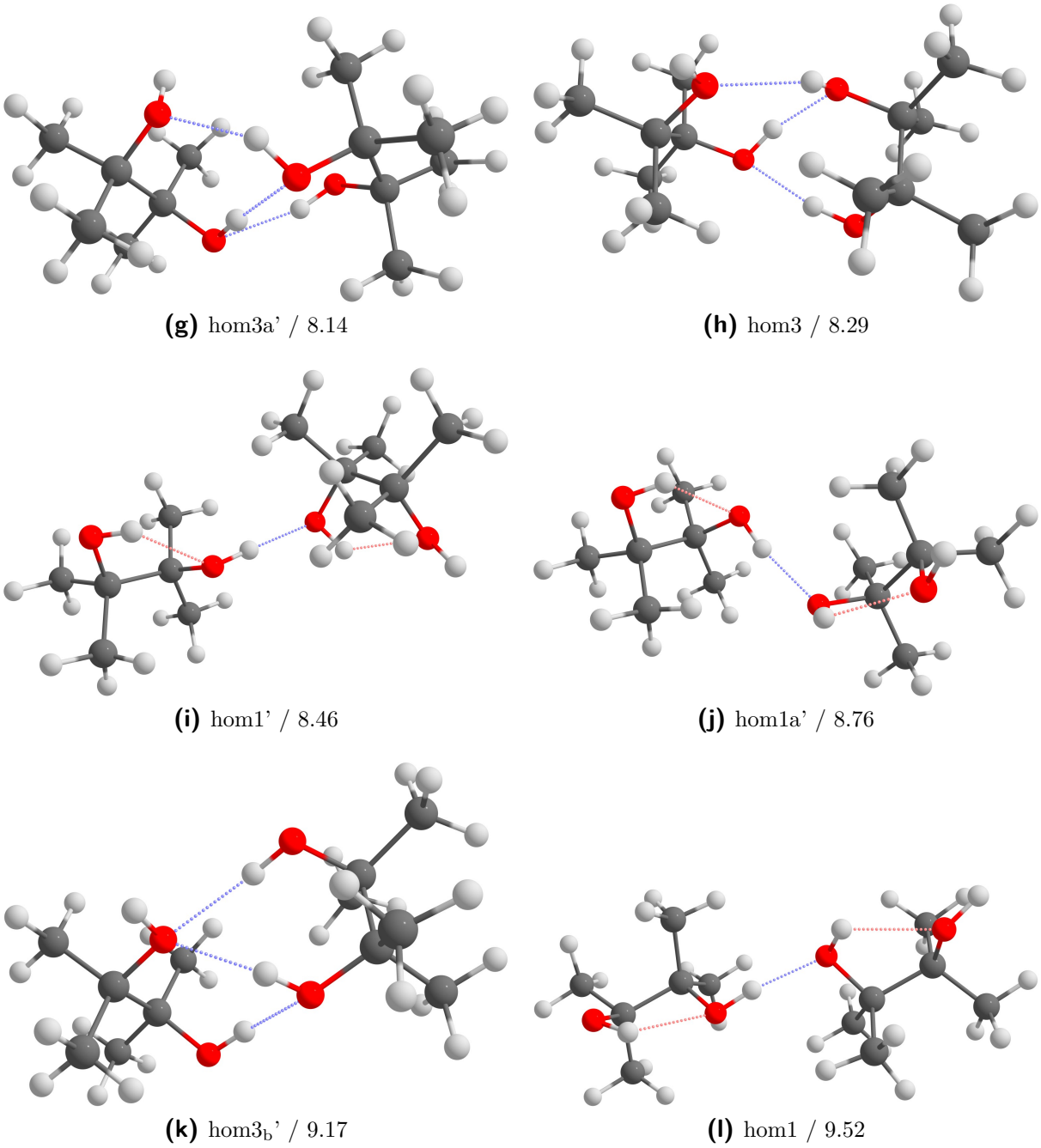

(g) hom3a' / 8.14 **(h)** hom3 / 8.29

(i) hom1' / 8.46 **(j)** hom1a' / 8.76

(k) hom3$_b$' / 9.17 **(l)** hom1 / 9.52

Fig. 4.9: Continuation of Fig. 4.9.

The experimental Raman spectrum as well as the predicted one are shown in Fig. 4.10. The typical intensity pattern of het4 is appears to be present, although the splitting between the degenerate E band (2/3) and A band (4) is significantly overestimated by B3LYP/maTZ. However, it may very well be the case that an overlap of hom4, hom2' and hom2 is responsible for the proposed E band. For 0-0 and t6-6, B3LYP/maTZ captured the B-E-A exciton splitting quite well and general substitution effects should have been already present going from 0-0 to t6-6. Therefore, the homo-chiral explanation appears

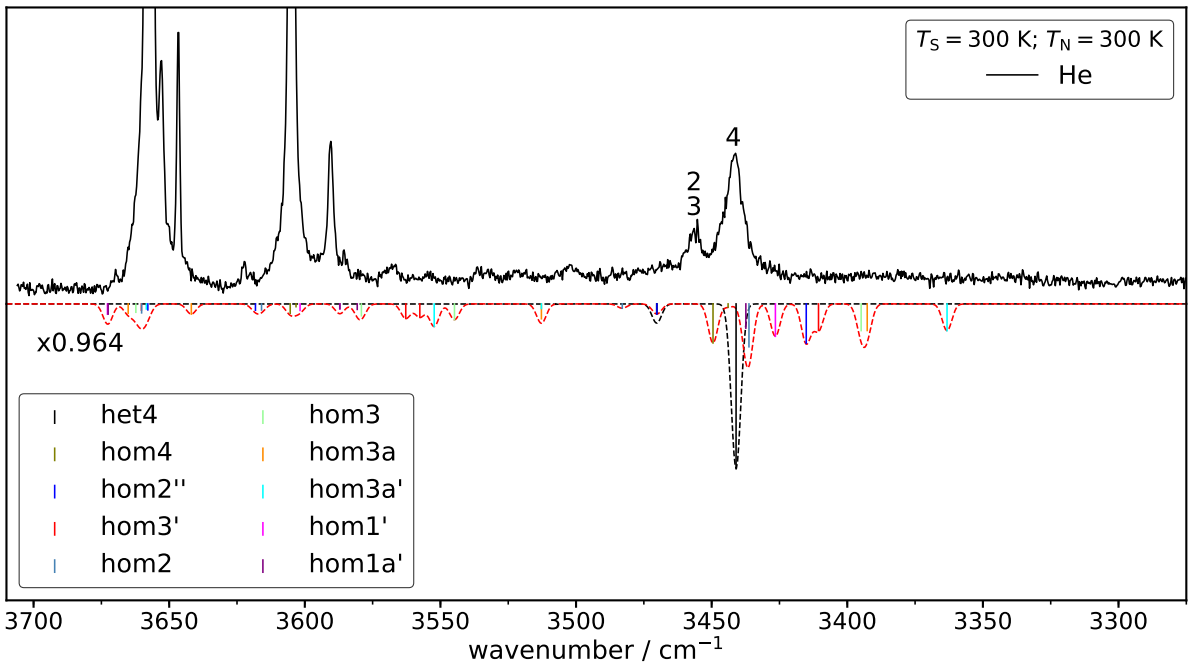

Fig. 4.10: Experimental Raman data (plotted upwards) and simulated data (plotted downwards) of pinacol. The saturator temperature (T_S) as well as the nozzle temperature (T_N) are given. The simulated spectra are based on B3LYP/maTZ and are scaled by 0.964 to match band 4 of het4.

to be more likely, but tetra-methylation could potentially be responsible. To establish a link to the methylation, butane-2,3-diol can be investigated, where the E-A splitting is expected to be larger but smaller than for 0-0. Butane-2,3-diol can also serve as an open analogue to t6-6, but similar, although smaller, effects can be expected for propane-1,2-diol.

The remaining unassigned bands are all expected to be caused by homo-dimers and therefore are considerably smaller in intensity. Furthermore, the most intense band of the most stable homo-dimer likely overlaps with het4. Given the plethora of possible candidates for the bands occurring in the range between 3575 cm^{-1} and 3460 cm^{-1} no clear assignments can be made. Even more so, since the vibrational counterparts for many conformers, *i.e.* hom2', hom3', hom3, hom3a and hom3a', are missing in the wavenumber region below band 4 (het4). Furthermore, some of the smaller bands in the monomer region could potentially be assigned to free OH modes of the homo-dimers. However, the signals at 3670 cm^{-1}, 3622 cm^{-1} and 3585 cm^{-1} are already present under monomer conditions. Hence, the free OH modes of the homo-dimers are likely all hidden underneath the intense monomer bands. Additionally, at the time the spectra were recorded, the residual water content was fairly high, but the three bands do not match those of water monomers[275]

or oligomers[276]. Pinacol-water dimers have not yet been ruled out as potential causes.

To solve the uncertainties with regards to the homo-dimers, a combination of more experimental and theoretical work is needed. Higher level computations could help to narrow the field of homo-dimers that have to be considered. However, given the size of the systems, geometry optimisations at the coupled cluster level are likely not feasible. The Raman spectrum can be improved by increasing the concentration of pinacol. By doing so, the weak homo-chiral bands would become more visible. The spectrum in Fig. 4.10 was recorded at room temperature leaving a lot of head room to increase the vapour pressure. Additionally, recent instrumental improvements at the *curry*-jet have lowered the amounts of residual water significantly. Therefore, pinacol-water dimers can also be ruled out. Moreover, IR spectra would help to confirm or contradict an overlap of homo-dimer bands with band 4 of het4, since this band is not IR active. Hom4 is also IR active in that region and given its stability should be the most prominent of all homo-dimers. Additionally, band 1 of het4 could be detected in the IR spectrum so that the entirety of the B-E-A splitting can be investigated. If the B symmetric band is also overestimated by theory the assignment of the E band can be confirmed. The Raman and IR simulations are contrasted in Fig. C.13 (page 283). Moreover, a microwave spectrum has been recorded in the 2 GHz – 8 GHz region that could further clear up the homo-chiral assignments. The presence of eight methyl rotors may complicate the microwave spectra significantly since each of them can potentially lead to additional splittings. However, given the close proximity of the methyl groups, they may act as hindered rotors and no special treatment for the large amplitude motions is required. Should they behave as free rotors the spectra can likely not be assigned since no program can handle that many rotors as of yet.

4.1.4 Butane-2,3-diol

Butane-2,3-diol can be considered an open version of *trans*-cyclohexane-1,2-diol and Raman spectra of the racemic and the enantiopure compound have been recorded. The achiral *meso* version was not studied here, but would be the equivalent to *cis*-cyclohexane-1,2-diol. Moreover, when comparing the *meso* and chiral compounds, chirality recognition is already present in the monomer[230]. Additionally, the monomers with a *gauche* (rM-M and rM-M') and anti-periplanar (rM-Ma and rM-Ma') C-CC-C dihedral angle are populated in the jet (see Fig. 3.9 (page 46)), adding more flexibility to the dimers in comparison to t6-6. Due to the ring, t6-6 is forced into *gauche* angles. However, *gauche* arrangements are favoured by about 2.8 kJ mol^{-1}. Both (*R*,*R*) and (*S*,*S*)-butane-2,3-diol are readily commercially available, but the racemic mixture is not. Therefore, test and

enantiopure measurements have been conducted with the cheaper (*S*,*S*)-butane-2,3-diol. The racemate was created by thoroughly mixing equal amounts of both enantiomers, with the spectra being recorded under conditions optimised for the enantiopure compound.

Despite some commonalities with t6-6, the energetic landscape is vastly different for rM-M, as can be seen from Tab. 4.4. The structures are shown in Fig. 4.11. The previous strong preference for het4 is no longer present with both a homo-chiral (hom2") and hetero-chiral (het2") dimer being isoenergetic after zero point correction, within the accuracy of the method. It is also evident that hydrogen bond motifs with two or four intermolecular hydrogen bonds are favoured. In the t6-6 case, motifs with three hydrogen bonds were still among the most stable homo-chiral dimers (see 4.2). Judging from the relative energies het3/hom3 type structures are not expected to be detected in the expansion. Moreover, the energy differences of dimers with three intermolecular hydrogen bonds to het4 is comparable to those of t6-6. This suggests that het4 and hom3/het3 type dimers are either consistently destabilised or hom2/het2 structures are specifically stabilised. A mix of both effects is also possible. het4, hom2" and het2" are expected to be present in the expansion and given their energetic proximity equal populations can be assumed. hom4 may also be present but likely with smaller populations. For simplicity, equal populations will be assumed and deviations discussed.

The stabilisation of hom4 can be explained by the increased flexibility since a rM-Ma type monomer is present. For t6-6, hom4 is $9.7\,\mathrm{kJ\,mol^{-1}}$ higher in energy than het4, with two long (2.05 Å) and two short (1.85 Å) hydrogen bonds[101]. Such an all *gauche* arrangement is also possible for butane-2,3-diol at a very similar relative energy, with hydrogen bond lengths of 2×2.07 Å and 2×1.82 Å, illustrating their analogous behaviour. However, for the mixed *gauche* – anti-periplanar case, shorter hydrogen bonds are possible, *i.e.* 2×1.96 Å and 2×1.91 Å. Additionally, cooperative effects introduce further stabilisation. Moreover, the anti-periplanar arrangement in hom4 also allows for two CH$\cdots$O contacts, which may also contribute to the stabilisation. Curiously, the energetic separation between het4 and hom4 is about the energy difference of a *gauche* and anti-periplanar monomer.

Tab. 4.4: Overview of computational B3LYP/maTZ results for the relative energies of the dimers of butane-2,3-diol. Electronic (E_{el}) and zero point corrected (E_0) values are given in kJ mol^{-1}.

	het4	hom2"	het2"	het2a"	hom4	het4a	het2b"	het3'	hom3$_b$'	hom3'
E_{el}	0	2.28	3.17	4.17	2.71	5.21	9.17	9.84	11.20	10.45
E_0	0	0.11	0.19	2.45	3.03	5.67	6.37	6.52	6.65	7.30

Similarly, het4a with two anti-periplanar conformers is twice as high in energy. Here, four CH$\cdots$O contacts are possible. Hence, it could be argued that the binding energy of the hydrogen bond motif is about equal to that of het4 and the relative energies are instead determined by the less stable monomer subunits.

In the context of structures with four intermolecular hydrogen bonds it is also worth discussing their strained nature. het4 has four hydrogen bonds with lengths of 1.90 Å (t6-6: 1.93 Å) each. In comparison to the previously discussed structures, these bonds are

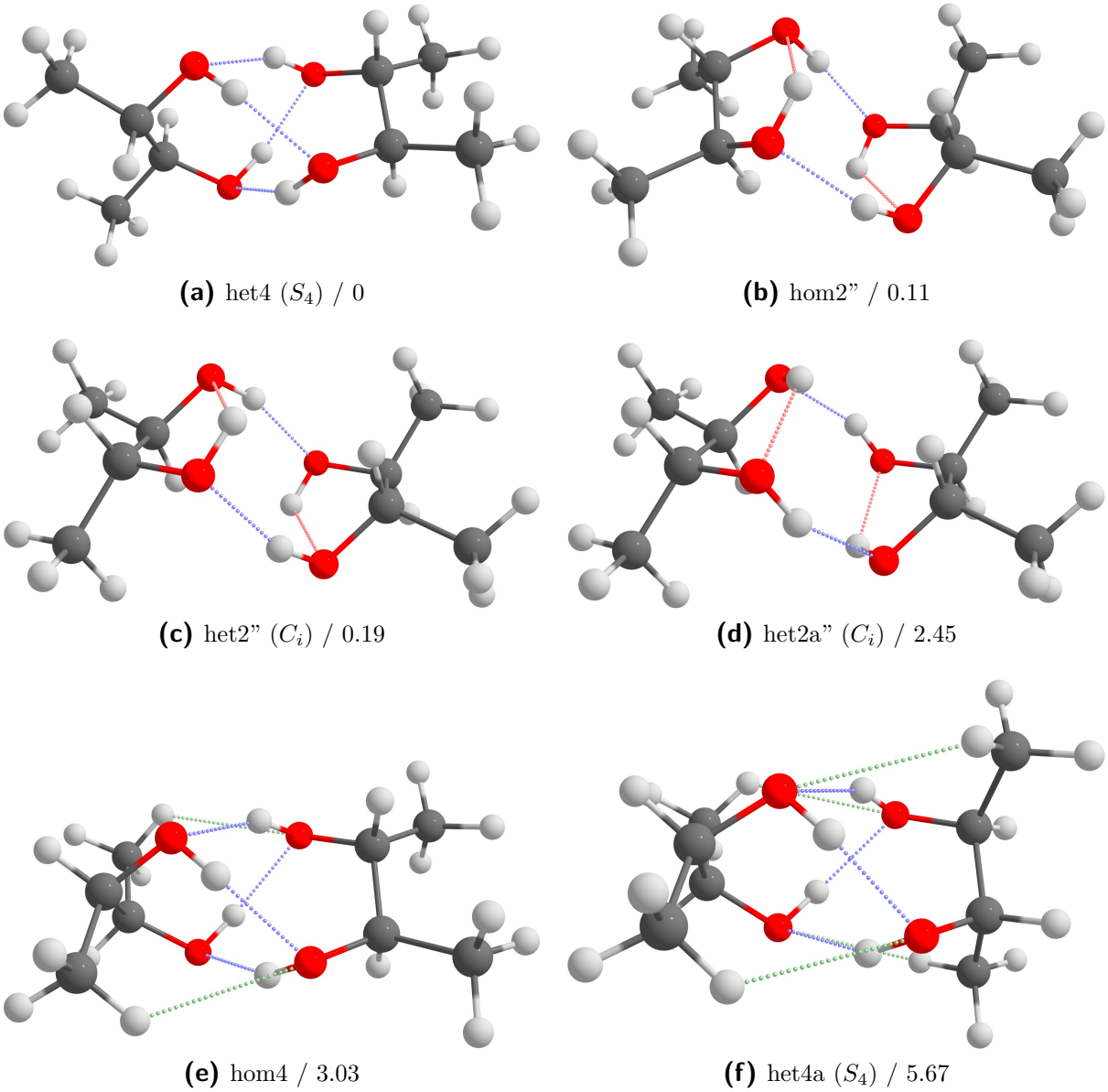

(a) het4 (S_4) / 0 **(b)** hom2" / 0.11

(c) het2" (C_i) / 0.19 **(d)** het2a" (C_i) / 2.45

(e) hom4 / 3.03 **(f)** het4a (S_4) / 5.67

Fig. 4.11: Dimers of butane-2,3-diol. Intermolecular hydrogen bonds are highlighted in blue and intramolecular ones in red. Proposed CH$\cdots$O contacts are highlighted in green. Relative zero-point corrected energies at the B3LYP/maTZ level are given in kJ mol^{-1}.

quite short on average. The strain, as indicated by the oxygen donor - hydrogen donor - oxygen acceptor angle ($\angle O_D H_D O_A$), is largest for het4. The water dimer binding situation can be taken as an unstrained reference point and exhibits an $\angle O_D H_D O_A$ of 173.5°. For het4, het4a and hom4 angles of 152.6° (t6-6: 151.5°), 152.7° and 149.6° were computed, respectively. Therefore, het4 and het4a should behave very similarly, which is reflected by the fact that their energetic separation almost exactly matches the doubled energy difference between a *gauche* and an anti-periplanar monomer. hom4 on the other hand is slightly more strained and shows a slightly larger energy difference than the monomer differentiation would suggest.

The stabilisation of hom2 and het2 type dimers appears to be largely influenced by a comparatively stronger shortening of the hydrogen bonds relative to t6-6. For hom2" of t6-6, hydrogen bond lengths of 1.92 Å, 1.97 Å, 2.21 Å and 2.35 Å have been computed, with the shorter two bonds being intermolecular and the longer ones intramolecular. For the rM-M counterpart 1.88 Å, 1.91 Å, 2.00 Å and 2.11 Å are found. This constitutes a

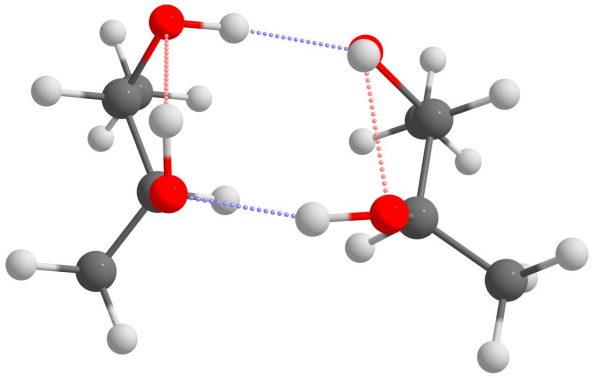

(g) het2b" / 6.37

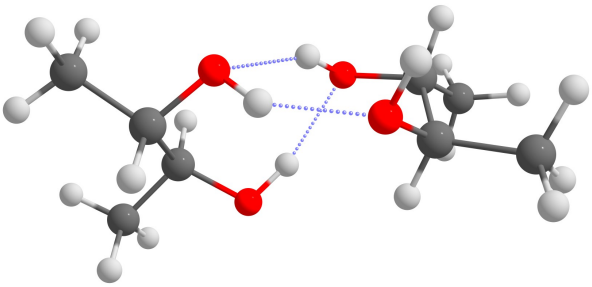

(h) het3' / 6.52

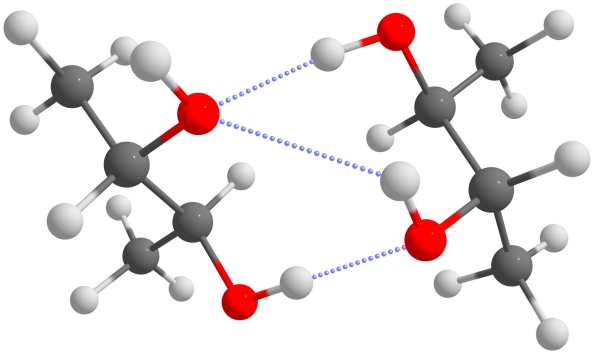

(i) hom3$_b$' / 6.65

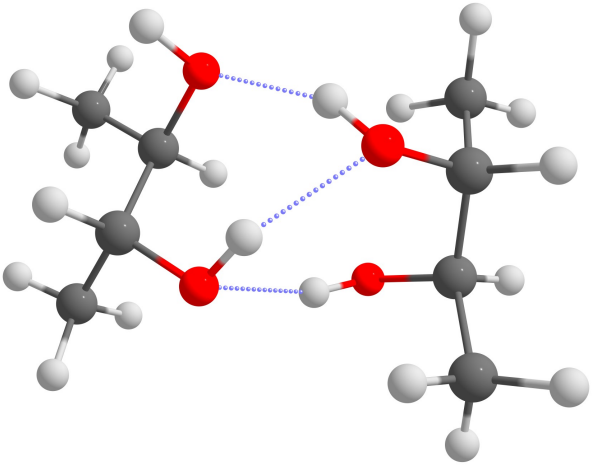

(j) hom3' / 7.30

Fig. 4.11: Continuation of Fig. 4.11.

significantly stronger shortening of the intermolecular hydrogen bonds than for het4 and hom3/het3 type dimers. The shorter intramolecular hydrogen bonds likely also allow for stronger cooperativity given the cyclic hydrogen bond network. Moreover, the hydrogen bonds are significantly less strained, so that shorter hydrogen bonds are expected to have a stronger impact. For the intermolecular ones an $\angle O_D H_D O_A$ of 164.8° and 158.1° have been computed for the shorter and longer one, respectively. Similar observations can be made for het2", with the intermolecular and intramolecular hydrogen bonds having the same lengths allowing for C_i symmetry. Moreover, the deformation energy of the monomers within het4 is significantly higher than in hom2", as was the case for t6-6 which has been discussed in detail in Ref. [166]. Furthermore, CH$\cdots$O contacts are also possible for the hom2"/het2" structures. These were already present for t6-6 but shorten in case of rM-M. het3', as the most stable dimer with three intermolecular hydrogen bonds shows much smaller changes when moving from t6-6 to rM-M. Here, one hydrogen bond does not change significantly in length, while the other two shorten by 0.01 Å and 0.03 Å. These small changes could explain the fact that het3' is slightly higher in energy for rM-M in comparison to t6-6 (see 4.2 (page 135)). Further insights into the stabilisation could be gained by employing energy decomposition schemes such as the one applied in section 4.3 (page 180).

The experimental spectrum is shown in Fig. 4.12. Comparing the racemic and enantiopure spectra some bands display an approximate doubling. These can be identified as of pure homo-chiral origin. However, all hetero-chiral signals appear to overlap to some degree with homo-chiral ones, as no signal vanishes in the enantiopure spectrum. The two bands at 3573 cm^{-1} and 3393 cm^{-1}, which are roughly doubling in intensity, can be attributed to the most stable homo-dimer. The signal at 3550 cm^{-1} decreases slightly when moving to the enantiopure case indicating that overlap with a hetero-chiral dimer is present. Given the simulations, an overlap of het2" and hom2" is the most plausible. However, the predictions for het2" are significantly separated from the matching hom2" ones. It may be the case that the energetic order of het2" and het2a" should be switched, since for the latter one band coincides with band 2 of hom2". Simulations using het2a" instead of het2" are shown in Fig. C.14 (page 284). The remaining band of hom2" likely belongs to the signal at 3466 cm^{-1}. In the enantiopure spectrum, some increase can be observed but not as strongly as for band 1 and 4. This could be due to an overlap with het2", however, based on the simulated intensities, a decrease would be expected in the enantiopure case. Here het2a" might again be a better match, since an overlap with band 4 of het4 would be expected. The slight increase could instead be attributed to an overlap with the degenerate E band of het4, which is much weaker in intensity. An overestimation of the A-E splitting would be in line with the previous results for pinacol (see Fig. 4.10 (page

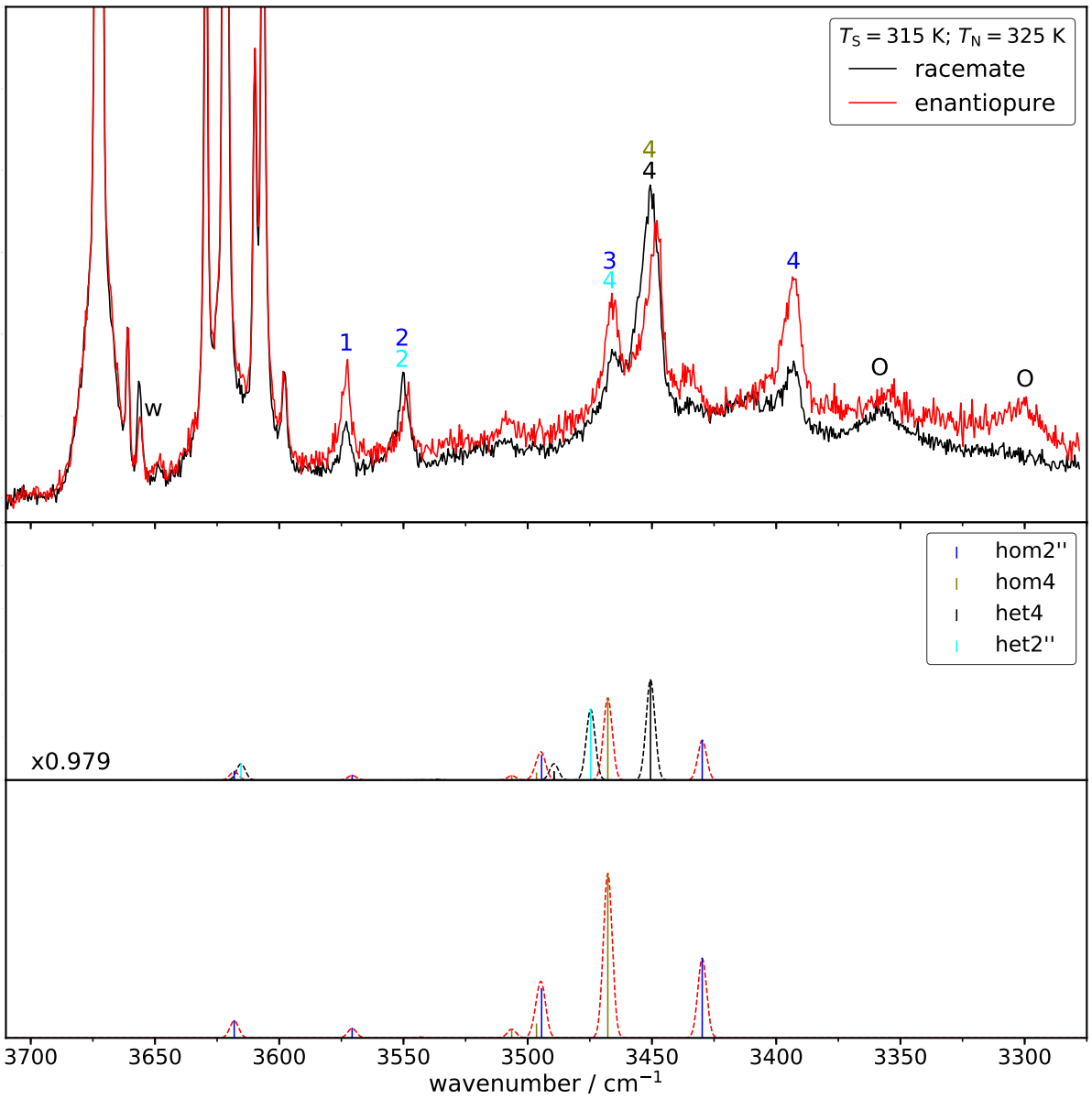

Fig. 4.12: Experimental Raman (top), simulated racemic Raman (middle) and simulated enantiopure Raman data (bottom) of butane-2,3-diol. The saturator temperature (T_S) as well as the nozzle temperature (T_N) are given. The simulated spectra are based on B3LYP/maTZ and are scaled by 0.979 to match band 4 of het4. w indicates a water band and O oligomer bands.

143)). Additionally, the scaling factor for band 4 of het4 is unusually high in comparison to the other diols that have been studied so far (0-0: 0.969, t6-6: 0.966, MM-MM: 0.964). Scaling to hom2" is more in line with the other factors, for instance one obtains 0.968 for band 4. There is also no trend evident. It remains to be seen if the dimers of propane-1,2-diol show somewhat similar behaviour.

The most prominent band in the spectrum is likely due to an overlap of band 4 of het4 and

hom4. hom4 is predicted to be about $3\,\mathrm{kJ\,mol^{-1}}$ higher in energy but, as the enantiopure spectrum shows, is still significantly populated, although the simulated intensities suggest that hom4 is less abundant than hom2". Two bands at $3508\,\mathrm{cm^{-1}}$ and $3436\,\mathrm{cm^{-1}}$ remain unassigned but should be of dimer origin. The former could be caused by hom4, while for the latter no good candidate explanation exists. It is also evident that a substantial background is present in the area of the latter. Less concentrated spectra could help to rule out the possibility of a trimer. Moreover, the relative experimental intensities could be compared more accurately with regards to the homo-chiral doubling. For the enantiopure spectrum, the baseline is considerably higher as soon as the dimer region is reached. Additionally, two distinct bands around $3354\,\mathrm{cm^{-1}}$ and $3300\,\mathrm{cm^{-1}}$, likely caused by trimers, can be observed in the enantiopure spectrum. The former is shifted slightly higher in the racemic case, while the latter disappears. This can be explained by overlapping hetero and homo-chiral trimers for the band at $3354\,\mathrm{cm^{-1}}$ and the statistical advantage of hetero-chiral trimers (see Fig. 2.7 (page 26)) for the band at $3300\,\mathrm{cm^{-1}}$.

Besides the assignment of hom2", the other assignments are somewhat ambiguous and leave room for speculation. To combat the rather high baseline, more dilute Raman spectra can be recorded. However, the most information can be gained from recording IR spectra. As was the case before, het4 is S_4 symmetric and is expected to show its typical band pattern. Band 1 can be observed in that manner which provides a general idea of where band 2/3 is located. Moreover, het2" and het2a" are both C_i symmetric so that the principle of mutual exclusion applies. Hence, the IR active modes can help to distinguish between the two. In this way, not only the assignment but also the energetic order can be further elucidated. Furthermore, hom4 in terms of its spectral pattern behaves very similarly to het4, with the degeneracy being lifted. It may also be the case that the splitting of the bands of hom4 is overestimated by B3LYP/maTZ. A comparison of Raman and IR simulations is shown in Fig. C.15 (page 285) including het2a". Additionally, higher level computational methods can be used to get a better understanding of the conformational landscape. To rule out the possibility of missing relevant conformers, the structure search can be extended. Lastly, microwave spectroscopy could be employed. However, the most stable conformers either have no permanent dipole moment due to symmetry (het4 and het2"/het2a") or very weak ones (hom2" and hom4).

4.1.5 *trans*-Cyclopentane-1,2-diol

trans-Cyclopentane-1,2-diol (t5-5) constitutes a more ring-strained version of *trans*-cyclohexane-1,2-diol. One consequence of the decreased ring size is the fact that the oxygen

atoms are dragged apart, which influences the hydrogen bond arrangements of the dimers. However, the same structural motifs are still possible as were for t6-6. Moreover, di-axial arrangements (designated with a t) are energetically feasible for the monomers and may play a role in the dimer formation, unlike in t6-6. As can be seen from Fig. 3.18b (page 60), the barriers for relaxation to the more stable di-equatorial conformations are quite low. Hence, upon formation of a dimer, di-axial conformers can convert to di-equatorial ones in the expansion.

As Tab. 4.5 shows, the energetic landscape of t5-5 is vastly different from that of t6-6 (see Tab. 4.2 (page 135)). Most prominently, the het-hom gap shrinks from $6.58\,\mathrm{kJ\,mol^{-1}}$ in case of t6-6 to an isoenergetic case within the uncertainty of the B3LYP/maTZ. However, formally het4 still constitutes the global minimum. The next most stable hetero dimer het3', closely follows at $0.61\,\mathrm{kJ\,mol^{-1}}$. Additionally, hom2" and het2" type structures are significantly higher in energy ($> 10\,\mathrm{kJ\,mol^{-1}}$), in stark contrast to t6-6. The corresponding structures are shown in Fig. 4.13. As can been seen, di-axial conformations are not relevant for the dimers. het4, het3', het4, hom3', hom3 and hom3a are expected to be present in the expansion based on the relative energies. het3 and het3' can in principle convert to het4 under jet conditions, however, they are very close in energy so that the conversion is lacking a strong thermodynamic driving force. Hence, they may still be present in the expansion contrary to the case of t6-6. het3' would convert to het4 *via* het3. Moreover, het3 can also convert to het3'. In a similar fashion, hom3 can relax to hom3' but the thermodynamic driving force is again limited. Due to very similar spectral patterns between het3/het3' and hom3/hom3' only the more stable species is assumed to be present to simplify the simulation. With regards to the latter this assumption was already made for t6-6 with no loss of explanatory power. It should be kept in mind that these conformers could very well still be present and are not categorically ruled out. Furthermore, equal populations will be assumed and possible deviations discussed.

The energetic differences between t6-6 and t5-5 can be explained by the increased distance of the oxygen atoms in each monomer subunit. This is due to the fact that the smaller

Tab. 4.5: Overview of computational B3LYP/maTZ results for the relative energies of the dimers of *trans*-cyclopentane-1,2-diol. Electronic (E_{el}) and zero point corrected (E_0) values are given in kJ mol^{-1}.

	het4	hom3'	het3'	het3	hom3	hom3a	het3a	het3b'	hom3a'	het3a'
E_{el}	0	2.83	3.26	3.16	3.67	5.43	6.56	9.19	8.55	9.30
E_0	0	0.33	0.61	0.71	1.03	2.26	3.64	5.09	5.09	6.12

ring drags the O atoms apart. To illustrate this point het4, hom3', het3' and hom2" will be compared with regards to their average O–O d(O–O) and hydrogen bond d(HB) distance. The distances are summarised in Tab. B.21 (page 258). For t5-5, d(O–O) ranges from 3.02 Å – 3.10 Å at the B3LYP/maTZ level of theory, while for t6-6 distances around 2.92 Å – 2.95 Å, with the exception of hom2" where 2.78 Å is computed, are found. For het4, this increase necessarily leads to an elongation of the hydrogen bonds, since the two monomers behave akin to a key and lock. Effectively, het4 only has the monomer–monomer distance as a degree of freedom. This is due to the fact that all four hydrogen bonds must remain equal in length as is required by its symmetry. hom3' and het3' are

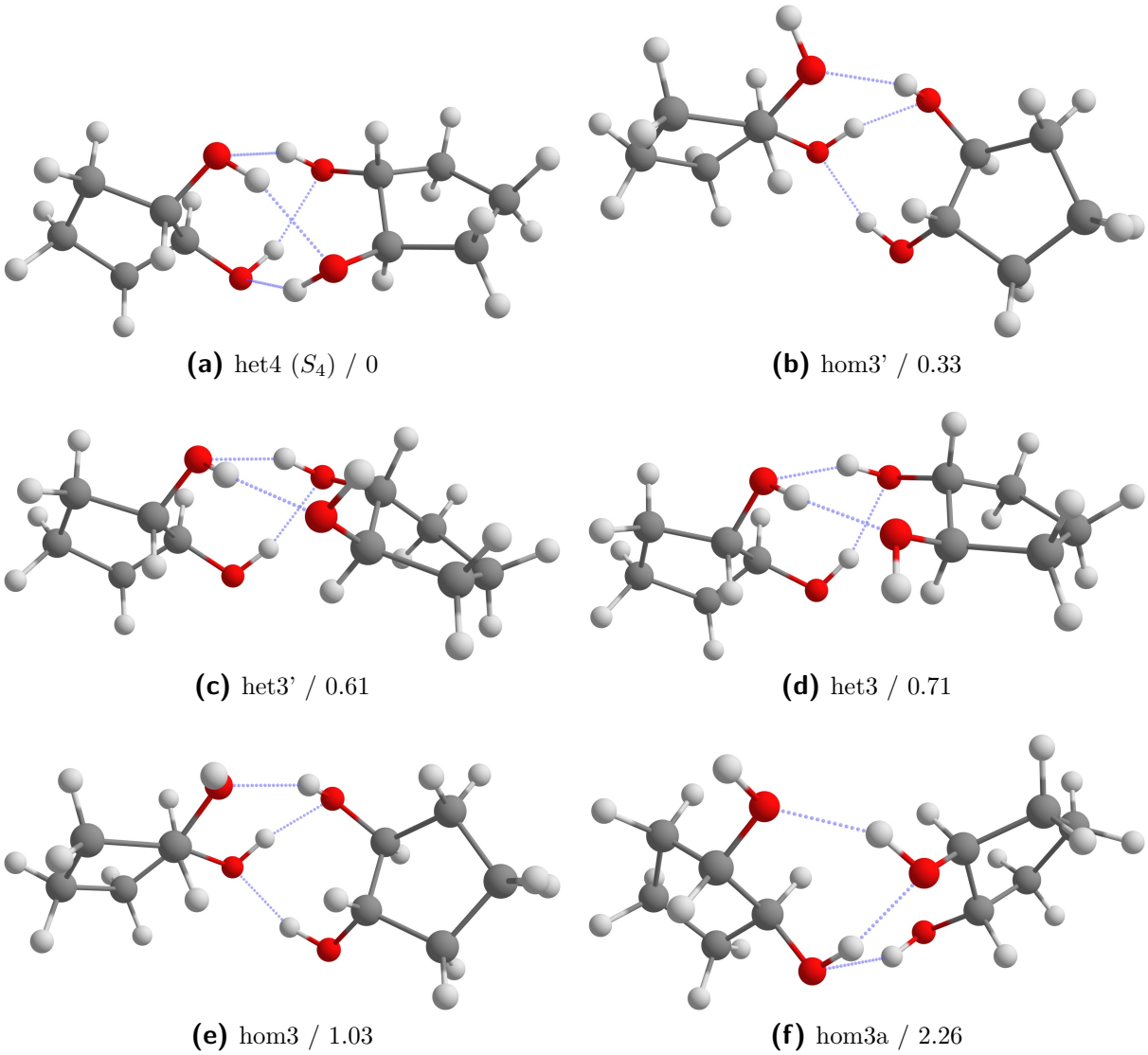

(a) het4 (S_4) / 0 **(b)** hom3' / 0.33

(c) het3' / 0.61 **(d)** het3 / 0.71

(e) hom3 / 1.03 **(f)** hom3a / 2.26

Fig. 4.13: Dimers of *trans*-cyclopentane-1,2-diol. Intermolecular hydrogen bonds are highlighted in blue and intramolecular ones in red. Relative zero-point corrected energies at the B3LYP/maTZ level are given in kJ mol^{-1}.

not limited in such a way, *i.e.* the monomers can rotate relative to each other to allow for more stable arrangements. Moreover, the rings can independently adjust themselves while this is not possible for het4 due to symmetry. The binding motif of hom2", on the other hand, has an analogous flexibility to the structures with 3 hydrogen bonds, but an increase of d(O–O) necessarily leads to significantly longer intramolecular hydrogen bonds.

As Tab. B.21 (page 258) shows, d(O–O) of hom3' and het3' hardly differs at all between t5-5 and t6-6. Similarly, the intermolecular hydrogen bond distances for hom2" do not change significantly but the intramolecular ones increase in case of t5-5. For het4 an overall increase of 0.4 Å can be found. Hence, het4 gets specifically destabilised while hom3' and het3' remain close in energy, as was the case for t6-6 (see Tab. 4.2 (page 135)). Since the intramolecular hydrogen bonds of hom2" also increase considerably (about 0.8 Å in total), it is also destabilised. Due to hom2" being higher in energy for t5-5 (14.10 kJ mol^{-1}) than t6-6 (7.47 kJ mol^{-1}), hom2" is destabilised to a larger extent than het4.

Fig. 4.14 shows the experimental as well as the simulated Raman spectrum of t5-5. The most prominent band can immediately be assigned to band 4 of het. The remaining

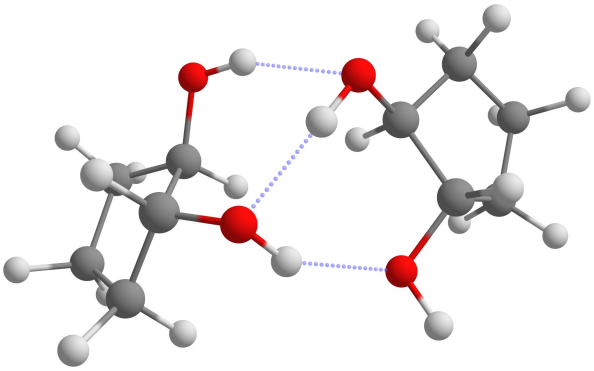

(g) het3a / 3.64

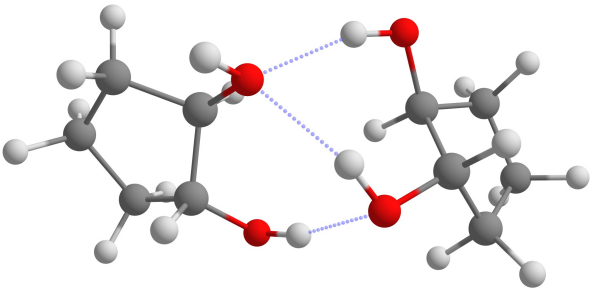

(h) het3$_b$' / 5.09

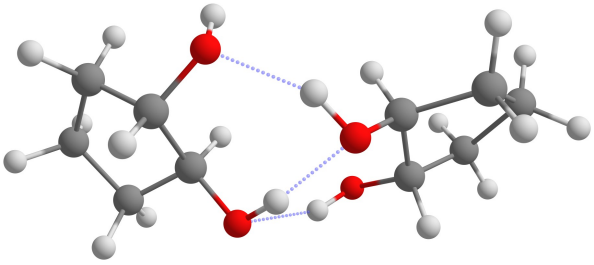

(i) hom3a' / 5.09

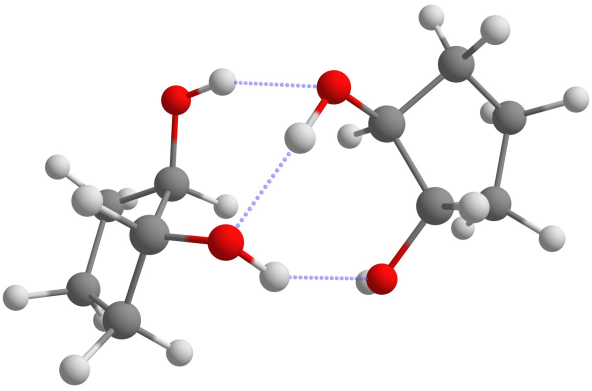

(j) het3a' / 6.12

Fig. 4.13: Continuation of Fig. 4.13.

Raman active band of het4 on the other hand cannot be definitively assigned, but may contribute to some of the broadening found around 3485 cm^{-1}. Moreover, with 3466 cm^{-1}, the position of band 4 is the highest in wavenumber of het4 for all systems studied so far, highlighting the increased hydrogen bond lengths. Additionally, the scaling factor (0.962) is the smallest of all systems. The three band pattern found at higher wavenumbers than het4 can be attributed to hom3a, het3' and hom3' in descending order. Band 3 of hom3' likely contributes to the broadening between band 2 of hom3' and band 4 of het4. It is evident that the applied scaling factor based on het4 is not applicable to the other dimers. Moreover, the splitting between het3' and hom3a relative to hom3' is underestimated by theory. Using the scaling factor of t6-6 (0.966) leads to very good agreement for band 2 of hom3' and to a lesser extent also for het3' and hom3a. However, the description of band 4 of these dimers suffers in that case. This indicates that the anharmonicity between the dimers but also the modes is quite different, hampering the error compensation. It might also be the case that this is an artefact of the method itself and not caused by differences in the anharmonicity of the OH modes. A comparison of the simulated and experimental intensities of band 2 of het3' suggests that equal populations cannot be assumed. As previously discussed, this is either caused by the energy difference itself, relaxation to het4 or a mix of both. The broad band around 3362 cm^{-1} can be assigned

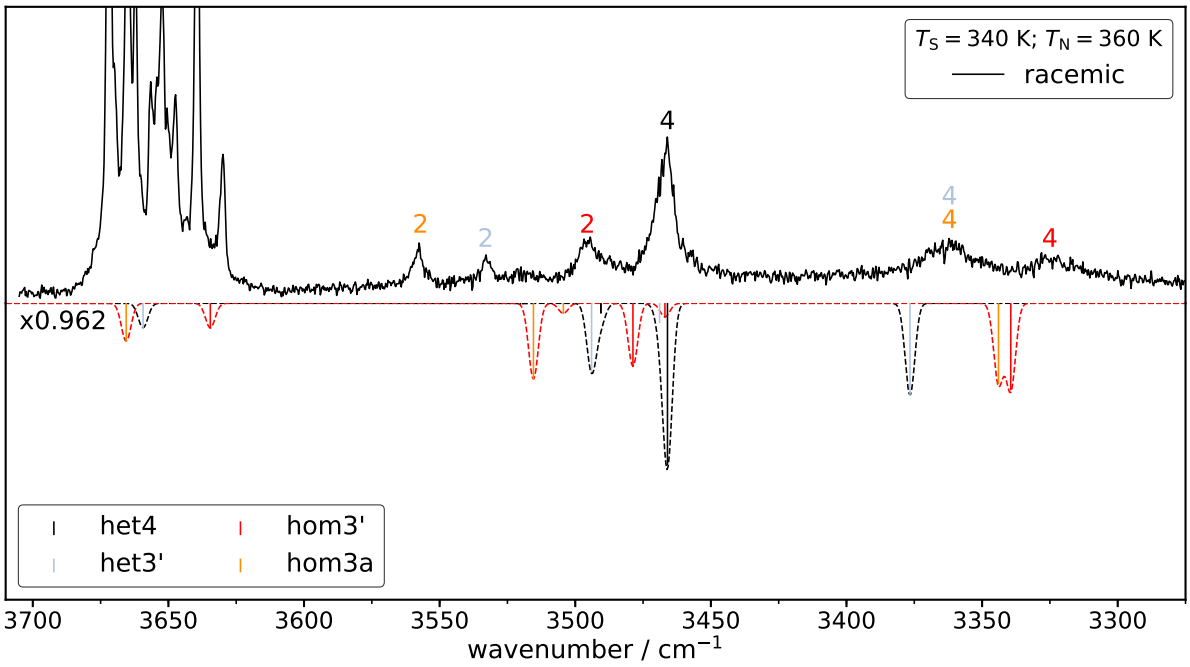

Fig. 4.14: Experimental (plotted upwards) and simulated Raman data (plotted downwards) of *trans*-cyclopentane-1,2-diol. The saturator temperature (T_S) as well as the nozzle temperature (T_N) are given. The simulated spectra are based on B3LYP/maTZ and are scaled by 0.962 to match band 4 of het4.

to an overlap of het3' and hom3a, while the band at 3325 cm^{-1} is assigned to hom3'. Given the comparatively high intensity of the band at 3362 cm^{-1}, an overlap of het3' and hom3a is assumed. Considering the limited accuracy of the method, it may also be an overlap of het3' and hom3'. The choice of hom3a is made due to the close spectral proximity. Purely based on the band positions, an overlap of hom3' and hom3a is suggested as being responsible for the signal at 3325 cm^{-1}. Such an overlap was found previously for ethane-1,2-diol as can be seen from Fig. 4.4 (page 133). Lastly, the free OH modes cannot be assigned due to the very complex monomer region, as was discussed in section 3.1.7 (page 59).

Of great help to confirm these assignments would be the measurement of the enantiopure compound, which might also allow for the assignment of band 2 of hom3'. The enantiopure compound was bought, however, the spectra showed no changes relative to the racemate. Hence, measurements with the enantiopure compound from a different vendor should be conducted. Moreover, IR spectra would also provide additional information. An IR simulation contrasted with the experimental Raman spectrum is shown in C.16 (page 286). The only IR active mode of het4 could be measured but also the position of the E can be narrowed down. Curiously, the simulated most intense band of het4 is only slightly larger than that of the other dimers. This indicates that the transition dipole moment is more sensitive to the increased hydrogen bond length than the change in polarisability. Furthermore, band 3 of het3' can be detected as it no longer overlaps with het4. Lastly, microwave spectra of t5-5 have been recorded in the 2 GHz – 8 GHz range, which could also be used to confirm the presence of the assigned conformers in the future.

4.1.6 *trans*-Cycloheptane-1,2-diol

An extension of the ring size of t6-6 leads to *trans*-cycloheptane-1,2-diol (t7-7). As was the case for t6-6, di-axial arrangements are significantly higher in energy than di-equatorial ones. Therefore, they are not expected to play a role in the formation of dimers. However, t7-7 is significantly more floppy, which is reflected in the more complicated energetic landscape of the monomers (*cf.* 3.20b (page 64) *vs.* 3.1 (page 31)). Hence, dimers with the same binding motif and slight modifications to the ring arrangement may be found to be very close in energy. Moreover, given the small barriers between different ring orientations found in the monomer, it is also expected that such relaxation should be present in the dimers.

From the previous section and the behaviour with regards to the ring size some predictions can be made for the energetic dimer landscape. As opposed to t5-5, the oxygen-oxygen

distance is expected to decrease, as the larger ring size pushes the oxygen atom/OH-groups together. These shorter distances would favour the formation of intramolecular hydrogen bonds. Therefore, a stabilisation of hom2"/het2" structural motifs is expected. For conformers with three or four hydrogen bonds, the shorter d(O–O) is expected to hamper the flexibility of the hydrogen arrangement, as there is less space to insert into the intramolecular hydrogen bond. Based on these assumptions, energetic behaviour more similar to butane-2,3-diol (see Tab. 4.4 (page 145)) is expected.

Due to the added flexibility, the energetic landscape is vastly more complicated with similar structural motifs occurring multiple times within a small energy window, as Fig. 4.6 shows. Within $2\,\mathrm{kJ\,mol^{-1}}$ above the global minimum, eight different hom2" variants can be found. As was previously suggested hom2"/het2" type structures dominate the conformational space. Curiously, it is also the first system showing a preference for homo-chiral dimers. A comparison of d(O–O) and d(HB) can again be made for the most stable representative of the het4, het3', hom3' and hom2" families. This is shown in Tab. B.21 (page 258). The intramolecular hydrogen bonds of hom2" shorten very significantly in comparison to t6-6 and to a lesser extent the intermolecular ones do as well. Thus the cyclic nature of hom2" is increased and stronger cooperative effects are expected. For het4, d(HB) also decreases but to a lesser extent. Furthermore, this is at the cost of a much higher deformation energy of almost $8\,\mathrm{kJ\,mol^{-1}}$ relative to hom2". Curiously, het3' and hom3' show fairly similar d(O–O) distances as was the case for t6-6. Moreover, in case of hom3', d(O–O) even increases relative to t6-6. Additionally, d(HB) also slightly decreases. In case of het3' only marginal changes occur. Furthermore, the linearity,*i.e.* $\angle \mathrm{O_D H_D O_A}$, of the hydrogen bond between t6-6 and t7-7 are comparable. Overall, the unique stability of the hom2"/het2" binding motif can be explained by these observations. However, it remains unclear why the homo-chiral preference occurs. This might be answered in the future by employing energy decomposition schemes, such as the one used in section 4.3. It should be kept in mind, that given the flexibility of the system, the structural search might not have been exhaustive. Because of the complex conformational space it is assumed for simplicity that only het2" and hom2" are present. Higher level electronic structure methods are necessary to explore the spectrum in more detail. In the future this can be done by performing coupled cluster single point calculations on the B3LYP structures.

To further illustrate the dependence on ring size of d(HB) and d(O–O), these quantities are plotted in Fig. 4.15 for het4, hom3' and hom2". Ring sizes of 4 up to 7 carbon atoms are compared. It can be seen immediately that d(HB) increases for het4 as the oxygen atoms are dragged apart. For the intermolecular OH bonds of hom2" and hom3' only minor changes can be observed as they can better accommodate longer d(O–O). Hence, it becomes clear that het4 is specifically destabilised as the ring size decreases. However,

Tab. 4.6: Overview of computational B3LYP/maTZ results for the relative energies of the dimers of *trans*-cycloheptane-1,2-diol. Electronic (E_{el}) and zero point corrected (E_0) values are given in kJ mol^{-1}.

	hom2"	hom2a"	hom2b"	hom2c"	hom2d"	hom2e"	hom2f"	het2"
E_{el}	0.90	0	0.92	1.69	2.19	1.71	2.87	3.22
E_0	0	0.06	0.24	1.10	1.20	1.23	1.47	1.83
	hom2g"	hom2h"	hom2i"	het2a"	het2b"	het2c"	het2d"	het2e"
E_{el}	3.04	3.03	3.07	2.48	2.08	2.08	1.71	3.09
E_0	1.83	1.85	2.09	2.08	2.10	2.10	2.13	3.02
	hom3'	hom3a'	hom2j"	het2f"	het2g"	het4	het2h"	het3
E_{el}	5.30	5.38	3.06	4.15	4.41	2.84	4.57	6.74
E_0	3.09	3.36	3.50	3.69	3.76	3.85	3.90	3.95
	het2i"	het3a	hom3b'	hom2k"	hom3c'	het4a	hom3d'	hom3e'
E_{el}	3.85	6.75	6.70	4.17	7.23	4.07	7.43	7.43
E_0	4.03	4.09	4.11	4.16	4.30	4.45	4.61	4.66
	het4b	het2l"	het3'	het3a'	hom3f'			
E_{el}	4.06	5.38	8.38	8.38	8.88			
E_0	4.70	4.98	5.78	5.96	6.07			

in case of hom2" the intramolecular hydrogen bonds also significantly increase in length as d(O–O) elongates. The hydrogen bond length nicely correlates with hom2" being the most stable species for t7-7, being on par with other motifs in case of t6-6 and not being energetically relevant at all in case of t5-5. No hom2" type minimum is found for t4-4. The data for het3' is also provided in Tab. B.21 (page 258) but not shown in Fig. 4.15 since it closely resembles hom3'.

Given the flexibility of the system only the most stable representative of each motif is shown in Fig. 4.16, with exception of hom2j" and het2h". The similarities between hom2" and het2" can be seen with the conformation of the same enantiomer being identical. hom2j" and het2h" suggest strong dispersion interactions between the rings. This type of structures also exist for t6-6 but previously where above 9 kmol^{-1}. However, relative to the most stable hom2" type dimer very similar energy differences can be found between t6-6 and t7-7. Moving to even larger ring sizes this dimer could be stabilised even further and may constitute the global minimum at some point. Moreover, despite the fact that het4 is no longer S_4 symmetric, it still resembles the point-group enough so that an approximate B-E-A splitting is expected, as well as a negligible permanent

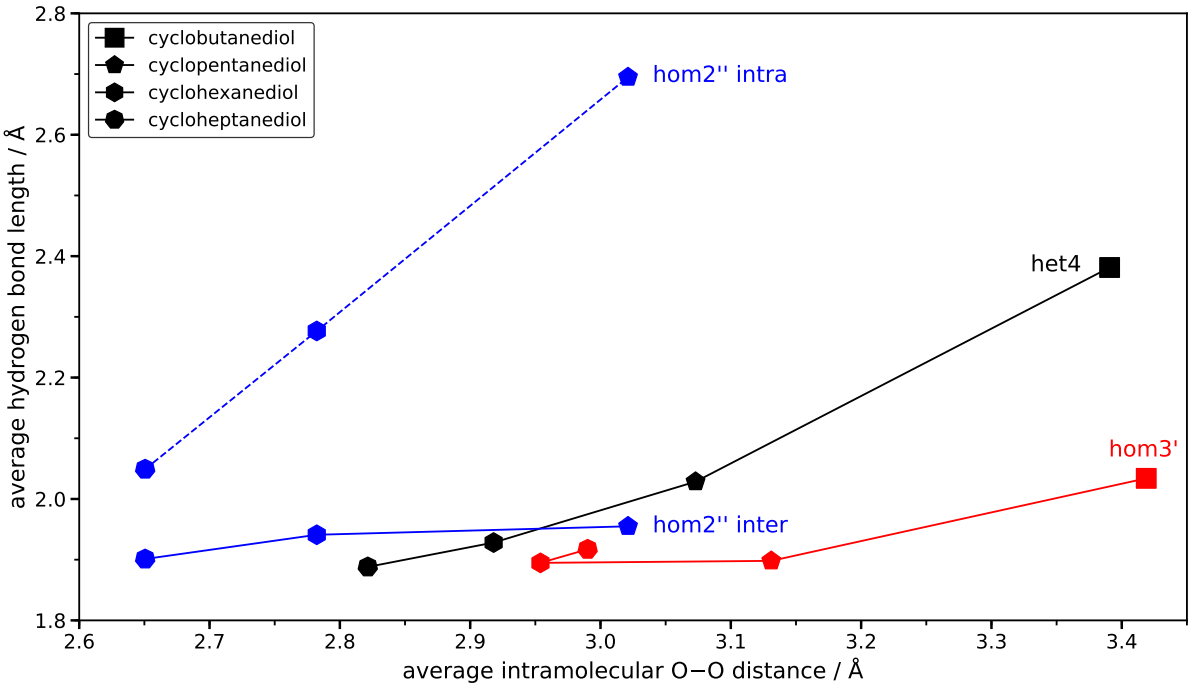

Fig. 4.15: Graphic illustration of the correlation of the average hydrogen bond length and the average intramolecular O–O distance in cyclic diols. Ring-sizes from 4 up to 7 carbon atoms are considered. The behaviour of het4, hom3' and hom2'' is shown. The latter is divided between intramolecular and intermolecular hydrogen bonds. All data points are shown in Tab. B.21 (page 258).

dipole moment. Similarly, most hom2"/het2" structures have very small dipole moments, so that this systems does not lend itself to a microwave investigation. hom2"/het2" structures where the rings overlap have a large dipole moment but are not expected to be strongly populated. Structures with three intermolecular hydrogen bonds behave analogously. Moreover, hom2b" and hom2j" show C_2 symmetry while het2a", het2d" and het2g" show C_i symmetry. In the C_i case, the permanent dipole moment is 0 debye due to symmetry.

The experimental spectrum is shown in Fig. 4.17. Some distinct but mostly broad bands can be observed with the spectrum being somewhat noisy. To aid in the assignment a scaling factor is derived based on butane-2,3-diol where hom2"/het2" type structures have previously been relevant (see Fig. 4.12 (page 149)). Here, band 4 of hom2" has been used as a reference. This approach yields a good match in the 3375 cm^{-1} – 3450 cm^{-1} region. The bands at 3396 cm^{-1} and 3448 cm^{-1} can be assigned to hom2", while the very prominent band in the middle between the two can be assigned to het2". The intensity pattern also matches fairly well. It should be kept in mind that given the complexity of the conformational landscape these assignments are tentative. Furthermore, some additional

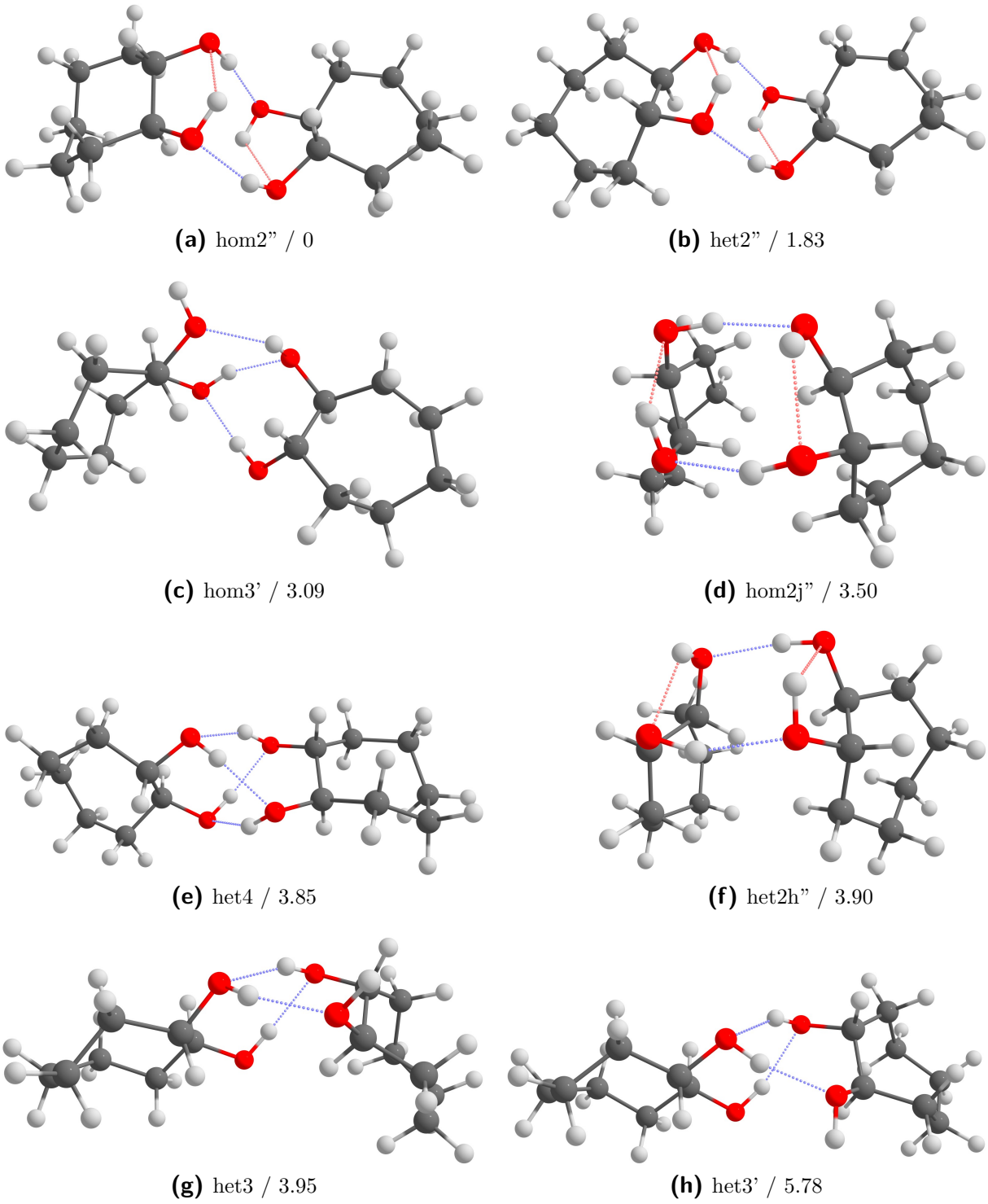

(a) hom2” / 0 **(b)** het2” / 1.83

(c) hom3’ / 3.09 **(d)** hom2j” / 3.50

(e) het4 / 3.85 **(f)** het2h” / 3.90

(g) het3 / 3.95 **(h)** het3’ / 5.78

Fig. 4.16: Dimers of *trans*-cycloheptane-1,2-diol. Intermolecular hydrogen bonds are highlighted in blue and intramolecular ones in red. Relative zero-point corrected energies at the B3LYP/maTZ level are given in kJ mol^{-1}.

features can be made out at 3405 cm^{-1}, 3439 cm^{-1} and 3462 cm^{-1} in that region. These features clearly indicate that more conformers are necessary to explain the spectrum.

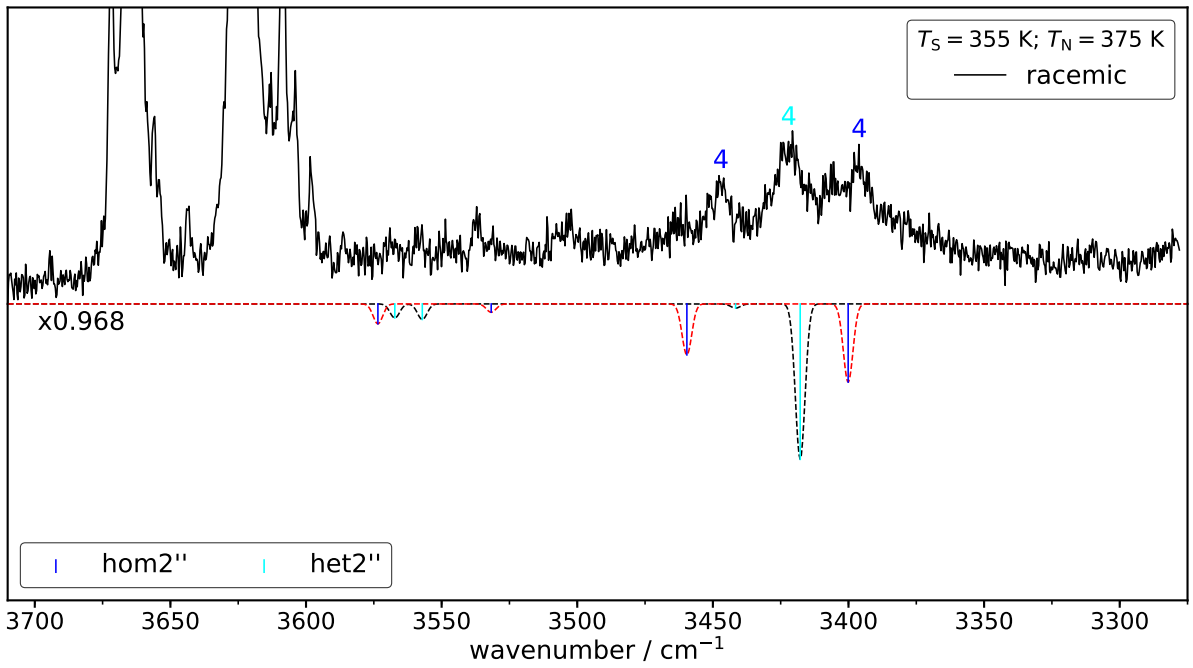

Fig. 4.17: Experimental (plotted upwards) and simulated Raman data (plotted downwards) of *trans*-cycloheptane-1,2-diol. The saturator temperature (T_S) as well as the nozzle temperature (T_N) are given. The simulated spectra are based on B3LYP/maTZ and are scaled by 0.968. The scaling factor is derived from band 4 of hom2'' of rM-M (see Fig. 4.12 (page 149)).

Moreover, the bands around 3405 cm^{-1} and 3462 cm^{-1} may in fact belong to hom2''. For the intramolecular OH modes towards the monomer region, small matching bands can be found. However, the noise is fairly significant so that no assignment is made. Moreover, slightly larger signals at 3537 cm^{-1} and 3503 cm^{-1} also remain unaccounted for. These two bands would generally match what would be expected for hom3'/hom3 or het3'/het3 type structures. hom3' is a fairly decent match although it is predicted to be 3.09 kJ mol^{-1} higher in energy than hom2''.

It is clear that for a more reliable analysis of the spectrum more accurate relative energies are necessary. An interesting method to apply might be CAM-B3LYP, which yielded energies that were remarkably close to CCSD(T) in case of the monomers of 3-chloro-propane-1,2-diol and 3-bromo-propane-1,2-diol. These two systems have been discussed in detail in sections 3.1.10 (page 96) and 3.1.10 (page 103). Single point coupled cluster calculations may also help to resolve the energetic ambiguities. Moreover, the conformational space should also be explored further. Besides that, enantiopure spectra can be recorded. Such an attempt was made, but the compound likely polymerised leading to a very small vapour pressure and different signals. The polymerisation likely has occurred while the saturator was filled. The compound was shipped in a small vial and could only

be removed by heating the vial with a heat gun, melting it in the process. Otherwise, the vial would have had to be broken. Unfortunately, this may have been an excessive amount of heat. The racemic mixture arrived as a fine powder so that this issue did not occur. Furthermore, IR spectra could help the assignments since the intermolecular OH modes of the hom2"/het2" binding motifs behave exclusionary to some extent. Hence, the band that appears smaller in the Raman spectrum should appear larger in the IR spectrum and *vice versa*. A very drastic example of this is het2", as can be seen from the simulations in Fig. C.17 (page 287). Additionally, as was previously alluded to, microwave spectroscopy is likely not of great help due to the fact that dipole moments are quite small for hom2"/het2" type structures. However, if the predicted energies are off and hom3' in fact plays a role in the spectrum it could be detected *via* rotational spectroscopy.

4.2 Non-symmetric diols

4.2.1 Propane-1,2-diol

Propane-1,2-diol (0-M) can be considered the simplest extension of ethane-1,2-diol (0-0), but as was already seen for the monomers, the conformational landscape proved to be vastly more complicated (*cf.* Figs. 3.1 (page 31) and 3.6 (page 39)). Therefore, the added flexibility may also lead to more relevant dimer structures than was the case for 0-0. Moreover, 0-M is permanently chiral and might share more similarities with butane-2,3-diol (rM-M) than with 0-0. Analogously to rM-M, the O-CC-O *gauche* + and − conformers are no longer enantiomers, as was the case for 0-0. The different orientations may also be involved in the dimers and in principle the monomer populations could limit the formation of some dimers. For (*S*)-propane-1,2-diol, the + conformers are more populated (0-M, 0-M', 0-Ma and 0-Ma') than the − ones (0-Mb, 0-Mb', 0-Mc and 0-Mc'), as can be seen from Fig. 3.7 (page 41). In case of (*R*)-propane-1,2-diol, the signs are reversed. Both the racemic and the enantiopure compounds are readily commercially available. For the enantiopure spectra, (*S*)-propane-1,2-diol has been used.

The energetic dimer landscape of 0-M is shown in Tab. 4.7. With a het-hom gap of $3.44\,\mathrm{kJ\,mol^{-1}}$, 0-M fits nicely in between 0-0 and rM-M with a gap of $6.73\,\mathrm{kJ\,mol^{-1}}$ and $0.11\,\mathrm{kJ\,mol^{-1}}$, respectively. Moreover, relative to 0-0, het2"/hom2" type dimers gain more relevance (*cf.* Tab. 4.1 (page 130)), albeit not as much as for rM-M (*cf.* Tab. 4.4 (page 145)). Curiously, in comparison to rM-M, hom4 and hom2" dimers switch their energetic order. As was the case for all systems, with the exception of t7-7, the het4 dimer constitutes the global minimum. However, due to the methyl groups, the S_4 symmetry

Tab. 4.7: Overview of computational B3LYP/maTZ and B3LYP-D3(BJ)/6-311+G(2d,p)[225] results for the relative energies of the dimers of propane-1,2-diol. Electronic (E_{el}) and zero point corrected (E_0) values are given in kJ mol^{-1}.

	het4	hom4	hom4a	het2"	hom2"	hom2a"	het2a"	hom2b"	het3'
E_{el}	0	3.20	3.29	8.21	7.94	7.83	9.85	8.56	9.74
E_0	0	3.44	3.54	4.65	4.79	5.21	6.16	6.31	6.42
	hom3$_b$'	het4a	het4b	hom3	het3a'	hom3'	het3b'	hom2c"	
E_{el}	10.64	6.34	6.39	10.00	10.65	10.75	11.16	10.79	
E_0	6.45	6.87	6.95	7.13	7.45	7.71	7.97	8.02	
	het4	hom4	hom4a	het2"	hom2"	hom2a"	het2a"	hom2b"	het3'
E_{el}[225]	0	3.0	2.8	8.8	8.4	8.1	-	-	9.8
E_0[225]	0	3.2	4.0	5.5	5.3	5.9	-	-	7.1
	hom3$_b$'	het4a	het4b	hom3	het3a'	hom3'	het3b'	hom2c"	
E_{el}[225]	-	5.9	-	-	-	-	-	-	
E_0[225]	-	6.9	-	-	-	-	-	-	

is broken. Given the structural similarities that have been found in case of the 0-M and 3-methyl-butane-2,3-diol (M-MM) monomers (see section 3.1.4 (page 39)), it may be the case that a het-hom gap of 3.5 kJ mol^{-1} can also be found for M-MM. The calculations suggest that het4 should be the only hetero-chiral dimer present in the expansion. On the homo-chiral side, hom4, hom4a, hom2" and hom2a" are likely present given their relative energies. Assuming equal populations for all conformers, with separated hetero- and homo-chiral populations, the intensities of het4 has to be scaled by a factor of 4. The B3LYP-D3(BJ)/6-311+G(2d,p) calculations by F. Kollipost[225] would generally lead to the same predictions, although hom2"/het2" type dimers are consistently predicted higher in energy than at the B3LYP/maTZ level of theory. Moreover, for both methods zero point correction can have a massive influence for hom2"/het2" type dimers and those with three hydrogen bonds. Changes of up to 4.2 kJ mol^{-1} can be observed. It is also noticeable that for conformers with four hydrogen bonds the zero point contributions mostly cancel at the B3LYP/maTZ level of computation. B3LYP-D3(BJ)/6-311+G(2d,p) shows some larger differences overall. Furthermore, some structures were identified that were missing in Ref. [225] although none of which are likely relevant for the interpretation of the spectra.

The structures up to 7 kJ mol^{-1} are shown in Fig. 4.18. As can be seen, CH$\cdots$O contacts are possible in het4/hom4 type arrangements if the monomer adopts the unfavoured O-

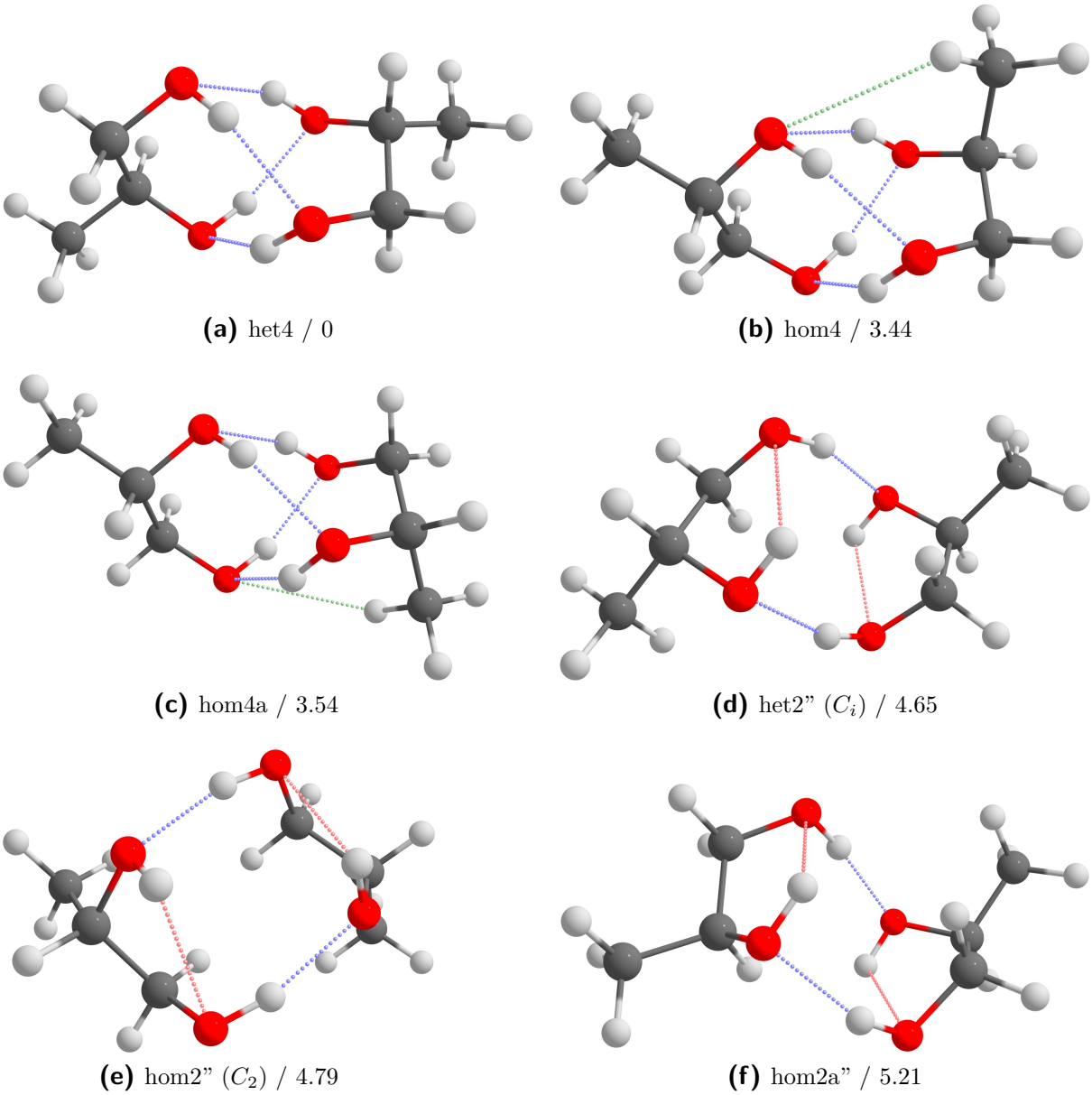

(a) het4 / 0 **(b)** hom4 / 3.44

(c) hom4a / 3.54 **(d)** het2" (C_i) / 4.65

(e) hom2" (C_2) / 4.79 **(f)** hom2a" / 5.21

Fig. 4.18: Dimers of propane-1,2-diol (0-M). Intermolecular hydrogen bonds are highlighted in blue and intramolecular ones in red. Proposed CH$\cdots$O contacts are highlighted in green. Relative zero-point corrected energies at the B3LYP/maTZ level are given in kJ mol^{-1}.

CC-O *gauche* angle. In case of rM-M, two of these contacts are possible for each monomer. Curiously, despite this fact, hom2" dimers are favoured over hom4 dimers for rM-M, while the opposite is true for 0-M. Moreover, hom2" (see Fig. 4.18e) shows a rather unexpected binding motif for such a small system, since it was previously only found to be energetically relevant for t7-7 (see Fig. 4.16d (page 159)). In these types of structures, the backbones interact directly. For the hetero-chiral case these dimers are not relevant due to some unfavourable CH-CH interactions. For hom2", the CH groups facing the other monomer

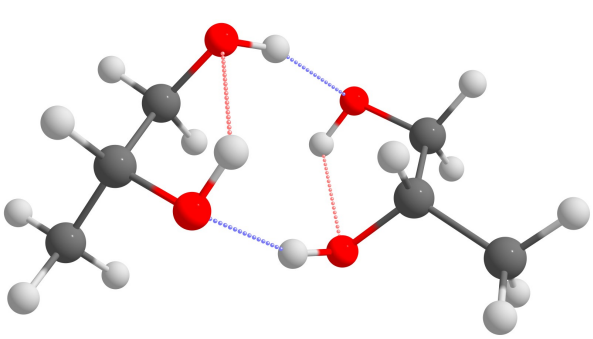

(g) het2a" / 6.16

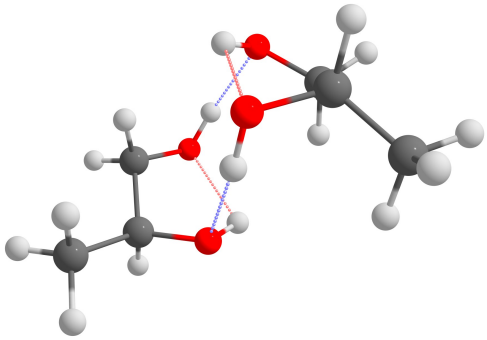

(h) hom2b" / 6.31

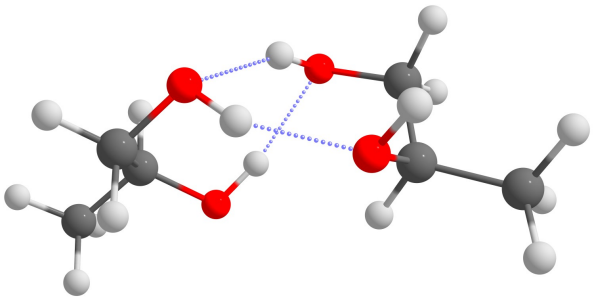

(i) het3' / 6.42

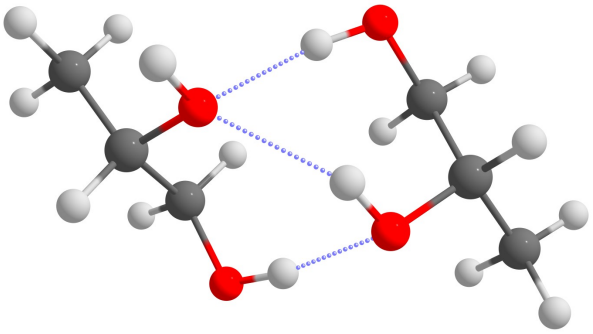

(j) hom3$_b$' / 6.45

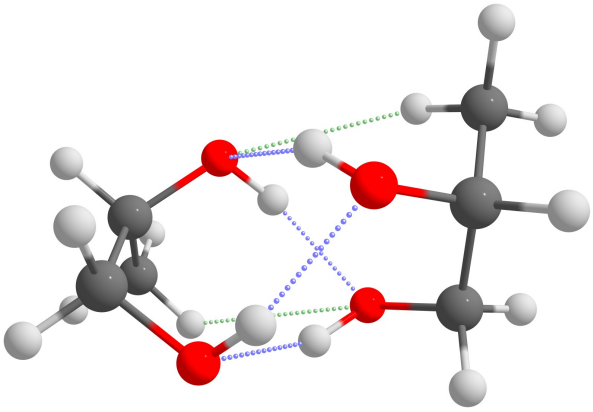

(k) het4a / 6.87

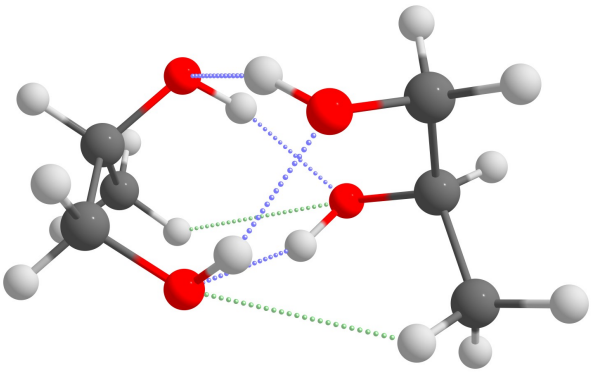

(l) het4b / 6.95

Fig. 4.18: Continuation of Fig. 4.18.

"slot in", while for the hetero-chiral analogue they directly face each other. Furthermore, hom2" and het2" exhibit C_2 and C_i symmetry, respectively.

Regarding the energetic order of hom2" and hom4 for 0-M in comparison to rM-M, the fact that hom4 can be found at similar energies ($\approx 3\,\mathrm{kJ\,mol^{-1}}$) above het4 in either case indicates that hom2" might be especially stabilised in case of rM-M ($0.11\,\mathrm{kJ\,mol^{-1}}$ above het4). Structurally, only minimal changes occur between the directly comparable hom2" of rM-M and hom2a" of 0-M. Therefore, changes in the hydrogen bond lengths and geometries cannot account for the energetic changes. It could be argued that the

added methyl group makes the neighbouring OH group a better hydrogen bond acceptor. This can in fact be seen for the hom2"/het2" motifs of 0-M, where the intermolecular hydrogen bond donor always binds at the methyl side. For rM-M, the additional methyl group would strengthen the intramolecular hydrogen bonds. However, this stabilising effect would also be present in hom4. It may be the case that this effect is stronger for hom2"/het2" type dimers, since the hydrogen bonds are more linear than for hom4. Another possibility would be a change in the deformation energy. However, this effect would amount to a sub $\mathrm{kJ\,mol^{-1}}$ destabilisation of hom4 relative to rM-M. Therefore, the origin of the hom4 and hom2" preference switch cannot be adequately explained. Applying local energy decomposition analysis to these system could help to understand this phenomenon in the future.

The experimental Raman-spectra as well as the simulations for the racemate and the enantiopure compound are shown in Fig. 4.19. In the racemic spectrum, the most intense band can be identified as band 4 of het4. However, as the enantiopure spectrum shows, there is significant overlap with homo-chiral dimers. At slightly higher wavenumbers ($3460\,\mathrm{cm^{-1}}$), an overlap of band 2 and 3 of het4 are likely present. This can be inferred by the fact that there is no signal in the corresponding enantiopure spectrum. Moreover, as was previously stated, het4 is not strictly S_4 symmetric but effectively behaves as such. Hence, band 4 corresponds to A and band 2 and 3 to the degenerate E character. The predictions for band 2 and 3 differ by only $0.2\,\mathrm{cm^{-1}}$. The splitting between E-A is slightly overestimated by B3LYP/maTZ in line with the results of 0-0 and t6-6. The unusually strong overestimation in case of pinacol (see Fig. 4.10) is therefore likely tied to the tetramethylation and no continuous substitution effect can be made out. The scaling factor used closely resembles the one of t6-6 (0.966). With 0.967, 0-M lies in between 0-0 (0.969) and t6-6, but above pinacol with 0.964. Therefore, 0-M matches the substitutional trend making the unusually high scaling factor of rM-M (0.979) even more exceptional.

As was the case for previous systems, upon switching from the racemate to the enantiopure compound, a doubling in intensity is expected for purely homo-chiral signals. An approximate doubling can be seen for all bands except the one at $3428\,\mathrm{cm^{-1}}$. The bands overlapping with het4 can be attributed to hom4 and hom4a. Since hom4 is predicted to only have one strongly Raman active band (4) it is assigned to the signal at $3421\,\mathrm{cm^{-1}}$. The more intense neighbouring band can be assigned to band 4 of hom4a. Based on band positions, the assignment would be switched. However, the predicted intensities do not match such an interpretation. Moreover, given the very broad nature of the band assigned to hom4a, the energetic order of hom4 and hom4a likely should be switched. The very intense signal at $3477\,\mathrm{cm^{-1}}$ can also be attributed to hom4, with band 2 and 3 likely at least partially overlapping. The flank towards lower wavenumbers could be

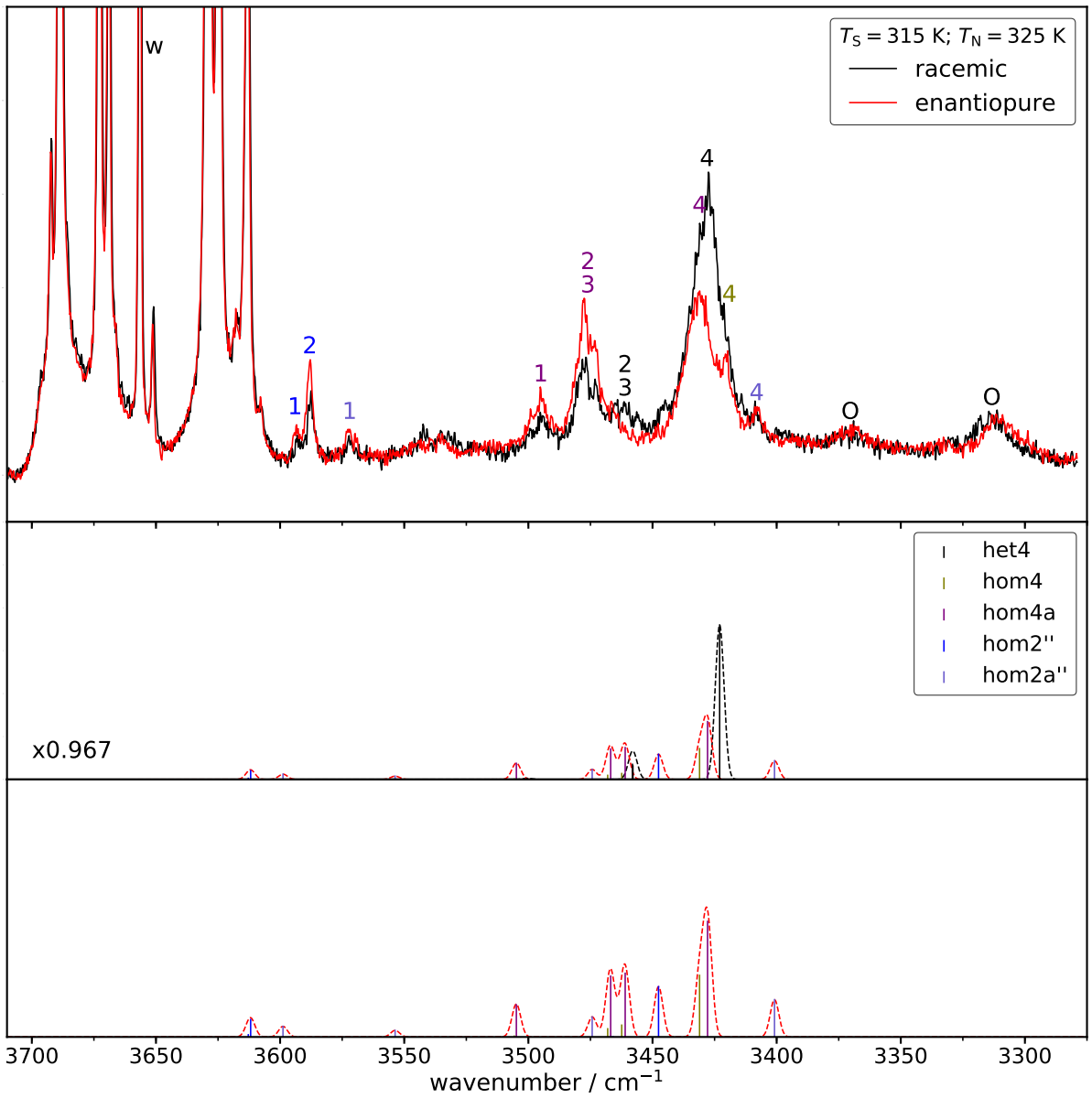

Fig. 4.19: Experimental Raman (top), simulated racemic Raman (middle) and simulated enantiopure Raman data (bottom) of propane-1,2-diol (0-M). The saturator temperature (T_S) as well as the nozzle temperature (T_N) are given. The simulated spectra are based on B3LYP/maTZ and are scaled by 0.967 to match band 4 of het4. w indicates a water band and O oligomer bands.

caused by band 4 of hom2". Some smaller contributions from hom4 and hom2a" may also be present. The neighbouring smaller band at 3495 cm^{-1} can be assigned to band 1 of hom4. The small signal at 3408 cm^{-1} is likely caused by hom2a". The three remaining signals near the monomer region can be assigned to hom2" and hom2a". For hom2", band 1 and 2 are predicted very close to each other, with the former also being much lower in intensity. Therefore, it may be the case that band 1 cannot be distinguished from band

2. This assignment is tentative but it is made due to a lack of other explanations.

Moreover, some broad signals exist between $3560\,\mathrm{cm}^{-1}$ and $3510\,\mathrm{cm}^{-1}$, which to some degree are present in both the racemic and the enantiopure spectrum. Some contributions to this feature are likely due to band 2 of hom2a", but the expected increase in the enantiopure case is not present. This would indicate the presence of another hetero-chiral dimer. However, given the energetic separation between het4 and the next most stable hetero dimer (het2") of $4.65\,\mathrm{kJ\,mol}^{-1}$ this appears unlikely. Moreover, het2" exhibits no matching signals. It may be possible that these bands are caused by dimers of 0-M and water. Since some advancements at the curry jet greatly reduced the amount of residual water in the vacuum chamber, spectra could be re-recorded to rule out this possibility.

Furthermore, towards lower wavenumbers, two signals appear which belong to higher oligomers. Most likely, these can be attributed to trimers. Curiously, both oligomer bands are present at about equal intensities in the enantiopure and racemic spectrum. Due to the lack of discernible changes, the hetero and homo oligomers likely behave very similarly spectroscopically. The trimers of 0-M can be explored in the future.

In case of 0-M, IR spectra would be of great help to confirm the assignments since not only het4, but also hom4 and hom4a show (partial) exclusionary behaviour with regards to the Raman and IR activity. This is also the case for the intermolecular OH modes of hom2". A comparison fo the simulated Raman and IR spectra is shown in C.18 (page 288). A previous IR study, using the *popcorn*-jet, by F. Kollipost suggests that het4, hom4, hom4a and hom2" are present[225]. However, recent experimental developments improved the quality of spectra significantly that can be obtained with the *popcorn*-jet[166,277]. Hence, revisiting 0-M in the IR is worthwhile. Given the prevalence of cyclic binding motifs, the permanent dipole moments are quite small throughout with the exception of hom2" ($\mu_a = \mu_b = 0\,\mathrm{Debye}$, $\mu_c = 2.0\,\mathrm{Debye}$).

4.2.2 2-Methyl-propane-1,2-diol

A simple extension of 0-M is 2-methyl-propane-1,2-diol (0-MM) which has the same degree of substitution (n_D) as rM-M, *i.e.* $n_\mathrm{D} = 2$. Therefore, it may be the case that 0-MM also requires an atypically high scaling factor for the simulated spectra. However, unlike rM-M, 0-MM is a transiently chiral system with *gauche* + and − conformers (O-CC-O dihedral angle), acting as enantiomers. Moreover, the fact that one carbon atom is doubly methylated makes the attached oxygen atom an even better hydrogen bond acceptor than in the single methylated cases of 0-M and rM-M. hom2"/het2" type binding motifs are

expected to profit the most from this change since very strong and linear intermolecular hydrogen bonds can be formed. However, the methyl groups may be sterically too demanding to properly form the motif, as was the case for the tetra-methylated pinacol (see Tab. 4.3 (page 140)).

The energetic landscape of 0-MM dimers is shown in Tab. 4.8. het4 is yet again the most stable conformer, although two het4 motifs share that position. The two het4 structures differ in the relative position of the methyl groups. As Fig. 4.20 shows, in case of het4, the methyl groups are opposite each other, while for het4a they are on the same side regarding the plane of projection. It can indeed be seen that hom2" and het2" motifs profit from the double methylation, being the most stable homo-chiral and second most stable hetero-chiral conformers, respectively. The het-hom gap shrinks to about $1\,\mathrm{kJ\,mol^{-1}}$, so that energetic chirality recognition is no longer present. Out of the methylated systems studied here, only rM-M shows a smaller gap (0-0: $6.73\,\mathrm{kJ\,mol^{-1}}$, 0-M: $3.44\,\mathrm{kJ\,mol^{-1}}$, rM-M: $0.11\,\mathrm{kJ\,mol^{-1}}$, MM-MM: $6.80\,\mathrm{kJ\,mol^{-1}}$). 0-MM shares the most similarities with rM-M in terms of their energetic landscape, which is also reflected in the very small het-hom gap in either case. However, a major difference is the instability of hom4 motifs. Similarly to 0-0, MM-MM and t6-6 only rather long hydrogen bonds can be formed. This is illustrated in Fig. A.27 (page 239), comparing the most stable hom4 motif of 0-0, 0-M, 0-MM, rM-M and MM-MM. It can be seen that when the degeneracy between the *gauche* + and − conformers (O-CC-O dihedral angle), is lifted, much shorter hydrogen bonds are possible. Moreover, hom4 in the 0-MM case is no longer C_2 symmetric, as was the case for the comparable transiently chiral systems 0-0 and MM-MM. It can also be seen that the

Tab. 4.8: Overview of computational B3LYP/maTZ results for the relative energies of the dimers of 2-methyl-propane-1,2-diol. Electronic (E_{el}) and zero point corrected (E_0) values are given in kJ mol^{-1}.

	het4	het4a	hom2"	het2"	hom3$_\mathrm{b}$'	het3$_\mathrm{b}$'	hom2a"	het2"
E_{el}	0.00	0.04	4.48	5.04	6.47	7.16	5.85	8.81
E_0	0.00	0.06	1.07	1.39	2.19	2.92	3.24	3.94
	het3'	hom3	het3a'	hom3'	hom3a'	hom3b'	hom3a	het3b'
E_{el}	6.96	7.52	7.42	7.65	8.04	10.26	10.22	9.80
E_0	3.95	4.09	4.20	4.31	4.64	5.82	6.25	6.47
	het3c'	het3$_\mathrm{b}$a'	hom3c'	hom3$_\mathrm{b}$a'	het2a"	het3		
E_{el}	9.58	10.58	10.44	10.90	11.62	10.54		
E_0	6.51	6.56	6.71	6.78	6.79	6.81		

hydrogen bond lengths in case of the symmetric rM-M behave more as one would expect for C_2 symmetry (two pairs of equal hydrogen bond lengths). 0-M starts deviating while 0-MM has vastly different hydrogen bond lengths. Although not explicitly shown, *trans*-cyclohexane-1,2-diol (t6-6) behaves very similarly to 0-0. Moreover, zero point effects are again quite substantial reaching up to $4.9\,\mathrm{kJ\,mol^{-1}}$. An exception to this is het4a where the zero point energy difference to het4 cancels.

Furthermore, bifurcated arrangements, as indicated by a lower case b ($_\mathrm{b}$), are also much

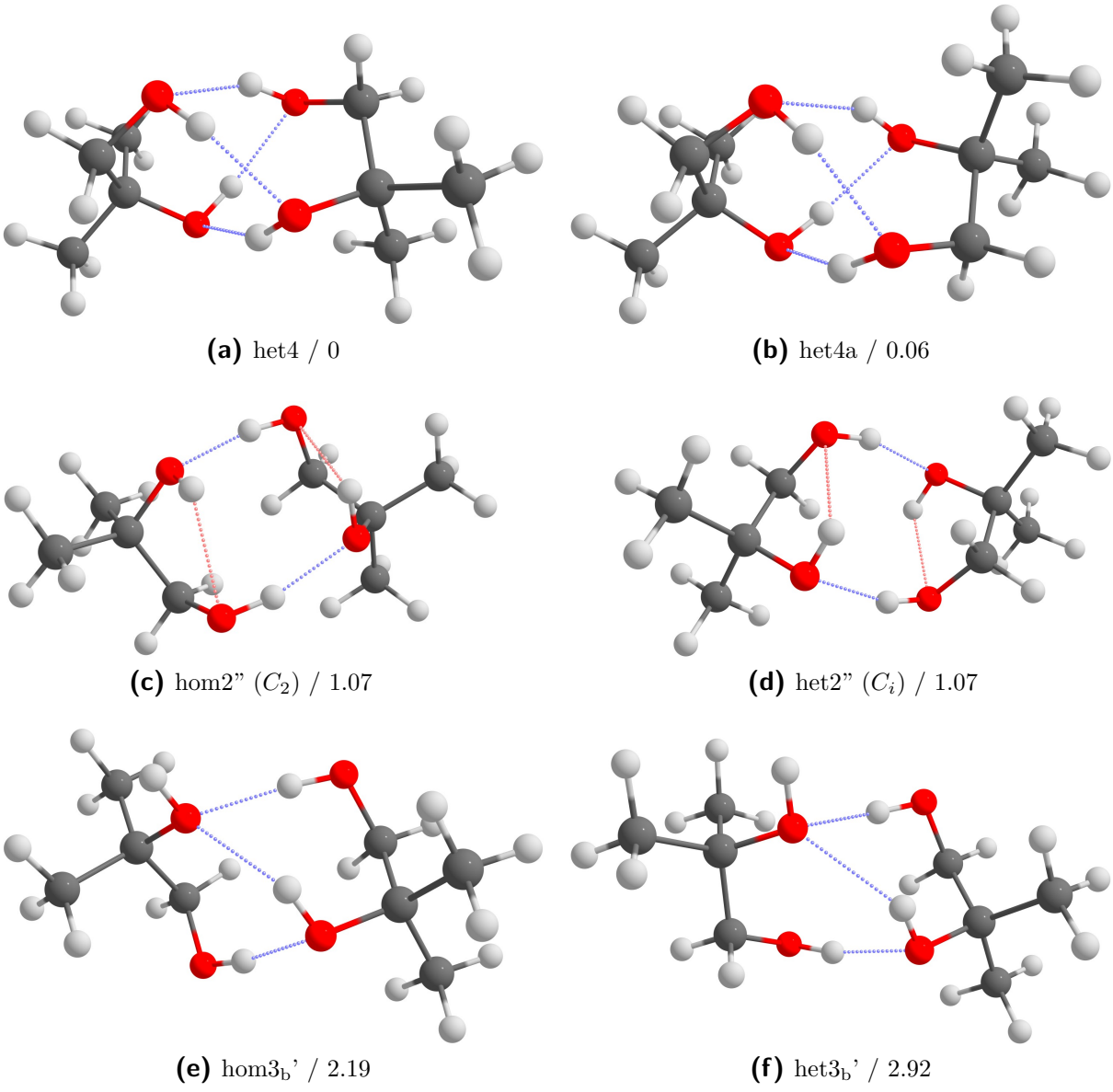

(a) het4 / 0 **(b)** het4a / 0.06

(c) hom2" (C_2) / 1.07 **(d)** het2" (C_i) / 1.07

(e) hom3$_\mathrm{b}$' / 2.19 **(f)** het3$_\mathrm{b}$' / 2.92

Fig. 4.20: 12 most stable dimers of 2-methyl-propane-1,2-diol. Intermolecular hydrogen bonds are highlighted in blue and intramolecular ones in red. Relative zero-point corrected energies at the B3LYP/maTZ level are given in kJ mol^{-1}.

lower in energy. Similarly to hom2”/het2”, these motifs benefit from the double methylation on a single carbon atom. For these motifs, the bifurcation occurs towards the oxygen at the doubly methylated side, so that three intermolecular hydrogen bonds towards the higher substituted side can be formed in total. For other patterns with three intermolecular hydrogen bonds this is not possible, as can be seen from Fig. 4.20. A stabilisation of bifurcated arrangements was also found for the dimers of 2-methoxyethanol and ethane-1,2-diol (relative to 0-0 and 0-0 dimers), where the methoxy group constitutes the better acceptor[111]. Furthermore, an unusual binding motif is observed for het2a”, where one of the intramolecular hydrogen bonds is no longer present. In case of the

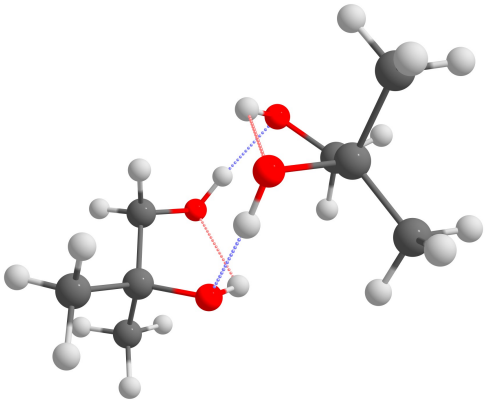

(g) hom2a” / 3.24

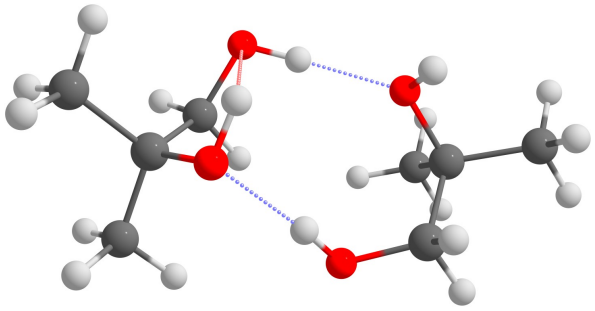

(h) het2a” / 3.94

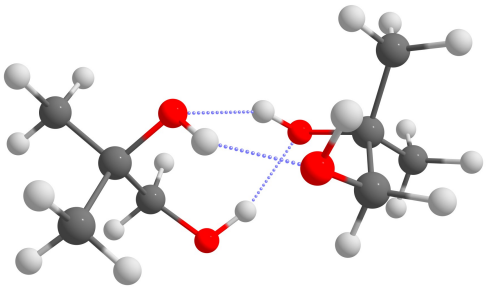

(i) het3’ / 3.95

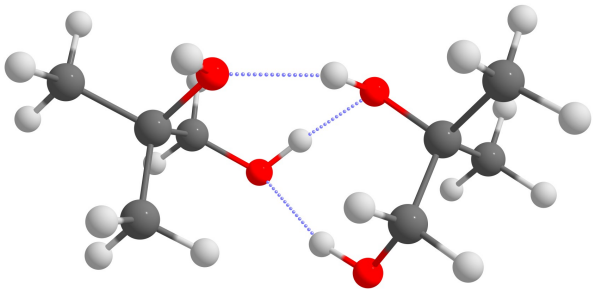

(j) hom3 / 4.09

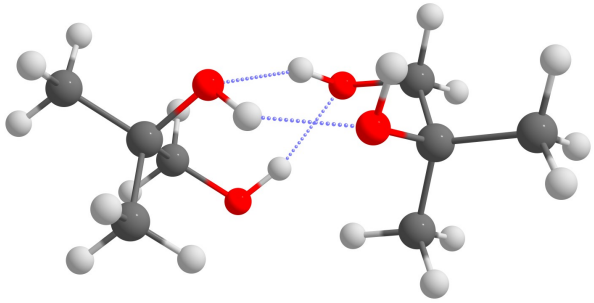

(k) het3a’ / 4.20

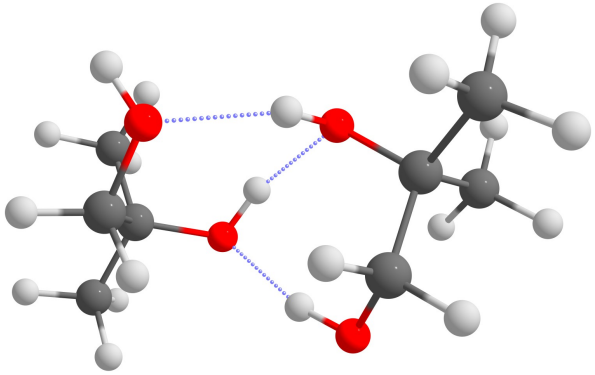

(l) hom3’ / 4.31

Fig. 4.20: Continuation of Fig. 4.20.

hom2", the motif where the backbones are directly interacting is favoured. This was also the case for 0-M (see Fig. 4.18e (page 163)). Moreover, the energy difference between the directly interacting (hom2") and not directly interacting (hom2a") hom2" structures increases significantly going from 0-M to 0-MM. For 0-M, direct interaction is favoured by $0.4\,\mathrm{kJ\,mol^{-1}}$ while for 0-MM, the preference increases to $2.2\,\mathrm{kJ\,mol^{-1}}$. This change can be attributed to the fact that for 0-MM only one intermolecular hydrogen bond to the higher substituted side is present, highlighting the fact that the oxygen atom on the doubly methylated side is the better hydrogen bond acceptor. A hom2a" motif similar to 0-M leads to unfavourable interactions with the additional methyl group. This hypothetical conformer is shown in Fig. A.28 (page 240). Moreover, analogously to 0-M, hom2" and het2" exhibit C_2 and C_i symmetry, respectively.

For the experimental spectra, het4, het4a and het2" are expected to be present in the expansion out of the hetero chiral dimers. However, het4 and het4a behave very similarly in terms of their spectral signatures. Therefore, to simplify the analysis only het4 will be simulated but with doubled intensities. On the homo chiral side, hom2", hom3_b' and hom2a" are likely present. Assuming equal populations no intensity scaling is required between the homo- and hetero-chiral dimers.

The experimental Raman spectrum as well as the simulations are shown in Fig. 4.21. The most intense and rather broad band at $3426\,\mathrm{cm^{-1}}$ can be assigned to the combined het4/het4a species. Further contributing to the broadening is likely band 3 of hom3_b'. For het4, the simulations also clearly show the departure from S_4 symmetry as band 2 and 3 are no longer degenerate. However, they likely still overlap spectrally resulting in the broad feature at $3473\,\mathrm{cm^{-1}}$. Moreover, hom2a" likely also contributes to that band. The band at $3460\,\mathrm{cm^{-1}}$ can be attributed to an overlap of band 3 and 4 of het2" and hom2", respectively. The added intensities of the two conformers match well between theory and experiment. In principle, an overlap of hom2" with het4 is possible, but would lead to an intensity mismatch. The most strongly downshifted band at $3397\,\mathrm{cm^{-1}}$ can be assigned to hom2a". A comparison of the experimental to the predicted intensities suggest that less hom2a" is present than simulated. This is in line with the fact that hom2a" is predicted to be $2.2\,\mathrm{kJ\,mol^{-1}}$ above the homo-chiral minimum.

Two distinct signals towards the monomer region remain unassigned. The more intense band can be assigned to an overlap of band 1 and 2 of hom2" and band 2 of hom3_b'. The smaller band can be assigned to an overlap of band 2 of het2" and band 1 of hom2a". A very broad and shallow band between $3550\,\mathrm{cm^{-1}}$ and $3515\,\mathrm{cm^{-1}}$ is also present, similarly to 0-M (see Fig. 4.19 (page 166)). It could possibly be assigned to hom3_b', but given the undefined nature of the signal, such an assignment is not made. Some broadening could

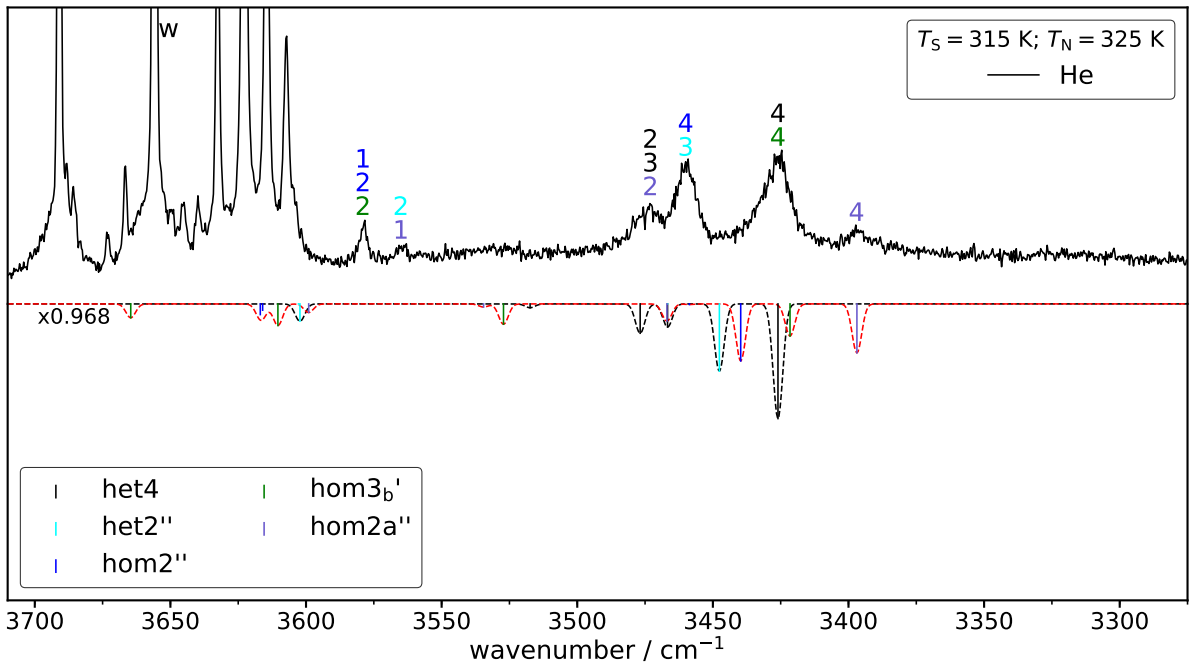

Fig. 4.21: Experimental Raman data (plotted upwards) and simulated data (plotted downwards) of 2-methyl-propane-1,2-diol (0-MM). The saturator temperature (T_S) as well as the nozzle temperature (T_N) are given. The simulated spectra are based on B3LYP/maTZ and are scaled by 0.968 to match band 4 of het4. w indicates a water band.

be caused by hom2a" and het4. For t6-6, which has the same degree of substitution, hom3$_b$' has been previously assigned in the same spectral region. However, it appeared as a sharp signal there (see Fig. 4.7 (page 137)). Lastly, the free OH mode of hom3$_b$' cannot be assigned since it overlaps with the monomer region. In comparison to a spectrum under monomer conditions, no new bands arise. Furthermore, the scaling factor does not fit in the progression found for 0-0, 0-M, t6-6 and MM-MM. The scaling factor would be expected to be very similar to t6-6 (0.966), but is in fact higher. However, the scaling factor is far removed from the extreme value of 0.979 found for rM-M. Therefore, the degree of substitution does not appear to be causal to this phenomenon. t6-6 also shares the same n_D as rM-M but due to its ring is not necessarily a good reference point. It is clear that given its atypical behaviour rM-M requires re-examination.

A great aid to substantiate the assignment is yet again IR spectroscopy. In case of het2", which is C_i symmetric, this is obvious since the principle of mutual exclusion strictly holds. However, the intermolecular OH modes of the C_2 symmetric hom2" behave in the same way. Moreover, het4 is still close enough to S_4 symmetry that band 1 (approximate B character) is effectively only IR active and band 4 (approximate A character) only Raman active. Hence, due to their exclusionary nature, three assignments can be confirmed in

this way. Moreover, band 4 of hom3$_b$' is expected to be significantly IR active, so that its presence can be confirmed since no overlap with band 4 of het4 is present. An IR simulation contrasted with the experimental Raman spectrum is shown in Fig. C.19 to illustrate this point. Since the permanent dipole moments of the hetero-chiral dimers are either very small or 0 debye, microwave spectroscopy is blind with regards to hetero dimers. Fortunately, all three assigned homo dimers have significantly large dipole components so that their presence might also be confirmed *via* rotational spectroscopy.

4.2.3 3-Butene-1,2-diol

All systems discussed previously focus on diols where only oxygen can act as a hydrogen bond acceptor. The inclusion of other acceptors allows for new structural motifs which will influence the energetic chiral recognition. 3-Butene-1,2-diol (0-V) constitutes a small system that introduces π interactions. In terms of its substitution pattern it is most similar to 0-M. Therefore, comparisons between the two are the most warranted. In principle, hom2"/het2" type dimers that involve π-stacking are possible. However, given the small size of the π-system, the stabilising effect is likely too small to compete with the other hydrogen bonds. In the future, it can be explored if such dimers are relevant for the larger 1-phenyl-ethane-1,2-diol. Another possibility would be to add a vinyl group on the other side as well, *i.e.* 1,5-hexadiene-3,4-diol. OH$\cdots\pi$ (intermolecular) contacts are expected to be the most prominent in hydrogen bond motifs with three hydrogen bonds (OH$\cdots$O), where such an additional π contact can be formed. Since het4 type structures cannot benefit from OH$\cdots\pi$ interactions, the het-hom gap might be further reduced relative to 0-M ($3.44\,\mathrm{kJ\,mol^{-1}}$).

The energetic landscape of the 0-V dimers can be found in Tab 4.9. As can be seen, the introduction of the vinyl group leads to a significantly more complex conformational space. However, some key similarities remain in comparison to 0-M, *i.e* het4 remains the global and hom4 the homo-chiral minimum (*cf.* Tab. 4.7 (page 162)). Moreover, the het-hom gap is fairly small with $2.75\,\mathrm{kJ\,mol^{-1}}$ in comparison to $3.44\,\mathrm{kJ\,mol^{-1}}$ of 0-M. The hetero-chiral dimers can be narrowed down to het4, het4a and het4b being relevant in the expansion. For the homo-chiral ones, on the other hand, 21 dimers can be found within $3\,\mathrm{kJ\,mol^{-1}}$ above the homo-chiral minimum. It is expected that, similar to 0-M, hom4 and hom4a should be the most prominent in the spectrum. Unlike 0-M, structures with three hydrogen bonds are favoured over those with two intermolecular hydrogen bonds.

A selection of different conformers, based on energetic relevance and representation of a binding motif, is shown in 4.22. As can be seen, the het4 structures only differ in the

Tab. 4.9: Overview of computational B3LYP/maTZ results for the relative energies of the dimers of 3-butene-1,2-diol. Electronic (E_{el}) and zero point corrected (E_0) values are given in kJ mol^{-1}.

	het4	het4a	het4b	hom4	het3'	het3a'	het3b'	hom4a
E_{el}	0	2.15	2.25	2.95	6.37	5.61	5.58	3.32
E_0	0	1.64	1.78	2.75	2.98	2.98	3.03	3.03
	het3c'	het4c	hom3'	het3d'	het3e'	hom3	het2"	$hom3_b$'
E_{el}	5.57	4.40	6.32	6.27	6.80	7.46	6.69	7.72
E_0	3.03	3.41	3.59	3.64	3.80	3.82	3.83	3.93
	hom2"	hom3a	$hom3_b$a'	het3f'	hom4b	hom3b	hom4c	hom4d
E_{el}	6.26	7.40	8.09	6.98	4.91	8.83	5.45	5.09
E_0	3.94	4.15	4.39	4.47	4.52	4.54	4.56	4.68
	hom4e	hom3c	$hom3_b$b'	hom3a'	hom3d	het2'	$hom3_b$c'	hom3b'
E_{el}	5.58	8.24	9.33	7.93	8.27	8.56	9.46	8.34
E_0	4.78	4.82	4.93	5.11	5.15	5.20	5.25	5.37
	hom3c'	het3g'	hom2a"	het3h'	het3i'	hom3e	het2a"	het4d
E_{el}	8.42	7.71	8.33	8.52	8.62	9.70	9.52	6.36
E_0	5.40	5.41	5.48	5.56	5.60	5.63	5.82	5.91
	hom2b"	hom2c"	hom3f	hom2d"	hom4f	hom4g	het2b"	het2c"
E_{el}	8.53	8.52	10.08	8.89	7.13	7.25	10.37	9.97
E_0	5.98	5.99	6.11	6.23	6.32	6.35	6.41	6.52
	hom3g	het2d"	hom2e"	hom2f"	het3j'	hom2g"		
E_{el}	10.46	10.33	9.86	9.77	9.50	9.55		
E_0	6.55	6.56	6.85	6.94	6.95	6.97		

orientation of the vinyl group. In case of het4, it appears as if CH contacts (highlighted in green) with the vinyl group determine the energetic ranking. For het4, two such contacts are possible, while in case of het4a and het4b only a single contact can be formed. Between the two latter systems, this interaction appears to be of very similar magnitude since they are very close in energy. Curiously, the OH acceptor bond of the interacting oxygen gets elongated, relative to the non interacting-ones. Moreover, their spectral patterns are very similar, so that they can be approximately considered as one degenerate conformer. A similar approximation was made for het4 and het4a of 0-MM (see section 4.2.2 (page 167)). For hom4 and hom4a, another such dynamic can be found. Here, the monomer on the right hand side of the structure is rotated by 180° (see Figs. 4.22d and 4.22h).

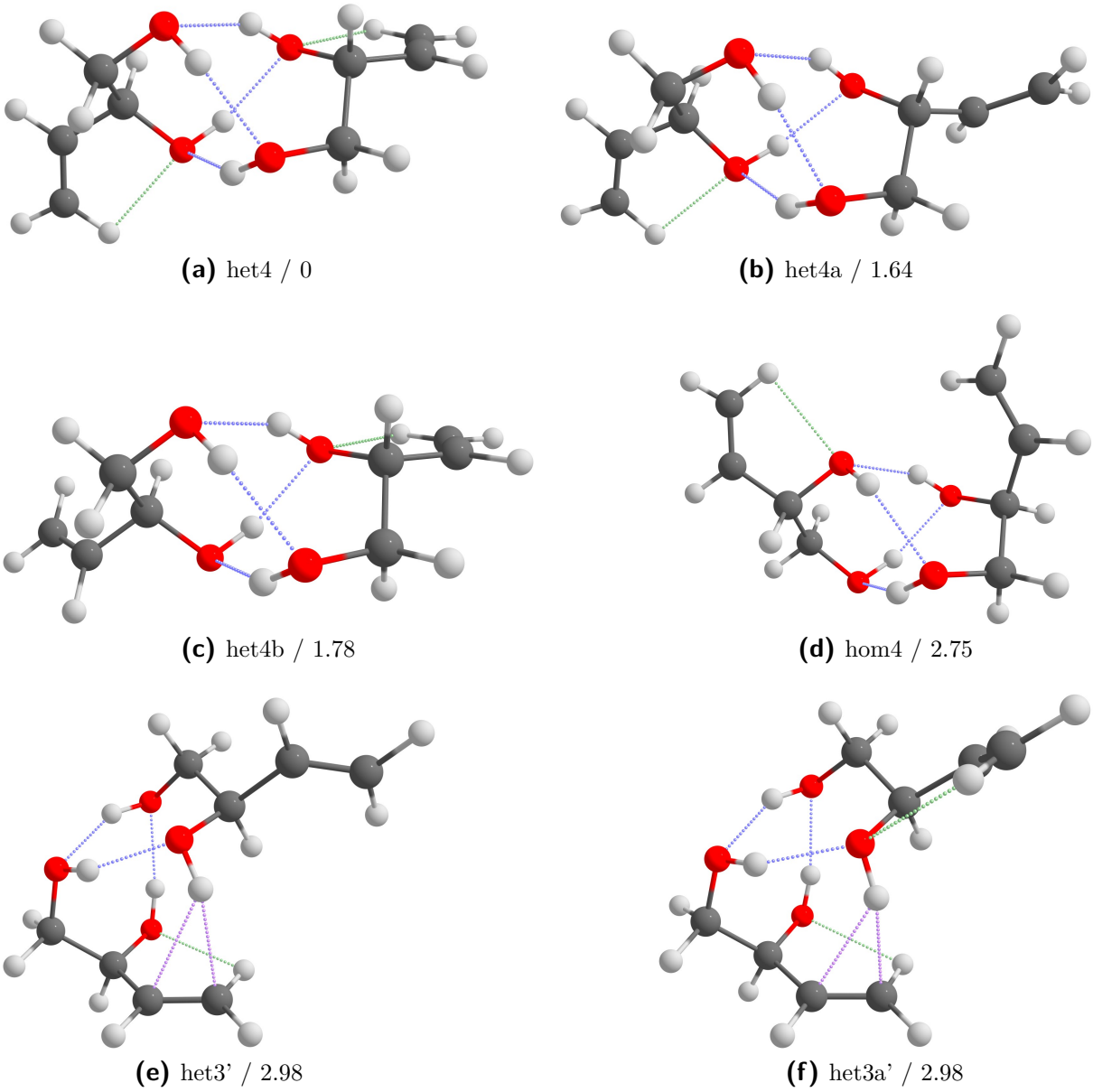

(a) het4 / 0 **(b)** het4a / 1.64 **(c)** het4b / 1.78 **(d)** hom4 / 2.75 **(e)** het3' / 2.98 **(f)** het3a' / 2.98

Fig. 4.22: Dimers of 3-butene-1,2-diol (0-V). Intermolecular hydrogen bonds are highlighted in blue and intramolecular ones in red. Proposed CH$\cdots$O contacts are highlighted in green and OH$\cdots\pi$ contacts in purple. Relative zero-point corrected energies at the B3LYP/maTZ level are given in kJ mol^{-1}.

However, with about 0.3 kJ mol^{-1}, the energetic separation is slightly larger. The OH modes are very similar, showing deviations below 1 cm^{-1}, with the exception of a single mode which differs by about 5 cm^{-1}. The fact that hom4 is slightly more stable relative to 0-M (3.44 kJ mol^{-1} *vs.* 2.95 kJ mol^{-1}), could be attributed to some long range interactions of the vinyl groups. Furthermore, het4 most closely resembles the S_4 point group in the sense that the hydrogen bonds are still about the same length. For het4a and het4b, the deviation of the mean hydrogen bond length increases roughly four fold, indicating

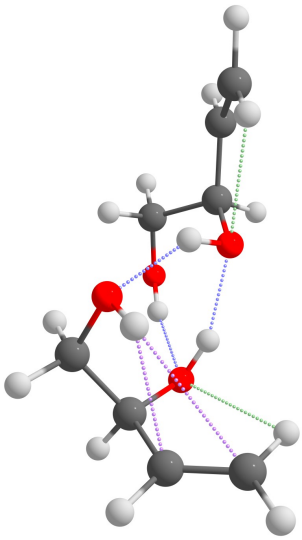

(g) het3b' / 3.03

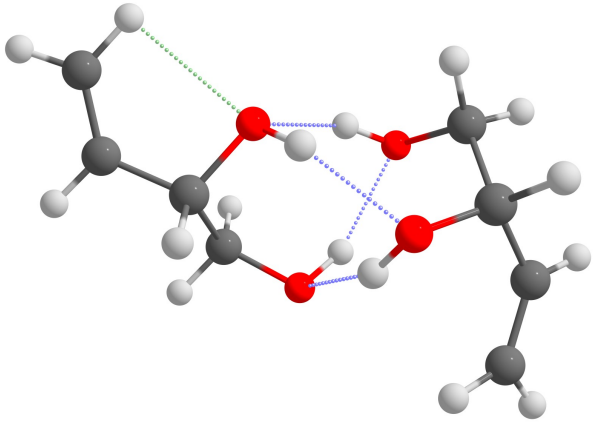

(h) hom4a / 3.03

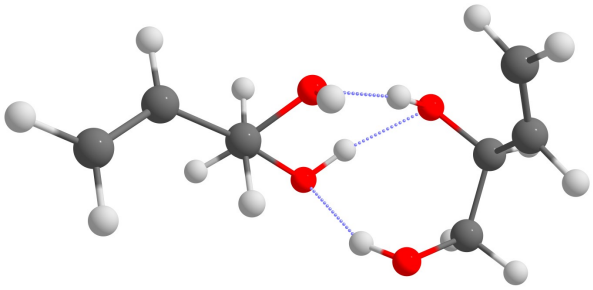

(i) hom3' / 3.59

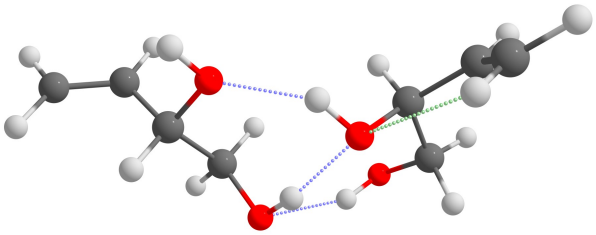

(j) hom3 / 3.82

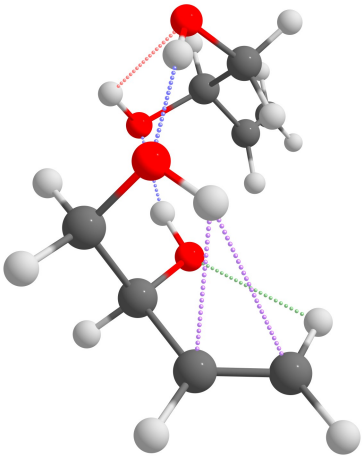

(k) het2" / 3.83

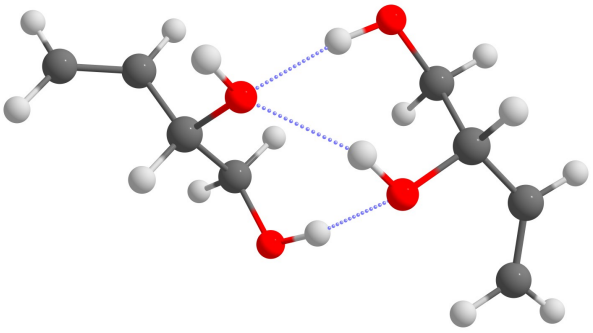

(l) hom3$_b$' / 3.93

Fig. 4.22: Continuation of Fig. 4.22.

a stronger departure from S_4 symmetry. hom4 and hom4a are far removed from C_2 symmetry and follow more along the lines of 0-MM for such motifs (*cf.* Fig. A.27c (page 239)).

As was previously stated for het3/hom3 type motifs, an additional intermolecular OH$\cdots\pi$

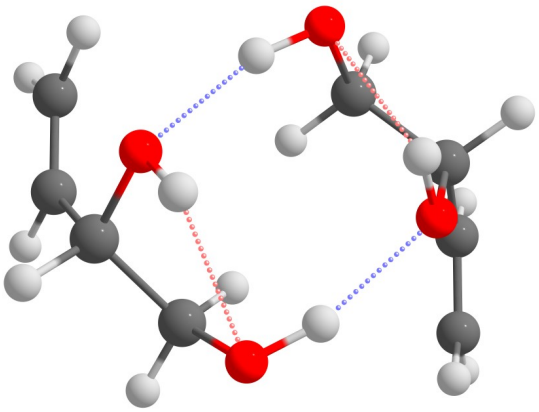

(m) hom2" (C_2) / 3.94

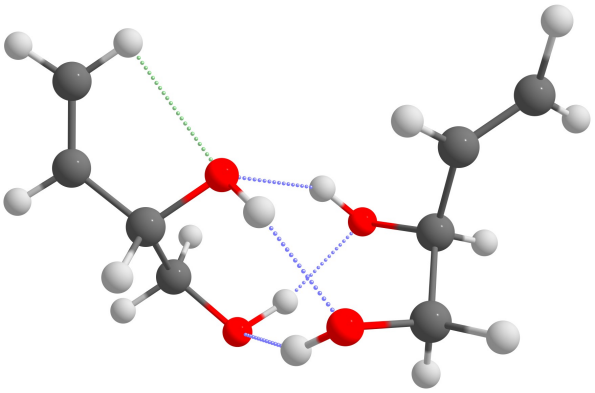

(n) hom4b / 4.52

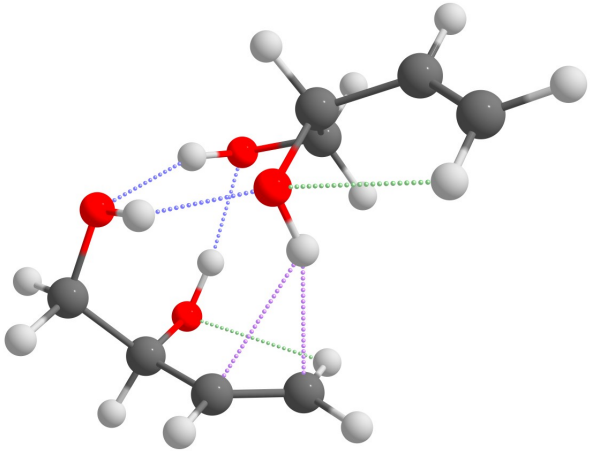

(o) hom3a' / 5.11

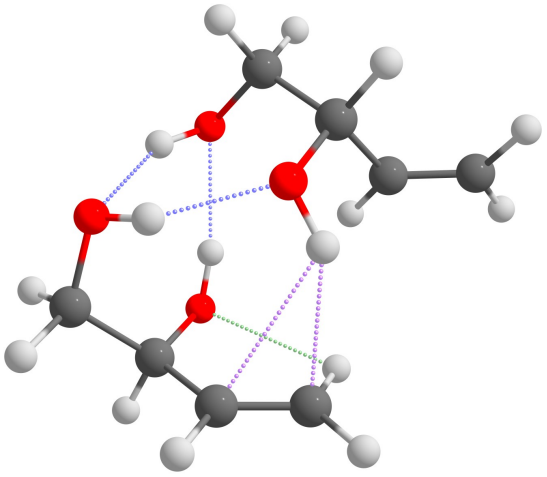

(p) hom3c' / 5.40

Fig. 4.22: Continuation of Fig. 4.22.

contact can be formed. For the hetero-chiral dimers, these follow around 3 kJ mol^{-1} with het3' and het3a'. From the observations of het4 and the het4a/het4b pair, it would be expected that het3a' should be more stable since two CH contacts can be formed. However, this is not the case with them being essentially isoenergetic. The hydrogen bond lengths of het3' and het3a' overall hardly differ, while the π contacts are shorter for het3a'. Hence, the hydrogen bond lengths cannot account for the isoenergetic behaviour. The deformation energy of het3a' relative to het3' amounts to the kind of stabilisation expected for the CH contact (about 1.7 kJ mol^{-1} per contact), as indicated by the het4 and het4a or het4b energy differences. het3b' also follows very close in energy, but exhibits an intramolecular π contact and two CH contacts similar to het3a'. The lack of a shorter intermolecular π contact is likely balanced out by the fact that the hydrogen bonds are overall shorter than for het3' and het3a'. Additionally, the most stable hetero-chiral motif with two intermolecular hydrogen bonds also exhibits an intramolecular π contact.

The homo-chiral dimers generally show more similar motifs to the other systems studied

without π contacts. For instance, the first homo dimer with a π contact (hom3a') follows $1.5\,\mathrm{kJ\,mol^{-1}}$ above the most stable hom3' type structure. The interacting dimers hom3a' and hom3c' are closely related to het3a' and het3', respectively. Despite this relationship, they are higher in energy by more than $2\,\mathrm{kJ\,mol^{-1}}$. This is especially surprising since hom3a' exhibits even shorter hydrogen bonds than het3'. Structurally, no clear feature sticks out between the homo- and hetero-chiral variants to explain the energetic differences. The deformation energies again provide a possible explanation. Relative to het3', hom3a' has a deformation penalty of $4.3\,\mathrm{kJ\,mol^{-1}}$ which is then counteracted by the shorter hydrogen bonds, leading to an ultimate energy gap of $2.1\,\mathrm{kJ\,mol^{-1}}$. In case of hom3c' the deformation energy is significantly smaller ($1.7\,\mathrm{kJ\,mol^{-1}}$), but longer hydrogen bonds then lead to an energy difference of $2.4\,\mathrm{kJ\,mol^{-1}}$ relative to het3'. Moreover, bifurcated hydrogen bond motifs are only energetically relevant for homo-chiral dimers, with hetero-chiral equivalents completely missing, similarly to 0-M. Another similarity to 0-M is the fact that the most stable hom2" motif is a directly interacting one in terms of the backbone. It is also C_2 symmetric as was the case for 0-M (see Fig. 4.18e (page 163)). The relative energies are also comparable (0-M: $4.79\,\mathrm{kJ\,mol^{-1}}$, 0-V: $3.94\,\mathrm{kJ\,mol^{-1}}$). hom2" or het2" structures with π stacking character are more than $12\,\mathrm{kJ\,mol^{-1}}$ above the global minimum. Hence, π stacking effects do not provide sufficient stabilisation to make them energetically relevant.

To simplify the simulations, het4a and het4b as well as hom4 and hom4a will be treated together, as was previously alluded to. The more stable dimer acts as the namesake for the two pairs. het4 will be simulated as a distinct species. Furthermore, only the four most stable homo-chiral dimers will be considered. Besides, hom4/hom4a this includes hom3' and hom3. In all cases, equal populations will be assumed, but hetero- and homo-dimers are treated as separate. For hom4 and het4a the populations are doubled. Under these assumptions, the overall homo-chiral population has to be scaled by 0.75 relative to the hetero-chiral one. The experimental and predicted Raman spectra are shown in Fig. 4.23. The scaling factor used is derived from 0-M (see Fig. 4.19 (page 166)). The most prominent and very broad band fits well to the predictions of het4, het4a and hom4. However, an exact band position cannot be discerned, although the slope of the flank towards higher wavenumbers is considerably steeper than at lower wavenumbers.

Unfortunately, the remaining bands cannot be assigned with any certainty. The two bands at $3464\,\mathrm{cm^{-1}}$ and $3481\,\mathrm{cm^{-1}}$, are likely caused by het4, het4a and hom4 to some extent. The spectral shifts would indicate that the former belongs to het4 and the latter broader one to an overlap of het4a and hom4. Some contributions of hom3' may be present in the het4 case. The bands around $3530\,\mathrm{cm^{-1}}$ may be due to an overlap of hom3' and hom4, but no clear assignments can be made. The prominent hom3 signal in that region, similarly

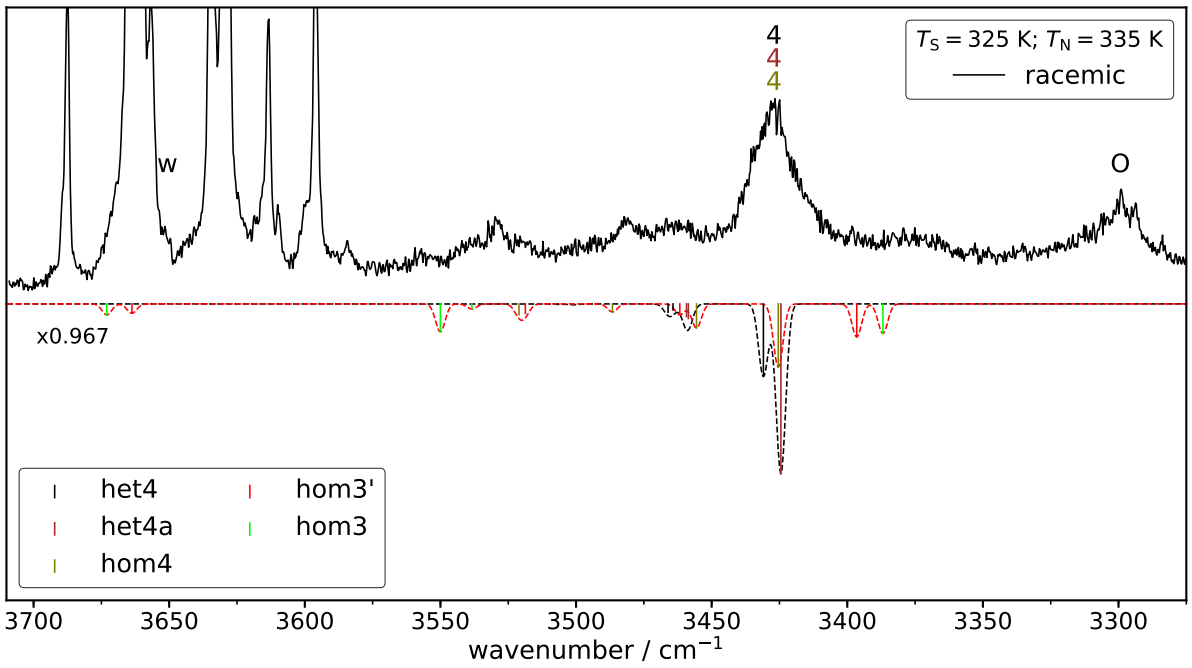

Fig. 4.23: Experimental Raman data (plotted upwards) and simulated data (plotted downwards) of 3-butene-1,2-diol (0-V). The saturator temperature (T_S) as well as the nozzle temperature (T_N) are given. The simulated spectra are based on B3LYP/maTZ and are scaled by 0.967 according to the factor derived for propane-1,2-diol (see Fig. 4.19 (page 166)). w indicates a water band and O oligomer bands.

can also not be assigned. Furthermore, the rather broad signal around 3375 cm^{-1} could be due to an overlap of hom3' and hom3.

Additionally, around 3300 cm^{-1}, a comparatively large signal can be observed that likely belongs to oligomers, due to the strong downshift. Curiously, the band already appeared at moderate backing pressures of 0.5 bar, while the spectrum shown in Fig. 4.23 was measured at 1.4 bar. Given the strong downshift, it is still more likely to be caused by a oligomer (trimer). Out of all computed structures, the one with the strongest downshift has a scaled band at 3338 cm^{-1}, hence, being somewhat close to the signal. However, the corresponding dimer lies 10 kJ mol^{-1} above the global minimum. Therefore, said dimer is a very unlikely candidate. Other dimers do not match in terms of their downshift. Consequently, the clustering propensity of 0-V is most likely quite high. Moreover, three distinct signals can be made out at 3299 cm^{-1}, 3294 cm^{-1} and 3284 cm^{-1} on top of the broader structure. Such narrow signals are highly unusual for trimers or higher clusters, since lifetime broadening is quite substantial in those cases. This phenomenon can be investigated in the future. Furthermore, a concentration series could make sure that the band at 3300 cm^{-1} is in fact due to a trimer or higher oligomers.

The assignments could be greatly aided by measuring the enantiopure compound. In this way, the overlap of hom4 and het4/het4a can be removed. Moreover, homo chiral bands in general can be clearly identified due to their increase in intensity. If no signal enhancement can be observed an overlap with a hetero-chiral dimer can be confirmed. Furthermore, given the exclusionary behaviour of the motifs with four hydrogen bonds, IR spectroscopy is another great tool for assignment. A simulated IR spectrum contrasted with the Raman predictions and experiment is shown in Fig. C.20 (page 290) to illustrate this point. As was the case before for 0-M, the permanent dipole moments of the structures with four hydrogen bonds are very small. Therefore they do not lend themselves to an investigation with microwave spectroscopy. However, the non cyclic homo-chiral dimers could be measured *via* rotational spectroscopy. Furthermore, higher level electronic structure methods could help narrow down the relevant homo-chiral dimers in a meaningful way. Additionally, given the flexibility of the systems, the structure search should be extended.

4.3 Influence of dispersion on chirality recognition

The results presented here have been published in Ref. [101]. With ethane-1,2-diol (0-0), *trans*-cyclohexane-1,2-diol (t6-6) and pinacol (MM-MM) examples have been found that energetically strongly favour a hetero-chiral pairing, *i.e.* chirality recognition is taking place. Judging from the systems studied in the previous sections, this phenomenon appears to be rare and the exact origin of this effect is unclear. For hydrogen bonded systems, as discussed here, charge transfer and electrostatic interactions are generally assumed to be the driving force of stabilisation. Another type of interaction, whose importance has been recognised more and more in the past two decades, is dispersion also referred to as London forces. In this section the influence of dispersion on the het-hom gap will be discussed.

To judge the influence of dispersion local variants of MP2 and SCS-MP2 are used. Computational details can be found in Ref. [101]. In this local framework, the double excitations can be grouped in types of interactions, including dispersion (see Fig. 2.4 (page 22)). This also allows for the computation of dispersion free gradients and Hesse-matrices, as the dispersion contributions can be excluded from the electronic energy. These wavefunction theory based results can be compared to DFT calculations including and neglecting dispersion correction (D3(BJ,abc)). However, it is important to recognise, that neglecting D3(BJ,abc) is not synonymous with a dispersion free case. DFT already includes London forces at short distances and the D3(BJ,abc) term cannot be taken as the dispersion

energy. Moreover, D3 introduces four additional empirical parameters, which may also correct for other deficiencies of a given functional (*e.g.* exchange part). The commonly used BP86, PBE, PBE0 and B3LYP functionals have been investigated. A comparison with the rigorously defined dispersion contributions of WFT allows to judge the use of D3 term as a dispersion indicator, as it is often done. Previous studies suggest that the agreement between the two varies greatly[278]. In the following no dispersion in the context of DFT means the neglect of D3.

Firstly, structural effects will be discussed. A total of 11, 10 and 6 dimers are compared for 0-0, t6-6 and MM-MM, respectively. The set of conformers is limited due to some conformers converting to completely different structures without dispersion. Hence, a structural comparison is not possible in these cases. An easy way to gauge such effects, is to analyse the difference of the distance between the centre of mass of the monomer subunits in the dispersion (d) and no dispersion (nd) case $\Delta R(\mathrm{CM}-\mathrm{CM})$. This is illustrated in Fig. A.26 (page 238) for LMP2, SCS-LMP2 and B3LYP. In all cases the monomers start separating once dispersion is excluded. This effect is the strongest for LMP2 followed by SCS-LMP2 and B3LYP. The fact that B3LYP shows comparatively small changes can be explained by the short range dispersion contributions that are already included in DFT. The higher sensitivity of LMP2 in comparison to SCS-LMP2 can be attributed to typical overestimation of London forces of MP2, which the spin component scaling (SCS) approach at least partially remedies[124]. For LMP2 and SCS-LMP2 the distances increase consistently by about 0.30 Å and 0.23 Å upon the exclusion of dispersion, respectively. In case of B3LYP, the results are less consistent, with 0.12 Å, 0.20 Å and 0.16 Å for 0-0, t6-6 and MM-MM, respectively. Therefore, t6-6 most closely resembles the effects found in the WFT case.

Another structural quantity is the change of the intermolecular hydrogen bond lengths. Such a comparison is shown in Fig. 4.24. This is done in the form of kernel density estimates (KDE), whereby a histogram is transformed into a continuous curve. More details about the creation can be found in the ESI of Ref. [101]. The different methods show very similar behaviour to the $\Delta R(\mathrm{CM}-\mathrm{CM})$ case, *i.e.* B3LYP shows small changes upon neglect of dispersion while this effect is much more pronounced for LMP2 and SCS-LMP2. Moreover, the changes for LMP2 are again slightly more prominent than for SCS-LMP2. Additionally, the distributions get much broader for the MP2 variants in comparison to B3LYP, with the exception of MM-MM. For MM-MM, the distributions are already much broader for all methods including dispersion. Overall, it is evident that the neglect of D3 does not accurately reflect the structural changes expected when dispersion is rigorously excluded.

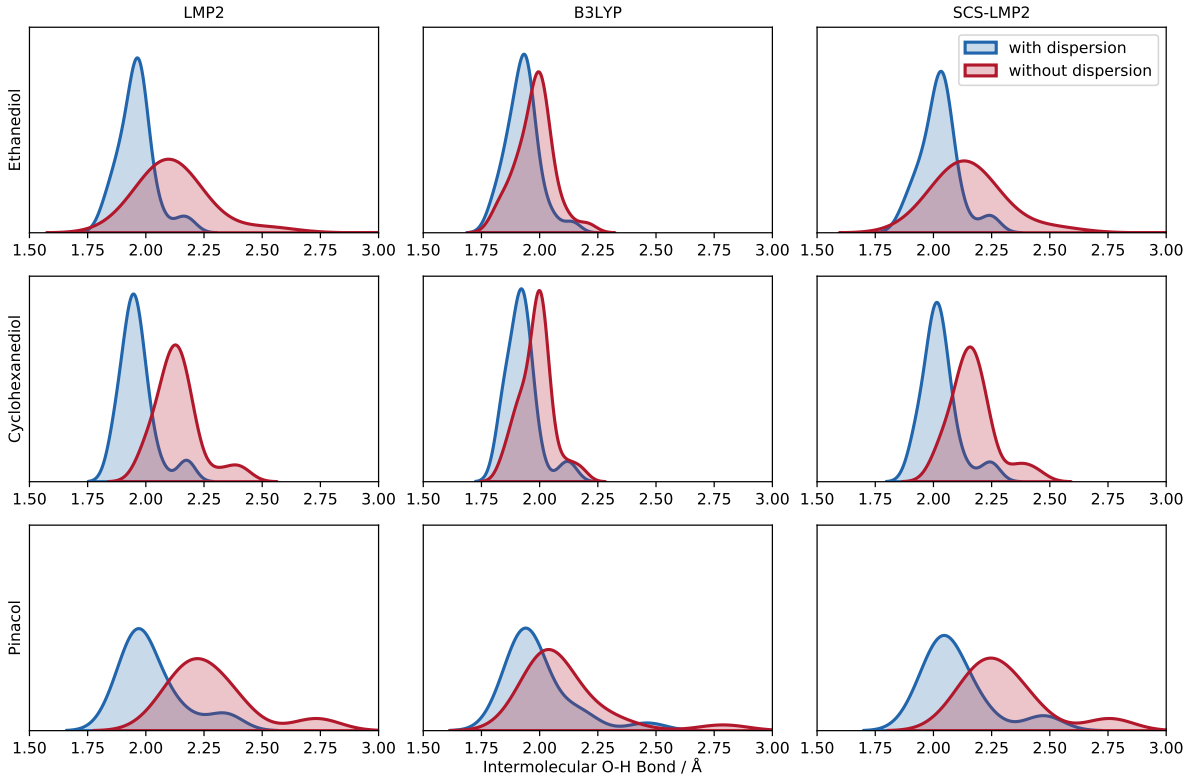

Fig. 4.24: Kernel density estimate (KDE) plot of the intermolecular O–H bond distance for the three molecular systems (top to bottom) evaluated at different levels of theory (left to right). Blue indicates results with dispersion while red shows the results without dispersion. Each O–H bond distance is represented in the density plot to illustrate the frequency and distribution. This figure is taken from Ref. [101] and more information regarding the KDE can be found therein.

The exclusion of dispersion also heavily influences the energetic het-hom gap, which is illustrated in Fig. 4.25. It can be seen that B3LYP, LMP2 and SCS-LMP2 are very sensitive with the het-hom gap shrinking significantly when dispersion is excluded. BP86 shows fairly large relative changes, but since the starting point is higher the het-hom gap remains substantial. PBE and PBE0 are comparatively indifferent with regards to the exclusion of dispersion, with the exception of PBE in case of pinacol. It is also noticeable, that SCS-MP2 exhibits a smaller het-hom gap for the dispersion case than the other methods. However, PNO-LCCSD(T)-F12b calculations, using the geometries of B3LYP and the LMP2 variants, with the corresponding zero point vibrational energies, are more in line with the results of B3LYP, PBE0 and LMP2. Of the tested DFT methods only B3LYP behaves in line with the WFT ones. Hence, one should be very cautious when judging the influence of dispersion based on D3. Such an analysis based on PBE0, for instance, would indicate that dispersion only plays a minor role. Furthermore, instead of re-optimising geometries obtained with D3, the D3 term is often just subtracted. Doing so leads to

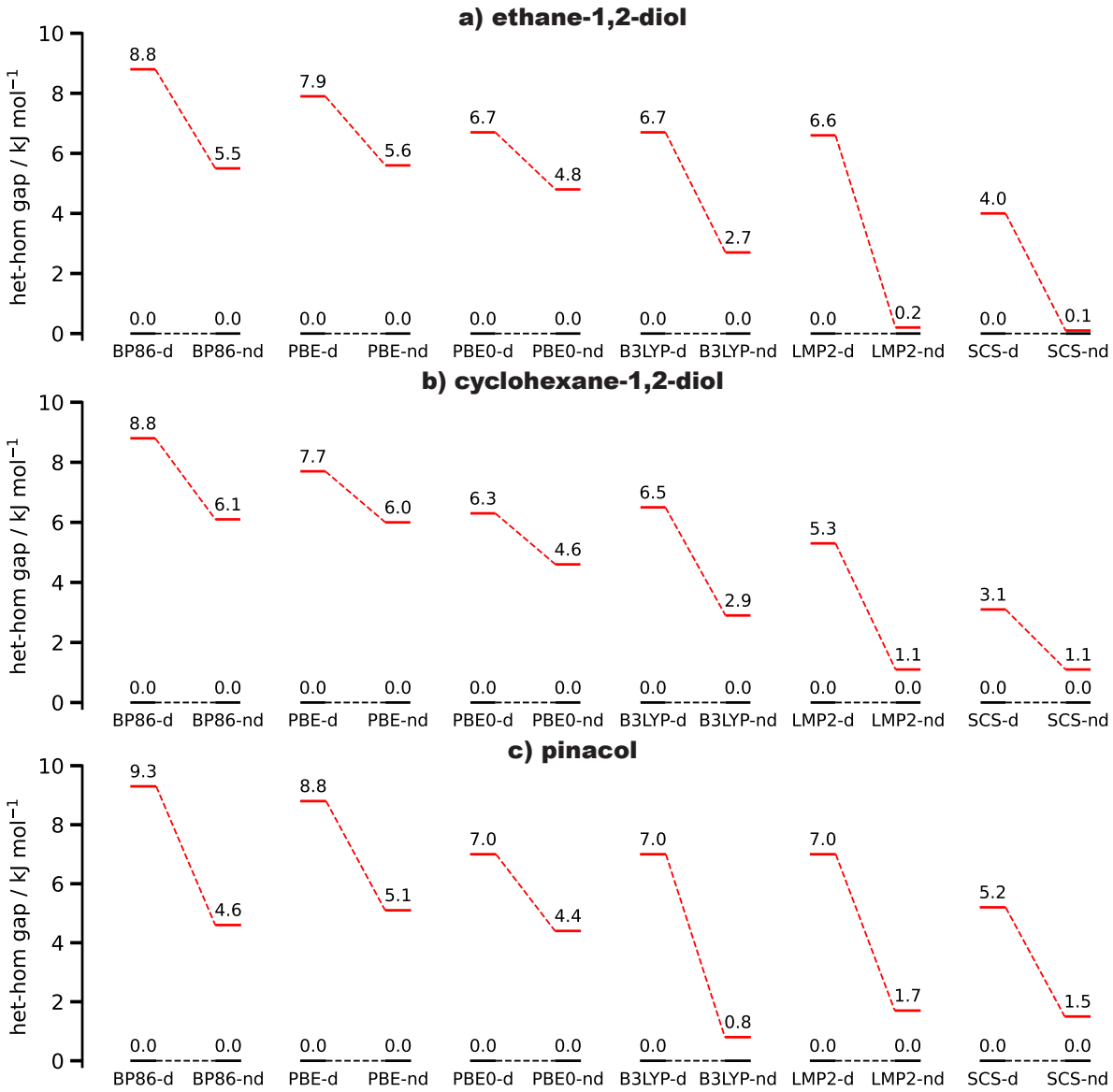

Fig. 4.25: Change of the het-hom gap when dispersion is included (d) and excluded (nd) at different levels of theory for ethane-1,2-diol, *trans*-cyclohexane-1,2-diol and pinacol. This figure has been adapted from Ref. [101].

smaller changes of the het-hom gap in comparison to fully re-optimised structures, as it was done in Fig. 4.25. This difference is especially large for pinacol. For example, B3LYP would exhibit a non-dispersion het-hom gap of 4.5 kJ mol^{-1} in comparison to 0.8 kJ mol^{-1} for the re-optimised case. Curiously, LMP2-d single point calculations with geometries optimised at LMP2-nd level (LMP2-d//LMP2-nd), show an almost unchanged het-hom gap in comparison to the full LMP2-d case. Similarly, LMP2-nd//LMP2-d calculations closely resemble the LMP2-nd//LMP2-nd case. Therefore, it can be concluded that for WFT the het-hom gap is not significantly impacted by the structure, but instead by electron correlation.

Although, it was previously mentioned that energetic chirality recognition is present, it is unclear where the line should be drawn for such a phenomenon. It can be argued that chirality recognition will always be present in terms of the populations, once sufficiently low temperatures have been reached. Hence, the question can be reframed to ask: "At what temperature does chirality recognition no longer manifests itself?". To this end, the relative standard Gibbs energies (ΔG) have been computed for different temperatures ranging from 0 K up to 400 K. ΔG can then be compared to the thermal energy (RT). As a qualitative measure once RT reaches the energy of the most stable homo-chiral dimer, it can be said that chirality recognition no longer manifests. Details with regards to the calculation of ΔG can be found in Ref. [101].

Such a comparison is shown in Fig. 4.26 for B3LYP. Since B3LYP behaves very similar to the LMP2 variants, a close resemblance is also expected for ΔG. To gauge the influence of dispersion, the crossing point of the lowest lying homo chiral dimer (red lines) with the thermal energy (green line) has to be determined. For ethanediol, this is around 270 K for the dispersion and 160 K for the no dispersion case. Therefore, chirality recognition is still present at much higher temperatures when dispersion is included. Cyclohexanediol shows similar behaviour, with values around 240 K and 140 K with and without D3, respectively. Pinacol yet again shows a higher sensitivity than the other two systems, with a shift of about 260 K. Overall, it can be shown that dispersion is an important factor in the manifestation of chirality recognition. For these diols it could be argued, that chirality recognition would be a low temperature phenomenon without dispersion. Such an analysis can also be applied to other systems, as it is cheap and generally applicable. However, it should be kept in mind, that this is a qualitative measure.

Moreover, the local approach allows to segment the dispersion interactions of the two monomer subunits. In this way, the contributions of the backbone and the OH groups can be differentiated. Specifically, the interaction of one entire monomer with the OH groups and the backbone of the other monomer have been investigated. Everything that is not an OH group is considered part of the backbone. Advantage of dividing the interactions in this way is that the sum of the backbone and OH contribution will be equal to the total dispersion energy.

This is illustrated in Fig. 4.27 for SCS-LMP2. It can be seen, that het4 has the largest dispersion contributions in all cases. By simply looking at the energy differences based on the dispersion energy (E_{Disp}) the het-hom gap can be reproduced, highlighting the importance of London forces for these systems. Moreover, E_{Disp} increases along 0-0, t6-6 and MM-MM. The fact that E_{Disp} is higher for MM-MM than t6-6, despite having almost the same number of electrons, shows that dispersion favours more compact structures rather

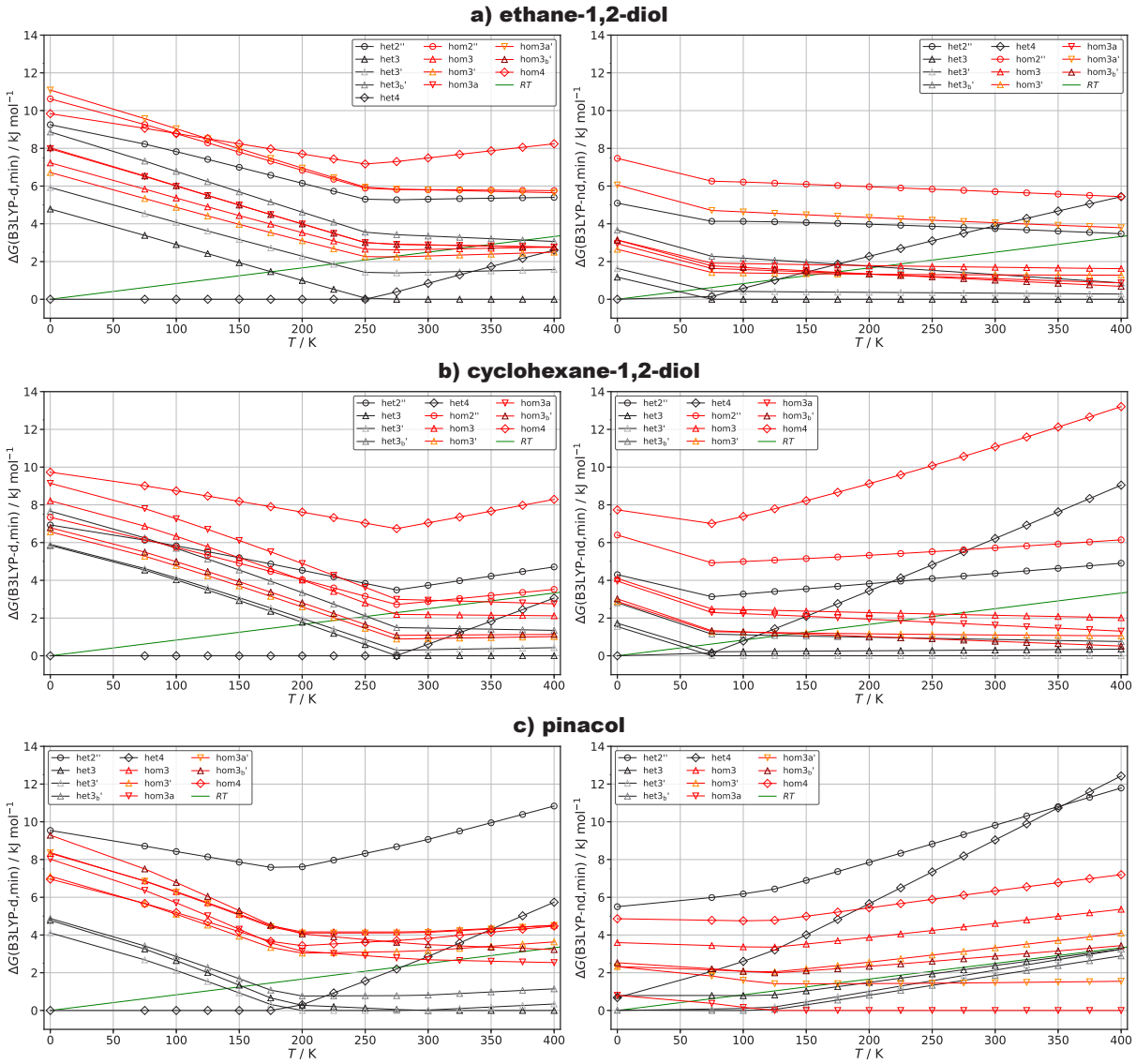

Fig. 4.26: Harmonic standard Gibbs energies (ΔG) relative to the minimum at different temperatures shown for ethane-1,2-diol (top), *trans*-cyclohexane-1,2-diol (mid) and pinacol (bottom). The results are shown for B3LYP-d (left side) and B3LYP-nd (right side). Hetero dimers are highlighted in black and homo dimers in red. The thermal energy (RT) is shown in green. This figure has been adapted from Ref. [101].

than extended ones as is the case for t6-6. Furthermore, the largest contributions to E_{Disp} come from the OH groups as one might expect. However, the importance of the backbone increases continuously along the lines of 0-0, t6-6 and MM-MM. This is especially true for MM-MM where the backbone contributes up to 41% to the total E_{Disp} in case of het2". Moving to larger groups such as ethyl- or phenyl-groups would likely lead to the backbone contributing most the to E_{Disp}. LMP2 shows very similar behaviour, although hom4 becomes slightly more competitive for 0-0 and t6-6. Moreover, LMP2 yields about 13% higher E_{Disp} on average than SCS-LMP2, which is commonly observed[124].

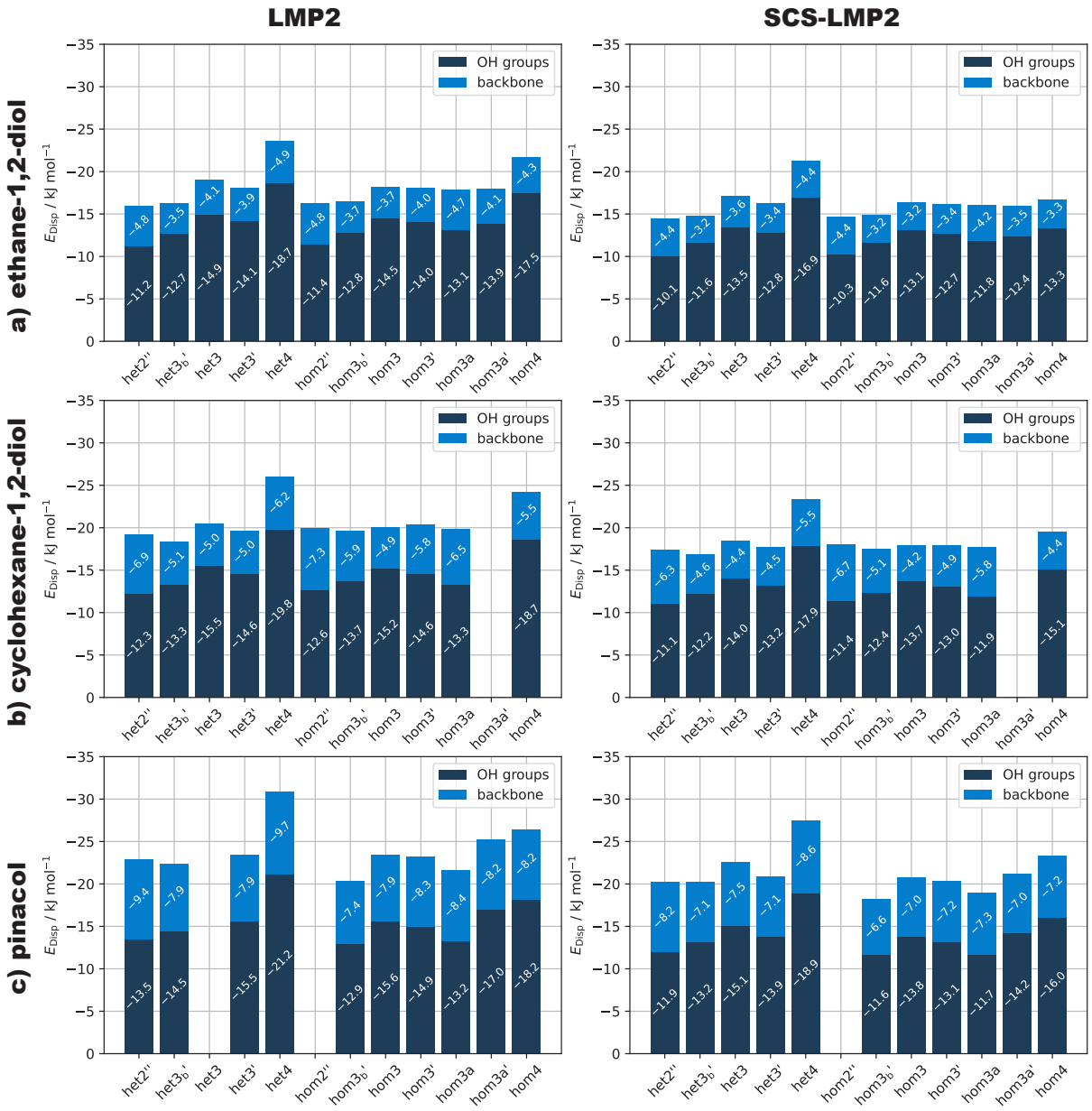

Fig. 4.27: Overview of the intermolecular dispersion contributions of the OH groups (dark blue) and the backbone (light blue) for a) ethanediol (top row), b) cyclohexanediol (middle row) and c) pinacol (bottom row) for the LMP2-d (left side) and SCS-LMP2-d (right side) results. Zero values indicate that a conformer either converges to a different one or exhibits an imaginary frequency. This figure has been adapted from Ref. [101].

Furthermore, the dispersion energy can be visualised by using the dispersion interaction density (DID)[279,280]. Here the dispersion energy is mapped upon the orbital density. In this way interacting fragments can quickly be spotted and differences made clear. In case of the S_4 symmetric het4, even the symmetry is retained.

5 Summary

The monomers of 17 different vicinal diols have been characterised vibrationally. These systems included varied methylation patterns, π-systems, fluorine interactions and vicinally as well as geminally bridged alkane rings. The experimental OH-stretching frequencies have been compared with harmonic frequencies obtained with the four commonly used density functionals BP86 PBE, PBE0 and B3LYP. Based on some unambiguous initial assignments for each degree of substitution (n_D), *i.e.* amount of substituted CH groups of ethane-1,2-diol (0-0), a linear model was derived and its predictive capabilities were tested. As was found in a previous study for mono-ols[31], B3LYPs performance heavily depends on the degree of substitution while the other tested functionals behaved indifferent to n_D. Furthermore, to describe the training sets, the BP86 and PBE fits had to be heavily scaled and to a lesser extent PBE0 as well. Out of the tested functionals, B3LYP performed the best, able to describe intramolecular hydrogen bond shifts remarkably well. However, if ring strain is introduced, as was the case with *trans*-cyclo-butane-1,2-diol (t4-4) and [1,1'-bicyclopentyl]-1,1'-diol (CP-CP), its predictive capabilities suffer. Systems including π interactions also were described worse. For phenyl-groups, a correction of $-8\,\mathrm{cm}^{-1}$ was successfully applied to related systems. Additionally, different fitting strategies were tested and a division into conformational families, separating donor and acceptor modes, appears to be promising to improve the results for BP86 and PBE.

Moreover, SCS-LMP2 and LCCSD(T)-F12 calculations have been conducted on some selected systems. Wavefunction theory also showed no dependence upon n_D, but improvements can be made by the division into conformational families. LCCSD(T)-F12 behaved especially uniform with regards to n_D. Furthermore, tri-*tert*-butyl-methanol was investigated as a potential "intermolecular diol" in terms of its dimer. This is due to the fact that the intermolecular hydrogen bonds are rather long given the bulkiness of the *tert*-butyl groups. The successfulness of the model is limited in this case, however, clear evidence was found for the formation of hydrogen bonded dimers opposite to results for the solid[237,239] and liquid phase[237,238]. Additionally, 3-chloro-propane-1,2-diol (0-Cl_1) and 3-bromo-propane-1,2-diol (0-Br_1) have been studied, for which the linear model is not sufficient. Some initial testing was done for the simpler 1-bromo-propan-2-ol and

2-bromo-propan-1-ol as well as for its chlorine derivatives. For these systems, anharmonic calculations (VPT2) were conducted and it was found that B2PLYP performed the best. Here, a correction of $+12\,\mathrm{cm}^{-1}$ was derived from the mono-ols and extended to the diols making assignments possible.

For the Cl- and Br-containing systems microwave spectra were analysed. The vibrational assignments for the mono-ols were confirmed, with the Cl case having been previously characterised by Goldstein *et al.*[244] rotationally. For the diols, all conformers that have been assigned in the OH stretching region were also found in the microwave spectra for 0-Cl_1. In case of 0-Br_1, four of the six conformers found in the Raman spectra were assigned. However, the missing conformers are likely present but could not be assigned due to the high density of lines in the microwave spectra. The rotational assignments include the ^{35}Cl, ^{37}Cl, ^{79}Br and ^{81}Br isotopologues. For these quadrupolar nuclei the nuclear quadrupole coupling constants (NQCC, χ_{ij}) were determined and its asymmetry parameter (η) calculated. η was correlated with the OH-stretching mode involved in an intramolecular OH contact to the halogen atom. It was found that η could potentially be used as a probe for hydrogen bond strengths. However, it appears as if at some point a value of maximal asymmetry is reached for vicinal diols ($\eta \approx 0.064$). Furthermore, the obtained η are very similar between the corresponding Cl and Br conformers. For the description of the rotational constants, B2PLYP again performed the best, while CCSD(T) yielded the best description of the NQCC. Furthermore, a significant impact of relativistic corrections was found for Br, while Cl was unaffected. It should be kept in mind that computed constants were derived from the equilibrium geometry, but are compared to experimental results derived from the vibrational ground state.

Moreover, the self aggregation of ethane-1,2-diol (0-0), *trans*-cyclohexane-1,2-diol (t6-6), pinacol (MM-MM), *trans*-cyclopentane-1,2-diol (t5-5), *trans*-cycloheptane-1,2-diol (t7-7), propane-1,2-diol (0-M), 2-methyl-propane-1,2-diol (0-MM) and 3-butene-1,2-diol (0-V) was studied. The het-hom gaps of these systems are shown in Fig. 5.1. It can be seen that only MM-MM, 0-0 and t6-6 show a strong energetic preference for hetero-dimers. These systems are also the most similar with regards to their monomers. 0-M and 0-V still show a preference for hetero-dimers but the het-hom gap is approximately cut in half. 0-MM, t5-5 and rM-M show no clear favourite. This is especially true for t5-5 and rM-M where the hetero- and homo-dimers behave isoenergetically. t7-7 is the only system which could be identified that favours homo-dimers. A het4 type dimer dominates the hetero-chiral conformational landscape, with t7-7 being the only system where it does not constitute the hetero-chiral (het2") as well as global minimum (hom2"). The most stable homo-chiral dimers showed significantly more variation. Trends observed regarding ring

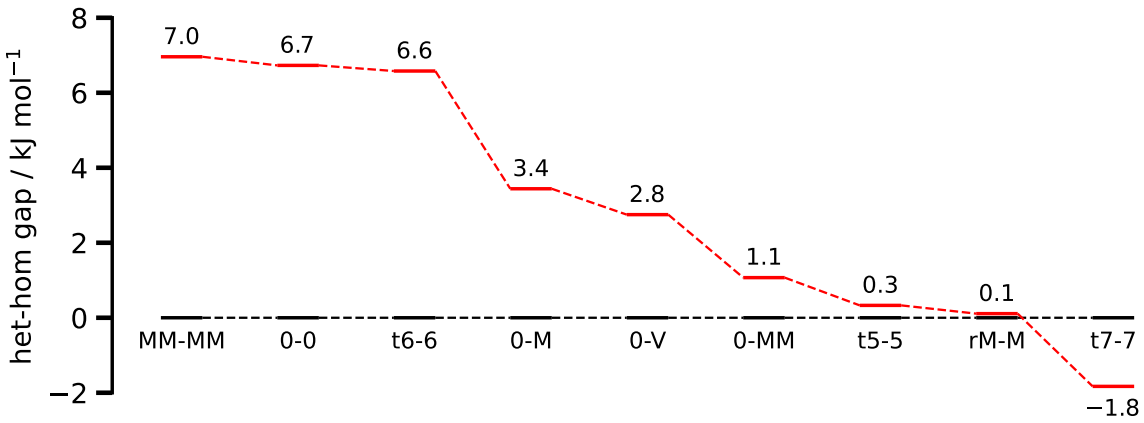

Fig. 5.1: Overview of the het-hom gap of ethane-1,2-diol (0-0), *trans*-cyclohexane-1,2-diol (t6-6), pinacol (MM-MM), *trans*-cyclopentane-1,2-diol (t5-5), *trans*-cycloheptane-1,2-diol (t7-7), propane-1,2-diol (0-M), 2-methyl-propane-1,2-diol (0-MM) and 3-butene-1,2-diol (0-V). Hetero-dimers are indicated by black and homo-dimers by red energy levels.

size can be explained by the increase (t5-5) or decrease (t7-7) of the monomer oxygen-oxygen distance relative to t6-6. In either case, het4 is specifically destabilised.

The apparent lack of homo-dimers in the vibrational spectra for the transiently chiral 0-0, described in Ref. [18] was resolved. By spectral analogy with the permanently chiral t6-6, the homo-dimers of 0-0 were identified. It was found that 0-0 behaves as permanently chiral in supersonic expansions, with dimers forming largely statistically. Additionally, the homo-chiral assignments for t6-6 were verified *via* microwave spectroscopy. Moreover, the complementary use of Raman and IR spectra was highlighted for 0-0 and t6-6. For the transiently chiral MM-MM, only the most stable hetero-dimer could be conclusively identified, due to the homo-chiral conformational landscape being very complicated. In case of rM-M, which shares structural similarities with t6-6, homo-chiral and hetero-chiral dimers were observed. Additionally, an unusually high scaling factor was found for rM-M. Using some simplifying strategies, the spectra of t5-5 were adequately explained. t7-7 provided a significant challenge due its conformational flexibility. Therefore, the amount of considered conformers was heavily reduced providing tentative evidence for homo- and hetero-chiral dimers. For 0-M, the Raman spectra recorded could confirm assignments previously made based on FT-IR results[225]. Furthermore, an additional conformer with two intermolecular hydrogen bonds was assigned in the Raman spectra. For the transiently chiral 0-MM, the experimental spectrum could be explained, again utilising some simplifying strategies. Moreover, the introduction of a π-system (0-V) vastly complicated the homo-chiral conformational landscape. The most stable hetero-chiral dimers were spectrally identified, however, no clear homo-dimer assignments could

be made.

Using local energy decomposition analysis (LMP2, SCS-LMP2), dispersion was identified as an important driving force for energetic chirality recognition found in 0-0, t6-6 and MM-MM. In the local framework dispersion can be rigorously excluded in the optimisation and frequency calculation, unlike the functional dependent D3 dispersion correction used for density functional theory (DFT). A comparison of wavenfunction theory (WFT) with DFT showed that one should be very cautious when judging the influence of dispersion based on D3. Of the BP86, PBE, PBE0 and B3LYP functionals, only the latter showed a similar behaviour as the WFT side. Furthermore, the structural changes are significantly stronger for WFT than for DFT, once dispersion is neglected or no dispersion correction used in the latter case. This can be rationalised by the fact that short range dispersion is already included in DFT. Additionally, it was found that the het-hom gap is an electron correlation effect for WFT and not significantly impacted by the structural changes. For DFT, on the other hand, differences in structure due to the neglect of D3 are important to the het-hom gap and full optimisations should be carried out with and without D3 if the influence of dispersion is supposed to be judged.

Moreover, an analysis of relative Gibbs energies (ΔG) at different temperatures illustrated the importance of London forces for the manifestation of chirality recognition. Here, manifestation refers to the fact that at sufficiently low temperatures any energy difference will result in chirality recognition in terms of the populations. This tipping point is estimated to be reached once the thermal energy (RT) reaches ΔG of the most stable homo-chiral dimer (hetero-chiral dimer constitutes the global minimum). It was found that this point is reached at much lower temperatures when D3 is not used. This is especially true for pinacol, where chirality recognition would be considered a low temperature phenomenon without D3. Additionally, within the local framework the dispersion energy can be divided in contributions from the OH groups and the backbone. Going along the series of 0-0, t6-6 and MM-MM the dispersion energy increases and the backbone becomes more important. However, in all cases the main contributions stem from the OH groups. Furthermore, despite having a very similar amount of electrons MM-MM benefits more from dispersion than t6-6, highlighting the importance of compact structures for London forces.

6 Outlook

The derived correlations from section 3.1 (page 29) can be tested with a more diverse set of systems in the future. For tri-*tert*-butyl-methanol, indications were found that not only the α, but β or even γ substitution as well may play a role. A publication analysing these effects is currently in preparation. Good candidate diols for such an investigation would be: butane-1,2-diol, 3-methyl-butane-1,2-diol, 3,3-dimethyl-butane-1,2-diol, pentane-1,2-diol, pentane-2,3-diol and 2-methyl-butane-1,2-diol. All structures proposed for further investigation are shown in Fig. 6.1. Other interesting test cases would include 1,2-diphenyl-1,2-ethanediol (hydrobenzoin) and hexa-1,5-diene-3,4-diol. In these cases, the indicated systematic shift caused by phenyl groups and possibly also vinyl groups could be tested. However, for the former, a sufficient vapour pressure may not be reached. Furthermore, the poor performance of the linear model for the mono-halogenated species can be investigated. Since the model yielded accurate results for 3,3,3-trifluoro-propane-1,2-diol, the corresponding chlorine or bromine derivatives could be tested. Alternatively, the mono-fluorinated compound could be investigated. In this way, the tri- and mono-substitutions can be decoupled from the choice of halogen. Given the better commercial availability of 3-fluoropropane-1,2-diol, it would be a better starting point. Additionally, a strong dependence of the shifting parameter $a2$ was found for strained geminally and vicinally bridged rings. Here, the vicinally bridged *trans*-cyclopropane-1,2-diol and geminally bridged 1-hydroxymethyl-cyclohexanol, 1-hydroxymethyl-cyclopentanol and 1-hydroxymethyl-cyclobutanol could be studied. Furthermore, overtones, hot bands and combination bands could measured to gain information about the anharmonicity constants. In this way it could be determined if the degree of substitution and/or different conformational families actually result in different anharmonicities.

Moreover, the stronger mode coupling computed for systems involving non-oxygen hydrogen bonds/contacts can be explored in more detail. The hydrogens of each OH group can be replaced with deuterium or tritium separately, this way coupling can be removed. The predictive capabilities of the linear model may improve by removing the coupling. Furthermore, evidence was found that a combined model for mono-ols and diols could be derived. The practicality of such an approach can be further investigated. Additionally,

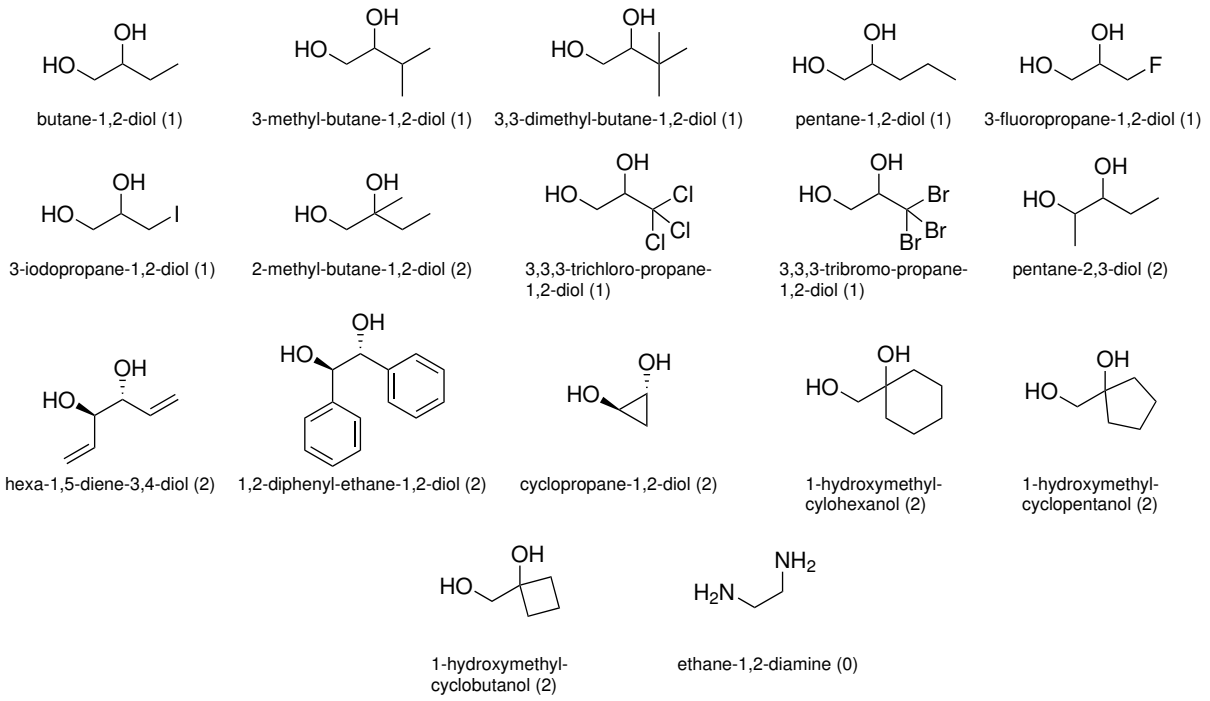

Fig. 6.1: Overview of the proposed systems for further investigation. The degree of substitution n_{D} is shown in parentheses.

1-chloropropan-2-ol and 2-chloropropan-1-ol and their bromine derivatives were vibrationally characterised and can be used to test the mono-ol model derived by R. Medel[31]. Besides, high level harmonic coupled cluster calculations as well as anharmonic density functional calculations have been performed for the mono-halogenated systems. The harmonic calculations can be combined with the computed anharmonicity constants and may provide very good predictions, as other studies have shown before[168,247–249].

The anharmonic calculations also provide rotational distortion constants (D_J, D_{JK}, D_K, d_1 and d_2). These have not yet been systematically compared to the experimental microwave data. Furthermore, the zero point averaged rotational constants predicted by VPT2 can be compared to the experimental ones. Moreover, the performance of the model to predict nuclear quadrupole coupling constants (NQCC, χ_{ij}), as derived by W. C. Bailey[253], can be tested. Additionally, instead of fitting the nuclear spin-rotation coupling constants (C_{ii}), the distortion constants of the NQCC (χ_J, χ_K) could be used for the Br-containing compounds. Furthermore, 3-iodopropane-1,2-diol could be investigated to explore the possibility of a maximal asymmetry of the NQCC (η). Here, stronger relativistic effects would also be expected. Besides, the good performance of anharmonic B2PLYP frequency predictions can be tested. Interestingly, it may be possible to make predictions for η once the frequencies have been measured or *vice versa*. Moreover, some

of the off-diagonal NQCC (χ_{ab}, χ_{ac} and χ_{bc}) could not be accurately determined for the Cl-containing compounds. To resolve this issue measurements with the newly developed cavity microwave setup of the Obenchain group can be conducted for some select conformers.

Additionally, the microwave spectra of 3-bromopropane-1,2-diol can be further analysed to find two more conformers which are expected to be present. Furthermore, for the most stable conformer of 3-chloropropane-1,2-diol (^{35}Cl), the three different singly ^{13}C substituted isotopomers ($^{12}C_2{}^{13}C^1H_7{}^{16}O_2{}^{35}Cl$) have been fitted, but not yet closer analysed. Here, the substitution structure (r_S), according to Kraitchman's method[281], can be determined and compared to computed structures. The r_S structure provides information about the positions of the chlorine and all three carbon atoms within the molecule. Deuteration experiments would also allow for the determination of the position of the hydrogen atoms. More sophisticated approaches can also be used for the structure determination, such as the methods developed by Watson *et al.*[282] and others using Z. Kisiel's STRFIT program[283]. Furthermore, the microwave spectra of 3-chloropropane-1,2-diol show a large variety of unassigned lines which can be investigated with regards to dimers or possibly other isotopologues.

Besides the halogen systems, microwave spectra of ethane-1,2-diol (0-0), *trans*-cyclopentane-1,2-diol (t5-5), pinacol (MM-MM) and *cis*-cyclohexane-1,2-diol (c6-6) have been recorded, which have not yet been analysed. For ethane-1,2-diol, the monomers have been characterised *via* rotational spectroscopy[178,210–213], while the other systems have not been yet investigated with regards to their monomers and dimers. In case of 0-0, Luca Evangelisti (University of Bologna) and his group agreed to join their data with the microwave spectra recorded here and have made some preliminary dimer and trimer assignments already. Moreover, the monomers of t5-5 are also of considerable interest due to difficulties assigning bands in the Raman spectrum.

For the dimers studied in this work, IR spectra can be measured to validate the assignments or in some cases make an assignment possible at all, with the exception of 0-0 and t6-6 where such spectra have already been recorded. In general, the comparison of simulated Raman and IR spectra highlights the complementary behaviour of the symmetric species studied in this work. Furthermore, higher level electronic structure methods are necessary to study the conformational landscape of some systems. This is especially true for *trans*-cycloheptane-1,2-diol (t7-7) and 3-butene-1,2-diol (0-V), where a lot of conformers are within very close energetic proximity. t7-7 would also lend itself to an investigation with energy decomposition schemes to understand its homo-chiral preference. Moreover, enantiopure spectra of t5-5, t7-7 and 0-V can be measured to corroborate the homo- and

hetero-dimer assignments. Additionally, Raman spectra of 1-phenyl-ethane-1,2-diol (0-Ph) have been recorded under dimer conditions but not yet analysed. Here, π stacking effects may play a role. Another interesting possibility is the investigation of transiently chiral systems in the shock-wave of the supersonic expansion. Given the temperature increase in the shock-wave region it might be possible to observe chirality synchronisation.

Furthermore, higher oligomers can be analysed which was already done for 0-0 and t6-6 at the B3LYP-D3(BJ,abc)/def2-TZVP level of theory[165]. An overview of the het-hom gap up to tetramers is shown in Fig. 6.2. As can be seen, the het-hom gap increases with the size of the oligomer. This can be attributed to the fact that the more extended cyclic systems allow for more linear hydrogen bonds. For instance, the cyclic hetero-dimers show a progression of the average $\angle O_D H_D O_A$ of 150°, 160° and 168° for the dimer (het4), trimer (hot6) and tetramer (het8), respectively. BSSE effects for the larger oligomers are expected to be small given the similar structural motifs. Curiously, the cyclic dimers can

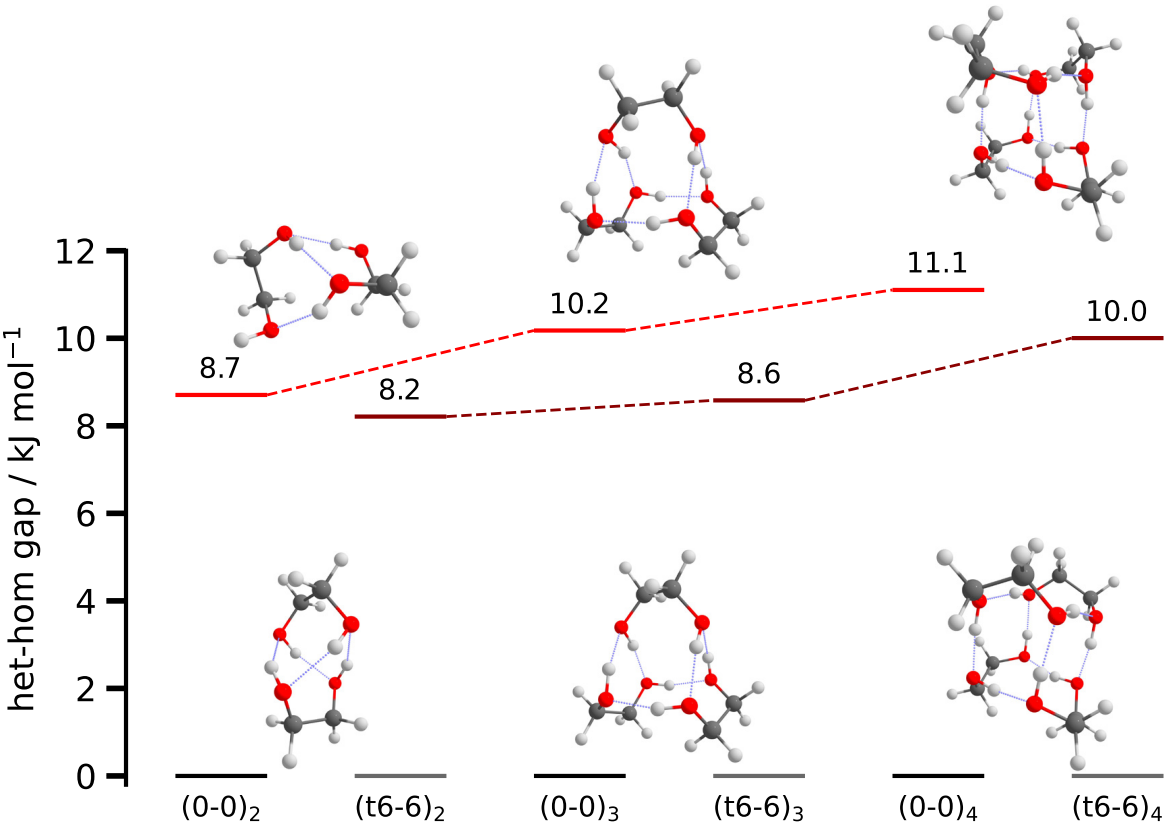

Fig. 6.2: Overview of the het-hom gap for the dimers (0-0)$_2$/(t6-6)$_2$, trimers (0-0)$_3$/(t6-6)$_3$ and tetramers (0-0)$_4$/(t6-6)$_4$ of ethane-1,2-diol (0-0) and *trans*-cyclohexane-1,2-diol (t6-6). Red and dark-red energy levels indicate homo-dimers and black and grey energy levels hetero-dimers. The most stable hetero- and homo-oligomers are shown for 0-0. The t6-6 equivalents are closely related. The energies are computed at the B3LYP-D3(BJ,abc)/def2-TZVP level of theory and zero-point corrected.

be generated easily by inserting a monomer into the previous structure. Furthermore, the structures of the trimers and tetramers are closely related to the water hexamer (cage)[284] and octamer[285], respectively. Additionally, the symmetry of the water clusters is retained with hot6 being C_2 and het8 being S_4 symmetric. These similarities may still hold for the 0-0 pentamers with the water decamers[286]. The evolution of the het-hom gap has some very interesting implications for 0-0 since it crystallises in separate *gauche* + and − hydrogen bonded networks[287]. Hence, in very large assemblies the hetero-chiral preference should reverse at some point. Experimental spectra have been recorded of 0-0 that indicate the presence of tetramers or even pentamers but not yet analysed. Moreover, other systems that have been studied in this work showed clear evidence of higher clusters which can be investigated in the future. These include: butane-2,3-diol (rM-M), propane-1,2-diol (0-M) and 3-butene-1,2-diol (0-V).

Lastly, a plethora of different dimer systems have been studied computationally at the B3LYP-D3(BJ,abc)/ma-def2-TZVP and B3LYP-D3(BJ,abc)/def2-TZVP level of computation. An overview of the het-hom gap is shown in Fig. 6.3. It should be kept in mind that the results are preliminary and the structural searches non exhaustive. However, it can be seen that energetic chirality recognition appears to be an exceedingly rare (otherwise observed for 0-0, t6-6 and MM-MM) phenomenon with only [1,1'-bicylopentyl]-1,1'-diol (CP-CP) and 3-fluoropropane-1,2-diol (0-F_1) showing a very pronounced preference

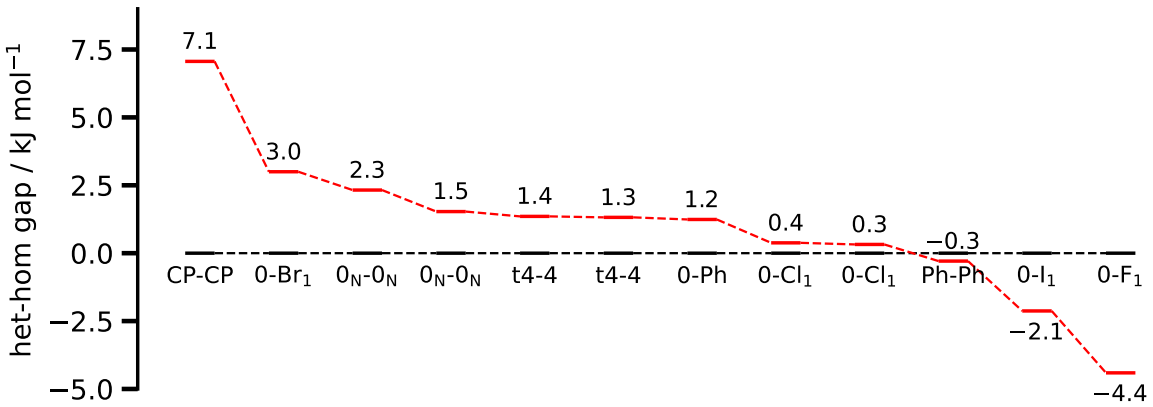

Fig. 6.3: Overview of the het-hom gap for the dimers of [1,1'-bicylopentyl]-1,1'-diol (CP-CP), 3-bromopropane-1,2-diol (0-Br_1), ethane-1,2-diamine (0_N-0_N), *trans*-cyclobutane-1,2-diol (t4-4), 1-phenyl-ethane-1,2-diol (0-Ph), 3-chloropropane-1,2-diol (0-Cl_1), 1,2-diphenyl-ethane-1,2-diol (Ph-Ph), 3-iodopropane-1,2-diol (0-I_1) and 3-fluoropropane-1,2-diol (0-F_1). Hetero-dimers are indicated by black and homo-dimers by red energy levels. The energies are computed at the B3LYP-D3(BJ,abc)/def2-TZVP level of theory and zero-point corrected. If an entry occurs a second time, the calculation has been conducted at the B3LYP-D3(BJ,abc)/ma-def2-TZVP instead. The change in basis set results in minor differences.

for a specific chirality. Curiously, in case of the latter, the preference is for homo-chiral dimers and has not been observed for any other system with that magnitude. These systems can be studied in more detail and it remains to be seen if the het-hom gaps remain unchanged once more exhaustive structural searches are employed. Additionally, the results may be skewed by the def2-TZVP basis set, which is more prone to BSSE than the augmented variant.

Literature

[1] S. Mauskopf, *Chiral Analysis*, (Eds.: K. W. Busch, M. A. Busch), Elsevier Science, **2006**.

[2] T. D. Lee, C. N. Yang, "Question of Parity Conservation in Weak Interactions", *Phys. Rev.* **1956**, *104*, 254–258.

[3] C. S. Wu, E. Ambler, R. W. Hayward, D. D. Hoppes, R. P. Hudson, "Experimental Test of Parity Conservation in Beta Decay", *Phys. Rev.* **1957**, *105*, 1413–1415.

[4] J. Crassous, C. Chardonnet, T. Saue, P. Schwerdtfeger, "Recent experimental and theoretical developments towards the observation of parity violation (PV) effects in molecules by spectroscopy", *Org. Biomol. Chem.* **2005**, *3*, 2218–2224.

[5] M. Quack, M. Willeke, "Stereomutation Tunneling Switching Dynamics and Parity Violation in Chlorineperoxide Cl−O−O−Cl", *J. Phys. Chem. A* **2006**, *110*, 3338–3348.

[6] F. De Montigny, R. Bast, A. Severo Pereira Gomes, G. Pilet, N. Vanthuyne, C. Roussel, L. Guy, P. Schwerdtfeger, T. Saue, J. Crassous, "Chiral oxorhenium(V) complexes as candidates for the experimental observation of molecular parity violation: a structural, synthetic and theoretical study", *Phys. Chem. Chem. Phys.* **2010**, *12*, 8792–8803.

[7] R. Bast, A. Koers, A. S. P. Gomes, M. Iliaš, L. Visscher, P. Schwerdtfeger, T. Saue, "Analysis of parity violation in chiral molecules", *Phys. Chem. Chem. Phys.* **2011**, *13*, 864–876.

[8] C. Stoeffler, B. Darquié, A. Shelkovnikov, C. Daussy, A. Amy-Klein, C. Chardonnet, L. Guy, J. Crassous, T. R. Huet, P. Soulard, P. Asselin, "High resolution spectroscopy of methyltrioxorhenium: towards the observation of parity violation in chiral molecules", *Phys. Chem. Chem. Phys.* **2011**, *13*, 854–863.

[9] R. Bentley, "The Nose as a Stereochemist. Enantiomers and Odor", *Chem. Rev.* **2006**, *106*, 4099–4112.

[10] P. Cintas, *Biochirality*, Springer Berlin Heidelberg, **2013**.

[11] F. Carey, *Advanced organic chemistry*, Springer, New York, NY, **2007**.

[12] E. Francotte, W. Lindner, *Chirality in Drug Research*, Wiley-VCH Verlag GmbH & Co. KGaA, **2006**.

[13] B. Testa, "Mechanisms of chiral recognition in xenobiotic metabolism and drug-receptor interactions", *Chirality* **1989**, *1*, 7–9.

[14] S. W. Smith, "Chiral Toxicology: It's the Same Thing... Only Different", *Toxicol. Sci.* **2009**, *110*, 4–30.

[15] W. Heger, H.-J. Schmahl, S. Klug, A. Felies, H. Nau, H.-J. Merker, D. Neubert, "Embryotoxic effects of thalidomide derivatives in the non-human primate Callithrix jacchus. IV. Teratogenicity of µg/kg doses of the EM12 enantiomers", *Teratog. Carcinog. Mutagen.* **1994**, *14*, 115–122.

[16] T. Eriksson, S. Björkman, B. Roth, P. Höglund, "Intravenous Formulations of the Enantiomers of Thalidomide: Pharmacokinetic and Initial Pharmacodynamic Characterization in Man", *J. Pharm. Pharmacol.* **2000**, *52*, 807–817.

[17] N. Vargesson, "Thalidomide-induced teratogenesis: History and mechanisms", *Birth Defects Res. Embry Today* **2015**, *105*, 140–156.

[18] F. Kollipost, K. E. Otto, M. A. Suhm, "A Symmetric Recognition Motif between Vicinal Diols: The Fourfold Grip in Ethylene Glycol Dimer", *Angew. Chem. Int. Ed.* **2016**, *55*, 4591–4595.

[19] M. S. G. Ahlquist, P.-O. Norrby, "Dispersion and Back-Donation Gives Tetracoordinate $[Pd(PPh_3)_4]$", *Angew. Chem. - Int. Ed.* **2011**, *50*, 11794–11797.

[20] I. Fenández López, M. Solà i Puig, F. M. Bickelhaupt, "Why do cycloaddition reactions involving C_{60} prefer [6,6] over [5,6] bonds?", *Chem. Eur. J.* **2013**, *19*, 7416–7422.

[21] E. Lyngvi, I. A. Sanhueza, F. Schoenebeck, "Dispersion makes the difference: Bisligated transition states found for the oxidative addition of $Pd(P\mathit{t}Bu_3)_2$ to Ar-OSO_2R and dispersion-controlled chemoselectivity in reactions with $Pd[P(\mathit{i}Pr)(\mathit{t}Bu_2)]_2$", *Organometallics* **2015**, *34*, 805–812.

[22] T. H. Meyer, W. Liu, M. Feldt, A. Wuttke, R. A. Mata, L. Ackermann, "Manganese(I)-Catalyzed Dispersion-Enabled C−H/C−C Activation", *Chem. Eur. J.* **2017**, *23*, 5443–5447.

[23] E. Detmar, V. Müller, D. Zell, L. Ackermann, M. Breugst, "Cobalt-catalyzed C–H cyanations: Insights into the reaction mechanism and the role of London dispersion", *Beilstein J. Org. Chem.* **2018**, *14*, 1537–1545.

[24] D. Yepes, F. Neese, B. List, G. Bistoni, "Unveiling the Delicate Balance of Steric and Dispersion Interactions in Organocatalysis Using High-Level Computational Methods", *J. Am. Chem. Soc.* **2020**, *142*, 3613–3625.

[25] C. Eschmann, L. Song, P. R. Schreiner, "London Dispersion Interactions Rather than Steric Hindrance Determine the Enantioselectivity of the Corey-Bakshi–Shibata Reduction", *Angew. Chem. - Int. Ed.* **2021**, *60*, 4823–4832.

[26] K. B. Lipkowitz, B. Coner, M. A. Peterson, A. Morreale, "ENANTIOSELECTIVE BINDING IN GAS CHROMATOGRAPHY:A COMPUTATIONAL STUDY OF CHIRAL SELECTION BYPERMETHYL-β-CYCLODEXTRIN", *J. Phys. Org. Chem.* **1997**, *10*, 311–322.

[27] K. B. Lipkowitz, R. Coner, M. A. Peterson, A. Morreale, J. Shackelford, "The Principle of Maximum Chiral Discrimination: Chiral Recognition in Permethyl-β-cyclodextrin", *J. Org. Chem.* **1998**, *63*, 732–745.

[28] V. Schurig, "Separation of enantiomers by gas chromatography", *J. Chromatogr. A* **2001**, *906*, Chiral Separations, 275–299.

[29] C. Cagliero, B. Sgorbini, C. Cordero, E. Liberto, P. Rubiolo, C. Bicchi, "Enantioselective Gas Chromatography with Derivatized Cyclodextrins in the Flavour and Fragrance Field", *Isr. J. Chem.* **2016**, *56*, 925–939.

[30] J. P. Wagner, P. R. Schreiner, "London Dispersion in Molecular Chemistry – Reconsidering Steric Effects", *Angew. Chem. - Int. Ed.* **2015**, *54*, 12274–12296.

[31] R. Medel, M. A. Suhm, "Predicting OH stretching fundamental wavenumbers of alcohols for conformational assignment: different correction patterns for density functional and wave-function-based methods", *Phys. Chem. Chem. Phys.* **2021**, *23*, 5629–5643.

[32] R. A. Mata, M. A. Suhm, "Benchmarking Quantum Chemical Methods: Are We Heading in the Right Direction?", *Angew. Chem. - Int. Ed.* **2017**, *56*, 11011–11018.

[33] B. Hartwig, "PhD Beppo Hartwig", *Göttingen Research Online / Dataverse* **2021**, https://data.goettingen-research–online.de/dataverse/phd_hartwig.

[34] M. Morse, "2. Supersonic Beam Sources", *Experimental Methods in the Physical Sciences* **1996**, *29*, 21–47.

[35] R. S. Ruoff, T. D. Klots, T. Emilsson, H. S. Gutowsky, "Relaxation of conformers and isomers in seeded supersonic jets of inert gases", *J. Chem. Phys.* **1990**, *93*, 3142–3150.

[36] K. Meyer, "Carboxylic Acids Under Vibrational Scrutiny: Experimental Reference Data to Benchmark Quantum Chemical Calculations", PhD thesis, Georg-August-Universität Göttingen, Germany, **2020**.

[37] A. Amirav, U. Even, J. Jortner, "Cooling of large and heavy molecules in seeded supersonic beams", *Chem. Phys.* **1980**, *51*, 31–42.

[38] A. Smekal, "Zur Quantentheorie der Dispersion", *Naturwissenschaften* **1923**, *11*, 873–875.

[39] P. Zielke, "Ramanstreuung am Überschallstrahl: Wasserstoffbrückendynamik aus neuer Perspektive", PhD thesis, Georg-August-Universität Göttingen, Germany, **2006**.

[40] T. N. Wassermann, "Umgebungseinflüsse auf die C−C und C−O-Torsionsdynamik in Molekülen und Molekülaggregaten: Schwingungsspektroskopie bei tiefen Temperaturen", PhD thesis, Georg-August-Universität Göttingen, Germany, **2009**.

[41] Z. Xue, "Raman spectroscopy of carboxylic acid and water aggregates", PhD thesis, Georg-August-Universität Göttingen, Germany, **2010**.

[42] N. O. B. Lüttschwager, "Raman Spectroscopy of Conformational Rearrangements at Low Temperatures", PhD thesis, Georg-August-Universität Göttingen, Germany, **2014**.

[43] K. Otto, "Raman-Spektroskopie kleiner Moleküle und Molekülaggregate im Überschallstrahl nach thermischer Anregung", PhD thesis, Georg-August-Universität Göttingen, Germany, **2015**.

[44] S. Bocklitz, "Conformational spectroscopy of flexible chain molecules near the folding limit", PhD thesis, Georg-August-Universität Göttingen, Germany, **2017**.

[45] T. Forsting, "Schwingungsspektroskopische Untersuchung der Aggregation und Isomerisierung von Modellpeptiden in der Jet-Expansion am Beispiel kleiner sekundärer Amide", PhD thesis, Georg-August-Universität Göttingen, Germany, **2021**.

[46] M. Gawrilow, "Ramanspektroskopische Untersuchung der Esterfaltung in Überschallexpansionen, Oder: Wie man bei der Suche nach der Haarnadel im Esterhaufen fünf auf einmal findet", PhD thesis, Georg-August-Universität Göttingen, Germany, **2022**.

[47] M. Gawrilow, personal communication.

[48] T. Forsting, M. Suhm, "Curry-Jet SETUP", *FigShare* **2019**, DOI 10.6084/m9.figshare.6395840.v1.

[49] National Institute of Standards and Technology, http://physics.nist.gov/PhysRefData/ASD/lines_form.html, last visited on 01.09.2022.

[50] D. Schmitz, V. Alvin Shubert, T. Betz, M. Schnell, "Multi-resonance effects within a single chirp in broadband rotational spectroscopy: The rapid adiabatic passage regime for benzonitrile", *J. Mol. Spectrosc.* **2012**, *280*, Broadband Rotational Spectroscopy, 77–84.

[51] M. Fatima, C. Pérez, B. E. Arenas, M. Schnell, A. L. Steber, "Benchmarking a new segmented K-band chirped-pulse microwave spectrometer and its application to the conformationally rich amino alcohol isoleucinol", *Phys. Chem. Chem. Phys.* **2020**, *22*, 17042–17051.

[52] G. G. Brown, B. C. Dian, K. O. Douglass, S. M. Geyer, B. H. Pate, "The rotational spectrum of epifluorohydrin measured by chirped-pulse Fourier transform microwave spectroscopy", *J. Mol. Spectrosc.* **2006**, *238*, 200–212.

[53] G. G. Brown, B. C. Dian, K. O. Douglass, S. M. Geyer, S. T. Shipman, B. H. Pate, "A broadband Fourier transform microwave spectrometer based on chirped pulse excitation", *Rev. Sci. Instrum.* **2008**, *79*, 053103.

[54] C. M. Western, "PGOPHER: A program for simulating rotational, vibrational and electronic spectra", *J. Quant. Spectrosc. Radiat. Transf.* **2017**, *186*, Satellite Remote Sensing and Spectroscopy: Joint ACE-Odin Meeting, October 2015, 221–242.

[55] C. M. Western, PGOPHER version 10.1, University of Bristol Research Data Repository, **2018**.

[56] B. S. Ray, "Über die Eigenwerte des asymmetrischen Kreisels", *Z. Phys.* **1932**, *78*, 74–91.

[57] W. Gordy, R. Cook, *Microwave Molecular Spectra*, Interscience Pub., **1970**.

[58] J. Watson, *Vibrational Spectra and Structure*, (Ed.: J. Durig), Elsevier, Amsterdam, **1977**.

[59] M. Born, R. Oppenheimer, "Zur Quantentheorie der Molekeln", *Ann. Phys.* **1927**, *389*, 457–484.

[60] S. Grimme, "Exploration of Chemical Compound, Conformer, and Reaction Space with Meta-Dynamics Simulations Based on Tight-Binding Quantum Chemical Calculations", *J. Chem. Theory Comput.* **2019**, *15*, 2847–2862.

[61] P. Pracht, F. Bohle, S. Grimme, "Automated exploration of the low-energy chemical space with fast quantum chemical methods", *Phys. Chem. Chem. Phys.* **2020**, *22*, 7169–7192.

[62] S. Grimme, C. Bannwarth, P. Shushkov, "A Robust and Accurate Tight-Binding Quantum Chemical Method for Structures, Vibrational Frequencies, and Noncovalent Interactions of Large Molecular Systems Parametrized for All spd-Block Elements ($Z = 1$–86)", *J. Chem. Theory Comput.* **2017**, *13*, 1989–2009.

[63] C. Bannwarth, S. Ehlert, S. Grimme, "GFN2-xTB—An Accurate and Broadly Parametrized Self-Consistent Tight-Binding Quantum Chemical Method with Multipole Electrostatics and Density-Dependent Dispersion Contributions", *J. Chem. Theory Comput.* **2019**, *15*, 1652–1671.

[64] J. G. Brandenburg, C. Bannwarth, A. Hansen, S. Grimme, "B97-3c: A revised low-cost variant of the B97-D density functional method", *J. Chem. Phys.* **2018**, *148*, 064104.

[65] F. Neese, "The ORCA Program System", *WIREs Comput. Mol. Sci.* **2012**, *2*, 73–78.

[66] F. Neese, "Software Update: The ORCA Program System, Version 4.0", *WIREs Comput. Mol. Sci.* **2017**, *8*, e1327.

[67] F. Neese, F. Wennmohs, U. Becker, C. Riplinger, "The ORCA quantum chemistry program package", *J. Chem. Phys.* **2020**, *152*, 224108.

[68] F. Neese, "Software update: The ORCA program system—Version 5.0", *WIREs Comput. Mol. Sci. 12*, e1606.

[69] M. J. Frisch, G. W. Trucks, H. B. Schlegel, G. E. Scuseria, M. A. Robb, J. R. Cheeseman, G. Scalmani, V. Barone, G. A. Petersson, H. Nakatsuji, X. Li, M. Caricato, A. V. Marenich, J. Bloino, B. G. Janesko, R. Gomperts, B. Mennucci, H. P. Hratchian, J. V. Ortiz, A. F. Izmaylov, J. L. Sonnenberg, D. Williams-Young, F. Ding, F. Lipparini, F. Egidi, J. Goings, B. Peng, A. Petrone, T. Henderson, D. Ranasinghe, V. G. Zakrzewski, J. Gao, N. Rega, G. Zheng, W. Liang, M. Hada, M. Ehara, K. Toyota, R. Fukuda, J. Hasegawa, M. Ishida, T. Nakajima, Y. Honda, O. Kitao, H. Nakai, T. Vreven, K. Throssell, J. A. Montgomery, Jr., J. E. Peralta, F. Ogliaro, M. J. Bearpark, J. J. Heyd, E. N. Brothers, K. N. Kudin, V. N. Staroverov, T. A. Keith, R. Kobayashi, J. Normand, K. Raghavachari, A. P. Rendell, J. C. Burant, S. S. Iyengar, J. Tomasi, M. Cossi, J. M. Millam, M. Klene, C. Adamo, R. Cammi, J. W. Ochterski, R. L. Martin, K. Morokuma, O. Farkas, J. B. Foresman, D. J. Fox, *Gaussian 16 Revision A.03*, Gaussian Inc. Wallingford CT, **2016**.

[70] J. P. Perdew, "Density-functional approximation for the correlation energy of the inhomogeneous electron gas", *Phys. Rev. B* **1986**, *33*, 8822–8824.

[71] J. P. Perdew, "Erratum: Density-functional approximation for the correlation energy of the inhomogeneous electron gas", *Phys. Rev. B* **1986**, *34*, 7406–7406.

[72] A. D. Becke, "Density-Functional Exchange-Energy Approximation with Correct Asymptotic Behavior", *Phys. Rev. A* **1988**, *38*, 3098–3100.

[73] J. P. Perdew, K. Burke, M. Ernzerhof, "Generalized Gradient Approximation Made Simple", *Phys. Rev. Lett.* **1996**, *77*, 3865–3868.

[74] C. Lee, W. Yang, R. G. Parr, "Development of the Colle-Salvetti Correlation-Energy Formula into a Functional of the Electron Density", *Phys. Rev. B* **1988**, *37*, 785–789.

[75] B. Miehlich, A. Savin, H. Stoll, H. Preuss, "Results obtained with the correlation energy density functionals of becke and Lee, Yang and Parr", *Chem. Phys. Lett.* **1989**, *157*, 200–206.

[76] A. D. Becke, "Density-functional thermochemistry. III. The role of exact exchange", *J. Chem. Phys.* **1993**, *98*, 5648–5652.

[77] C. Adamo, V. Barone, "Toward reliable density functional methods without adjustable parameters: The PBE0 model", *J. Chem. Phys.* **1999**, *110*, 6158–6170.

[78] M. Ernzerhof, G. E. Scuseria, "Assessment of the Perdew–Burke–Ernzerhof exchange-correlation functional", *J. Chem. Phys.* **1999**, *110*, 5029–5036.

[79] H. Iikura, T. Tsuneda, T. Yanai, K. Hirao, "A long-range correction scheme for generalized-gradient-approximation exchange functionals", *J. Chem. Phys.* **2001**, *115*, 3540–3544.

[80] T. Yanai, D. P. Tew, N. C. Handy, "A new hybrid exchange–correlation functional using the Coulomb-attenuating method (CAM-B3LYP)", *Chem. Phys. Lett.* **2004**, *393*, 51–57.

[81] C. Møller, M. S. Plesset, "Note on an Approximation Treatment for Many-Electron Systems", *Phys. Rev.* **1934**, *46*, 618–622.

[82] S. Grimme, "Semiempirical hybrid density functional with perturbative second-order correlation", *J. Chem. Phys.* **2006**, *124*, 034108.

[83] T. Schwabe, S. Grimme, "Double-hybrid density functionals with long-range dispersion corrections: higher accuracy and extended applicability", *Phys. Chem. Chem. Phys.* **2007**, *9*, 3397–3406.

[84] M. Casanova-Páez, M. B. Dardis, L. Goerigk, "ωB2PLYP and ωB2GPPLYP: The First Two Double-Hybrid Density Functionals with Long-Range Correction Optimized for Excitation Energies", *J. Chem. Theory Comput.* **2019**, *15*, PMID: 31298850, 4735–4744.

[85] R. Eisenschitz, F. London, "Über das Verhältnis der van der Waalsschen Kräfte zu den homöopolaren Bindungskräften", *Z. Physik* **1930**, *60*, 491–527.

[86] F. London, "Zur Theorie und Systematik der Molekularkräfte", *Z. Physik* **1930**, *63*, 245–279.

[87] S. Grimme, J. Antony, S. Ehrlich, H. Krieg, "A consistent and accurate ab initio parametrization of density functional dispersion correction (DFT-D) for the 94 elements H-Pu", *J. Chem. Phys.* **2010**, *132*, 154104.

[88] S. Grimme, S. Ehrlich, L. Goerigk, "Effect of the Damping Function in Dispersion Corrected Density Functional Theory", *J. Comput. Chem.* **2011**, *32*, 1456–1465.

[89] B. M. Axilrod, E. Teller, "Interaction of the van der Waals Type Between Three Atoms", *J. Chem. Phys.* **1943**, *11*, 299–300.

[90] Y. Muto, "Force between nonpolar molecules", *J. Phys. Math. Soc. Jpn* **1943**, *17*, 629.

[91] L. A. Burns, Á. V. Mayagoitia, B. G. Sumpter, C. D. Sherrill, "Density-functional approaches to noncovalent interactions: A comparison of dispersion corrections (DFT-D), exchange-hole dipole moment (XDM) theory, and specialized functionals", *J. Chem. Phys.* **2011**, *134*, 084107.

[92] N. Mardirossian, M. Head-Gordon, "Thirty years of density functional theory in computational chemistry: an overview and extensive assessment of 200 density functionals", *Mol. Phys.* **2017**, *115*, 2315–2372.

[93] L. Goerigk, A. Hansen, C. Bauer, S. Ehrlich, A. Najibi, S. Grimme, "A look at the density functional theory zoo with the advanced GMTKN55 database for general main group thermochemistry, kinetics and noncovalent interactions", *Phys. Chem. Chem. Phys.* **2017**, *19*, 32184–32215.

[94] F. Weigend, R. Ahlrichs, "Balanced Basis Sets of Split Valence, Triple Zeta Valence and Quadruple Zeta Valence Quality for H to Rn: Design and Assessment of Accuracy", *Phys. Chem. Chem. Phys.* **2005**, *7*, 3297.

[95] D. Rappoport, F. Furche, "Property-optimized Gaussian basis sets for molecular response calculations", *J. Chem. Phys.* **2010**, *133*, 134105.

[96] J. Zheng, X. Xu, D. G. Truhlar, "Minimally augmented Karlsruhe basis sets", *Theor. Chem. Acc.* **2011**, *128*, 295–305.

[97] T. H. Dunning, "Gaussian basis sets for use in correlated molecular calculations. I. The atoms boron through neon and hydrogen", *J. Chem. Phys.* **1989**, *90*, 1007–1023.

[98] R. A. Kendall, T. H. Dunning, R. J. Harrison, "Electron affinities of the first-row atoms revisited. Systematic basis sets and wave functions", *J. Chem. Phys.* **1992**, *96*, 6796–6806.

[99] F. Jensen, "Unifying General and Segmented Contracted Basis Sets. Segmented Polarization Consistent Basis Sets", *J. Chem. Theory Comput.* **2014**, *10*, 1074–1085.

[100] F. Jensen, *Introduction to Computational Chemistry*, Third Edition, Wiley, **2017**.

[101] X. Aniban, B. Hartwig, A. Wuttke, R. A. Mata, "Dispersion forces in chirality recognition – a density functional and wave function theory study of diols", *Phys. Chem. Chem. Phys.* **2021**, *23*, 12093–12104.

[102] S. Reiling, J. Brickmann, M. Schlenkrich, P. A. Bopp, "Theoretical investigations on 1,2-ethanediol: The problem of intramolecular hydrogen bonds", *J. Comput. Chem.* **1996**, *17*, 133–147.

[103] F. Jensen, "Using valence bond methods to estimate intramolecular basis set superposition errors", *J. Chem. Phys.* **2017**, *146*, 184109.

[104] D. Bykov, T. Petrenko, R. Izsák, S. Kossmann, U. Becker, E. Valeev, F. Neese, "Efficient implementation of the analytic second derivatives of Hartree–Fock and hybrid DFT energies: a detailed analysis of different approximations", *Mol. Phys.* **2015**, *113*, 1961–1977.

[105] F. Weigend, "Accurate Coulomb-Fitting Basis Sets for H to Rn", *Phys. Chem. Chem. Phys.* **2006**, *8*, 1057.

[106] F. Neese, F. Wennmohs, A. Hansen, U. Becker, "Efficient, Approximate and Parallel Hartree–Fock and Hybrid DFT Calculations. A 'Chain-of-Spheres' Algorithm for the Hartree–Fock Exchange", *Chem. Phys.* **2009**, *356*, 98–109.

[107] M. Gawrilow, M. A. Suhm, "Quantifying Conformational Isomerism in Chain Molecules by Linear Raman Spectroscopy: The Case of Methyl Esters", *Molecules* **2021**, *26*, DOI 10.3390/molecules26154523.

[108] D. A. Long, *The Raman Effect: A Unified Treatment of the Theory of Raman Scattering by Molecules*, Wiley, **2002**.

[109] V. Ásgeirsson, B. O. Birgisson, R. Bjornsson, U. Becker, F. Neese, C. Riplinger, H. Jónsson, "Nudged Elastic Band Method for Molecular Reactions Using Energy-Weighted Springs Combined with Eigenvector Following", *J. Chem. Theory Comput.* **2021**, *17*, 4929–4945.

[110] B. Helmich-Paris, "A trust-region augmented Hessian implementation for restricted and unrestricted Hartree–Fock and Kohn–Sham methods", *J. Chem. Phys.* **2021**, *154*, 164104.

[111] L. N. Schiebel, *Spectroscopic Investigation of Ethane-1,2-diol and 2-Methoxyethanol*, Bachelor thesis, **2022**.

[112] F. Neese, "The SHARK integral generation and digestion system", *J. Comput. Chem.* **2022**, *n/a*, DOI 10.1002/jcc.26942.

[113] H. H. Nielsen, "The Vibration-Rotation Energies of Molecules", *Rev. Mod. Phys.* **1951**, *23*, 90–136.

[114] V. Barone, "Anharmonic vibrational properties by a fully automated second-order perturbative approach", *J. Chem. Phys.* **2005**, *122*, 014108.

[115] V. Barone, J. Bloino, C. A. Guido, F. Lipparini, "A fully automated implementation of VPT2 Infrared intensities", *Chem. Phys. Lett.* **2010**, *496*, 157–161.

[116] A. Nejad, personal communication.

[117] H.-J. Werner, P. J. Knowles, G. Knizia, F. R. Manby, M. Schütz, "Molpro: a general-purpose quantum chemistry program package", *WIREs Comput. Mol. Sci.* **2012**, *2*, 242–253.

[118] H.-J. Werner, P. J. Knowles, F. R. Manby, J. A. Black, K. Doll, A. Heßelmann, D. Kats, A. Köhn, T. Korona, D. A. Kreplin, Q. Ma, T. F. Miller, A. Mitrushchenkov, K. A. Peterson, I. Polyak, G. Rauhut, M. Sibaev, "The Molpro quantum chemistry package", *J. Chem. Phys.* **2020**, *152*, 144107.

[119] H.-J. Werner, P. J. Knowles, G. Knizia, F. R. Manby, M. Schütz, P. Celani, W. Györffy, D. Kats, T. Korona, R. Lindh, A. Mitrushenkov, G. Rauhut, K. R. Shamasundar, T. B. Adler, R. D. Amos, S. J. Bennie, A. Bernhardsson, A. Berning, D. L. Cooper, M. J. O. Deegan, A. J. Dobbyn, F. Eckert, E. Goll, C. Hampel, A. Hesselmann, G. Hetzer, T. Hrenar, G. Jansen, C. Köppl, S. J. R. Lee, Y. Liu, A. W. Lloyd, Q. Ma, R. A. Mata, A. J. May, S. J. McNicholas, W. Meyer, T. F. M. III, M. E. Mura, A. Nicklass, D. P. O'Neill, P. Palmieri, D. Peng, T. Petrenko, K. Pflüger, R. Pitzer, M. Reiher, T. Shiozaki, H. Stoll, A. J. Stone, R. Tarroni, T. Thorsteinsson, M. Wang, M. Welborn, MOLPRO, version 2020.2, a package of ab initio programs, see https://www.molpro.net, **2020**.

[120] H.-J. Werner, P. J. Knowles, G. Knizia, F. R. Manby, M. Schütz, P. Celani, W. Györffy, D. Kats, T. Korona, R. Lindh, A. Mitrushenkov, G. Rauhut, K. R. Shamasundar, T. B. Adler, R. D. Amos, S. J. Bennie, A. Bernhardsson, A. Berning, D. L. Cooper, M. J. O. Deegan, A. J. Dobbyn, F. Eckert, E. Goll, C. Hampel, A. Hesselmann, G. Hetzer, T. Hrenar, G. Jansen, C. Köppl, S. J. R. Lee, Y. Liu, A. W. Lloyd, Q. Ma, R. A. Mata, A. J. May, S. J. McNicholas, W. Meyer, T. F. M. III, M. E. Mura, A. Nicklass, D. P. O'Neill, P. Palmieri, D. Peng, T. Petrenko, K. Pflüger, R. Pitzer, M. Reiher, T. Shiozaki, H. Stoll, A. J. Stone, R. Tarroni, T. Thorsteinsson, M. Wang, M. Welborn, MOLPRO, version 2021.2, a package of ab initio programs, see https://www.molpro.net, **2021**.

[121] M. J. Frisch, M. Head-Gordon, J. A. Pople, "A direct MP2 gradient method", *Chem. Phys. Lett.* **1990**, *166*, 275–280.

[122] M. J. Frisch, M. Head-Gordon, J. A. Pople, "Semi-direct algorithms for the MP2 energy and gradient", *Chem. Phys. Lett.* **1990**, *166*, 281–289.

[123] M. Head-Gordon, T. Head-Gordon, "Analytic MP2 frequencies without fifth-order storage. Theory and application to bifurcated hydrogen bonds in the water hexamer", *Chem. Phys. Lett.* **1994**, *220*, 122–128.

[124] S. Grimme, "Improved second-order Møller–Plesset perturbation theory by separate scaling of parallel- and antiparallel-spin pair correlation energies", *J. Chem. Phys.* **2003**, *118*, 9095–9102.

[125] G. Hetzer, P. Pulay, H.-J. Werner, "Multipole approximation of distant pair energies in local MP2 calculations", *Chem. Phys. Lett.* **1998**, *290*, 143–149.

[126] M. Schütz, G. Hetzer, H.-J. Werner, "Low-order scaling local electron correlation methods. I. Linear scaling local MP2", *J. Chem. Phys.* **1999**, *111*, 5691–5705.

[127] G. Hetzer, M. Schütz, H. Stoll, H.-J. Werner, "Low-order scaling local correlation methods II: Splitting the Coulomb operator in linear scaling local second-order Møller–Plesset perturbation theory", *J. Chem. Phys.* **2000**, *113*, 9443–9455.

[128] S. Saebo/, W. Tong, P. Pulay, "Efficient elimination of basis set superposition errors by the local correlation method: Accurate ab initio studies of the water dimer", *J. Chem. Phys.* **1993**, *98*, 2170–2175.

[129] M. Schütz, G. Rauhut, H.-J. Werner, "Local treatment of electron correlation in molecular clusters: Structures and stabilities of $(H2O)_n$, $n = 2 - 4$", *J. Phys. Chem. A* **1998**, *102*, 5997–6003.

[130] R. A. Mata, H.-J. Werner, "Calculation of smooth potential energy surfaces using local electron correlation methods", *J. Chem. Phys.* **2006**, *125*, 184110.

[131] J. Pipek, P. G. Mezey, "A fast intrinsic localization procedure applicable for ab initio and semiempirical linear combination of atomic orbital wave functions", *J. Chem. Phys.* **1989**, *90*, 4916–4926.

[132] J. M. Foster, S. F. Boys, "Canonical Configurational Interaction Procedure", *Rev. Mod. Phys.* **1960**, *32*, 300–302.

[133] F. Weigend, A. Köhn, C. Hättig, "Efficient use of the correlation consistent basis sets in resolution of the identity MP2 calculations", *J. Chem. Phys.* **2002**, *116*, 3175–3183.

[134] F. Weigend, "A fully direct RI-HF algorithm: Implementation, optimised auxiliary basis sets, demonstration of accuracy and efficiency", *Phys. Chem. Chem. Phys.* **2002**, *4*, 4285–4291.

[135] R. Lindh, "The reduced multiplication scheme of the Rys-Gauss quadrature for 1st order integral derivatives", *Theor. Chem. Acc.* **1993**, *85*, 423–440.

[136] F. Eckert, P. Pulay, H.-J. Werner, "Ab initio geometry optimization for large molecules", *J. Comput. Chem.* **1997**, *18*, 1473–1483.

[137] M. Schütz, H.-J. Werner, R. Lindh, F. R. Manby, "Analytical energy gradients for local second-order Møller–Plesset perturbation theory using density fitting approximations", *J. Chem. Phys.* **2004**, *121*, 737–750.

[138] G. Rauhut, A. El Azhary, F. Eckert, U. Schumann, H.-J. Werner, "Impact of local approximations on MP2 vibrational frequencies", *Spectrochim. Acta A* **1999**, *55*, 647–658.

[139] H.-J. Werner, M. Schütz, "An efficient local coupled cluster method for accurate thermochemistry of large systems", *J. Chem. Phys.* **2011**, *135*, 144116.

[140] T. B. Adler, H.-J. Werner, "An explicitly correlated local coupled cluster method for calculations of large molecules close to the basis set limit", *J. Chem. Phys.* **2011**, *135*, 144117.

[141] H.-J. Werner, K. Pflüger in (Ed.: D. C. Spellmeyer), Annual Reports in Computational Chemistry, Elsevier, **2006**, pp. 53–80.

[142] K. A. Peterson, T. B. Adler, H.-J. Werner, "Systematically convergent basis sets for explicitly correlated wavefunctions: The atoms H, He, B–Ne, and Al–Ar", *J. Chem. Phys.* **2008**, *128*, 84102.

[143] K. E. Yousaf, K. A. Peterson, "Optimized auxiliary basis sets for explicitly correlated methods", *J. Chem. Phys.* **2008**, *129*, 184108.

[144] K. E. Yousaf, K. A. Peterson, "Optimized complementary auxiliary basis sets for explicitly correlated methods: aug-cc-pVnZ orbital basis sets", *Chem. Phys. Lett.* **2009**, *476*, 303–307.

[145] A. Wuttke, "Computational Study of Dispersion Interactions through Local Orbital Analysis", PhD thesis, Georg-August-Universität Göttingen, Germany, **2019**.

[146] G. Bistoni, "Finding chemical concepts in the Hilbert space: Coupled cluster analyses of noncovalent interactions", *WIREs Comput. Mol. Sci.* **2020**, *10*, e1442.

[147] T. B. Adler, G. Knizia, H.-J. Werner, "A simple and efficient CCSD(T)-F12 approximation", *J. Chem. Phys.* **2007**, *127*, 221106.

[148] G. Knizia, T. B. Adler, H.-J. Werner, "Simplified CCSD(T)-F12 methods: Theory and benchmarks", *J. Chem. Phys.* **2009**, *130*, 054104.

[149] W. Győrffy, G. Knizia, H.-J. Werner, "Analytical energy gradients for explicitly correlated wave functions. I. Explicitly correlated second-order Møller-Plesset perturbation theory", *J. Chem. Phys.* **2017**, *147*, 214101.

[150] W. Győrffy, H.-J. Werner, "Analytical energy gradients for explicitly correlated wave functions. II. Explicitly correlated coupled cluster singles and doubles with perturbative triples corrections: CCSD(T)-F12", *J. Chem. Phys.* **2018**, *148*, 114104.

[151] J. G. Hill, K. A. Peterson, "Correlation consistent basis sets for explicitly correlated wavefunctions: Pseudopotential-based basis sets for the post-d main group elements Ga–Rn", *J. Chem. Phys.* **2014**, *141*, 094106.

[152] K. A. Peterson, D. Figgen, E. Goll, H. Stoll, M. Dolg, "Systematically convergent basis sets with relativistic pseudopotentials. II. Small-core pseudopotentials and correlation consistent basis sets for the post-d group 16–18 elements", *J. Chem. Phys.* **2003**, *119*, 11113–11123.

[153] F. Weigend, "Hartree–Fock exchange fitting basis sets for H to Rn", *J. Comput. Chem.* **2008**, *29*, 167–175.

[154] K. A. Peterson, T. H. Dunning, "Accurate correlation consistent basis sets for molecular core-valence correlation effects: The second row atoms Al-Ar, and the first row atoms B-Ne revisited", *J. Chem. Phys.* **2002**, *117*, 10548–10560.

[155] N. J. DeYonker, K. A. Peterson, A. K. Wilson, "Systematically Convergent Correlation Consistent Basis Sets for Molecular Core-Valence Correlation Effects: The Third-Row Atoms Gallium through Krypton", *J. Phys. Chem. A* **2007**, *111*, 11383–11393.

[156] A. Aerts, A. Brown, "A revised nuclear quadrupole moment for aluminum: Theoretical nuclear quadrupole coupling constants of aluminum compounds", *J. Chem. Phys.* **2019**, *150*, 224302.

[157] M. Douglas, N. M. Kroll, "Quantum electrodynamical corrections to the fine structure of helium", *Ann. Physics* **1974**, *82*, 89–155.

[158] B. A. Hess, "Relativistic electronic-structure calculations employing a two-component no-pair formalism with external-field projection operators", *Phys. Rev. A* **1986**, *33*, 3742–3748.

[159] G. Jansen, B. A. Hess, "Revision of the Douglas-Kroll transformation", *Phys. Rev. A* **1989**, *39*, 6016–6017.

[160] L. Visscher, K. Dyall, "DIRAC–FOCK ATOMIC ELECTRONIC STRUCTURE CALCULATIONS USING DIFFERENT NUCLEAR CHARGE DISTRIBUTIONS", *At. Data. Nucl. Data Tables* **1997**, *67*, 207–224.

[161] F. Neese, A. Wolf, T. Fleig, M. Reiher, B. A. Hess, "Calculation of electric-field gradients based on higher-order generalized Douglas–Kroll transformations", *J. Chem. Phys.* **2005**, *122*, 204107.

[162] D. E. Woon, T. H. Dunning, "Gaussian basis sets for use in correlated molecular calculations. V. Core-valence basis sets for boron through neon", *J. Chem. Phys.* **1995**, *103*, 4572–4585.

[163] W. A. de Jong, R. J. Harrison, D. A. Dixon, "Parallel Douglas–Kroll energy and gradients in NWChem: Estimating scalar relativistic effects using Douglas–Kroll contracted basis sets", *J. Chem. Phys.* **2001**, *114*, 48–53.

[164] N. Stone, *Table of Nuclear Magnetic Dipole and Electric Quadrupole Moments (INDC(NDS)–0658)*, International Atomic Energy Agency (IAEA), **2014**.

[165] B. Hartwig, M. A. Suhm, "Subtle hydrogen bonds: benchmarking with OH stretching fundamentals of vicinal diols in the gas phase", *Phys. Chem. Chem. Phys.* **2021**, *23*, 21623–21640.

[166] B. Hartwig, M. Lange, A. Poblotzki, R. Medel, A. Zehnacker, M. A. Suhm, "The reduced cohesion of homoconfigurational 1,2-diols", *Phys. Chem. Chem. Phys.* **2020**, *22*, 1122–1136.

[167] G. Herzberg, *Infrared and Raman Spectra of Polyatomic Molecules*, Van Nostrand, **1945**.

[168] M. Heger, "Diagonal and Off-Diagonal Anharmonicity in Hydrogen-Bonded Systems", PhD thesis, Georg-August-Universität Göttingen, Germany, **2016**.

[169] E. Vogt, P. Bertran Valls, H. G. Kjaergaard, "Accurate Calculations of OH-Stretching Intensities with a Reduced-Dimensional Local Mode Model Including Eckart Axis Embedding", *J. Phys. Chem. A* **2020**, *124*, 932–942.

[170] G. Herzberg, J. SPINKS, *Molecular Spectra and Molecular Structure. I. Spectra of Diatomic Molecules ... Second Edition. [Translated by John W.T. Spinks.]*. D. van Nostrand Company, **1950**.

[171] S. Califano, *Vibrational States*, Wiley, **1976**.

[172] B. Hartwig, M. A. Suhm, "xyz Structure Files of Diols", *Göttingen Research Online / Data* **2021**, *version V1*, DOI: 10.25625/VJF95K.

[173] B. Hartwig, M. A. Suhm, "Monomer Raman-Jet Spectra of Diols in the 3700 to 3560 Wavenumber Range", *Göttingen Research Online / Data* **2021**, *version V1*, DOI: 10.25625/CVAGRL.

[174] B. Hartwig, "Monomer Raman-Spectra of Mono- and Diols in the 3700 to 3560 Wavenumber Range", *Göttingen Research Online / Data* **2022**, *version V1*, DOI: 10.25625/EJVBHD.

[175] B. J. Teppen, M. Cao, R. F. Frey, C. van Alsenoy, D. M. Miller, L. Schäfer, "An investigation into intramolecular hydrogen bonding: impact of basis set and electron correlation on the ab initio conformational analysis of 1,2-ethanediol and 1,2,3-propanetriol", *J. Mol. Struct. THEOCHEM* **1994**, *314*, Theoretical Aspects of Hydrogen Bonding, 169–190.

[176] C. J. Cramer, D. G. Truhlar, "Quantum Chemical Conformational Analysis of 1,2-Ethanediol: Correlation and Solvation Effects on the Tendency To Form Internal Hydrogen Bonds in the Gas Phase and in Aqueous Solution", *J. Am. Chem. Soc.* **1994**, *116*, 3892–3900.

[177] T.-S. Yeh, Y.-P. Chang, T.-M. Su, I. Chao, "Global Conformational Analysis of 1,2-Ethanediol", *J. Phys. Chem.* **1994**, *98*, 8921–8929.

[178] D. Christen, L. Coudert, J. Larsson, D. Cremer, "The Rotational-Torsional Spectrum of the g'Gg Conformer of Ethylene Glycol: Elucidation of an Unusual Tunneling Path", *J. Mol. Spectrosc.* **2001**, *205*, 185–196.

[179] D. L. Howard, P. Jørgensen, H. G. Kjaergaard, "Weak Intramolecular Interactions in Ethylene Glycol Identified by Vapor Phase OH-Stretching Overtone Spectroscopy", *J. Am. Chem. Soc.* **2005**, *127*, 17096–17103.

[180] D. L. Howard, H. G. Kjaergaard, "Influence of Intramolecular Hydrogen Bond Strength on OH-Stretching Overtones", *J. Phys. Chem. A* **2006**, *110*, 10245–10250.

[181] O. Guvench, A. D. MacKerell, "Quantum Mechanical Analysis of 1,2-Ethanediol Conformational Energetics and Hydrogen Bonding", *J. Phys. Chem. A* **2006**, *110*, 9934–9939.

[182] K. Takahashi, "Theoretical study on the effect of intramolecular hydrogen bonding on OH stretching overtone decay lifetime of ethylene glycol, 1,3-propanediol, and 1,4-butanediol", *Phys. Chem. Chem. Phys.* **2010**, *12*, 13950–13961.

[183] P. Das, P. K. Das, E. Arunan, "Conformational Stability and Intramolecular Hydrogen Bonding in 1,2-Ethanediol and 1,4-Butanediol", *J. Phys. Chem. A* **2015**, *119*, 3710–3720.

[184] J. S. Lomas, "1H NMR spectra of ethane-1,2-diol and other vicinal diols in benzene: GIAO/DFT shift calculations", *Magn. Reson. Chem.* **2013**, *51*, 32–41.

[185] A. Lopes Jesus, J. Redinha, "Self-association of 1,2-cyclohexanediols: A spectroscopic and computational study", *J. Mol. Struct.* **2014**, *1067*, 104–111.

[186] L. Paoloni, G. Mazzeo, G. Longhi, S. Abbate, M. Fusè, J. Bloino, V. Barone, "Toward Fully Unsupervised Anharmonic Computations Complementing Experiment for Robust and Reliable Assignment and Interpretation of IR and VCD Spectra from Mid-IR to NIR: The Case of 2,3-Butanediol and *trans*-1,2-Cyclohexanediol", *J. Phys. Chem. A* **2020**, *124*, 1011–1024.

[187] M. Dahlqvist, M. Hotokka, M. Räsänen, "Structures and vibrational spectra of pinacol.: 1. Infrared and matrix infrared spectra of monomeric pinacol. Ab initio calculations on conformers and vibrational frequencies", *Chem. Phys.* **1998**, *229*, 137–147.

[188] M. Olschewski, J. Lindner, P. Vöhringer, "A Hydrogen-Bond Flip-Flop through a Bjerrum-Type Defect", *Angew. Chem. - Int. Ed.* **2013**, *52*, 2602–2605.

[189] J. S. Lomas, L. Joubert, F. Maurel, "Association of symmetrical alkane diols with pyridine: DFT/GIAO calculation of 1H NMR chemical shifts", *Magn. Reson. Chem.* **2016**, *54*, 805–814.

[190] G. Scalmani, M. J. Frisch, "Continuous surface charge polarizable continuum models of solvation. I. General formalism", *J. Chem. Phys.* **2010**, *132*, 114110.

[191] L. P. Kuhn, "The Hydrogen Bond. I. Intra- and Intermolecular Hydrogen Bonds in Alcohols", *J. Am. Chem. Soc.* **1952**, *74*, 2492–2499.

[192] E. L. Eliel, C. Pillar, "The Conformation of a Six-membered Ring *cis*-1,2 Fused to a Five-membered Ring1", *J. Am. Chem. Soc.* **1955**, *77*, 3600–3604.

[193] J. Brimacombe, A. Foster, M. Stacey, D. Whiffen, "Aspects of stereochemistry—I: Properties and reactions of some diols", *Tetrahedron* **1958**, *4*, 351–360.

[194] A. Foster, A. Haines, M. Stacey, "Intramolecular hydrogen bonding in some acyclic alcohols", *Tetrahedron* **1961**, *16*, 177–184.

[195] P. Krueger, H. Mettee, "Spectroscopic studies of alcohols: Part VII. Intramolecular hydrogen bonds in ethylene glycol and 2-methoxyethanol", *J. Mol. Spectrosc.* **1965**, *18*, 131–140.

[196] C. W. Davey, E. L. McGinnis, J. M. McKeown (née Chancellor), G. D. Meakins, M. W. Pemberton, R. N. Young, "Hydroxy-steroids. Part XI. The preparation and infrared spectra of vicinal cholestanediols", *J. Chem. Soc. C* **1968**, 2674–2682.

[197] W. Busfield, M. Ennis, I. McEwen, "An infrared study of intramolecular hydrogen bonding in α, ω diols", *Spectrochim. Acta A* **1973**, *29*, 1259–1264.

[198] D. A. Partridge, "A simple demonstration of conformational equilibrium", *J. Chem. Educ.* **1980**, *57*, 508.

[199] J. Bacon, J. van der Maas, J. Dixon, W. George, P. McIntyre, "Structural information from OH stretching frequencies – conformations of cyclohexanol and cyclohexandiols", *Spectrochim. Acta A* **1989**, *45*, 1313–1318.

[200] F. Singelenberg, J. Van Der Maas, "Fourier transform – infrared study of hydrogen-bonding between an OH-donor and a vicinal oxygen acceptor", *J. Mol. Struct.* **1990**, *240*, 213–223.

[201] F. Singelenberg, J. Van Der Maas, "Hydrogen-bonding in non-cyclic vicinal diols and their mono-methyl ethers: an ftir study", *J. Mol. Struct.* **1991**, *243*, 111–122.

[202] K. Yamamoto, Y. Nakao, Y. Kyogoku, H. Sugeta, "Vibrational circular dichroism in hydrogen bond systems: Part III. Vibrational circular dichroism of the OH stretching vibrations of 1,2-diols and β-methoxyalcohols", *J. Mol. Struct.* **1991**, *242*, 75–86.

[203] A. J. Lock, J. J. Gilijamse, S. Woutersen, H. J. Bakker, "Vibrational relaxation and coupling of two OH-stretch oscillators with an intramolecular hydrogen bond", *J. Chem. Phys.* **2004**, *120*, 2351–2358.

[204] X. Ma, J. Wang, "Differentiating Subtle Variation of Weak Intramolecular Hydrogen Bond in Vicinal Diols by Linear Infrared Spectroscopy", *J. Phys. Chem. A* **2009**, *113*, 6070–6076.

[205] P. Buckley, P. A. Giguère, "Infrared studies on rotational isomerism. I. Ethylene glycol", *Can. J. Chem.* **1967**, *45*, 397–407.

[206] T.-K. Ha, H. Frei, R. Meyer, H. H. Günthard, "Conformation of ethylene glycol: Isometric group, ab initio study of internal H bonding and ir-matrix spectra of the species CH_2OHCH_2OH, CD_2OHCD_2OH and CH_2ODCH_2OD", *Theor. Chim. Acta* **1974**, *34*, 277–292.

[207] H. Frei, T.-K. Ha, R. Meyer, H. Gūnthard, "Ethylene glycol: Infrared spectra, AB initio calculations, vibrational analysis and conformations of 5 matrix isolated isotopic modifications", *Chem. Phys.* **1977**, *25*, 271–298.

[208] H. Takeuchi, M. Tasumi, "Infrared-induced conformational isomerization of ethylene glycol in a low-temperature argon matrix", *Chem. Phys.* **1983**, *77*, 21–34.

[209] C. G. Park, M. Tasumi, "Reinvestigation of infrared-induced conformational isomerizations of 1,2-ethanediol in low-temperature argon matrixes and reverse reaction in the dark", *J. Phys. Chem.* **1991**, *95*, 2757–2762.

[210] W. Caminati, G. Corbelli, "Conformation of ethylene glycol from the rotational spectra of the nontunneling O-monodeuterated species", *J. Mol. Spectrosc.* **1981**, *90*, 572–578.

[211] P.-E. Kristiansen, K.-M. Marstokk, H. Møllendal, V. D. Parker, L. Niinistö, "Microwave Spectrum of $HOCH_2CD_2OH$ and the Assignment of a Second Hydrogen-Bonded Conformation of Ethylene Glycol.", *Acta Chem. Scand.* **1987**, *41a*, 403–414.

[212] D. Christen, H. S. P. Müller, "The millimeter wave spectrum of aGg' ethylene glycol: The quest for higher precision", *Phys. Chem. Chem. Phys.* **2003**, *5*, 3600–3605.

[213] H. S. Müller, D. Christen, "Millimeter and submillimeter wave spectroscopic investigations into the rotation-tunneling spectrum of gGg' ethylene glycol, $HOCH_2CH_2OH$", *J. Mol. Spectrosc.* **2004**, *228*, Special Issue Dedicated to Dr. Jon T. Hougen on the Occasion of His 68th Birthday, 298–307.

[214] J. van der Maas, E. Lutz, "Structural information from OH stretching frequencies monohydric saturated alcohols", *Spectrochim. Acta Part Mol. Spectrosc.* **1974**, *30*, 2005–2019.

[215] B. T. Lutz, J. H. van der Maas, "The sensorial potentials of the OH stretching mode", *J. Mol. Struct.* **1997**, *436-437*, Structure, Properties and Dynamics of Molecular Systems, 213–231.

[216] F. Kollipost, K. Papendorf, Y.-F. Lee, Y.-P. Lee, M. A. Suhm, "Alcohol dimers – how much diagonal OH anharmonicity?", *Phys. Chem. Chem. Phys.* **2014**, *16*, 15948–15956.

[217] F. Lovas, D. Plusquellic, B. H. Pate, J. L. Neill, M. T. Muckle, A. J. Remijan, "Microwave spectrum of 1,2-propanediol", *J. Mol. Spectrosc.* **2009**, *257*, 82–93.

[218] Bossa, J.-B., Ordu, M. H., Müller, H. S. P., Lewen, F., Schlemmer, S., "Laboratory spectroscopy of 1,2-propanediol at millimeter and submillimeter wavelengths", *A&A* **2014**, *570*, A12.

[219] O. Zakharenko, J.-B. Bossa, F. Lewen, S. Schlemmer, H. Müller, "Millimeter and submillimeter wave spectroscopy of higher energy conformers of 1,2-propanediol", *J. Mol. Spectrosc.* **2017**, *333*, 23–26.

[220] B. E. Arenas, S. Gruet, A. L. Steber, M. Schnell, "A global study of the conformers of 1,2-propanediol and new vibrationally excited states", *J. Mol. Spectrosc.* **2017**, *337*, Spectroscopy and Inter/Intramolecular Dynamics in Honor of Walther Caminati - Part 2, 9–16.

[221] Favre, C., Pagani, L., Goldsmith, P. F., Bergin, E. A., Carvajal, M., Kleiner, I., Melnick, G., Snell, R., "The complexity of Orion: an ALMA view - II. gGg'-ethylene glycol and acetic acid", *A&A* **2017**, *604*, L2.

[222] M. Melosso, L. Dore, F. Tamassia, C. L. Brogan, T. R. Hunter, B. A. McGuire, "The Submillimeter Rotational Spectrum of Ethylene Glycol up to 890 GHz and Application to ALMA Band 10 Spectral Line Data of NGC 6334I", *J. Phys. Chem. A* **2020**, *124*, 240–246.

[223] T. J. Lockley, J. I. Hearn, A. K. King, B. J. Howard, "Detection and analysis of a new conformational isomer of propan-1,2-diol by Fourier transform microwave spectroscopy", *J. Mol. Struct.* **2002**, *612*, 199–206.

[224] J. S. Lomas, F. Maurel, A. Adenier, "1H NMR study of the hetero-association of non-symmetrical diols with pyridine; GIAO/DFT calculations on diols", *J. Phys. Org. Chem.* **2011**, *24*, 798–808.

[225] F. Kollipost, "Schwingungsdynamik in O−H$\cdots$O-verbrückten Aggregaten: FTIR-Spektroskopie vom Nah- bis zum Ferninfraroten", PhD thesis, Georg-August-Universität Göttingen, Germany, **2015**.

[226] C. Emmeluth, V. Dyczmons, M. A. Suhm, "Tuning the Hydrogen Bond Donor/Acceptor Isomerism in Jet-Cooled Mixed Dimers of Aliphatic Alcohols", *J. Phys. Chem. A* **2006**, *110*, 2906–2915.

[227] F. Wang, P. L. Polavarapu, "Predominant Conformations of (2*R*,3*R*)-(−)-2,3-Butanediol", *J. Phys. Chem. A* **2001**, *105*, 6991–6997.

[228] A. J. Lopes Jesus, M. T. S. Rosado, M. L. P. Leitão, J. S. Redinha, "Molecular Structure of Butanediol Isomers in Gas and Liquid States: Combination of DFT Calculations and Infrared Spectroscopy Studies", *J. Phys. Chem. A* **2003**, *107*, 3891–3897.

[229] A. J. Lopes Jesus, M. T. S. Rosado, I. Reva, R. Fausto, M. E. Eusébio, J. S. Redinha, "Conformational Study of Monomeric 2,3-Butanediols by Matrix-Isolation Infrared Spectroscopy and DFT Calculations", *J. Phys. Chem. A* **2006**, *110*, 4169–4179.

[230] J. Paul, I. Hearn, B. J. Howard, "Chiral recognition in a single molecule: a study of homo and heterochiral butan-2,3-diol by Fourier transform microwave spectroscopy", *Mol. Phys.* **2007**, *105*, 825–839.

[231] R. Medel, M. A. Suhm, "Understanding benzyl alcohol aggregation by chiral modification: the pairing step", *Phys. Chem. Chem. Phys.* **2020**, *22*, 25538–25551.

[232] E. Anslyn, D. Dougherty, E. Dougherty, *Modern Physical Organic Chemistry*, University Science Books, **2006**.

[233] A. S. Hansen, R. M. Huchmala, E. Vogt, M. A. Boyer, T. Bhagde, M. F. Vansco, C. V. Jensen, A. Kjærsgaard, H. G. Kjaergaard, A. B. McCoy, M. I. Lester, "Coupling of torsion and OH-stretching in tert-butyl hydroperoxide. I. The cold and warm first OH-stretching overtone spectrum", *J. Chem. Phys.* **2021**, *154*, 164306.

[234] E. Vogt, R. M. Huchmala, C. V. Jensen, M. A. Boyer, J. Wallberg, A. S. Hansen, A. Kjærsgaard, M. I. Lester, A. B. McCoy, H. G. Kjaergaard, "Coupling of torsion and OH-stretching in tert-butyl hydroperoxide. II. The OH-stretching fundamental and overtone spectra", *J. Chem. Phys.* **2021**, *154*, 164307.

[235] J. R. Lane, J. Contreras-García, J.-P. Piquemal, B. J. Miller, H. G. Kjaergaard, "Are Bond Critical Points Really Critical for Hydrogen Bonding?", *J. Chem. Theory Comput.* **2013**, *9*, 3263–3266.

[236] A. Jindal, V. Arunachalam, S. Vasudevan, "Search for H-Bonded Motifs in Liquid Ethylene Glycol Using a Machine Learning Strategy", *J. Phys. Chem. B.* **2021**, *125*, 5909–5919.

[237] Z. Malarski, "Solid Rotator Phases in 2,2,4,4- Tetramethyl-3-t-butyl-pentane-3-ol (t-Bu_3 COH)", *Mol. Cryst. Liq. Cryst.* **1974**, *25*, 259–272.

[238] E. M. Arnett, L. E. Small, R. T. McIver, J. S. Miller, "Ionization and fragmentation of tri-tert-butylcarbinol. Evidence for a transient tert-butyl carbanion in dimethyl sulfoxide", *J. Org. Chem.* **1978**, *43*, 815–817.

[239] I. Majerz, I. Natkaniec, "Experimental and theoretical IR, R, and INS spectra of 2,2,4,4-tetramethyl-3-t-butyl-pentane-3-ol", *J. Mol. Struct.* **2006**, *788*, 93–101.

[240] R. Medel, "Schwingungsspektroskopische Untersuchungen zur Chiralitätserkennung und Torsionsdynamik bei Alkoholen", PhD thesis, Georg-August-Universität, **2020**.

[241] T. N. Wassermann, M. A. Suhm, "Ethanol Monomers and Dimers Revisited: A Raman Study of Conformational Preferences and Argon Nanocoating Effects", *J. Phys. Chem. A* **2010**, *114*, 8223–8233.

[242] J. E. Anderson, "Chemical shifts of the protons within a methyl group in a saturated hydrocarbon. Slow methyl group rotation", *Chem. Commun.* **1996**, 93–95.

[243] B. Hartwig, "Dimer Raman-Spectra of Diols and tri-tert-Butylmethanol", *Göttingen Research Online / Data* **2022**, *version V1*, DOI: 10.25625/4Y9DNB.

[244] T. Goldstein, M. Snow, B. Howard, "Intramolecular hydrogen bonding in chiral alcohols: The microwave spectrum of the chloropropanols", *J. Mol. Spectrosc.* **2006**, *236*, 1–10.

[245] K. M. S. Gonçalves, D. R. Garcia, T. C. Ramalho, J. D. Figueroa-Villar, M. P. Freitas, "Conformational Analysis of 1-Chloro- and 1-Bromo-2-propanol", *J. Phys. Chem. A* **2013**, *117*, 10980–10984.

[246] K. A. E. Meyer, M. A. Suhm, "Stretching of *cis*-formic acid: warm-up and cool-down as molecular work-out", *Chem. Sci.* **2019**, *10*, 6285–6294.

[247] K. A. E. Meyer, A. Nejad, "CC-stretched formic acid: isomerisation, dimerisation, and carboxylic acid complexation", *Phys. Chem. Chem. Phys.* **2021**, *23*, 17208–17223.

[248] A. Nejad, K. A. E. Meyer, F. Kollipost, Z. Xue, M. A. Suhm, "Slow monomer vibrations in formic acid dimer: Stepping up the ladder with FTIR and Raman jet spectroscopy", *J. Chem. Phys.* **2021**, *155*, 224301.

[249] P. R. Franke, J. F. Stanton, G. E. Douberly, "How to VPT2: Accurate and Intuitive Simulations of CH Stretching Infrared Spectra Using VPT2+K with Large Effective Hamiltonian Resonance Treatments", *J. Phys. Chem. A* **2021**, *125*, 1301–1324.

[250] R. G. Azrak, E. B. Wilson, "Microwave Spectra and Intramolecular Hydrogen Bonding in the 2-Haloethanols: Molecular Structure and Quadrupole Coupling Constants for 2-Chloroethanol and 2-Bromoethanol", *J. Chem. Phys.* **1970**, *52*, 5299–5316.

[251] M. Hayashi, T. Inagusa, "Microwave spectrum, structure and nuclear quadrupole coupling constant tensor of ethyl chloride and vinyl chloride", *J. Mol. Struct.* **1990**, *220*, 103–117.

[252] T. Inagusa, M. Hayashi, "Microwave spectrum, r_s structure, dipole moment, and nuclear quadrupole coupling constant tensor of ethyl bromide", *J. Mol. Spectrosc.* **1988**, *129*, 160–171.

[253] W. C. Bailey, Calculation of Nuclear Quadrupole Coupling Constants in Gaseous State Molecules, http://nqcc.wcbailey.net/TOC.html, last visited on 10.06.2022.

[254] S. G. Kukolich, A. C. Nelson, "Chlorine Quadrupole Coupling in Methyl Chloride. Variation of Quadrupole Coupling Strength with Isotopic Substitution", *J. Am. Chem. Soc.* **1973**, *95*, 680–682.

[255] H.-T. Man, R. Butcher, "Laser-radiofrequency double-resonance spectroscopy of methyl chloride: Hyperfine structure of the ground and ν_6 states", *J. Mol. Spectrosc.* **1985**, *110*, 19–26.

[256] G. Wlodarczak, D. Boucher, R. Bocquet, J. Demaison, "The microwave and submillimeter-wave spectrum of methyl chloride", *J. Mol. Spectrosc.* **1986**, *116*, 251–255.

[257] L. Nová Stříteská, M. Šimečková, P. Kania, P. Musil, L. Kolesniková, J. Koubek, Š. Urban, "Precise ground state molecular parameters of chloromethane", *J. Mol. Struct.* **2009**, *919*, 89–93.

[258] D. R. Lide, M. Jen, "Microwave Spectrum of Tertiary Butyl Chloride. A Comparison of Tertiary Butyl Structures", *J. Chem. Phys.* **1963**, *38*, 1504–1507.

[259] M. Ellis, A. Legon, C. Rego, D. Millen, "Cl-nuclear quadrupole coupling in the microwave spectra of 1-chloroadamantane and t-butyl chloride", *J. Mol. Struct. THEOCHEM* **1989**, *200*, 353–359.

[260] J. H. Carpenter, R. Crane, J. G. Smith, "Millimeter-wave spectra of 2-chloro-2-methylpropane", *J. Mol. Spectrosc.* **1990**, *141*, 91–103.

[261] Z. Kisiel, E. Białkowska-Jaworska, O. Desyatnyk, B. Pietrewicz, L. Pszczółkowski, "The Gas-Phase Electric Dipole Moments of the Symmetric Top Tertiary Butyl Molecules tBuX, X=F, Cl, Br, I, CN, and NC", *J. Mol. Spectrosc.* **2001**, *208*, 113–120.

[262] W. J. O. Thomas, J. T. Cox, W. Gordy, "Millimeter Wave Spectra and Centrifugal Stretching Constants of the Methyl Halides", *J. Chem. Phys.* **1954**, *22*, 1718–1722.

[263] E. Arimondo, J. Baker, P. Glorieux, T. Oka, J. Sakai, "Radiofrequency spectroscopy inside a laser cavity: Nuclear quadrupole resonance and A1-A2 splitting of CH_3Br", *J. Mol. Spectrosc.* **1980**, *82*, 54–72.

[264] G. Graner, "The methyl bromide molecule: A critical consideration of perturbations in spectra", *J. Mol. Spectrosc.* **1981**, *90*, 394–438.

[265] S. Carocci, P. Minguzzi, M. Tonelli, A. Dilieto, "The Electric Dipole and the Nuclear Quadrupole Moment of Methyl Bromide in the Ground Vibrational State", *J. Mol. Spectrosc.* **1993**, *160*, 359–370.

[266] M. Ramos, B. J. Drouin, "Submillimeter spectrum of methyl bromide (CH_3Br)", *J. Mol. Spectrosc.* **2011**, *269*, 187–192.

[267] H. Harder, W. Stahl, H. Dreizler, "Hyperfine Structure in the Rotational Spectrum of tert-Butyl Bromide", *Z. Naturforsch.* **1990**, *45*, 807–810.

[268] J. Carpenter, C. Gowland, D. Read, J. Smith, "Rotational Spectra of 2-Bromo-2-methylpropane in Excited Vibrational States", *J. Mol. Spectrosc.* **1993**, *159*, 192–209.

[269] W. C. Bailey, Calculation of Nuclear Quadrupole Coupling Constants in Gaseous State Molecules; Ethyl Chloride, http://nqcc.wcbailey.net/CH3CH2Cl.html, last visited on 10.06.2022.

[270] A. de Luis, M. Sanz, F. J. Lorenzo, J. C. López, J. L. Alonso, "Internal Rotation and the Chlorine Nuclear Quadrupole Coupling Tensor of 1-Chloropropane", *J. Mol. Spectrosc.* **1997**, *184*, 60–77.

[271] E. Arunan, G. R. Desiraju, R. A. Klein, J. Sadlej, S. Scheiner, I. Alkorta, D. C. Clary, R. H. Crabtree, J. J. Dannenberg, P. Hobza, H. G. Kjaergaard, A. C. Legon, B. Mennucci, D. J. Nesbitt, "Definition of the hydrogen bond (IUPAC Recommendations 2011)", *Pure Appl. Chem.* **2011**, *83*, 1637–1641.

[272] Y. Niide, I. Ohkoshi, M. Takano, "Microwave spectrum of gauche normal propyl bromide", *J. Mol. Spectrosc.* **1981**, *89*, 387–396.

[273] M. Fujitake, M. Hayashi, "Microwave spectrum of 1-Iodopropane: The observation of the forbidden transitions", *J. Mol. Spectrosc.* **1988**, *127*, 112–124.

[274] M. A. Lloyd, G. E. Patterson, G. H. Simpson, L. L. Duncan, D. P. King, Y. Fu, B. O. Patrick, S. Parkin, C. P. Brock, "Solid-state compounds of stereoisomers: *cis* and *trans* isomers of 1,2-cyclohexanediol and 2,3-tetralindiol", *Acta Crystallogr. Sect. B: Struct. Sci.* **2007**, *63*, 433–447.

[275] G. Avila, J. Fernández, G. Tejeda, S. Montero, "The Raman spectra and cross-sections of H_2O, D_2O, and HDO in the OH/OD stretching regions", *J. Mol. Spectrosc.* **2004**, *228*, 38–65.

[276] K. E. Otto, Z. Xue, P. Zielke, M. A. Suhm, "The Raman spectrum of isolated water clusters", *Phys. Chem. Chem. Phys.* **2014**, *16*, 9849–9858.

[277] A. Poblotzki, "Intermolecular energy scales based on aromatic ethers and alcohols", PhD thesis, Georg-August-Universität Göttingen, Germany, **2019**.

[278] U. Ryde, R. A. Mata, S. Grimme, "Does DFT-D estimate accurate energies for the binding of ligands to metal complexes?", *Dalton Trans.* **2011**, *40*, 11176–11183.

[279] A. Wuttke, R. A. Mata, "Visualizing dispersion interactions through the use of local orbital spaces", *J. Comput. Chem.* **2017**, *38*, 15–23.

[280] A. Wuttke, M. Feldt, R. A. Mata, "All That Binds Is Not Gold - The Relative Weight of Aurophilic Interactions in Complex Formation", *J. Phys. Chem. A* **2018**, *122*, 6918–6925.

[281] J. Kraitchman, "Determination of Molecular Structure from Microwave Spectroscopic Data", *Amer. J. Phys.* **1953**, *21*, 17–24.

[282] J. K. Watson, A. Roytburg, W. Ulrich, "Least-Squares Mass-Dependence Molecular Structures", *J. Mol. Spectrosc.* **1999**, *196*, 102–119.

[283] Z. Kisiel, "Least-squares mass-dependence molecular structures for selected weakly bound intermolecular clusters", *J. Mol. Spectrosc.* **2003**, *218*, 58–67.

[284] C. Pérez, M. T. Muckle, D. P. Zaleski, N. A. Seifert, B. Temelso, G. C. Shields, Z. Kisiel, B. H. Pate, "Structures of Cage, Prism, and Book Isomers of Water Hexamer from Broadband Rotational Spectroscopy", *Science* **2012**, *336*, 897–901.

[285] W. T. S. Cole, J. D. Farrell, D. J. Wales, R. J. Saykally, "Structure and torsional dynamics of the water octamer from THz laser spectroscopy near 215 µm", *Science* **2016**, *352*, 1194–1197.

[286] C. Pérez, D. P. Zaleski, N. A. Seifert, B. Temelso, G. C. Shields, Z. Kisiel, B. H. Pate, "Hydrogen Bond Cooperativity and the Three-Dimensional Structures of Water Nonamers and Decamers", *Angew. Chem. - Int. Ed.* **2014**, *53*, 14368–14372.

[287] A. D. Fortes, E. Suard, "Crystal structures of ethylene glycol and ethylene glycol monohydrate", *J. Chem. Phys.* **2011**, *135*, 234501.

[288] W. Caminati, "Conformation and hydrogen bond in 1,2-propanediol", *J. Mol. Spectrosc.* **1981**, *86*, 193–201.

[289] S. Vázquez, R. A. Mosquera, M. A. Rios, C. Van Alsenoy, "AB initio gradient optimized molecular geometry and conformational analysis of 1,2-propanediol at the 4-21G level", *J. Mol. Struct. Theochem* **1989**, *184*, 323–342.

A Structures

A.1 Monomers

A.1.1 Mono-ols

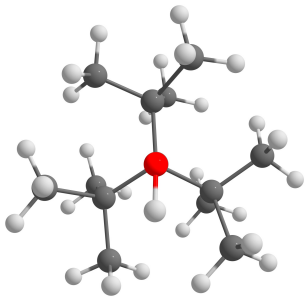

(a) min / 0

Fig. A.1: Structure of tri-*tert*-butyl-methanol at the B3LYP/maTZ level.

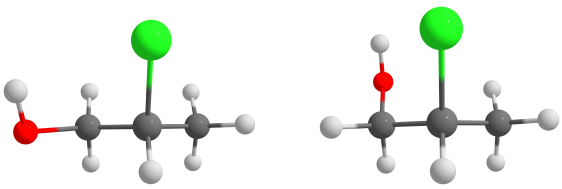

(a) g-ga / 0 **(b)** g'-gg / 1.89

Fig. A.2: Structures of 2-chloropropan-1-ol. Relative zero-point corrected energies at the B3LYP/maTZ level are given in kJ mol^{-1}.

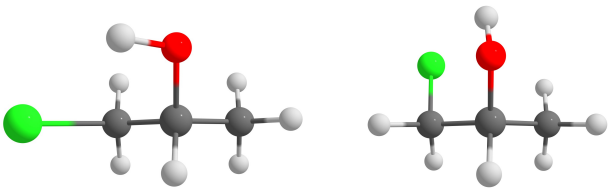

(a) m-ga / 0 **(b)** h-gg / 2.60

Fig. A.3: Structures of 1-chloropropan-2-ol. Relative zero-point corrected energies at the B3LYP/maTZ level are given in kJ mol^{-1}.

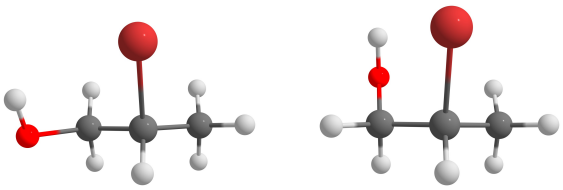

(a) g-ga / 0 **(b)** g'-gg / 1.73

Fig. A.4: Structures of 2-bromopropan-1-ol. Relative zero-point corrected energies at the B3LYP/maTZ level are given in kJ mol^{-1}.

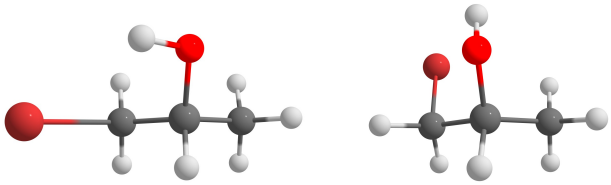

(a) m-ga / 0 **(b)** h-gg / 2.17

Fig. A.5: Structures of 1-bromopropan-2-ol. Relative zero-point corrected energies at the B3LYP/maTZ level are given in kJ mol^{-1}.

A.1.2 $n_D = 0$: Primary-Primary

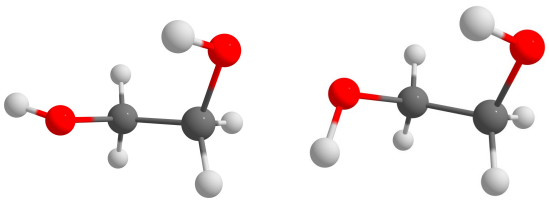

(a) 0-0 / 0 **(b)** 0-0' / 1.49

Fig. A.6: Structures of ethane-1,2-diol (0-0). Relative zero-point corrected energies at the B3LYP/maTZ level are given in kJ mol^{-1}.

A.1.3 $n_D = 1$: Primary-Secondary

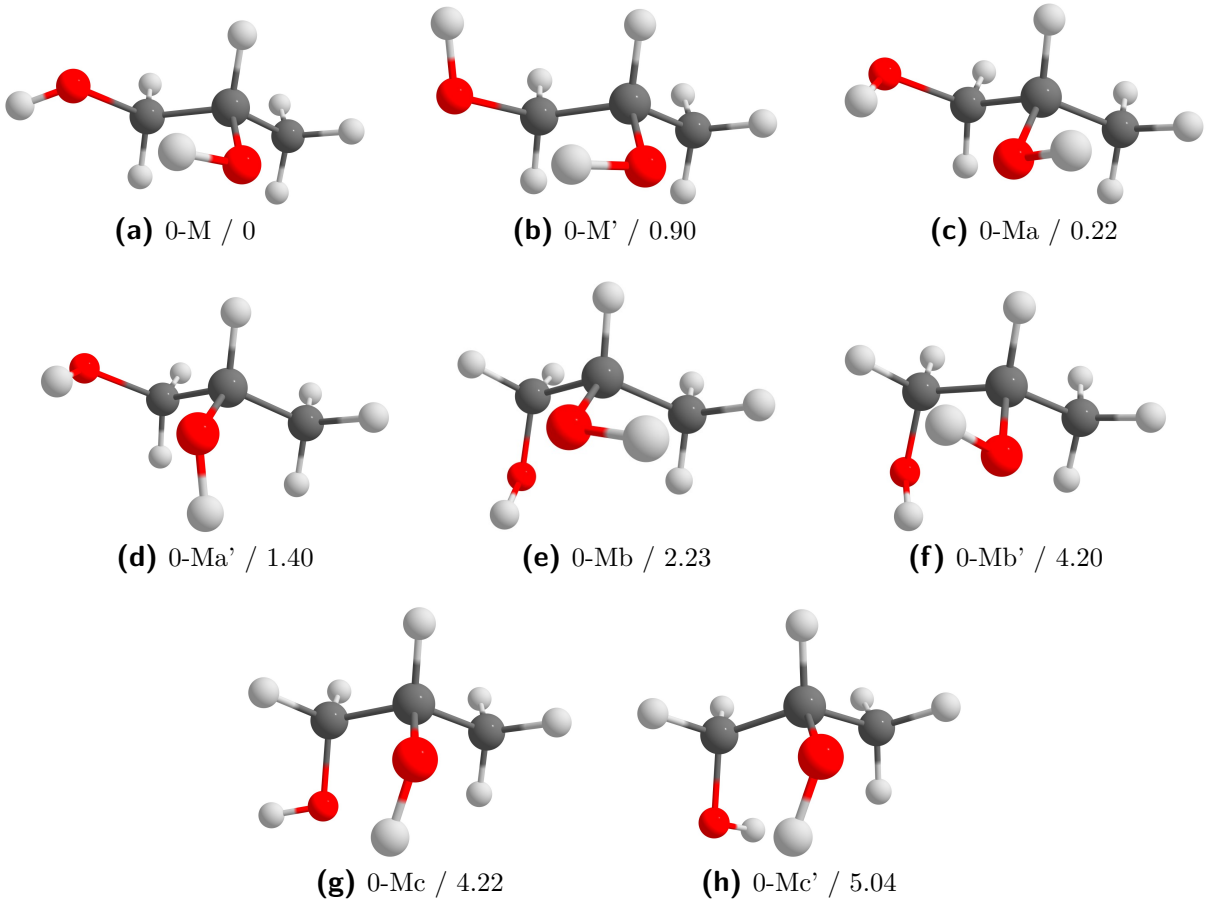

(a) 0-M / 0 **(b)** 0-M' / 0.90 **(c)** 0-Ma / 0.22

(d) 0-Ma' / 1.40 **(e)** 0-Mb / 2.23 **(f)** 0-Mb' / 4.20

(g) 0-Mc / 4.22 **(h)** 0-Mc' / 5.04

Fig. A.7: Structures of propane-1,2-diol (0-M). Relative zero-point corrected energies at the B3LYP/maTZ level are given in kJ mol^{-1}.

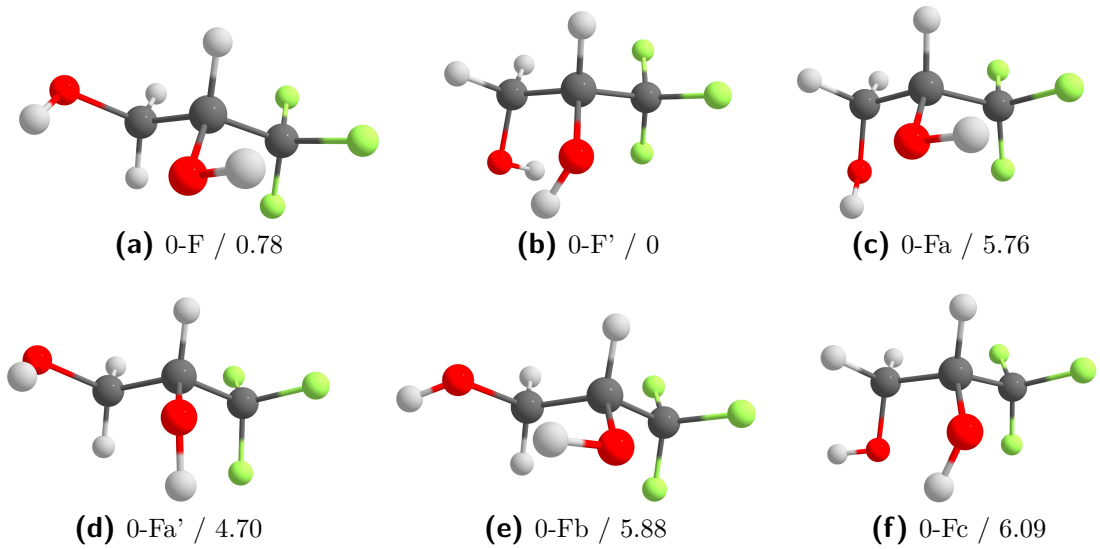

(a) 0-F / 0.78 **(b)** 0-F' / 0 **(c)** 0-Fa / 5.76

(d) 0-Fa' / 4.70 **(e)** 0-Fb / 5.88 **(f)** 0-Fc / 6.09

Fig. A.8: Structures of 3,3,3-trifluoro-propane-1,2-diol (0-F). Relative zero-point corrected energies at the B3LYP/maTZ level are given in kJ mol^{-1}.

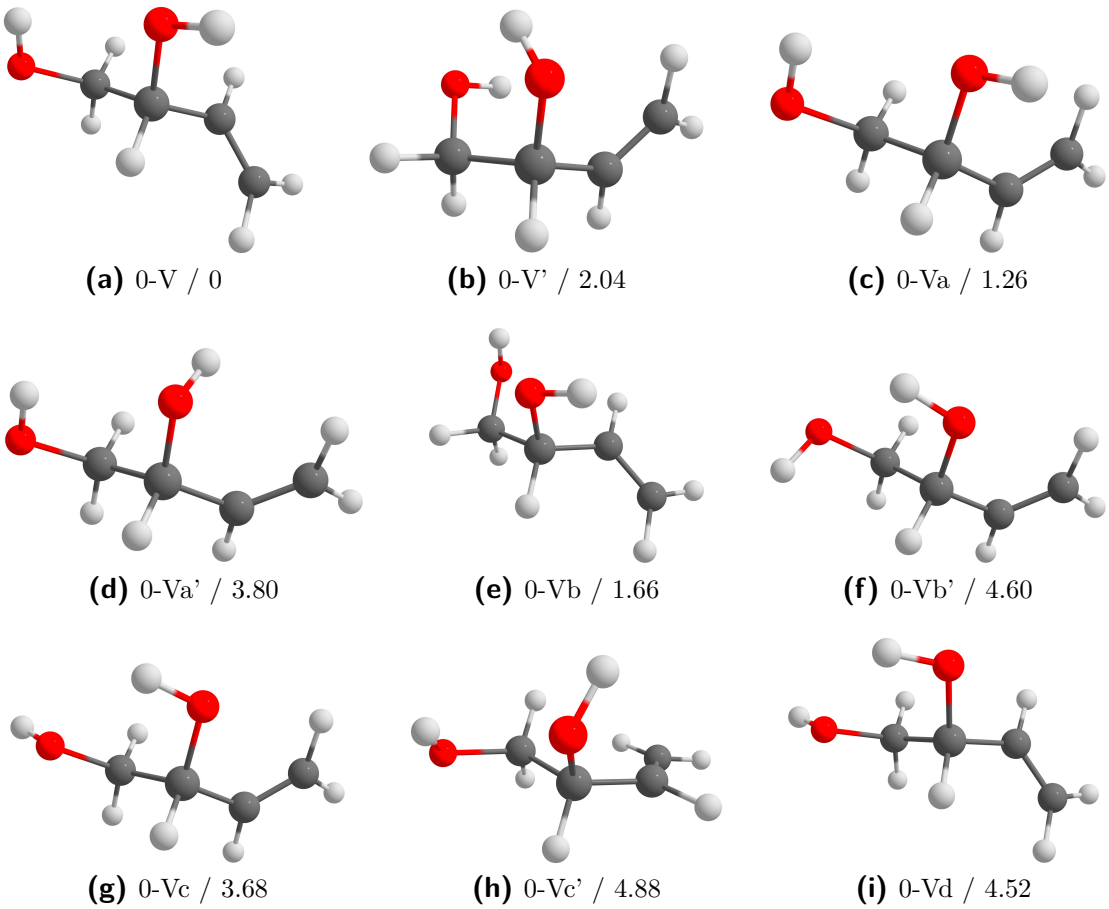

(a) 0-V / 0 **(b)** 0-V' / 2.04 **(c)** 0-Va / 1.26

(d) 0-Va' / 3.80 **(e)** 0-Vb / 1.66 **(f)** 0-Vb' / 4.60

(g) 0-Vc / 3.68 **(h)** 0-Vc' / 4.88 **(i)** 0-Vd / 4.52

Fig. A.9: Structures of 3-butene-1,2-diol (0-V). Relative zero-point corrected energies at the B3LYP/maTZ level are given in kJ mol^{-1}.

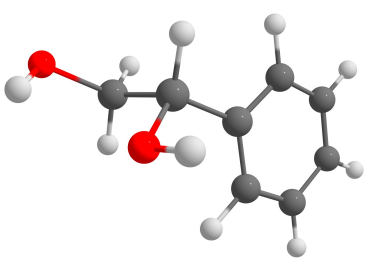

(a) 0-Ph / 0

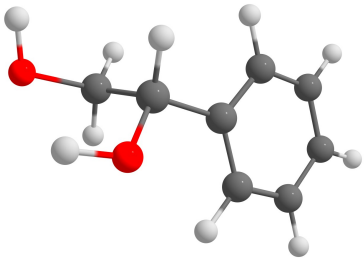

(b) 0-Ph' / 4.08

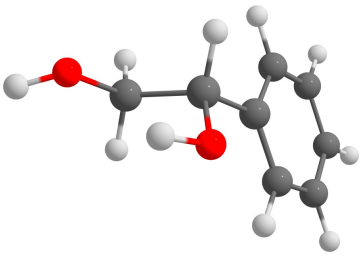

(c) 0-Pha / 3.46

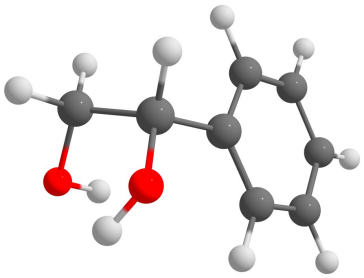

(d) 0-Pha' / 4.22

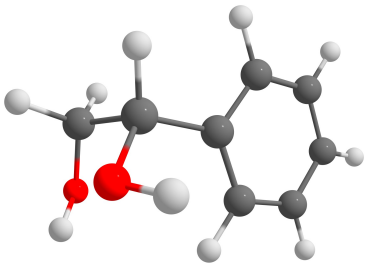

(e) 0-Phb / 5.60

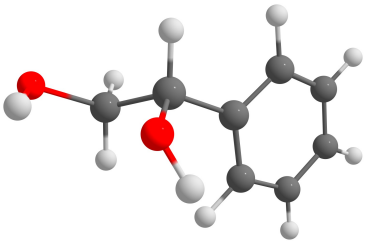

(f) 0-Phc / 5.74

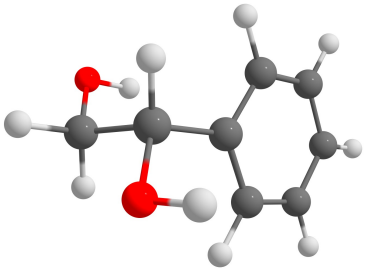

(g) 0-Pht / 5.75

Fig. A.10: Structures of 1-phenyl-ethane-1,2-diol (0-Ph). Relative zero-point corrected energies at the B3LYP/maTZ level are given in kJ mol^{-1}.

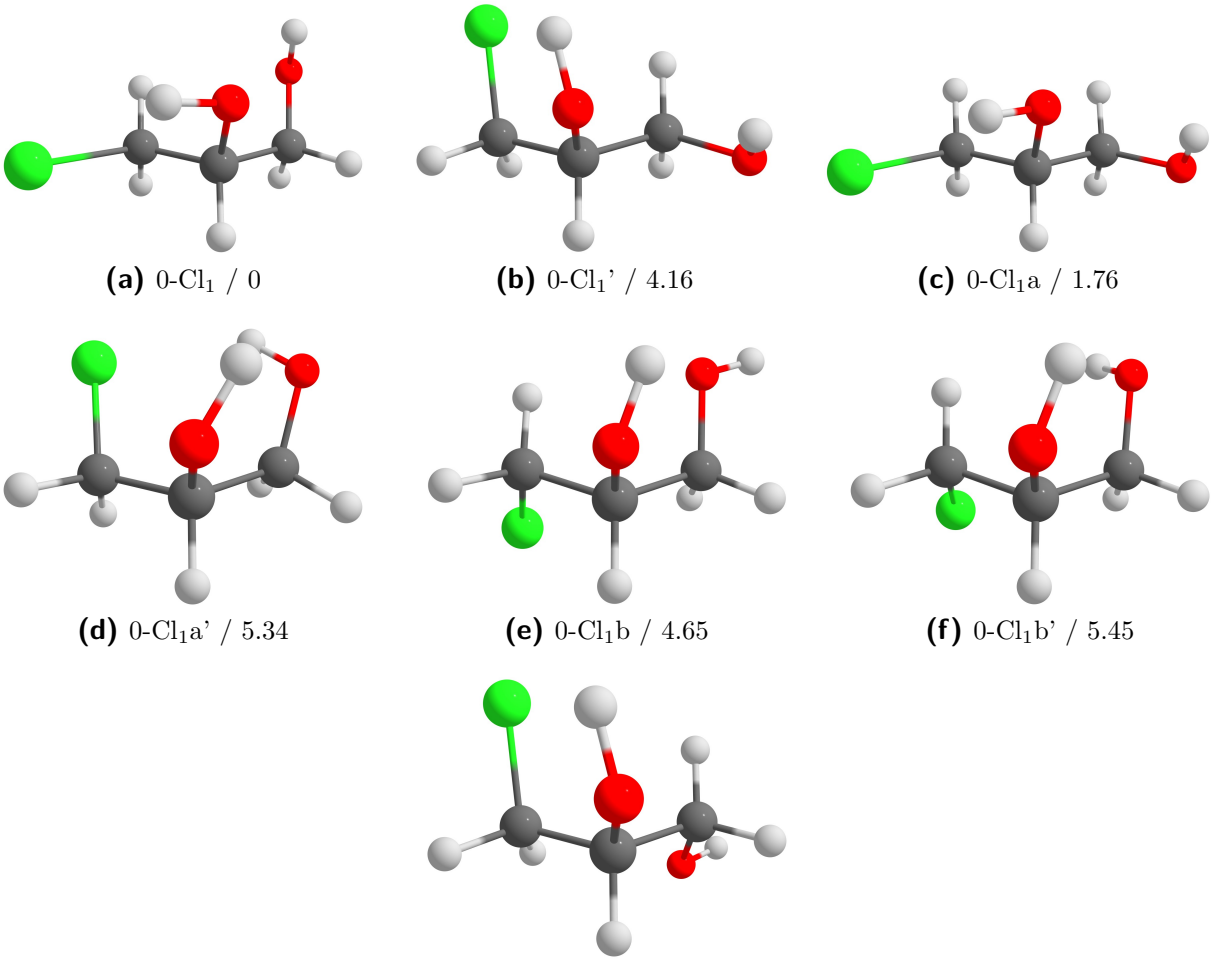

(a) 0-Cl_1 / 0 **(b)** 0-Cl_1' / 4.16 **(c)** 0-Cl_1a / 1.76

(d) 0-Cl_1a' / 5.34 **(e)** 0-Cl_1b / 4.65 **(f)** 0-Cl_1b' / 5.45

(g) 0-Cl_1t / 5.89

Fig. A.11: Structures of 3-chloro-propane-1,2-diol (0-Cl_1). Relative zero-point corrected energies at the B3LYP/maTZ level are given in kJ mol^{-1}.

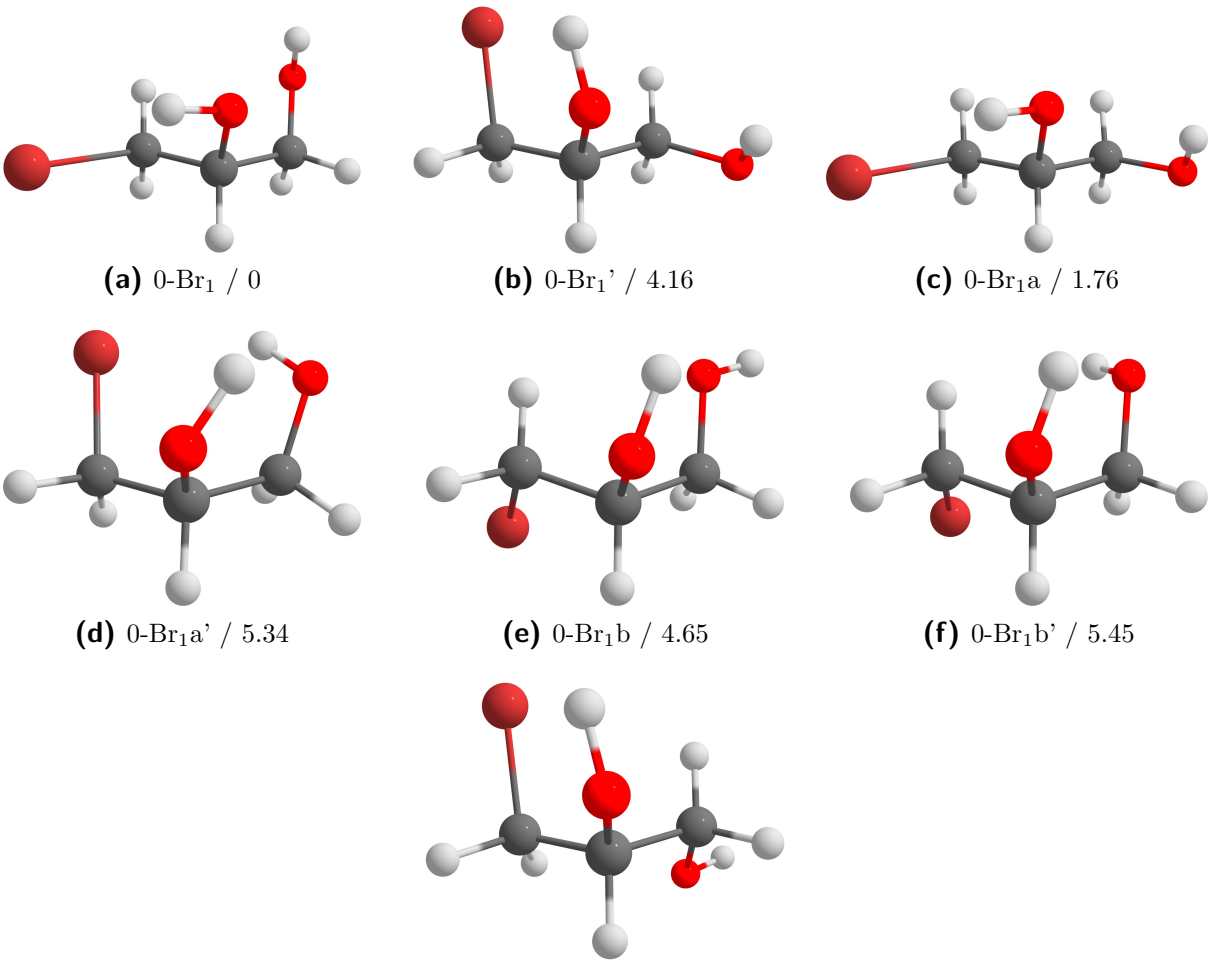

(a) 0-Br_1 / 0 **(b)** 0-Br_1' / 4.16 **(c)** 0-Br_1a / 1.76

(d) 0-Br_1a' / 5.34 **(e)** 0-Br_1b / 4.65 **(f)** 0-Br_1b' / 5.45

(g) 0-Br_1t / 5.89

Fig. A.12: Structures of 3-chloro-propane-1,2-diol (0-Br_1). Relative zero-point corrected energies at the B3LYP/maTZ level are given in kJ mol^{-1}.

A.1.4 $n_D = 2$: Primary-Tertiary

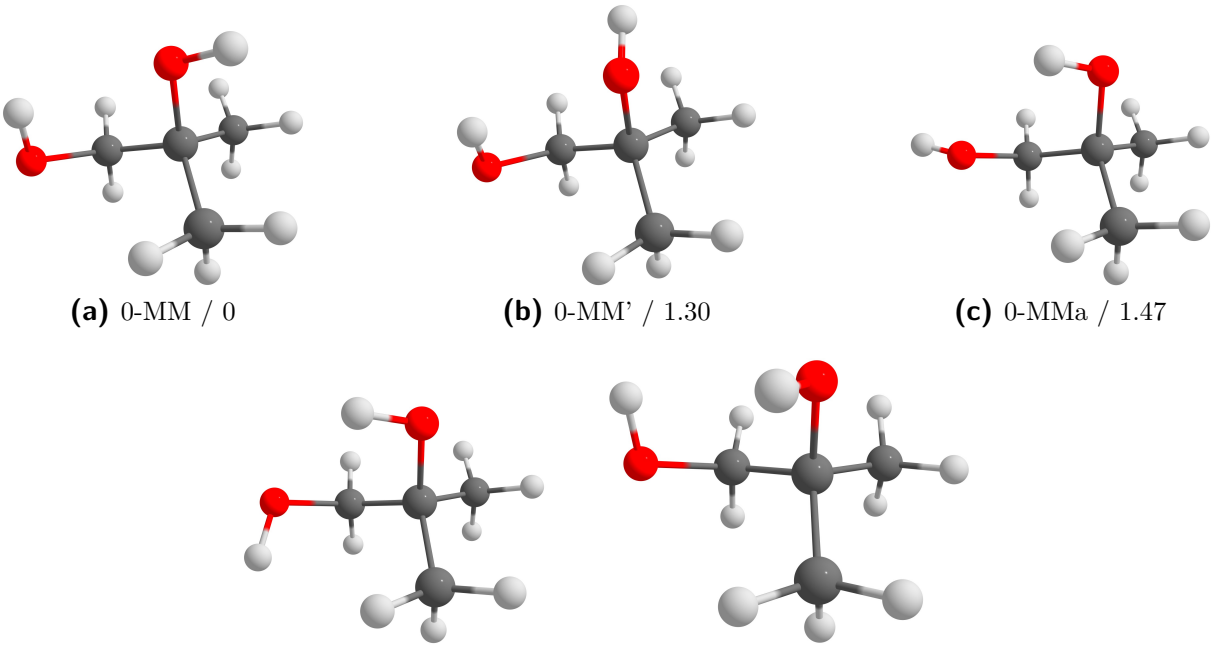

(a) 0-MM / 0 **(b)** 0-MM' / 1.30 **(c)** 0-MMa / 1.47

(d) 0-MMa' / 2.08 **(e)** 0-MM* / 3.00

Fig. A.13: Structures of 2-methyl-propane-1,2-diol (0-MM). Relative zero-point corrected energies at the B3LYP/maTZ level are given in kJ mol^{-1}.

A.1.5 $n_D = 2$: Secondary-Secondary

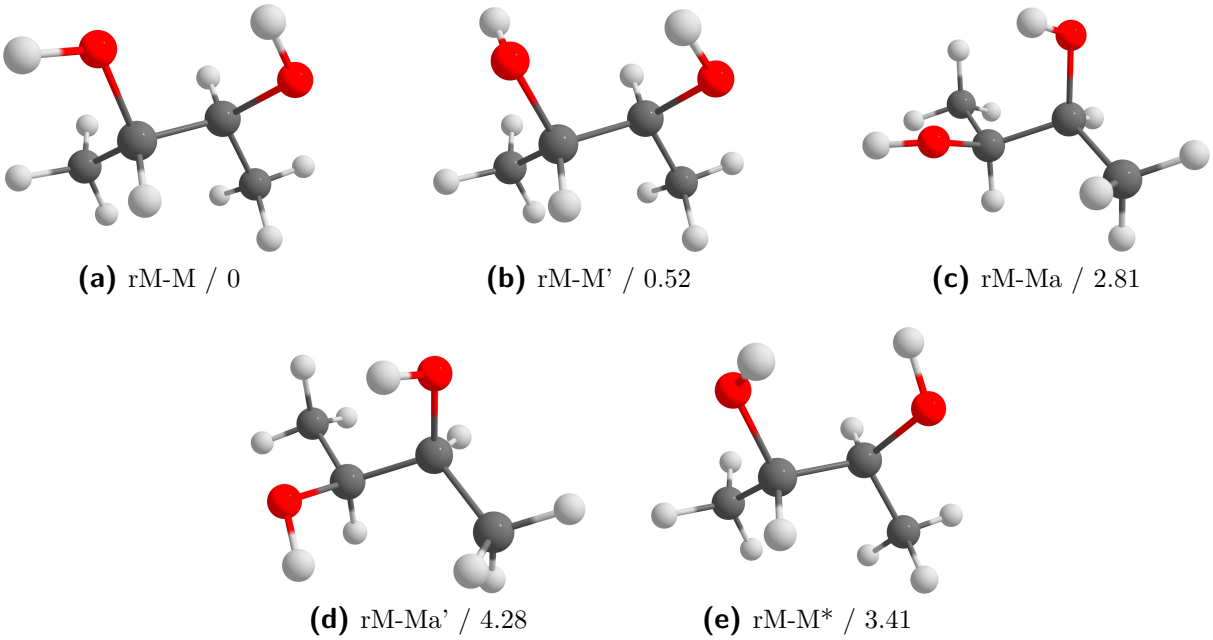

(a) rM-M / 0 **(b)** rM-M' / 0.52 **(c)** rM-Ma / 2.81

(d) rM-Ma' / 4.28 **(e)** rM-M* / 3.41

Fig. A.14: Structures of *rac*-butane-2,3-diol (rM-M). Relative zero-point corrected energies at the B3LYP/maTZ level are given in kJ mol^{-1}.

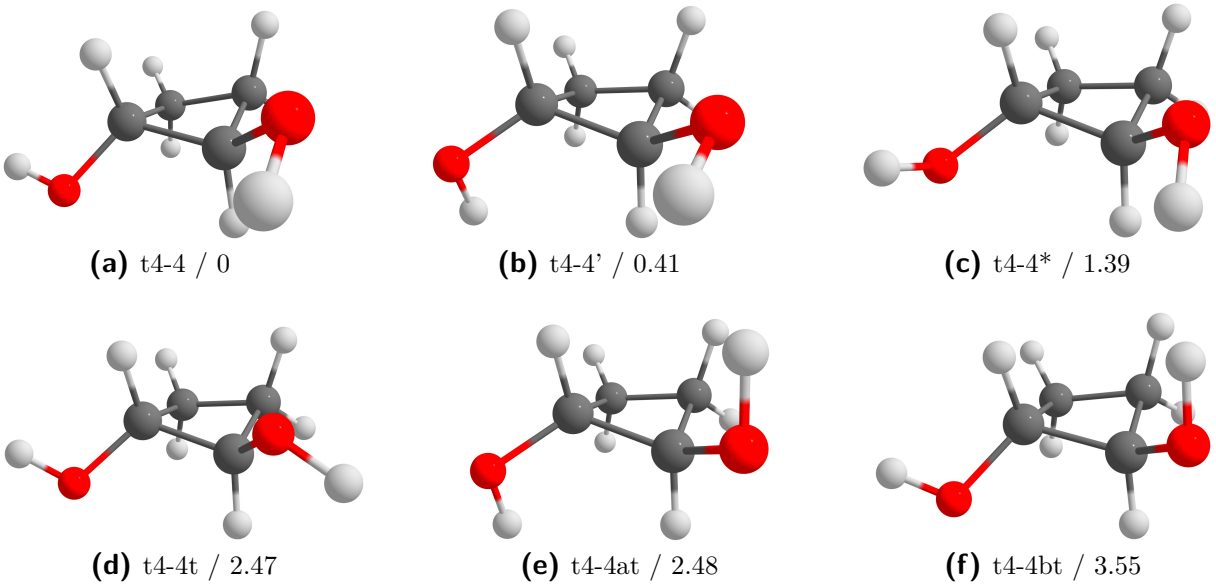

(a) t4-4 / 0 **(b)** t4-4' / 0.41 **(c)** t4-4* / 1.39

(d) t4-4t / 2.47 **(e)** t4-4at / 2.48 **(f)** t4-4bt / 3.55

Fig. A.15: Structures of *trans*-cyclobutane-1,2-diol (t4-4). Relative zero-point corrected energies at the B3LYP/maTZ level are given in kJ mol^{-1}.

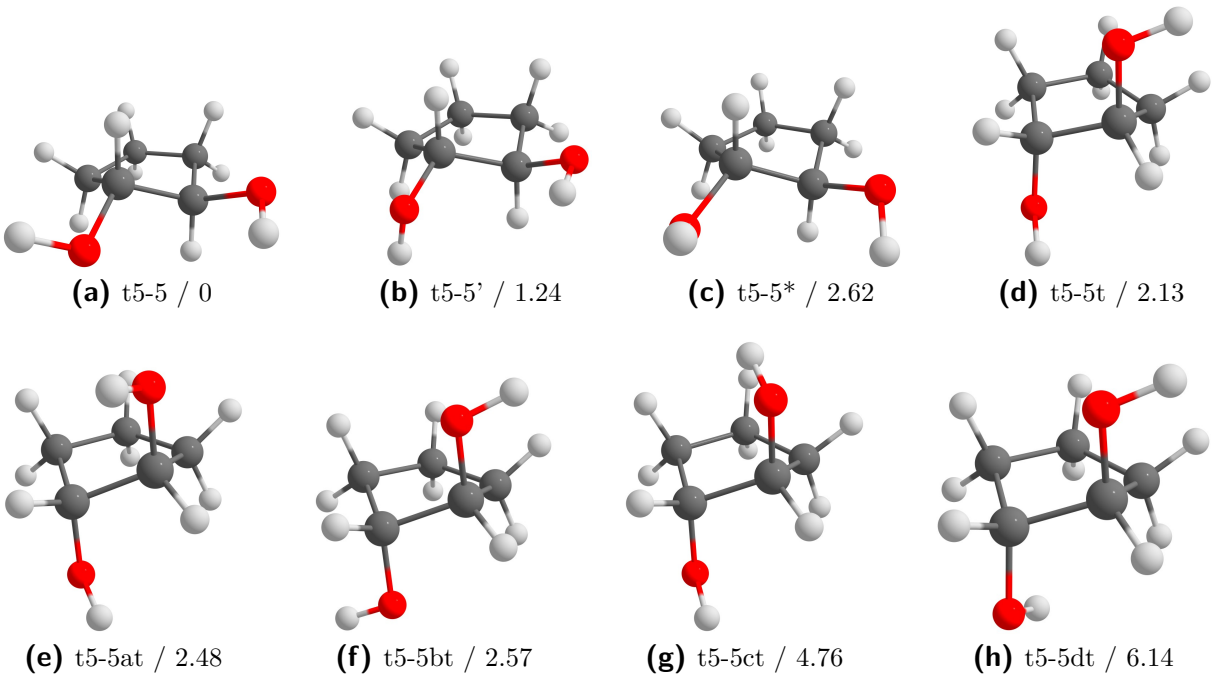

(a) t5-5 / 0 **(b)** t5-5' / 1.24 **(c)** t5-5* / 2.62 **(d)** t5-5t / 2.13

(e) t5-5at / 2.48 **(f)** t5-5bt / 2.57 **(g)** t5-5ct / 4.76 **(h)** t5-5dt / 6.14

Fig. A.16: Structures of *trans*-cyclopentane-1,2-diol (t5-5). Relative zero-point corrected energies at the B3LYP/maTZ level are given in kJ mol^{-1}.

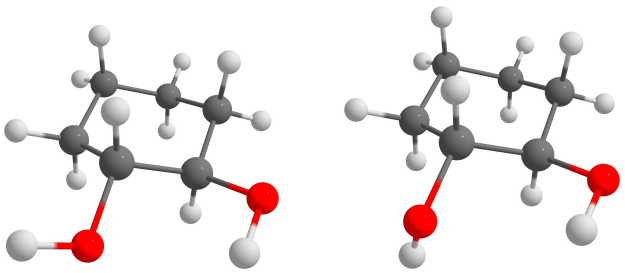

(a) t6-6 / 0 **(b)** t6-6' / 0.75

Fig. A.17: Structures of *trans*-cyclohexane-1,2-diol. Relative zero-point corrected energies at the B3LYP/maTZ level are given in kJ mol^{-1}.

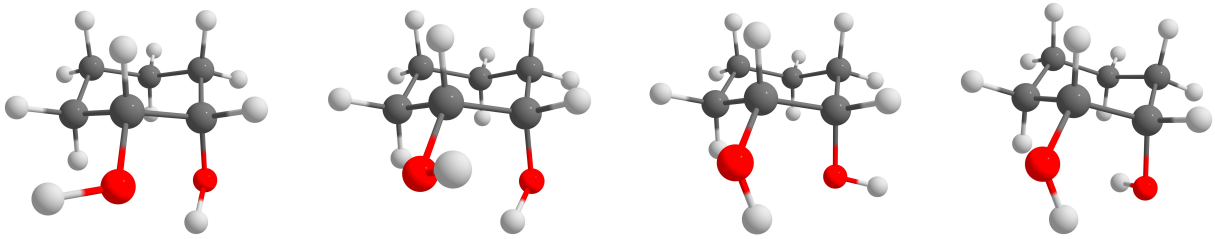

(a) c6-6 / 0 **(b)** c6-6' / 1.95 **(c)** c6-6a / 2.49 **(d)** c6-6a' / 5.09

Fig. A.18: Structures of *cis*-cyclohexane-1,2-diol. Relative zero-point corrected energies at the B3LYP/maTZ level are given in kJ mol^{-1}.

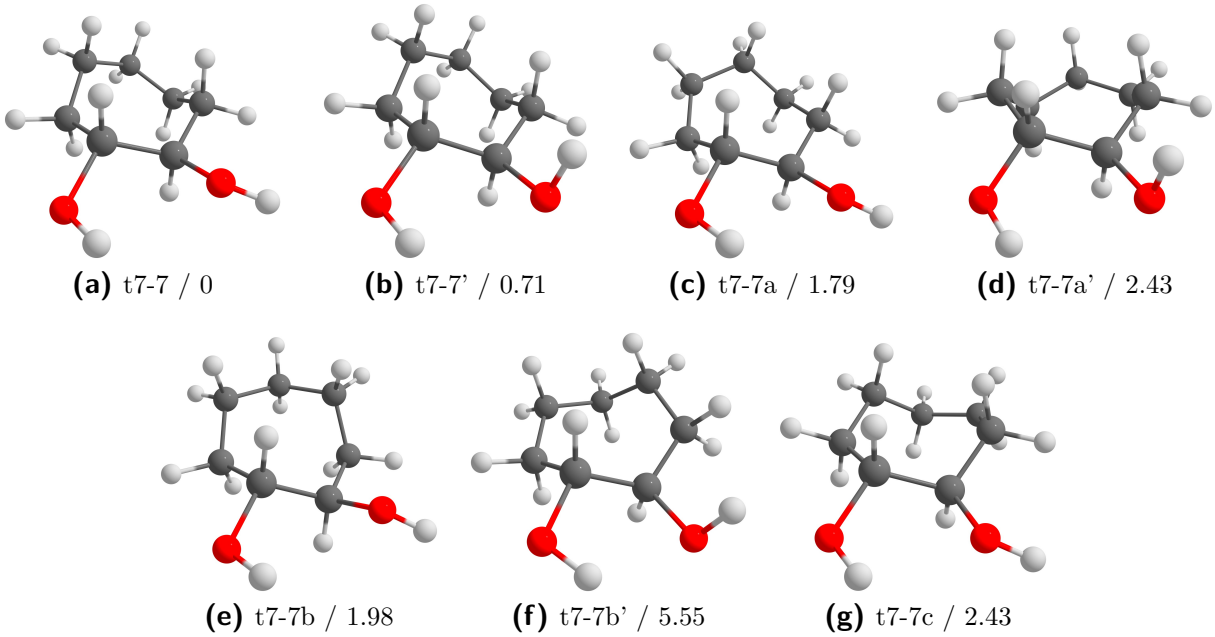

(a) t7-7 / 0 **(b)** t7-7' / 0.71 **(c)** t7-7a / 1.79 **(d)** t7-7a' / 2.43

(e) t7-7b / 1.98 **(f)** t7-7b' / 5.55 **(g)** t7-7c / 2.43

Fig. A.19: Structures of *trans*-cycloheptane-1,2-diol (t7-7). Relative zero-point corrected energies at the B3LYP/maTZ level are given in kJ mol^{-1}.

A.1.6 $n_D = 3$: Secondary-Tertiary

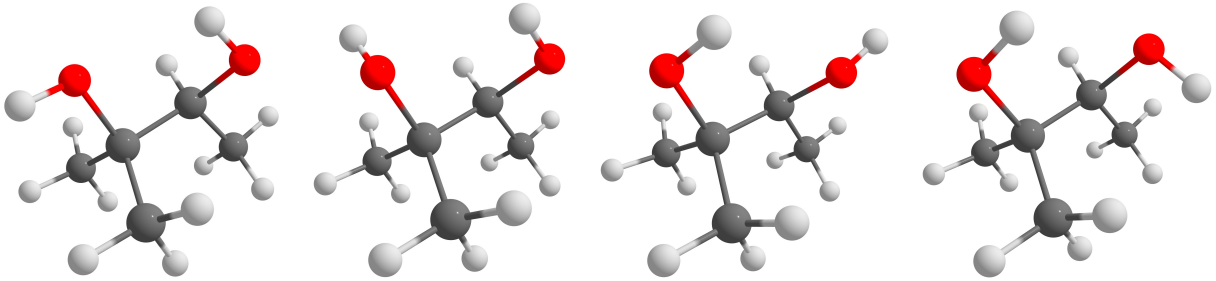

(a) M-MM / 0 **(b)** M-MM' / 0.87 **(c)** M-MMa / 2.15 **(d)** M-MMa' / 2.41

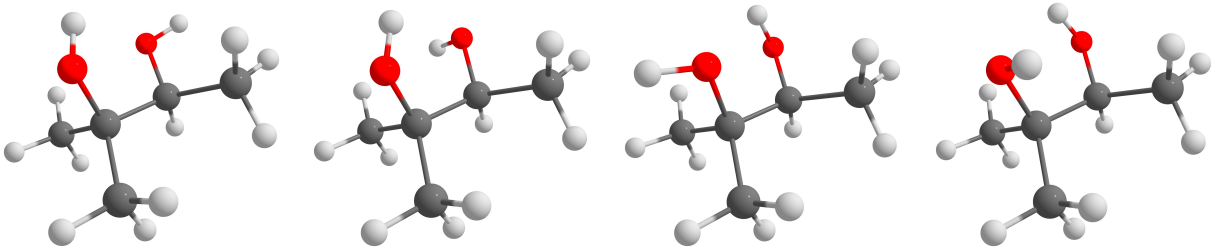

(e) M-MMb / 2.48 **(f)** M-MMb' / 4.31 **(g)** M-MMc / 3.59 **(h)** M-MMc' / 4.47

Fig. A.20: Structures of 2-methyl-butane-2,3-diol (M-MM). Relative zero-point corrected energies at the B3LYP/maTZ level are given in kJ mol^{-1}.

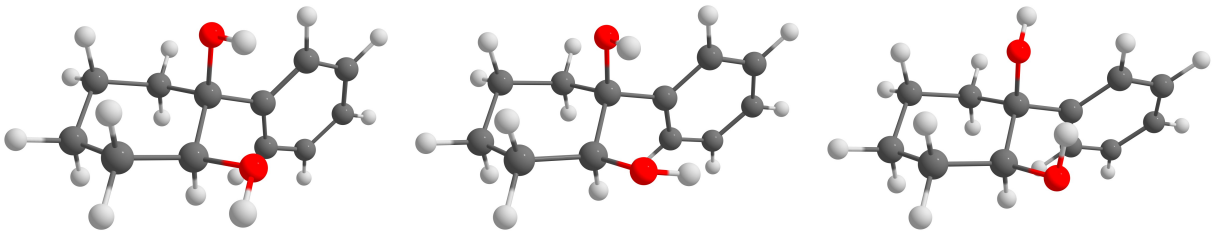

(a) c6-6Ph / 7.20 **(b)** c6-6Ph' / 0 **(c)** c6-6Pha / 10.16

Fig. A.21: Structures of 1-phenyl-*cis*-cyclohexane-1,2-diol (c6-6Ph). Relative zero-point corrected energies at the B3LYP/maTZ level are given in kJ mol^{-1}.

A.1.7 $n_D = 4$: Tertiary-Tertiary

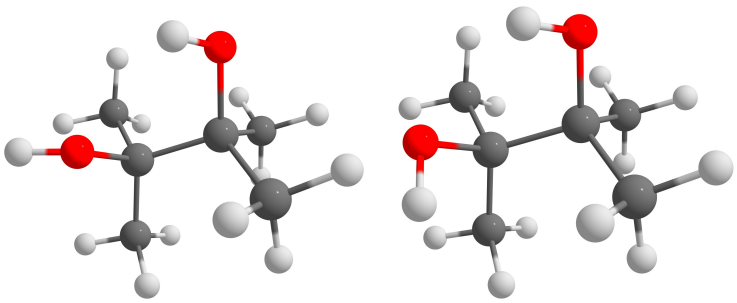

(a) MM-MM / 0 **(b)** MM-MM' / 1.16

Fig. A.22: Structures of pinacol (MM-MM). Relative zero-point corrected energies at the B3LYP/maTZ level are given in kJ mol^{-1}.

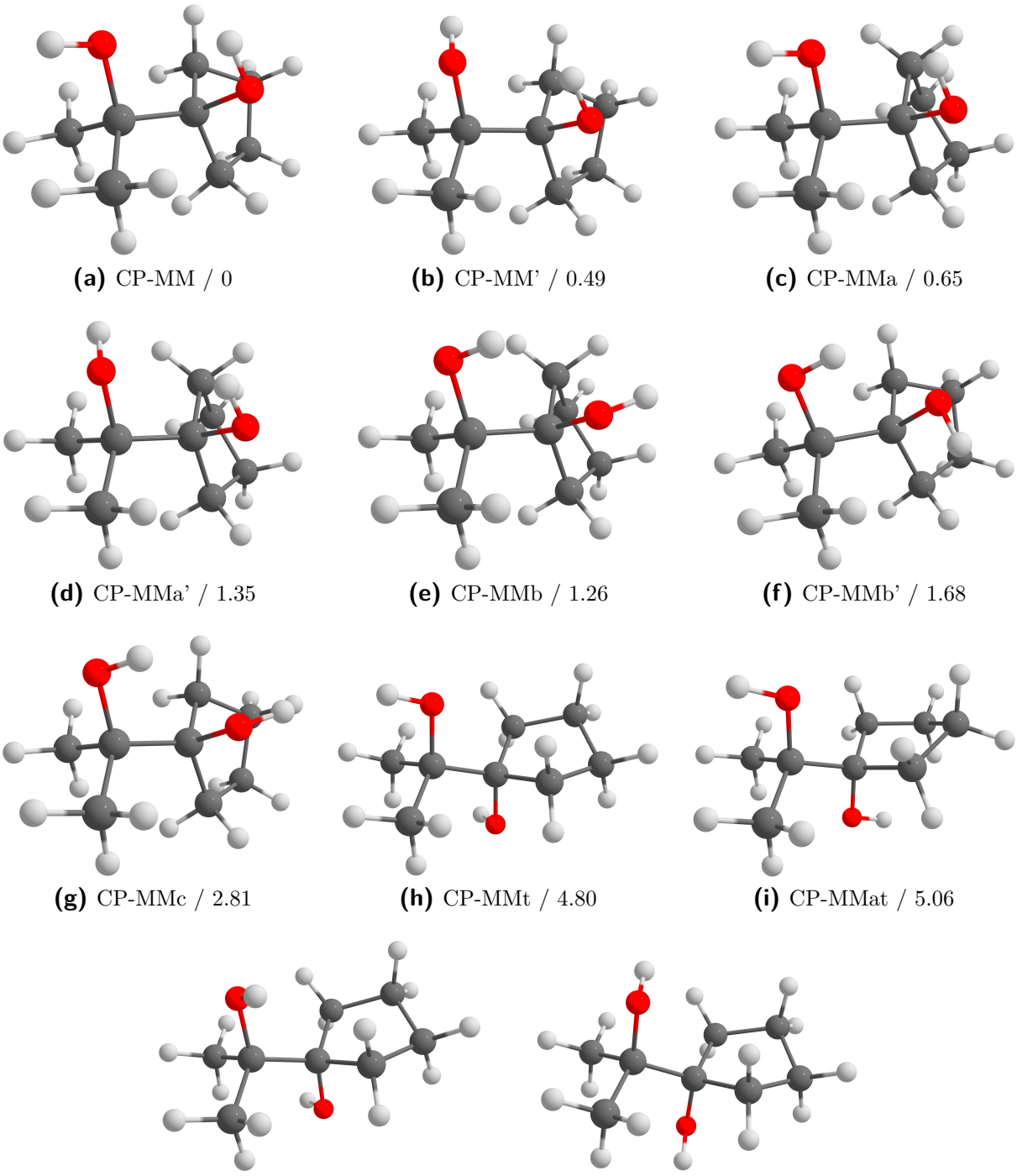

(a) CP-MM / 0 **(b)** CP-MM' / 0.49 **(c)** CP-MMa / 0.65

(d) CP-MMa' / 1.35 **(e)** CP-MMb / 1.26 **(f)** CP-MMb' / 1.68

(g) CP-MMc / 2.81 **(h)** CP-MMt / 4.80 **(i)** CP-MMat / 5.06

(j) CP-MMbt / 5.10 **(k)** CP-MMct / 5.20

Fig. A.23: Structures of 1-(1-hydroxy-1-methylethyl)-cyclopentanol (CP-MM). Relative zero-point corrected energies at the B3LYP/maTZ level are given in kJ mol^{-1}.

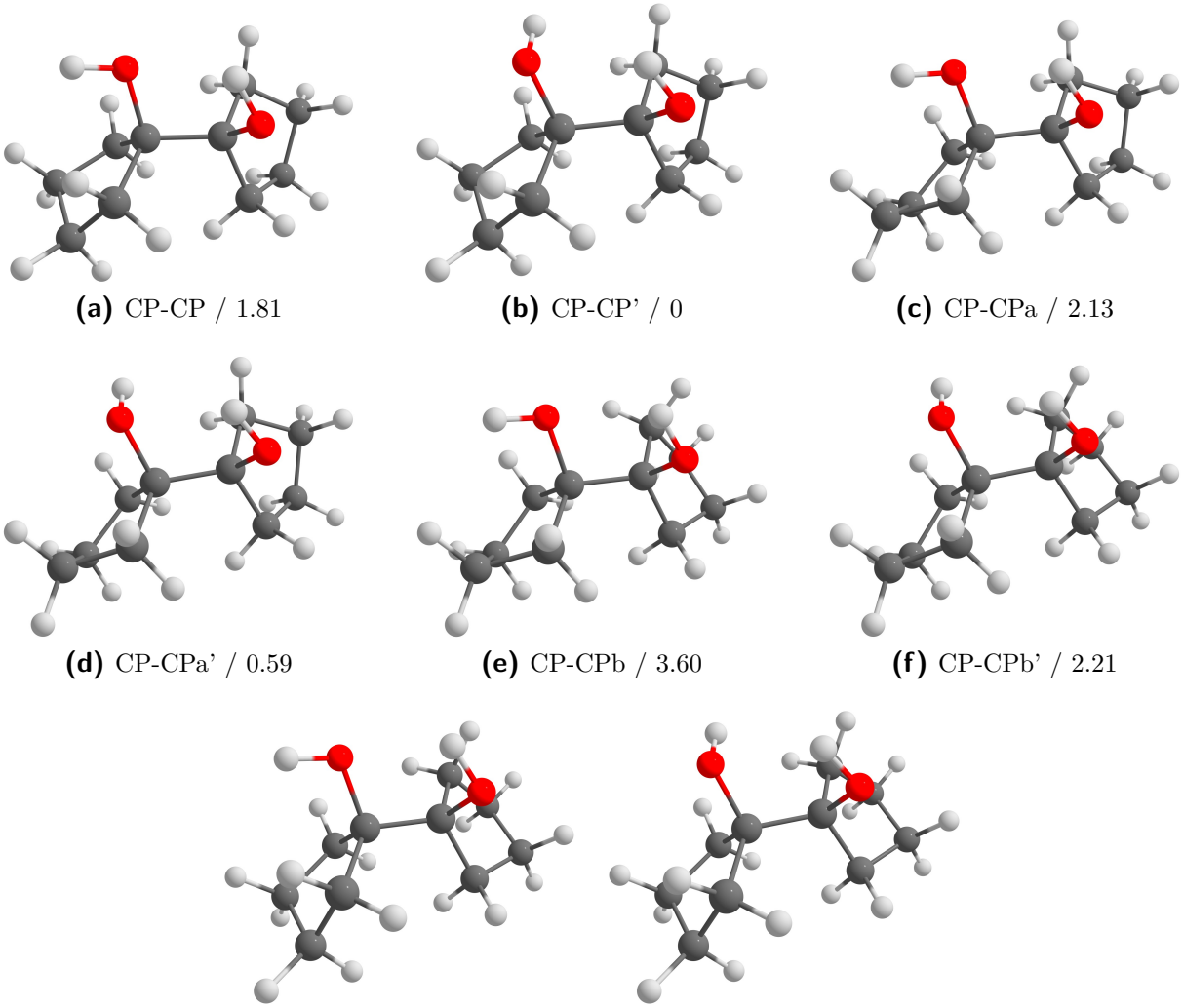

(a) CP-CP / 1.81 **(b)** CP-CP' / 0 **(c)** CP-CPa / 2.13

(d) CP-CPa' / 0.59 **(e)** CP-CPb / 3.60 **(f)** CP-CPb' / 2.21

(g) CP-CPc / 4.76 **(h)** CP-CPc' / 3.40

Fig. A.24: Structures of [1,1'-bicyclopentyl]-1,1'-diol (CP-CP). Relative zero-point corrected energies at the B3LYP/maTZ level are given in kJ mol^{-1}.

A.2 Dimers

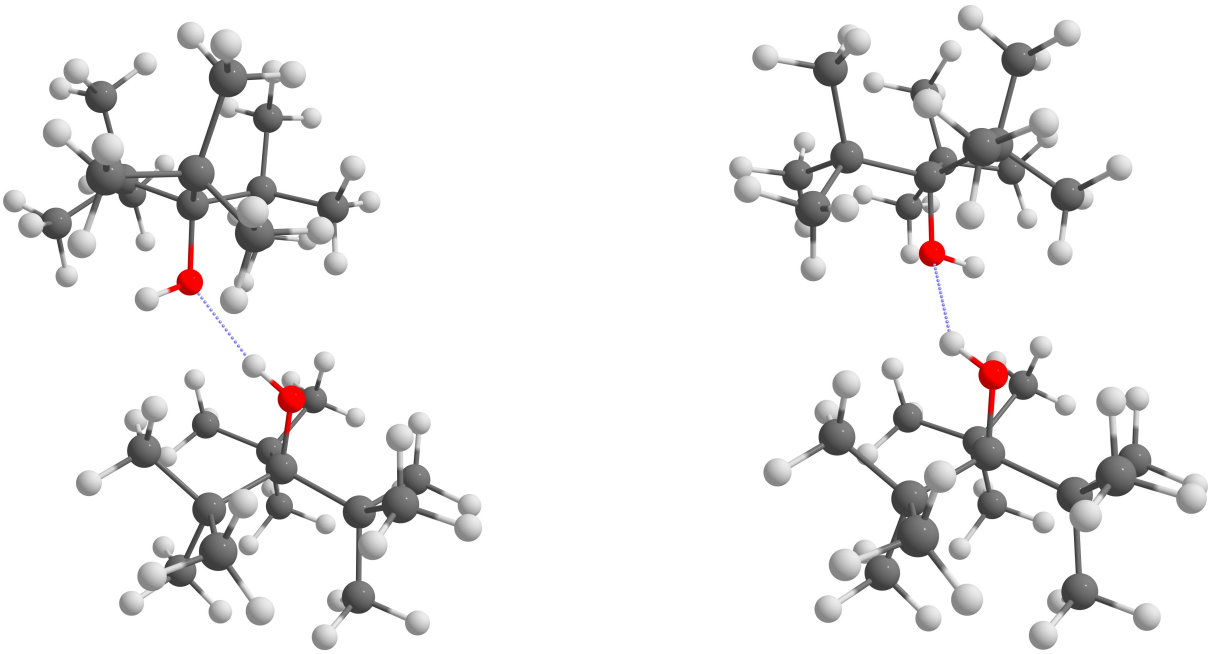

(a) hom1' / 0

(b) hom1a'/ 0.83

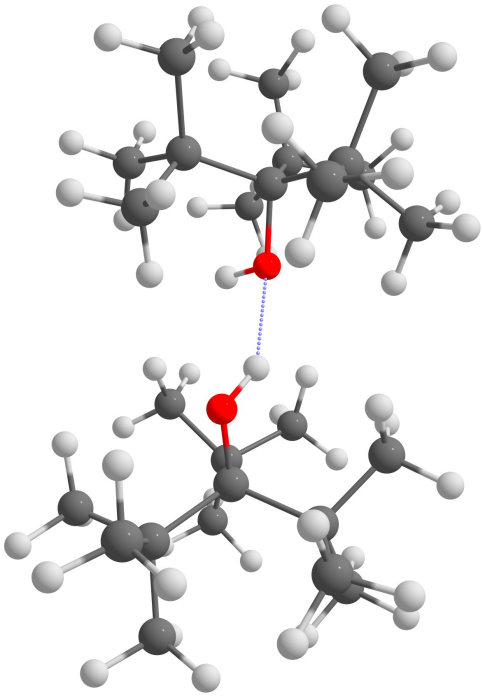

(c) het1' / 0.36

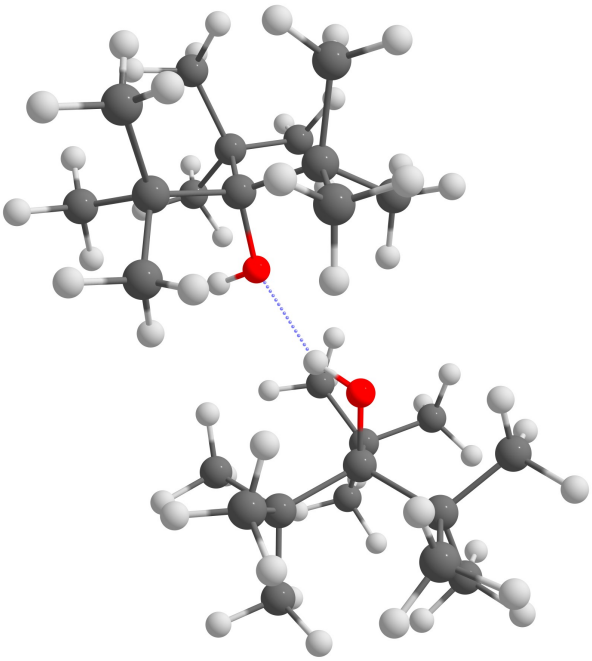

(d) het1a' / 1.50

Fig. A.25: Structures of tri-*tert*-butyl-methanol. Relative zero-point corrected energies at the B3LYP/maTZ level are given in kJ mol^{-1}.

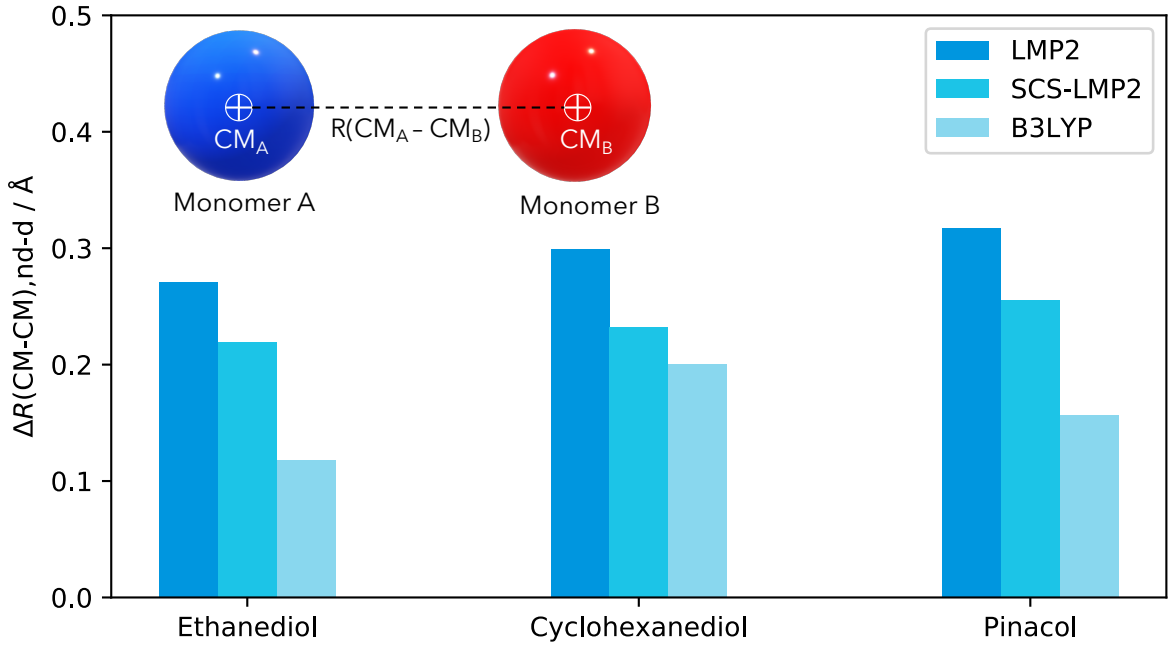

Fig. A.26: Average differences of the distance of the centre of mass (CM) of the monomer subunits ΔR(CM−CM) at the LMP2, SCS-LMP2 and B3LYP level of theory. The centre of mass distance is illustrated in the top left. nd indicates the no dispersion and d the dispersion case. Positive values indicate an increased separation of the monomers upon neglect of dispersion/dispersion correction. This figure is taken from Ref. [101].

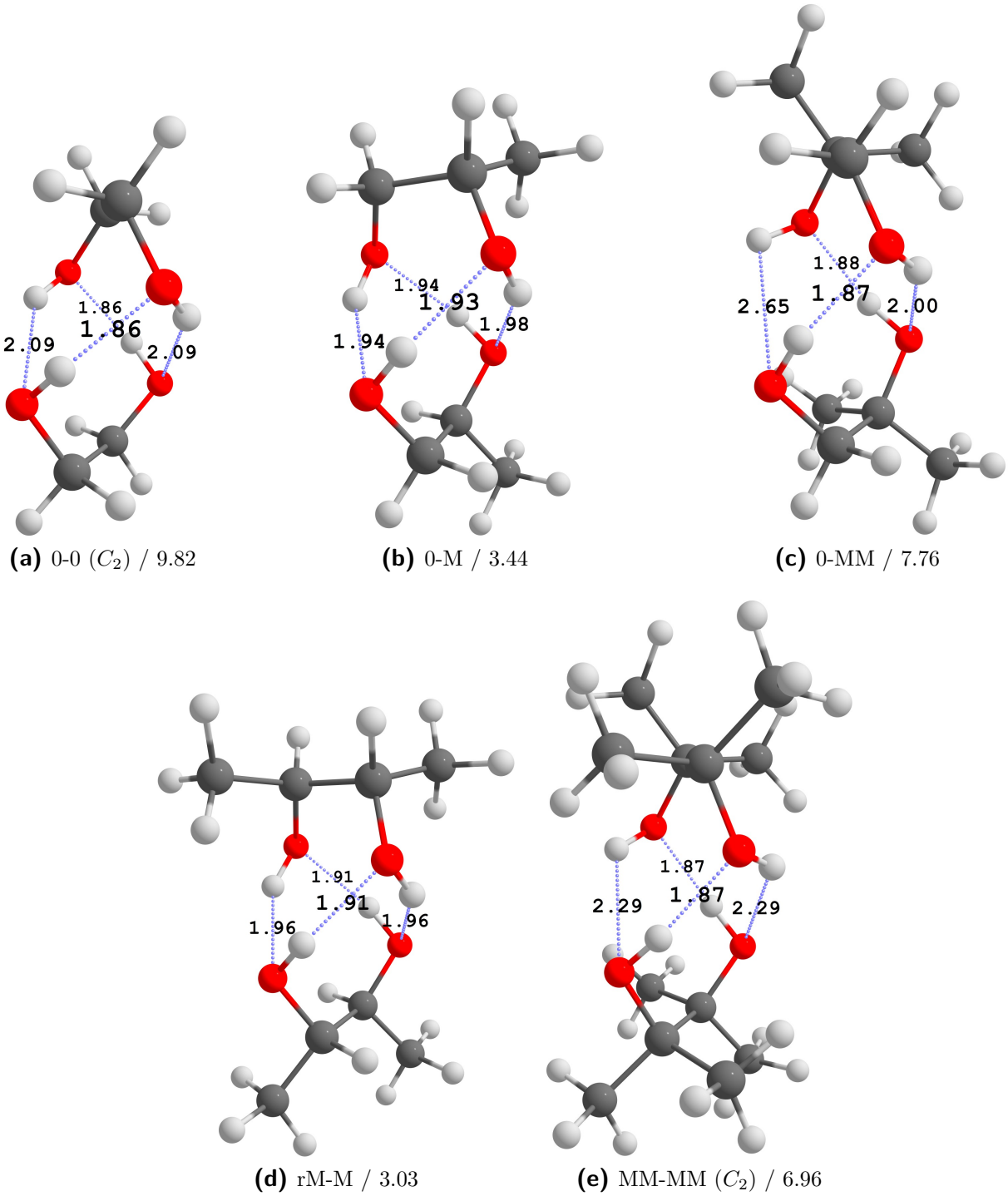

(a) 0-0 (C_2) / 9.82 **(b)** 0-M / 3.44 **(c)** 0-MM / 7.76

(d) rM-M / 3.03 **(e)** MM-MM (C_2) / 6.96

Fig. A.27: Overview of the most stable hom4 dimers of different systems. The systems shown are ethane-1,2-diol (0-0), propane-1,2-diol (0-M), 2-methyl-propane-1,2-diol (0-MM), butane-2,3-diol (rM-M) and pinacol (MM-MM). Hydrogen bond lengths are shown in Å. Relative zero-point corrected energies at the B3LYP/maTZ level are given in kJ mol^{-1}.

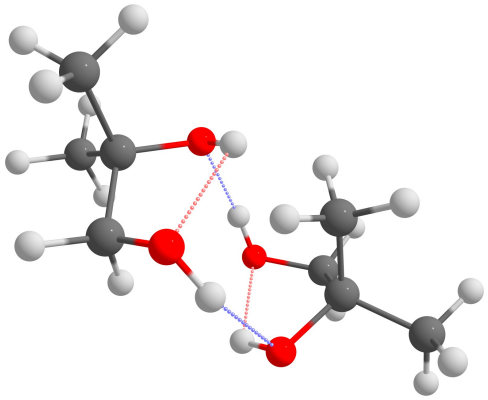

(a) hom2a”

Fig. A.28: Hypothetical hom2a” pattern analogous to that of propane-1,2-diol (0-M) for 2-methyl-propane-1,2-diol (0-MM). hom2a” of 0-M is shown in Fig. 4.18f (page 163).

B Energetic tables

B.1 Monomers

B.1.1 $n_D = 0$: Primary-Primary

Tab. B.1: Comparison of computational results for 0-0. Relative electronic energies (ΔE_{el}) and zero point corrected energies (ΔE_0) are given in kJ mol^{-1}. Conformers highlighted in bold text are assigned in the experimental Raman data. The corresponding structures can be found in Fig. A.6 (page 224).

	0-0	**0-0'**	
BP86/maTZ[165]	ΔE_{el}	0	0.13
	ΔE_0	0	0.49
PBE/maTZ[165]	ΔE_{el}	0	0.15
	ΔE_0	0	0.49
PBE0/maTZ[165]	ΔE_{el}	0	1.08
	ΔE_0	0	1.34
B3LYP/maTZ[165]	ΔE_{el}	0	1.21
	ΔE_0	0	1.49
B3LYP/TZ[166]	ΔE_{el}	0	0.6
	ΔE_0	0	1.1
B3LYP/QZ[166]	ΔE_{el}	0	1.1
	ΔE_0	0	1.3
PBE0/6-311+G(d,p)[184]	ΔE_{el}	0	1.8
	ΔE_0	0	2.0
B3LYP/6-31+G(d,p)[182]	ΔE_0	0	1.5
B3LYP/6-311++G**[183]	ΔE_0	0	2.4

B3LYP-D3(BJ)/6-311+G(2d,p)[18]	ΔE_0	0	1.4
B3LYP/aug-cc-pVDZ[183]	ΔE_0	0	1.7
B3LYP/aug-cc-pVTZ[179]	ΔE_0	0	1.8
MP2/6-31G**[209]	ΔE_{el}	0	0.83
MP2/6-311G**[175]	ΔE_{el}	0	0.3
MP2/6-311G(d, p)[178]	ΔE_{el}	0	0.38
	ΔE_0	0	1.34
MP2/6-311G(d,p)[181]	ΔE_{el}	0	0.3
MP2/6-311++G(d,p)[181]	ΔE_{el}	0	2.6
MP2/6-311+G(2d,p)//MP2/6-31G**[177]	ΔE_{el}	0	2.76
MP2/cc-pVDZ[176]	ΔE_{el}	0.17	0
MP2/cc-pVTZ//MP2/cc-pVDZ[176]	ΔE_{el}	0	1.30
MP2/cc-pVDZ[181]	ΔE_{el}	0	1.8
MP2/aug-cc-pVDZ[181]	ΔE_{el}	0	1.8
MP2/cc-pVTZ[181]	ΔE_{el}	0	1.3
QCISD/6-311++G(2d,2p)[180]	ΔE_{el}	0	2.2
	ΔE_0	0	2.5
HM-IE[181]	ΔE_{el}	0	1.5
CCSD(T)/cc-pVDZ//MP2/cc-pVDZ[176]	ΔE_{el}	0.50	0
CCSD(T)/aug'-cc-pVTZ[179]	ΔE_{el}	0	1.3
LCCSD(T0)-F12a/cc-pVDZ-F12[166]	ΔE_{el}	0	1.9
	ΔE_0	0	2.0

B.1.2 $n_D = 1$: Primary-Secondary

Tab. B.2: Comparison of computational data with those of Lockley *et al.*[223], Lovas *et al.*[217], Lomas and co-workers[184,224], Kollipost[225] and Arenas *et al.*[220] for 0-M. The values given by Arenas *et al.* have been converted from cm^{-1} to kJ mol^{-1}. Relative electronic energies (ΔE_{el}) and zero point corrected energies (ΔE_0) are given. All values are given in kJ mol^{-1}. Conformers highlighted in bold text are assigned in the experimental Raman data. Lovas *et al.*[217] experimentally observe the same conformers, while Arenas *et al.*[220] are missing 0-Mb'. 0-Ma and 0-Mb were initially observed by Caminati[288] and later extended by the global minimum structure 0-M by Lockley *et al.*[223]. Our nomenclature corresponds to that used originally by Vazquez *et al.*[289] in the following way: 0-M=tG'g, 0-Ma=gG't, 0-M'=g'G'g, 0-Ma'=gG'g', 0-Mb=g'Gt, 0-Mb'=g'Gg, 0-Mc=tGg' and 0-Mc'=gGg'. The corresponding structures can be found in Fig. A.7 (page 225).

		0-M	**0-Ma**	**0-M'**	**0-Ma'**	**0-Mb**	**0-Mb'**	
BP86/maTZ[165]	ΔE_{el}	0.57	0.74	0	0.14	2.08	3.30
	ΔE_0	0.14	0.14	0	0.04	1.91	3.26
PBE/maTZ[165]	ΔE_{el}	0.54	0.85	0	0.30	2.39	3.69
	ΔE_0	0.13	0.23	0	0.17	2.22	3.63
PBE0/maTZ[165]	ΔE_{el}	0	0.34	0.42	0.78	1.88	3.84
	ΔE_0	0	0.17	0.77	1.01	2.16	4.19
B3LYP/maTZ[165]	ΔE_{el}	0	0.34	0.53	1.10	1.94	3.84
	ΔE_0	0	0.22	0.90	1.40	2.23	4.20
HF/6-31G[223]	ΔE_{el}	0	0.79	4.68	-	2.21	7.34
PBE0/6-311+G(d,p)[224]	ΔE_0	0	0.36	1.08	1.62	2.09	4.37
PBE0/6-311+G(d,p)[184]	ΔE_0	0	0.17	1.29	1.75	2.47	4.79
B3LYP-D3(BJ)/	ΔE_{el}	0	0.3	0.4	0.9	1.8	-
6-311+G(2d,p)[225]	ΔE_0	0	0.1	0.7	1.3	2.1	-
MP2/6-311++G**[223]	ΔE_{el}	0	0.87	-	-	1.85	-
MP2/aVTZ[217]	ΔE_0	0	0.89	1.37	2.75	2.54	4.49
MP2/aVTZ[220]	ΔE_0	0	1.00	1.04	2.55	2.30	-

conformer / method		**0-Mc**	0-Mc'
BP86/maTZ[165]	ΔE_{el}	4.76	3.87
	ΔE_0	4.41	3.94

PBE/maTZ[165]	ΔE_{el}	5.07	4.30		
	ΔE_0	4.72	4.36		
PBE0/maTZ[165]	ΔE_{el}	4.28	4.58		
	ΔE_0	4.33	4.99		
B3LYP/maTZ[165]	ΔE_{el}	4.18	4.60		
	ΔE_0	4.22	5.04		
HF/6-31G[223]	ΔE_{el}	4.16	8.57		
PBE0/6-311+G(d,p)[224]	ΔE_0	-	-		
PBE0/6-311+G(d,p)[184]	ΔE_0	4.38	5.86		
B3LYP-D3(BJ)/	ΔE_{el}	3.9	-		
6-311+G(2d,p)[225]	4.0	-			
MP2/6-311++G**[223]	ΔE_{el}		-	-	
MP2/aVTZ[217]	ΔE_0	4.17	5.75		
MP2/aVTZ[220]	ΔE_0	4.04	-		

Tab. B.3: Comparison of computational data for 0-F. Relative electronic energies (ΔE_{el}) and zero point corrected energies (ΔE_0) are given. All values are given in kJ mol^{-1}. Conformers highlighted in bold text are assigned in the experimental Raman data. The corresponding structures can be found in Fig. A.8 (page 226).

		0-F'	**0-F**	0-Fa'	0-Fa	0-Fb	**0-Fc**	
BP86/maTZ[165]	ΔE_{el}	0	3.62	5.88	8.55	9.53	9.00	
	ΔE_0	0	2.26	4.80	6.99	7.83	7.62	
PBE/maTZ[165]	ΔE_{el}	0	3.38	5.73	8.34	9.20	8.82	
	ΔE_0	0	2.04	4.66	6.79	7.51	7.45	
PBE0/maTZ[165]	ΔE_{el}	0	2.36	5.81	7.38	7.61	7.56	
	ΔE_0	0	1.11	4.74	5.94	5.91	6.17	
B3LYP/maTZ[165]	ΔE_{el}	0	1.99	5.72	7.19	7.61	7.52	
	ΔE_0	0	0.78	4.70	5.76	5.88	6.09	

Tab. B.4: Comparison of computational data for 0-V. Relative electronic energies (ΔE_{el}) and zero point corrected energies (ΔE_0) are given. All values are given in kJ mol^{-1}. Conformers highlighted in bold text are assigned in the experimental Raman data. The corresponding structures can be found in Fig. A.9 (page 226).

		0-V	**0-Va**	**0-Vb**	**0-V'**	**0-Vc**	
BP86/maTZ[165]	ΔE_{el}	0.93	2.26	1.91	0	5.25
	ΔE_0	0	1.30	1.36	0.19	4.22
PBE/maTZ[165]	ΔE_{el}	0.46	1.76	1.68	0	4.44
	ΔE_0	0	1.25	1.59	0.62	3.89
PBE0/maTZ[165]	ΔE_{el}	0.67	1.05	1.89	0	3.60
	ΔE_0	0	0.42	1.61	0.37	2.81
B3LYP/maTZ[165]	ΔE_{el}	0	1.22	1.29	1.08	3.88
	ΔE_0	0	1.26	1.66	2.04	3.68
		0-Va'	**0-Vd**	0-Vb'	0-Vc'	
BP86/maTZ[165]	ΔE_{el}	3.31	6.51	4.55	6.40	
	ΔE_0	2.56	5.19	4.00	6.34	
PBE/maTZ[165]	ΔE_{el}	2.68	5.93	3.78	6.16	
	ΔE_0	2.40	5.10	3.71	6.54	
PBE0/maTZ[165]	ΔE_{el}	2.97	5.59	4.00	6.91	
	ΔE_0	2.51	4.50	3.62	7.05	
B3LYP/maTZ[165]	ΔE_{el}	3.59	5.02	4.84	4.37	
	ΔE_0	3.80	4.52	4.60	4.88	

Tab. B.5: Comparison of computational data for 0-Ph with those of Lomas[184]. The value marked with † is for benzene as a solvent since in Lomas calculations this conformer was not found to be stable in the gas phase. Relative electronic energies (ΔE_{el}) and zero point corrected energies (ΔE_0) are given. All values are given in kJ mol^{-1}. Conformers highlighted in bold text are assigned in the experimental Raman data. The corresponding structures can be found in Fig. A.10 (page 227).

		0-Ph	**0-Pha**	**0-Ph'**	**0-Pha'**	0-Phb
BP86/maTZ[165]	ΔE_{el}	0	4.10	3.02	1.19	5.00
	ΔE_0	0	3.91	3.36	2.26	5.11
PBE/maTZ[165]	ΔE_{el}	0	3.81	2.78	1.85	5.38
	ΔE_0	0	3.67	3.11	2.86	5.47
PBE0/maTZ[165]	ΔE_{el}	0	3.41	3.57	2.11	5.65
	ΔE_0	0	3.23	3.81	3.11	5.77
B3LYP/maTZ[165]	ΔE_{el}	0	3.73	3.92	3.25	5.50
	ΔE_0	0	3.46	4.08	4.22	5.60
PBE0/6-311+G(d,p)[184]	ΔE_0	0	3.30	4.52	4.95	6.59

method \ conformer		0-Pht	0-Phc
BP86/maTZ[165]	ΔE_{el}	5.58	5.45
	ΔE_0	5.41	5.01
PBE/maTZ[165]	ΔE_{el}	6.29	5.55
	ΔE_0	6.11	5.47
PBE0/maTZ[165]	ΔE_{el}	5.83	7.15
	ΔE_0	5.66	6.01
B3LYP/maTZ[165]	ΔE_{el}	5.89	6.84
	ΔE_0	5.74	5.75
PBE0/6-311+G(d,p)[184]	ΔE_0	7.10	7.43†

Tab. B.6: Comparison of energetical computational data of 3-chloro-propane-1,2-diol (0-Cl_1). The relative electronic energy (ΔE_{el}) and harmonically zero point corrected energy (ΔE_0^h) as well as the anharmonically corrected energies (ΔE_0^{an}) if available are shown. The conformers are ordered according to the ΔE_0^h results of B3LYP/maTZ. All values are given in kJ mol^{-1}.

		0-Cl_1	0-Cl_1a	0-Cl_1'	0-Cl_1b	0-Cl_1a'	0-Cl_1b'	0-Cl_1t
BP86/ maTZ	E_{el}	0	2.84	2.97	5.43	1.93	4.70	7.38
	E_0^h	0	2.19	2.91	5.20	2.65	4.77	6.12
	E_0^{an}	-	-	-	-	-	-	-
PBE/ maTZ	E_{el}	0	2.51	3.45	5.82	3.08	5.39	7.98
	E_0^h	0	1.87	3.36	5.59	3.74	5.41	6.73
	E_0^{an}	-	-	-	-	-	-	-
PBE0/ maTZ	E_{el}	0	2.47	4.29	5.64	5.05	6.36	7.62
	E_0^h	0	1.87	4.19	5.39	5.73	6.24	6.48
	E_0^{an}	-	-	-	-	-	-	-
B3LYP/ maTZ	E_{el}	0	2.27	4.24	4.89	4.67	5.48	7.02
	E_0^h	0	1.76	4.16	4.65	5.34	5.45	5.89
	E_0^{an}	-	-	-	-	-	-	-
PBE0/ aVTZ	E_{el}	0	2.40	4.19	5.79	4.70	6.30	7.22
	E_0^h	0	1.84	4.07	5.50	5.38	6.19	6.14
	E_0^{an}	0	1.89	4.02	5.44	5.32	6.05	6.15
B3LYP/ aVTZ	E_{el}	0	2.18	4.11	4.81	4.35	5.27	6.48
	E_0^h	0	1.71	4.00	4.56	5.05	5.23	5.44
	E_0^{an}	0	1.83	3.95	4.79	5.06	5.43	5.75
CAM-B3LYP/ aVTZ	E_{el}	0	2.13	5.06	4.79	5.78	6.18	7.11
	E_0^h	0	1.65	4.97	4.54	6.53	5.96	6.09
	E_0^{an}	0	1.72	4.92	4.53	6.28	5.86	6.12
B2PLYP/ aVTZ	E_{el}	0	2.31	4.81	4.59	5.55	5.55	6.62
	E_0^h	0	1.84	4.72	4.32	6.26	5.23	5.63
	E_0^{an}	0	2.00	4.58	4.31	6.21	5.30	5.81
MP2/ aVTZ	E_{el}	0	2.86	5.33	4.58	6.27	5.90	6.66
	E_0^h	0	2.35	5.27	4.26	7.02	5.76	5.73
	E_0^{an}	0	2.42	5.25	4.16	6.85	5.53	5.71

CCSD(T)-F12/ VDZ-F12	E_{el}	0	2.82	5.15	4.79	6.16	5.62	7.23
	E_0^h	0	2.31	5.07	4.50	6.92	5.51	6.21
	E_0^{an}	-	-	-	-	-	-	-

Tab. B.7: Comparison of energetical computational data of 3-bromo-propane-1,2-diol (0-Br_1). The relative electronic energy (ΔE_{el}) and harmonically zero point corrected energy (ΔE_0^h) as well as the anharmonically corrected energies (ΔE_0^{an}) if available are shown. The conformers are ordered according to the ΔE_0^h results of B3LYP/maTZ. All values are given in kJ mol^{-1}.

		0-Br_1	0-Br_1a	0-Br_1'	0-Br_1a'	0-Br_1b	0-Br_1b'	0-Br_1t
BP86/ maTZ	E_{el}	0	2.44	2.35	1.25	5.09	4.10	6.50
	E_0^h	0	1.92	2.26	1.90	5.02	4.38	5.20
	E_0^{an}	-	-	-	-	-	-	-
PBE/ maTZ	E_{el}	0	2.10	3.08	2.75	5.65	5.05	7.38
	E_0^h	0	1.60	2.96	3.34	5.59	5.27	6.10
	E_0^{an}	-	-	-	-	-	-	-
PBE0/ maTZ	E_{el}	0	2.16	3.99	4.97	5.59	6.20	7.03
	E_0^h	0	1.66	3.85	5.58	5.45	6.22	5.86
	E_0^{an}	-	-	-	-	-	-	-
B3LYP/ maTZ	E_{el}	0	1.91	3.91	4.55	4.65	5.12	6.44
	E_0^h	0	1.48	3.78	5.14	4.52	5.22	5.28
	E_0^{an}	-	-	-	-	-	-	-
PBE0/ aVTZ	E_{el}	0	2.09	3.88	4.65	5.68	6.11	6.67
	E_0^h	0	1.58	3.71	5.27	5.51	6.13	5.56
	E_0^{an}	0	1.31	3.74	5.17	5.59	5.87	5.71
B3LYP/ aVTZ	E_{el}	0	1.81	3.75	4.25	4.53	4.88	5.92
	E_0^h	0	1.39	3.60	4.87	4.40	4.98	4.85
	E_0^{an}	0	1.36	3.87	4.85	4.71	5.14	5.11
CAM-B3LYP/ aVTZ	E_{el}	0	1.76	4.86	5.97	4.53	5.88	6.73
	E_0^h	0	1.33	4.73	6.67	4.38	5.78	5.70
	E_0^{an}	0	1.37	4.65	6.44	4.24	5.49	5.51
B2PLYP/ aVTZ	E_{el}	0	2.03	4.51	5.31	4.42	5.24	6.02
	E_0^h	0	1.58	4.35	5.99	4.22	5.24	5.01

	E_0^{an}	0	1.60	4.21	5.89	4.27	4.82	4.95
MP2/ aVTZ	E_{el}	0	2.80	4.85	5.26	4.72	5.68	5.62
	E_0^{h}	0	2.26	4.67	6.04	4.37	5.59	4.67
	E_0^{an}	0	2.34	4.65	5.91	4.30	5.38	4.69
CCSD(T)-F12/ VDZ-F12	E_{el}	0	2.30	4.62	6.49	4.28	5.32	6.69
	E_0^{h}	0	1.89	4.32	6.75	4.14	5.00	5.44
	E_0^{an}	-	-	-	-	-	-	-

B.1.3 $n_{\mathrm{D}} = 2$: Primary-Tertiary

Tab. B.8: Comparison of computational results for 0-MM. 0-MM* converges to 0-MM for all functionals besides B3LYP. Relative electronic energies (ΔE_{el}) and zero point corrected energies (ΔE_0) are given. All values are given in kJ mol^{-1}. Conformers highlighted in bold text are assigned in the experimental Raman data. The corresponding structures can be found in Fig. A.13 (page 230).

		0-MM	**0-MM'**	**0-MMa**	**0-MMa'**	0-MM*	
BP86/maTZ[165]	ΔE_{el}	0.08	0	2.30	1.18	-
	ΔE_0	0	0.39	2.21	1.52	-
PBE/maTZ[165]	ΔE_{el}	0.06	0	2.10	1.11	-
	ΔE_0	0	0.39	2.05	1.48	-
PBE0/maTZ[165]	ΔE_{el}	0	0.76	1.73	1.76	-
	ΔE_0	0	1.19	1.72	2.15	-
B3LYP/maTZ[165]	ΔE_{el}	0	0.89	1.53	1.69	3.63
	ΔE_0	0	1.30	1.47	2.08	3.00

B.1.4 n_D = 2: Secondary-Secondary

Tab. B.9: Comparison of computational results for t4-4. Relative electronic energies (ΔE_{el}) and zero point corrected energies (ΔE_0) are given. All values are given in kJ mol^{-1}. Conformers highlighted in bold text are assigned in the experimental Raman data. The corresponding structures can be found in Fig. A.15 (page 231).

		t4-4	**t4-4'**	**t4-4***	**t4-4t**	t4-4at	t4-4bt	
BP86/maTZ[165]	ΔE_{el}	0.76	0	2.48	4.22	1.29	3.59	
	ΔE_0	0.35	0	1.34	2.67	1.35	3.03	
PBE/maTZ[165]	ΔE_{el}	0.71	0	2.36	4.12	1.35	3.56	
	ΔE_0	0.29	0	1.42	2.50	1.39	3.00	
PBE0/maTZ[165]	ΔE_{el}	0.17	0	2.36	4.12	1.35	3.66	
	ΔE_0	0	0.20	1.56	2.64	1.88	3.31	
B3LYP/maTZ[165]	ΔE_{el}	0.01	0	2.04	3.64	2.05	3.72	
	ΔE_0	0	0.41	1.39	2.47	2.48	3.55	

Tab. B.10: Comparison of computational results for t5-5. Relative electronic energies (ΔE_{el}) and zero point corrected energies (ΔE_0) are given. All values are given in kJ mol^{-1}. Conformers highlighted in bold text are assigned in the experimental Raman data. The corresponding structures can be found in Fig. A.16 (page 231).

		t5-5	**t5-5'**	t5-5t	t5-5at	t5-5bt	t5-5*	t5-5ct	t5-5dt	
BP86/maTZ[165]	ΔE_{el}	0	0.07	2.25	2.19	3.50	3.72	4.02	6.19	
	ΔE_0	0	0.33	1.72	1.51	2.67	2.46	3.38	5.06	
PBE/maTZ[165]	ΔE_{el}	0	0.12	2.94	2.88	4.18	3.70	4.81	7.02	
	ΔE_0	0	0.38	2.40	2.16	3.37	2.49	4.17	5.89	
PBE0/maTZ[165]	ΔE_{el}	0	0.79	3.41	3.92	4.12	4.19	6.09	7.85	
	ΔE_0	0	1.01	3.07	3.42	3.53	2.93	5.39	6.81	
B3LYP/maTZ[165]	ΔE_{el}	0	0.97	2.47	2.93	3.20	3.78	5.42	7.15	
	ΔE_0	0	1.24	2.13	2.48	2.57	2.62	4.76	6.14	

Tab. B.11: Comparison of computational results for t6-6 and those of Paoloni *et al.*[186]. Relative electronic energies (ΔE_{el}) and harmonically (also for Ref. [186]) zero point corrected energies (ΔE_0) are given. All values are given in kJ mol^{-1}. Conformers highlighted in bold text are assigned in the experimental Raman data. A general overview of other computational data can be found in the ESI of Ref. [166]. The corresponding structures can be found in Fig. A.17 (page 232).

		t6-6	**t6-6'**
BP86/maTZ[165]	ΔE_{el}	0.89	0
	ΔE_0	0.42	0
PBE/maTZ[165]	ΔE_{el}	0.82	0
	ΔE_0	0.36	0
PBE0/maTZ[165]	ΔE_{el}	0	0.07
	ΔE_0	0	0.47
B3LYP/maTZ[165]	ΔE_{el}	0	0.31
	ΔE_0	0	0.75
B3LYP/TZ[166]	ΔE_{el}	0	0.0
	ΔE_0	0	0.6
B3LYP/QZ[166]	ΔE_{el}	0	0.3
	ΔE_0	0	1.0
PBE0/6-311+G(d,p)[184]	ΔE_{el}	0	0.81
	ΔE_0	0	1.20
B3LYP/6-311++G**[185]	ΔE_{el}	0	1.27
B3LYP-D3(BJ)/jul-cc-pVDZ[186]	ΔE_{el}	0	0.31
	ΔE_0	0	0.72
B2PLYP-D3(BJ)/jun-cc-pVTZ[186]	ΔE_0	0	1.11

Tab. B.12: Comparison of computational results for c6-6 with those of Lomas[184]. Relative electronic energies (ΔE_{el}) and zero point corrected energies (ΔE_0) are given. All values are given in kJ mol^{-1}. Conformers highlighted in bold text are assigned in the experimental Raman data. The corresponding structures can be found in Fig. A.18 (page 232).

		c6-6	**c6-6'**	**c6-6a**	c6-6a'	
BP86/maTZ[165]	ΔE_{el}	0	0.88	3.02	2.43	
	ΔE_0	0	1.07	2.79	2.59	
PBE/maTZ[165]	ΔE_{el}	0	0.94	3.13	2.77	
	ΔE_0	0	1.12	2.88	2.91	
PBE0/maTZ[165]	ΔE_{el}	0	1.63	3.09	4.01	
	ΔE_0	0	1.77	2.79	4.09	
B3LYP/maTZ[165]	ΔE_{el}	0	1.53	2.82	4.23	
	ΔE_0	0	1.64	2.54	4.38	
PBE0/6-311+G(d,p)[184]	ΔE_0	0	1.95	2.49	5.09	

Tab. B.13: Comparison of computational results for t7-7. Relative electronic energies (ΔE_{el}) and zero point corrected energies (ΔE_0) are given. All values are given in kJ mol^{-1}. Conformers highlighted in bold text are assigned in the experimental Raman data. The corresponding structures can be found in Fig. A.19 (page 232).

		t7-7	**t7-7'**	**t7-7a**	**t7-7b**	t7-7c	**t7-7a'**	t7-7b'	
BP86/maTZ[165]	ΔE_{el}	0.85	0	2.53	2.80	3.30	1.78	3.43	
	ΔE_0	0.47	0	2.14	2.50	2.77	1.81	3.80	
PBE/maTZ[165]	ΔE_{el}	0.78	0	2.54	2.79	3.31	1.80	3.54	
	ΔE_0	0.42	0	2.16	2.53	2.79	1.83	3.93	
PBE0/maTZ[165]	ΔE_{el}	0	0.14	1.92	2.30	2.61	2.22	4.61	
	ΔE_0	0	0.42	1.90	2.47	2.47	2.62	5.30	
B3LYP/maTZ[165]	ΔE_{el}	0	0.38	1.81	1.82	2.57	2.02	4.88	
	ΔE_0	0	0.71	1.79	1.98	2.43	2.43	5.55	

Tab. B.14: Comparison of computational data with those of Wang *et al.*[227], Jesus *et al.*[228,229], Paul *et al.*[230], Lomas[184] and Paoloni *et al.*[186] for rM-M. The values given by Paul *et al.* and Paoloni *et al.* have been converted from cm^{-1} to $\mathrm{kJ\,mol}^{-1}$. The values marked with ‡ are saddle points at their respective level of computation. Relative electronic energies (ΔE_{el}) and harmonically (also for Ref. [186], where discrepancies between main text and supplementary information have been found, the supplementary information is used) zero point corrected energies (ΔE_0) are given. All values are given in kJ mol^{-1}. Conformers highlighted in bold text are assigned in the experimental Raman data. The corresponding structures can be found in Fig. A.14 (page 230).

		rM-M	**rM-M'**	**rM-Ma**	rM-M*	**rM-Ma'**	
BP86/maTZ[165]	ΔE_{el}	1.35	0	4.19	5.97‡	4.48
	ΔE_0	0.83	0	3.64	3.64‡	4.15
PBE/maTZ[165]	ΔE_{el}	1.30	0	4.26	5.93‡	4.73
	ΔE_0	0.81	0	3.71	4.10‡	4.41
PBE0/maTZ[165]	ΔE_{el}	0.27	0	3.10	5.58‡	4.44
	ΔE_0	0	0.16	2.73	3.90‡	4.25
B3LYP/maTZ[165]	ΔE_{el}	0	0.06	3.01	4.72	4.26
	ΔE_0	0	0.52	2.81	3.41	4.28
HF/6-311G[230]	ΔE_{el}	0	5.59	2.00	-	7.12
PBE0/6-311+G(d,p)[184]	ΔE_0	0	1.14	2.95	4.31‡	4.83
B3LYP/6-31G*[227]	ΔE_{el}	1.79	2.96	0.42	3.03	0
B3LYP/6-311++G**[228,229]	ΔE_0	0	1.67	3.13	3.60‡	5.10
B3LYP-D3(BJ)/jul-VDZ[186]	ΔE_{el}	0	0.19	3.56	4.47	4.74
	ΔE_0	0	0.54	3.04	3.67	4.33
B2PLYP-D3(BJ)/jun-VTZ[186]	ΔE_0	0	0.90	2.91	-	4.46
MP2/6-311++G**[229]	ΔE_0	0	2.07	2.86	4.21‡	5.50
MP2/6-311++G**[230]	ΔE_{el}	0	1.40	2.87	-	5.89

B.1.5 $n_D = 3$: Secondary-Tertiary

Tab. B.15: Comparison of computational results for M-MM. Relative electronic energies (ΔE_{el}) and zero point corrected energies (ΔE_0) are given. All values are given in kJ mol^{-1}. Conformers highlighted in bold text are assigned in the experimental Raman data. The corresponding structures can be found in Fig. A.20 (page 233).

	M-MM	**M-MM'**	**M-MMa**	**M-MMa'**	**M-MMb**	
BP86/maTZ[165]	ΔE_{el}	0.65	0	3.35	1.53	3.39
	ΔE_0	0.16	0	2.8	1.55	3.01
PBE/maTZ[165]	ΔE_{el}	0.60	0	3.26	1.57	3.13
	ΔE_0	0.16	0	2.74	1.60	2.77
PBE0/maTZ[165]	ΔE_{el}	0	0.27	2.47	1.78	2.30
	ΔE_0	0	0.68	2.35	2.20	2.33
B3LYP/maTZ[165]	ΔE_{el}	0	0.47	2.28	1.97	2.51
	ΔE_0	0	0.87	2.15	2.41	2.48

	M-MMc	M-MMb'	M-MMc'		
BP86/maTZ[165]	ΔE_{el}	4.51	4.07	3.67	
	ΔE_0	3.94	3.91	3.63	
PBE/maTZ[165]	ΔE_{el}	4.45	4.03	3.72	
	ΔE_0	3.86	3.88	3.67	
PBE0/maTZ[165]	ΔE_{el}	3.68	4.03	3.83	
	ΔE_0	3.44	4.25	4.14	
B3LYP/maTZ[165]	ΔE_{el}	3.85	4.17	4.20	
	ΔE_0	3.59	4.34	4.47	

Tab. B.16: Comparison of computational results for c6-6Ph. Relative electronic energies (ΔE_{el}) and zero point corrected energies (ΔE_0) are given. All values are given in kJ mol^{-1}. Conformers highlighted in bold text are assigned in the experimental Raman data. The corresponding structures can be found in Fig. A.21 (page 233).

		c6-6Ph'	c6-6Ph	c6-6Pha
BP86/maTZ	ΔE_{el}	0	9.67	13.02
	ΔE_0	0	8.54	11.46
PBE/maTZ	ΔE_{el}	0	9.14	12.80
	ΔE_0	0	8.06	11.23
PBE0/maTZ	ΔE_{el}	0	9.11	12.79
	ΔE_0	0	7.98	11.16
B3LYP/maTZ	ΔE_{el}	0	8.36	11.64
	ΔE_0	0	7.20	10.16

B.1.6 $n_{\text{D}} = 4$: Tertiary-Tertiary

Tab. B.17: Comparison of our computational results for MM-MM with those of Dahlqvist *et al.*[187], Olschewski *et al.*[188] and Lomas *et al.*[189]. The values given by Lomas have been converted from kcal mol^{-1} to kJ mol^{-1} and those from Olschewski from cm^{-1} to kJ mol^{-1}. Relative electronic energies (ΔE_{el}) and zero point corrected energies (ΔE_0) are given. All values are given in kJ mol^{-1}. Conformers highlighted in bold text are assigned in the experimental Raman data. The corresponding structures can be found in Fig. A.22 (page 234).

		MM-MM	**MM-MM'**
BP86/maTZ[165]	ΔE_{el}	0.57	0
	ΔE_0	0.08	0
PBE/maTZ[165]	ΔE_{el}	0.45	0
	ΔE_0	0	0.03
PBE0/maTZ[165]	ΔE_{el}	0	1.08
	ΔE_0	0	0.96
B3LYP/maTZ[165]	ΔE_{el}	0	0.67
	ΔE_0	0	1.16

HF/6-311G**[187]	ΔE_{el}	0	3.4
B3LYP/6-311++G**[188]	ΔE_{el}	0	0.60
PBE0/cc-pVTZ//B3LYP/6-311+G(d,p)[189]	ΔE_0	0	1.88
MP2/6-311G**[187]	ΔE_{el}	0	3.4

Tab. B.18: Comparison of our computational results for CP-MM. Relative electronic energies (ΔE_{el}) and zero point corrected energies (ΔE_0) are given. All values are given in kJ mol^{-1}. Conformers highlighted in bold text are assigned in the experimental Raman data. The corresponding structures can be found in Fig. A.23 (page 235).

		CP-MM	**CP-MM'**	**CP-MMa**	**CP-MMb**
BP86/maTZ[165]	ΔE_{el}	1.22	0	1.76	1.73
	ΔE_0	0.59	0	1.17	1.17
PBE/maTZ[165]	ΔE_{el}	1.11	0	1.87	1.93
	ΔE_0	0.48	0	1.26	1.34
PBE0/maTZ[165]	ΔE_{el}	0.41	0	1.04	1.32
	ΔE_0	0	0.21	0.69	1.02
B3LYP/maTZ[165]	ΔE_{el}	0.13	0	0.75	1.24
	ΔE_0	0	0.49	0.65	1.26

		CP-MMa'	**CP-MMb'**	CP-MMc	CP-MMt
BP86/maTZ[165]	ΔE_{el}	0.60	1.88	3.81	8.63
	ΔE_0	0.51	1.59	2.99	6.51
PBE/maTZ[165]	ΔE_{el}	0.83	2.02	3.80	8.23
	ΔE_0	0.71	1.72	2.99	6.14
PBE0/maTZ[165]	ΔE_{el}	0.97	1.80	3.30	6.97
	ΔE_0	1.07	1.77	2.65	5.21
B3LYP/maTZ[165]	ΔE_{el}	0.97	1.44	3.15	6.23
	ΔE_0	1.35	1.68	2.81	4.80

		CP-MMat	CP-MMbt	CP-MMct
BP86/maTZ[165]	ΔE_{el}	9.58	7.14	7.47
	ΔE_0	7.00	5.95	5.84
PBE/maTZ[165]	ΔE_{el}	9.06	7.56	7.37

	ΔE_0	6.53	5.79	5.72
PBE0/maTZ[165]	ΔE_{el}	7.66	6.87	6.97
	ΔE_0	5.35	5.40	5.53
B3LYP/maTZ[165]	ΔE_{el}	7.07	6.26	6.33
	ΔE_0	5.06	5.10	5.20

Tab. B.19: Comparison of our computational results for CP-CP. The values marked with ‡ correspond to a transition state. Relative electronic energies (ΔE_{el}) and zero point corrected energies (ΔE_0) are given. All values are given in kJ mol^{-1}. Conformers highlighted in bold text are assigned in the experimental Raman data. The corresponding structures can be found in Fig. A.24 (page 236).

		CP-CP'	**CP-CPa'**	**CP-CP**	**CP-CPa**	**CP-CPb'**
BP86/maTZ[165]	ΔE_{el}	0	1.41	3.44	4.24	2.96
	ΔE_0	0	1.14	2.46	3.25	2.53
PBE/maTZ[165]	ΔE_{el}	0	1.38	3.44	4.07	3.05
	ΔE_0	0	1.12	2.46	3.11	2.64
PBE0/maTZ[165]	ΔE_{el}	0	1.08	2.91	3.46	3.00
	ΔE_0	0	0.79	1.96	2.41	2.56
B3LYP/maTZ[165]	ΔE_{el}	0	0.84	2.75	3.20	2.69
	ΔE_0	0	0.59	1.81	2.13	2.21

		CP-CPc'	**CP-CPb**	**CP-CPc**
BP86/maTZ[165]	ΔE_{el}	3.47	5.74	6.73
	ΔE_0	3.22	4.52	5.56
PBE/maTZ[165]	ΔE_{el}	3.69	5.73	6.91
	ΔE_0	3.37	4.54	5.69
PBE0/maTZ[165]	ΔE_{el}	4.19‡	5.02	6.46
	ΔE_0	3.80‡	3.81	5.26
B3LYP/maTZ[165]	ΔE_{el}	3.75	4.81	5.93
	ΔE_0	3.40	3.60	4.76

B.2 Dimers

Tab. B.20: Comparison of computational results for tri-*tert*-butyl-methanol. Relative electronic energies (ΔE_{el}) and zero point corrected energies (ΔE_0) are given. All values are given in kJ mol^{-1}. Conformers highlighted in bold text are assigned in the experimental Raman data. The corresponding structures can be found in Fig. A.25 (page 237).

method \ conformer		**hom1'**	**het1'**	**hom1a'**	**het1a'**
B3LYP/maTZ	ΔE_{el}	0	0.79	0.62	2.86
	ΔE_0	0	0.36	0.83	1.50

Tab. B.21: Overview of the average oxygen-oxygen atom *d*(O–O) and hydrogen bond distance *d*(HB) of selected dimers for *trans*-cyclobutane-1,2-diol (t4-4), *trans*-cyclopentane-1,2-diol (t5-5), *trans*-cyclohexane-1,2-diol (t6-6) and *trans*-cycloheptane-1,2-diol (t7-7). In case of hom2" the intermolecular and intramolecular hydrogen bonds are average separately with intermolecular ones being shorter. All distances are given in Å and have been computed at the B3LYP/maTZ level of theory.

		het4	hom3'	het3'	hom2"	
t4-4	*d*(O–O)	3.39	3.42	3.42	-	
	d(HB)	2.38	2.03	2.01	-	-
t5-5	*d*(O–O)	3.07	3.13	3.10	3.02	
	d(HB)	2.03	1.90	1.90	1.95	2.69
t6-6	*d*(O–O)	2.92	2.95	2.93	2.78	
	d(HB)	1.93	1.90	1.90	1.94	2.28
t7-7	*d*(O–O)	2.82	2.99	2.91	2.65	
	d(HB)	1.89	1.92	1.90	1.90	2.05

C Assignments

C.1 Monomers

C.1.1 Mono-ols

Tab. C.1: Overview of the experimental assignments for 2-chloropropan-1-ol (g-ga and g'-gg) and 1-chloropropan-2-ol (m-ga and h-gg) at different levels of computation. The absolute wavenumbers by Goldstein *et al.*[244] were originally scaled by 0.95 and did not provide any decimal places. All values are given in cm^{-1} and unscaled.

	g-ga	g'-gg	m-ga	h-gg
Jet-Raman	3620	3620	3619	3609
BP86/maTZ	3621.07	3626.90	3623.18	3622.14
PBE/maTZ	3632.35	3638.32	3633.76	3633.01
PBE0/maTZ	3816.01	3819.92	3817.46	3813.04
B3LYP/maTZ	3761.89	3762.40	3761.78	3756.06
PBE0/aVTZ	3821.13	3824.49	3822.24	3816.91
B3LYP/aVTZ	3775.00	3777.97	3776.70	3770.54
CAM-B3LYP/aVTZ	3820.74	3823.19	3822.25	3814.25
B2PLYP/aVTZ	3791.56	3793.37	3788.70	3783.15
MP2/aVTZ	3792.61	3793.08	3783.05	3780.37
CCSD(T)-F12a/VDZ-F12	3808.94	3808.68	3805.09	3797.65
MP2/6-311++G(d,p)[244]	3862.11	3864.21	3852.63	3852.63

Tab. C.2: Overview of the experimental assignments for 2-bromopropan-1-ol (g-ga and g'-gg) and 1-bromopropan-2-ol (m-ga and h-gg) at different levels of computation. The VDZ-F12* basis set is defined as all = VDZ-F12 and Br = VDZ-PP-F12. All values are given in cm^{-1} and unscaled.

	g-ga	g'-gg	m-ga	h-gg
Jet	3607	3608	3608	3598
BP86/maTZ	3601.04	3607.85	3606.05	3604.68
PBE/maTZ	3611.71	3618.68	3615.94	3614.72
PBE0/maTZ	3801.03	3805.63	3804.33	3799.87
B3LYP/maTZ	3749.72	3753.52	3753.86	3748.00
PBE0/aVTZ	3805.79	3810.12	3809.09	3803.77
B3LYP/aVTZ	3762.90	3771.26	3766.58	3760.43
CAM-B3LYP/aVTZ	3812.09	3815.15	3815.20	3806.91
B2PLYP/aVTZ	3779.12	3783.35	3777.72	3772.35
MP2/aVTZ		3775.83	3766.79	3764.61
CCSD(T0)-F12a/VDZ-F12*	3794.68	3794.98	3790.80	3783.96

C.1.2 $n_D = 0$: Primary-Primary

Tab. C.3: Overview of the experimental[18,166] assignments for ethane-1,2-diol (0-0) at the BP86/maTZ, PBE/maTZ, PBE0/maTZ and B3LYP/maTZ level of computation[165]. All values are given in cm^{-1} and unscaled. This table was adopted from Ref. [165].

	Jet-Raman	BP86/maTZ	PBE/maTZ	PBE0/maTZ	B3LYP/maTZ
$0\text{-}0_1$	3636	3645.72	3657.05	3833.64	3775.45
$0\text{-}0_2$	3689	3713.88	3725.04	3891.23	3824.91
$0\text{-}0_1'$	3623	3622.15	3633.41	3816.42	3759.88
$0\text{-}0_2'$	3656	3670.95	3681.58	3855.74	3790.80

Tab. C.4: Overview of experimental frequencies measured in a jet-expansion[18,166], the gas phase[205], in a matrix[206–209] and in solution[191,194,195,197,204] of thane-1,2-diol (0-0). The values given by Park *et al.*[209], Ma *et al.*[204] and Das *et al.*[183] originally included one more decimal place. The intramolecular hydrogen bond shift for the 0-0 ($\Delta\tilde{\nu}$, 0-0_1−0-0_2) and 0-0' ($\Delta\tilde{\nu}'$, 0-$0'_1$−0-$0'_2$) conformers are also given. Since solution data cannot distinguish between 0-0 and 0-0' approximate values for 0-0 are given. All values are given in cm^{-1}.

conformer / method	0-0_1	0-0_2	0-$0'_1$	0-$0'_2$	$\Delta\tilde{\nu}_{21}$	$\Delta\tilde{\nu}'_{21}$
Raman/Jet[18,166]	3636	3689	3623	3656	53	33
IR/Matrix Ar[206]	3626	3666	-	-	40	-
IR/Matrix Ar[207]	3626	3667	-	-	41	-
IR/Matrix Ar[208]	3626	3671	3638	3671	45	33
FTIR/Matrix Ar[209]	3624	3663	3634	3665	39	31
IR/Matrix Xe[207]	3593	3644	-	-	51	-
IR/gas phase[205]	3644	3677	-	-	33	-
FTIR/gas phase[183]	3638	3683	-	-	45	-
IR/CCl_4[191]	3612	3644	-	-	32	-
IR/CCl_4[194]	3619	3645	-	-	26	-
IR/CCl_4[195]	3604	3644	-	-	40	-
IR/CCl_4[197]	3608	3643	-	-	35	-
FTIR/CCl_4[204]	3607	3643	-	-	36	-

C.1.3 $n_D = 1$: Primary-Secondary

Tab. C.5: Overview of the experimental assignments for propane-1,2-diol (0-M) at the BP86/maTZ, PBE/maTZ, PBE0/maTZ and B3LYP/maTZ level of computation[165]. All values are given in cm^{-1} and unscaled. The first 5 conformations were also correctly assigned based on the jet FTIR spectrum[225], where the 3669 and 3673 cm^{-1} (FTIR: ≈ 3673 cm^{-1}) as well as the 3625 and 3629 cm^{-1} (FTIR: ≈ 3626 cm^{-1}) transitions were not resolved, but otherwise the wavenumbers agree within 1 cm^{-1} with the sharper Raman transitions of Ref. [165]. This table was adopted from Ref. [165].

	Jet-Raman	BP86/maTZ	PBE/maTZ	PBE0/maTZ	B3LYP/maTZ
0-M_1	3625	3628.16	3639.03	3821.58	3767.12
0-M_2	3688	3714.99	3726.24	3892.21	3826.27
0-Ma_1	3629	3636.24	3648.55	3826.29	3770.15

0-Ma_2	3673	3701.71	3712.04	3879.26	3814.63
0-M_1'	3613	3606.38	3617.06	3805.25	3752.51
0-M_2'	3656	3672.95	3683.71	3857.74	3793.08
0-Ma_1'	3613	3605.86	3617.55	3804.42	3751.36
0-Ma_2'	3629	3647.71	3658.89	3833.69	3770.90
0-Mb_1	3629	3639.39	3650.77	3828.46	3772.25
0-Mb_2	3669	3695.24	3705.89	3875.00	3811.32
0-Mb_1'	-	3611.53	3623.09	3809.18	3755.54
0-Mb_2'	3651	3671.24	3681.80	3855.88	3792.13
0-Mc_1	-	3628.99	3640.06	3819.89	3763.95
0-Mc_2	3692	3720.96	3732.20	3896.84	3831.30
0-Mc_1'	-	3608.11	3619.09	3804.80	3750.83
0-Mc_2'	-	3682.61	3693.10	3868.50	3806.57

Tab. C.6: Overview of the experimental assignments for 3,3,3-trifluoro-propane-1,2-diol (0-F) at the BP86/maTZ, PBE/maTZ, PBE0/maTZ and B3LYP/maTZ level of computation[165]. All values are given in cm^{-1} and unscaled. This table was adopted from Ref. [165].

	Jet-Raman	BP86/maTZ	PBE/maTZ	PBE0/maTZ	B3LYP/maTZ
0-F_1'	3575	3556.32	3567.81	3763.70	3716.03
0-F_2'	3656	3670.23	3680.49	3854.93	3793.04
0-F_1	3641	3657.56	3668.62	3840.91	3781.24
0-F_2	3663	3689.60	3698.88	3865.50	3803.06
0-Fa_1'	-	3629.68	3640.53	3820.49	3761.41
0-Fa_2'	-	3640.74	3650.13	3824.05	3766.28
0-Fa_1	-	3655.71	3666.51	3837.69	3779.72
0-Fa_2	-	3681.01	3690.13	3858.27	3797.60
0-Fb_1	-	3612.93	3625.19	3812.69	3761.11
0-Fb_2	-	3715.87	3726.69	3891.07	3825.91
0-Fc_1	-	3593.16	3606.25	3794.46	3742.13
0-Fc_2	3689	3721.11	3731.70	3895.05	3829.66

Tab. C.7: Overview of the experimental assignments for 3-butene-1,2-diol (0-V) at the BP86/maTZ, PBE/maTZ, PBE0/maTZ and B3LYP/maTZ level of computation. All values are given in cm^{-1} and unscaled. This table was adopted from Ref. [165].

	Jet-Raman	BP86/maTZ	PBE/maTZ	PBE0/maTZ	B3LYP/maTZ
0-V_1	3629	3641.24	3652.59	3827.91	3771.35
0-V_2	3665	3691.46	3702.23	3871.06	3806.92
0-Va_1	3634	3648.75	3660.29	3834.03	3776.00
0-Va_2	3661	3687.72	3697.91	3866.40	3804.02
0-Vb_1	3629	3637.30	3648.86	3827.93	3771.75
0-Vb_2	3661	3684.32	3695.30	3866.21	3803.63
0-V_1'	3596	3594.62	3605.78	3792.58	3742.23
0-V_2'	3613	3614.51	3625.75	3808.68	3756.92
0-Vc_1	3629	3631.34	3642.61	3825.77	3772.25
0-Vc_2	3687	3713.76	3725.11	3890.84	3825.05
0-Va_1'	3610	3613.81	3625.23	3809.88	3754.78
0-Va_2'	-	3628.86	3639.87	3816.49	3758.82
0-Vd_1	3610	3605.62	3616.89	3807.06	3753.98
0-Vd_2	3687	3714.43	3725.60	3891.03	3824.95
0-Vb_1'	-	3608.82	3619.86	3808.30	3756.62
0-Vb_2'	-	3671.75	3682.37	3856.64	3792.09
0-Vc_1'	-	3607.77	3619.58	3805.51	3751.54
0-Vc_2'	-	3645.83	3657.27	3831.97	3769.51

Tab. C.8: Overview of the experimental assignments for 1-phenyl-ethane-1,2-diol (0-Ph) at the BP86/maTZ, PBE/maTZ, PBE0/maTZ and B3LYP/maTZ level of computation[165]. All values are given in cm^{-1} and unscaled. This table was adopted from Ref. [165].

	Jet-Raman	BP86/maTZ	PBE/maTZ	PBE0/maTZ	B3LYP/maTZ
0-Ph_1	3631	3645.47	3656.47	3831.87	3774.26
0-Ph_2	3660	3690.68	3701.41	3868.77	3805.36
0-Pha_1	3618	3619.68	3631.62	3816.88	3764.13
0-Pha_2	3685	3713.07	3724.37	3890.06	3824.12

0-Ph_1'	3605	3596.64	3607.80	3798.50	3747.35
0-Ph_2'	-	3672.74	3683.33	3857.22	3792.99
0-Pha_1'	3593	3593.07	3603.01	3790.04	3740.77
0-Pha_2'	3615	3626.53	3640.16	3819.13	3764.15
0-Phb_1	-	3644.17	3655.69	3833.90	3777.80
0-Phb_2	-	3683.48	3694.37	3863.65	3802.65
0-Pht_1	-	3640.44	3652.72	3830.36	3775.49
0-Pht_2	-	3680.21	3691.29	3862.25	3798.63
0-Phc_1	-	3607.95	3619.87	3808.78	3754.32
0-Phc_2	-	3670.37	3681.30	3861.89	3804.30

Tab. C.9: Overview of the experimental assignments for 3-chloro-propane-1,2-diol (0-Cl_1) at different levels of computation. All values are given in cm^{-1} and unscaled.

	0-Cl_{11}	0-Cl_{12}	0-Cl_1a_1	0-Cl_1a_2	0-Cl_{1_1}'	0-Cl_{1_2}'	0-Cl_1b_1
Jet-Raman	3617	3628	3629	3629	3587	3621	3604
BP86[a]	3610.89	3639.85	3645.97	3646.22	3591.24	3618.58	3605.71
PBE[a]	3621.67	3651.44	3655.91	3657.42	3601.97	3629.67	3617.19
PBE0[a]	3810.23	3828.39	3829.59	3834.58	3787.50	3814.63	3802.59
B3LYP[a]	3761.59	3771.95	3772.06	3779.97	3737.48	3759.93	3749.49
PBE0[b]	3813.88	3835.05	3837.00	3837.57	3791.61	3821.74	3810.53
B3LYP[b]	3773.28	3786.77	3786.63	3790.85	3749.91	3774.87	3764.13
CAM-B3L[b]	3818.55	3825.29	3824.74	3834.68	3793.12	3815.58	3802.39
B2PLYP[b]	3785.35	3800.26	3800.73	3801.65	3761.58	3790.03	3775.52
MP2[b]	3776.85	3798.61	3793.80	3801.42	3756.03	3790.46	3771.96
CCSD(T)-F12a[c]	3802.53	3813.64	3816.29	3818.56	3776.00	3805.45	3790.24
	0-Cl_1b_2	0-Cl_1a_1'	0-Cl_1a_2'	0-Cl_1b_1'	0-Cl_1b_2'	0-Cl_1t_1	0-Cl_1t_2
Jet-Raman	3694	3573	3604	-	-	3599	3689
BP86[a]	3721.66	3552.70	3584.35	3595.74	3693.62	3602.12	3710.34
PBE[a]	3732.47	3564.93	3599.16	3605.54	3704.20	3613.13	3721.31
PBE0[a]	3896.68	3763.88	3797.33	3794.24	3875.26	3797.77	3889.34
B3LYP[a]	3831.55	3719.41	3747.08	3741.83	3812.63	3746.44	3823.27

PBE0[b]	3903.03	3768.83	3801.14	3800.12	3883.22	3801.98	3896.41
B3LYP[b]	3845.43	3731.25	3758.81	3754.69	3827.74	3758.60	3837.95
CAM-B3LP[b]	3886.45	3770.50	3808.03	3794.28	3872.01	3803.06	3880.81
B2PLYP[b]	3856.50	3742.40	3778.93	3766.42	3840.94	3771.84	3850.27
MP2[b]	3855.04	3731.56	3780.19	3764.76	3841.21	3768.49	3851.02
CCSD(T)-F12a[c]	3872.43	3757.80	3800.91	3780.97	3851.08	3786.95	3866.18

[a] = maTZ, [b] = aVTZ, [c] = VDZ-F12

Tab. C.10: Overview of the experimental assignments for 3-bromo-propane-1,2-diol (0-Br_1) at different levels of computation. All values are given in cm^{-1} and unscaled.

	0-Br_{11}	0-Br_{12}	0-Br_1a_1	0-Br_1a_2	0-$Br_1{}_1^{'}$	0-$Br_1{}_2^{'}$	0-Br_1b_1
Jet-Raman	3605	3627	3620	3628	3574	3613	3600
BP86[a]	3590.81	3639.66	3627.45	3645.25	3571.19	3617.93	3604.21
PBE[a]	3600.75	3651.30	3636.64	3656.52	3581.14	3629.00	3615.41
PBE0[a]	3794.86	3828.33	3821.01	3829.05	3771.51	3814.33	3801.61
B3LYP[a]	3749.60	3772.18	3769.33	3771.36	3725.20	3760.35	3748.51
PBE0[b]	3798.40	3835.01	3823.51	3837.18	3775.87	3821.60	3809.53
B3LYP[b]	3761.21	3786.66	3780.51	3786.28	3737.67	3774.80	3763.08
CAM-B3LYP[b]	3810.23	3825.33	3824.46	3827.55	3784.05	3815.57	3801.79
B2PLYP[b]	3772.19	3799.95	3790.45	3800.41	3748.44	3789.74	3774.41
MP2[b]	3757.05	3797.56	3776.66	3801.24	3737.15	3789.42	3771.65
CCSD(T)-F12a[c]	3785.69	3810.99	3804.61	3812.80	3758.15	3802.98	3784.57
	0-Br_1b_2	0-$Br_1a_1^{'}$	0-$Br_1a_2^{'}$	0-$Br_1b_1^{'}$	0-$Br_1b_2^{'}$	0-Br_1t_1	0-Br_1t_2
Jet-Raman	3693	3568	3588	-	-	3584	3688
BP86[a]	3721.62	3541.47	3559.68	3598.39	3689.44	3582.72	3710.57
PBE[a]	3732.41	3554.37	3573.00	3606.81	3701.14	3592.68	3721.38
PBE0[a]	3896.57	3757.45	3778.78	3795.21	3872.55	3782.24	3889.39
B3LYP[a]	3831.51	3714.49	3731.88	3742.27	3810.01	3734.08	3823.42
PBE0[b]	3902.84	3761.96	3781.91	3800.31	3881.30	3786.13	3896.36
B3LYP[b]	3845.29	3725.76	3742.58	3754.65	3825.76	3745.90	3837.96
CAM-B3LYP[b]	3886.26	3766.17	3796.74	3794.26	3870.80	3793.68	3880.74
B2PLYP[b]	3856.22	3736.95	3761.99	3766.32	3838.26	3758.47	3850.06

MP2[b]	3854.63	3724.52	3757.07	3766.26	3834.96	3750.11	3850.56
CCSD(T)-F12a[c]	3872.51	3748.38	3780.52	3775.45	3851.21	3769.67	3865.08

[a] = maTZ, [b] = aVTZ, [c] = VDZ-F12

C.1.4 n_D = 2: Primary-Tertiary

Tab. C.11: Overview of the experimental assignments for 2-methyl-propane-1,2-diol (0-MM) at the BP86/maTZ, PBE/maTZ, PBE0/maTZ and B3LYP/maTZ level of computation[165]. All values are given in cm^{-1} and unscaled. 0-MM* converges to 0-MM for all functionals besides B3LYP. This table was adopted from Ref. [165].

	Jet-Raman	BP86/maTZ	PBE/maTZ	PBE0/maTZ	B3LYP/maTZ
0-MM_1	3623	3626.68	3638.36	3820.24	3766.20
0-MM_2	3656	3686.73	3696.96	3865.41	3802.98
0-MM_1'	3607	3596.06	3607.91	3797.89	3746.63
0-MM_2'	3633	3656.99	3667.94	3841.91	3780.46
0-MMa_1	3614	3620.20	3631.31	3814.86	3761.28
0-MMa_2	3691	3720.55	3731.83	3896.41	3830.85
0-MMa_1'	3607	3602.19	3613.00	3800.48	3748.83
0-MMa_2'	3667	3683.52	3694.18	3869.67	3807.57
0-MM_1^*	-	-	-	-	3793.63
0-MM_2^*	-	-	-	-	3804.51

C.1.5 n_D = 2: Secondary-Secondary

Tab. C.12: Overview of the experimental assignments for *rac*-butane-2,3-diol (rM-M) at the BP86/maTZ, PBE/maTZ, PBE0/maTZ and B3LYP/maTZ level of computation[165]. The values in italic correspond to those of a transition state. All values are given in cm^{-1} and unscaled. This table was adopted from Ref. [165].

	Jet-Raman	BP86/maTZ	PBE/maTZ	PBE0/maTZ	B3LYP/maTZ
rM-M_1	3622	3622.14	3634.40	3817.45	3764.06
rM-M_2	3673	3702.65	3713.30	3880.28	3815.68
rM-M_1'	3607	3592.37	3603.28	3795.42	3745.41

rM-M_2'	3630	3649.63	3660.69	3835.36	3773.07
rM-Ma_1	3610	3618.58	3629.78	3812.01	3758.63
rM-Ma_2	3673	3700.68	3711.18	3879.49	3816.50
rM-M_1^*	-	*3677.32*	*3687.59*	*3865.94*	3804.45
rM-M_2^*	-	*3678.30*	*3688.58*	*3866.73*	3806.07
rM-Ma_1'	3598	3591.36	3602.86	3793.20	3742.00
rM-Ma_2'	3661	3679.68	3689.93	3866.41	3805.81

Tab. C.13: Overview of the experimental assignments for *trans*-cyclobutane-1,2-diol (t4-4) at the BP86/maTZ, PBE/maTZ, PBE0/maTZ and B3LYP/maTZ level of computation[165]. The assignment in italic is done base on VPT2 calculations. All values are given in cm^{-1} and unscaled. This table was adopted from Ref. [165].

	Jet-Raman	BP86/maTZ	PBE/maTZ	PBE0/maTZ	B3LYP/maTZ
t4-4_1	3664	3683.34	3694.13	3863.22	3796.12
t4-4_2	3666	3688.05	3699.26	3869.29	3802.10
t4-$4_1'$	*3644*	3667.70	3678.21	3852.34	3787.53
t4-$4_2'$	3654	3677.22	3687.75	3857.92	3790.75
t4-4_1^*	3669	3694.68	3705.96	3876.11	3808.64
t4-4_2^*	3669	3695.71	3706.95	3877.33	3809.84
t4-4t_1	3674	3699.74	3712.81	3880.16	3813.11
t4-4t_2	3674	3700.17	3713.23	3880.27	3813.28
t4-4ta_1	-	3670.42	3680.92	3854.04	3788.81
t4-4ta_2	-	3671.93	3682.44	3855.50	3790.17
t4-4ta_1	-	3669.83	3680.35	3854.41	3788.99
t4-4ta_2	-	3686.99	3698.12	3868.84	3801.64

Tab. C.14: Overview of the experimental assignments for *trans*-cyclopentane-1,2-diol (t5-5) at the BP86/maTZ, PBE/maTZ, PBE0/maTZ and B3LYP/maTZ level of computation[165]. All values are given in cm^{-1} and unscaled. This table was adopted from Ref. [165].

	Jet-Raman	BP86/maTZ	PBE/maTZ	PBE0/maTZ	B3LYP/maTZ
t5-5_1	3640	3663.73	3673.61	3845.24	3783.15

t5-5_2	3672	3699.31	3710.18	3878.22	3812.46
t5-$5'_1$	3630	3647.30	3657.27	3833.23	3772.23
t5-$5'_2$	-	3651.84	3662.41	3837.94	3775.16
t5-$5t_1$	-	3673.87	3685.02	3858.58	3793.94
t5-$5t_2$	-	3686.44	3697.33	3868.97	3804.49
t5-$5ta_1$	-	3668.26	3678.80	3853.88	3789.98
t5-$5ta_2$	-	3668.48	3679.02	3854.54	3790.65
t5-$5tb_1$	-	3692.99	3703.67	3874.52	3810.10
t5-$5tb_2$	-	3694.50	3705.18	3875.71	3811.33
t5-5^*_1	-	3691.51	3701.88	3874.71	3809.57
t5-5^*_2	-	3699.32	3709.74	3881.62	3815.94
t5-$5tc_1$	-	3673.38	3683.75	3855.97	3793.82
t5-$5tc_2$	-	3674.71	3685.56	3858.37	3796.09
t5-$5td_1$	-	3673.37	3684.05	3858.60	3797.72
t5-$5td_2$	-	3687.23	3697.95	3870.73	3806.20

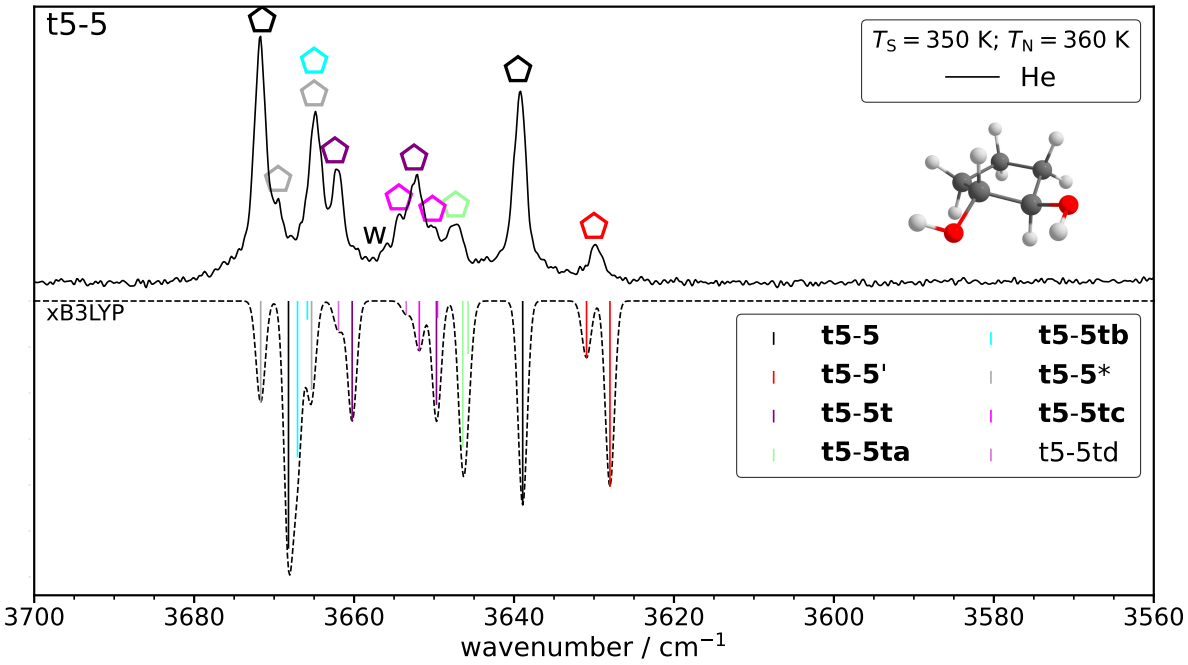

Fig. C.1: Alternative assignments of *trans*-cyclopentane-1,2-diol in analogy to Fig. 3.19 (page 62).

Tab. C.15: Overview of the experimental[166] assignments for *trans*-cyclohexane-1,2-diol (t6-6) at the BP86/maTZ, PBE/maTZ, PBE0/maTZ and B3LYP/maTZ level of computation[165]. All values are given in cm^{-1} and unscaled. This table was adopted from Ref. [165].

	Jet-Raman	BP86/maTZ	PBE/maTZ	PBE0/maTZ	B3LYP/maTZ
t6-6_1	3628	3641.26	3652.51	3829.15	3773.19
t6-6_2	3667	3696.77	3707.04	3875.31	3810.58
t6-$6'_1$	3616	3617.44	3628.32	3811.62	3757.47
t6-$6'_2$	3628	3651.07	3662.02	3836.96	3774.68

Tab. C.16: Overview of experimental frequencies measured in a jet-expansion[166], in a matrix[199] and in solution[185,191–193,196,199,200,202] of *trans*-cyclohexane-1,2-diol (t6-6). Given the limited resolution of the data of Bacon *et al.*[199] a peak average is taken. The intramolecular hydrogen bond shift for the t6-6 ($\Delta\tilde{\nu}$, t6-6_1−t6-6_2) and t6-6' ($\Delta\tilde{\nu}'$, t6-$6'_1$−t6-$6'_2$) conformers are also given. Since solution data cannot distinguish between t6-6 and t6-6' approximate values for 0-0 are given. All values are given in cm^{-1}.

method \ conformer	t6-6_1	t6-6_2	t6-$6'_1$	t6-$6'_2$	$-\Delta\tilde{\nu}$	$-\Delta\tilde{\nu}'$
Raman/Jet[166]	3628	3667	3616	3628	39	12
FTIR/Matrix Ar[199]	3618	3654	-	-	36	-
IR/CCl_4[192]	3602	3633	-	-	31	-
IR/CCl_4[193]	3602	3633	-	-	31	-
IR/CCl_4[185]	3598	3631	-	-	33	-
IR/CCl_4[191]	3602	3634	-	-	32	-
IR/CCl_4[196]	3601	3633	-	-	32	-
IR/CCl_4[200]	3598	3632	-	-	34	-
FTIR/CCl_4[199]	3598	3631	-	-	33	-
VCD,IR/CCl_4[202]	3600	3632	-	-	32	-
FTIR/$CDCl_3$[199]	3545	3609	-	-	36	-
IR/CS_2[200]	3588	3615	-	-	27	-

Tab. C.17: Overview of the experimental assignments for *cis*-cyclohexane-1,2-diol (c6-6) at the BP86/maTZ, PBE/maTZ, PBE0/maTZ and B3LYP/maTZ level of computation[165]. All values are given in cm^{-1} and unscaled. This table was adopted from Ref. [165].

	Jet-Raman	BP86/maTZ	PBE/maTZ	PBE0/maTZ	B3LYP/maTZ
c6-6_1	3617	3622.59	3633.82	3817.09	3764.35
c6-6_2	3660	3685.55	3696.07	3867.48	3804.67
c6-$6'_1$	3604	3597.46	3608.50	3798.37	3746.88
c6-$6'_2$	3648	3668.51	3679.29	3854.18	3791.20
c6-$6a_1$	3613	3622.49	3633.76	3814.53	3759.60
c6-$6a_2$	3674	3708.07	3718.49	3883.86	3820.40
c6-$6a'_1$	-	3595.44	3606.62	3793.82	3742.06
c6-$6a'_2$	-	3661.34	3672.82	3850.58	3794.92

Tab. C.18: Overview of the experimental assignments for *trans*-cycloheptane-1,2-diol (t7-7) at the BP86/maTZ, PBE/maTZ, PBE0/maTZ and B3LYP/maTZ level of computation[165]. All values are given in cm^{-1} and unscaled. This table was adopted from Ref. [165].

	Jet-Raman	BP86/maTZ	PBE/maTZ	PBE0/maTZ	B3LYP/maTZ
t7-7_1	3623	3629.28	3640.78	3821.60	3767.20
t7-7_2	3664	3694.41	3704.91	3874.00	3810.41
t7-$7'_1$	3604	3603.64	3614.46	3802.90	3750.79
t7-$7'_2$	3626	3648.95	3659.84	3834.79	3772.60
t7-$7a_1$	3608	3607.20	3619.71	3805.99	3753.97
t7-$7a_2$	3672	3700.33	3710.56	3877.75	3814.09
t7-$7b_1$	3626	3643.37	3653.95	3831.18	3773.92
t7-$7b_2$	3662	3691.36	3702.20	3872.08	3807.95
t7-$7c_1$	-	3613.37	3625.91	3812.43	3760.55
t7-$7c_2$	-	3702.73	3713.37	3880.78	3816.83
t7-$7a'_1$	3613	3616.06	3626.21	3811.81	3757.35
t7-$7a'_2$	3626	3645.90	3656.58	3832.86	3770.54
t7-$7b'_1$	-	3542.84	3555.44	3755.98	3713.52
t7-$7b'_2$	-	3648.87	3660.61	3838.84	3778.25

C.1.6 $n_D = 3$: Secondary-Tertiary

Tab. C.19: Overview of the experimental assignments for 2-methyl-butane-2,3-diol (M-MM) at the BP86/maTZ, PBE/maTZ, PBE0/maTZ and B3LYP/maTZ level of computation[165]. All values are given in cm^{-1} and unscaled. This table was adopted from Ref. [165].

	Jet-Raman	BP86/maTZ	PBE/maTZ	PBE0/maTZ	B3LYP/maTZ
M-MM$_1$	3617	3616.14	3628.05	3813.65	3762.43
M-MM$_2$	3655	3685.10	3695.49	3864.49	3802.82
M-MM$'_1$	3602	3587.07	3598.89	3791.82	3743.30
M-MM$'_2$	3629	3652.74	3663.92	3838.10	3777.65
M-MMa$_1$	3612	3615.20	3627.77	3810.93	3759.24
M-MMa$_2$	3675	3706.86	3717.23	3883.50	3819.50
M-MMa$'_1$	3602	3588.41	3599.94	3790.68	3742.04
M-MMa$'_2$	3642	3660.97	3671.88	3847.90	3788.02
M-MMb$_1$	3609	3613.16	3624.65	3809.51	3758.00
M-MMb$_2$	3670	3699.38	3709.89	3879.34	3817.06
M-MMc$_1$	-	3606.17	3618.11	3804.11	3752.54
M-MMc$_2$	3659	3691.38	3701.83	3869.54	3807.82
M-MMb$'_1$	-	3589.30	3600.80	3791.64	3742.62
M-MMb$'_2$	-	3683.02	3693.70	3870.62	3811.32
M-MMc$'_1$	-	3579.28	3591.18	3782.99	3734.63
M-MMc$'_2$	-	3665.88	3676.58	3852.60	3793.67

Tab. C.20: Overview of the experimental assignments for 1-phenyl-*cis*-cyclohexane-1,2-diol (c6-6Ph) at the BP86/maTZ, PBE/maTZ, PBE0/maTZ and B3LYP/maTZ level of computation. All values are given in cm^{-1} and unscaled.

	Jet-Raman	BP86/maTZ	PBE/maTZ	PBE0/maTZ	B3LYP/maTZ
c6-6Ph$'_1$	3574	3571.25	3582.06	3773.36	3727.77
c6-6Ph$'_2$	3612	3630.20	3642.09	3818.77	3766.04
c6-6Ph$_1$	-	3592.12	3603.37	3788.85	3741.79
c6-6Ph$_2$	-	3686.69	3696.72	3868.68	3806.99

c6-6Pha$_1$	-	3636.53	3647.78	3824.51	3769.51
c6-6Pha$_2$	-	3669.87	3679.66	3850.84	3793.58

C.1.7 n_D = 4: Tertiary-Tertiary

Tab. C.21: Overview of the experimental assignments for pinacol (MM-MM) at the BP86/maTZ, PBE/maTZ, PBE0/maTZ and B3LYP/maTZ level of computation[165]. Dahlqvist *et al.* did FT-IR measurements in a Ar matrix and also provide gas phase values of 3603 and 3648 for MM-MM$_1$ and MM-MM$_2$ respectively[187]. All values are given in cm^{-1} and unscaled. This table was adopted from Ref. [165].

	Jet-Raman	FT-IR/Ar	BP86/ maTZ	PBE/ maTZ	PBE0/ maTZ	B3LYP/ maTZ
MM-MM$_1$	3605	3593	3602.50	3614.47	3802.56	3753.52
MM-MM$_2$	3658	3642	3690.96	3701.29	3870.05	3808.85
MM-MM$_1^{'}$	3591	-	3575.35	3586.65	3780.29	3734.59
MM-MM$_2^{'}$	3647	-	3667.50	3678.07	3855.30	3797.67

Tab. C.22: Overview of experimental frequencies measured in a jet-expansion[165], in a matrix[187] and in solution[187,188,191,198,201,203] of pinacol (MM-MM). The values given by Singelenberg *et al.*[201] are originally given with one more decimal place. The intramolecular hydrogen bond shift for the t6-6 ($\Delta\tilde{\nu}$, MM-MM$_1$−MM-MM$_2$) and t6-6' ($\Delta\tilde{\nu}^{'}$, MM-MM$_1^{'}$−MM-MM$_2^{'}$) conformers are also given. Since solution data cannot distinguish between MM-MM and MM-MM' approximate values for MM-MM are given. All values are given in cm^{-1}.

method \ conformer	MM-MM$_1$	MM-MM$_2$	MM-MM$_1^{'}$	MM-MM$_2^{'}$	$\Delta\tilde{\nu}_{21}$	$\Delta\tilde{\nu}_{21}^{'}$
Raman/Jet[165]	3605	3658	3591	3647	53	56
FTIR/Matrix Ar[187]	3593	3642	-	-	49	-
FTIR/gas phase[187]	3603	3648	-	-	45	-
IR/CCl$_4$[191]	3583	3626	-	-	43	-
IR/CCl$_4$[198]	3565	3610	-	-	45	-
IR/CCl$_4$[201]	3580	3625	-	-	45	-
FTIR/CCl$_4$[188]	3579	3626	-	-	47	-
IR/CDCl$_3$[203]	3570	3612	-	-	42	-
FTIR/CS$_2$[201]	3571	3613	-	-	42	-

IR/CS_2[187]	3571	3613	-	-	42	-

Tab. C.23: Overview of the experimental assignments for 1-(1-hydroxy-1-methylethyl)-cyclopentanol (CP-MM) at the BP86/maTZ, PBE/maTZ, PBE0/maTZ and B3LYP/maTZ level of computation[165]. All values are given in cm^{-1} and unscaled. This table was adopted from Ref. [165].

	Jet-Raman	BP86/maTZ	PBE/maTZ	PBE0/maTZ	B3LYP/maTZ
CP-MM_1	3599	3599.50	3611.34	3799.09	3750.87
CP-MM_2	3652	3685.16	3696.11	3865.84	3803.92
CP-MM'_1	3587	3577.19	3587.61	3780.78	3734.43
CP-MM'_2	3635	3661.94	3671.96	3847.52	3788.93
CP-MMa_1	3604	3606.09	3617.89	3804.32	3753.83
CP-MMa_2	3652	3685.55	3695.75	3865.35	3803.88
CP-MMb_1	3604	3606.26	3618.07	3806.12	3755.93
CP-MMb_2	3662	3695.95	3706.53	3876.83	3817.25
CP-MMa'_1	3587	3577.75	3589.04	3782.63	3735.95
CP-MMa'_2	3635	3656.60	3666.99	3844.74	3788.40
CP-MMb'_1	3587	3581.50	3592.96	3784.56	3737.66
CP-MMb'_2	3652	3674.55	3684.49	3861.15	3803.58
CP-MMc_1	-	3606.08	3617.65	3804.88	3755.07
CP-MMc_2	-	3682.92	3693.59	3867.76	3812.35
CP-MMt_1	-	3680.06	3690.56	3861.64	3799.88
CP-MMt_2	-	3682.31	3692.79	3866.64	3807.97
CP-$MMat_1$	-	3685.30	3695.65	3865.81	3804.71
CP-$MMat_2$	-	3686.95	3697.28	3868.19	3810.43
CP-$MMbt_1$	-	3671.27	3685.19	3861.37	3803.03
CP-$MMbt_2$	-	3681.67	3693.97	3866.65	3808.18
CP-$MMct_1$	-	3668.05	3678.34	3855.42	3797.59
CP-$MMct_2$	-	3669.82	3679.75	3857.51	3800.25

Tab. C.24: Overview of the experimental assignments for [1,1'-bicyclopentyl]-1,1'-diol (CP-CP) at the BP86/maTZ, PBE/maTZ, PBE0/maTZ and B3LYP/maTZ level of computation[165]. All values are given in cm^{-1} and unscaled. This table was adopted from Ref. [165].

	Jet-Raman	BP86/maTZ	PBE/maTZ	PBE0/maTZ	B3LYP/maTZ
CP-CP'_1	3589	3587.74	3587.74	3788.65	3739.24
CP-CP'_2	3622	3651.98	3661.97	3838.18	3781.24
CP-CPa'_1	3592	3598.17	3607.96	3795.98	3744.95
CP-CPa'_2	3635	3663.24	3673.45	3848.40	3791.60
CP-CP_1	3600	3603.78	3614.73	3802.63	3752.25
CP-CP_2	3656	3691.50	3701.98	3871.99	3812.12
CP-CPa_1	3603	3614.68	3624.49	3809.47	3758.31
CP-CPa_2	3650	3678.69	3688.87	3861.62	3803.65
CP-CPb'_1	3589	3585.83	3596.53	3788.79	3741.10
CP-CPb'_2	3630	3655.54	3665.93	3844.28	3788.30
CP-CPc'_1	3589	3575.30	3586.78	3784.88	3737.90
CP-CPc'_2	3622	3645.39	3655.83	3834.99	3778.72
CP-CPb_1	3603	3610.49	3621.34	3807.47	3757.56
CP-CPb_2	3650	3683.04	3692.90	3864.14	3805.44
CP-CPc_1	3600	3602.53	3614.41	3803.78	3754.32
CP-CPc_2	3656	3690.54	3701.00	3871.68	3811.43

C.1.8 Additional correlation and spectra

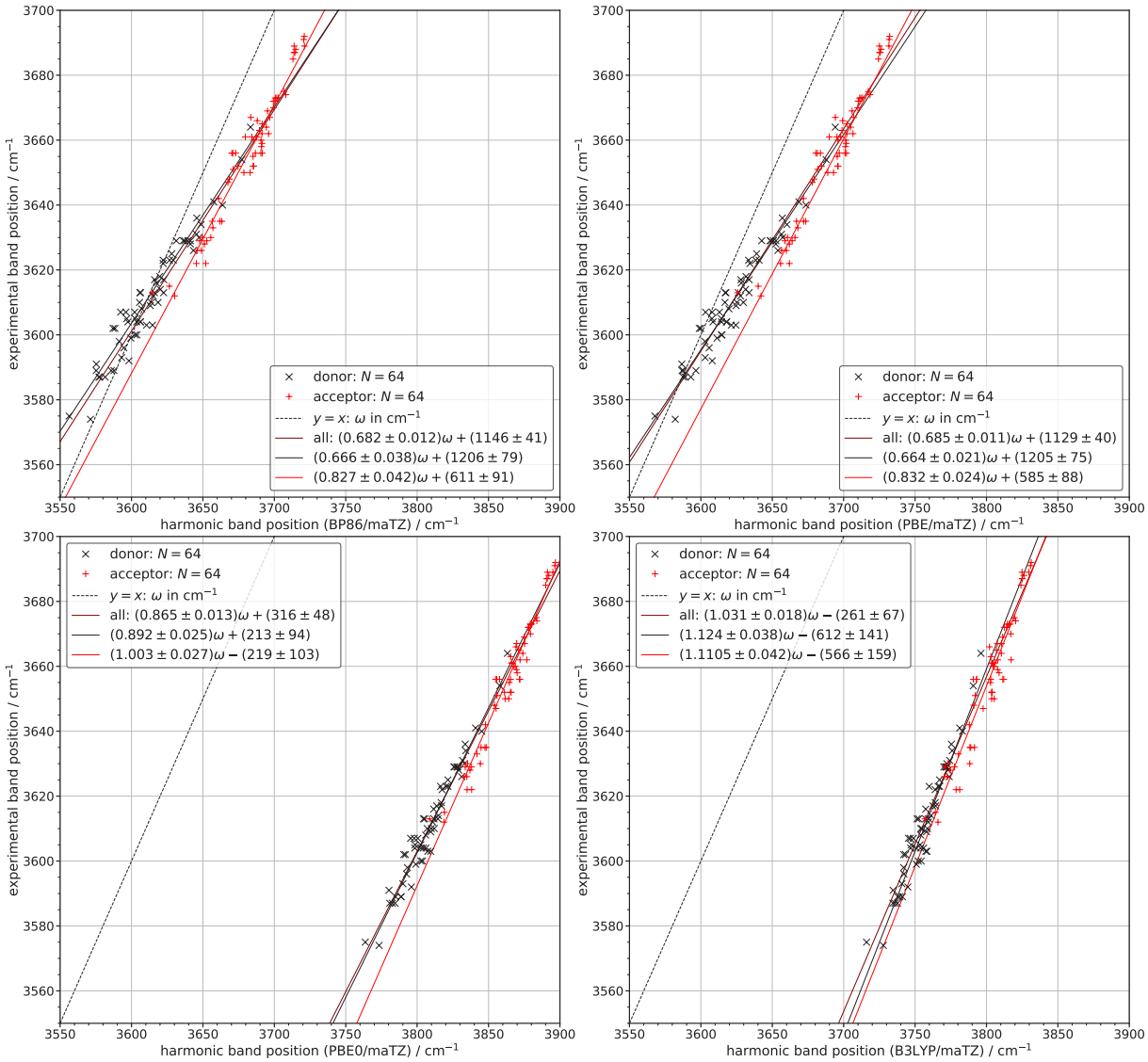

Fig. C.2: Fits for BP86/maTZ, PBE/maTZ, PBE0/maTZ and B3LYP/maTZ for hydrogen bond donors and acceptors separately. N indicates the number of data-points included.

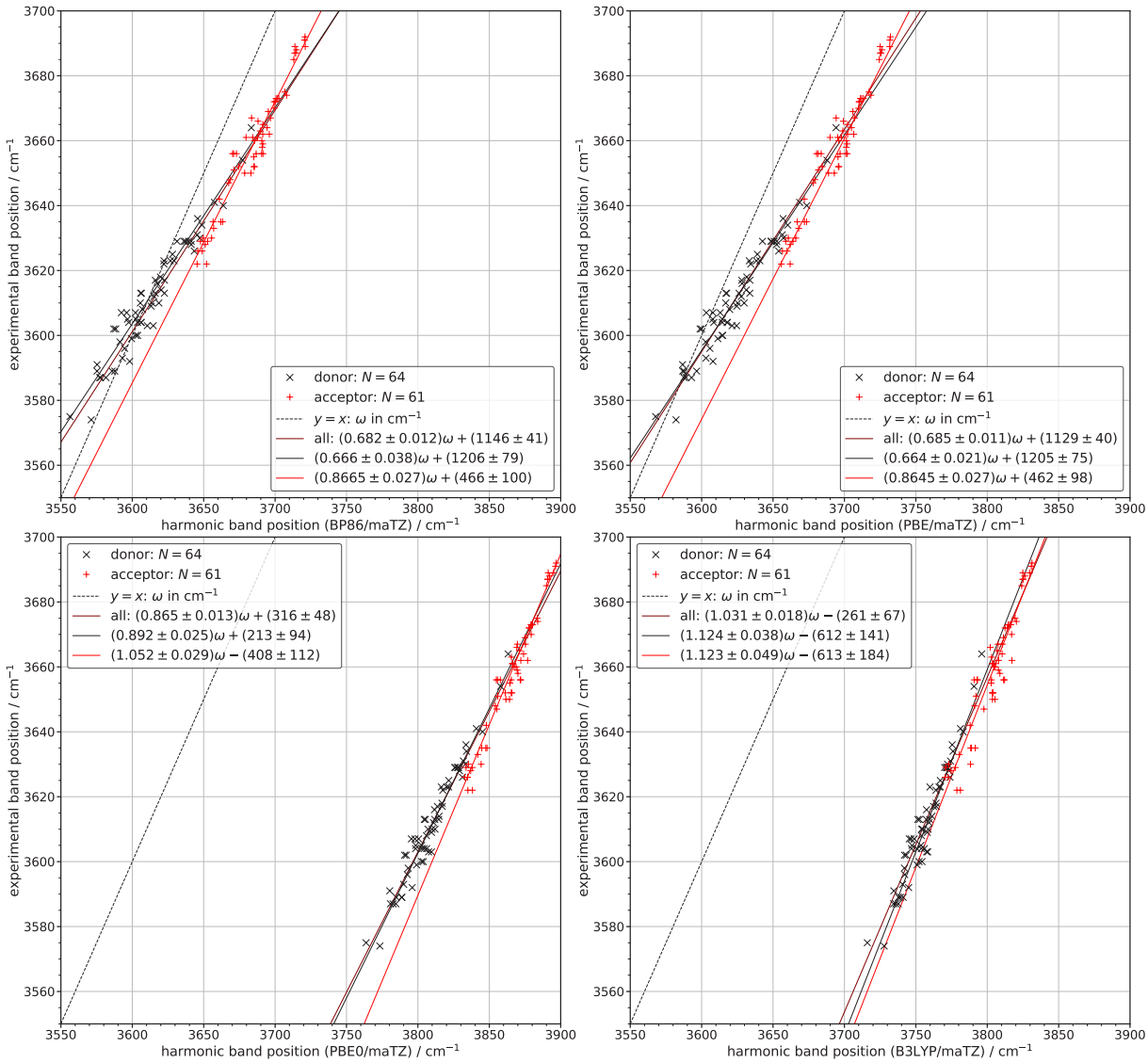

Fig. C.3: Reanalysis of the data provided in Fig. C.2 excluding the acceptor bands that involve π-systems directly (0-Va', 0-Ph' and c6-6Ph'). N indicates the number of data-points included.

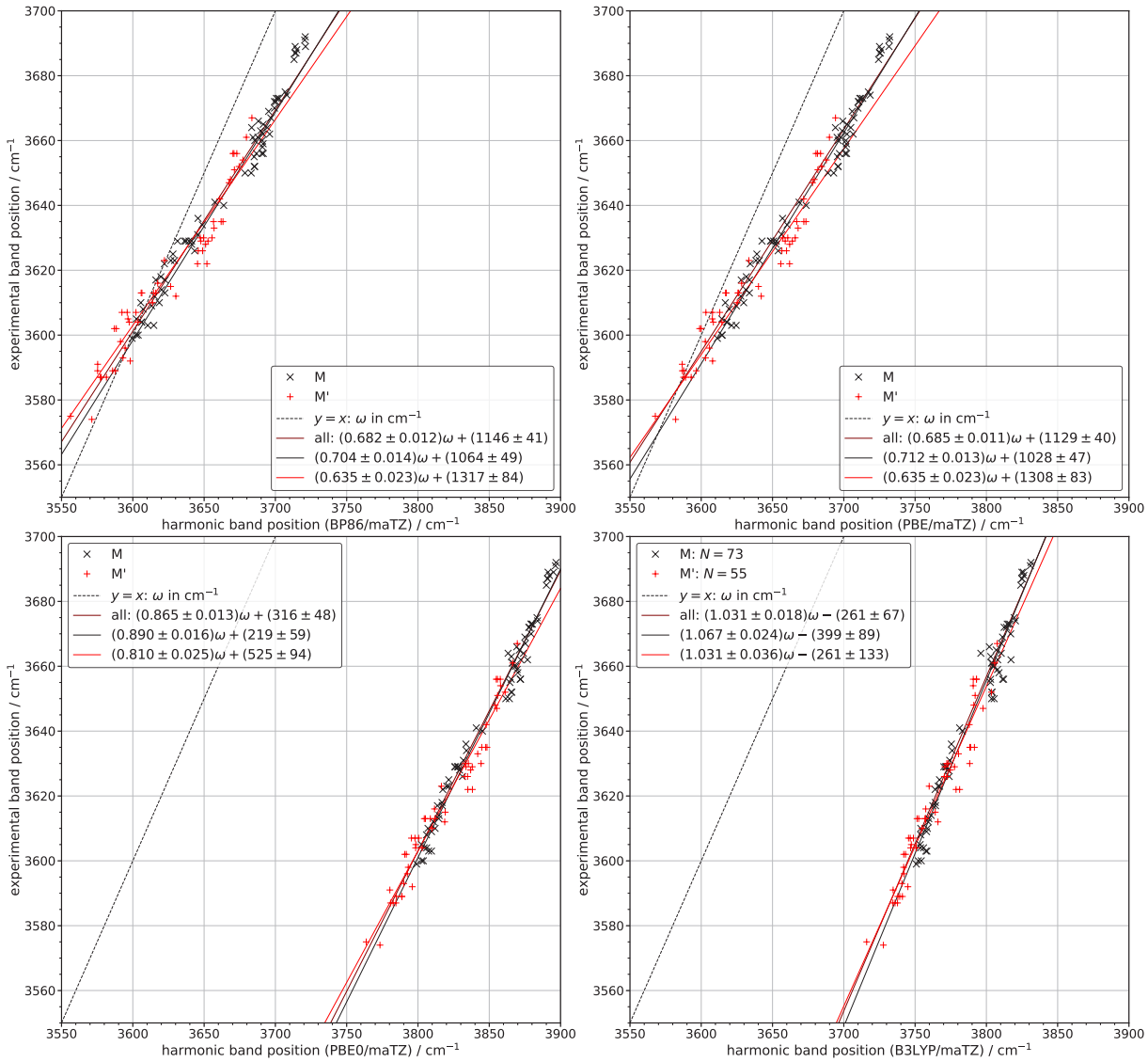

Fig. C.4: Fits for BP86/maTZ, PBE/maTZ, PBE0/maTZ and B3LYP/maTZ for the primed (M') and unprimed (M) conformers separately. N indicates the number of data-points included.

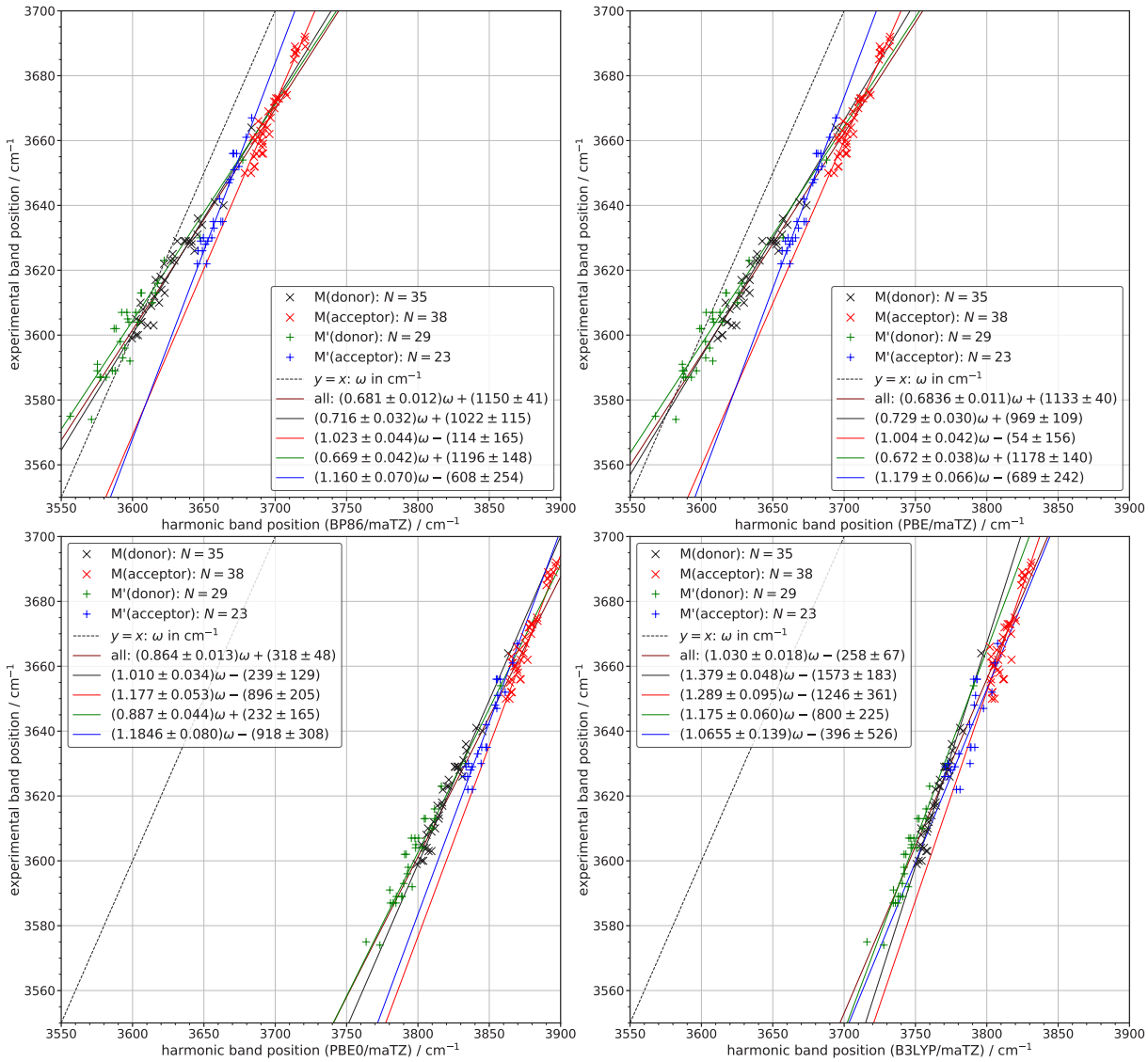

Fig. C.5: Reanalysis of the data provided in Fig. 3.29 (page 79) excluding the acceptor bands that involve π-systems directly (0-Va', 0-Ph' and c6-6Ph'). N indicates the number of data-points included.

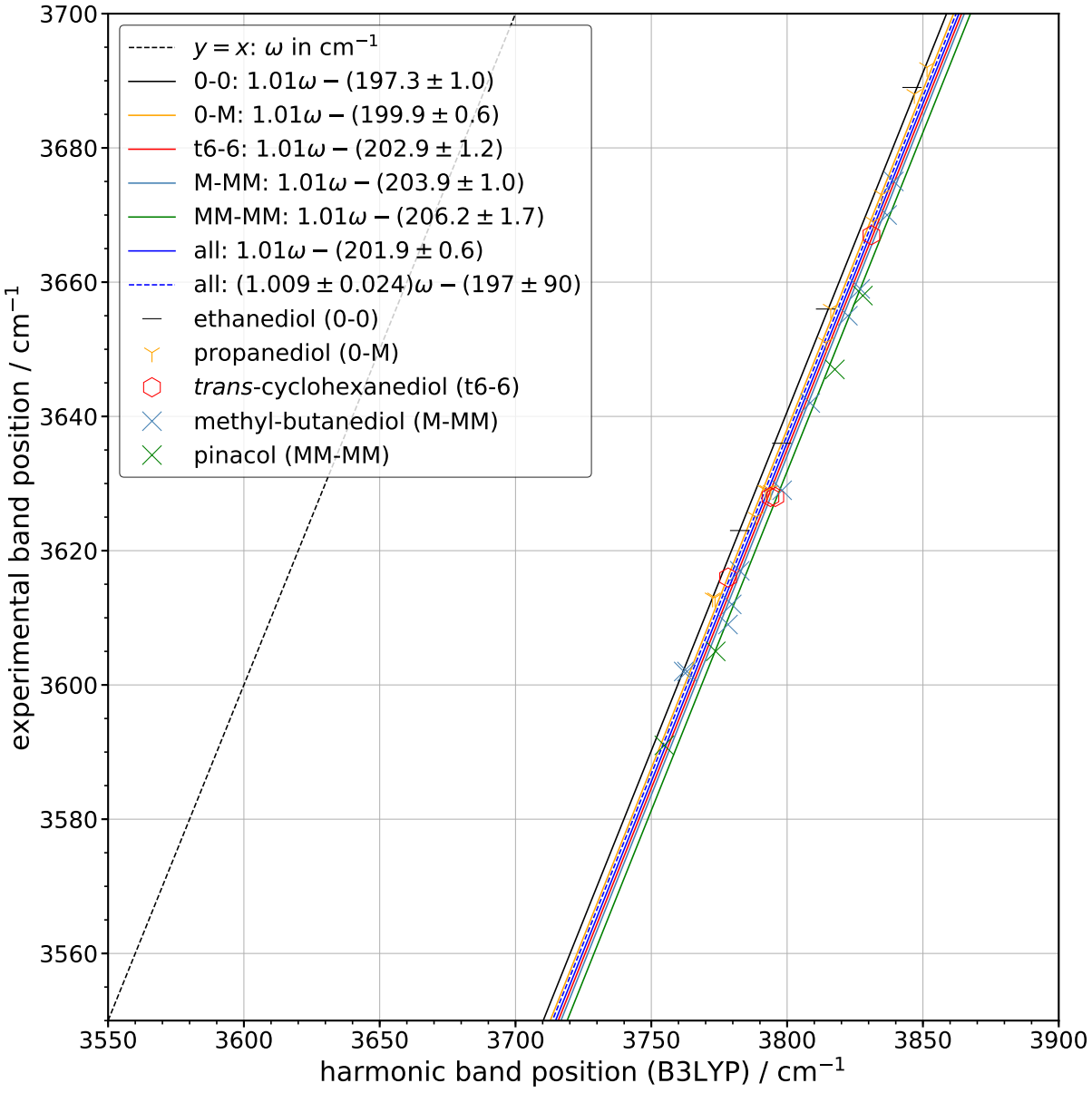

Fig. C.6: Fits according to n_D for B3LYP-D3(BJ)/may-cc-pVTZ. All data points are shown. The standard deviations (σ) as well as the number of included data points (N) are shown as well.

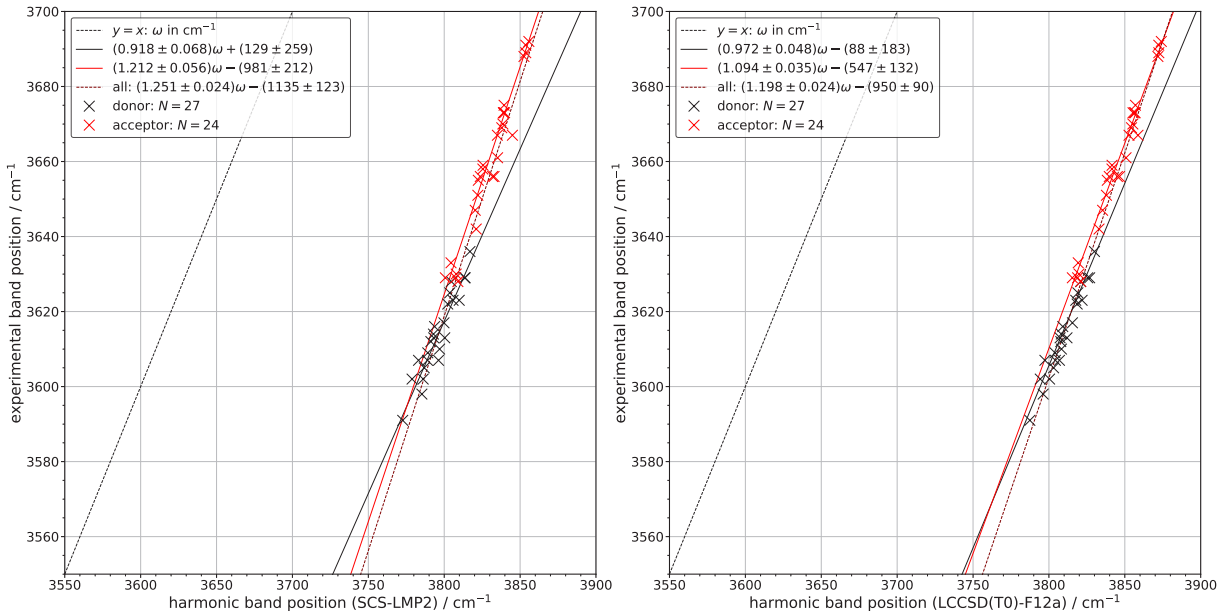

Fig. C.7: Fits for SCS-LMP2/aVTZ* (aVTZ*; aVTZ=all, H=VTZ) and LCCSD(T0)-F12a/VDZ-F12 for hydrogen bond donors and acceptors separately. The standard deviations (σ) as well as the number of included data points (N) are shown as well.

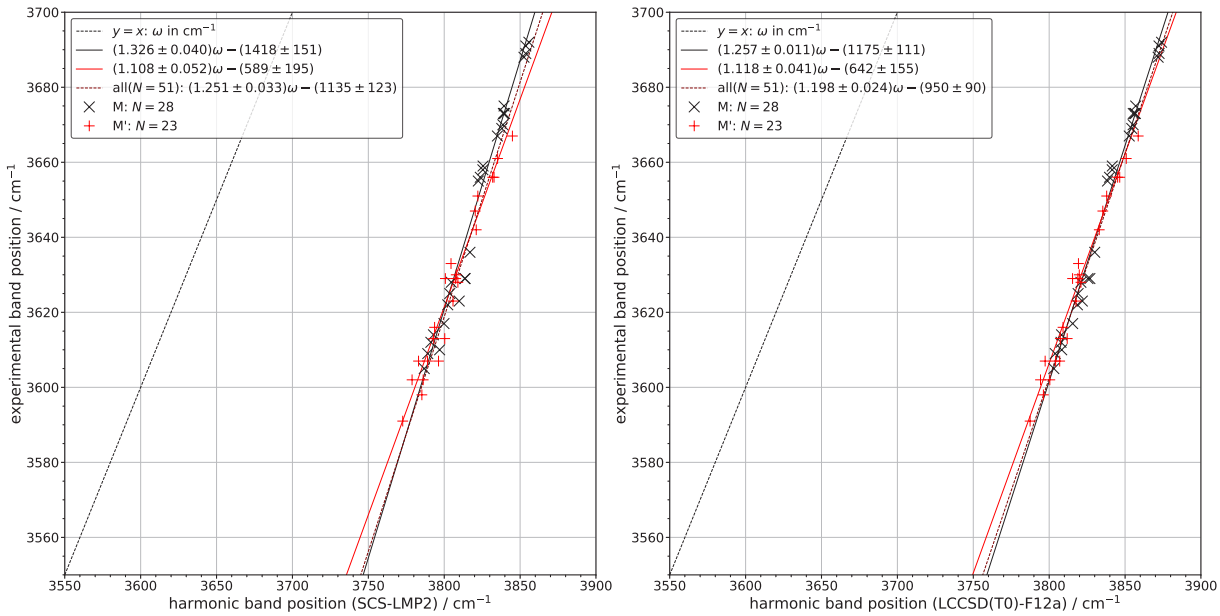

Fig. C.8: Fits for SCS-LMP2/aVTZ* (aVTZ*; aVTZ=all, H=VTZ) and LCCSD(T0)-F12a/VDZ-F12 for primed and unprimed conformers separately. The standard deviations (σ) as well as the number of included data points (N) are shown as well.

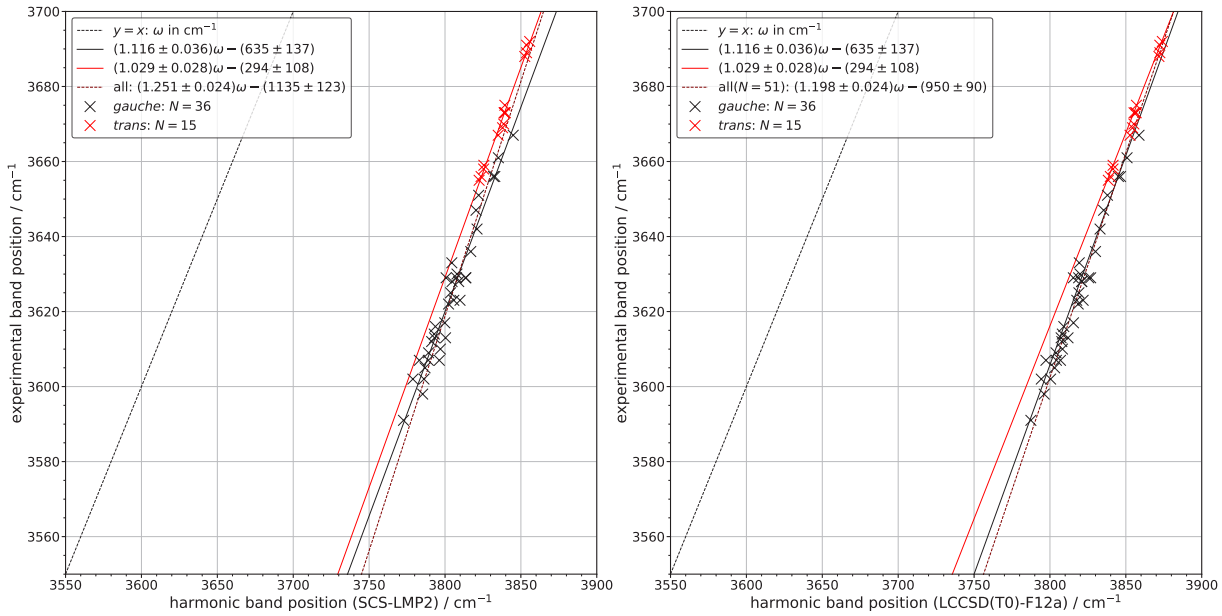

Fig. C.9: Fits for SCS-LMP2/aVTZ* (aVTZ*; aVTZ=all, H=VTZ) and LCCSD(T0)-F12a/VDZ-F12 for *gauche* and *trans* oriented OH groups separately. The standard deviations (σ) as well as the number of included data points (N) are shown as well.

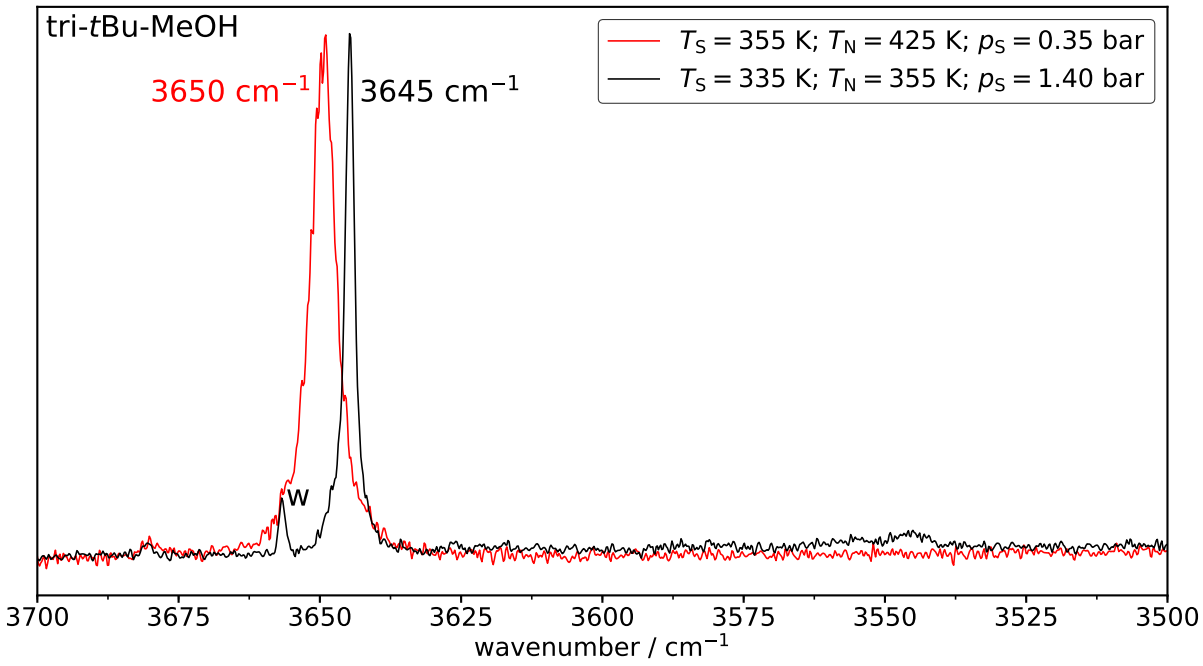

Fig. C.10: Spectra of tri-*tert*-butyl-methanol illustrating the influence of hot bands on the band centre of the most stable monomer. Pure He was used as a carrier gas for the red spectrum and an admixture of 10% Ar in He were used for the black spectrum. A full width at half maximum of about 2.0 and 5.2 cm^{-1} can be found for the black and red spectrum assuming a Lorentz-profile (better fit in comparison to Gaussian-Profile), respectively. The corresponding dimer spectrum is shown in 3.32 (page 86).

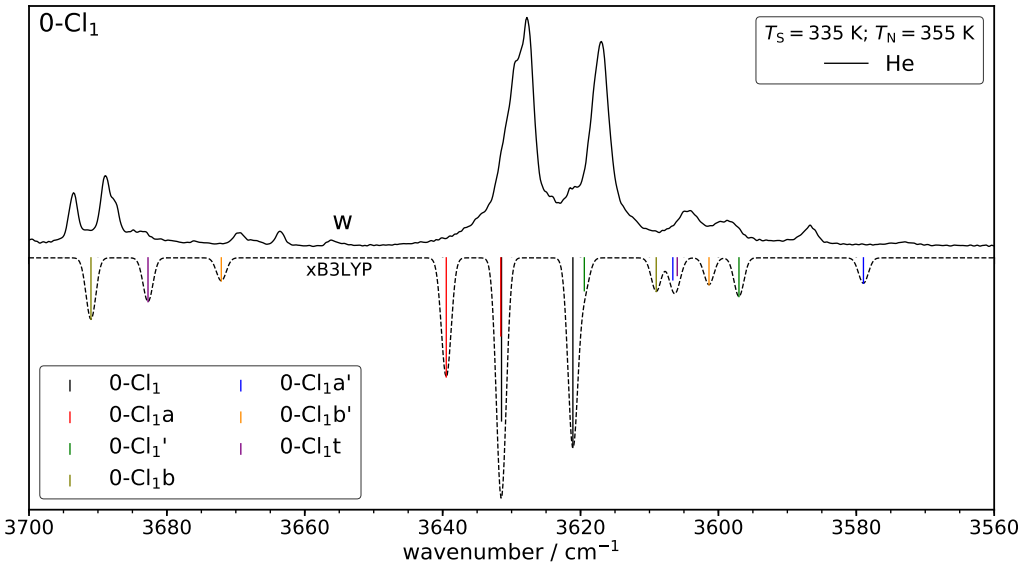

Fig. C.11: Experimental Raman data (plotted upwards) and simulated data (plotted downwards) of 3-chloro-propane-1,2-diol (0-Cl_1). The saturator temperature (T_S) as well as the nozzle temperature (T_N) are given. The simulated spectra are based on B3LYP/maTZ and are Boltzmann weighted based on T_N according to the relative energies given in Fig. B.6 (page 247). The derived correlation ($n_D = 1$) for B3LYP was used for the predictions. w indicates a water band.

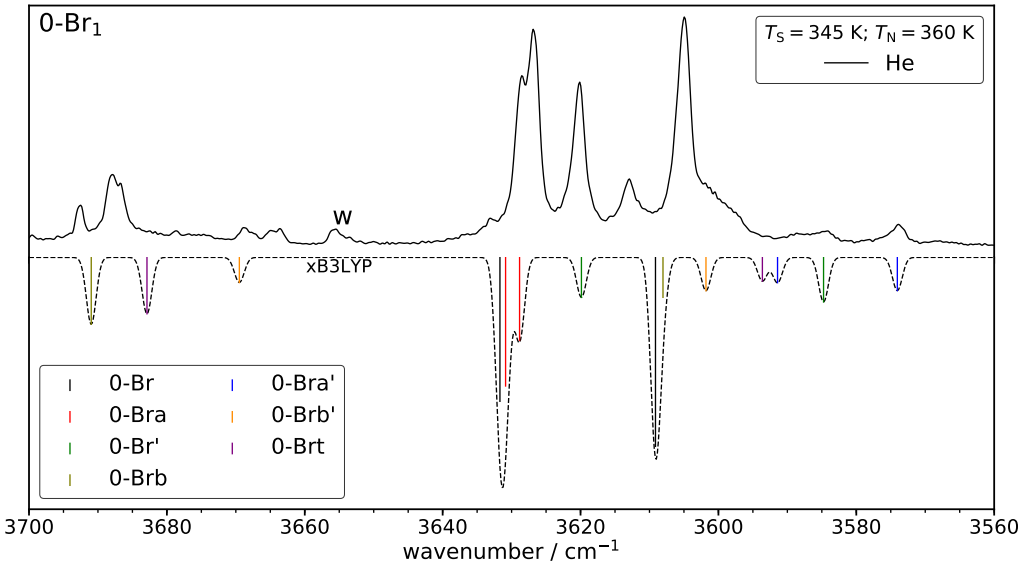

Fig. C.12: Experimental Raman data (plotted upwards) and simulated data (plotted downwards) of 3-bromo-propane-1,2-diol (0-Br_1). The saturator temperature (T_S) as well as the nozzle temperature (T_N) are given. The simulated spectra are based on B3LYP/maTZ and are Boltzmann weighted based on T_N according to the relative energies given in Fig. B.7 (page 248). The derived correlation ($n_D = 1$) for B3LYP was used for the predictions. w indicates a water band.

C.2 Dimers

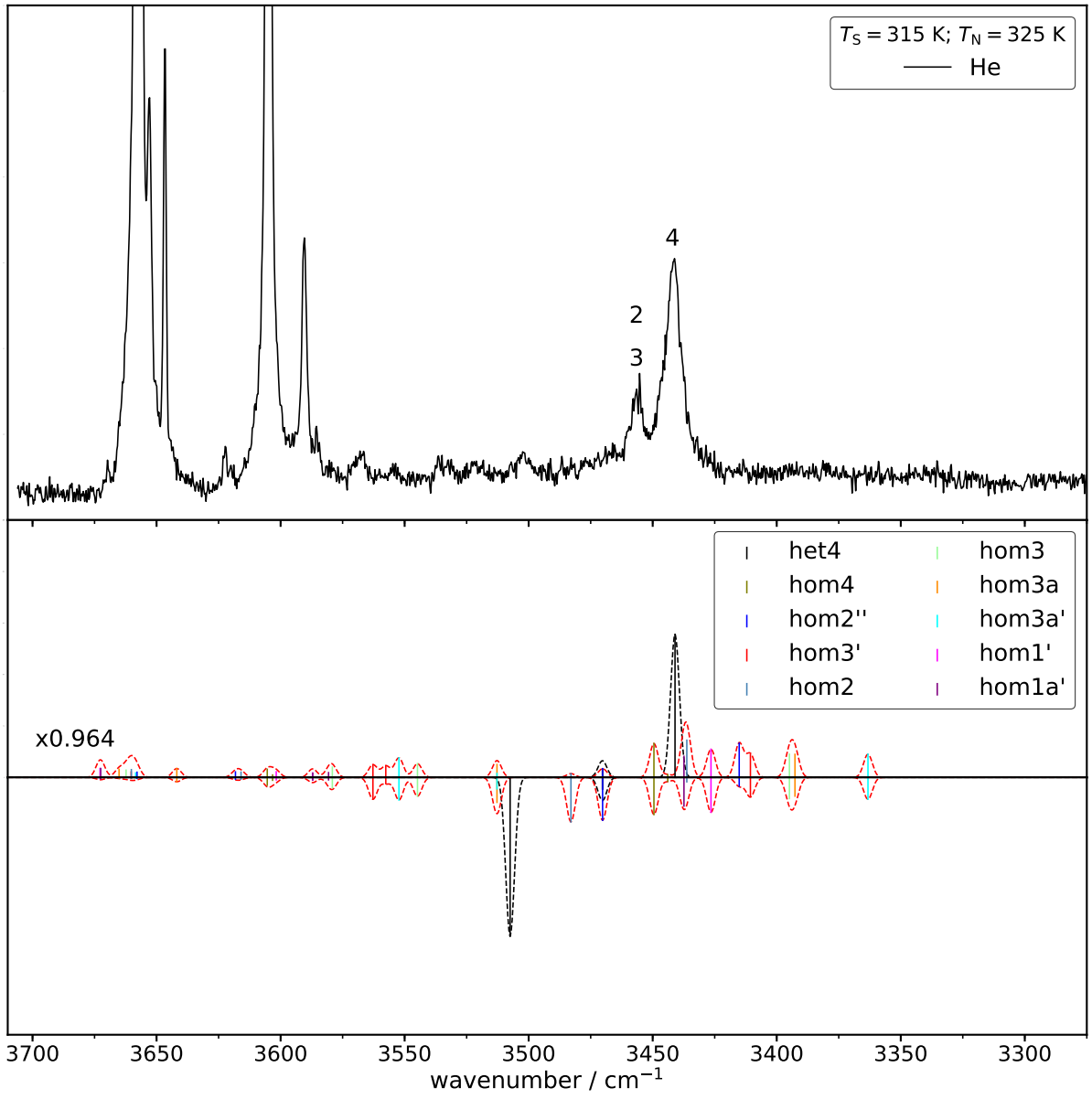

Fig. C.13: Experimental Raman (top), simulated Raman (middle) and simulated IR data (bottom) of pinacol (MM-MM). The saturator temperature (T_S) as well as the nozzle temperature (T_N) are given. The simulated spectra are based on B3LYP/maTZ and are scaled to band 4 of het4. w indicates a water band.

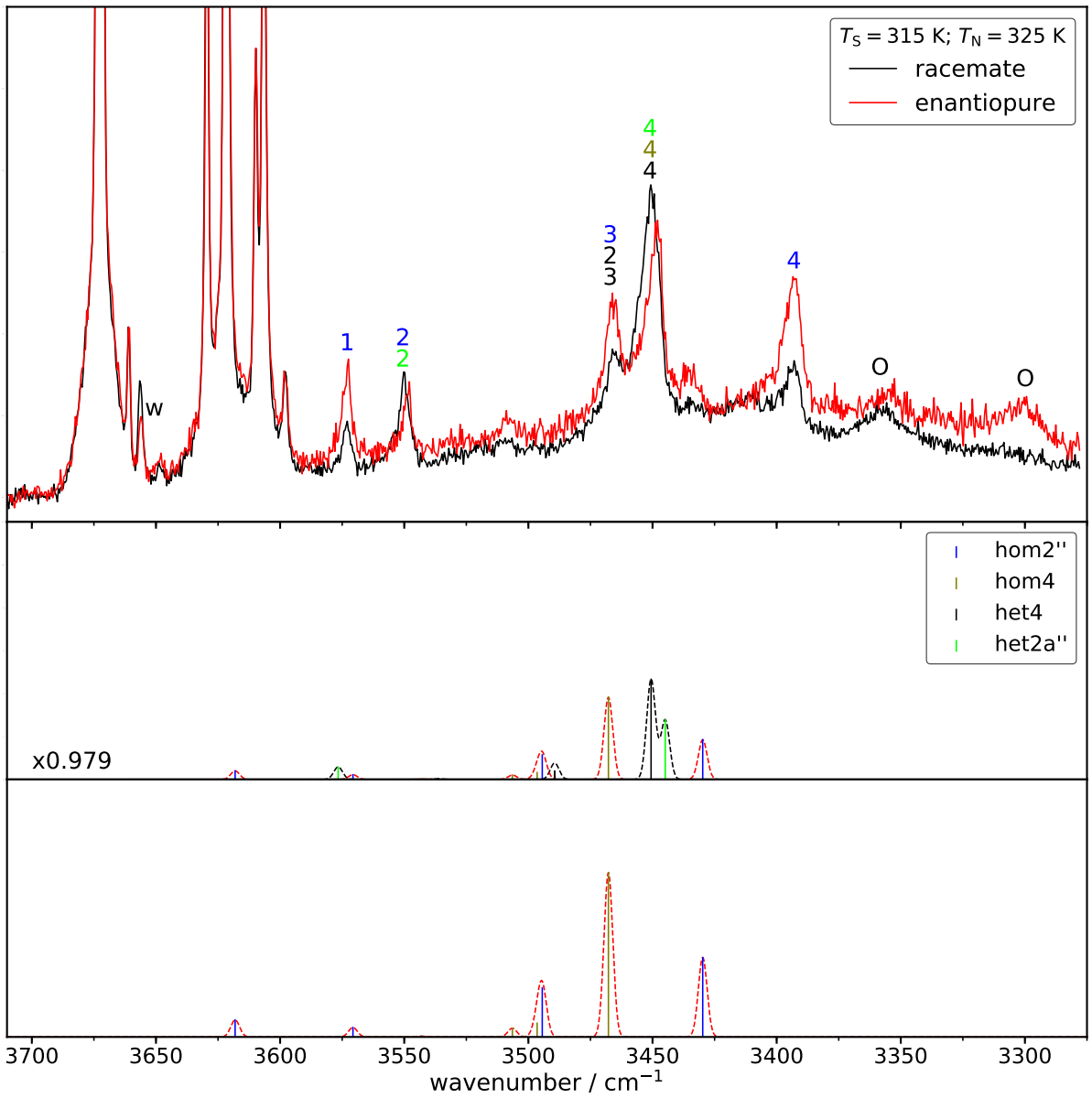

Fig. C.14: Experimental data (plotted upwards) and simulated data (plotted downwards) of butane-2,3-diol (rM-M). Like the simulation shown in Fig. 4.12 (page 149) but het2'' has been switched with het2a''. Alternative assignments are shown as well. The saturator temperature (T_S) as well as the nozzle temperature (T_N) are given. The simulated spectra are based on B3LYP/maTZ. w indicates a water band and O oligomer bands.

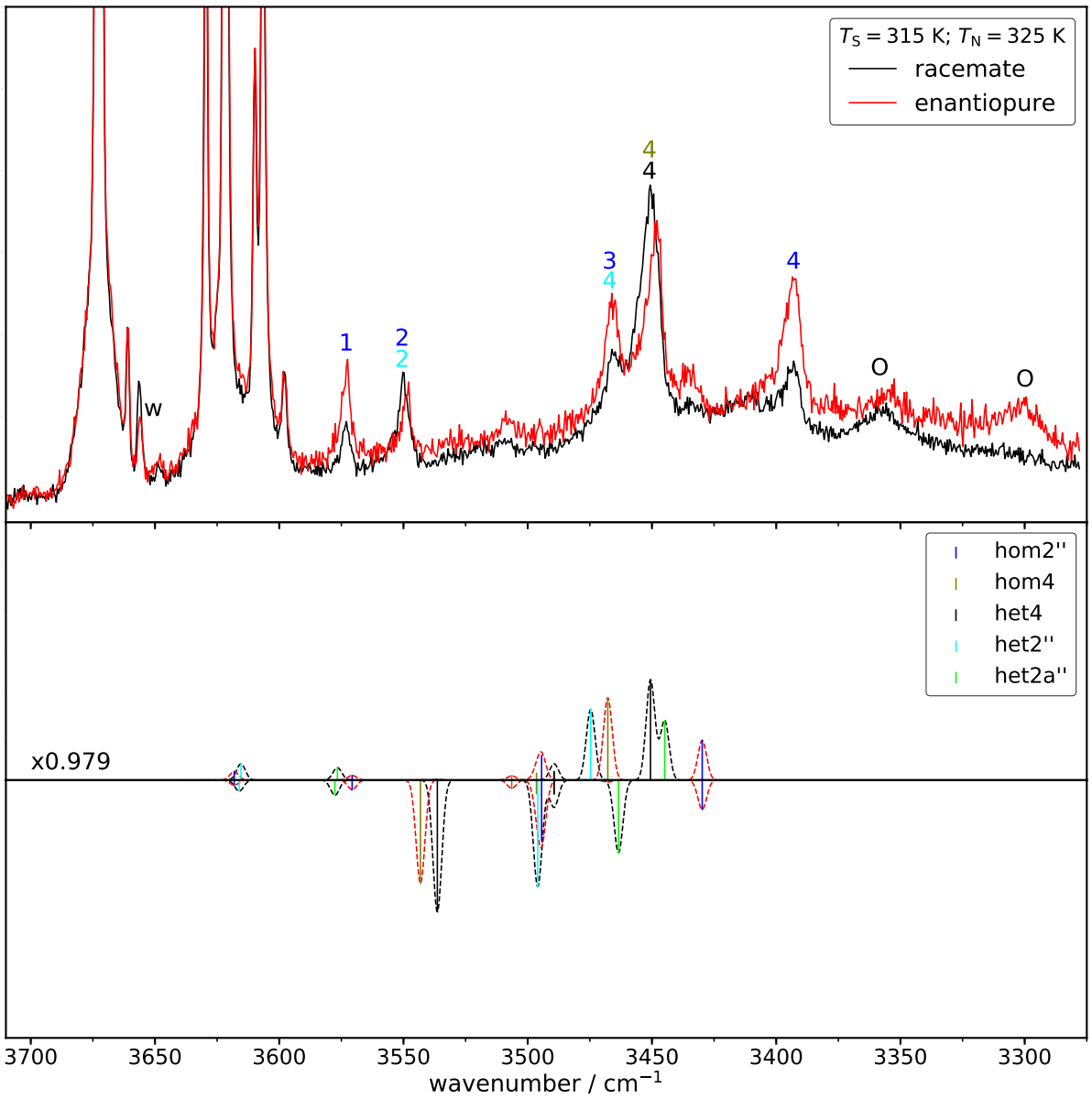

Fig. C.15: Experimental Raman (top), simulated Raman (middle) and simulated IR data (bottom) of butane-2,3-diol (rM-M). The saturator temperature (T_S) as well as the nozzle temperature (T_N) are given. The simulated spectra are based on B3LYP/maTZ and are scaled to band 4 of het4. w indicates a water band and O oligomer bands.

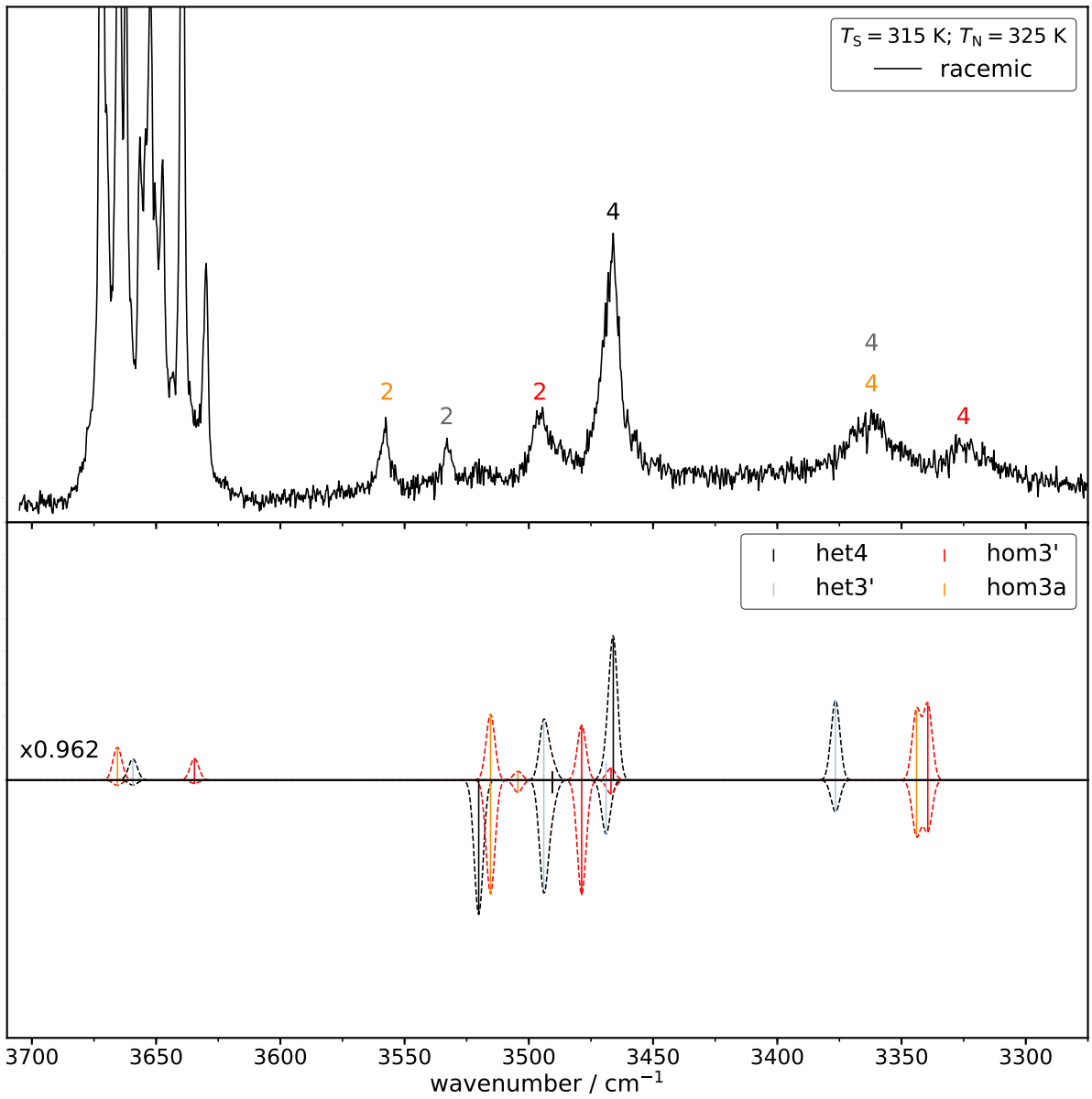

Fig. C.16: Experimental Raman (top), simulated Raman (middle) and simulated IR data (bottom)of *trans*-cyclopentane-1,2-diol (t5-5). The saturator temperature (T_S) as well as the nozzle temperature (T_N) are given. The simulated spectra are based on B3LYP/maTZ and are scaled to band 4 of het4.

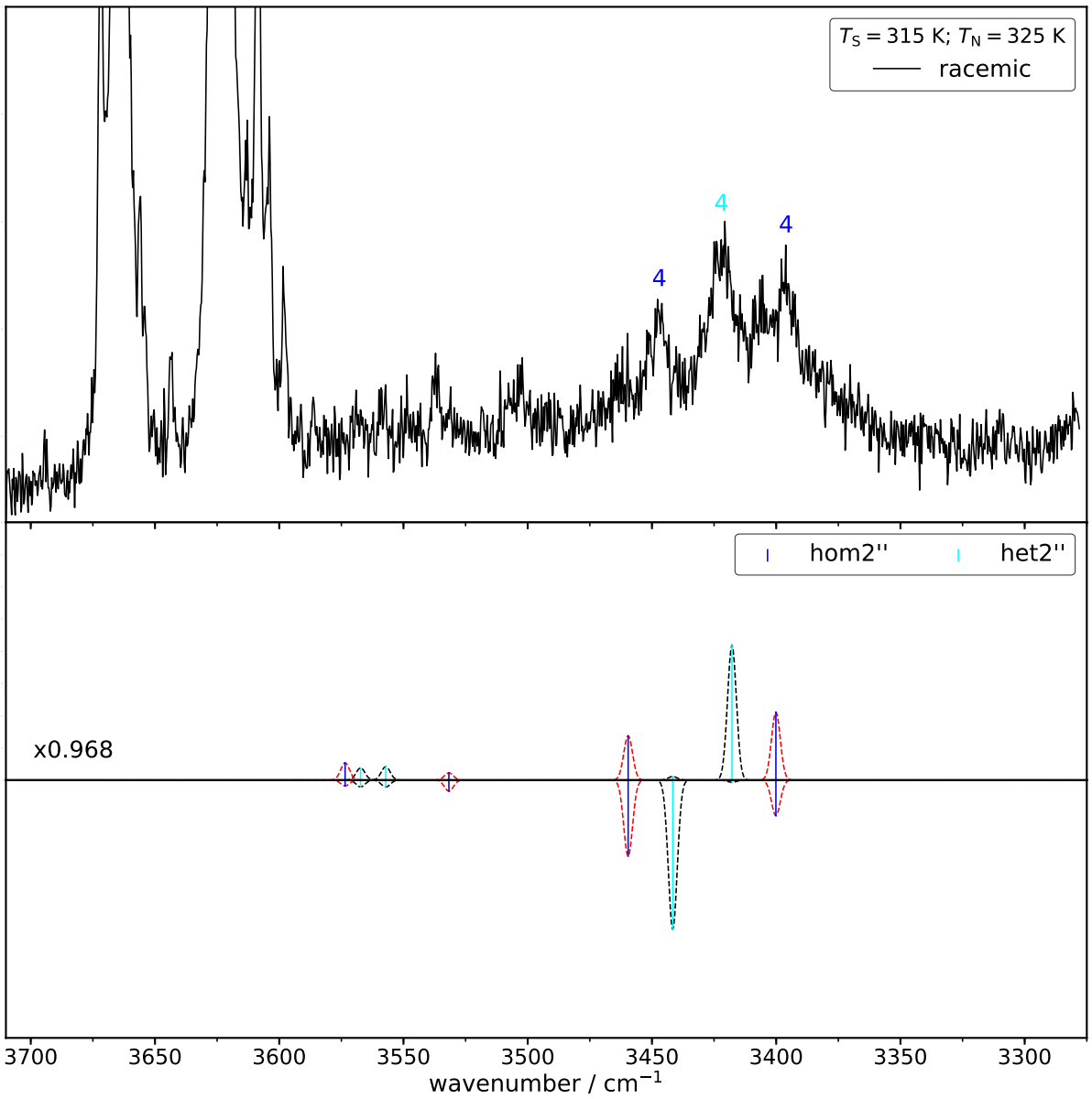

Fig. C.17: Experimental Raman (top), simulated Raman (middle) and simulated IR data (bottom) of *trans*-cycloheptane-1,2-diol (t7-7). The saturator temperature (T_S) as well as the nozzle temperature (T_N) are given. The simulated spectra are based on B3LYP/maTZ and are scaled. The scaling factor is derived from band 4 of hom2'' of rM-M (see Fig. 4.12 (page 149)).

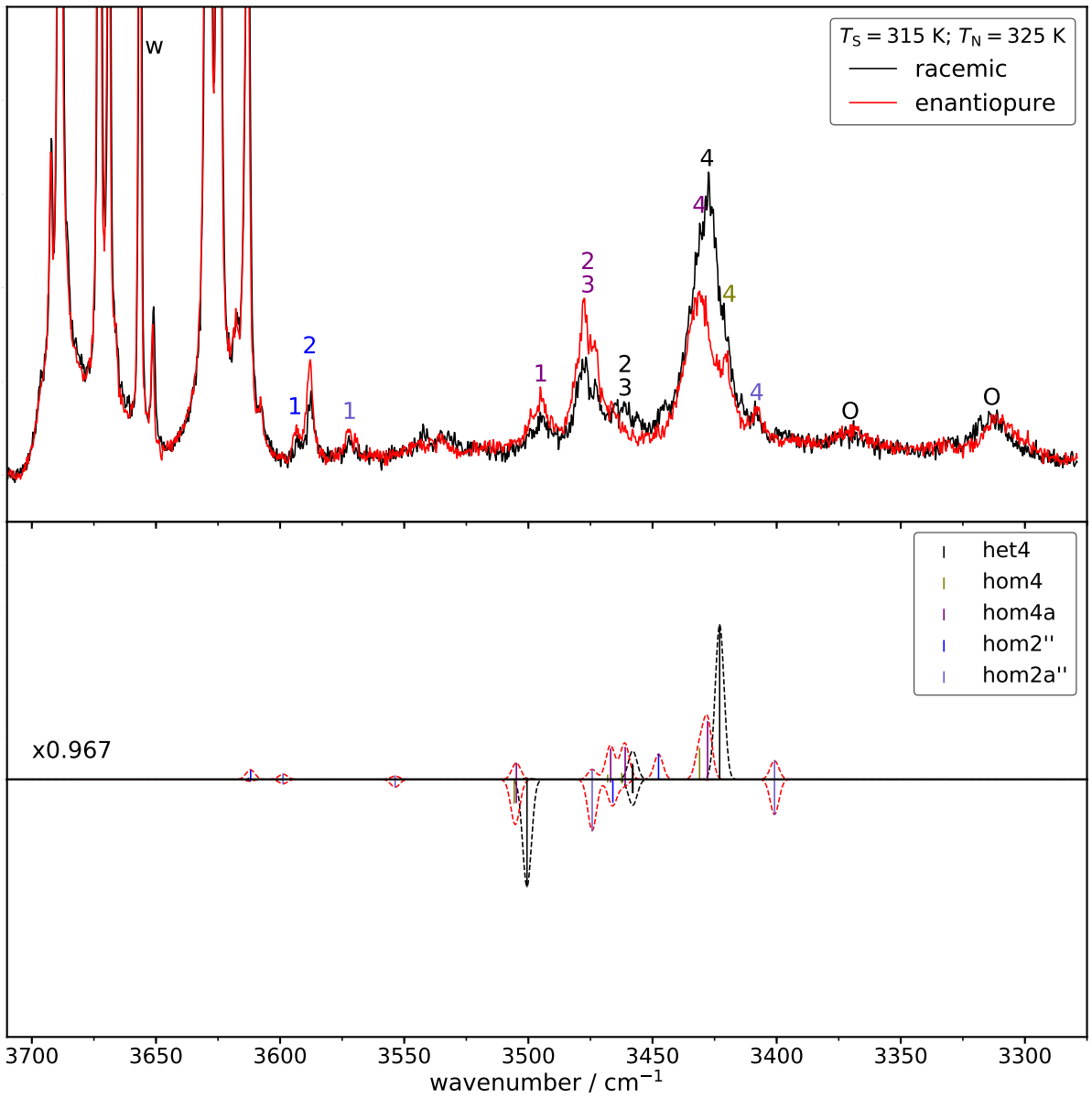

Fig. C.18: Experimental Raman (top), simulated Raman (middle) and simulated IR data (bottom) of propane-1,2-diol (0-M). The saturator temperature (T_S) as well as the nozzle temperature (T_N) are given. The simulated spectra are based on B3LYP/maTZ and are scaled to band 4 of het4. w indicates a water band and O oligomer bands.

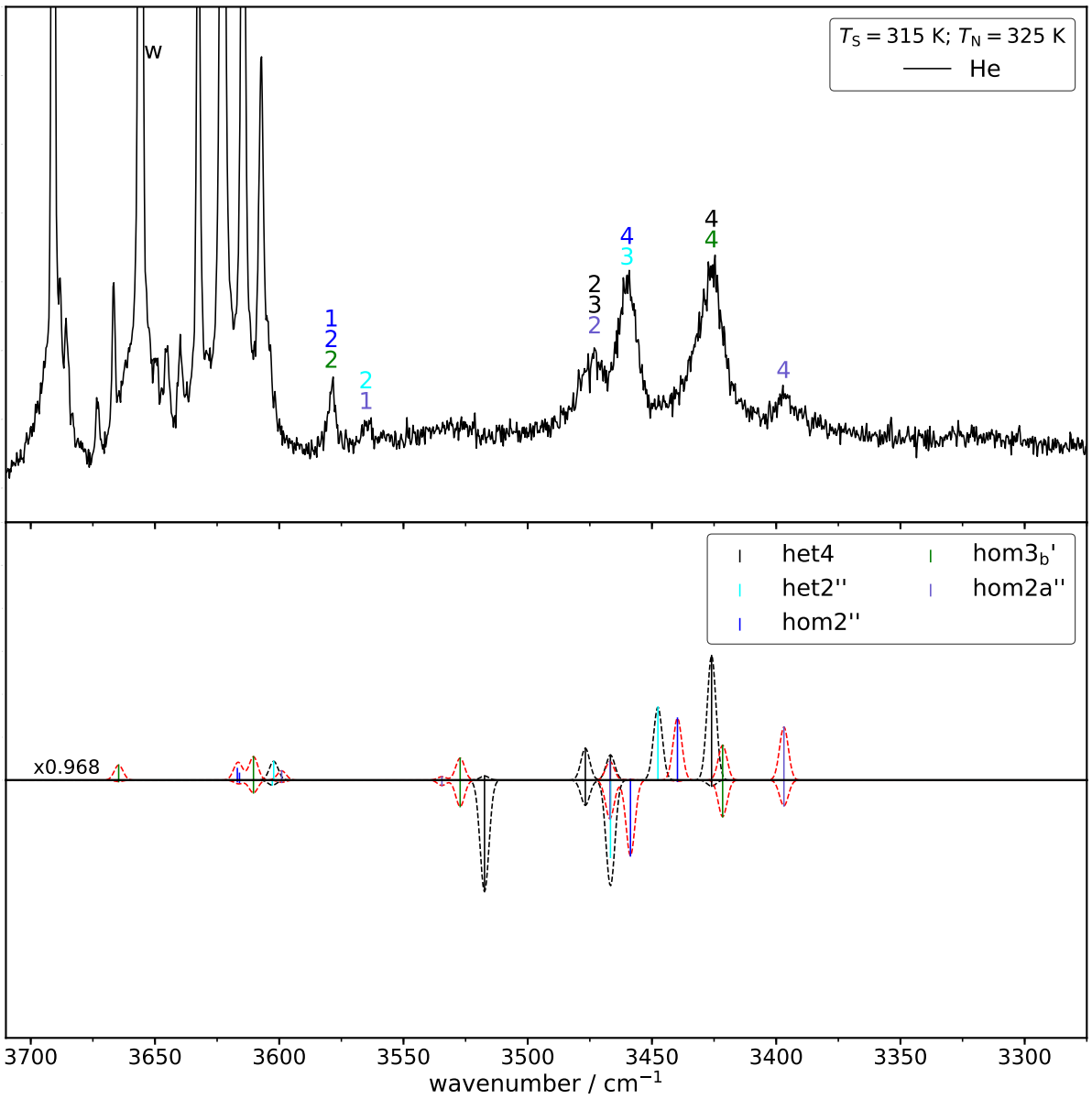

Fig. C.19: Experimental Raman (top), simulated Raman (middle) and simulated IR data (bottom) of 2-methyl-propane-1,2-diol (0-MM). The saturator temperature (T_S) as well as the nozzle temperature (T_N) are given. The simulated spectra are based on B3LYP/maTZ and are scaled to band 4 of het4. w indicates a water band.

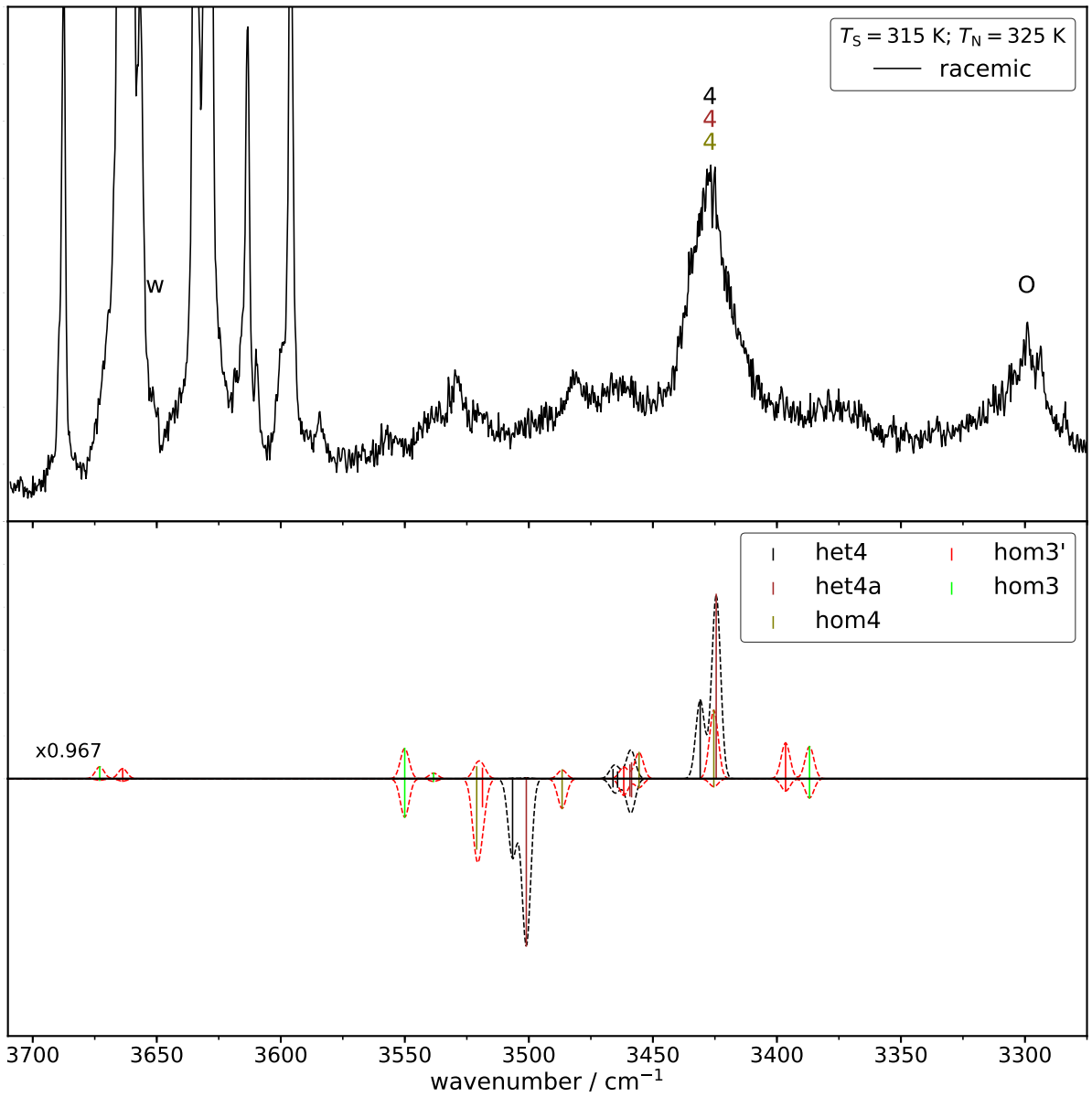

Fig. C.20: Experimental Raman (top), simulated Raman (middle) and simulated IR data (bottom) of 3-butene-1,2-diol (0-V). The saturator temperature (T_S) as well as the nozzle temperature (T_N) are given. The simulated spectra are based on B3LYP/maTZ and are scaled according to the factor derived for propane-1,2-diol (see Fig. 4.19 (page 166)) w indicates a water band and O oligomer bands.

D Anharmonic calculations

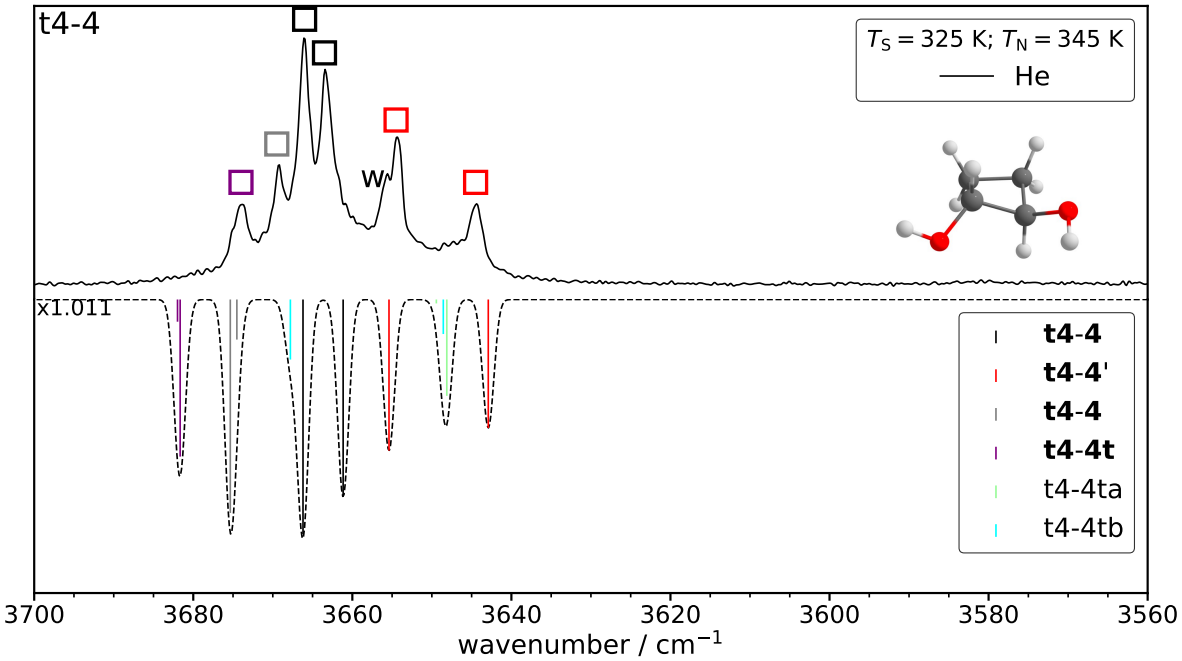

Fig. D.1: Spectral comparison with scaled B3LYP-D3(BJ)/def2-TZVP VPT2 calculations for *trans*-cyclobutane-1,2-diol. The Raman cross-section and population factors are taken from B3LYP/maTZ calculations.

Tab. D.1: Results of a VPT2[114] calculation for the t5-5 conformer with Gaussian16 (Revision A.03)[69] at the B3LYP-D3(BJ)/def2-TZVP level of computation. ω_i are the respective calculated harmonic frequencies, $\tilde{\nu}_i$ the anharmonic frequencies and $x_{i,44}$ the coupling constants for the bound OH mode and $x_{i,45}$ the ones for the free OH mode. Modes 18 – 32 are ring breathing vibrations. Significant off-diagonal constants may indicate spectrally identifiable hot transitions, if the coupling mode remains thermally populated in the jet. This table was adopted from Ref. [165].

mode	18	19	21	23	29	32
ω_i / cm^{-1}	1075.236	1110.600	1173.130	1235.281	1356.468	1438.726
$\tilde{\nu}_i$ / cm^{-1}	1050.540	1082.496	1149.484	1205.165	1322.233	1401.172
$x_{i,44}$ / cm^{-1}	−1.657	0.012	−0.551	−1.211	−0.303	−0.917
$x_{i,45}$ / cm^{-1}	−2.930	−1.100	−1.581	−3.095	−1.833	−3.05

mode	44	45
ω_i / cm^{-1}	3783.942	3813.614
$\tilde{\nu}_i$ / cm^{-1}	3605.346	3635.292
$x_{i,44}$ / cm^{-1}	−86.031	0.211
$x_{i,45}$ / cm^{-1}	0.211	−85.567

Tab. D.2: Overview of the experimental assignments for 2-chloropropan-1-ol (g-ga and g'-gg) and 1-chloropropan-2-ol (m-ga and h-gg) at different levels of computation. Frequencies are computed with VPT2. All calculations utilise the aVTZ basis set. All values are given in cm^{-1} and unscaled.

	g-ga	g'-gg	m-ga	h-gg
Jet-Raman	3620	3620	3619	3609
PBE0	3635.89	3640.49	3641.52	3633.68
B3LYP	3587.81	3592.13	3593.12	3584.26
CAM-B3LYP	3642.89	3645.58	3647.49	3637.56
B2PLYP	3606.23	3609.14	3606.33	3598.85
MP2	3611.03	3611.62	3603.04	3599.60

Tab. D.3: Overview of the experimental assignments for 2-bromopropan-1-ol (g-ga and g'-gg) and 1-bromopropan-2-ol (m-ga and h-gg) at different levels of computation. Frequencies are computed with VPT2. All calculations utilise the aVTZ basis set. All values are given in cm^{-1} and unscaled.

	g-ga	g'-gg	m-ga	h-gg
Jet	3607	3608	3608	3598
PBE0	3617.99	3621.99	3625.22	3616.82
B3LYP	3573.48	3582.15	3581.12	3571.55
CAM-B3LYP	3632.72	3636.97	3639.09	3629.12
B2PLYP	3592.11	3596.97	3593.68	3585.97
MP2		3591.35	3583.87	3580.81

Tab. D.4: Overview of the experimental assignments for 3-chloro-propane-1,2-diol (0-Cl_1) at different levels of computation. Frequencies are computed with VPT2. All calculations utilise the aVTZ basis set. All values are given in cm^{-1} and unscaled.

	Jet-Raman	PBE0	B3LYP	CAM-B3LYP	B2PLYP	MP2
0-Cl_{11}	3617	3632.13	3588.79	3643.81	3604.01	3597.20
0-Cl_{12}	3628	3652.65	3601.52	3649.60	3616.97	3620.20
0-Cl_1a_1	3629	3652.30	3606.48	3650.05	3617.91	3612.88
0-Cl_1a_2	3629	3659.05	3601.86	3658.75	3617.83	3623.11
0-$Cl_{1_1}^{'}$	3587	3607.95	3564.60	3616.39	3577.58	3575.42
0-$Cl_{1_2}^{'}$	3621	3642.04	3590.71	3642.31	3608.30	3613.87
0-Cl_1b_1	3604	3629.98	3580.43	3626.36	3591.81	3592.10
0-Cl_1b_2	3694	3729.13	3669.26	3717.18	3680.16	3682.12
0-$Cl_1a_1^{'}$	3573	3587.50	3548.41	3594.69	3558.23	3549.63
0-$Cl_1a_2^{'}$	3604	3610.54	3564.47	3626.63	3590.38	3596.50
0-$Cl_1b_1^{'}$		3621.19	3573.41	3621.53	3584.45	3585.62
0-$Cl_1b_2^{'}$		3707.11	3649.83	3707.20	3664.77	3670.84
0-Cl_1t_1	3599	3618.25	3572.36	3625.98	3586.09	3587.26
0-Cl_1t_2	3689	3723.79	3662.10	3711.77	3675.14	3680.30

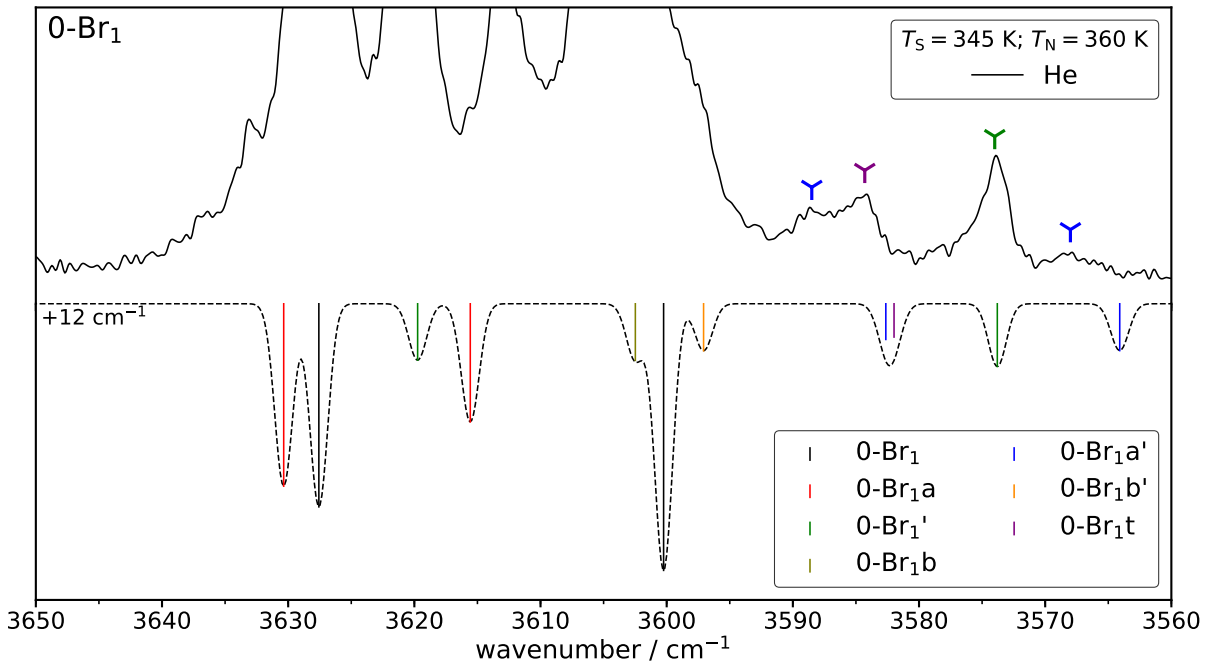

Fig. D.2: Zoom in of Fig. 3.39 (page 104).

Tab. D.5: Overview of the experimental assignments for 3-bromo-propane-1,2-diol (0-Br_1) at different levels of computation. Frequencies are computed with VPT2. All calculations utilise the aVTZ basis set. All values are given in cm^{-1} and unscaled.

	Jet-Raman	B3LYP	PBE0	CAM-B3LYP	B2PLYP	MP2
0-Br_{11}	3605	3575.14	3613.85	3632.80	3588.24	3573.08
0-Br_{12}	3627	3600.02	3650.76	3649.00	3615.57	3617.20
0-Br_1a_1	3620	3588.51	3632.99	3649.52	3603.57	3592.27
0-Br_1a_2	3628	3605.90	3657.80	3650.65	3618.36	3621.15
0-Br_1'$_1$	3574	3547.55	3585.80	3606.04	3561.80	3551.64
0-Br_1'$_2$	3613	3594.24	3644.41	3642.20	3607.74	3611.49
0-Br_1b_1	3600	3580.43	3628.22	3626.50	3590.48	3589.94
0-Br_1b_2	3693	3667.63	3727.98	3716.29	3679.01	3681.07
0-Br_1a'$_1$	3568	3540.69	3578.05	3589.67	3552.09	3540.83
0-Br_1a'$_2$	3588	3548.10	3587.93	3614.80	3570.63	3568.79
0-Br_1b'$_1$	-	3572.03	3621.09	3619.86	3585.08	3585.90
0-Br_1b'$_2$	-	3647.79	3703.00	3702.31	3659.19	3661.31
0-Br_1t_1	3584	3557.39	3598.96	3614.23	3569.98	3564.12
0-Br_1t_2	3688	3661.12	3722.42	3710.65	3672.37	3678.02

E Fitting constants

Tab. E.1: Fit parameters for B3LYP/maTZ. The parameters in parentheses of the all fit indicate which ones were varied. Fits with $h = 1.00$ can be seen in Fig. **??** for a comparison with PBE0. The sections refer to the main text.

section	n_D	h	$a2$ / cm^{-1}
	0	1.01	174.6(9)
	2	1.01	182.0(1.1)
3.1.3	4	1.01	186.1(1.9)
	all($a2$)	1.01	180.9(1.6)
	all($h, a2$)	1.008(65)	170(250)
	0	1.00	136.8(1.0)
	1	1.00	140.5(6)
	2	1.00	144.2(1.1)
3.1.5	3	1.00	146.0(9)
	4	1.00	148.4(1.7)
	all($a2$)	1.00	143.1(7)
	all($h, a2$)	0.999(28)	140(76)

Tab. E.2: Corresponding covariance matrices for the fits shown in Tab. E.1 illustrating the parameter correlation. The errors (σ) in Tab. E.1 can be obtained by diagonalising the matrix and then taking the square root.

section	n_D	hh	$(a2)(a2)$ / cm^{-2}	$h(a2) = (a2)h$ / cm^{-1}
4.2	all($h, a2$)	0.004 248	60 706	−16.058
4.4	all($h, a2$)	0.000 771	11 033	−2.917

Tab. E.3: Fit parameters for PBE0/maTZ. The parameters in parentheses of the all fit indicate which ones were varied. Despite the strong parameter correlation, the standard deviations for $a2$ in one-parameter fits profit significantly from a lowering of h.

section	n_D	h	$a2$ / cm^{-1}
3.1.3	0	0.84	−417.6(1.0)
	2	0.84	−410.6(2.0)
	4	0.84	−410.5(1.8)
	all($a2$)	0.84	−412.9(1.3)
	all($h, a2$)	0.837(44)	−420(170)
3.1.3 ($h = 1.00$)	0	1.00	198.3(1.9)
	2	1.00	203.5(3.2)
	4	1.00	201.8(5.2)
	all($a2$)	1.00	201.2(2.0)
3.1.5	0	0.84	−417.6(1.0)
	1	0.84	−414.9(8)
	2	0.84	−410.6(2.0)
	3	0.84	−411.3(1.1)
	4	0.84	−410.5(1.8)
	all($a2$)	0.84	−413.1(7)
	all($h, a2$)	0.835(21)	−432(81)

Tab. E.4: Fit parameters for BP86/maTZ. The parameters in parentheses of the all fit indicate which ones were varied. The sections refer to the main text.

section	n_D	h	$a2$ / cm^{-1}
3.1.3	0	0.66	−1233.3(1.7)
	2	0.66	−1224.7(2.3)
	4	0.66	−1226.8(1.9)
	all($a2$)	0.66	−1228.2(1.5)
	all($h, a2$)	0.664(40)	1210(150)
3.1.5	0	0.66	−1233.3(1.7)
	1	0.66	−1230.5(1.2)
	2	0.66	−1224.7(2.3)
	3	0.66	−1226.8(1.5)
	4	0.66	−1226.8(1.9)
	all($a2$)	0.66	−1228.6(8)
	all($h, a2$)	0.658(20)	−1235(75)

Tab. E.5: Fit parameters for PBE/maTZ. The parameters in parentheses of the all fit indicate which ones were varied. The sections refer to the main text.

section	n_D	h	$a2$ / cm^{-1}
	0	0.67	−1189.2(1.5)
	2	0.67	−1180.9(2.3)
3.1.3	4	0.67	−1183.0(2.0)
	all($a2$)	0.67	−1184.4(1.5)
	all($h, a2$)	0.670(40)	−1180(150)
	0	0.66	−1226.0(1.7)
	1	0.66	−1223.2(1.2)
	2	0.66	−1217.5(2.3)
3.1.5	3	0.66	−1219.4(1.4)
	4	0.66	−1219.5(1.8)
	all($a2$)	0.66	−1221.3(8)
	all($h, a2$)	0.664(20)	−1206(75)

F Microwave data

A short explanation of the constants used can be found in Tab. 2.1 (page 13). All values are given in the Ir representation using the Watson S reduction.

Tab. F.1: Overview of the experimentally determined rotational constants for 2-bromo-propan-1-ol (top) and 1-bromo-propan-2-ol (bottom) for the two naturally abundant bromine isotopes. All other isotopes are in their most naturally abundant form. All values are given in MHz.

	g-ga		g'-gg	
	^{79}Br	^{81}Br	^{79}Br	^{81}Br
A	3948.083 03(47)	3944.437 98(48)	4677.437 35(67)	4675.665 73(73)
B	2349.194 08(34)	2328.608 29(28)	2079.364 11(28)	2061.302 89(29)
C	1553.406 48(24)	1543.825 55(21)	1675.648 81(25)	1663.689 85(27)
D_J	0.000 729(10)	0.000 715 6(76)	0.000 659 0(75)	0.000 659 3(92)
D_K	0.001 656(35)	0.001 654(36)	0.004 299(76)	0.004 595(99)
D_{JK}	−0.000 872(14)	−0.000 824(17)	−0.000 933(17)	−0.000 934(17)
d_1	−0.000 310 8(42)	−0.000 300 8(24)	−0.000 193 9(22)	−0.000 188 9(22)
d_2	−0.000 044 5(15)	−0.000 042 9(12)	−0.000 021 62(84)	−0.000 016 9(10)
χ_{aa}	304.3578(21)	257.0362(21)	317.5495(25)	266.3215(25)
χ_{bb-cc}	144.5718(40)	118.1307(39)	68.1420(48)	56.1226(49)
χ_{ab}	304.968(87)	253.023(71)	266.32(10)	221.81(13)
χ_{ac}	144.41(27)	121.10(22)	−199.71(17)	−166.71(21)
χ_{bc}	87.55(19)	72.44(11)	−103.811(62)	−86.347(80)
C_{aa}	0.003 28(31)	0.003 49(33)	0.003 82(42)	0.003 10(43)
C_{bb}	0.003 62(20)	0.003 64(22)	0.003 02(24)	0.002 71(23)
C_{cc}	0.002 38(21)	0.002 90(20)	0.002 66(25)	0.002 80(27)

	m-ga		h-gg	
	^{79}Br	^{81}Br	^{79}Br	^{81}Br
A	8428.620 09(92)	8428.400 17(95)	5881.084 58(71)	5879.488 43(81)
B	1438.940 37(15)	1426.181 45(16)	1710.469 92(26)	1695.947 75(24)
C	1284.319 38(17)	1274.149 15(18)	1608.463 64(25)	1595.726 89(23)
D_J	0.000 191 4(28)	0.000 180 1(29)	0.000 452 4(47)	0.000 432 4(50)
D_K	0.005 89(13)	0.005 72(15)	-	−0.000 318(92)
D_{JK}	0.002 116(32)	0.001 983(37)	0.002 371(27)	0.002 329(21)
d_1	−0.000 021 50(50)	−0.000 024 28(67)	−0.000 009 18(84)	−0.000 010 08(60)
d_2	-	-	-	-
χ_{aa}	367.4396(28)	306.9964(29)	222.9665(26)	186.9364(27)
χ_{bb-cc}	126.1196(49)	105.4239(49)	−338.5509(63)	−282.1508(64)
χ_{ab}	291.536(26)	243.609(29)	−14.63(91)	−12.6(1.3)
χ_{ac}	−138.425(69)	−115.329(78)	−386.920(42)	−323.071(53)
χ_{bc}	−72.933(29)	−60.876(34)	−1.03(17)	−0.48(48)
C_{aa}	0.002 71(82)	-	-	-
C_{bb}	0.001 72(22)	0.001 46(22)	-	-
C_{cc}	0.001 38(20)	0.001 21(20)	-	-

Tab. F.2: Overview of the experimentally determined rotational constants for 3-chloro-propane-1,2-diol (0-Cl_1) for the two naturally abundant bromine isotopes. All other isotopes are in their most naturally abundant form. All values are given in MHz.

	0-Cl_1		0-Cl_1'	
	^{35}Cl	^{37}Cl	^{35}Cl	^{37}Cl
A	6167.483 35(42)	6164.233 31(51)	5283.117 33(78)	5258.8173(10)
B	1463.305 64(16)	1426.220 93(20)	1552.635 32(28)	1517.944 29(34)
C	1342.809 29(15)	1311.465 94(19)	1441.042 46(29)	1411.189 60(35)
D_J	0.000 223 8(10)	0.000 221 5(18)	0.000 320 9(30)	0.000 302 1(29)
D_K	0.008 940(35)	0.008 858(52)	0.008 094(23)	0.008 16(10)
D_{JK}	0.000 031 5(62)	0.000 057 6(85)	−0.000 634(26)	−0.000 681(30)
d_1	−0.000 010 84(34)	−0.000 015 16(51)	−0.000 013 7(27)	−0.000 011 9(30)
d_2	-	-	-	-

χ_{aa}	−54.8680(44)	−43.1392(48)	−0.9107(73)	−1.2169(91)
χ_{bb-cc}	−17.6738(86)	−14.0396(92)	55.459(11)	42.892(15)
χ_{ab}	35.89(33)	28.21(19)	−18.78(13)	−16.74(87)
χ_{ac}	−5.8(2.3)	−3.5(1.9)	46.024(46)	35.86(4.10)
χ_{bc}	-	-	21.65(15)	17.43(18)

	0-Cl_1a		0-Cl_1a'	
	^{35}Cl	^{37}Cl	^{35}Cl	^{37}Cl
A	7946.885 21(94)	7941.7761(12)	3756.5317(10)	3748.3973(16)
B	1296.403 11(15)	1264.238 26(15)	2169.526 72(67)	2118.518 51(99)
C	1176.648 38(15)	1150.196 83(15)	1763.711 60(75)	1728.7774(17)
D_J	0.000 091 4(11)	0.000 088 5(12)	0.000 479(10)	0.000 741(43)
D_K	0.011 30(19)	0.011 13(24)	−0.001 41(12)	−0.000 94(20)
D_{JK}	0.001 061(12)	0.001 012(15)	0.002 048(58)	0.001 20(19)
d_1	−0.000 008 49(79)	-	−0.000 102(13)	-
d_2	-	-	-	-
χ_{aa}	−40.6275(38)	−32.1047(48)	4.5884(76)	2.769(17)
χ_{bb-cc}	−16.1856(68)	−12.8187(84)	−32.824(14)	−25.557(23)
χ_{ab}	−40.41(18)	−31.71(18)	−32.9(4.0)	−24(11)
χ_{ac}	23.93(48)	20.16(50)	−23.6(6.8)	-
χ_{bc}	14.39(15)	11.19(19)	−34.8(1.2)	−27.02(93)

	0-Cl_1b		0-Cl_1t	
	^{35}Cl	^{37}Cl	^{35}Cl	^{37}Cl
A	4436.654 95(37)	4433.917 59(52)	3654.891 63(64)	3637.8100(10)
B	1736.850 42(25)	1689.879 44(35)	2028.568 17(31)	1981.766 39(50)
C	1427.141 55(21)	1395.021 61(30)	1558.662 85(24)	1529.015 89(36)
D_J	0.000 545 1(30)	0.000 536 9(39)	0.001 326 0(48)	0.001 251 1(63)
D_K	0.004 881(22)	0.004 905(32)	0.010 058(64)	0.009 20(11)
D_{JK}	0.000 595 7(93)	0.000 618(16)	−0.005 154(19)	−0.004 769(62)
d_1	−0.000 168 2(22)	−0.000 135 8(32)	−0.000 478 7(32)	−0.000 456 5(48)
d_2	−0.000 029 3(10)	−0.000 032 2(19)	−0.000 029 6(22)	−0.000 029 1(35)
χ_{aa}	−35.3033(40)	−28.1243(63)	−12.3322(44)	−10.4866(66)
χ_{bb-cc}	−7.8265(79)	−5.965(12)	45.0052(85)	35.373(13)
χ_{ab}	39.607(19)	30.88(56)	14.5(2.6)	-
χ_{ac}	30.002(76)	22.4(1.0)	49.9(1.1)	40.6(2.3)

χ_{bc}	$-17.26(31)$	$-14.38(56)$	$-13.9(1.1)$	-

Tab. F.3: Overview of the experimentally determined rotational constants for 3-bromo-propane-1,2-diol (0-Br_1) for the two naturally abundant bromine isotopes. All other isotopes are in their most naturally abundant form. All values are given in MHz.

	0-Br_1		0-Br_1'	
	^{79}Br	^{81}Br	^{79}Br	^{81}Br
A	6148.144 49(51)	6147.499 60(43)	4861.6639(14)	4856.9400(16)
B	959.192 62(12)	950.041 34(10)	1061.745 70(18)	1052.343 90(22)
C	905.980 68(12)	897.808 742(91)	1009.354 52(18)	1000.810 07(22)
D_J	0.000 099 2(11)	0.000 098 05(83)	0.000 170 5(14)	0.000 142 5(27)
D_K	0.009 458(70)	0.009 563(74)	-	-
D_{JK}	$-0.000\,028\,5(96)$	$-0.000\,037\,3(98)$	$-0.000\,755(44)$	$-0.000\,891(66)$
d_1	$-0.000\,004\,36(44)$	$-0.000\,003\,70(22)$	-	-
d_2	-	-	-	-
χ_{aa}	424.0536(36)	354.1088(36)	108.6463(54)	91.8287(58)
χ_{bb-cc}	136.8656(60)	114.5271(59)	$-268.447(12)$	$-222.933(12)$
χ_{ab}	$-272.585(11)$	$-227.891(12)$	198.857(46)	166.468(49)
χ_{ac}	30.591(99)	25.40(13)	350.593(34)	292.768(39)
χ_{bc}	$-11.940(55)$	$-9.922(71)$	176.638(14)	147.427(16)
C_{aa}	-	0.002 12(71)	-	-
C_{bb}	0.001 17(24)	0.001 56(22)	-	-
C_{cc}	0.001 45(19)	0.001 34(20)	-	-
	0-Br_1a		0-Br_1b	
	^{79}Br	^{81}Br	^{79}Br	^{81}Br
A	7809.464 62(93)	7808.156 90(87)	4379.3030(10)	4378.8910(12)
B	862.792 70(12)	854.699 18(13)	1110.364 09(19)	1099.250 89(20)
C	809.025 33(13)	801.917 89(13)	973.392 13(19)	964.824 17(21)
D_J	0.000 051 06(69)	0.000 045 89(84)	0.000 244 1(12)	0.000 234 9(22)
D_K	0.013 68(18)	0.013 79(17)	0.004 639(68)	0.004 441(69)
D_{JK}	0.000 432(12)	0.000 403(12)	0.000 489(31)	0.000 510(36)
d_1	$-0.000\,002\,11(52)$	$-0.000\,002\,06(50)$	$-0.000\,049\,81(92)$	$-0.000\,041\,4(13)$
d_2	$-0.000\,001\,90(46)$	$-0.000\,001\,66(47)$	-	-

χ_{aa}	340.7550(38)	284.8205(36)	327.0627(44)	273.5763(46)
χ_{bb-cc}	124.2535(70)	103.9347(67)	33.5196(86)	27.7881(86)
χ_{ab}	−304.228(20)	−254.181(24)	−279.130(57)	−232.993(63)
χ_{ac}	−175.611(11)	−146.505(21)	224.373(85)	187.444(99)
χ_{bc}	96.4629(98)	80.468(11)	−108.646(38)	−90.589(44)
C_{aa}	0.002 57(88)	0.002 85(78)	-	-
C_{bb}	0.000 63(29)	0.001 57(27)	0.001 38(39)	0.001 86(39)
C_{cc}	0.000 95(29)	0.001 17(27)	0.001 80(43)	0.001 77(42)

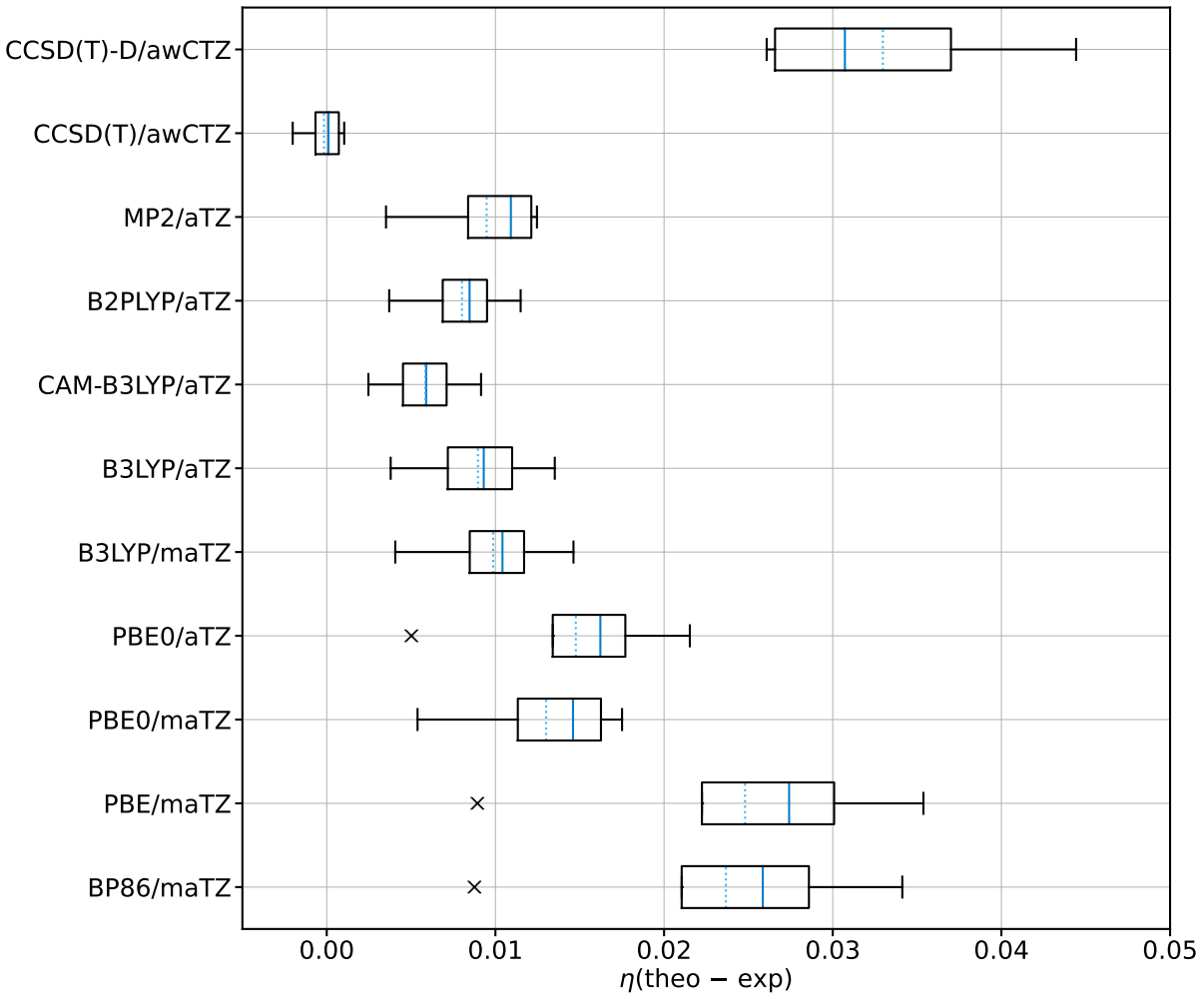

Fig. F.1: Box-plot comparing the experimental and predicted asymmetry parameter of 3-bromopropane-1,2-diol at different levels of theory.

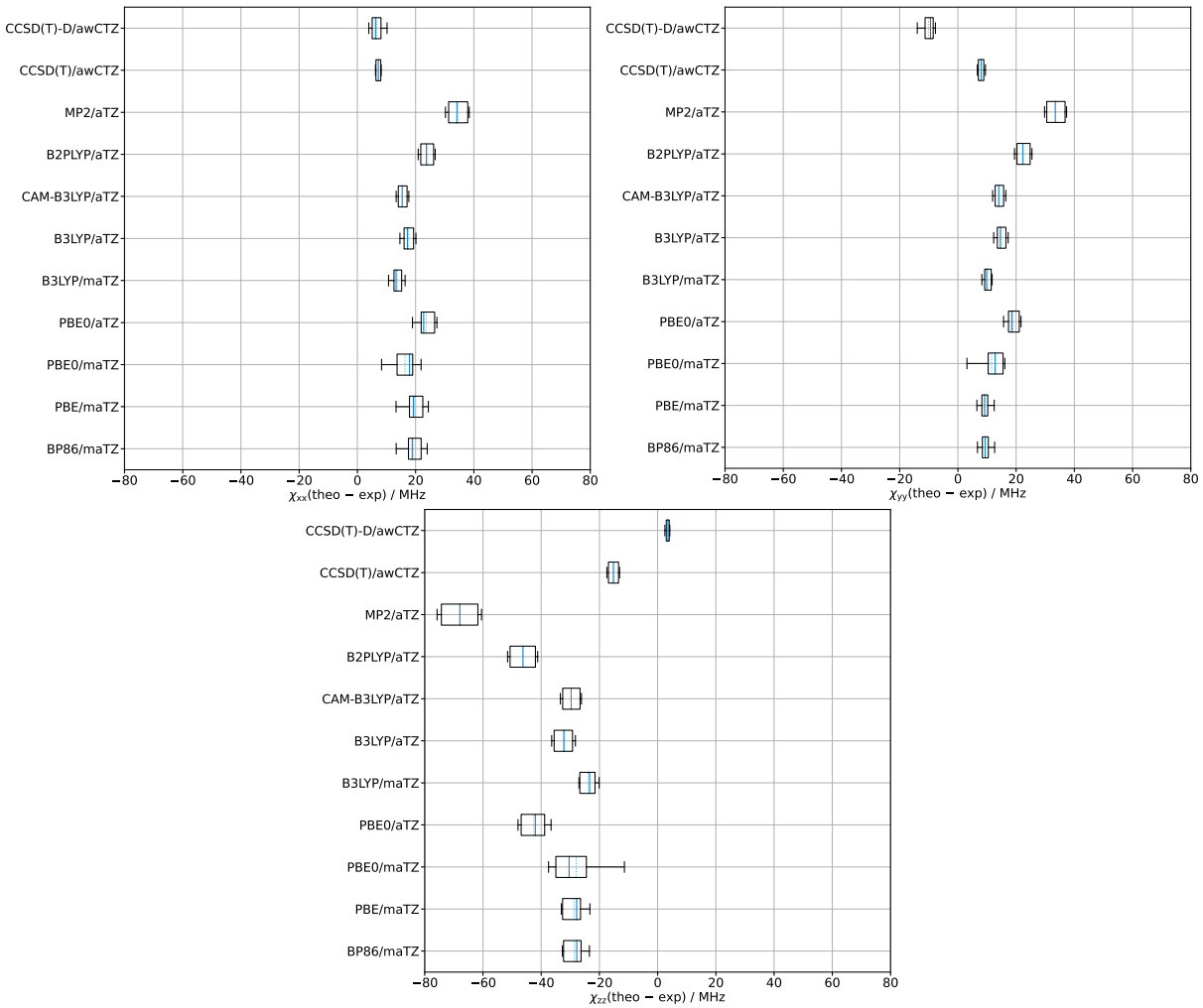

Fig. F.2: Box-plot comparing the experimental and predicted χ_{xx}, χ_{yy} and χ_{zz} of 3-bromo-propane-1,2-diol at different levels of theory. As can be seen, CCSD(T) does not provide the best description of all components individually but yields the best results for η (see Fig. F.1).

G Example inputs

G.1 ORCA

Tab. G.1: Example inputs for the ORCA 4.2.1 calculations. Numerical frequency calculations are needed to compute the Raman activities. For BP86 and PBE the RI-J approximation was used for the analytical frequency calculations. The %eprnmr block follows after the geomtry input. Only the method block is shown.

calculation	input
optimisation + analytical frequencies	`!B3LYP D3BJ abc UseSym ma-def2-TZVP TightOpt TightSCF Freq Grid5 NoFinalGrid Mass2016` `%method SymThresh 5.0e-2 end`

optimisation + numerical frequencies	`!B3LYP D3BJ abc UseSym RIJCOSX def2/J ma-def2-TZVP TightOpt TightSCF NumFreq Grid5 NoFinalGrid GridX4 Mass2016`
	`%method SymThresh 5.0e-2 end`
	`%elprop Polar 1 end`

nudged-elastic band scan	`!NEB-CI B3LYP D3BJ abc ma-def2-TZVP TightSCF Grid5 NoFinalGrid Mass2016`
	`%neb`
	`NEB_End_XYZFile "XXXX.xyz"`
	`SpringType DOF`
	`PerpSpring cosTan`
	`Tol_MaxF_CI 2.e-3`
	`Tol_RMSF_CI 1.e-3`
	`Tol_Scale 10.0`
	`Local true`
	`Nimages 12`
	`end`

transition state optimisation	`!B3LYP D3BJ abc ma-def2-TZVP SlowConv OptTS TightSCF Grid5NoFinalGrid Freq Mass2016`
	`%geom`
	`Calc_Hess true`
	`Recalc_Hess 3 end`

electric field gradient	`!CCSD(T) aug-cc-pwCVTZ NoFrozenCore NoRI TightSCF Grid7 Mass2016`
	`%eprnmr`
	`nuclei = all Br fgrad`
	`end`

electric field gradient + DKH2	`!CCSD(T) DKH2 aug-cc-pwCVTZ NoFrozenCore NoRI TightSCF Grid7 Mass2016`
	`%rel`
	`FiniteNuc true`
	`picturechange 2`
	`end`
	`%eprnmr`
	`nuclei = all Br {fgrad}`
	`end`

Tab. G.2: Example inputs for the ORCA 5.0.3 calculations at the B3LYP level of computation. Numerical frequency calculations are needed to compute the Raman activities. RI-JCOSX is used by default. Only the method block is shown.

calculation	input

optimisation + analytical frequencies	`!B3LYP D3BJ abc ma-def2-TZVP SlowConv VeryTightOpt VeryTightSCF Freq DefGrid3 Mass2016`
	`%geom`
	`MaxIter 500`
	`ENFORCESTRICTCONVERGENCE true`
	`end`

optimisation + numerical frequencies	`!B3LYP D3BJ abc ma-def2-TZVP SlowConv VeryTightOpt VeryTightSCF NumFreq DefGrid3 Mass2016`
	`%geom`
	`MaxIter 500`
	`ENFORCESTRICTCONVERGENCE true`

```
end
%elprop Polar 1 end
```

G.2 Gaussian

Tab. G.3: Example inputs for the Gaussian 16 (Rev. A.03) calculations at the B3LYP level of computation. The `Print` and `Resonances` settings follow one line after the geometry input. Only the method block is shown.

calculation	input

optimisation DFT + VPT2	`# B3LYP aug-cc-pVTZ Int=SuperFine output=pickett`
	`# Opt=VeryTight empiricaldispersion=gd3bj`
	`# Freq=(anharmonic,ReadAnharm)`
	`Print=(NMOrder=AscNoIrrep)`
	`Resonances=No11Res`

optimisation WFT + VPT2	`# MP2 aug-cc-pVTZ output=pickett`
	`# Opt=VeryTight`
	`# Freq=(anharmonic,ReadAnharm)`
	`Print=(NMOrder=AscNoIrrep)`
	`Resonances=No11Res`

G.3 Molpro

Tab. G.4: Example input for the MOLPRO 2020.2 calculations at CCSD(T) level with specialised option for the use of the VDZ-PP-F12 basis set. For CI th definitions simplify to `basis=vdz-f12` with all other auxiliary basis set definitions becoming obsolete. Only the method block is shown.

```
basis={default=vdz-f12;
br=VDZ-PP-F12
set,df
default=AUG-CC-PVDZ/mp2fit;
br=VDZ-PP-F12/mp2fit
set,jk
```

```
default=AUG-CC-PVDZ/jkfit;
br=def2-QZVPP/jkfit
set,ri
default=vdz-f12/optri;
br=VDZ-PP-F12/optri}
gthresh,OPTSTEP=6.d-5,OPTGRAD=1.d-6,ENERGY=1.d-10,ZERO=1.d-16
orient,NOORIENT
symmetry
MASS,ISO
geomtyp=xyz
angstrom
geometry=GEOM_START.xyz
explicit,ri_basis=ri,df_basis=dfmp,df_basis_exch=jk
{hf,accu,16}
{df-ccsd(t)-f12a,ansatz=3*C(FIX,HY1),cabs=0,cabs_singles=0,
ri_basis=ri,df_basis=df,df_basis_exch=jk}
{OPTG,GAUSSIAN,GRMS=1.d-5,SRMS=1.d-5}
put,xyz,GEOM.xyz
{frequencies
PRINT,HESSIAN,LOW}
```

Tab. G.5: Example inputs for the MOLPRO 2021.2 calculations at the CCSD(T) level of theory, with specialised options for the use of the VDZ-PP-F12 basis set. For CI th definitions simplify to `basis=vdz-f12` with all other auxiliary basis set definitions becoming obsolete. Only the method block is shown.

calculation	input

SCS-LMP2 optimisation + numerical frequencies	`basis=aug-cc-pVTZ,h=cc-pVTZ`
	`nosym`
	`MASS,ISO`
	`set,geomtyp=xyz`
	`geometry=GEOM_START.xyz`
	`{optg,gaussian,gradient=1.5E-5,grms=1E-5,`
	`step=6E-5,srms=4E-5,energy=1E-8,`
	`procedure=runmp2}`
	`put,xyz,GEOM.xyz`
	`runmp2={df-hf;accu,16;df-lmp2,scsgrd=1,`

	npasel=0.03,cpldel=2} frequencies,symm=no
LCCSD(T0) optimisation + numerical frequencies	basis=aug-cc-pVTZ,h=cc-pVTZ nosym basis={default=vdz-f12; {gthresh,OPTSTEP=6.d-5,OPTGRAD=1.d-6, ENERGY=1.d-10,ZERO=1.d-16} orient,NOORIENT symmetry,nosym MASS,ISO geomtyp=xyz angstrom geometry=GEOM_START.xyz {df-hf,accu,16} {df-lccsd(t)-f12a,SCALE_TRIP=1,ri_basis=optri local,loc_method=pipek,npasel=0.03,interact=1 pipek,delete=2} {OPTG,GAUSSIAN,GRMS=1.d-5,SRMS=1.d-5} put,xyz,GEOM.xyz {frequencies PRINT,HESSIAN,LOW}

H Spectral directory

In the following T_S is the saturator temperature, T_N the nozzle temperature, d_N the distance of the laser from the nozzle, N the number of averaged exposures, t_{exp} the length of each exposure, p_S the stagnation pressure, Ar in He the fraction of argon in helium and ν the frequency range if applicable. The following abbreviations were used for the different compounds: 0-0 (ethane-1,2-diol), 0-M (propane-1,2-diol), 0-F (3,3,3-trifluoro-propane-1,2-diol), 0-V (but-3-ene-1,2-diol), 0-Ph (1-phenyl-ethane-1,2-diol), 0-Cl_1 (3-chloro-propane-1,2-diol), 0-Br_1 (3-bromo-propane-1,2-diol), 0-MM (2-methyl-propane-1,2-diol), rM-M (*rac*-butane-2,3-diol), M-MM (2-methyl-butane-2,3-diol), MM-MM (pinacol), t4-4 (*trans*-cyclobutane-1,2-diol), t5-5 (*trans*-cyclopentane-1,2-diol), t6-6 (*trans*-cyclohexane-1,2-diol), c6-6 (*cis*-cyclohexane-1,2-diol (c6-6), t7-7 (*trans*-cycloheptane-1,2-diol), 1-phenyl-*cis*-cyclohexane-1,2-diol (c6-6Ph), CP-MM (1-(1-hydroxy-1-methylethyl)-cyclopentanol), CP-CP ([1,1'-bicylopentyl]-1,1'-diol), (tBu)$_3$COH (tri-*tert*-butyl-methanol), 1-Cl (1-chloropropan-2-ol), 2-Cl (2-chloropropan-1-ol), 1-Br (1-bromopropan-2-ol) and 2-Br (2-bromopropan-1-ol).

Tab. H.1: Overview of the experimental conditions for the Raman spectra discussed in the monomer chapter (see section 3.1 (page 29)) of this work. The raw spectra have been made available in Ref. [173] and [174].

compound	T_S / K	T_N / K	d_N / mm	$N \times t_{exp}$ / min	p_S / bar	Ar in He / %
0-0	315	325	2.0	10 × 10	1.0	0
0-M	315	325	1.5	9 × 10	1.4	0
	315	325	1.5	10 × 10	1.4	6
	315	325	1.5	10 × 10	1.4	14
0-F	330	340	1.0	8 × 4	0.35	0
0-V	325	335	1.5	21 × 4	1.4	0
0-Ph	355	375	1.0	9 × 4	0.35	0
	355	375	1.0	11 × 4	0.35	15

	355	375	1.0	14 × 4	0.35	27
0-Cl_1	335	365	1.0	15 × 4	0.4	0
0-Br_1	345	365	1.0	10 × 4	0.35	0
0-MM	315	325	1.25	12 × 4	1.0	0
rM-M	315	325	1.0	12 × 4	0.8	0
M-MM	315	325	0.75	5 × 3	0.35	0
MM-MM	300	300	1.5	12 × 12	1.2	0
t4-4	325	345	0.5	17 × 3	0.35	0
t5-5	350	360	1.5	15 × 4	1.4	0
t6-6	375	395	1.25	8 × 4	1.4	0
	375	395	1.25	10 × 4	1.4	2.5
	375	395	1.25	17 × 4	1.4	10
c6-6	355	370	1.25	7 × 4	1.4	0
	355	370	2.0	10 × 4	1.4	0
c6-6Ph	395	425	1.0	18 × 4	0.4	0
t7-7	355	375	1.5	12 × 4	1.4	0
CP-MM	325	345	1.0	7 × 4	0.35	0
CP-CP	395	415	1.0	8 × 4	0.35	0
$(t\mathrm{Bu})_3\mathrm{COH}$	355	425	1.0	4 × 4	0.35	0
	335	355	1.25	8 × 4	1.4	10
1-Cl	275	300	1.0	24 × 4	0.4	0
2-Cl	275	300	1.0	18 × 4	0.4	0
1-Br	285	300	1.0	10 × 4	0.6	0
2-Br	285	300	1.0	8 × 4	0.6	0

Tab. H.2: Overview of the experimental conditions for the microwave spectra discussed in the monomer chapter (see section 3.2 (page 108)) of this work. For the microwave setups the nozzle acts as the saturator. Hence, only T_N is given. Here, N refers to the amount of averaged free induction decays (FIDs). All spectra have been recorded in pure Ne.

compound	ν / GHz	T_N / K	N / 10^6	p_S / bar
0-Cl_1	2 – 8	375	5.4	2.2
	8 – 13	375	0.8	2.3
	13 – 15.5	375	3.0	2.3
	18 – 26	375	4.4	2.0
0-Br_1	2 – 8	375	3.3	2.2
	18 – 26	395	0.4	2.0
1-Br	2 – 8	325	4.7	2.4
2-Br	2 – 8	300	4.3	2.4

Tab. H.3: Overview of the experimental conditions for the Raman spectra discussed in the dimer chapter (see section 4 (page 129)) of this work. Additional information about the chirality of the system is provided. The raw spectra have been made available in Ref. [243].

compound	chirality	T_S / K	T_N / K	d_N / mm	$N \times t_{exp}$ / min	p_S / bar
0-0	transient	315	325	2.0	10 × 10	1.0
0-M	racemic	315	325	1.5	9 × 10	1.4
	(*S*)	315	325	1.5	10 × 10	1.4
0-V	racemic	325	345	1.5	21 × 4	1.4
0-MM	transient	315	325	1.25	12 × 4	1.0
rM-M	racemic	315	325	1.0	12 × 4	0.8
rM-M	(*S*,*S*)	315	325	1.0	10 × 4	0.8
MM-MM	transient	300	300	1.5	12 × 12	1.2
t5-5	racemic	375	395	1.5	7 × 4	1.4
t6-6	racemic	355	375	1.25	7 × 4	1.4
	(*S*,*S*)	355	375	1.25	10 × 4	1.4
t7-7	racemic	355	375	1.5	12 × 4	1.4

I Curriculum vitae and publications

I.1 Curriculum vitae

Beppo Hartwig	Bamberg, Germany
Nationality	German

Education

2019 – 2022	**Ph.D. candidate, Georg-August-Universität Göttingen, Germany**
2017 – 2018	**Master of Science in Chemistry, Georg-August-Universität Göttingen, Germany** master thesis - "Raman Spectroscopy concerning the Conformation and Aggregation of Cyclohexane Derivatives"
2013 – 2017	**Bachelor of Science in Chemistry, Georg-August-Universität Göttingen, Germany** bachelor thesis - "Isomerism and aggregation of a realistic peptide bond model"
2012	**Allgemeine Hochschulreife (Abitur)**
2004 – 2012	**Advanced Secondary Education, Johann-Georg-Lingemann-Gymnasium, Heilbad Heiligenstadt, Germany**

Research Stay

Aug 2020 – Sep 2020	**Deutsches Elektronen-Synchrotron Hamburg, Germany** microwave measurements of diols in the group of Prof. Dr. Melanie Schnell

I.2 Publications

I. T. Forsting, H.C. Gottschalk, B. Hartwig, Michel Mons and M. A. Suhm, "Correcting the record: the dimers and trimers of *trans*-*N*-methylacetamide", *Phys. Chem. Chem. Phys.* **2017**, *19*, 10727–10737.

II. B. Hartwig, Manuel Lange, Robert Medel, Anne Zehnacker and M. A. Suhm, "The reduced cohesion of homoconfigurational 1,2-diols", *Phys. Chem. Chem. Phys.* **2020**, *22*,1122–1136.

III. X. Aniban‡, B. Hartwig‡, Axel Wuttke and R. A. Mata, "Dispersion forces in chirality recognition – a density functional and wave function theory study of diols", *Phys. Chem. Chem. Phys.* **2021**, *23*, 12093–12104.

IV. B. Hartwig and M. A. Suhm, "Subtle hydrogen bonds: benchmarking with OH stretching fundamentals of vicinal diols in the gas phase", *Phys. Chem. Chem. Phys.* **2021**, *23*, 21623–21640.

‡These authors contributed equally to this work.